THE LOCATION OF LOCAL EARTHQUAKES IN A ZONE OF ANISOTROPY

by

Mark A. Doyle

(B.Sc., Univ. of Southampton)

Thesis submitted for degree of Ph.D

University of Edinburgh, Department of Geophysics

November 1981

I hereby declare that this thesis was composed by myself and that the work described in it is entirely my own unless explicitly stated otherwise.

ABSTRACT

Analysis of three-component seismograms of events detected on a section of the North Anatolian Fault in north-west Turkey reveals clear and consistent examples of shear-wave splitting. Shear-wave splitting is strongly indicative of seismic-wave propagation through anisotropic media. This is supported by the joint-inversion of suites of arrival-times for both hypocentral locations and the parameters that describe seismic-wave propagation through an anisotropic half-space. This analysis indicates that the principal axes in the anisotropic structure are close to the stress axes of a composite fault-plane solution, with a low velocity direction close to the direction of least compression. This is consistent with a system of pre-existing cracks being preferentially aligned by the action of a deviatoric stress system. If such dilatancy-anisotropy is typical of the structure in most seismic regions, it is likely to have important consequences for the interpretation of any velocity dependent data, and of any precusory variations.

Failure to take account of the anisotropic variations in an earthquake location procedure will introduce systematic errors to the hypocentral locations in such a region of up to 20% of the average path length through the structure. Temporal variations in the degree and orientation of the variations may result in illusory migrations of earthquake foci. The amplitude of such mislocations may be sufficient to invalidate any conclusions based on the earthquake locations. A simple modification to the location procedure, that incorporates the anisotropic variations, allows the accurate determination of hypocentres in such regions providing that P- and shear-wave arrival-times are employed.

ACKNOWLEDGMENTS

The work in this Thesis was undertaken in the Global Seismology Unit of the Institute of Geological Sciences, under the supervision of Dr. Stuart Crampin, and was supported by a grant from the Natural Environment Research Council. I would like to express my gratitude to Stuart whose original ideas and hard work made this thesis possible in the first place. Stuart's constant encouragement, criticism, faith, enthusiasm and his constant availability and willingness to discuss my problems played a significant part in the conception and the eventual completion of this Thesis.

Bob McGonigle provided significant assistance in writing various computer programs. His patience and ability to provide straightforward and understandable answers to, what appeared to me as, insurmountable problems, helped to maintain my enthusiasm during those times when I regarded computers as one of mankind's lesser achievments. The numerous discussions over the even more numerous beers, and Bob's friendship were of great value to me. [redacted]

Without Russ Evans this thesis would not have been possible. Russ organised, made by far the most important contribution to, and was largely responsible for the success of the TDP projects. His widespread knowledge made him an important source of information for me, and his time, patience and advice were very much appreciated. Russ also supplied the shear-wave delays and the TDP2 arrival-times that I used in Chapter 7.

I was very lucky at IGS to be surrounded by experts in most aspects of seismological research, and I would particularly like to thank Graham Neilson, Charlie Fyfe and Paul Burton for valuable advice and assistance. In addition, I would like to thank the staff of Kandilli Observatory, and in particular, Balamir Üçer, Alastair Miller and their families for making our stay in Turkey both enjoyable and profitable. I would also like to

thank Bruce Hobbs for being reasonable over my computing bills.

Lastly, but certainly not least, I would like to thank my wife Jayne for her patience, and for putting up with my thesis over the past year.

CONTENTS

CHAPTER 1

INTRODUCTION

One of the major goals in modern seismology is an understanding of the process, or processes, that culminate in a major earthquake. Several models of earthquake preparation have been proposed during the last decade to explain phenomena observed prior to major earthquakes, the most notable seismological phenomenon being the reduction and return to normal of the velocity ratio Vp/Vs (Semonov, 1969; Aggarwal, Sykes, Simpson & Richards 1975; Sobolev & Slavina 1977; Robinson, Wesson & Ellsworth 1974; Whitcomb, Garmany & Anderson 1973 - but see Lindh, Lockner & Lee, 1978, for an alternative explanation). These models (Nur 1972; Scholz, Sykes & Aggarwal 1973; Stuart 1974; Nur 1975; Mjachkin, Brace, Sobolev & Dieterich 1975) all involve the concept of dilatancy occuring in the source region. Dilatancy is the anelastic increase in volume of rock subjected to high stress levels and is due to the opening of cracks in the stressed rock (Brace 1978). Such cracks will, by necessity, be preferentially aligned by the action of any deviatoric stress system, and would be effectively anisotropic to seismic waves with wavelengths greater than the crack dimensions (Crampin 1978).

Dilatancy-anisotropy has been verified in laboratory experiments by Nur & Simmons (1969), Hadley (1975), and Scholz & Koczynski (1979), and by field observations of shear-wave splitting, which is strongly indicative of anisotropy (Crampin 1978). These field observations have been made in areas of possible dilatancy-anisotropy by Yegorkina, Rakitov, Garetovsky & Yegorova (1977); Crampin, Evans, Üçer, Doyle, Davis, Yegorkina & Miller (1980); and possibly by Gupta (1973a), - but see Crampin, Evans, Doyle & Davis (1981), and imply dilatancy with aligned cracks over a large volume surrounding the earthquake source. Such extensive dilatancy-anisotropy is

unlikely to be caused by high stress levels but must be a comparatively low stress phenomenon. A possible mechanism is the effect of cyclic loading in the seismic region (Scholz & Koczynski, 1979) such that the onset of dilatancy-anisotropy along an active fault occurs at substantially lower stress levels than those predicted by simple laboratory experiments on intact rock. In addition, the Earth's crust is permeated by a variety of cracks, joints and fractures (Simmons & Richter 1969), and it is expected that the stress required to preferentially open and close these pre-existing cracks would be substantially less than that necessary to open new cracks (Byerlee 1978; Crampin & Evans 1982). On this basis the occasionally observed Vp/Vs anomalies are just the result of fortuitous source/receiver geometry (Crampin 1978). It is quite possible that Vp/Vs anomalies would not be observed with particular station geometries even though substantial dilatancy-anisotropy might exist. This would be the case particularly for ratios measured from a few observations where a scatter in the ratios is most likely to be observed and interpreted in some way other than in terms of dilatancy-anisotropy.

In such a region of dilatancy-anisotropy, three body waves can propagate, (a quasi- compressional, qP, and two quasi-shear waves qS1 and qS2), each with a different velocity and with mutually orthogonal polarisations with respect to the direction of phase propagation. This feature of seismic-wave propagation through anisotropic media gives rise to the phenomenon known as shear-wave splitting, (or shear-wave polarisation anomalies), where at least two shear-waves can be identified arriving separately, and with almost orthogonal polarisations, on suitably processed three-component seismograms. In addition, the velocities of the body-waves can have strong directional variations that cannot be adequately modelled by any isotropic approximation. Therefore, any model that does not

correctly allow for the anisotropic variations may produce misleading results and conclusions.

The first, and possibly the most important, stage in the data analysis from any micro-earthquake survey in a seismically active region, is the determination of the hypocentral locations of events that were detected during the experiment. Accurate hypocentral locations are required for many purposes such as testing for correlation with surficial geological features, as basic data for determining fault-plane solutions for focal mechanism studies, and for monitoring seismicity for earthquake prediction and seismic hazard purposes. The usual location procedure involves minimising travel-time residuals and as a consequence is very sensitive to the choice of velocity model. The accurate location of earthquakes, therefore, requires detailed knowledge of the velocity-structure that exists beneath the monitoring network. This structure is usually defined by parameters such as, amongst many others, layer velocities; depths to, and dip of, refractors; or blocks of differing velocity that can be used to model three-dimensional structural variations. The basic assumption, however, is that within each block or layer, the structure is characterised by homogeneity and isotropy. The assumption of isotropy, in particular, is likely to be invalid in regions of dilatancy-anisotropy.

Clearly, if extensive dilatancy-anisotropy exists in seismic regions, it will be important to be able to identify the form of the anisotropy, and take account of it when using and interpreting any velocity dependent data. This thesis will examine the problem of locating earthquakes in regions of dilatancy-anisotropy, and of quantifying the anisotropic variations by the inversion of suites of earthquake arrival-times. This will be achieved with particular reference to the field study of Crampin et al. (1980), and to a subsequent experiment in the same area.

CHAPTER 2

TWO EXPERIMENTS TO MONITOR DILATANCY-ANISOTROPY

2.1 Introduction

During the summers of 1979 and 1980, two micro-earthquake surveys, TDP1 (Turkish Dilatancy Project) and TDP2 respectively, were conducted a few kilometres south of Izmit, near the Northern Anatolian Fault at the eastern margin of the Marmara Sea in Turkey (Fig.2.1). The networks of three component stations were specifically designed to monitor shear-wave polarisation-anomalies in a region of possible dilatancy-anisotropy, as suggested by theoretical and numerical investigations (Crampin 1978). The area was chosen on the basis of consistent swarm activity during the winter of 1978-9, which was identified during routine epicentral locations at Kandilli Observatory, Istanbul, from analysis of records provided by MARNET - a radio-linked seismic network spanning the Marmara Sea (Üçer, Crampin & Miller, 1982). The author was extensively involved in all stages of the TDP projects and it forms the necessary background to this thesis. This Chapter will describe these two surveys and present preliminary earthquake locations and examples of shear-wave polarisation-anomalies.

2.2 Preliminary analysis of the TDP1 experiment.

2.2.1 Earthquake locations

The TDP1 experiment deployed six three-component stations and one vertical instrument (CA - Fig.2.1). Each station was radio-linked into a base station at SE where it was recorded on analogue magnetic tape. In addition, KLT was a three-component station of MARNET which was radio-linked to Istanbul where the records were made available for the TDP1 experiment. The network was fully operational for a period of six weeks during which several hundred earthquakes were detected within or near the network. Preliminary locations of the better located events are shown in

Figure 2.1. A map showing the locations of the stations of the TDP networks. The heavy dashed line indicates the approximate boundaries of the Northern Anatolian Fault. The inset illustrates the area in relation to Istanbul, the Black Sea, and the Maramara Sea.
△ denotes stations of the TDP1 network.
◇ denotes stations of the TDP2 network.
⊠ denotes stations common to both networks.

Figure 2.2. Preliminary locations by HYP071 of 326 events detected during the TDP1 experiment. All events shown have an RMS error of < 0.1s. The TDP1 stations are marked by a solid triangle.

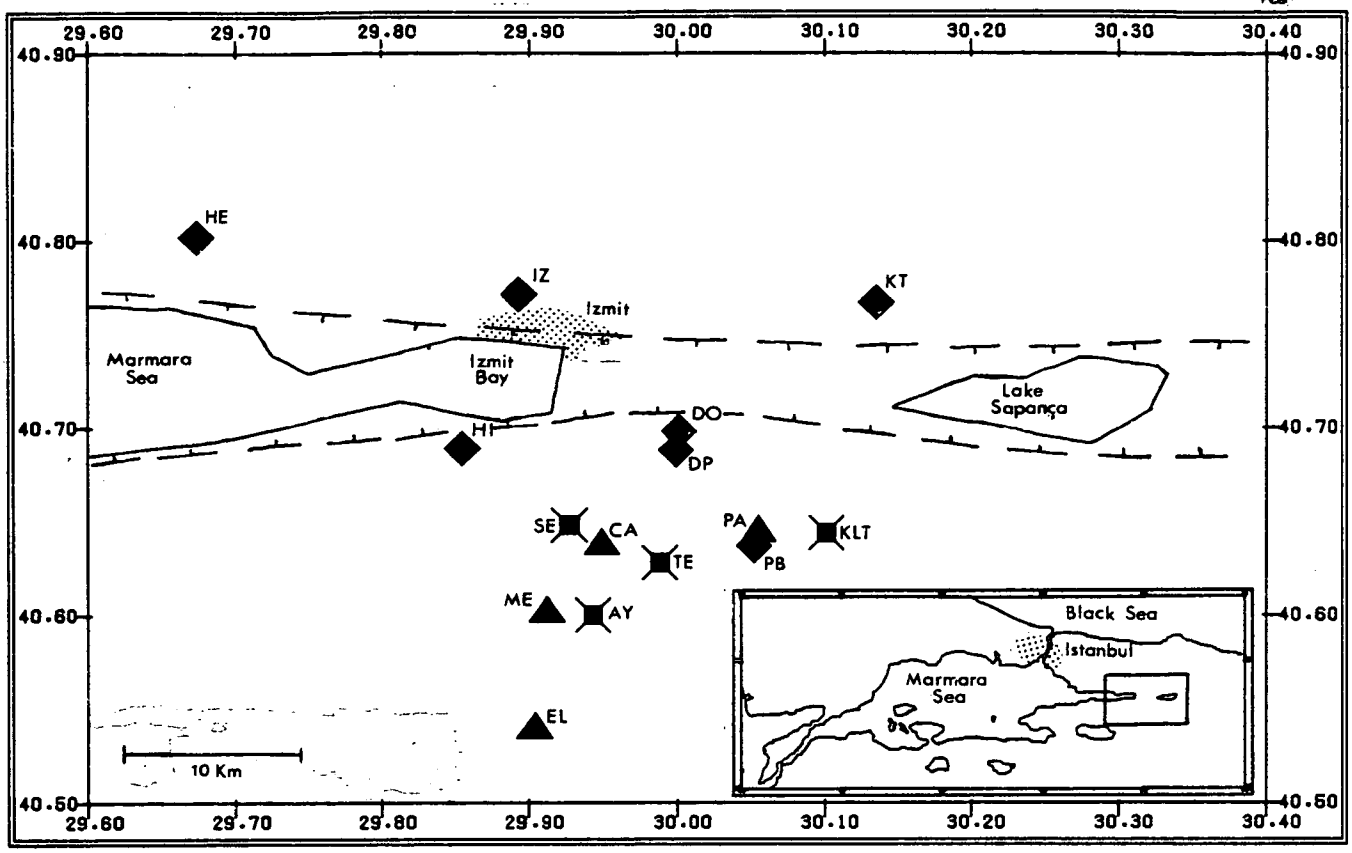
29.60
29.70
29.80
29.90
30.00
30.10
30.20
30.30
30.40
40.90
40.80
40.70
40.60
40.50
HE
IZ
KT
Izmit
Marmara Sea
Izmit Bay
Lake Sapança
HI
DO
DP
SE
CA
TE
PA
PB
KLT
ME
AY
EL
10 Km
Black Sea
Istanbul
Marmara Sea

Figure 2.1

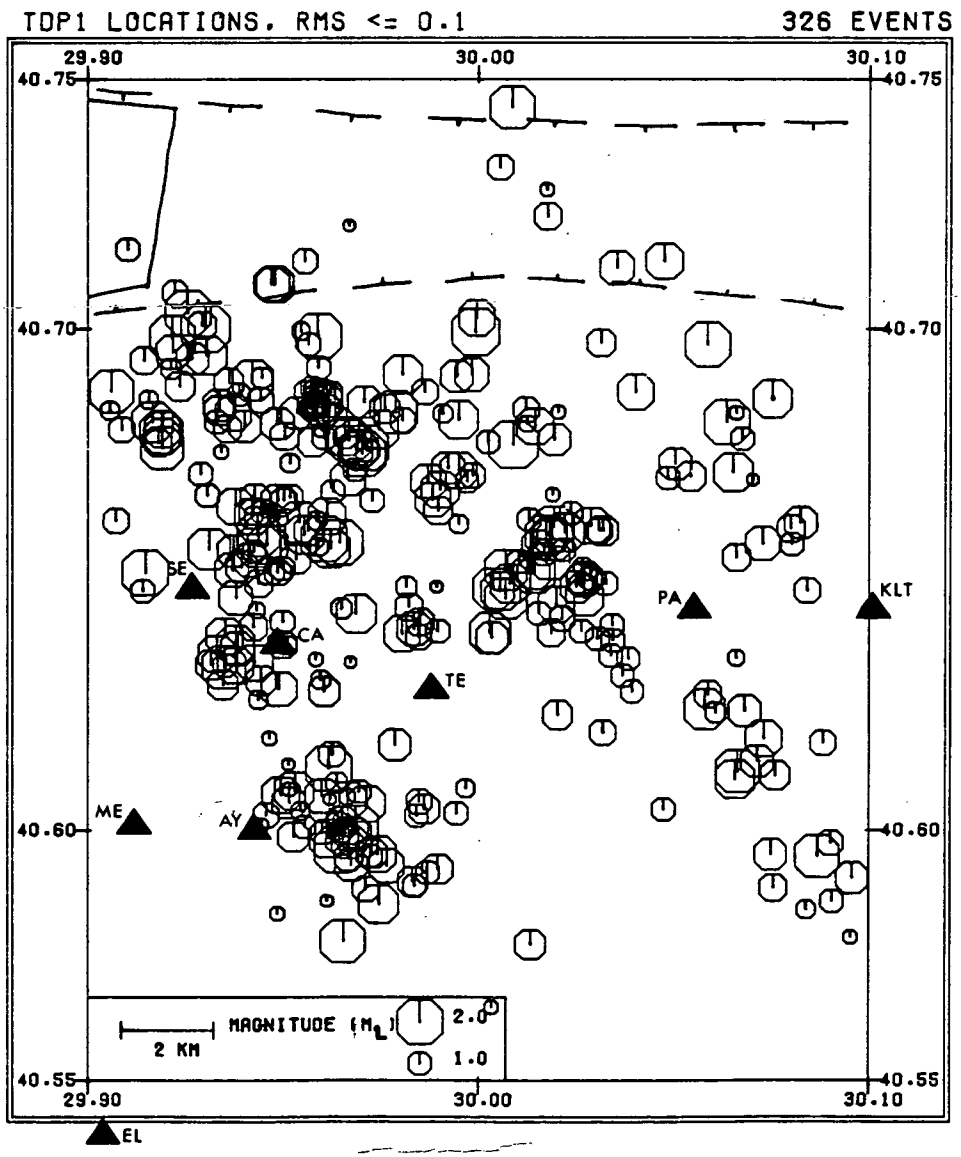
TDP1 LOCATIONS, RMS <= 0.1
326 EVENTS
29.90
30.00
30.10
40.75
40.70
40.60
40.55
SE
CA
TE
PA
KLT
ME
AY
EL
MAGNITUDE (M_L)
2.0
1.0
2 KM

Fig.2.2. These locations were performed by HYPO71 (Lee & Lahr, 1975) using a simple isotropic crustal structure determined using local quarry blasts. This structure is summarised in Table 2.1. Individual station corrections were determined on the basis of the station elevation, the surface layer P-wave velocity and an assumed Vp/Vs ratio of 1.73. P- and S-arrival times used for these locations were picked from analogue, jet-pen records and were read to the nearest 1/20 of a second. The events are located in a depth range of 8km to 15km, and have a magnitude (M_L) in the range 0.8 to 2.5. The RMS of the travel-time residuals are typically equal to 0.07s and the standard epicentral and focal depth errors average approximately 1km.

Table 2.1. The isotropic structure used to determine the preliminary locations of the TDP earthquakes.

	Vp	Vp/Vs	Depth
Surface layer	5.1	1.73	0 - 1 km
Half-space	5.7	1.73	1 - ? km

The pattern of seismicity appears to indicate several NW-SE trends beneath the network. However, these are ill-defined and cannot be taken to indicate any small-scale structural feature. Notice that most of the locations appear to be to the south of the strike of the main fault. This may be due to poor network resolution for events to the north of the network. Cross-sections through the hypocentral locations reveal a marked dip to the north, and not to the south as might be anticipated. However, we shall see in Chapter 7 that this is probably another result of poorly constrained locations for events outside the network.

2.2.2 Observations of shear-wave splitting

The purpose of this experiment was to analyse the shear-waves for evidence of shear-wave splitting that would indicate seismic-wave propagation through a zone of anisotropy. The analogue seismograms from TDP1 display impulsive P- and S-wave arrivals that are very suitable for further

analysis of arrival-time data and, in particular, shear-wave polarisations. Shear-wave splitting (also known as shear-wave polarisation anomalies, shear-wave birefringence and acoustic double refraction) is the phenomenon resulting from two almost orthogonally-polarised shear-waves propagating at a different velocity in most directions through anisotropic media. It can most easily be identified on three-component seismograms as abrupt changes in the direction of shear-wave particle motion when the waveforms are drawn in polarisation-diagrams. These diagrams are projections of the particle motion onto the three orthogonal planes defined by the rotated seismograms.

The analogue records were digitised at 100 samples/sec and were examined for evidence of shear-wave splitting. Approximately 10% of the records show shear-waves arriving at different times on the unrotated horizontal seismograms from events at all azimuths. Fig.2.3 shows an example of this for a ray path from an event located just to the west of the network. Separate shear-waves can be seen on both the unrotated and the rotated horizontal seismograms. The polarisation diagrams clearly show that the first shear-wave has linear particle motion and that the second shear-wave arrives approximately 0.1s later with an almost orthogonal polarisation. The majority however show shear-waves arriving at the same time on both horizontal traces, and display shear-wave splitting only when plotted in polarisation diagrams. Further examples of shear-wave splitting from the TDP1 experiment can be seen in Crampin et al. (1980), a copy of which appears in Appendix E.

2.3 Preliminary analysis of the TDP2 experiment

2.3.1 Earthquake locations

The TDP2 experiment took place during the summer of 1980 in the same area as the TDP1 experiment a year earlier. The purpose of the second experiment was twofold. 1) To identify any changes in the form or degree

Figure 2.3. An example of a three-component seismogram and polarisation-diagrams for an earthquake on 14 September 1979, with epicentre 40.657N, 29.796E, depth 9.81km, and magnitude M_L = 1.9. The seismograms were recorded at station TE at a hypocentral distance of 19.7km and at an azimuth of N100E from the epicentre. The seismograms are, from the top: unrotated horizontals N354E and N84E, vertical, and rotated radial and transverse components. The numbered polarisation-diagrams for shear-wave arrivals are the projections of the particle motion onto the three orthogonal planes for the correspondingly numbered 0.15s time-windows marked above each of the lower seismograms. Directions: U - up; D - down; T - towards the source; A - away from the source; L - left, and R - right in the direction of the station. Each set of three diagrams has been normalised and the relative multiplication factor is marked at the bottom left of each diagram. The heavy arrows on the horizontal projection of the shear-waves mark the first S-wave arrival and the subsequent arrival of phases with a different polarisation. Cross bars are marked on the polarisation-diagrams at every 0.01s to allow the delays between shear-wave arrivals to be estimated.

PMPLOT V4.01 08-JUL-81 31:59:46 A2284 NETWORK: TDP-A TAPE: A19 EVENT: A19/11STATION TEV
START: 14-SEP-79 22: 7:59 MOTION FROM START + 2.19 WINDOW LENGTH 0.15
HYPOCENTRAL DISTANCE 19.70 AZIMUTH (FROM STN TO EPI) -79.7 F1= 0.10 F2=20.00

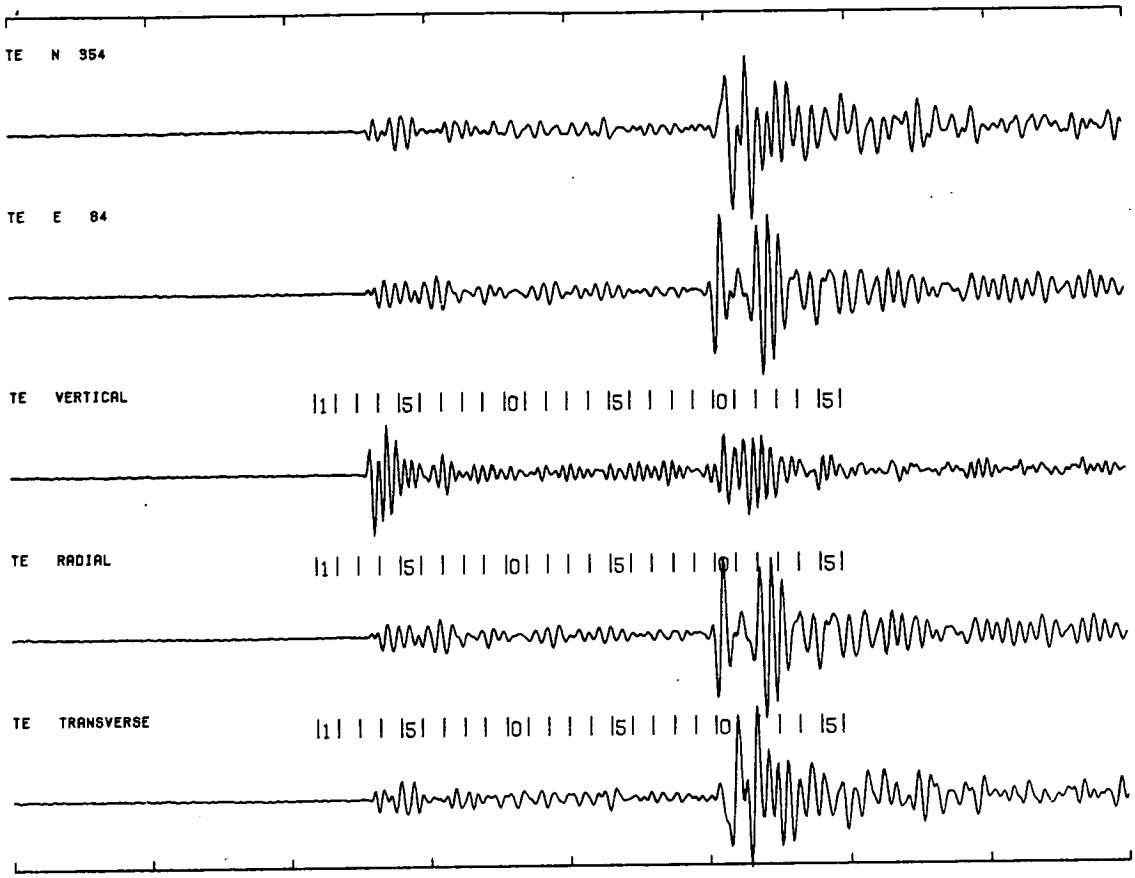

PMPLOT V4.01 08-JUL-81 31:59:46 A2284 NETWORK: TDP-A TAPE: A19 EVENT: A19/11STATION TEV
START: 14-SEP-79 22: 7:59 MOTION FROM START + 2.19 WINDOW LENGTH 0.15
HYPOCENTRAL DISTANCE 19.70 AZIMUTH (FROM STN TO EPI) -79.7 F1= 0.10 F2=20.00

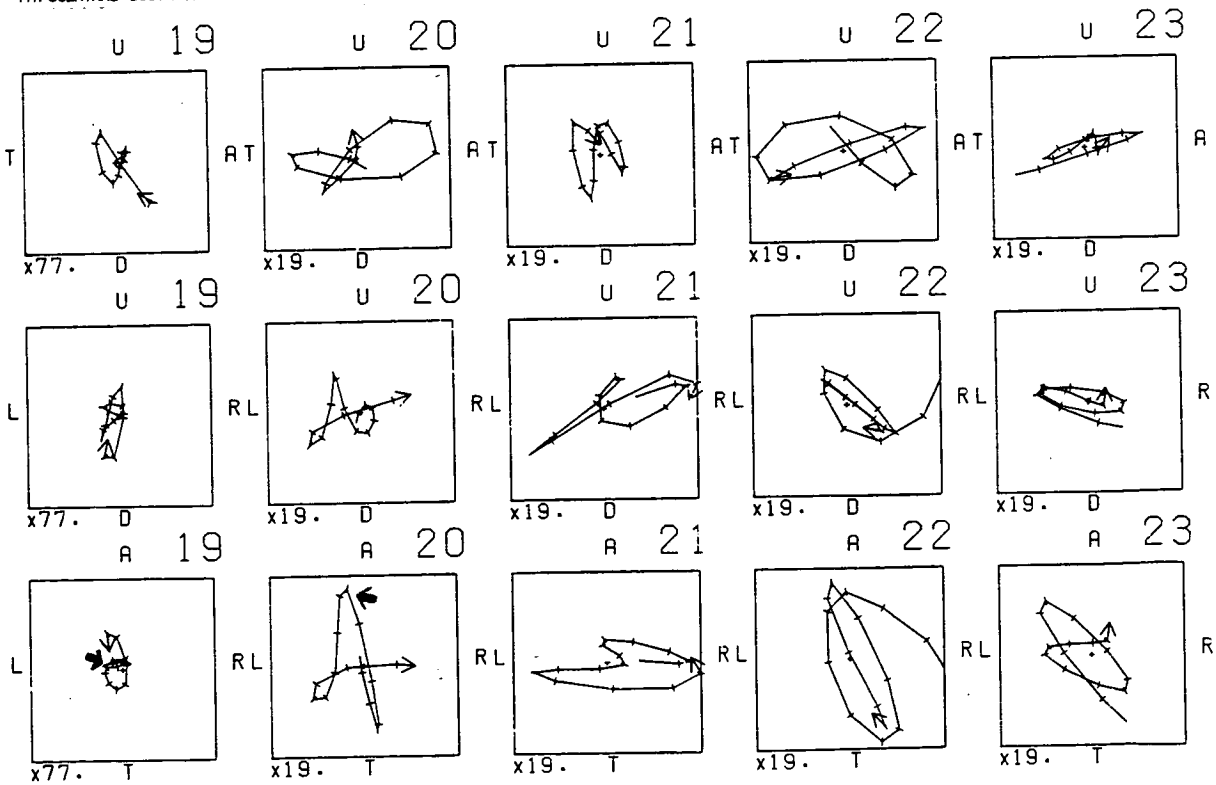

of the dilatancy-anisotropy from the analysis of shear-wave polarisations. Any change would provide a strong indication that the anisotropy beneath the TDP networks is due to stress-induced dilatancy, as this would be expected to vary in response to changes in the level and the orientation of the stress-field in the area. 2) The TDP1 events were located deeper than expected and so the stations only examine a small segment of the focal sphere. An increased network-aperture would examine a much larger segment and dilatancy-anisotropy would be more clearly identified.

Eleven sites were occupied during TDP2 by, at any one time, a maximum of nine three-component stations and one vertical (Fig.2.1), each station being radio-linked to a base station at IZ. Three of the sites, SE, AY, and TE were reoccupied from TDP1, and PB was near the same village as PA (also from TDP1). The MARNET station KLT was in operation during the early stages of the TDP2 experiment, and DP and DO were never occupied simultaneously. The network was fully operational for a period of twelve weeks during which approximately 500 events with magnitudes (M_L) 1.0-3.0 were detected within or near the network. Fig.2.4 shows the preliminary locations of these events. The locations were again performed by HYPO71 using the isotropic crustal model determined during the TDP1 experiment (Table 2.1). This structure can only be a first approximation to the true structure beneath the TDP2 network. The stations of the network lie on both sides of the North Anatolian Fault and it is anticipated that there will be a different velocity structure on either side of the fault, together with a low velocity region within the fault zone, which in this area appears to be a graben structure. Such a structure has been identified on the similar San Andreas Fault in California (Healy & Peake 1975). With this model the majority of these events are located at depths of between 8km and 15km. The absence of earthquakes in the area surrounding the swarm shown in Fig.2.4 may not be real. It is more likely to be an

Figure 2.4. Preliminary locations by HYPO71 of 347 events detected during the TDP2 experiment. All events shown have an RMS error of < 0.1. The TDP2 station are marked by a solid triangle.

Figure 2.5. Preliminary locations of the TDP2 events on the same scale as Fig.2.2.

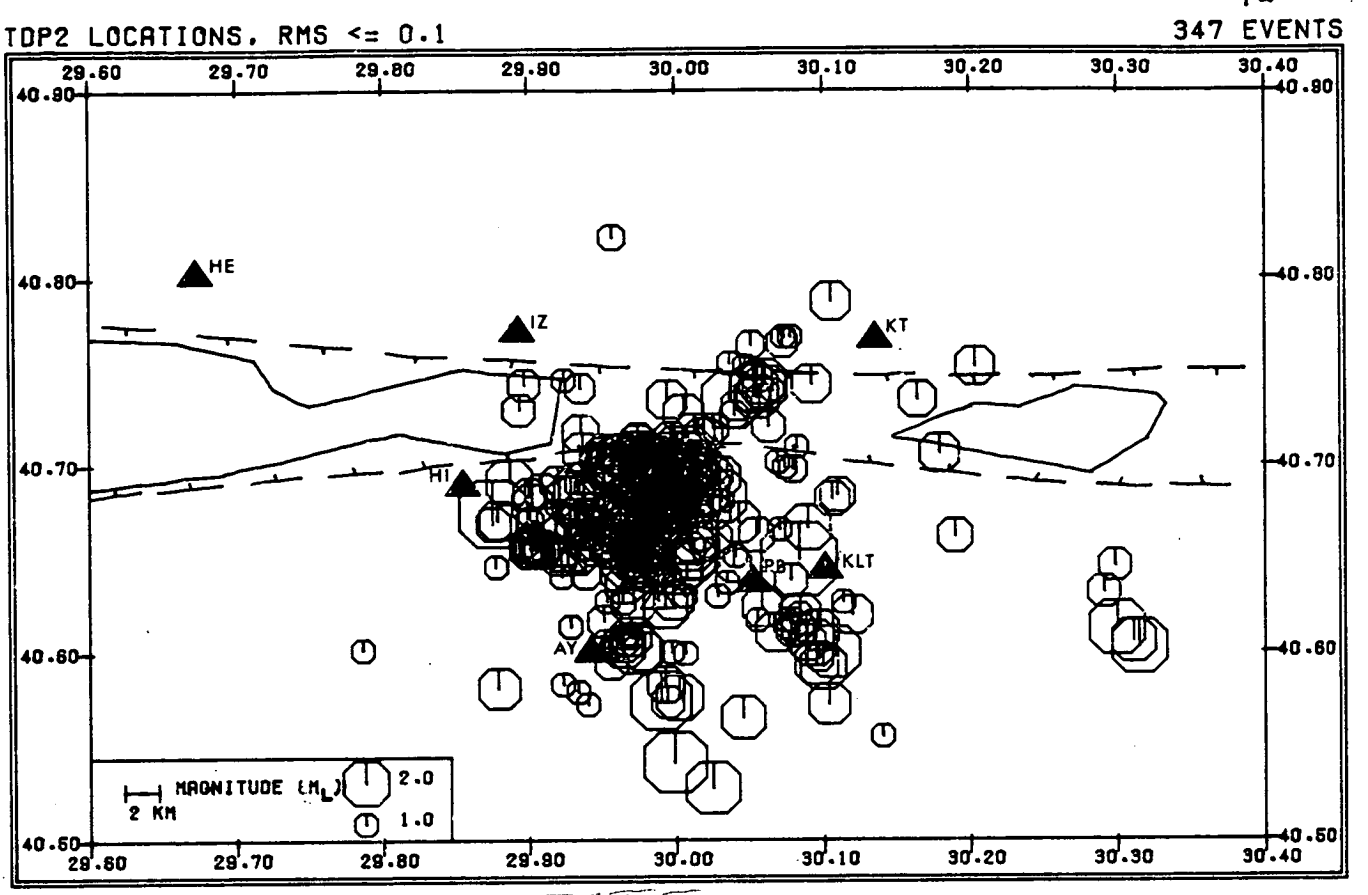

Figure 2.4

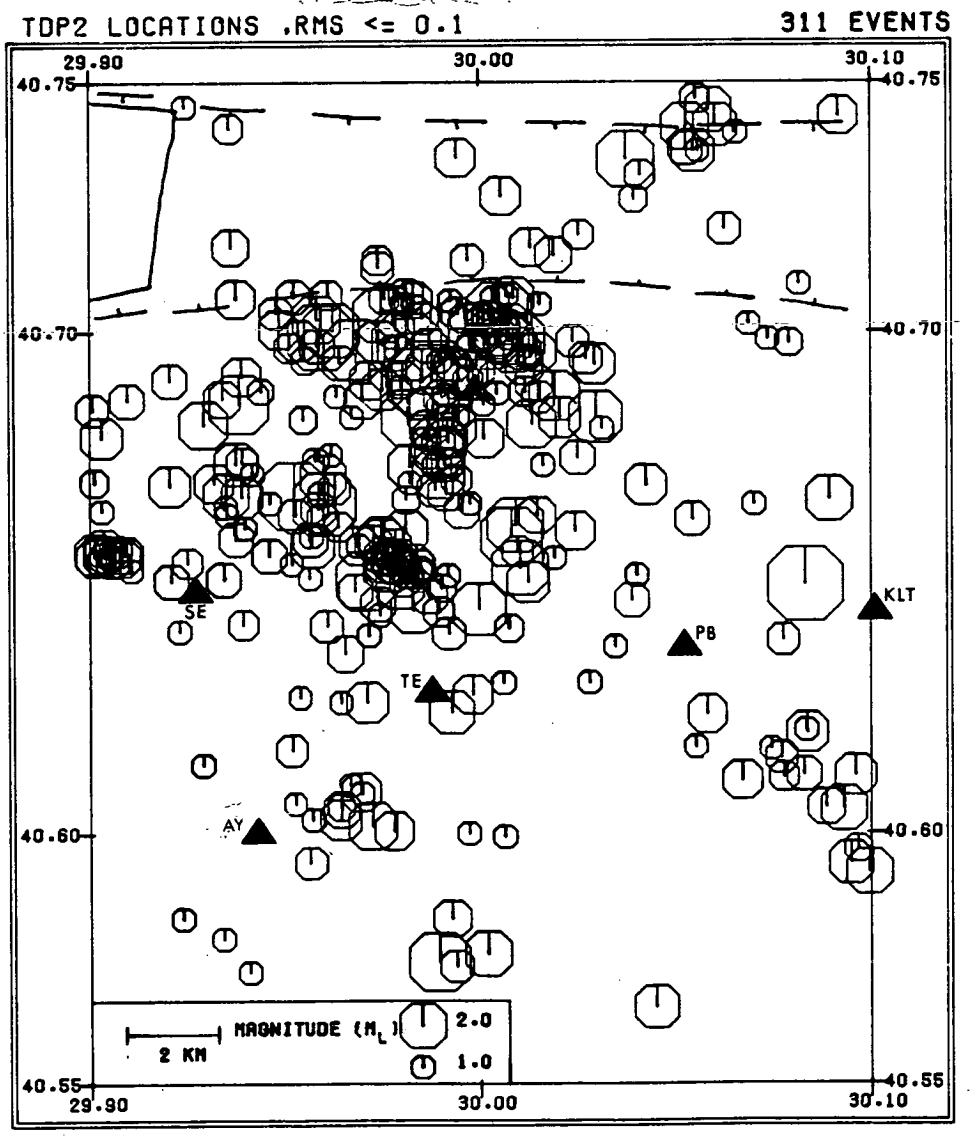

Figure 2.5

effect of poor location accuracy due to reduced network resolution away from the centre of the network. However, as noted in the TDP1 experiment, most events are located to the south of the southern margin of the main fault.

Fig.2.5 shows the epicentres plotted in the same area as in Fig.2.2 for the TDP1 events. The level and spatial extent of the seismic activity is similar in both surveys. However there are some differences that can be explained either as an actual migration of earthquakes or an effect of the altered station distribution. For instance, the apparent decrease in activity in the small cluster directly to the east of AY is because the TDP2 stations were too distant to provide a sufficient number of recorded arrival-times for small events in this area to be located. The apparent increase in activity underneath DO and DP may be result of these stations, and stations to the north of the fault, providing a better constraint on the earthquake locations in this region. This area was outside the TDP1 network and so locations in this area would be poorly constrained. As for the TDP1 events, there is little indication of linear trends in the seismic activity that might be associated with any small-scale structural feature. In addition, cross-sections through the locations do not reveal any dip to the seismicity away from the fault. The hypocentres are located in a horizontal band, approximately 4km in depth, and centred at a depth of 10km.

2.3.2 Fault-plane solutions

Evans, Asudeh & Crampin (1982) have undertaken a study of the focal mechanisms of over 100 of the best recorded events from TDP2. Composite fault plane solutions of first P-wave motion suggest that the dominant mechanism is strike-slip with a small component of normal motion. A typical example is shown in Fig.2.6. The P and T axes are at an azimuth of N112E and N207E, and are inclined above the surface by 29 and 12 degrees

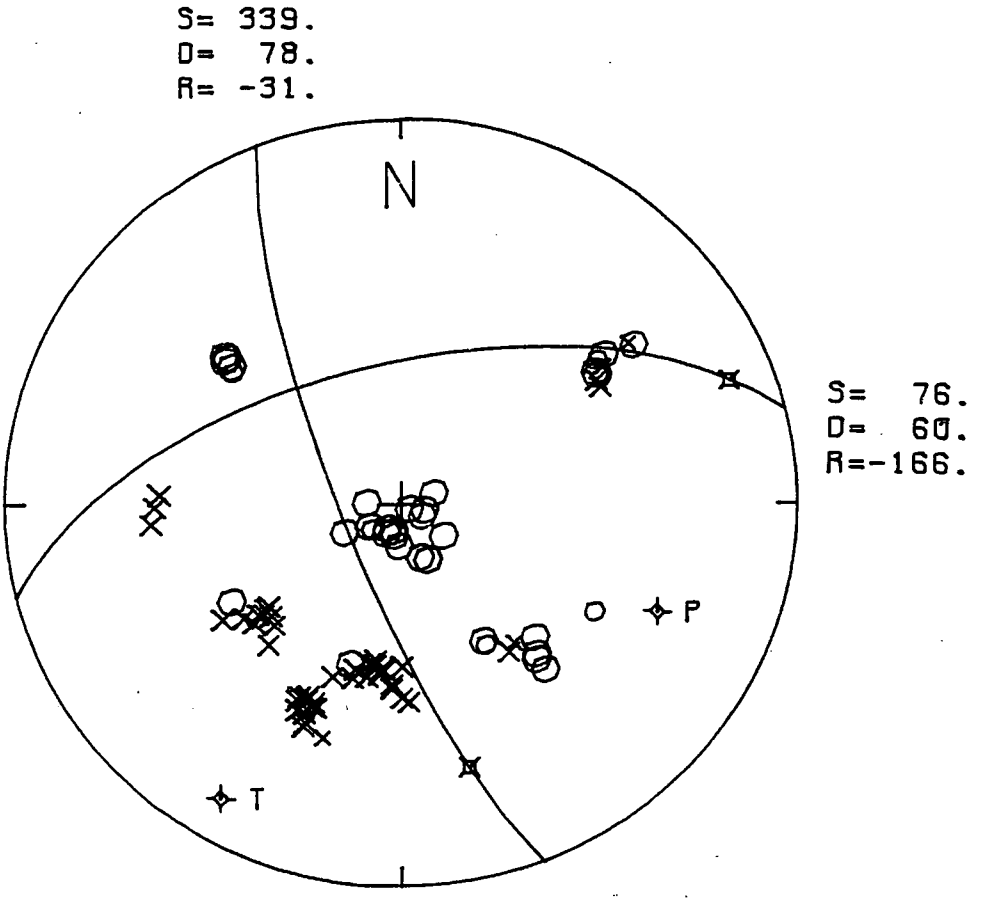

Figure 2.6. A typical example of a fault plane solution of P-wave first motions from events recorded during the TDP2 experiment. The plot is an equal area projection of the upper hemisphere with open circles denoting dilatations and crosses denoting compressions. S, D and R are the strike, dip and rake, respectively, of each plane. P and T axes denote possible directions of maximum and minimum compressions respectively. A star on each plane marks the position of the rake vector. (Courtesy of Evans, Asudeh & Crampin, 1982).

respectively. It is not possible to undertake a similar study for the TDP1 events because the TDP1 network lacks the necessary azimuthal coverage. However, the first motions from the TDP1 events are consistent with the fault plane solution shown in this figure.

The fact that most of the events from TDP1 and TDP2 conform to this radiation pattern is encouraging because it suggests that the orientation of the dilatancy-anisotropy beneath the networks is likely to be homogeneous. This will facilitate the determination of the anisotropic structure at a later stage in this thesis, as the orientation of the P and T axesis likely to reflect the orientation of the dilatancy-anisotropy. Note however, that these axes do not necessarily place a great constraint on the direction of the maximum and minimum stresses if the earthquakes are occuring on pre-existing fault-planes.

2.3.3 Observations of shear-wave splitting

As with the TDP1 data set, the analogue records were digitised at 100 samples/sec and display impulsive shear-wave arrivals that are very suitable for the analysis of shear-wave polarisations. The majority of records from TDP2 display clear evidence of shear-wave splitting and Fig.2.7 shows an example. Separate shear-wave arrivals are not apparent on the unrotated seismograms, but are seen more clearly on the rotated seismograms. The polarisation-diagrams show the first shear-wave arriving with linear particle motion and followed approximately 0.1s later by a second shear-wave arrival with a different polarisation.

2.4 Discussion

This Chapter has presented the preliminary results from two micro-earthquake surveys on a section of the North Anatolian Fault. In total about 600 well-recorded, small earthquakes were detected immediately beneath the networks providing several thousand three-component records.

Figure 2.7. An example of a three-component seismogram and polarisation-diagrams for an earthquake on 30 June 1980 with epicentre 40.674N, 29.939E, depth 9.82km, and magnitude, M_L = 1.4. The seismograms were recorded at station SE at a hypocentral distance of 10km and at an azimuth of N203E from the epicentre. Notation and format as in Fig.2.3.

PMPLOT V4.01 08-JUL-81 39:05:11 MA3772 NETWORK: TDP-D2 TAPE: D4 EVENT: D4/01 STATION SEV
START: 30-JUN-80 14:21:23 MOTION FROM START + 2.38 WINDOW LENGTH 0.15
HYPOCENTRAL DISTANCE 10.00 AZIMUTH (FROM STN TO EPI) 23.0 F1= 0.10 F2=20.00

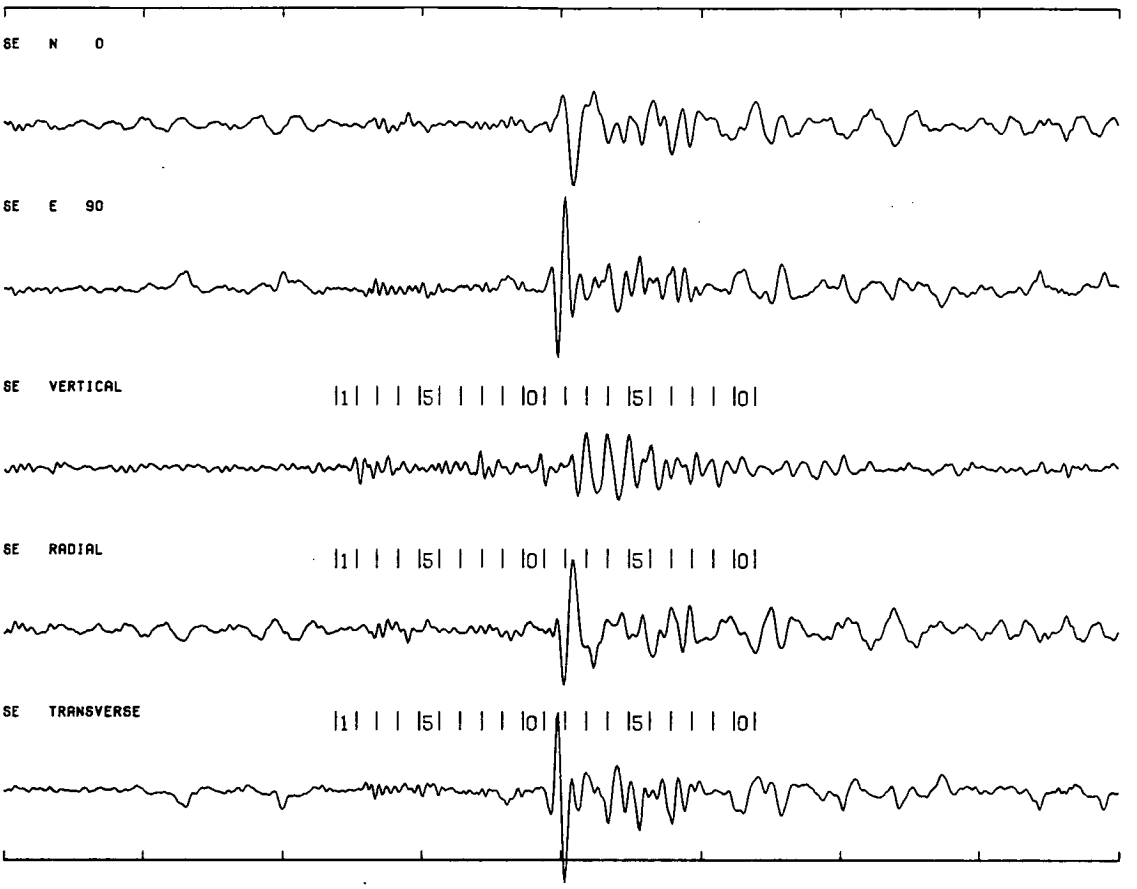

PMPLOT V4.01 08-JUL-81 39:05:11 MA3772 NETWORK: TDP-D2 TAPE: D4 EVENT: D4/01 STATION SEV
START: 30-JUN-80 14:21:23 MOTION FROM START + 2.38 WINDOW LENGTH 0.15
HYPOCENTRAL DISTANCE 10.00 AZIMUTH (FROM STN TO EPI) 23.0 F1= 0.10 F2=20.00

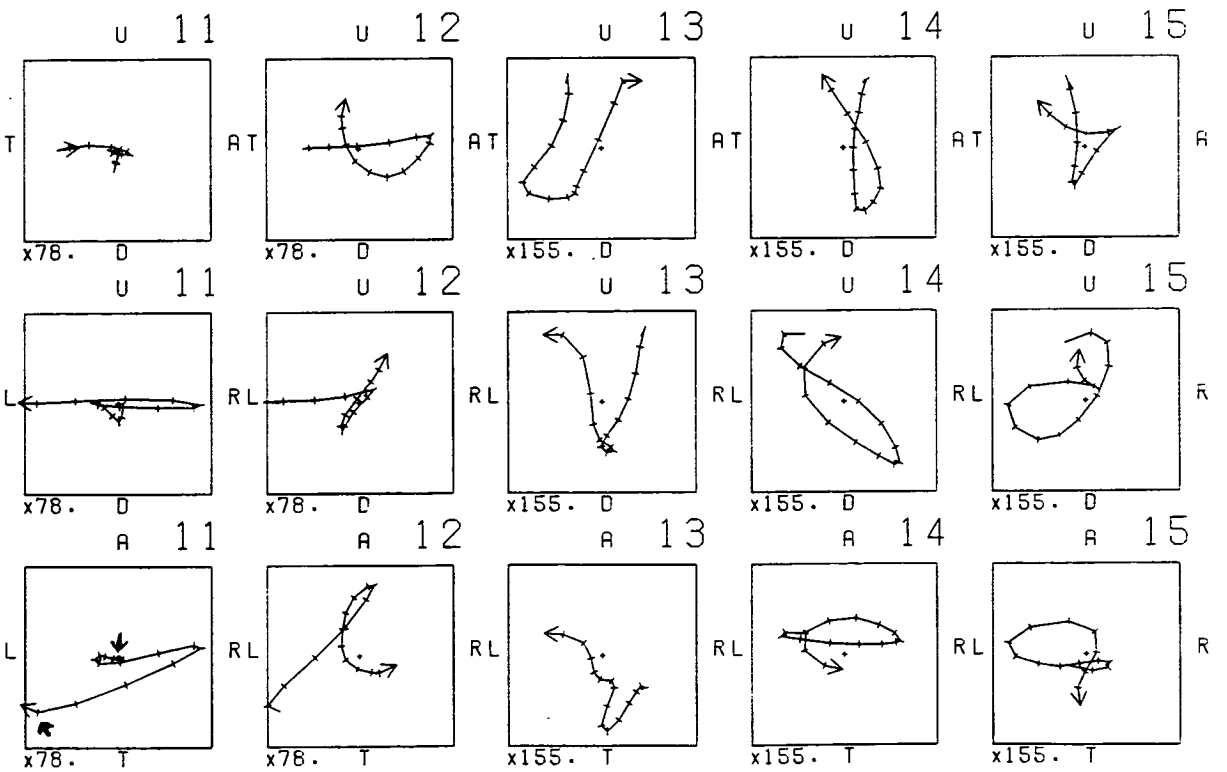

The majority of these records display evidence of shear-wave splitting which is strongly indicative of shear-wave propagation through an anisotropic structure. (Note that the two examples shown in this Chapter are not general. They were chosen as being particularly obvious examples of shear-wave splitting and represent only about 10% of the seismic records. Shear-wave spltting in the remainder can only be seen in polarisation-diagrams. This phenomenon will be discussed in more detail in Chapter 5). It is anticipated that the anisotropy is a result of preferentially aligned cracks in an extensive region of dilatancy-anisotropy. At the time of writing (November 1981) there have been no large earthquakes detected in this area and the dilatancy-anisotropy is thought to be a result of the ambient stress field. However, there is a suggestion (Toksöz, Shakal & Michael, 1979) that this area may be a seismic gap and we cannot rule out the possibility that we are witnessing the preporatory period to a large ($M > 6$) earthquake. The analysis of shear-wave polarisations and delays is currently in progress in order to confirm dilatancy-anisotropy in this region. Initial results suggest that the structure is strongly anisotropic with at least 10% differential shear-wave anisotropy (Stuart Crampin, private communication). This thesis will independently attempt to determine the anisotropic structure by the analysis of the arrival-times of seismic body-waves. However, we shall first consider the effect of such anisotropy on the hypocentral locations when an isotropic velocity structure is assumed in the location procedure.

CHAPTER 3

THE EFFECTS OF DILATANCY-ANISOTROPY ON THE HYPOCENTRAL LOCATIONS OF LOCAL EARTHQUAKES WHEN ISOTROPY IS ASSUMED.

3.1 Introduction

Clear observations of shear-wave splitting, presented in Chapter 2, provide strong evidence that the structure on this section of the North Anatolian Fault is anisotropic. Much of the further analysis of the TDP data, including the identification of the type of dilatancy-anisotropy, detailed structural analysis, focal mechanism studies and the search for any temporal, precursory variations, will depend on reliably accurate hypocentral locations. However, the preliminary locations of the TDP events have been determined under the assumption that the structure is isotropic. It is therefore necessary to consider the validity of the isotropic approximation when locating earthquakes in an anisotropic structure. This Chapter examines this problem for a variety of possible orientations and symmetry systems of the dilatancy-anisotropy in seismic source regions by exact modelling of the earthquake location procedure and of anisotropic seismic-wave propagation. We shall demonstrate that the assumption of isotropy can result in serious and systematic mislocations, and may lead to observations of apparent hypocentral migrations as the nature of the anisotropic variations change in response to conditions in the source region.

3.2 Possible models for dilatancy-anisotropy in seismic regions

The initial decrease in the velocity ratio Vp/Vs that has been observed to occur prior to earthquakes is thought to be due to the opening of dry cracks in the source region. The return to normal of this ratio could be due to several mechanisms, including, the migration of pore fluid into this

newly created pore space (Nur 1972, Scholz et al.1973); the reduction of crack density by unstable deformation in the source region, and some release of regional stress (Mjachkin et al.1975); the reduction of crack density by pre-seismic fault creep (Nur 1975); or the reduction of crack density by the reorientation of stress axes in the focal region (Brady 1975). In both dry and saturated states, an aligned crack system would possess anisotropic properties and would display anisotropic velocity variations, but of a different form. The reduction of crack density would reduce the degree of velocity-anisotropy until, when all the cracks are closed, the system would be characterised by isotropy. Thus the form of dilatancy-anisotropy may be characterised by dry cracks initially, but may develop into that characterised by saturated cracks, reduced crack density, and even isotropy at a later stage immediately prior to the impending earthquake. Note, however, that the occurence of dilatancy-anisotropy in seismic regions need not be specifically related to an impending earthquake. The effect of a deviatoric stress system, as exists in most seismic regions, will be to preferentially align pre-existing cracks (Crampin & Evans, 1982). In this case the anisotropy is just a reflection of the ambient stress field, and the cracks are likely to be saturated.

The possible symmetry systems and orientations of dilatancy-anisotropy are not known at present, and any attempt to model the velocity structure must be purely speculative. However there have been many laboratory experiments on dilatancy in rock samples, and there appear to be three ways in which dilatancy can develop in such samples.

1) Where one of the stress axes is much smaller than the other two, cracks close parallel to the direction of maximum compressive stress and open perpendicular to it (Gupta 1973b). Such a crack system possesses hexagonal symmetry in which there is an axis of rotational symmetry perpendicular to the open faces of the cracks (Fig.3.1(a)). This direction would correspond

Figure 3.1. Schematic diagrams of possible crack systems that may characterise dilatancy-anisotropy. The crack systems are dependent on the ratios of the principal stresses (σ_1 - maximum, σ_2 - intermediate, σ_3 - minimum). P_{max} , P_{int} , P_{min} refer to maximum, intermediate and minimum P-wave velocities respectively on the assumption that the cracks are dry.

(a) Model 1 - ($\sigma_1 \simeq \sigma_2 > \sigma_3$) - a system of parallel cracks possessing hexagonal symmetry with rotational symmetry about the direction of least compression.

(b) Model 2 - ($\sigma_1 >> \sigma_2 = \sigma_3$) - a system of coplanar-normal cracks possessing hexagonal symmetry with rotational symmetry about the direction of maximum compression.

(c) Model 3 - ($\sigma_1 > \sigma_2 > \sigma_3$) - a system of orthogonal, biplanar cracks of unequal crack density. This system possesses orthorhombic symmetry with three symmetry planes - parallel to the major and minor cracks, and perpendicular to the direction of crack intersections.

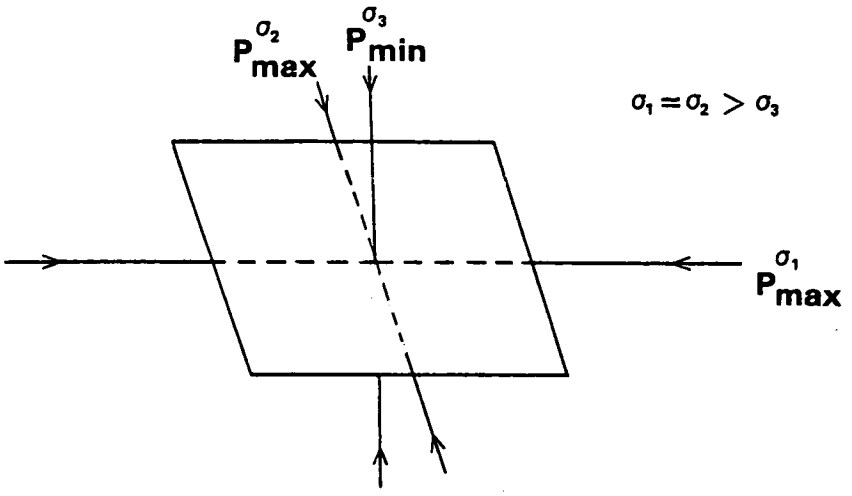

(a) Model 1

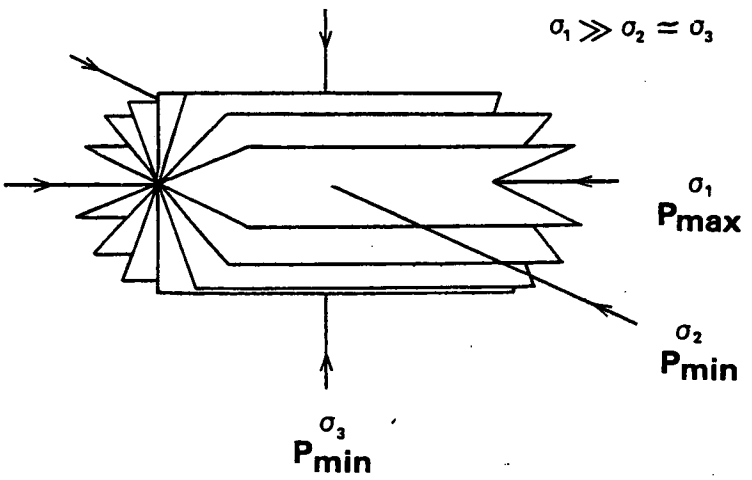

(b) Model 2

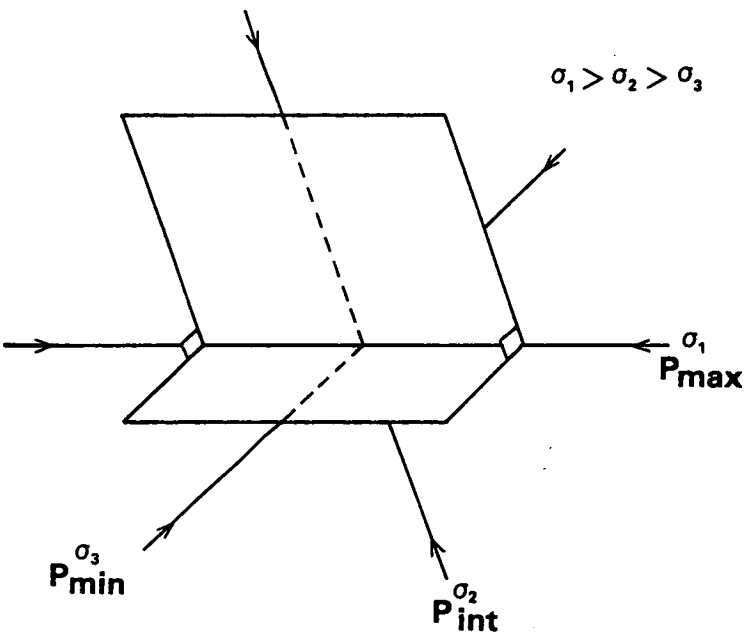

(c) Model 3

to the direction of least compression in earthquake mechanisms.

2) Tri-axial experiments, where there is one dominant compressive stress direction, suggest that a system of random cracks with coplanar normals about the axis of maximum compression would be created (Hadley 1975). This system of cracks also possesses hexagonal symmetry but in this case the system has an axis of rotational symmetry about the direction of maximum compressive stress (Fig.3.1(b)).

3) A more general crack structure may result from poly-axial stress distributions where the magnitudes of the principal stress axes are all distinct. This may result in a system of orthogonal, biplanar cracks with unequal crack densities, with both sets of cracks orthogonal to the direction of maximum compression (Fig.3.1(c)). This system would possess orthorhombic symmetry in which there are three planes of symmetry - parallel to the major and minor cracks, and perpendicular to the direction of crack intersections.

These crack systems can be modelled by the numerical techniques of Crampin (1978). Figs.3.2(a) and 3.2(b) show quadrant sections through the symmetry axes of the wave-surfaces, (the group-velocity-surfaces), of GKFF1 and GKLF1 (from Crampin 1978) which model systems of parallel, penny-shaped, dry and saturated cracks respectively. Each model has a crack density of:

$$\varepsilon = \underline{N}\underline{a}^3 / \underline{v} = 0.1 \qquad (3.1)$$

where $\underline{N}$ is the number of cracks with radius $\underline{a}$ in volume $\underline{v}$ of an initially intact isotropic solid. These models correspond to crack model 1 above. Figs.3.2(c) and 3.2(d) show sections through the wave-surfaces of CPFF1 and CPLF1 corresponding to the dry and saturated crack systems of crack model 2 above with a crack density of 0.1. Figs.3.2(e), 3.2(f) and 3.2(g), and Figs.3.2(h), 3.2(i) and 3.2(j) are sections through the wave-surfaces of GK2FFA and GK2LFA respectively (from Crampin & McGonigle 1981). These

Figure 3.2. Quadrant sections through the wave-surfaces of various anisotropic models used in this Thesis. The horizontal axis measures the number of degrees away from a principal axis in the system.

(a) GKFF1 - a system of dry, parallel cracks with an axis of rotational symmetry perpendicular to the open faces of the cracks.
(b) GKLF1 - a system of saturated parallel cracks with an axis of rotational symmetry perpendicular to the open faces of the cracks.
(c) CPFF1 - a system of dry cracks with coplanar-normals and an axis of rotational symmetry perpendicular to the plane of the crack normals.
(d) CPLF1 - a system of saturated cracks with coplanar-normals and an axis of rotational symmetry perpendicular to the plane of the crack normals.
(e) GK2FFA - a system of orthogonal, biplanar dry cracks with unequal crack densities and possessing orthorhombic symmetry. Section perpendicular to direction of crack intersections.
(f) GK2FFA - as (e) for a section parallel to minor crack system
(g) GK2FFA - as (e) for a section parallel to major crack system
(h) GK2LFA - a system of orthogonal, biplanar saturated cracks with unequal crack densities and possessing orthorhombic symmetry. Section perpendicular to direction of crack intersections.
(i) GK2LFA - as (h) for a section parallel to minor crack system
(j) GK2LFA - as (h) for a section parallel to major crack system

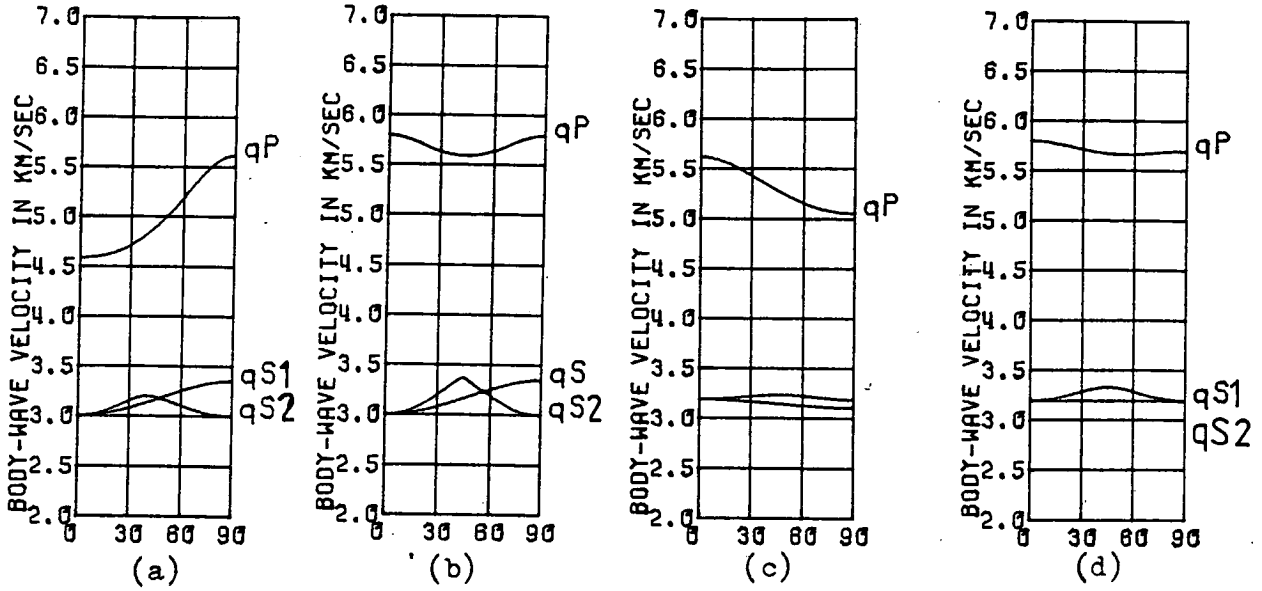
BODY-WAVE VELOCITY IN KM/SEC
7.0
6.5
6.0
5.5
5.0
4.5
4.0
3.5
3.0
2.5
2.0
0
30
60
90
qP
qS1
qS2
qS
(a)
(b)
(c)
(d)

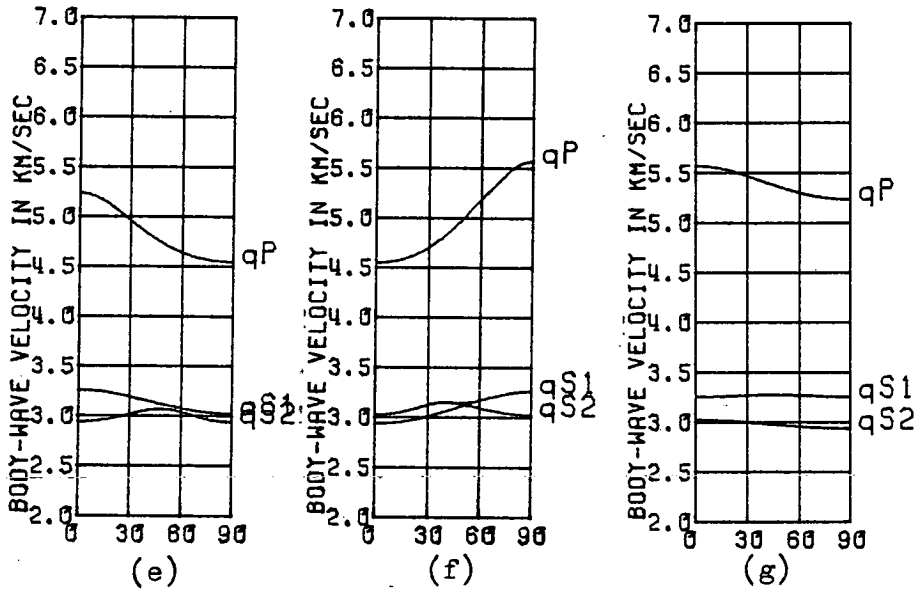
BODY-WAVE VELOCITY IN KM/SEC
7.0
6.5
6.0
5.5
5.0
4.5
4.0
3.5
3.0
2.5
2.0
0
30
60
90
qP
qS1
qS2
(e)
(f)
(g)

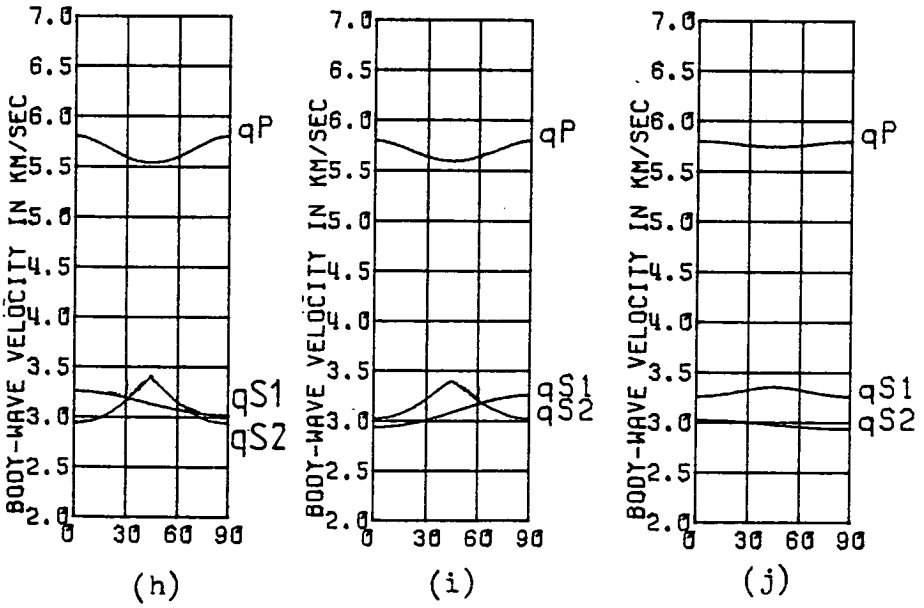
BODY-WAVE VELOCITY IN KM/SEC
7.0
6.5
6.0
5.5
5.0
4.5
4.0
3.5
3.0
2.5
2.0
0
30
60
90
qP
qS1
qS2
(h)
(i)
(j)

correspond to the dry and saturated crack systems of crack model 3 where the minor and major crack systems have a crack density of 0.025 and 0.1 respectively.

Obviously these crack models can only be an approximation to any in situ crack system. In seismic regions the cracks are unlikely to be penny-shaped and homogeneous throughout the region. Until we have more information about cracked structures, the investigation in this Chapter can only be a qualitive rather than a quantitative study. However, Crampin (1978) shows that dilatancy-anisotropy as modelled by GKFF1 and GKLF1 is consistent with the observed Vp/Vs anomalies, such as those of Aggarwal et al.(1975).

The orientation of the crack system in a seismic region is also unknown, but to a first approximation will be primarily dependent on the stress system associated with the seismically active fault. Under the assumption that two of the stress axes are horizontal (as they must be at the free-surface), there are three fundamental types of fault; pure thrust (minimum stress axis vertical), pure strike-slip (intermediate axis vertical), and pure normal (maximum axis vertical). Each of these faults will be characterised by a different orientation of the dilatancy-anisotropy and will have completely different effects on the location of earthquakes.

3.3 Network and event distribution

Fig.3.3 shows the network used in this study and the epicentral positions of simulated earthquakes that are to be relocated. An idealised network (SQ1) consisting of nine stations is formed on a grid, with the epicentres, spaced at one kilometre intervals, lying along one of the network's axes of symmetry. Such a small network is necessary in micro-earthquake surveys in order to isolate the masking effects of large-scale hetereogeneities, and

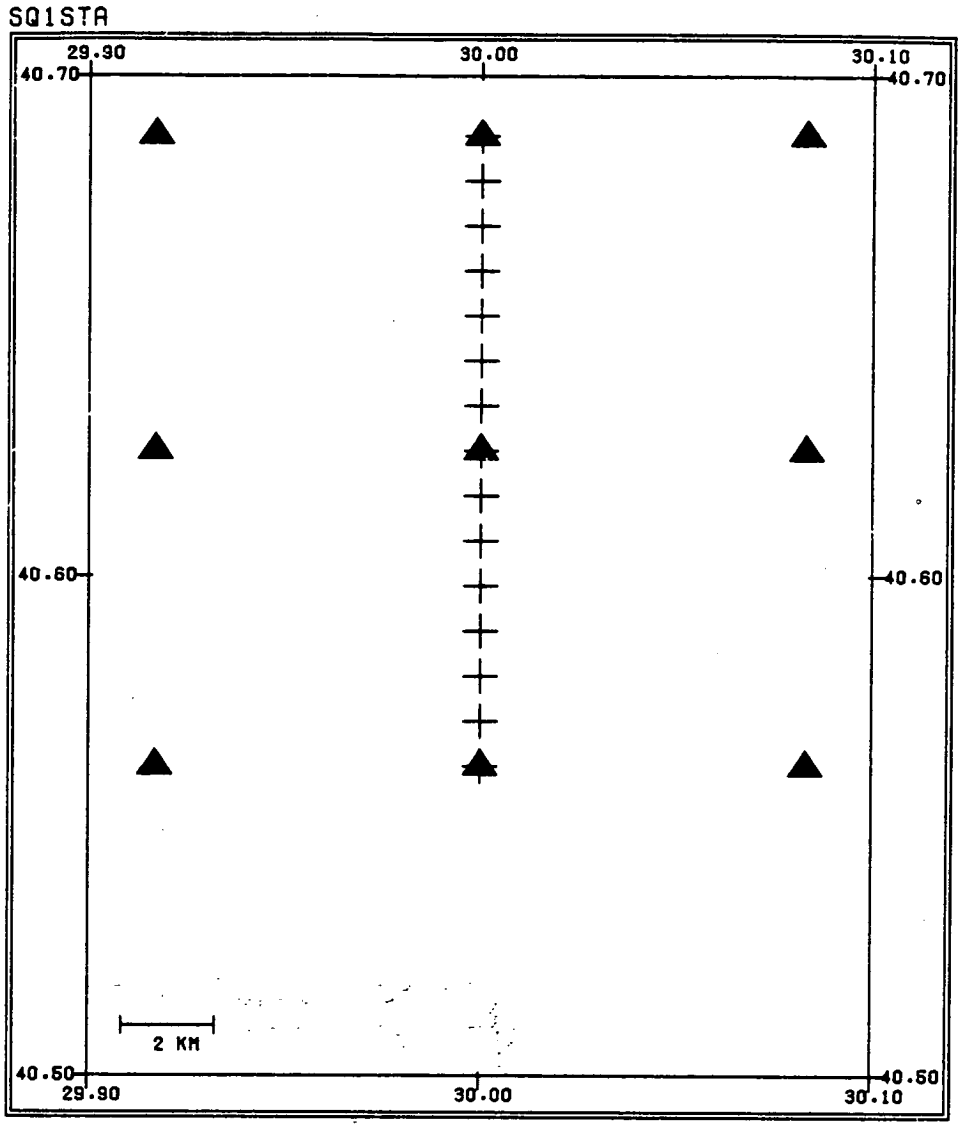

Figure 3.3. Map showing the locations of the stations (solid triangles) of an idealised network (SQ1) used to locate simulated earthquakes. A cross denotes the epicentral positions of three foci at depths of 5, 10 and 15km. The epicentres are spaced at 1km intervals.

so be able to make a detailed study of the velocity structure, and monitor and interpret any temporal variations. At each epicentre in the figure there are three hypocentres at depths of 5, 10 and 15km. Only in the case of a vertical strike-slip fault will this be a realistic distribution of events. This distribution is maintained for the other fault models in order to preserve the symmetry of the station/event system, and not to introduce, at this stage, any effects that may be due to impaired network resolution. Consequently, any anomalous effects in this system will be due entirely to the incorrect assumption of isotropy in an anisotropic structure.

For simplicity, the structure is assumed to homogeneous in a half-space. This approximation may not be too unrealistic as large velocity variations due to dilatancy-anisotropy seem likely to dominate any velocity contrasts across local velocity-discontinuities. This would particularly be the case for small networks sited immediately above the seismic activity, as was the case in the TDP experiments.

3.4 The generation of anisotropic travel-times and the relocation of hypocentres

The most important property of anisotropic propagation in regions of dilatancy-anisotropy, (with regard to earthquake location procedures), is that the P- and shear-wave velocities can display strong directional variations. These cannot be adequately modelled by any isotropic approximation. However, there are two, more subtle, characteristics of anisotropic propagation that must be taken into account in the modelling procedure. Firstly, except for particular symmetry directions, energy in anisotropic media, unlike in isotropic media, propagates with a component, usually small, parallel to the surface of constant phase, and the energy travels along a ray at an angle to the propagation direction and at the

group-velocity. It is this group-velocity that is measured in most observations of arrival-times rather than the phase-velocity that appears in equations of motion and most other analytical expressions. For this reason all velocities in this Chapter refer to the group-velocity unless otherwise specified. Secondly, in many seismic records the shear-wave polarisations will be mixed and the biplanar propagation of shear-waves easily overlooked, resulting in the picking of the first shear-wave arrival as the unique S-phase. In the rest of this Chapter the S-phase refers to the fastest of the shear-waves propagating in a given direction.

The computation of the body-wave group-velocities in an anisotropic solid is described in Appendix A, following the techniques of Crampin & McGonigle (1981), where a look-up table is created containing each group-velocity at intervals of nine degrees in azimuth and angle of incidence from the focal sphere, together with the derivative of each velocity with respect to the angles at the same points. This technique may be applied for any particular anisotropic solid. Suites of synthetic travel-times are generated through various anisotropic structures from each hypocentre to each station in Fig.3.3 by interpolating the P- and shear-wave velocities from this look-up table. The arrival-times are then rounded to 1/20 of a second to simulate the scatter of real data for very near earthquake arrivals.

The relocation of the hypothetical earthquakes of Fig.3.3 is performed by a least-squares procedure which minimises travel-time residuals. A simple location program was written that assumes the structure is an isotropic half-space. The theory for such a program is well known and is outlined in Appendix B. Fig.3.4 is a control calculation and illustrates the relocation of the events of Fig.3.3 by this program, for the case where the travel-times have been generated through an isotropic half-space. Figs.3.4(a) and 3.4(b) are the relocations determined using P- arrivals,

Figure 3.4. A summary of the relocation of the events of Fig.3.3 in an isotropic half-space by an isotropic location program.

(a) Relocation by the half-space location program using P-arrivals at every station (model ASQ1XZ, Table C.1).

(b) Relocation by the half-space location program using P- and S-arrivals at every station (model ASQ1XY, Table C.1).

(c) Relocation by HYPO71 using P-arrivals at every station (model HYPOP, Table C.1).

(d) Relocation by HYPO71 using P- and S-arrivals at every station (model HYPOPS, Table C.1).

Each part consists of three diagrams, from left to right:- 1) a plan view (equal N-S and E-W scales) of the relocations where the crosses denote the correct epicentres (spaced at 1km intervals), and circles denote the relocated epicentre with the diameter of the circle being inversely proportional to the correct focal depth of 5, 10 and 15km; 2) a cross-section of the relocations where the vertical solid lines indicate the correct hypocentral depth, and the asterisks, placed opposite the correct epicentral position, denote the relocated depth; 3) a summary of the root-mean-square (RMS) of the travel-time residuals associated with each relocation, with the length of each vertical bar being inversely proportional to the correct hypocentral depth and placed opposite the correct epicentral position.

ISOTROPIC LOCATIONS

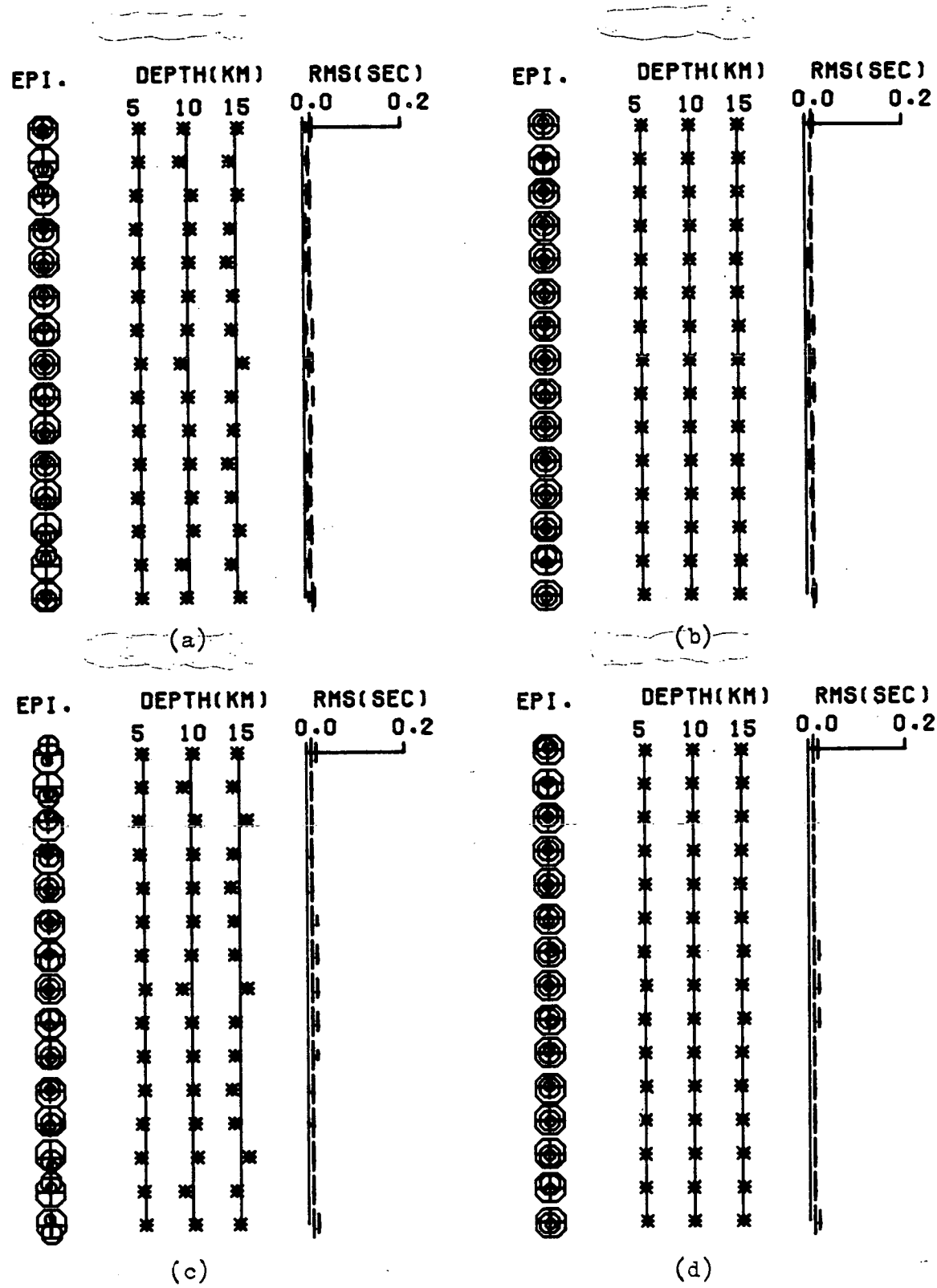

and P- and S-arrivals at every station respectively. Figs.3.4(c) and 3.4(d), similarly, show the relocations determined from the same data set by the widely used HYPO71 location program (Lee & Lahr 1975). The locations and the estimated errors of the hypocentral parameters are very similar in both cases (Table C.1, Appendix C, where the model references are indicated in the figure captions). The scatter on the epicentral locations and the non-zero RMS values are due to the errors introduced to the data in order to simulate the scatter of real data. The apparent uniformity of the RMS values determined by HYPO71, compared to the half-space location program, is merely a reflection of differing degrees of mathematical precision used in the calculation.

3.5 Earthquake locations in anisotropic structures.

Section 3.2 described some crack models that may result from particular combinations of principal stress axes. This section will use those crack models in conjunction with the orientation of stress axes associated with the three fundamental types of faults to illustrate the effects of assuming isotropy when locating events in anisotropic structures. The location program uses the average P-, and the average shear-wave velocity determined from the corresponding anisotropic look-up table as the isotropic velocities. For this network, the choice of the isotropic velocities would have little effect on the epicentral locations, but will obviously effect the depth of the relocated hypocentres. This point will be considered in more detail at a later stage.

3.5.1 Events on a pure-strike-slip fault

In the case of a pure strike-slip fault, the axis of intermediate stress would be vertical with the other two horizontal. In addition, the axis of maximum compression would be oriented at an acute angle to the strike of

the fault. This angle depends on many factors, but in this section it will be assumed to be 45 degrees (corresponding to the case where faulting takes place in the plane of maximum shear, and not on a pre-existing fault plane (Aki & Richards 1980). Therefore in order to model right lateral motion on the fault as defined by the epicentres in Fig.3.3, the direction of maximum compression strikes at N45E. In order to model the orientation of the dilatancy-anisotropy associated with such a fault, the axis of rotational symmetry strikes along the axis of least compression for crack model 1, and along the direction of maximum compression for crack model 2. In the biplanar crack model 3, the normal to the minor crack system is vertical, and the normal to the major crack system strikes along the direction of least compression (i.e. N135E).

Figs.3.5, 3.6 and 3.7 illustrate the relocation of the events of Fig.3.3 for each of the possible crack systems that may develop around a pure strike-slip fault. In almost all the dry crack systems , the relocations define a plane that strikes at an angle to the true fault plane. This is particularly obvious where the relocations have been determined using only P-arrivals. The rotation away from the fault is always towards the direction of least compression, and can be as much as 7 degrees as in Fig.3.5(a). This phenomenon is a consequence of the strong 2θ azimuthal variation of P-wave velocity in these models, and can be simply understood in terms of the travel-time equation of epicentral distance divided by velocity. If the velocity used in the relocation is lower than the true velocity, then epicentral distance is reduced. The opposite is true if the assumed velocity is higher than the true velocity. In effect the epicentres are 'pulled' closer to stations if they lie in high velocity directions, and 'pushed' away from stations in low velocity directions - resulting in an overall alignment towards the low velocity direction. The addition of shear-arrivals to the location procedure

modifies this effect because the fastest shear-wave surface has a much reduced 2θ variation. In the saturated crack models the P-wave has a weak 4θ variation, so this effect is not observed with this particular source/station distribution.

The depths of the relocations in almost all cases are too shallow, particularly when just P-arrivals are used. These depth variations require a more complicated explanation than the epicentral distributions, because it is well known that there is a trade-off between the depth and the origin-time when only P-arrivals are used in the location procedure. There appear to be two factors controlling the hypocentral depth. The first is valid for the shallow events where the outer stations in the network influence the depth determination. When the assumed velocity is higher than the true velocity, then the events migrate towards the surface and the large depth errors are accommodated in the origin-time, which is poorly constrained. The second factor is similar to the way the epicentres are perturbed. For deeper events, epicentral stations exert most control over the depth of focus. In this model vertical propagation is a high velocity direction and so the deeper events are again located at shallower depths. The depths are more accurately determined when shear-arrivals are used because the S-P times place a much greater constraint on the origin-time which in turn constrains the other hypocentral parameters.

The high resolution afforded by such a symmetric network is reflected by the high RMS errors associated with the poorly determined relocations in the strongly anisotropic dry crack structures. The variation of the RMS errors between each depth interval is due to differences in the degree of anisotropy sampled by the ray paths from a particular depth. The deeper events in the dry crack model have a lower RMS because the ray paths to the surface define a narrower cone than those for the shallower events, and so the difference between the highest and lowest velocity sampled by the ray

Figure 3.5. A summary of the relocations, by an isotropic half-space program, of the events of Fig.3.3 in a half-space that models dilatancy-anisotropy on a strike-slip fault with a system of parallel cracks.
(a) Locations determined using P-arrivals at every station in the dry crack model GKFF1 (model MSQ1SZ, Table C.2).
(b) Locations determined using P- and S-arrivals at every station in the dry crack model GKFF1 (model MSQ1SY, Table C.2).
(c) Locations determined using P-arrivals at every station in the saturated crack model GKLF1 (model NSQ1SZ, Table C.2).
(d) Locations determined using P- and S-arrivals at every station in the saturated crack model GKLF1 (model NSQ1SY, Table C.2).
Notation and parameters as in Fig.3.4.

STRIKE-SLIP FAULT

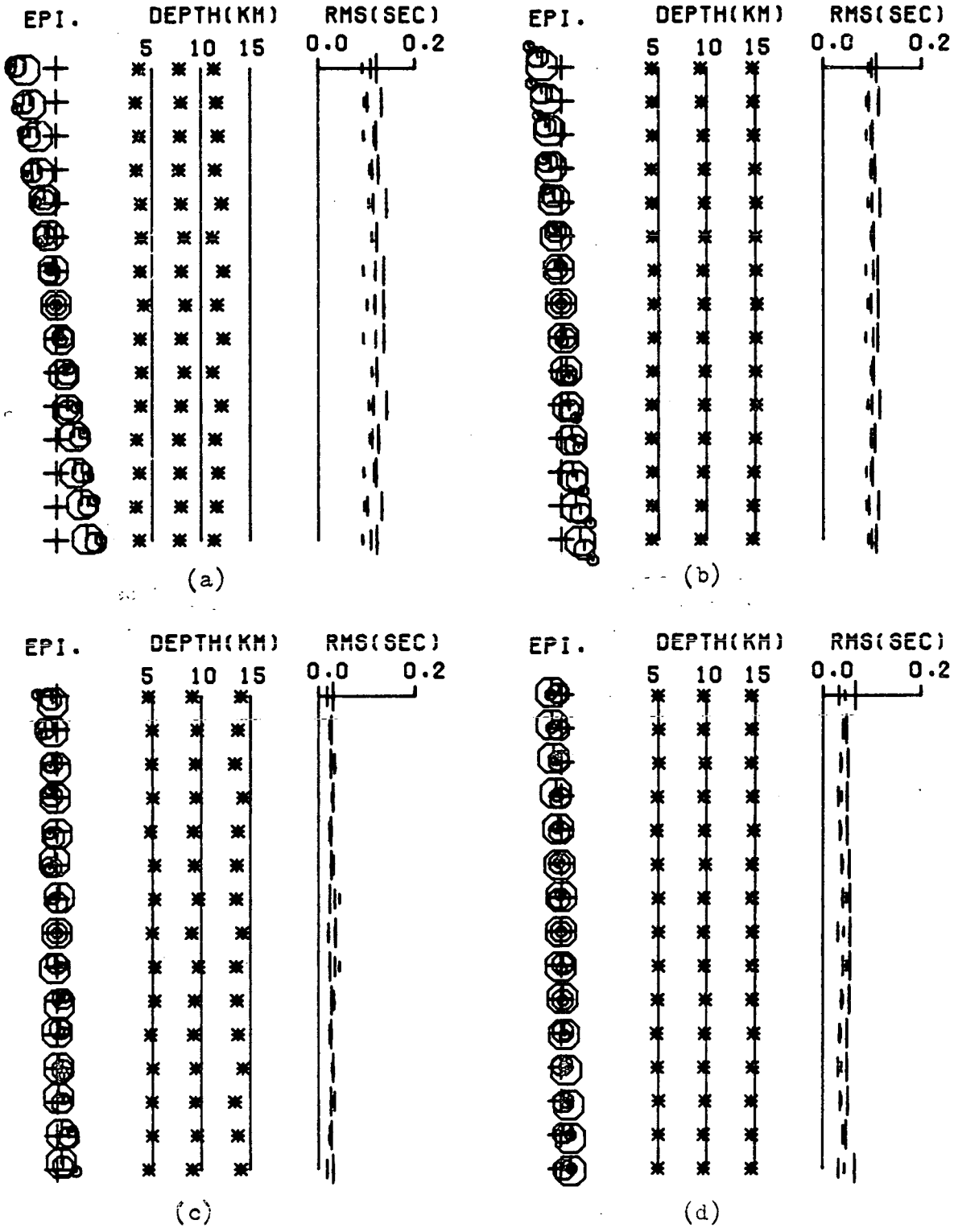

Figure 3.6. A summary of the relocations, by an isotropic half-space program, of the events of Fig.3.3 in a half-space that models dilatancy-anisotropy on a strike-slip fault with a system of coplanar cracks
(a) Locations determined using P-arrivals at every station in the dry crack model CPFF1 (model OSQ1SZ, Table C.2).
(b) Locations determined using P- and S-arrivals at every station in the dry crack model CPFF1 (model OSQ1SY, Table C.2).
(c) Locations determined using P-arrivals at every station in the saturated crack model CPLF1 (model PSQ1SZ, Table C.2).
(d) Locations determined using P- and S-arrivals at every station in the saturated crack model CPLF1 (model PSQ1SY, Table C.2).
Notation and parameters as in Fig.3.4.

STRIKE-SLIP FAULT

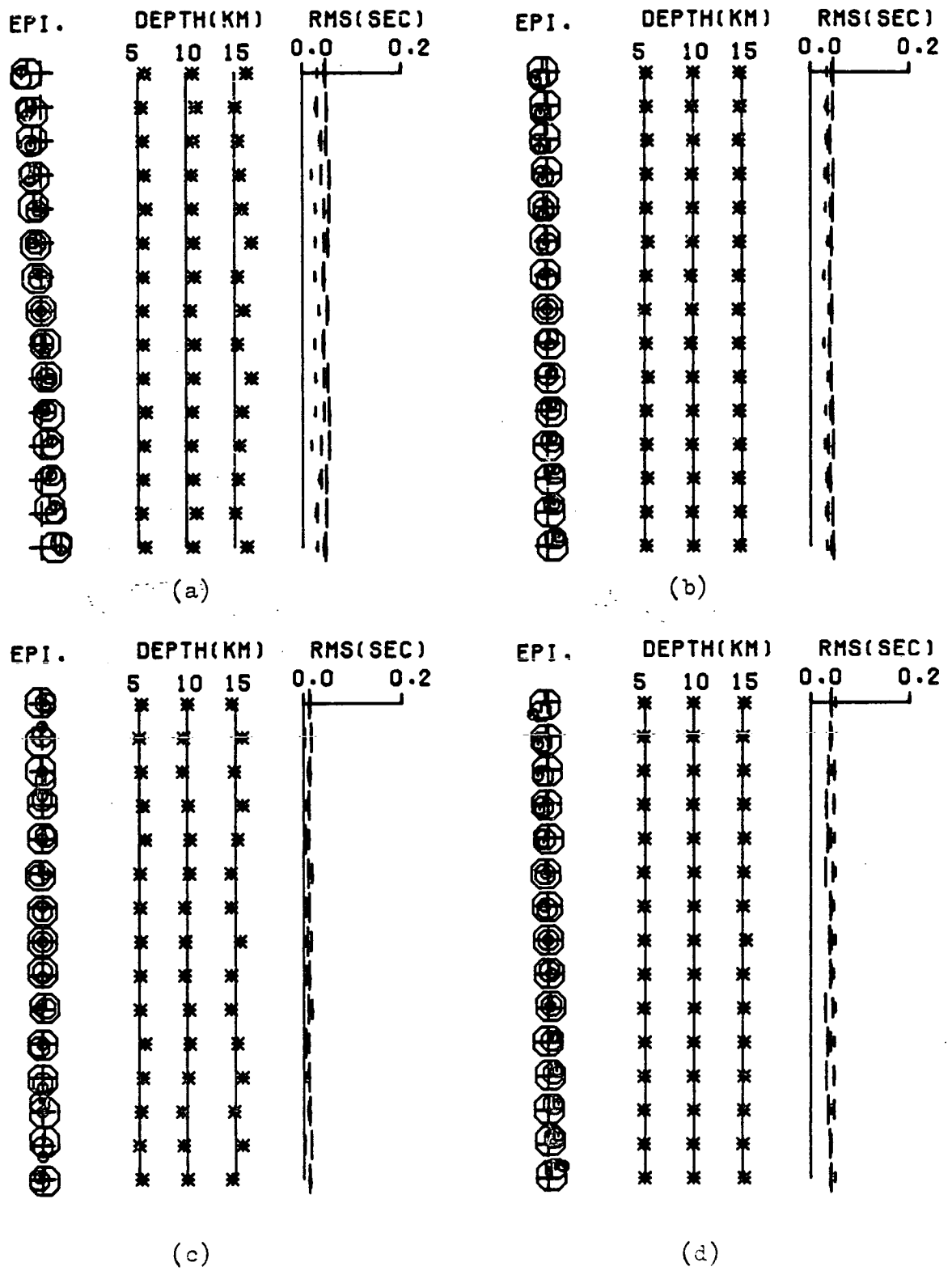

Figure 3.7. A summary of the relocations, by an isotropic half-space program, of the events of Fig.3.3 in a half-space that models dilatancy-anisotropy on a strike-slip fault with a system of orthogonal bi-planar cracks
(a) Locations determined using P-arrivals at every station in the dry crack model GK2FFA (model QSQ1SZ, Table C.2).
(b) Locations determined using P- and S-arrivals at every station in the dry crack model GK2FFA (model QSQ1SY, Table C.2).
(c) Locations determined using P-arrivals at every station in the saturated crack model GK2LFA (model RSQ1SZ, Table C.2).
(d) Locations determined using P- and S-arrivals at every station in the saturated crack model GK2LFA (model RSQ1SY, Table C.2).
Notation and parameters as in Fig.3.4.

STRIKE-SLIP FAULT

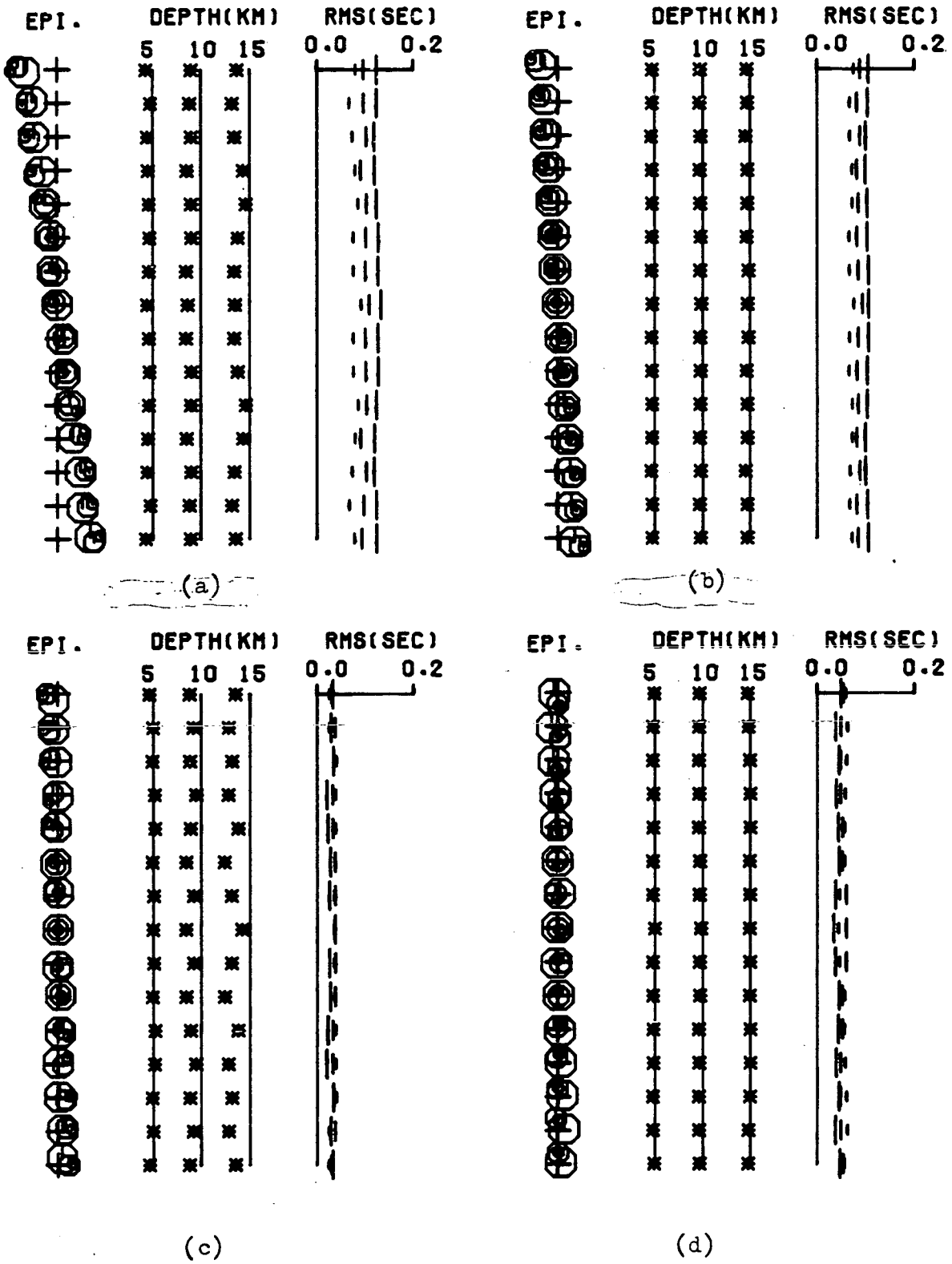

paths is less. Consequently, the RMS of the residuals about the mean velocity used to locate the events is less. This effect is not so noticeable in the saturated crack structure because of the lower degree of velocity anisotropy.

The estimated hypocentral errors are typically equal to, or greater than, the true hypocentral errors in all cases, (Table C.2, Appendix C). This is to be expected for such a regular network.

3.5.2 Events on a pure-thrust fault

Pure-thrust faults are characterised by a vertical axis of least compression, with the axis of maximum compression oriented horizontal and perpendicular to the strike of the fault plane. In this case the hypothetical events of Fig.3.3 do not define a fault plane as this plane dips at a shallow angle for thrust faults, but should be thought of as delineating three possible depths of seismic activity beneath the network. In order to model the orientation of the dilatancy-anisotropy associated with such a fault, the axis of rotational symmetry is vertical for crack model 1, and for crack model 2 it is horizontal and perpendicular to the line of epicentres along the direction of maximum compression. In crack model 3 the normal to the major crack system is vertical, and the normal to the minor crack system is parallel to the line of epicentres.

Figs.3.8, 3.9 and 3.10 illustrate the relocation of the events in the crack systems that may develop around a pure-thrust fault. The epicentres have been located fairly accurately and in the true hypocentral plane. This can be explained in terms of the velocity-anisotropy and the station/event distribution. The axes of the velocity-anisotropy coincide with the axes in the station/event system (unlike the case for the pure-strike-slip fault) so that stations on opposite sides of the fault have an equal and opposite effect on the epicentres. The apparent

contraction of relocated epicentres along the fault trace, (Fig.3.8a), or expansion (Fig.3.9a), depends on whether the north-south direction for particular angles of emergence is characterised by a higher than average velocity (contraction), or a lower than average velocity (expansion).

The depths of the relocations provide two contrasting features. In this model there is very little azimuthal variation of velocities (crack model 1 is now oriented to be transversely isotropic). This effectively limits the control of the outer stations over the hypocentral depths. Therefore the epicentral stations have the greatest control, and the depth determination depends on whether the vertical direction is characterised by high or low velocity. In the dry crack models the vertical direction of propagation is characterised by low P- and S-velocities resulting in the foci being located too deep and in the footwall (Figs.3.8a and 3.10a). However in the saturated crack structures, the vertical direction is a high velocity direction for P-waves resulting in the hypocentres being located too shallow and in the hanging wall (Figs.3.8c and 3.10c). These effects are again reduced when shear-arrivals are used because the S-P times provide a greater constraint on hypocentre determination.

The RMS errors are quite low in this case reflecting the accuracy of the epicentral locations. Figs.3.10d and 3.8d illustrate the opposite effect to that in the pure-strike-slip fault. The ray paths from the deeper events sample a greater degree of anisotropy than the shallower events, and consequently have a larger RMS error associated with their relocation. The estimated errors of the hypocentres calculated by the location program are shown in Table C.3 of Appendix C. In the models where the depths have been poorly determined, the true hypocentral error is more than twice the estimated error. At the 95% confidence limit, these relocations are significantly different from the true locations. This difference is mainly accounted for by the depth parameter and suggests that

Figure 3.8. A summary of the relocations, by an isotropic half-space program, of the events of Fig.3.3 in a half-space that models dilatancy-anisotropy on a thrust fault with a system of parallel cracks.
(a) Locations determined using P-arrivals at every station in the dry crack model GKFF1 (model MSQ1TZ, Table C.3).
(b) Locations determined using P- and S-arrivals at every station in the dry crack model GKFF1 (model MSQ1TY, Table C.3).
(c) Locations determined using P-arrivals at every station in the saturated crack model GKLF1 (model NSQ1TZ, Table C.3).
(d) Locations determined using P- and S-arrivals at every station in the saturated crack model GKLF1 (model NSQ1TY, Table C.3).
Notation and parameters as in Fig.3.4.

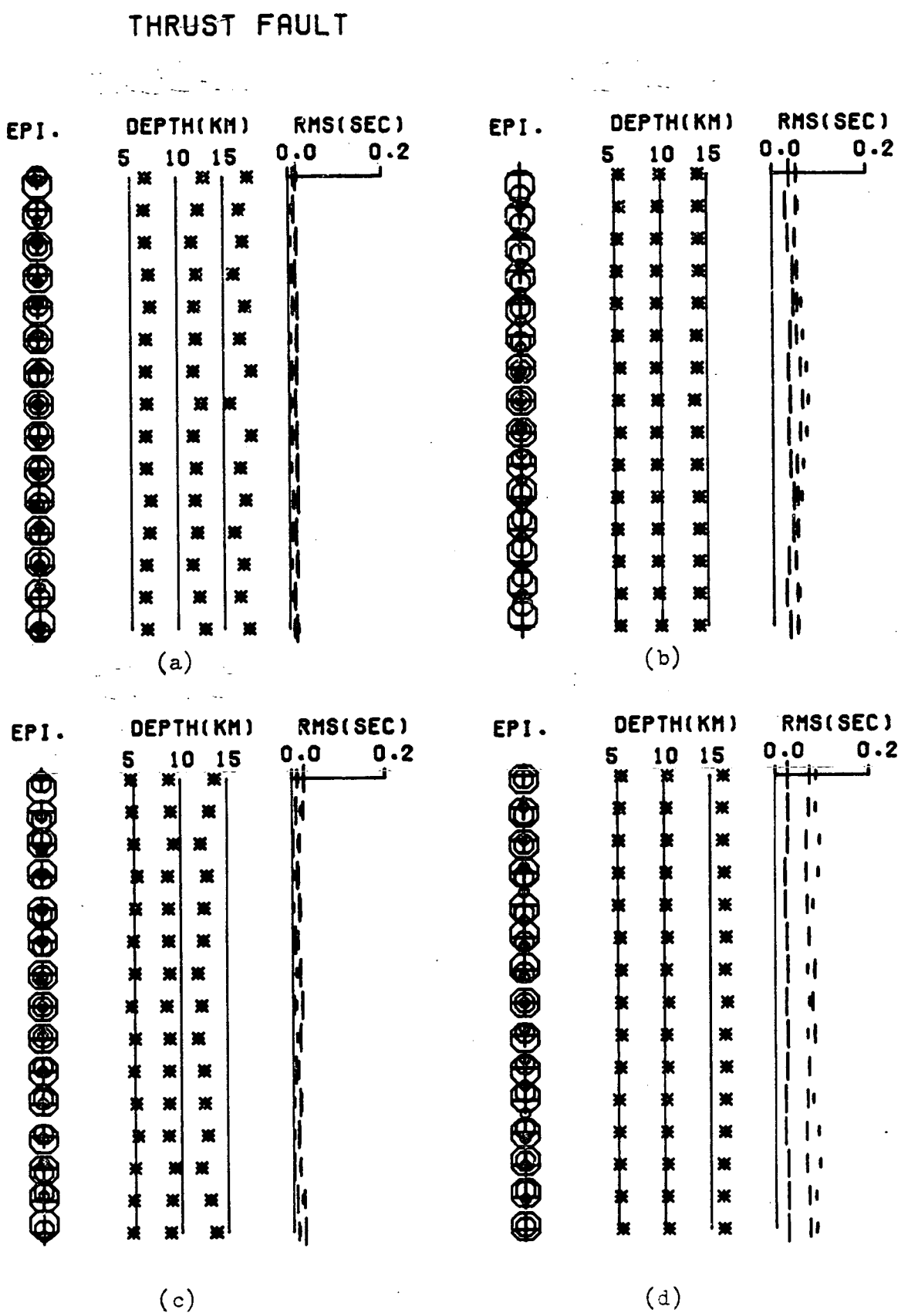
THRUST FAULT
EPI.
DEPTH(KM)
5 10 15
RMS(SEC)
0.0 0.2
(a)
EPI.
DEPTH(KM)
5 10 15
RMS(SEC)
0.0 0.2
(b)
EPI.
DEPTH(KM)
5 10 15
RMS(SEC)
0.0 0.2
(c)
EPI.
DEPTH(KM)
5 10 15
RMS(SEC)
0.0 0.2
(d)

Figure 3.9. A summary of the relocations, by an isotropic half-space program, of the events of Fig.3.3 in a half-space that models dilatancy-anisotropy on a thrust fault with a system of coplanar normal cracks.
(a) Locations determined using P-arrivals at every station in the dry crack model CPFF1 (model OSQ1TZ, Table C.3).
(b) Locations determined using P- and S-arrivals at every station in the dry crack model CPFF1 (model OSQ1TY, Table C.3).
(c) Locations determined using P-arrivals at every station in the saturated crack model CPLF1 (model PSQ1TZ, Table C.3).
(d) Locations determined using P- and S-arrivals at every station in the saturated crack model CPLF1 (model PSQ1TY, Table C.3).
Notation and parameters as in Fig.3.4.

THRUST FAULT

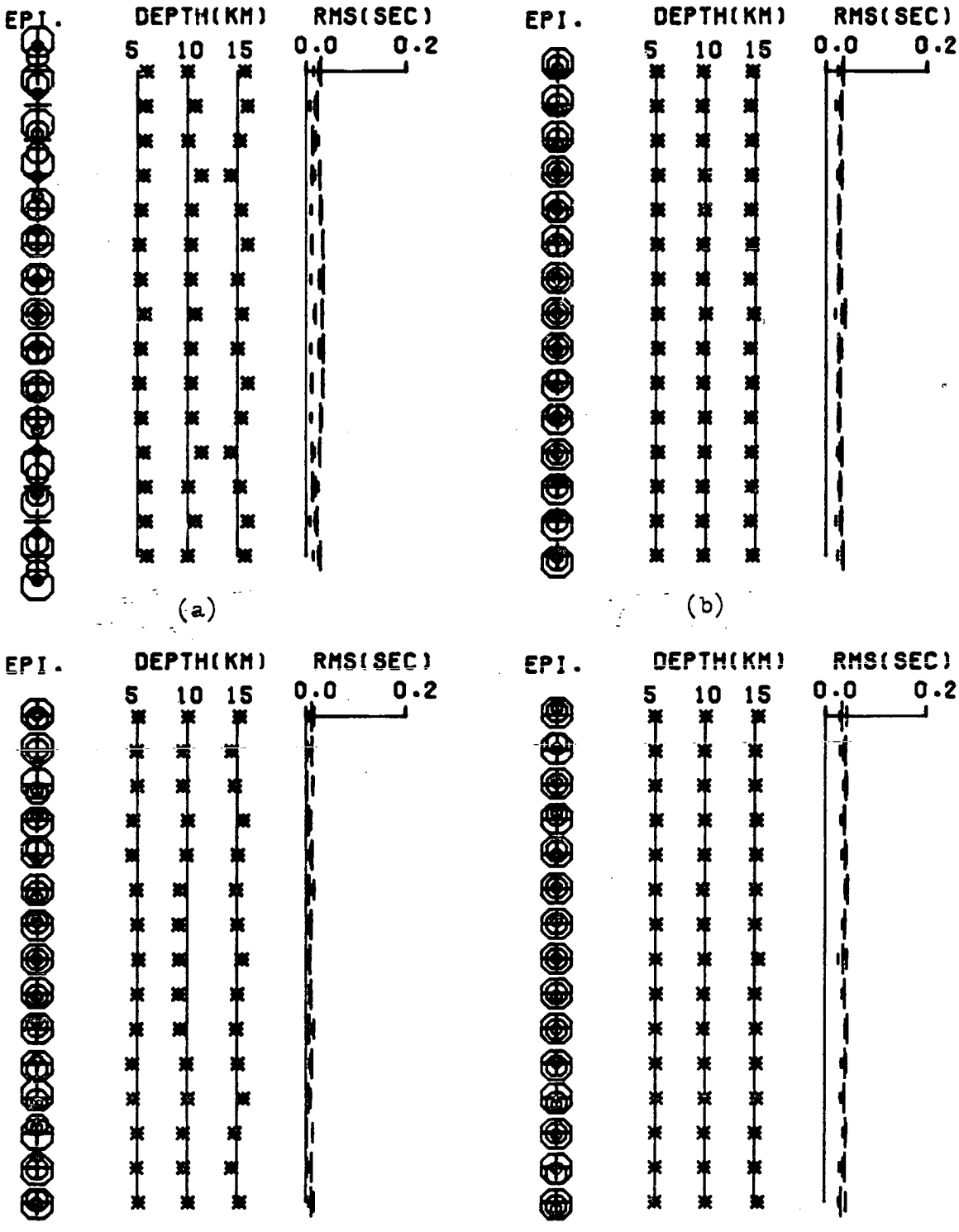

Figure 3.10. A summary of the relocations, by an isotropic half-space program, of the events of Fig.3.3 in a half-space that models dilatancy-anisotropy on a thrust fault with a system of orthogonal, bi-planar cracks.
(a) Locations determined using P-arrivals at every station in the dry crack model GK2FFA (model QSQ1TZ, Table C.3).
(b) Locations determined using P- and S-arrivals at every station in the dry crack model GK2FFA (model QSQ1TY, Table C.3).
(c) Locations determined using P-arrivals at every station in the saturated crack model GK2LFA (model RSQ1TZ, Table C.3).
(d) Locations determined using P- and S-arrivals at every station in the saturated crack model GK2LFA (model RSQ1TY, Table C.3).
Notation and parameters as in Fig.3.4.

THRUST FAULT

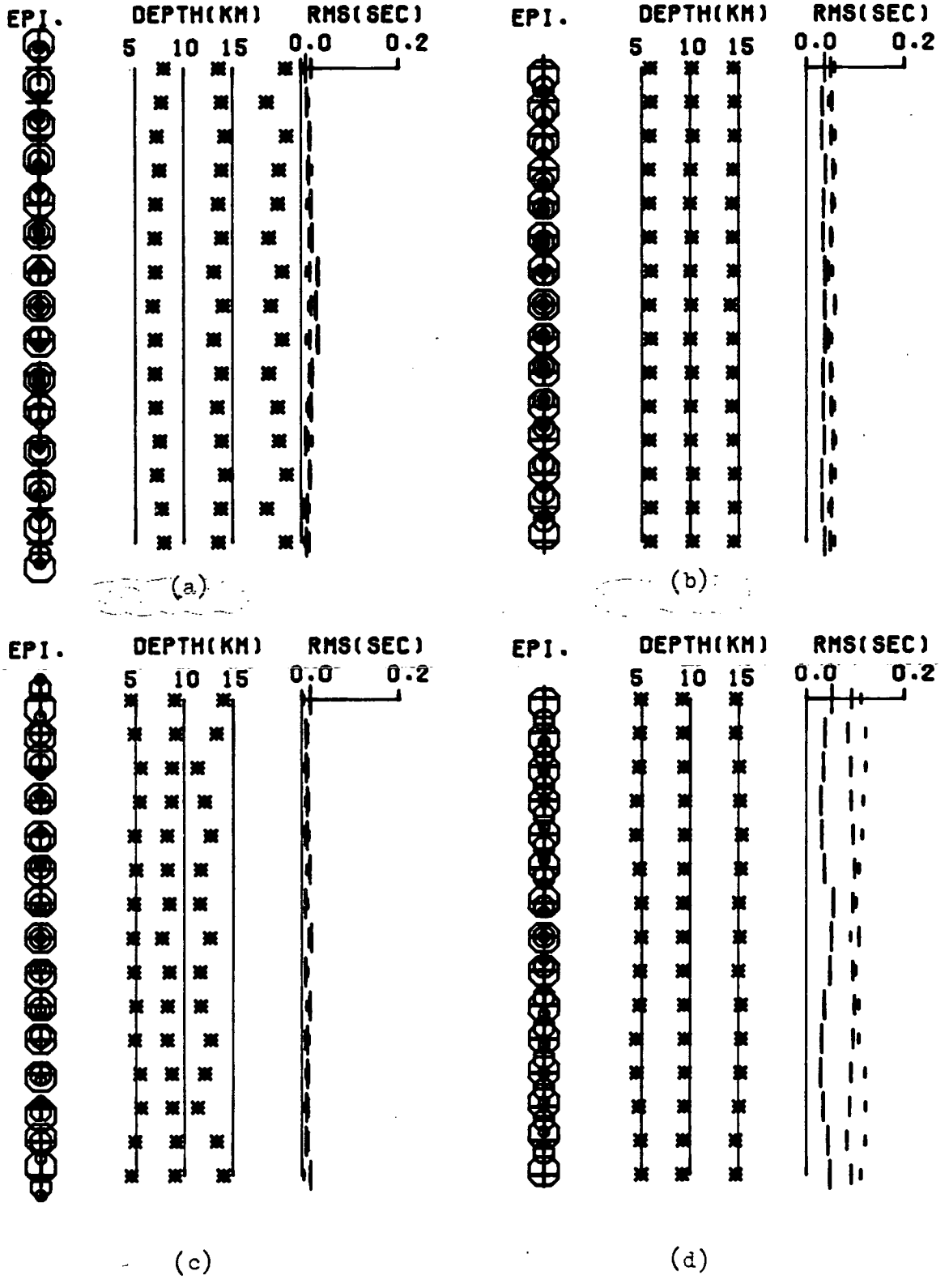

the depth of the true fault plane would not lie within the error bounds of the fault plane determined from these locations. In effect isotropy is an inadequate approximation for this particular model.

3.5.3 Events on a pure normal fault

In the case of a pure normal fault the axis of maximum compression is vertical, and the direction of least compression is horizontal and perpendicular to the strike of the fault plane. Again the hypothetical events in Fig.3.3 do not define a realistic fault plane. In this case in order to model the orientation of the associated dilatancy-anisotropy the axis of rotational symmetry for crack model 1 is horizontal and perpendicular to the line of epicentres, and it is vertical for crack model 2. In crack model 3 the normal to the major crack system is horizontal and perpendicular to the line of epicentres, and the normal to the minor crack system is parallel to the line of epicentres.

Figs.3.11, 3.12 and 3.13 illustrate the relocation of the events in these crack structures that may develop around a pure-normal fault. As in the case of the thrust fault, the hypocentres have been located in the plane defined by the true hypocentres owing to the symmetry of the station/event/velocity-anisotropy system. In all cases the epicentres have been shifted closer together because the north-south direction is characterised by a higher than average velocity.

The depths of the relocations can again be explained by the outer stations controlling the depth of the shallow events, but the epicentral stations controlling the depth of the deeper events. The vertical direction of propagation is characterised by a higher than average velocity in both dry and saturated crack models for both P and S-waves. This has resulted in the depth of the locations being too shallow in all cases - particularly in the cases of P-arrivals only. The use of shear-arrivals in

Figure 3.11. A summary of the relocations, by an isotropic half-space program, of the events of Fig.3.3 in a half-space that models dilatancy-anisotropy on a normal fault with a system of parallel cracks.
(a) Locations determined using P-arrivals at every station in the dry crack model GKFF1 (model MSQ1NZ, Table C.4).
(b) Locations determined using P- and S-arrivals at every station in the dry crack model GKFF1 (model MSQ1NY, Table C.4).
(c) Locations determined using P-arrivals at every station in the saturated crack model GKLF1 (model NSQ1NZ, Table C.4).
(d) Locations determined using P- and S-arrivals at every station in the saturated crack model GKLF1 (model NSQ1NY, Table C.4).
Notation and parameters as in Fig.3.4.

NORMAL FAULT

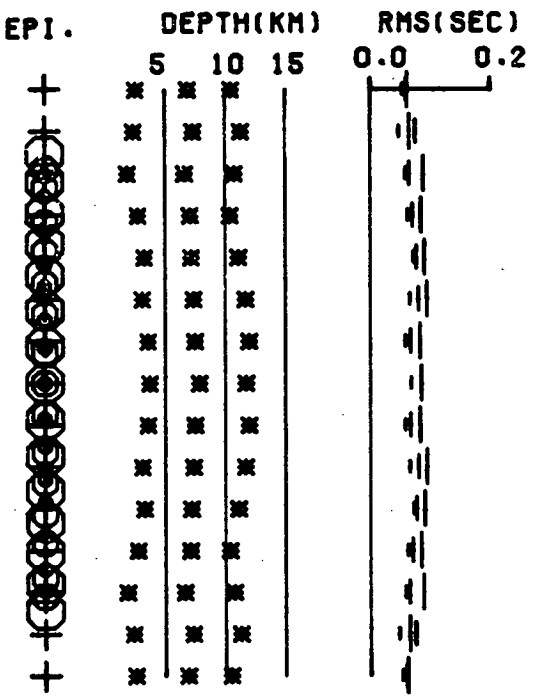

(a)

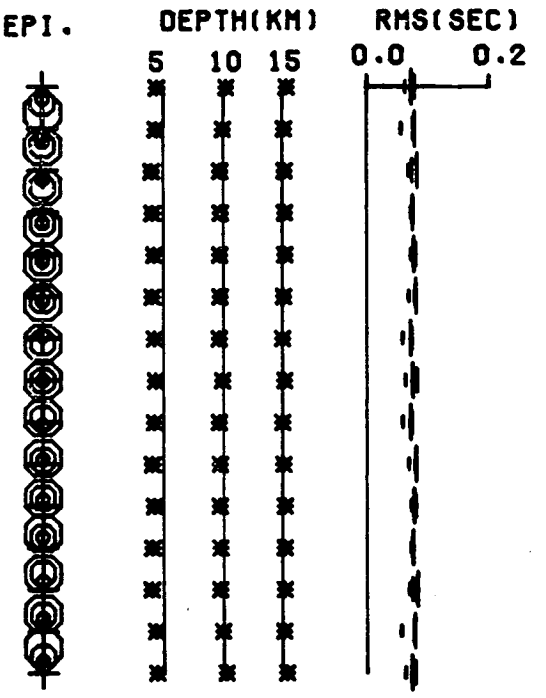

(b)

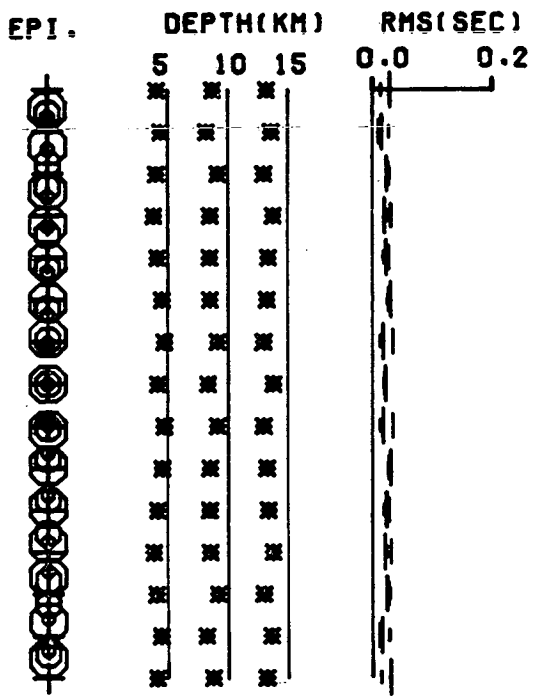

(c)

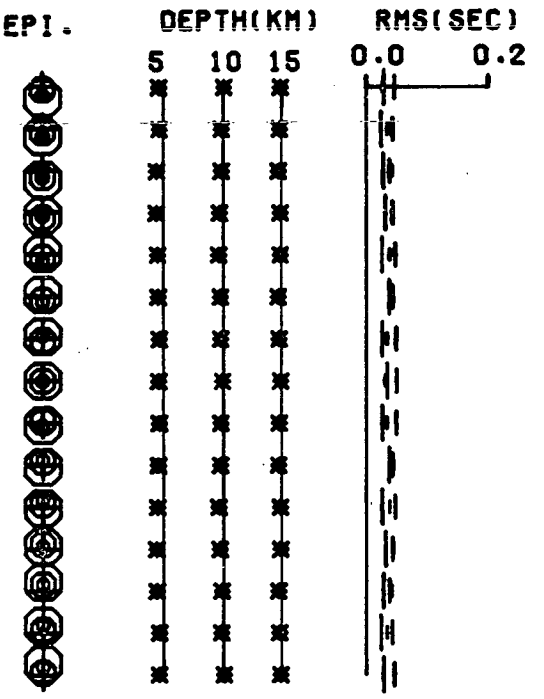

(d)

Figure 3.12. A summary of the relocations, by an isotropic half-space program, of the events of Fig.3.3 in a half-space that models dilatancy-anisotropy on a normal fault with a system of coplanar normal cracks.
(a) Locations determined using P-arrivals at every station in the dry crack model CPFF1 (model OSQ1NZ, Table C.4).
(b) Locations determined using P- and S-arrivals at every station in the dry crack model CPFF1 (model OSQ1NY, Table C.4).
(c) Locations determined using P-arrivals at every station in the saturated crack model CPLF1 (model PSQ1NZ, Table C.4).
(d) Locations determined using P- and S-arrivals at every station in the saturated crack model CPLF1 (model PSQ1NY, Table C.4).
Notation and parameters as in Fig.3.4.

NORMAL FAULT

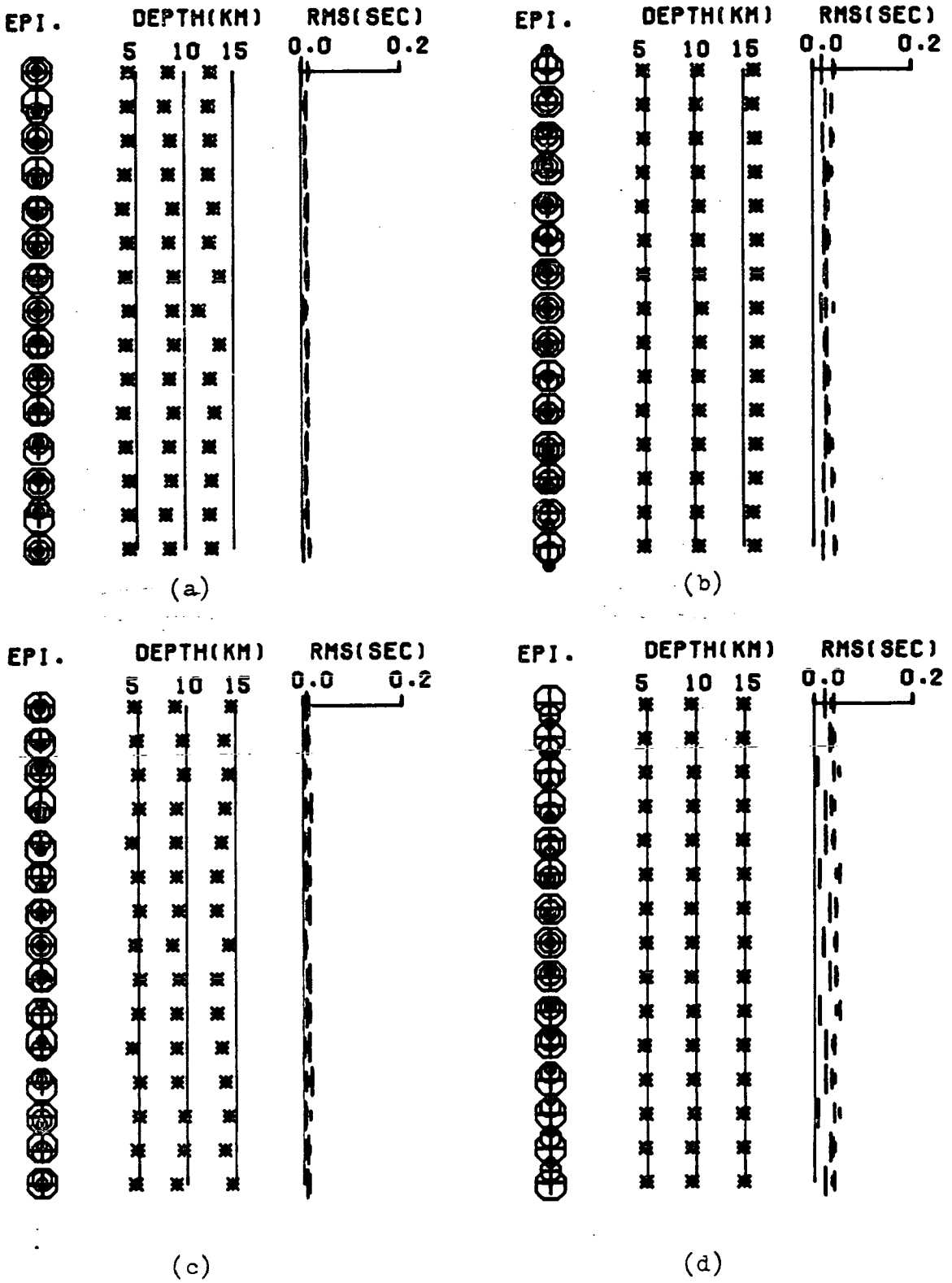

Figure 3.13. A summary of the relocations, by an isotropic half-space program, of the events of Fig.3.3 in a half-space that models dilatancy-anisotropy on a normal fault with a system of orthogonal, biplanar cracks.
(a) Locations determined using P-arrivals at every station in the dry crack model GK2FFA (model QSQ1NZ, Table C.4).
(b) Locations determined using P- and S-arrivals at every station in the dry crack model GK2FFA (model QSQ1NY, Table C.4).
(c) Locations determined using P-arrivals at every station in the saturated crack model GK2LFA (model RSQ1NZ, Table C.4).
(d) Locations determined using P- and S-arrivals at every station in the saturated crack model GK2LFA (model RSQ1NY, Table C.4).
Notation and parameters as in Fig.3.4.

NORMAL FAULT

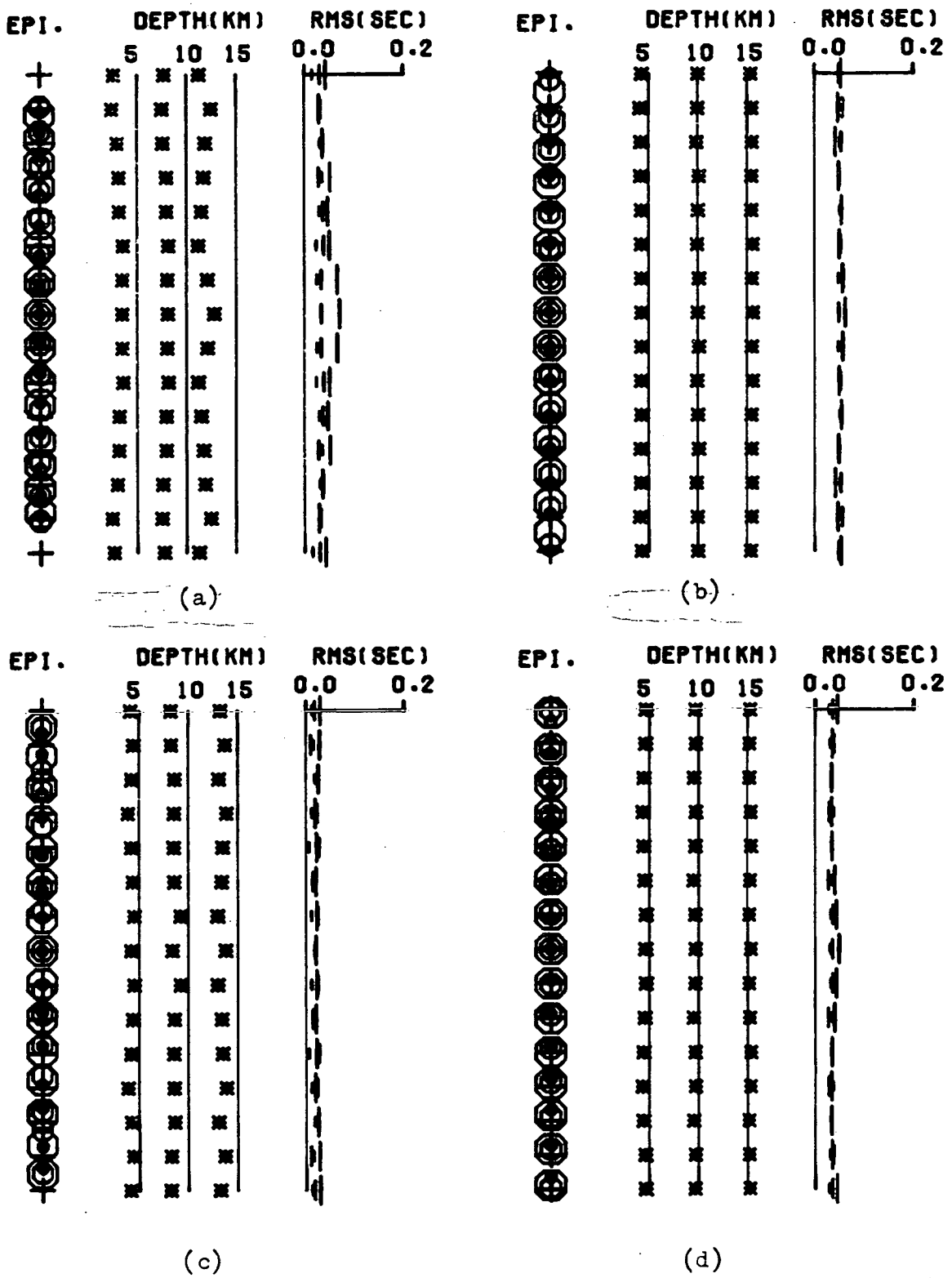

the location procedure again results in more accurate depth determinations.

The RMS errors associated with the relocations are generally quite low. The estimated errors of the hypocentres (Table C.4, Appendix C) are again significantly smaller than the true error in those cases where the depth of foci have been poorly determined.

3.6 Additional cases

The previous section illustrated that for some anisotropic structures failure to take account of anisotropic velocity variations when locating earthquakes can lead to some very large hypocentral errors even though the events have been located with a high resolution network. However the examples shown should not be considered as general. This section will show that modifications to the network and anisotropic structure can give rise to very different effects.

3.6.1 Location with an irregular network

It is unlikely that a regular network like SQ1 could be deployed in practice. The station locations will be influenced by many factors including access to the site, distance from environmental noise, and, in the case of a radio-linked network, line of sight to the recording station. This will in turn effect the resolution possible for locating earthquakes within or near the network.

We shall use as an irregular network the TDP1 network described in section 2.2. Fig.3.14 shows this network in relation to the hypothetical earthquakes that are to be relocated. This roughly corresponds to a concentration of epicentres detected in the TDP1 experiment (see Fig.2.2, N.B. this does not correspond to the surface trace of the Northern Anatolian Fault). Figs.3.15, 3.16 and 3.17 illustrate the relocations of these events by the TDP1 network where the dilatancy-anisotropy on each of

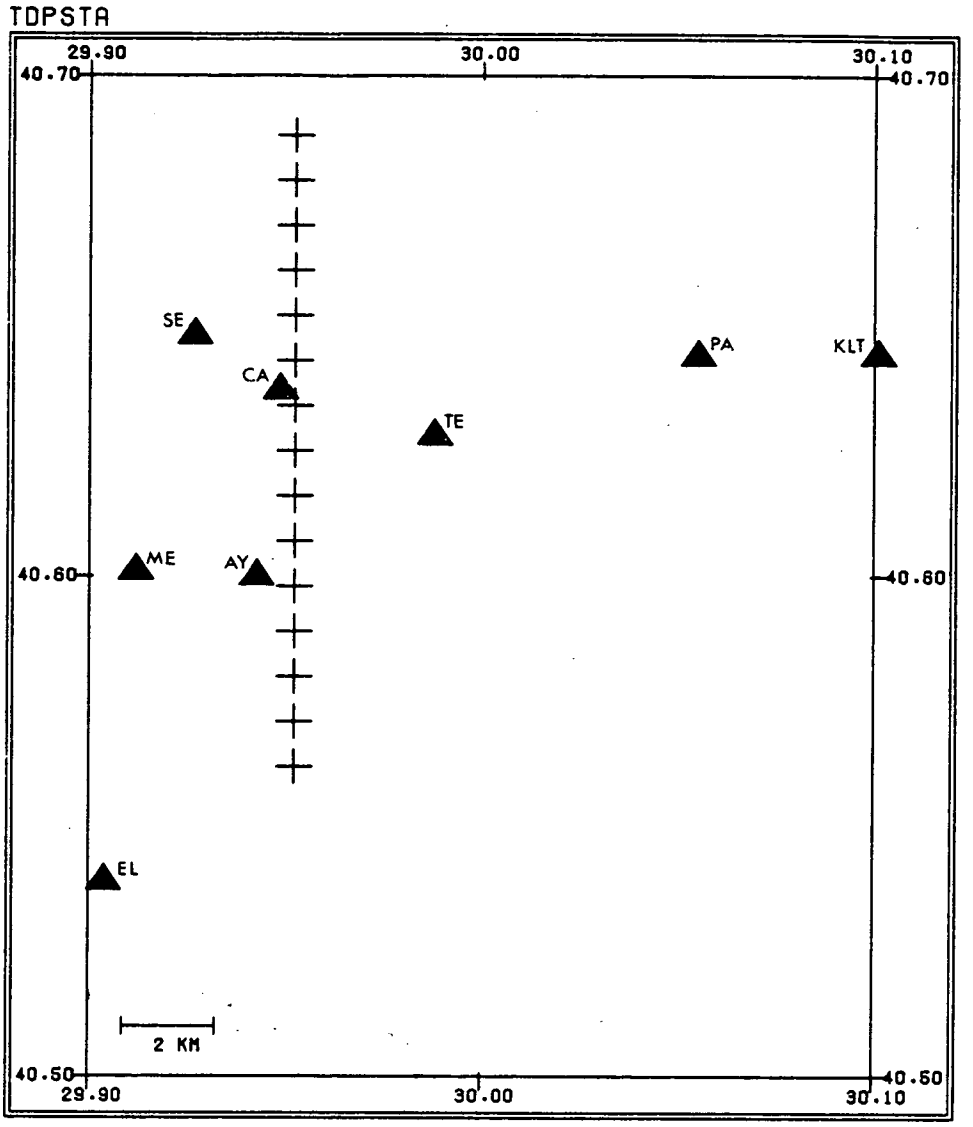

Figure 3.14. Map showing stations of the TDP1 network in relation to the simulated earthquakes that are to be relocated. As in Fig.3.3 a cross denotes the epicentral position of three foci at depths of 5, 10 and 15km. The epicentres are spaced at 1km intervals.

Figure 3.15. A summary of the relocations, by an isotropic half-space program, of the events of Fig.3.14 in a half-space that models dilatancy-anisotropy on a strike-slip fault with a system of parallel cracks.
(a) Locations determined using P-arrivals at every station in the dry crack model GKFF1 (model MTP1SZ, Table C.5).
(b) Locations determined using P- and S-arrivals at every station in the dry crack model GKFF1 (model MTP1SY, Table C.5).
(c) Locations determined using P-arrivals at every station in the saturated crack model GKLF1 (model NTP1SZ, Table C.5).
(d) Locations determined using P- and S-arrivals at every station in the saturated crack model GKLF1 (model NTP1SY, Table C.5).
Notation and parameters as in Fig.3.4.

STRIKE-SLIP FAULT

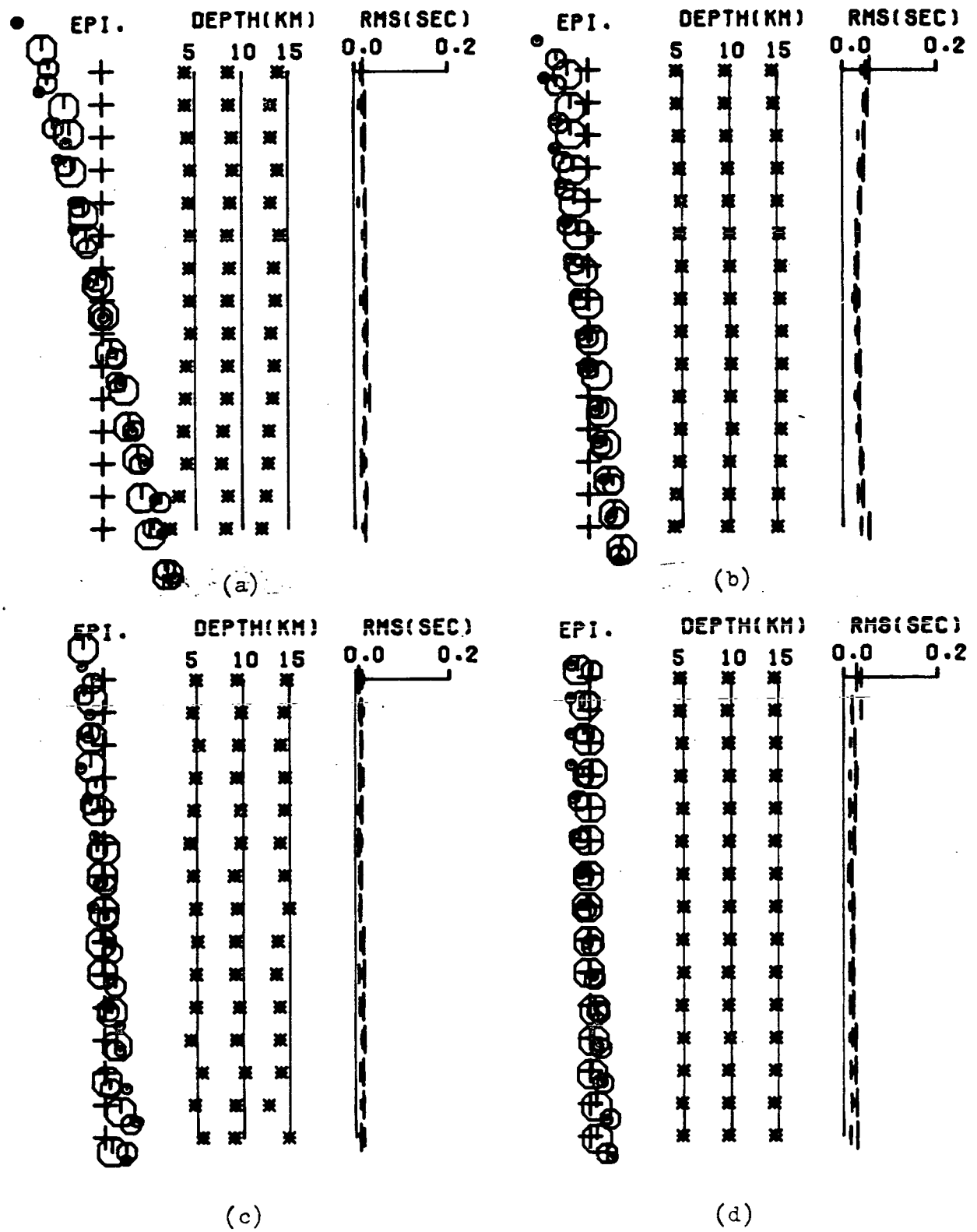

Figure 3.16. A summary of the relocations, by an isotropic half-space program, of the events of Fig.3.14 in a half-space that models dilatancy-anisotropy on a thrust fault with a system of parallel cracks.
(a) Locations determined using P-arrivals at every station in the dry crack model GKFF1 (model MTP1TZ, Table C.5).
(b) Locations determined using P- and S-arrivals at every station in the dry crack model GKFF1 (model MTP1TY, Table C.5).
(c) Locations determined using P-arrivals at every station in the saturated crack model GKLF1 (model NTP1TZ, Table C.5).
(d) Locations determined using P- and S-arrivals at every station in the saturated crack model GKLF1 (model NTP1TY, Table C.5).
Notation and parameters as in Fig.3.4.

THRUST FAULT

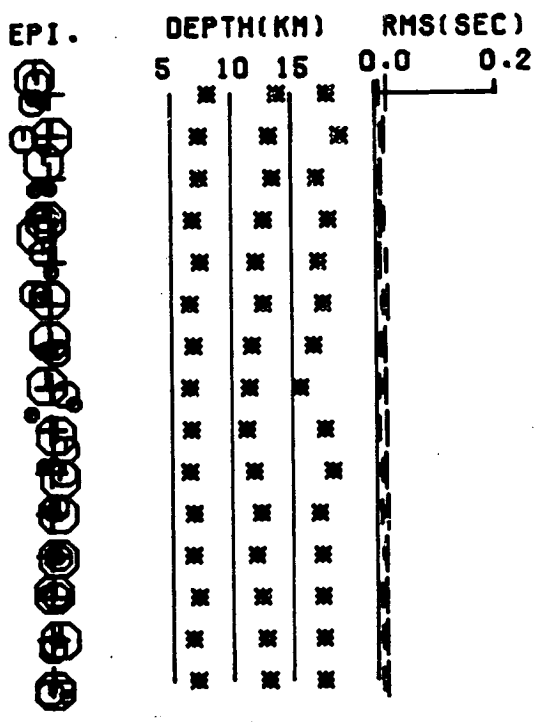

(a)

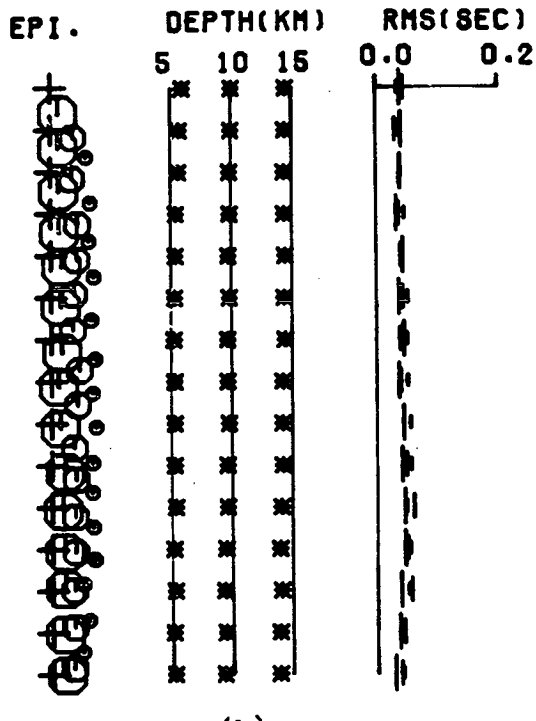

(b)

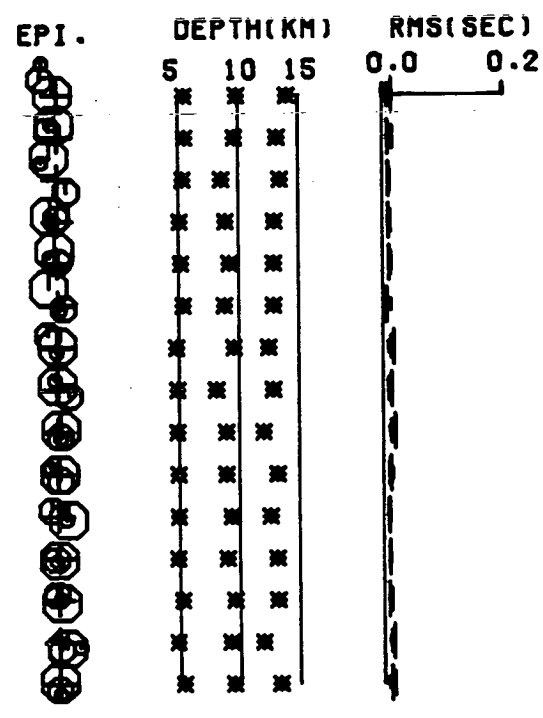

(c)

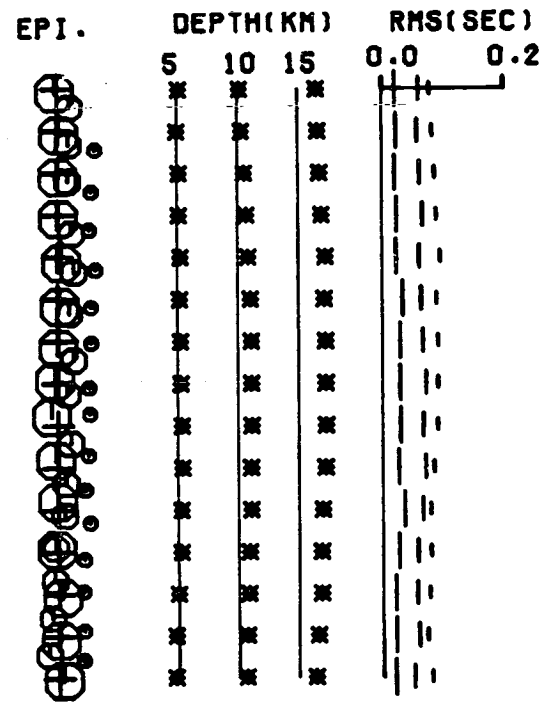

(d)

Figure 3.17. A summary of the relocations, by an isotropic half-space program, of the events of Fig.3.14 in a half-space that models dilatancy-anisotropy on a normal fault with a system of parallel cracks.
(a) Locations determined using P-arrivals at every station in the dry crack model GKFF1 (model MTP1NZ, Table C.5).
(b) Locations determined using P- and S-arrivals at every station in the dry crack model GKFF1 (model MTP1NY, Table C.5).
(c) Locations determined using P-arrivals at every station in the saturated crack model GKLF1 (model NTP1NZ, Table C.5).
(d) Locations determined using P- and S-arrivals at every station in the saturated crack model GKLF1 (model NTP1NY, Table C.5).
Notation and parameters as in Fig.3.4.

NORMAL FAULT

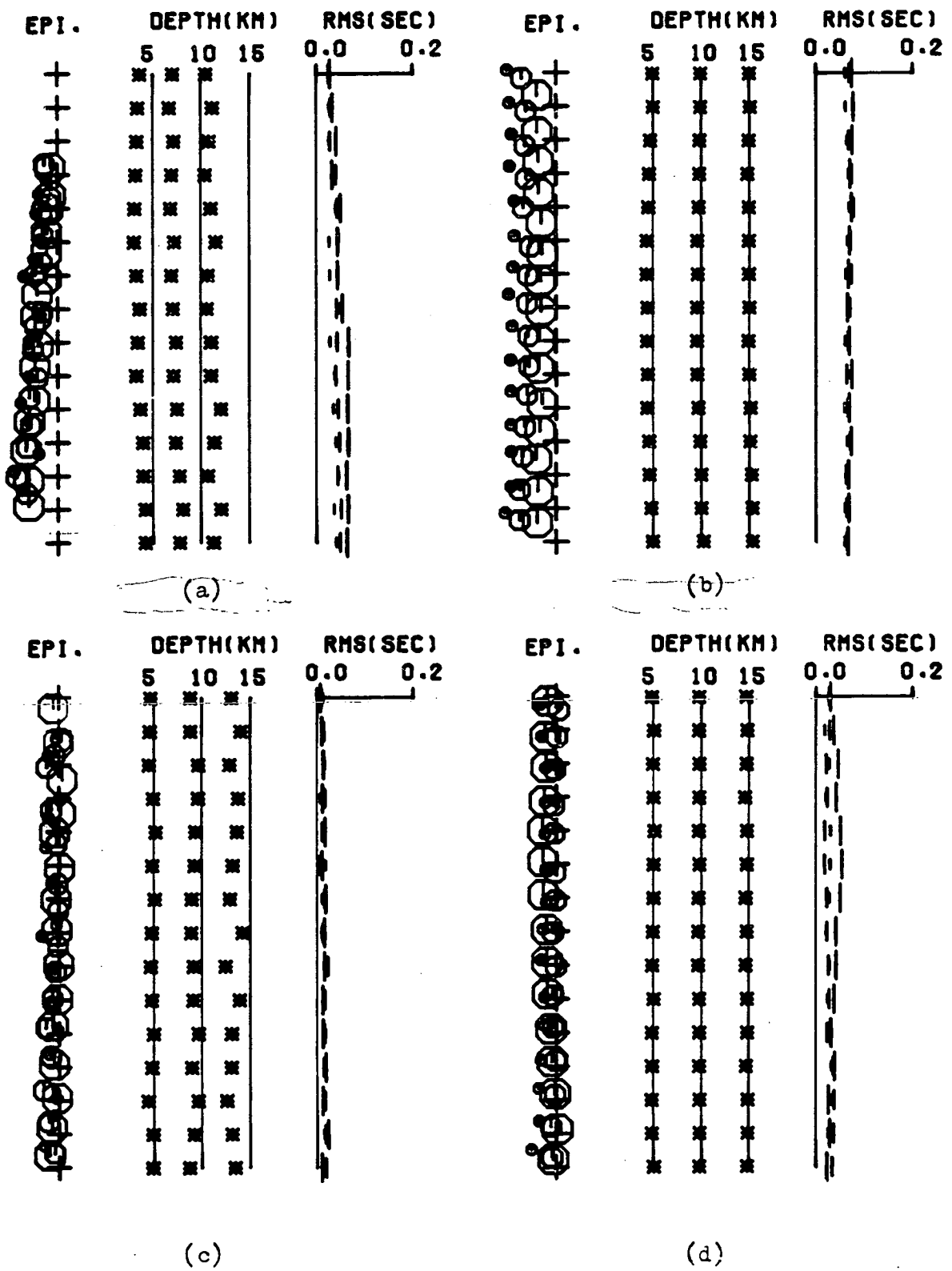

the pure faults has been modelled by the parallel crack system of crack model 1. These figures correspond to Figs.3.5, 3.8 and 3.11 for the SQ1 network. In the case of the strike-slip fault (Fig.3.15) the angle between the plane of the relocations and the true fault plane is greater in all cases with the TDP1 network, although the error in depths is slightly less. For the pure-thrust (Fig.3.16) and pure-normal (Fig.3.17) faults there is more scatter on the epicentral locations and in some cases the relocated epicentres display a clear offset from the fault plane (Figs.3.16(b) and 3.17(b)). This is due to the irregular nature of the network resulting in stations on one side of the fault having a greater effect than stations on the opposite side. In these two cases the depth mislocations are similar to those with the SQ1 network. In all cases the RMS errors are less for the relocations by the TDP1 network, despite the true errors being greater. In some cases the RMS errors are almost as low as in the isotropic control case (Fig.3.4), particularly when only P-arrivals are used to locate the events. Although this effect can be expected to a certain extent, because of the fewer stations in this network, the estimated errors of the relocated hypocentres are less than with the SQ1 network, and are less than half the true error (Table C.5, Appendix C). The mislocations by the TDP1 network can be considered as being significant at the 95% confidence level. The assumption of isotropy when locating earthquakes in an anisotropic half-space with the TDP1 network, is an inadequate approximation. Such an approximation would mean that the fault planes associated with events located by the TDP1 network would not correspond with the true fault plane.

3.6.2 Increased crack density

In previous sections the crack density of all the models has been 0.1. This value stems from the theoretical work of Griggs, Jackson, Knopoff & Shreve (1975) on Vp/Vs anomalies. They assume a crack density of 0.2 for

randomly oriented cracks corresponding to a Vp reduction of 18%, which is approximately that observed in field observations. The corresponding crack density for parallel cracks is 0.1 (Crampin 1978). Obviously the crack density could be greater either due to an increased number of cracks per unit volume, or because of cracks with greater dimensions. Fig.3.18 shows the group-velocity-surfaces through a system of parallel, saturated cracks, with crack density 0.4 (model GKLF4 - Table A.1). This corresponds to crack model 1 with an increased crack density. Locating the events of Fig.3.3 using the SQ1 network in this crack structure, oriented to model a strike-slip fault, produces the locations shown in Fig.3.19. This figure should be compared with Fig.3.5c and 3.5d. This figure is particularly interesting because, unlike all the other examples, the use of shear-arrivals results in greater errors. This is because of the complicated variation in the fastest shear-wave group-velocity-surface dominating the weaker variation of the P-wave surface. However the RMS errors are considerably increased with the addition of shear-wave data in the location procedure. This example illustrates that systematic mislocation effects produced by the dry crack model can be reproduced by saturated cracks with a greater crack density, but apparently at the expense of larger RMS errors. The estimated error of the hypocentres are typically equal to, or greater than, the true error (Table C.6, Appendix C). Obviously, decreasing the crack density will result in more accurate locations due to the lower degree of velocity-anisotropy.

3.6.3 Crack systems of intermediate orientation

The preceding sections considered only pure-fault motion. This is a reasonable approximation at, or near, the Earth's surface where one of the stress directions must be vertical. However, at depth, there is usually a component of motion associated with the pure motion. This means that the

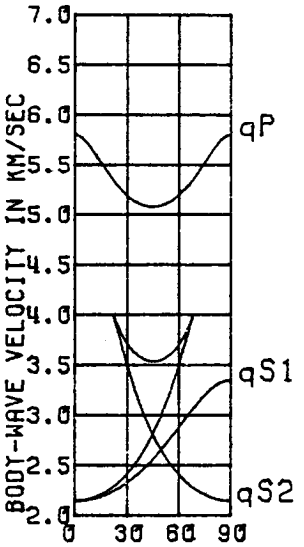

Figure 3.18. Quadrant sections through the wave-surfaces of a system of saturated parallel cracks with crack density 0.4, set in an originally isotropic matrix.

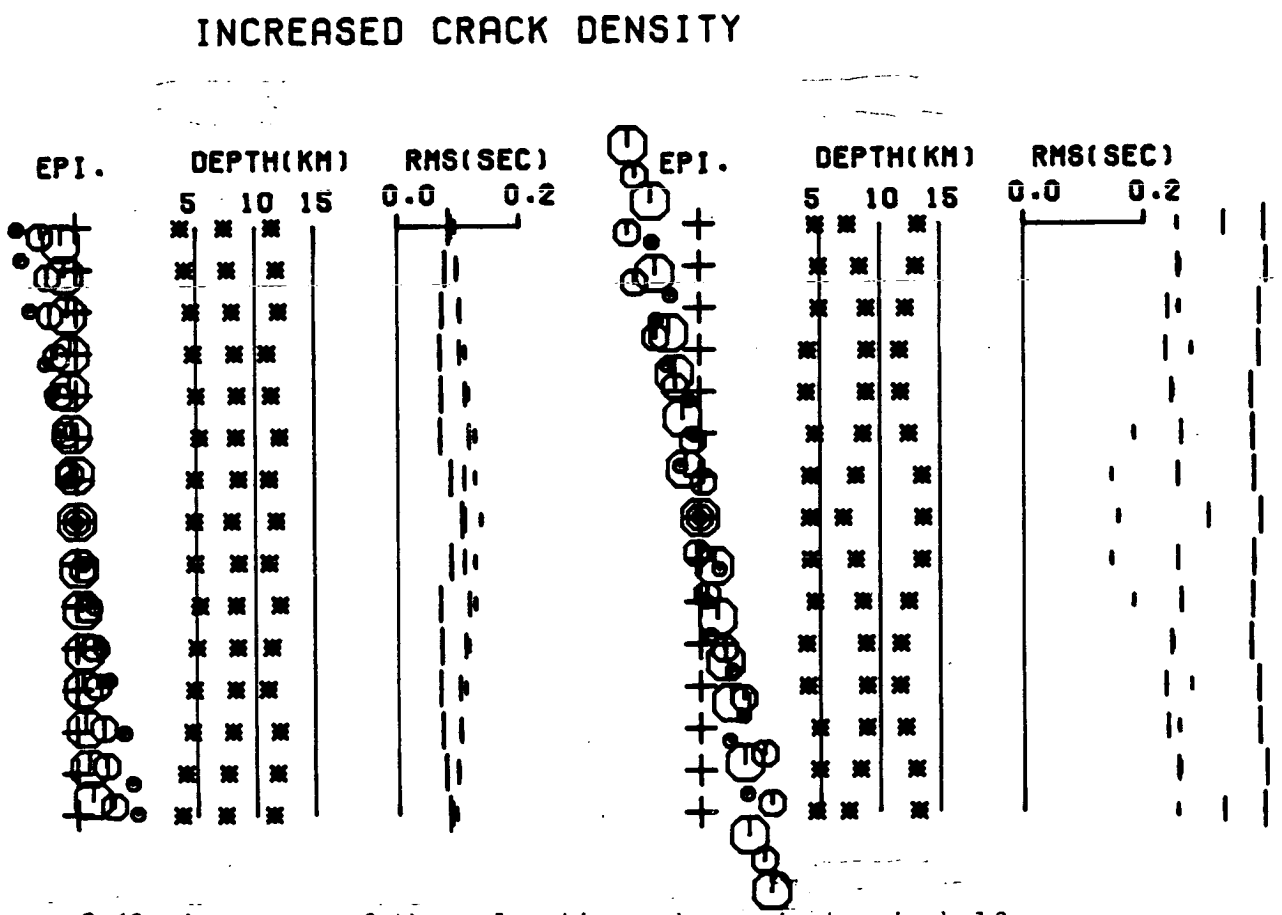

Figure 3.19. A summary of the relocations, by an isotropic half-space program, of the events of Fig.3.3 in a half-space that models dilatancy-anisotropy on a strike-slip fault with a system of parallel cracks of crack density 0.4.
(a) Locations determined using P-arrivals at every station (model N1SQSZ, Table C.6).
(b) Locations determined using P- and S-arrivals at every station (model N1SQSY, Table C.6).
Notation and parameters as in Fig.3.4.

stress axes no longer lie in the vertical/horizontal planes, and one would expect the orientation of the crack system to be modified accordingly. Another cause of crack orientations departing from the vertical/horizontal plane is the effect of pre-existing rock fabric. Hadley (1975) suggests that even a slight foliation such as is found in Westerly granite, can produce more than 10% departures from axial symmetry of cracks, if that foliation does not coincide with the maximum stress direction. Spetzler, Sobolev, Sondergeld, Salov, Getting & Koltsoz (1981) find that the cracks that were created in a sample of pyrophillite under polyaxial stress conditions were aligned closer to the direction of maximum shear stress, about 30-40 degrees from the direction of maximum compression. This effect may have been observed because the layering in the pyrophillite was always perpendicular to the direction of maximum compressive stress in their experiments. Haimson (1981) suggested that similar phenomena would be observed in large-scale testing of hydraulic fracturing of rocks. These experiments suggest that the axes of the dilatancy-anisotropy need not coincide with the principal stress directions. Figs.3.20, 3.21 and 3.22 illustrate the effect on the hypocentral locations caused by rotating the axis of rotational symmetry in crack model 1, 30 degrees away from the direction that might be associated with pure-fault motion.

Fig.3.20 illustrates the relocations on the strike-slip fault model. In this case the axis of rotational symmetry has been rotated 30 degrees above the horizontal about the direction of maximum compression. Therefore the axis of maximum compression is still horizontal and at an azimuth of 45 degrees. In the dry crack structures, the relocated hypocentres define a dipping plane that strikes at an angle to the true hypocentral plane. The depth of the relocations show an improvement compared to the pure-fault motion (Fig.3.5). The locations in the saturated crack structure show little difference when compared to those in the pure-fault model. The RMS

errors in Fig.3.20a are noticeably smaller than the corresponding values of Fig.3.5a, despite the increased epicentral errors. The estimated errors of the hypocentres (Table C.7, Appendix C) are generally equal to the true error.

Fig.3.21 illustrates the relocations on a thrust fault where the axis of rotational symmetry is no longer vertical but has been offset by 30 degrees from the upward vertical towards the east. For relocations determined in the dry crack model this results in a very large, linear offset to one side of the fault. This is because stations to the east of the true hypocentral plane are in low velocity directions, while the stations to the west are in high velocity directions. This results in each hypocentre being offset to the west in the high velocity direction. Fig.3.21c illustrates the complicated effect of a 4θ variation in P-wave velocity. Ray paths from the shallow (5km) events to the stations to the west are in high velocity directions (being ~90 degrees away from the axis of symmetry), and so are offset to the west. The deepest events (15km) have high velocity paths to the eastern stations (along the direction of the axis of symmetry) and are therefore offset to the east. This effect disappears when shear-wave data, with a strong 2θ variation is included. The depth of the relocations is similar to the case in the pure fault model (Fig.3.8), and the RMS errors are almost identical despite the actual hypocentral error being substantially increased. The estimated hypocentral errors (Table C.7) in the dry crack models do not provide any indication of the very large errors, and are typically less than 1/3 of the true error. This is not the case for the saturated crack model.

Fig.3.22 shows the case where the axis of rotational symmetry on a pure-normal fault has been rotated by 30 degrees below the surface to the west about the intermediate axis parallel to the line of epicentres. Again there are very large offsets in the epicentral relocations to the west of

Figure 3.20. A summary of the relocations, by an isotropic half-space program, of the events of Fig.3.3 in a half-space that models dilatancy-anisotropy on a strike-slip fault with a system of parallel cracks where the axis of rotational symmetry strikes at an angle of 135 degrees from North and is inclined above the surface by 30 degrees.
(a) Locations determined using P-arrivals at every station in the dry crack model GKFF1 (model MDSQSZ, Table C.7).
(b) Locations determined using P- and S-arrivals at every station in the dry crack model GKFF1 (model MDSQSY, Table C.7).
(c) Locations determined using P-arrivals at every station in the saturated crack model GKLF1 (model NDSQSZ, Table C.7).
(d) Locations determined using P- and S-arrivals at every station in the saturated crack model GKLF1 (model NDSQSY; Table C.7).
Notation and parameters as in Fig.3.4.

STRIKE-SLIP FAULT

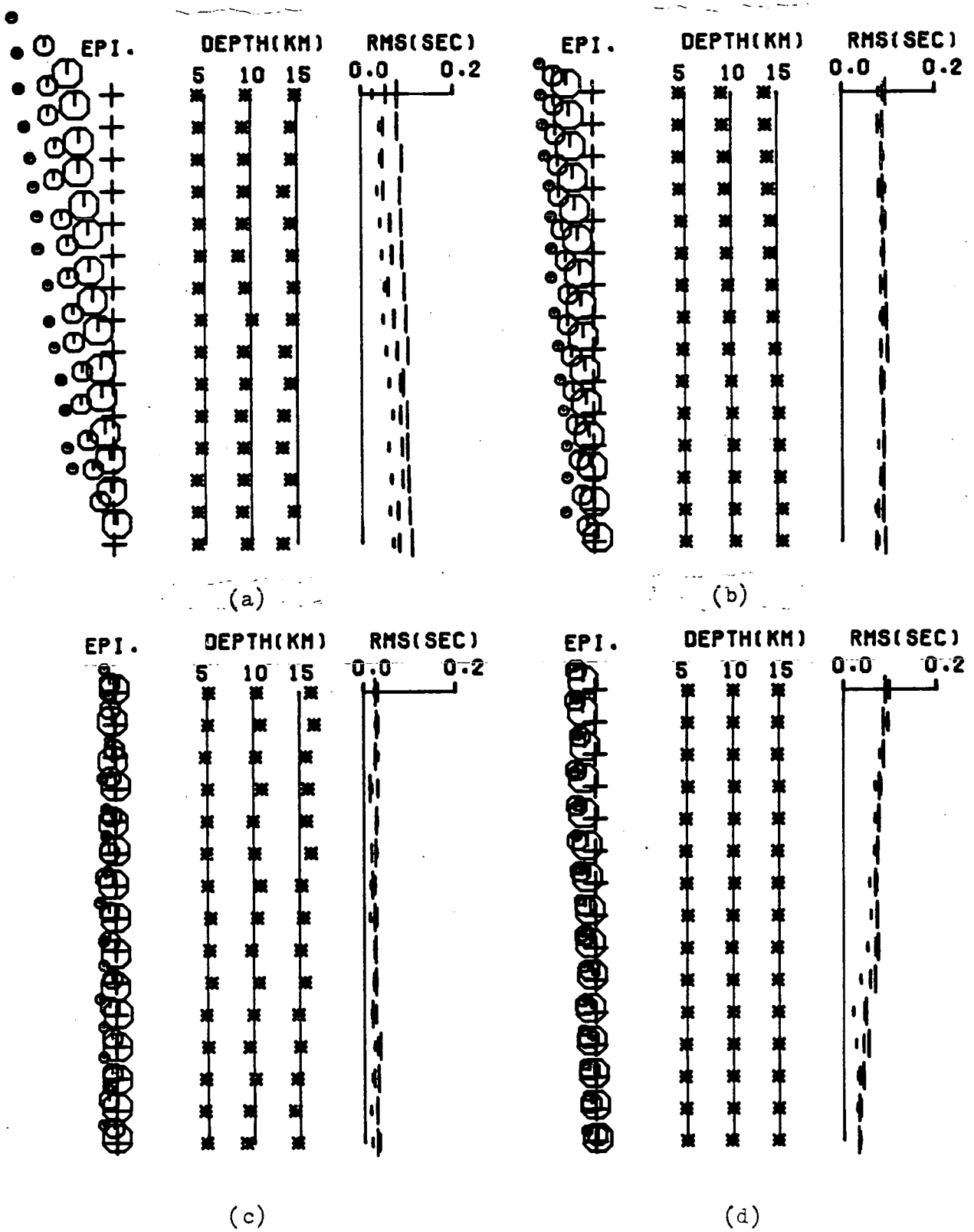

Figure 3.21. A summary of the relocations, by an isotropic half-space program, of the events of Fig.3.3 in a half-space that models dilatancy-anisotropy on a thrust fault with a system of parallel cracks where the axis of rotational symmetry dips below the surface by 60 degrees to the West.
(a) Locations determined using P-arrivals at every station in the dry crack model GKFF1 (model MDSQTZ, Table C.7).
(b) Locations determined using P- and S-arrivals at every station in the dry crack model GKFF1 (model MDSQTY, Table C.7).
(c) Locations determined using P-arrivals at every station in the saturated crack model GKLF1 (model NDSQTZ, Table C.7).
(d) Locations determined using P- and S-arrivals at every station in the saturated crack model GKLF1 (model NDSQTY, Table C.7).
Notation and parameters as in Fig.3.4.

THRUST FAULT

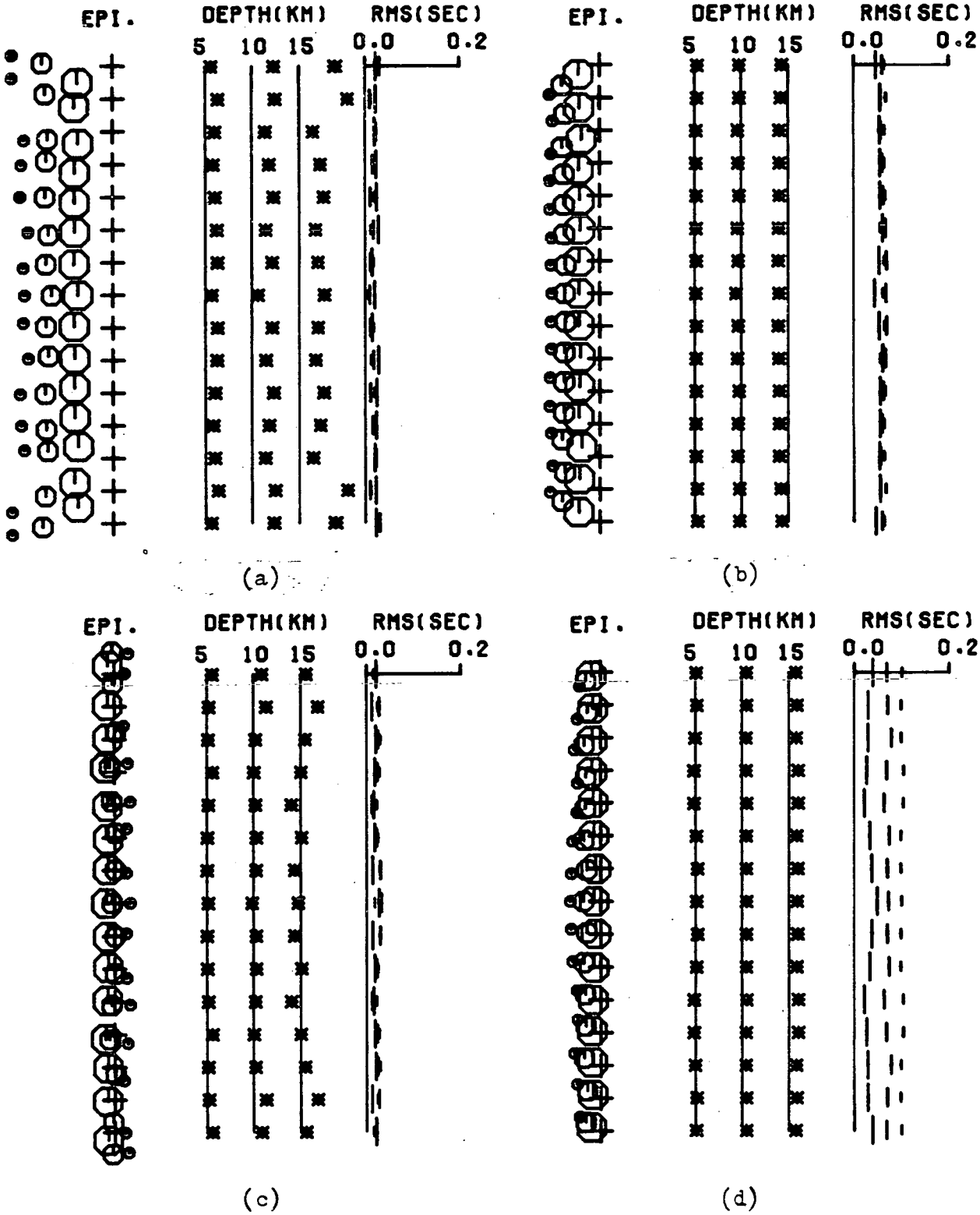

Figure 3.22. A summary of the relocations, by an isotropic half-space program, of the events of Fig.3.3 in a half-space that models dilatancy-anisotropy on a normal fault with a system of parallel cracks where the axis of rotational symmetry dips below the surface by 30 degrees to the West.
(a) Locations determined using P-arrivals at every station in the dry crack model GKFF1 (model MDSQNZ, Table C.7).
(b) Locations determined using P- and S-arrivals at every station in the dry crack model GKFF1 (model MDSQNY, Table C.7).
(c) Locations determined using P-arrivals at every station in the saturated crack model GKLF1 (model NDSQNZ, Table C.7).
(d) Locations determined using P- and S-arrivals at every station in the saturated crack model GKLF1 (model NDSQNY, Table C.7).
Notation and parameters as in Fig.3.4.

NORMAL FAULT

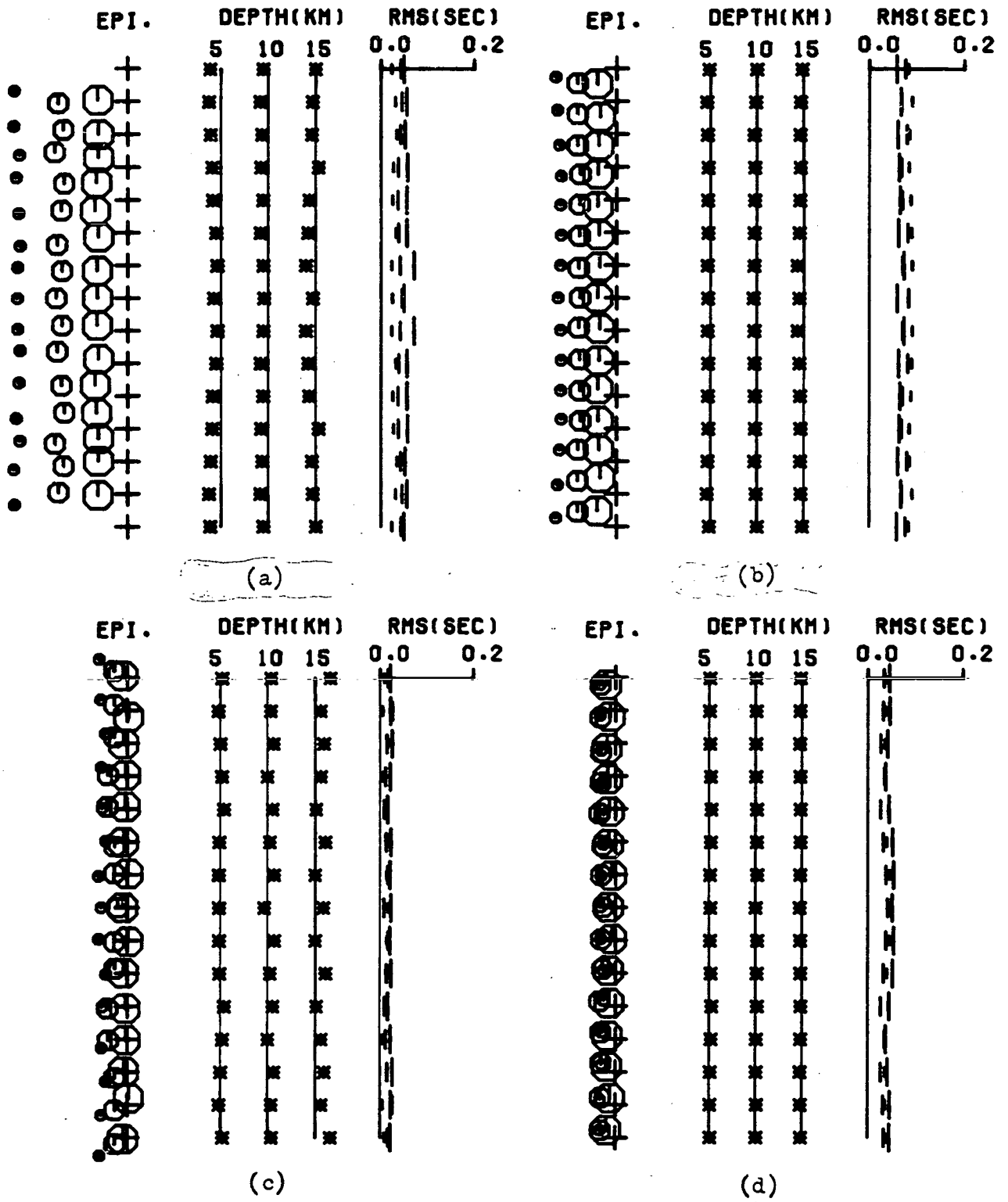

the true hypocentral plane in the apparent high velocity direction. The depth of the relocations, controlled by the stations immediately above the hypocentres, are approximately correct as the velocity in the vertical direction is about equal to the assumed velocity. Again the RMS errors are almost the same as in the pure-fault model (Fig.3.11) although the true hypocentral errors are greatly increased. Again, the estimated hypocentral errors (Table C.7) in the dry crack model are significantly less than the true error, but this is not the case in the saturated crack model.

3.7 Apparent hypocentral migrations during an idealised dilatancy-anisotropy episode

It is unlikely that the form and degree of dilatancy-anisotropy will remain constant during the earthquake preparation process. The anisotropic velocity variations are likely to vary in response to changes in the level of stress, degree of saturation of the cracks, and with variations in the orientation of the stress field. A simple interpretation of the dilatancy-diffusion model of earthquake preparation (Nur, 1972; Scholz et al. 1973) suggests that initially a system of aligned dry cracks will be created in the source region and that these will later become saturated by the migration of pore fluid from peripheral areas. The assumption of a consistent, isotropic velocity model when locating earthquakes throughout such an episode will not only lead to systematic mislocations as demonstrated in the previous sections, but also to apparent migrations of hypocentres. In order to simulate such a sequence, the dilatancy episode can be divided into four stages on the basis of the dilatancy-diffusion model. These stages are: A) isotropic propagation (possibly through a system of randomly oriented, saturated or partially saturated cracks); B) anisotropic propagation through aligned, dry cracks; C) anisotropic propagation through aligned, saturated cracks; and, D) isotropic

propagation after the main event (possibly again through a system of randomly oriented, saturated or partially saturated cracks).

From the previous section it can be seen that there may be a small, apparent epicentral migration as the impending earthquake source region progresses through the various stages described above. In the case of a strike-slip fault (Fig.3.5), the epicentres would appear to migrate away from the true fault plane in the first stage, and migrate back to the impending source region in the second stage. This form of apparent epicentral migration would also be observed on thrust or normal faults if the orientation of the anisotropy deviated from the horizontal/vertical plane, or if an irregular network such as TDP1 was used to locate the earthquakes. There would be no migrational effect on such faults in the unlikely case where a regular network was used, and the orientation of the velocity-anisotropy was symmetrical with the source/reciever geometry. Although the effect on epicentres is very small, the effect on the depth of the relocations is much more significant.

In order to model apparent depth migrations, the isotropic P- and S-velocities used to locate the earthquakes must be carefully selected. The choice of these velocities will have little effect on the epicentral relocations by the SQ1 network, but would obviously alter the depth of foci determined by the location program. It will be assumed that, in practise, the velocity structure beneath the network has been determined in stage A - before the onset of dilatancy-anisotropy in the source region, and that there would be no change in overall crack density during the process whereby an aligned system of cracks was created from a pre-existing system of randomly oriented, saturated cracks. The anisotropic crack models used in previous sections had a crack density of 0.1, and intrinsic P- and S-velocities of 5.8km/sec and 3.349km/sec respectively (Crampin 1978). Using these parameters in conjunction with the expressions for elastic moduli

derived by Garbin & Knoppoff (1975), for a medium with randomly-oriented, liquid-filled cracks, provides effective P- and S-velocities of 5.686km/sec and 3.206km/sec. These velocities will be used to locate the events of Fig.3.3 in order to model possible depth migrations, rather than the average velocities from the anisotropic velocity look-up tables, as have been used previously.

Possible forms of a temporal variation in the depth of seismic activity are illustrated in Figs.3.23, 3.24a and 3.24b where crack model 1 of section 3.2 has been used to model dilatancy on each of the pure faults and the SQ1 network has been used to relocate the events in Fig.3.3. The figures show the apparent migrations of foci determined by isotropic relocations of events in an idealised episode of dilatancy-anisotropy. If the absolute value of the Student's t-ratio, marked at each depth interval is greater than a critical level, the hypothesis that the means are from the same population can be rejected. The critical level of the Student's t-ratio at the 95% significance level in this study is approximately 2.2 (Haber & Runyon 1973). The figures illustrate a marked variation in the apparent depth of seismic activity occurring throughout the history of a dilatancy zone. In almost all cases the depths of the events decrease in the dry crack stage and increase in the saturated crack stage. The exception is Fig.3.23c, which illustrates the locations on a thrust fault determined using only P-arrivals. In this case the events appear to be deeper in the dry crack stage, and decrease in the saturated crack stage. Figs.3.24c and 3.24d illustrate the case where the TDP1 network has been used to locate events using the pure-strike-slip fault model. The error bars are smaller in both stages of the idealised dilatancy episode, compared to the locations by the SQ1 network, but the Student's t-ratios in comparison show a decrease in the dry crack stage, and an increase in the saturated stage. However the diagram illustrates that for both networks a

Figure 3.23. A summary of the apparent focal depth migration of the events of Fig.3.3 throughout an idealised dilatancy episode, modelled by a system of parallel cracks, and when the same isotropic velocity model is used throughout the complete episode.

(a) Locations using P-arrivals at every station and where the dilatancy-anisotropy models that associated with a strike-slip fault.

(b) Locations using P- and S-arrivals at every station and where the dilatancy-anisotropy models that associated with a strike-slip fault.

(c) Locations using P-arrivals at every station and where the dilatancy-anisotropy models that associated with a thrust fault.

(d) Locations using P- and S-arrivals at every station and where the dilatancy-anisotropy models that associated with a thrust fault.

Each part consists of three diagrams:- 1) the upper diagram - the apparent depth migration of the three foci at 5, 10 and 15km depth at the central epicentre in Fig.3.3 at four stages in a possible dilatancy episode. Time from left to right: A) unstressed isotropic structure; B) stressed distribution of dry cracks; C) stressed distribution of saturated cracks; and D) de-stressed isotropic structure. The error bars indicate the standard deviation of the depth determination of the location at that particular depth interval. The depth determinations in the isotropic stages represent the correct depth of focus and no error bar has been plotted. 2) bottom left - a histogram of the depth distributions of the 15 events at each depth interval in the dry-crack stage of dilatancy. The dashed lines represent the true hypocentral depths. The number plotted at each depth interval is the Student t-ratio calculated for the events at that particular depth interval; 3) bottom right - equivalent to part (2) for the saturated crack stage of the episode.

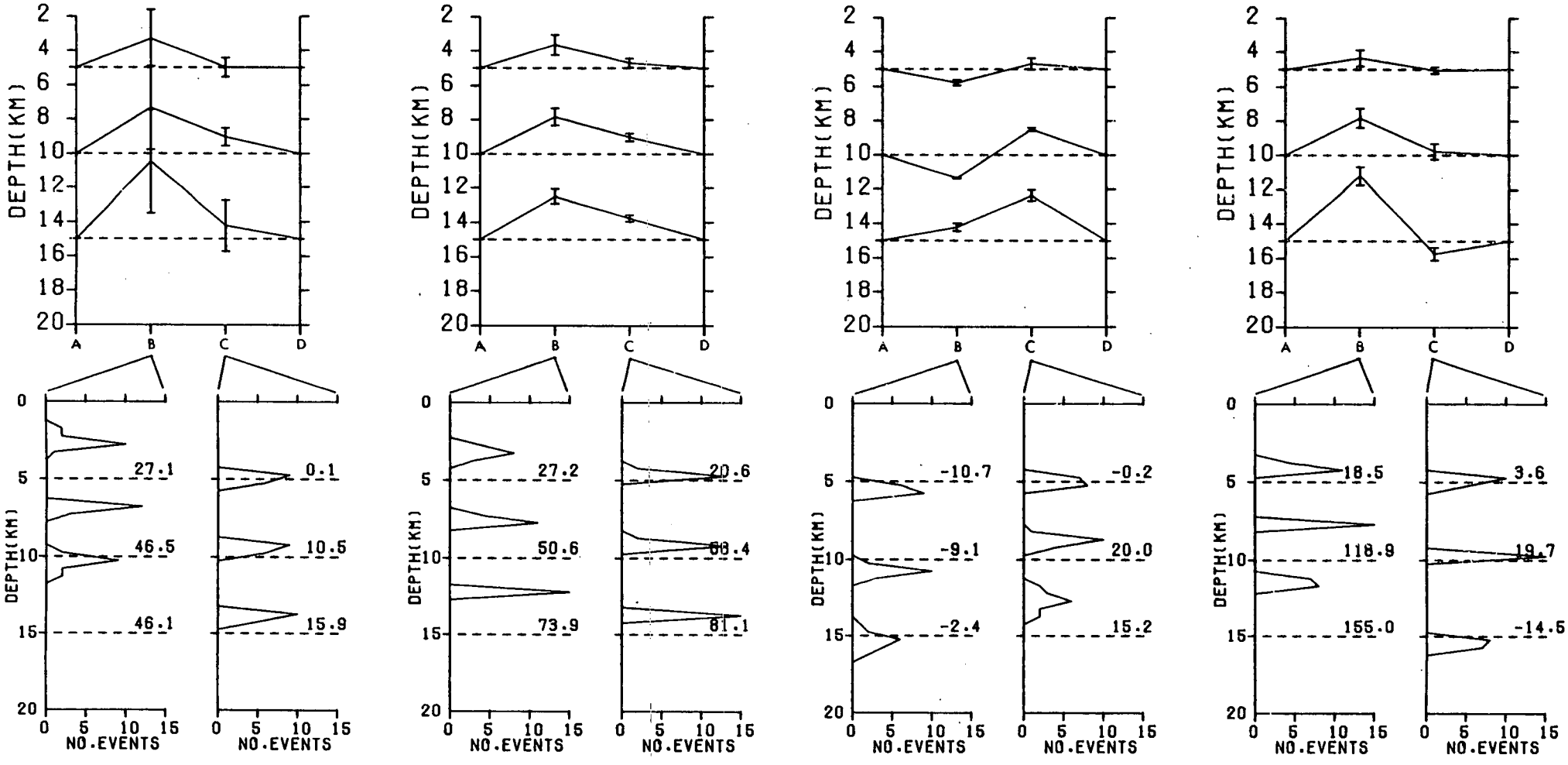
DEPTH(KM)
2
4
6
8
10
12
14
16
18
20
A
B
C
D
0
5
10
15
20
27.1
46.5
46.1
0.1
10.5
15.9
27.2
50.6
73.9
20.6
-10.7
-9.1
-2.4
-0.2
20.0
15.2
18.5
118.9
155.0
3.6
19.7
-14.5
NO.EVENTS
(a)
(b)
(c)
(d)

Figure 3.24. A summary of the apparent focal depth migration of the events of Fig.3.3 and Fig.3.14 throughout an idealised dilatancy episode, modelled by a system of parallel cracks, and when the same isotropic velocity model is used throughout the complete episode.
(a) Locations using P-arrivals at every station in the SQ1 network and where the dilatancy-anisotropy models that associated with a normal fault.
(b) Locations using P- and S-arrivals at every station in the SQ1 network and where the dilatancy-anisotropy models that associated with a normal fault.
(c) Locations using P-arrivals at every station in the TDP1 network and where the dilatancy-anisotropy models that associated with a strike-slip fault.
(d) Locations using P- and S-arrivals at every station in the TDP1 network and where the dilatancy-anisotropy models that associated with a strike-slip fault.
Notation and format as in Fig.3.23.

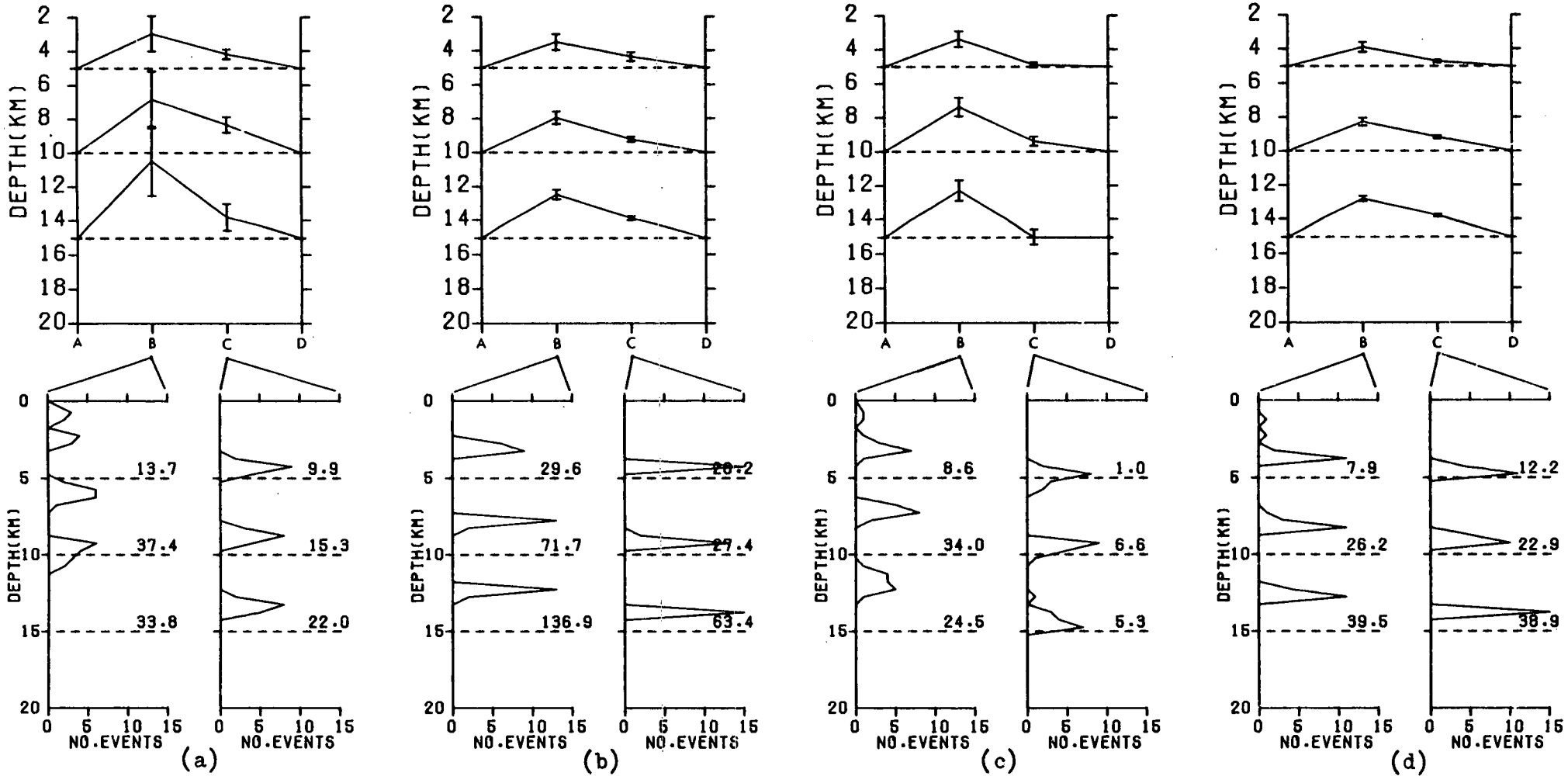
DEPTH(KM)
2
4
6
8
10
12
14
16
18
20
A
B
C
D
0
5
10
15
20
13.7
37.4
33.8
9.9
15.3
22.0
29.6
71.7
136.9
20.2
27.4
63.4
8.6
34.0
24.5
1.0
6.6
5.3
7.9
26.2
39.5
12.2
22.9
38.9
NO.EVENTS
(a)
(b)
(c)
(d)

similar migration effect would be observed. In almost all cases the value of the Student's t-ratio and the size of the estimated errors associated with the depth determinations are such that the variations would be interpreted as a real migration of earthquakes. The form of the depth variation is, however, dependent on the orientation of the dilatancy-anisotropy and on whether S-arrivals are incorporated in the location procedure.

3.8 Discussion

The previous sections presented examples of the effect of assuming isotropy when locating events in an anisotropic half-space. It has been clearly demonstrated that failure to take account of anisotropic velocity variations when locating earthquakes can lead to very large systematic errors. This is particularly true when only P-arrivals are used in the hypocentral determination, and when the structure is strongly anisotropic. The use of shear-arrivals, in addition to the P-arrivals, improves the accuracy the locations. This is a well known phenomenon (Buland 1976) and is a result of the S-P times constraining the origin time which in turn restricts the other hypocentral parameters. The normal indicators of location quality, the RMS of the travel-time residuals and the estimated errors, do not always reflect the general inaccuracy of the hypocentral location. This is nearly always the case for the locations determined by the irregular TDP1 network, and demonstrates the importance of the overall source-to-reciever geometry in deploying networks of seismic stations. The effect of anisotropy on hypocentral locations cannot be generalised. Although the effects are modified by the station distribution and the choice of isotropic model, the dominant factor in the locations is the orientation, form and degree of the anisotropic velocity variations. These parameters will determine whether the epicentres are located on the fault

trace, offset to one side, or at an angle across it. It is not possible to allow for the effects of anisotropy without being able to identify and quantify the variations in some way.

It is possible that the systematic mislocations only represent secondary minima in the earthquake location hypersurface, or that a more sophisticated location program, such as HYPO71 (Lee & Lahr 1975) would produce improved solutions. The first point has been checked by initiating the location procedure from the correct hypocentral locations. This process results in almost the same mislocations as before, demonstrating that these represent primary minima in the hypersurface. HYPO71 employs a process of 'step-wise' multiple regression which means that only the hypocentral parameters that will be significantly changed are varied at each iteration. This results in increased stability in the location procedure, but is usually only effective in cases where there are only a few arrivals, or if the earthquake has occurred outside the network. Fig.3.25 illustrates the locations determined by HYPO71 using the SQ1 network and where crack model 1 of section 3.2 is used to model dry crack dilatancy-anisotropy on a pure-strike-slip fault. This figure is equivalent to figures 3.5a and 3.5b. As can be seen the locations determined by HYPO71 are similar to those determined by the half-space location program. Table C.8 (Appendix C) illustrates that the estimated errors calculated by HYPO71 are also similar to those estimated by the simple half-space location program.

Rothman, Greenfield & Hardy (1974), in an attempt at a similar study, simplify the anisotorpic variations by expressing phase-velocities in terms of direction cosines. Crampin & McGonigle (1981), and Crampin & Kirkwood (1981), demonstrate that phase-velocities, modelled by cosines, are only a good approximation to observed group-velocity arrivals for weak anisotropy in planes of mirror symmetry. Group-velocities and the bi-planar nature of

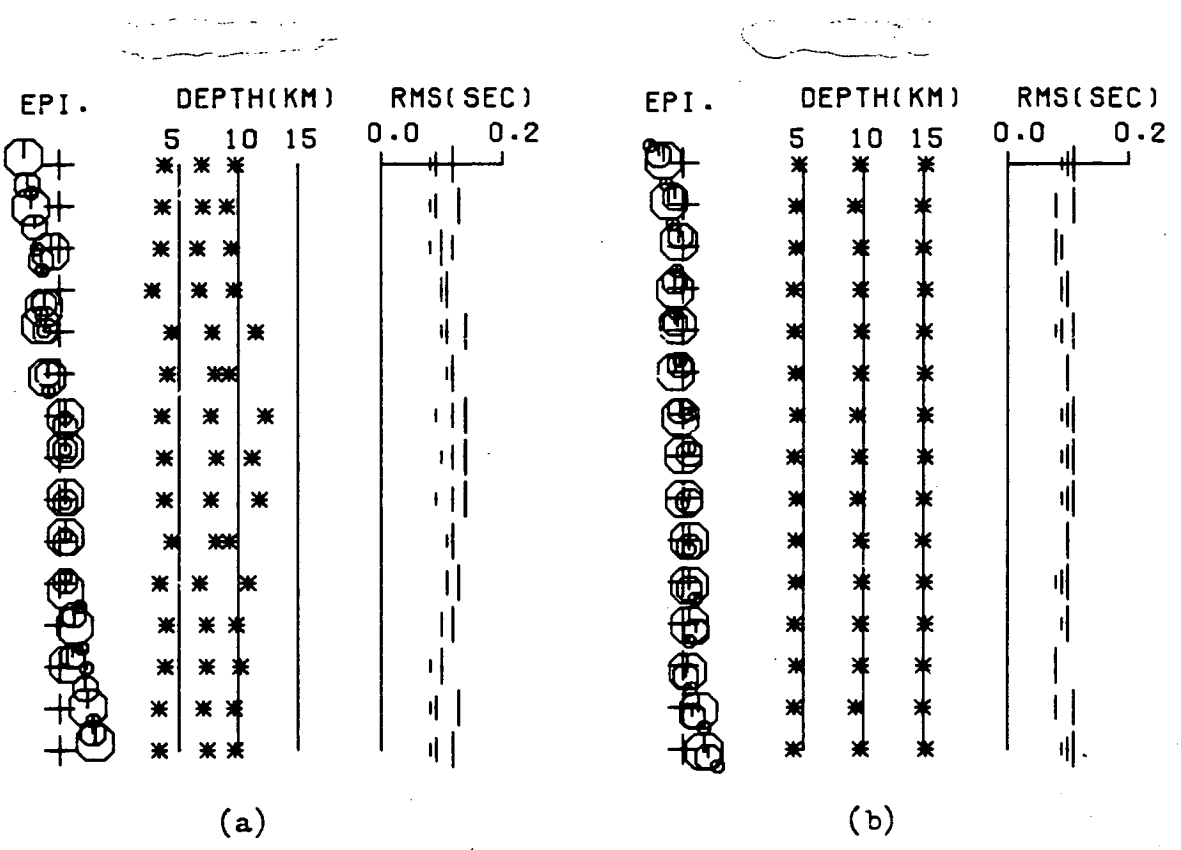

Figure 3.25. A summary of the relocations determined by HYP071 assuming an isotropic half-space and where the true structure is a system of dry, parallel cracks oriented to model dilatancy-anisotropy on a strike-slip fault.
(a) Locations determined using P-arrivals at every station in the SQ1 network (model HYP2P, Table C.8).
(b) Locations determined using P- and S-arrivals at every station in the SQ1 network (model HYP2PS, Table C.8).

shear-wave polarisations in anisotropic media can lead to large observational errors when they are not taken into account. Their analysis uses a high resolution network of stations with regular geometry and only consider P-arrivals with no attempt to simulate observational errors. The approximations of Rothman et al.(1974) are therefore inappropiate and insufficient to model the effect of anisotropy on hypocentral locations.

In order to relate what has been shown here to in situ observations involves many difficulties. The station geometry of most networks will be different from those considered here, and the locations would be based on a mixture of P- and shear-arrivals recorded at various stations in the network. The dilatancy-anisotropy is unlikely to be homogeneous from the source region to all recievers. In addition only a half-space has been modelled here. Although the large velocity variations due to dilatancy-anisotropy may dominate velocity contrasts from a layered structure for direct waves, this half-space approximation may not be adequate on a fault zone where the geological structure is frequently different on either side of the fault, or in a structure where the first arrivals at the network are a mixture of direct and refracted waves. It is particularly difficult to relate depth migrations modelled here to any observed in the field, as the depth parameter is not normally very well determined in local earthquake locations. The depths would be controlled by the station/event distribution and the velocity used to locate the earthquakes. Despite these simplifications, the results presented here do bear some remarkable similarities to 'anomalous' earthquake locations observed in field studies.

Gupta (1974) discusses five observations of aftershock distributions that define a plane that strikes at an angle to the known or inferred fault plane. The persistence of dilatancy-anisotropy after the main shock can be explained by the action of pore fluids and residual stresses maintaining

open cracks (Scholz & Kranz 1974), or by cracks being propped open by debris or because of irregularly matched faces (Batzle, Simmons & Siegfried 1980; Spetzler et al. 1981). However, in each of these observations the deviation is always towards the direction of maximum compression as determined by focal mechanism studies of the main event and its aftershocks. Only a rotation towards the direction of least compression has been modelled here. This contradiction may arise from one or more of several sources:

1) The anomalous observations may be due to a peculiar effect of station geometry coupled with a complicated, layered, isotropic velocity model.

2) The anomalous observations may be the result of a physical process. Gupta (1974) suggests that the preferred alignment of cracks parallel to the direction of maximum compression will provide a preferred direction of fluid flow. Violent perturbations of the pore fluid caused by a large earthquake may trigger aftershocks along this direction. Alternatively, transferral of stress after the main shock may trigger aftershocks in the stressed region surrounding the main source (Das & Scholz, 1981).

3) Cracks in the focal region may open parallel to the future fault strike, and open parallel to the direction of maximum compression only in the surrounding region (Mjachkin et al. 1975). In this case a correct anisotropic model would depend on the size of the focal region in relation to the size of the monitoring network, and may involve a complicated combination of two anisotropic structures.

4) Focal mechanisms of foreshocks have been observed to undergo rotation prior to the main shock (McNally, Kanamori & Pechman, 1978; Wyss 1975; Engdahl & Kisslinger 1978; Bowman and Kisslinger 1980). This rotation can be as much as 90 degrees, suggesting that very complicated stress episodes can take place in the focal region, and that the stress axes determined from events inside this region may not be the same as those that determined

the orientation of the crack structure beneath most of the monitoring network.

5) Aftershocks do not necessarily have the same focal mechanism as foreshocks (Lindh, Fuis & Mantis 1978). Therefore the stress axes determined from the focal mechanism of aftershocks may not reflect the orientation of the cracks persisting after the main earthquake.

It is not surprising that such anomalous earthquake locations have not been observed in foreshock sequences. Foreshocks that have been recorded are usually very few in number and occur irregularly and in very localised clusters in the source region. Aftershocks are numerous, well-recorded and occur along elongated sections of the ruptured fault plane, and so are similar in distribution to the hypothetical events modelled here. However, a recent study of foreshocks to the 1978 Oaxaca, Mexico earthquake (Stewart, Chael & McNally 1981) suggests that the foreshocks migrated towards the epicentre of the main shock during the preceding two days. This migration effect is qualitatively similar to that expected to occur as the degree of the anisotropy, and so the degree of the location errors, decreased immediately prior to the main shock either because of the saturation of cracks or because of reduced crack density.

It is well known that earthquakes on the San Andreas Fault system tend to be located away from the surface strike of the fault. This usually takes the form of an offset to the west by two or three kilometres. Although it has been shown in this Chapter that this effect can be reproduced by failing to take account of velocity-anisotropy, these anomalous observations can be explained from the evidence of refraction surveys and from the geology of the area. These indicate that the velocity structure is discontinuous across the strike of the fault, with faster velocities to the west. This can be allowed for by suitable selection of station corrections according to the source region (Healy & Peake 1975), or

by using ray tracing routines through complicated three dimensional structures (Engdahl & Lee 1976; Aki & Lee 1976). However there is some evidence that velocity anisotropy exists on the San Andreas Fault system. Healy & Peake (1975) observe an indication of an azimuthal variation of travel-time residuals near Bear Valley and suggest that it may be caused by tension fractures in the fault zone. The dominant cause of these anomalous earthquake locations on the San Andreas is undoubtedly the velocity contrast across the fault, but velocity-anisotropy may also be a contributory factor.

Bufe, Pfluke & Wesson (1974) observed that the mean apparent depth of micro-earthquakes occuring along a 20km stretch of the San Andreas Fault increased by 25% during a period of two to three months, and then returned to normal prior to magnitude 5.0 and 4.6 events in Stone Canyon, California. The station coverage and location procedure was the same throughout this study, and only P-arrivals were used to determine the hypocentral locations. Wu & Crosson (1975) attempted to model this depth anomaly by allowing a low velocity zone to exist in the source region. This would be the case if cracks that opened during a dilatancy episode possessed a random orientation, and were confined to a very small volume in the focal region of an impending earthquake. Both of these assumptions are unrealistic for stress-induced cracking in a structure that contains pre-existing cracks. Their experiment did not produce significant variations. Steppe, Bakun & Bufe (1977) relocated all the earthquakes in the study, again using only P-arrivals, and were unable to find any azimuthal variation, or any temporal variation, in travel-time residuals that would indicate the presence of, or changes in, horizontal P-wave anisotropy. Section 3.7 illustrated that such an apparent depth anomaly can be modelled in terms of dilatancy-anisotropy only in the case where the cracks are aligned in the horizontal plane (in order to model a

pure-thrust-fault), and when only P-arrivals are used to locate the events. In other models the increase in depth would be caused by an overall increase in velocity with the resaturation of dry cracks, and the main shock would be expected to occur at an anomalous depth. This would also be the case if the anomalous zone of Wu & Crosson were allowed to extend to all receivers, as their results seem to suggest. Finally, the anisotropic model that does reproduce the form of the observed depth anomaly is transversely-isotropic. This means that there is no azimuthal variation in velocities, and consequently one would not expect to observe any azimuthal variation in travel-time residuals.

It is not clear how the results of this Chapter can be applied to foreshock and aftershock sequences. The stress conditions along a fault are undoubtedly very complicated, and vary on a regional scale (Osokina, Nikonov & Tsvetkova 1979) and on a local scale before large earthquakes (Wyss, Johnston & Klein 1981). However, all locations in such regions will be in error if sufficient velocity-anisotropy exists and an isotropic velocity model is assumed. Such systematic mislocations, as presented in this Chapter, may be a contributory factor in the observed fore- and aftershock migrations and apparent mislocations that have been reported several times in the literature. The results of this Chapter clearly suggest that the assumption of isotropy when locating the TDP1 earthquakes, in particular, is not sufficient to provide accurate hypocentres. It is necessary to have a means of identifying and quantifying the anisotropy, and of taking account of it when locating earthquakes. This will be the subject of the following Chapters.

CHAPTER 4

LOCATING EARTHQUAKES IN REGIONS OF DILATANCY-ANISOTROPY.

4.1 Introduction

The previous Chapter demonstrated that failure to take account of the anisotropic velocity variations when locating earthquakes can result in serious mislocations. These mislocations can indicate spurious deviations from fault planes and other illusory migrations of foci from the true epicentral positions or true depths of foci. In some cases, and particularly for the irregular TDP1 network, the normal tests of location quality, (the RMS of the travel-time residuals and the standard deviation of a hypocentral parameter determination), indicate that these incorrect locations would be considered as being reasonably accurate. An important conclusion was that apparent, precursory hypocentral migrations may be due to dilatancy-anisotropy introducing location errors, rather than an actual migration of earthquakes.

It is clearly necessary to have some means of taking account of the velocity anisotropy when locating earthquakes. This will allow more accurate locations in regions of dilatancy-anisotropy, which will in turn help to isolate true precursory phenomena and so provide a better understanding of the earthquake preparation process. An example of this is the study of Lindh et al.(1978). They made a detailed study of the precursory activity before two magnitude 5 events on the San Andreas Fault in Central California for which temporal variations in P-wave travel-time residuals had been interpreted as evidence for material velocity changes. They notice that the travel-time residuals correlate with, among other things, the hypocentral depth. These depth migrations may have been real or may have been an effect of dilatancy-biasing of earthquake locations as modelled in the previous Chapter. An accurate method of locating earthquakes in such regions of possible dilatancy-anisotropy would have

allowed the clearer identification of real precursory phenomena.

Chapter 3 illustrated the great variety of different mislocation effects that velocity-anisotropy can produce. These mislocation effects cannot be generalised. The anisotropic structure must be quantified in some sense before the velocity variations can be taken into account in any earthquake location procedure. The problem of anisotropic structure determination will be considered in Chapters 5 and 6. This Chapter will present a method of locating events in anisotropic structures of known orientation and with known elastic constants. The structural models considered will be a homogeneous, anisotropic half-space, and an anisotropic half-space overlain by an isotropic layer.

4.2 The location of earthquakes in an anisotropic half-space

Appendix B describes a common method of locating earthquakes in an isotropic half-space. The method involves minimising travel-time residuals by an iterative least-squares procedure. It is shown that the process depends on the inversion of equations involving travel-time residuals and travel-time derivatives with respect to each of the hypocentral parameters. In an anisotropic half-space the travel-times, and their residuals can be found following the method outlined in Appendix A, where a look-up table is created containing the group-velocities at specified directions of propagation for any particular anisotropic solid. This look-up table can be stored internally within the location program and used to calculate travel-times. However, the travel-time derivatives for an anisotropic half-space are more complicated than in the isotropic case, because the velocity in the travel-time equation is not constant and varies with the direction of propagation.

From the equation for the travel-time, T_i, to the ith station:

$$T_i = p_1 + [(x_i - p_2)^2 + (y_i - p_3)^2 + (z_i - p_4)^2]^{\frac{1}{2}}/V_i \qquad \text{(B.9 - bis)}$$

where x_i, y_i and z_i are the station co-ordinates;

V_i is the velocity to the ith station;

p_1 is the origin time;

and p_2, p_3, p_4 are the hypocentral coordinates, (i.e x, y, and z);

and assuming that:

$$\frac{\partial V_i(\theta,\phi)}{\partial p_k} = \frac{\partial V_i}{\partial \theta}\frac{\partial \theta}{\partial p_k} + \frac{\partial V_i}{\partial \phi}\frac{\partial \phi}{\partial p_k} \qquad (4.1)$$

where θ is the azimuth of the station from the epicentre, and ϕ is the angle of incidence from the vertical. The travel-time derivatives can be written as;

$$\frac{\partial T_i}{\partial p_2} = -(\sin\phi \sin\theta)/V_i + \left((\cos\theta/\sin\phi \frac{\partial V_i}{\partial \theta}) + (\sin\theta \cos\phi \frac{\partial V_i}{\partial \phi})\right)/V_i^2$$

$$\frac{\partial T_i}{\partial p_3} = -(\sin\phi \cos\theta)/V_i - \left((\sin\theta/\sin\phi \frac{\partial V_i}{\partial \theta}) - (\cos\theta \cos\phi \frac{\partial V_i}{\partial \phi})\right)/V_i^2 \qquad (4.2)$$

$$\frac{\partial T_i}{\partial p_4} = -\cos\phi/V_i + (\sin\phi \frac{\partial V_i}{\partial \phi})/V_i^2$$

The travel-time derivative with respect to the origin-time being equal to unity as in the isotropic case.

The first term on the right hand sides of equations (4.2) represent the travel-time derivatives in an isotropic half-space, while the other terms represent the modifications required for an anisotropic half-space. These derivatives are now a function of the derivatives of the velocity with respect to the angles of incidence and azimuth. These parameters are calculated by the same routine that calculates the velocities in the anisotropic solid, and are stored in the same look-up table.

Following the theory outlined above, the half-space location program

used in Chapter 3 can be modified to take account of known anisotropic velocity variations by using the corresponding look-up table to calculate travel-times, their residuals and their derivatives. Fig.4.1 illustrates the relocation of the events of Figs.3.3 and 3.14 by this modified program. The half-space in this case models dry crack dilatancy-anisotropy surrounding a pure strike-slip fault. Figs.4.1a and 4.1c are the relocations determined by the SQ1 and TDP1 networks respectively, using P-and S-arrivals at every station. As can be seen, the locations are determined as accurately as those in the control calculation for an isotropic half-space (Fig.3.4). However the determination of the deepest events (15km) did not converge when only P-arrivals were used in the location procedure. This is due to poor network resolution at this depth, which can be improved by including shear-waves so that the S-P times provide a greater constraint on the origin-time. It was found that for convergence of these events to their correct solution, a minimum of two S-arrivals were required by the SQ1 network, and four S-arrivals for the TDP1 network. This performance can again be improved by using the hypocentres determined under the assumption of isotropy (i.e. those from figures 3.5 and 3.15), as the initial hypccentres, rather than the nearest station and some arbitrary depth (5km in Chapter 3), as is the usual case. For this case the requirement for convergence is only one shear-arrival at a central station in each of the networks. These locations are illustrated in Figs.4.1b and 4.1d for the SQ1 and TDP1 networks respectively. Notice that although the RMS errors of the relocations determined by the SQ1 network are noticeably lower than the equivalent isotropic locqations, the same is not true for the locations by the TDP1 network. Table C.9 compares the estimated and true errors of these locations with those in the same structure, but using an isotropic model. There is a clear reduction in the estimated errors for the locations determined by both networks. This feature of the locations will be important in Chpater 7 when we

Figure 4.1. A summary of the relocations of the events of Figs.3.3 and 3.14 by a program that takes account of velocity anisotropy in a half-space. The true structure is a system of dry, parallel cracks oriented to model dilatancy-anisotropy associated with a strike-slip fault.

(a) Locations using P- and S-arrivals at every station in the SQ1 network (model XBSQNY, Table C.9).

(b) Locations using P-arrivals at every station and one S-arrival at the central station of the SQ1 network (model Y1BQNZ, Table C.9).

(c) Locations using P- and S-arrivals at every station in the TDP1 network (model XBTPNY, Table C.9).

(d) Locations using P-arrivals at every station and one S-arrival at a central station of the TDP1 network (model Y1BTNZ, Table C.9).

Notation and format as in Fig.3.4

ANISOTROPIC LOCATIONS

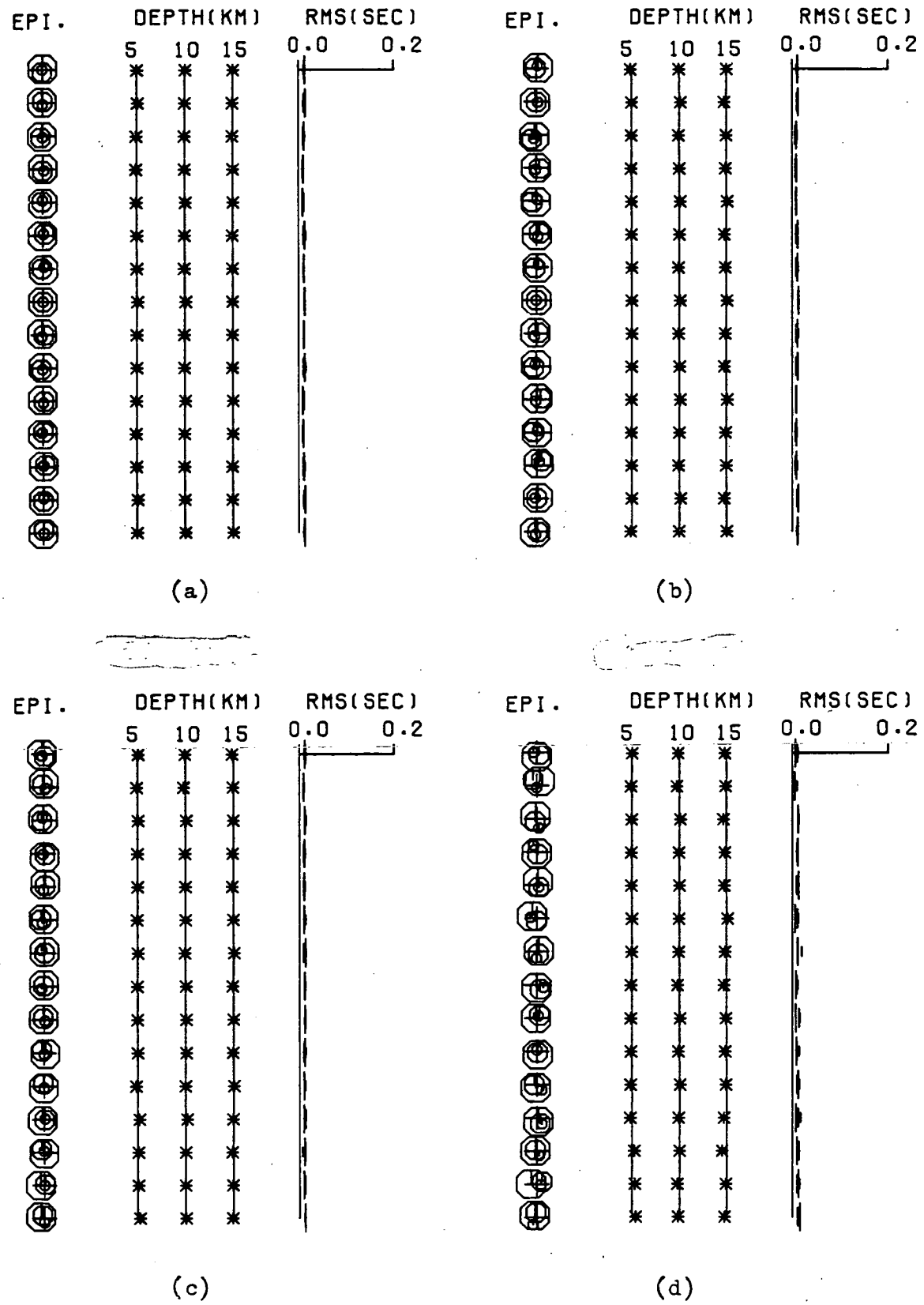

relocate the TDP events in various anisotropic structures.

The anisotropic location program operates in a batch processing mode and determines the hypocentres in approximately the same number of iterations as a conventional isotropic program. The overall time difference between the two location procedures is just the time required by the anisotropic program to store the look-up table of anisotropic velocities and derivatives.

4.3 The location of earthquakes in a layered anisotropic structure

A computer program that will locate earthquakes in a structure that consists of an isotropic layer above an anisotropic half-space needs to be considerably more sophisticated than a half-space location program. In most micro-earthquake applications, where local earthquakes are occuring immediately beneath the monitoring network, as in the TDP experiments, the travel-time of the direct wave between the source and the receiver is required. This requires some iterative scheme and can be achieved simply in the isotropic case, where the ray path is always in the same vertical plane as that defined by the source and the receiver. However, in the anisotropic case, although the travel-time is controlled by the group-velocity of the ray in a particular direction, the direction of the refracted ray is controlled by the magnitude and direction of the corresponding phase of the incident ray. In an anisotropic solid the direction and magnitude of phase propagation is usually different from that of the group, or energy propagation. This means that except for particular symmetry directions the ray that emerges at the receiver has travelled away from the vertical plane defined by the source and receiver. This is illustrated in Fig.4.2. The cross-over points of the solid lines represent the emergent points at the surface of rays propagating in specified directions from a source in an isotropic half-space, lying 1km below an interface with an isotropic layer of thickness 1km. The circles represent

Figure 4.2. An illustration of seismic-wave propagation through an anisotropic/isotropic interface. Rays are generated at directions spaced at nine degree intervals throughout the focal sphere from a source in a homogeneous half-space, 1km below a horizontal interface with a surface isotropic layer of thickness 1km. P-wave velocity in the isotropic layer is 4km/sec and the Vp/Vs ratio is equal to 1.73. The cross-over points of the solid lines mark the emergent pojnts of the rays when the half-space is isotropic (Vp = 5.62km/sec, Vs = 3.35km/sec). The numbers refer to take-off angles of the rays measured from the upward vertical. The triangles mark the emergent points of rays generated from the source in the same directions and where the half-space is anisotropic (model GKFF1 - dry, parallel cracks with the axis of rotational symmetry striking East-West).
(a) Emergent points of P-waves.
(b) Emergent points of shear-waves.

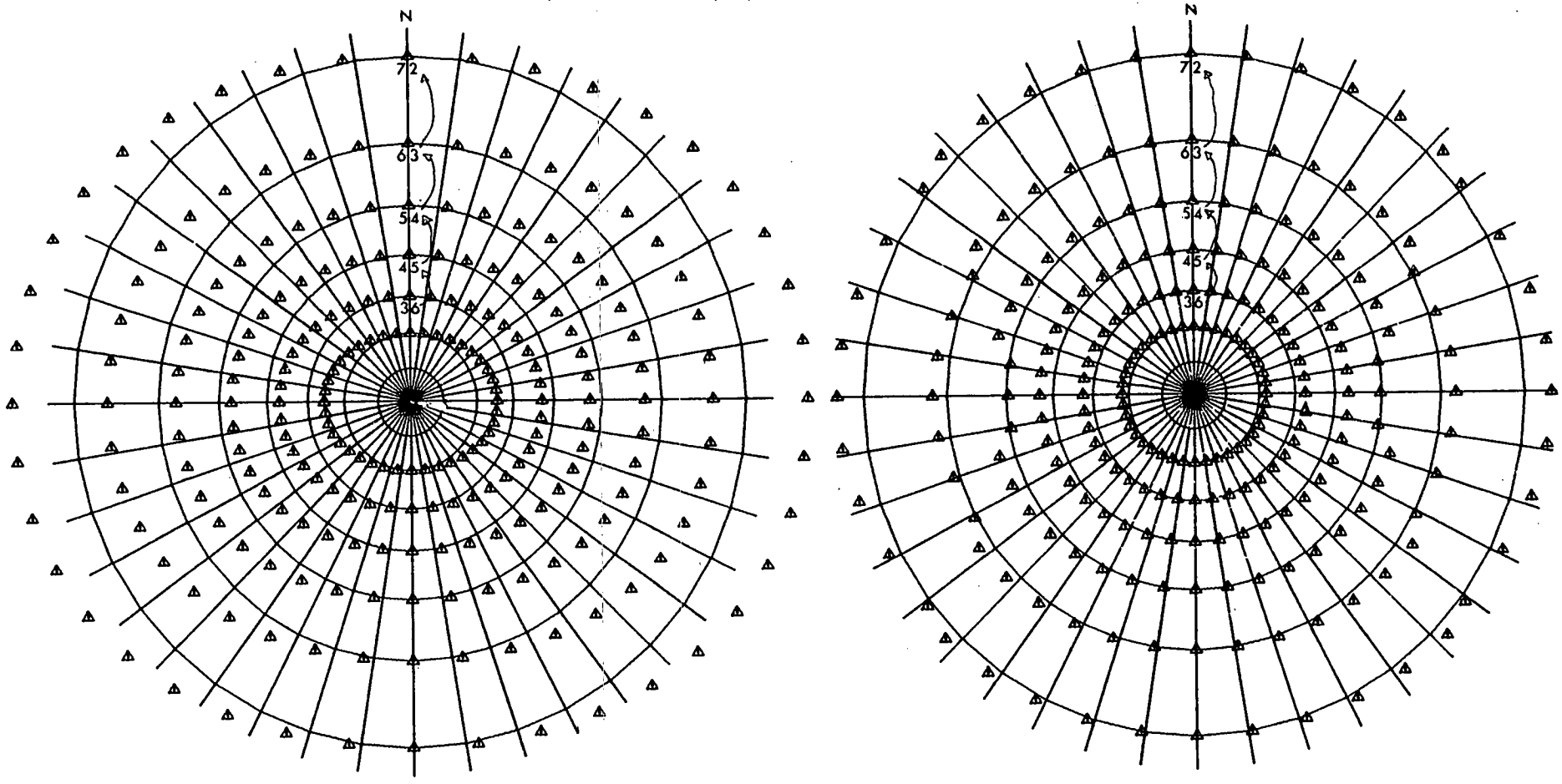

(a) (b)

points of emergence of the rays propagating in the same direction from the source in an anisotropic half-space. As can be seen, except for symmetry directions, the incident and refracted ray no longer have the same azimuth and the angle of emergence is not the same as in the isotropic case. The azimuth changes because the direction of phase- is different from the direction of energy-propagation, and the angle of emergence is different for the same reason and also because of the directional variations of velocity in the anisotropic half-space. Notice the irregular nature of the shear-wave emergent points. This is caused by the transition from one shear-wave surface to the other during the calculation of the fastest shear-wave.

This added complication has several consequences for an earthquake location program. Firstly, the calculation of the travel-time of the direct wave requires an iterative routine that operates in three dimensions. This is considerably more complicated than the two-dimensional isotropic situation. Secondly, we are not aware of any useful expression for the travel-time derivatives of such a direct wave. This means that the calculation has to be performed numerically, which increases computation time. Finally, although look-up tables could be used as before, a phase-velocity look-up table is also required. This look-up table would be irregularly spaced in two dimensions, with sparse coverage in some directions of group-velocity propagation and would require a complicated interpolating routine. Numerical tests suggest that interpolation of such a look-up table would not provide sufficient accuracy for the numerical calculation of travel-time derivatives, and therefore it is necessary to use the routine that calculates velocities in an anisotropic solid (Appendix A) as an integral part of the location program.

Although such a program would appear to be too expensive to use on a routine basis, it may be possible to introduce reasonable approximations that would save considerable expense. For example it may be possible to

approximate the structure by an anisotropic half-space coupled with extra station corrections. This section will describe such a program and discuss the possibility of using such an approximation. A structure consisting of a horizontal isotropic layer overlying an anisotropic half-space, and direct arrivals only will be considered.

4.3.1 Calculation of the travel-time of the direct wave

In order to generate synthetic data with which to test the program, and to investigate various approximations to the true structure, a routine is required that will calculate the travel-time of the direct wave from a source to a receiver. This routine will then form part of the final location program. There is no general criterion for finding the correct minimum path for the direct wave in a layered isotropic or anisotropic structure. This path has to be determined numerically by an efficient, iterative, search procedure operating in three dimensions for the anisotropic case. The first stage involves finding the direction cosines of a ray that leaves the source in the direction of the receiver. This ray is used as an initial trial ray. A window is set up around this ray within which the true ray must lie. The size of this window needs to be large enough to contain the true ray, and small enough to provide rapid convergence to the correct solution. In this application it was found that a size of 0.2 units in each direction cosine, centred on the initial ray, was suitable.

The next step involves calculating the emergent point for the initial ray leaving the source in the direction of the receiver. The trial ray is then perturbed according to whether the trial ray over- or undershot the receiver position. It is only necessary to consider perturbations to two of the direction cosines of this ray, as the third follows immediately. For instance, if the x-coordinate of the emergent point is greater than the x-coordinate of the receiver, the x-direction cosine of the trial ray is

decreased by a certain fraction of the window width. The limits of the window are then redefined. In this case the maximum limit of the window in the x-direction is reduced to the value of the x-direction cosine of the initial ray. Similarly, if the y-coordinate of the emergent point is less than the y-coordinate of the reciever, the y-direction cosine of the trial ray is increased by the same amount, and the minimum limit in the y-direction reset. The same procedure is then repeated on this new trial ray.

For the first two iterations, the ray is perturbed by 1/10 of the size of the window in order to redefine the window limits to a sensible region for the particular ray under consideration. This procedure is continued, increasing the perturbation to 8/10 of the window size in subsequent iterations, until the emergent point is within 1/50km of the reciever. The travel-time is then calculated on the basis of the group-velocity for the direction in the half-space, and the isotropic velocity of the layer. The direction of the P-wave is then used as a trial ray to determine the S-wave propagation direction, and the size of the window is increased by 0.1 (i.e. $\pm$ 0.05 centred on this trial ray).

In most cases the take-off direction for the ray is found after about 10 iterations. However, because of the rapid variations in the direction of the refracted ray for some directions in the anisotropic half-space, the window may be redefined after a few iterations, such that the true ray no longer lies within it. This is corrected for by increasing the window limits by $\pm$ 0.1 centred on the current ray position, if the solution has not converged after 15 iterations. The routine then converges to the correct solution after approximately another 10 iterations.

In the TDP experiments (Chapter 2), analysis of arrival-times from timed explosions indicates that the structure consists of a thin layer overlying a half-space. We shall assume that this layer is not anisotropic. In order to examine the effect of this layer on the location

of earthquakes in those experiments in particular, this routine was used to generate synthetic travel-times from each of the hypocentres in Fig.3.14 to the stations of the TDP1 network. Two cases were considered, consisting of an anisotropic half-space overlain by an isotropic layer (Vp = 4.0km/sec, Vp/Vs = 1.73), of thickness 1km and thickness 3km. In the first case the routine takes 24s of CPU time (on an ICL 2980 machine) to determine the travel times of the 720 direct ray paths. In the second case this time is doubled because with a thicker layer, small changes in the direction of the incident ray can produce large changes in the point of emergence, and so more iterations are required before convergence to the required degree of accuracy is achieved. This is particularly the case for rays from the shallow events (at a depth of 5km) only 2km below the interface.

This section will now consider the effects of assuming a variety of structures when locating events in a structure consisting of an isotropic layer above an anisotropic half-space. It has already been shown that HYPO71 produces the same locations as the simple half-space location program of Chapter 3. HYPO71 calculates travel-time derivatives analytically and is therefore more efficient than a program that calculates the derivatives numerically. Therefore in order to restrict computer costs, the locations performed under the assumption of isotropy have all been performed by HYPO71. The anisotropic structure that will be used is that of dry parallel cracks (crack model 1 of Chapter 3) oriented to model dilatancy-anisotropy surrounding a pure-normal fault (i.e. the axis of rotational symmetry is horizontal and perpendicular to the line of epicentres of Fig.3.14). In all cases where the half-space has been assumed to be isotropic, the velocities used to relocate the events correspond to the average velocities of all the ray paths that were actually sampled through the structure, rather than the average over the whole structure as was the case in the first part of Chapter 3.

4.3.2 An isotropic half-space approximation

Fig.4.3 illustrates the relocation of the events in each of the layered structures, when the structure has been assumed to be an isotropic half-space. For a thin layer the patterns of locations are very similar to those in a half-space (Fig.3.17). This demonstrates that the velocity anisotropy dominates the effect of the velocity discontinuity, that different assumed isotropic velocities have little effect on the pattern of mislocations, and that HYPO71 performs no better, in these simple cases, than the previous half-space location program. There is still no significant difference if the layer thickness is increased to 3km when only P-arrivals are used to locate the events. However using shear-arrivals in this case results in larger hypocentral errors. This is reflected in the higher RMS values associated with these locations.

4.3.3 An isotropic layered approximation

Fig.4.4 illustrates the effect on the relocations of assuming that the structure consists of an isotropic half-space overlain by a horizontal isotropic layer. The thickness and P-wave velocity of the layer are assumed known. In each of the layered cases, when only P-arrivals are used to locate the events, the addition of the isotropic layer has little effect on the epicentral relocations but sightly improves the depth determinations. With HYPO71 it is not possible to specify different values of Poisson's ratio for each layer, and so some overall Vp/Vs ratio for the whole structure must be assumed. The Vp/Vs ratio in the isotropic layer is 1.73, whereas the ratio of average sampled P- and average sampled S-velocity in the anisotropic half-space is 1.63. Assuming an overall ratio of 1.63 produces a small improvement in epicentral locations for the 1km layer (Fig.4.4b) when P- and S-arrivals are used, and a greater improvement for the case of the 3km layer (Fig.4.4d). Assuming a ratio of 1.68 (Fig.4.5a and 4.5b) produces a further improvement in both cases, and further still

Figure 4.3. A summary of the relocations of the events of Fig.3.14 by HYPO71 assuming that the structure is an isotropic half-space. The true structure is an anisotropic half-space overlain by an isotropic layer. (Vp = 4.0km/sec, Vp/Vs = 1.73)
(a) Locations using P-arrivals at every station and where the isotropic layer is 1km thick.
(b) Locations using P- and S-arrivals at every station and where isotropic layer is 1km thick.
(c) Locations using P-arrivals at every station and where the isotropic layer is 3km thick.
(d) Locations using P- and S-arrivals at every station and where isotropic layer is 3km thick.
Notation and format as in Fig.3.4

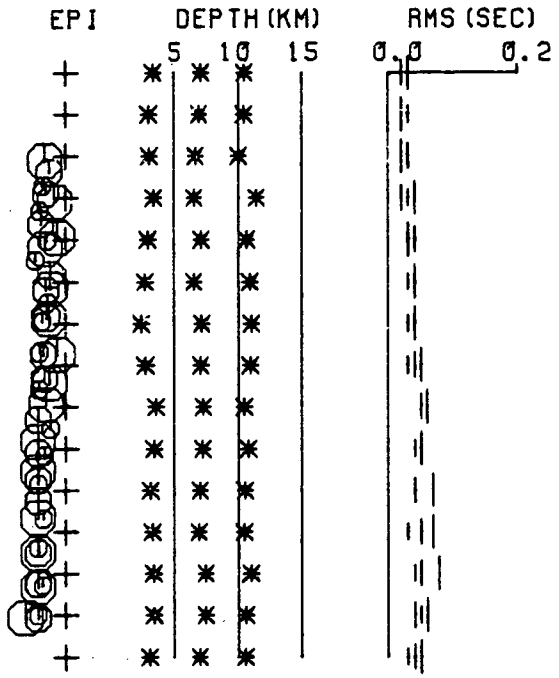
EPI
DEPTH (KM)
5 10 15
RMS (SEC)
0.0 0.2

(a)

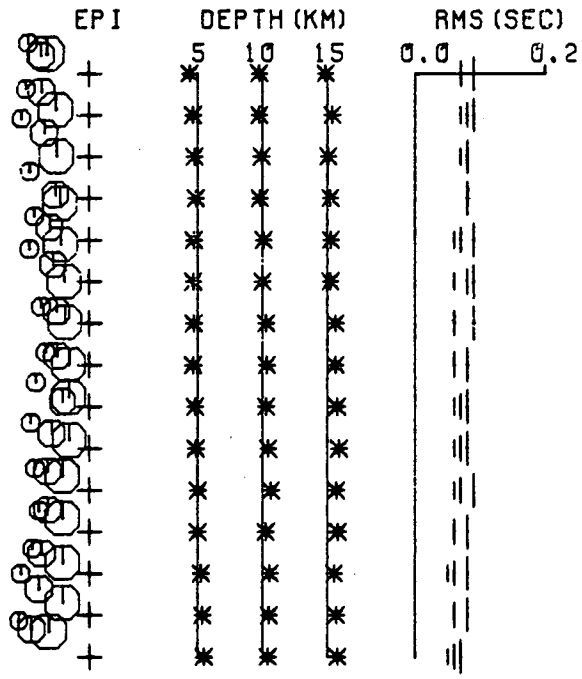
EPI
DEPTH (KM)
5 10 15
RMS (SEC)
0.0 0.2

(b)

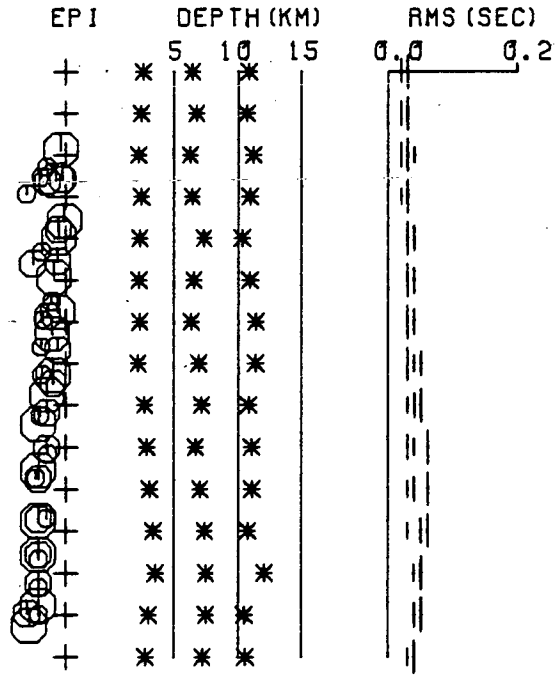
EPI
DEPTH (KM)
5 10 15
RMS (SEC)
0.0 0.2

(c)

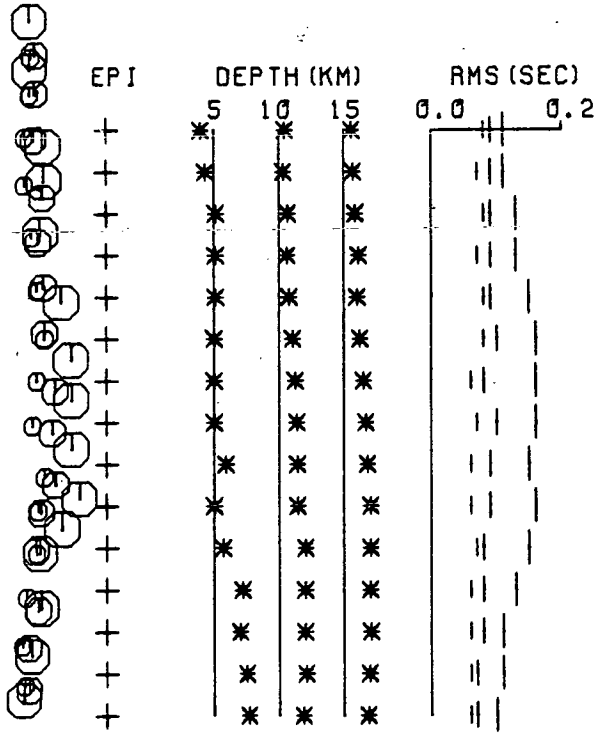
EPI
DEPTH (KM)
5 10 15
RMS (SEC)
0.0 0.2

(d)

Figure 4.4. A summary of the relocations by HYPO71 of the events of Fig.3.14 using a layered isotropic model. The thickness and P-wave velocity of the isotropic layer are assumed to be known. (Vp = 4.0km/sec, Vp/Vs = 1.73)

(a) Locations using P-arrivals at every station and where the isotropic layer is 1km thick.

(b) Locations using P- and S-arrivals at every station, where the isotropic layer is 1km thick and where the Vp/Vs ratio is assumed to be 1.63.

(c) Locations using P-arrivals at every station and where the isotropic layer is 3km thick.

(d) Locations using P- and S-arrivals at every station, where the isotropic layer is 3km thick and where the Vp/Vs ratio is assumed to be 1.63.

Notation and format as in Fig.3.4

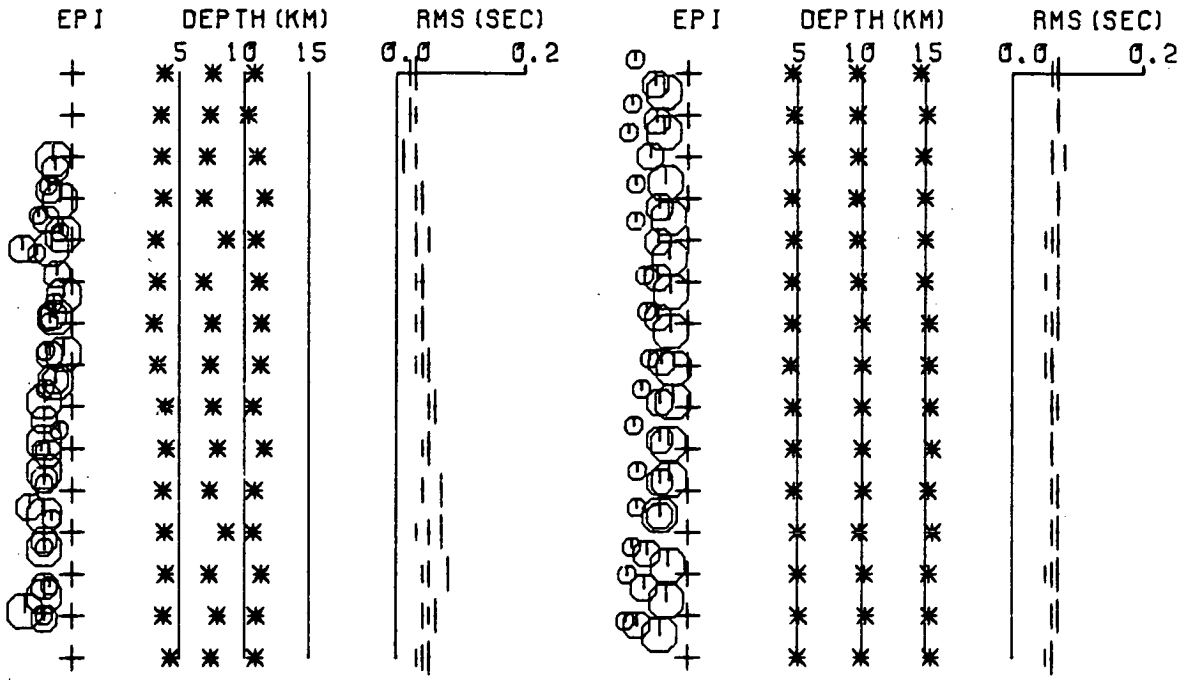
EPI
DEPTH (KM)
5 10 15
RMS (SEC)
0.0 0.2
(a)
EPI
DEPTH (KM)
5 10 15
RMS (SEC)
0.0 0.2
(b)

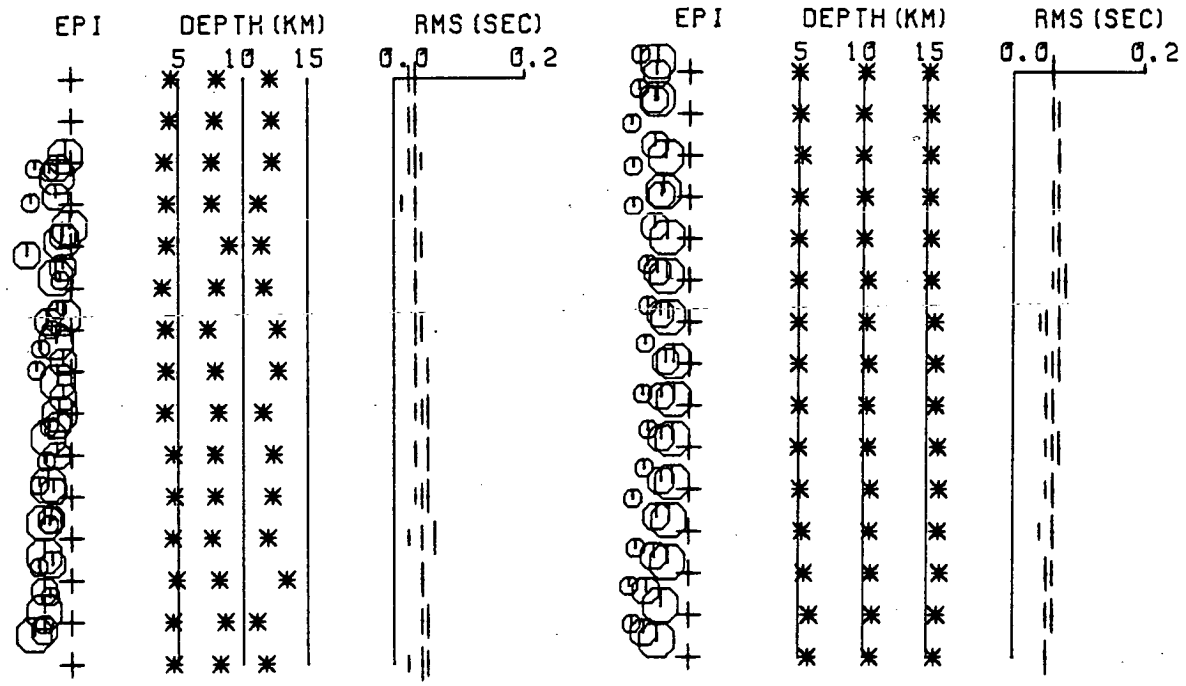
EPI
DEPTH (KM)
5 10 15
RMS (SEC)
0.0 0.2
(c)
EPI
DEPTH (KM)
5 10 15
RMS (SEC)
0.0 0.2
(d)

Figure 4.5. A summary of the relocation by HYPO71 of the events of Fig.3.14 using a layered isotropic model. The thickness and P-wave velocity of the layer are assumed to be known. (Vp = 4.0km/sec, Vp/Vs = 1.73)

(a) Locations using P- and S-arrivals at every station, where the isotropic layer is 1km thick and where the Vp/Vs ratio is assumed to be 1.68.

(b) Locations using P- and S-arrivals at every station, where the isotropic layer is 3km thick and where the Vp/Vs ratio is assumed to be 1.68.

(c) Locations using P- and S-arrivals at every station where the isotropic layer is 1km thick and where the Vp/Vs ratio is assumed to be 1.73.

(d) Locations using P- and S-arrivals at every station, where the isotropic layer is 3km thick and where the Vp/Vs ratio is assumed to be 1.73.

Notation and format as in Fig.3.4

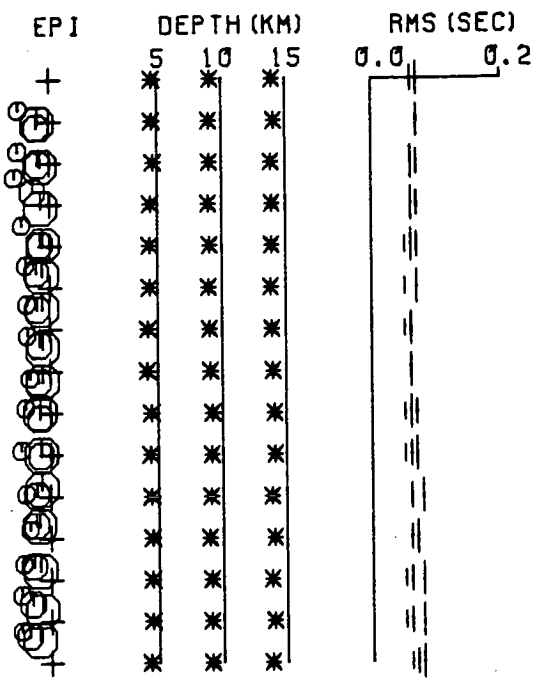
EPI
DEPTH (KM)
5
10
15
RMS (SEC)
0.0
0.2

(a)

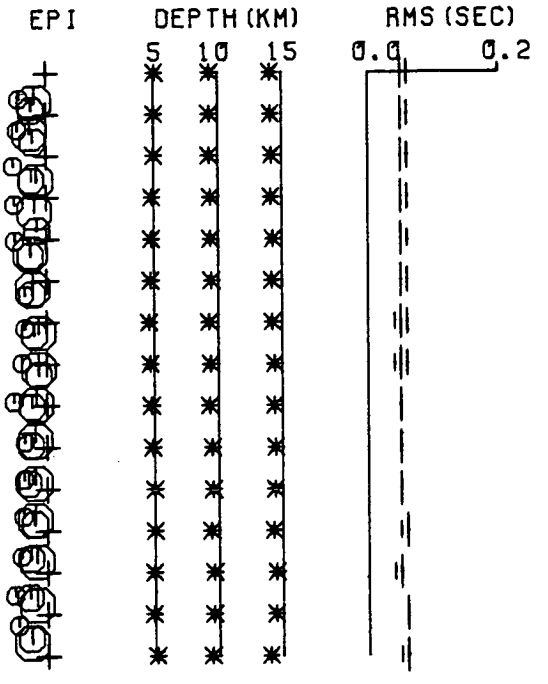
EPI
DEPTH (KM)
5
10
15
RMS (SEC)
0.0
0.2

(b)

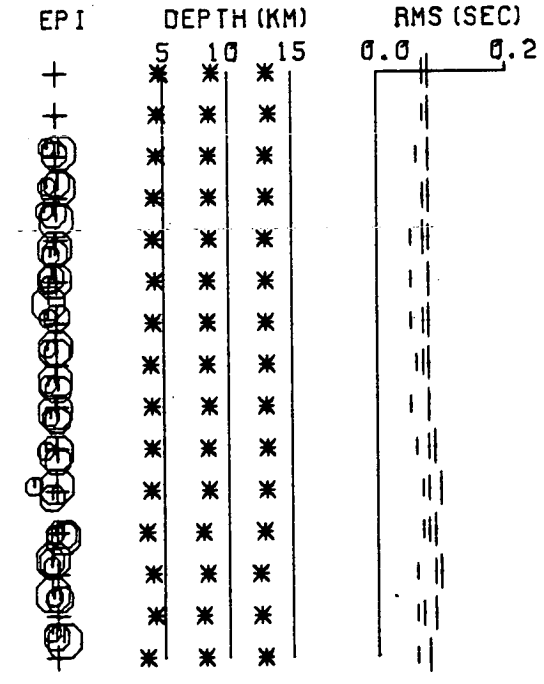
EPI
DEPTH (KM)
5
10
15
RMS (SEC)
0.0
0.2

(c)

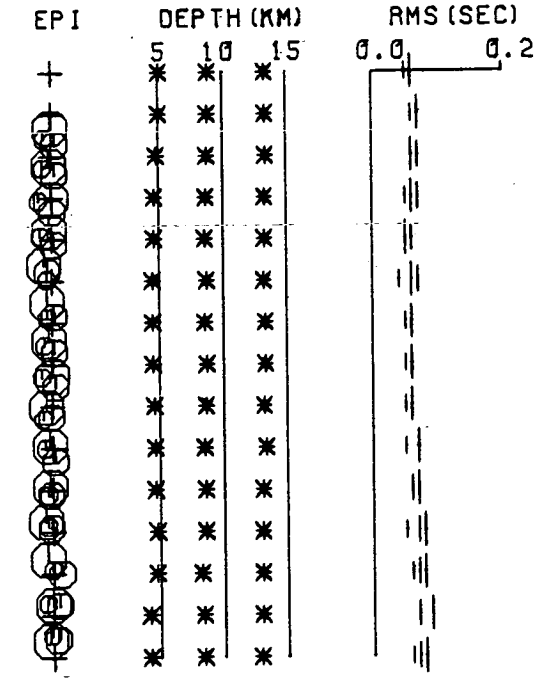
EPI
DEPTH (KM)
5
10
15
RMS (SEC)
0.0
0.2

(d)

when a ratio of 1.73 is assumed (Fig.4.5c and 4.5d). However increasing the Vp/Vs ratio from 1.63 through to 1.73 results in progressively larger focal depth errors, particularly for the deeper events.

4.3.4 An anisotropic half-space approximation

Fig.4.6 illustrates the effect of ignoring the presence of the 1km isotropic layer, and approximating the structure by an anisotropic half-space. The elastic constants and orientation of the anisotropic half-space are assumed to be known. We shall use as trial hypocentres those determined by assuming the structure is an isotropic half-space. Figs.4.6a and 4.6b demonstrate that the anisotropic half-space approximation produces better results than the isotropic layer approximation. This can be improved further by introducing station corrections of 0.07s to allow for the effect of the isotropic layer. These corrections have been calculated using the P-wave velocity of the layer, assuming an average hypocentral depth of 10km and a typical take-off angle of 25 degrees. The P-wave velocity at this angle in the anisotropic half-space corresponds to the average P-wave velocity used to locate the events under the assumption of isotropy. The resulting locations are shown in Figs.4.6c and 4.6d, where the events that lie inside the network have been very well determined.

Figure 4.7 shows the relocations determined under the assumption of an anisotropic half-space when the isotropic layer is 3km thick (Fig.4.7a and 4.7b). In this case the anisotropic half-space approximation is not superior to the isotropic layered approximation. However, introducing station corrections of 0.2s to allow for the effect of the layer does result in superior hypocentre determinations for those events that lie within the network (Figs.4.7c and 4.7d).

Figure 4.6. A summary of the relocations of the events of Fig.3.14 by a program that assumes the structure is an anisotropic half-space. The elastic constants and orientation of the half-space are assumed to be known. The isotropic layer is 1km thick. (Vp = 4.0km/sec, Vp/Vs = 1.73).
(a) Locations using P-arrivals at every station and one S-arrival at a central station.
(b) Locations using P- and S-arrivals at every station.
(c) Location using P-arrivals at every station and one S-arrival at a central station, and where station corrections of 0.07s have been introduced to allow for the effect of the isotropic layer.
(d) Locations using P- and S-arrivals at every station and where station corrections of 0.07s have been introduced to allow for the effect of the isotropic layer.
Notation and format as in Fig.3.4

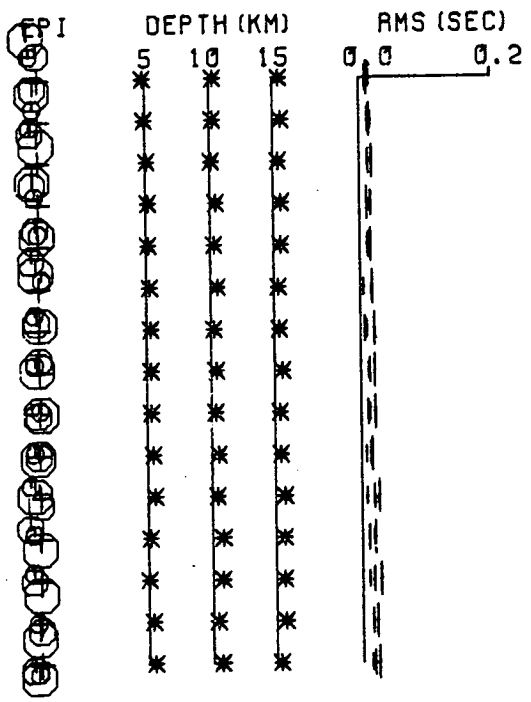
EPI
DEPTH (KM)
5 10 15
RMS (SEC)
0.0 0.2

(a)

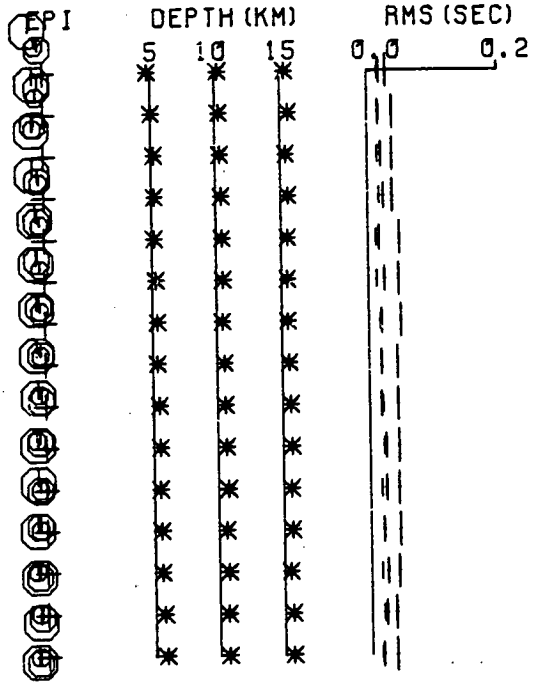
EPI
DEPTH (KM)
5 10 15
RMS (SEC)
0.0 0.2

(b)

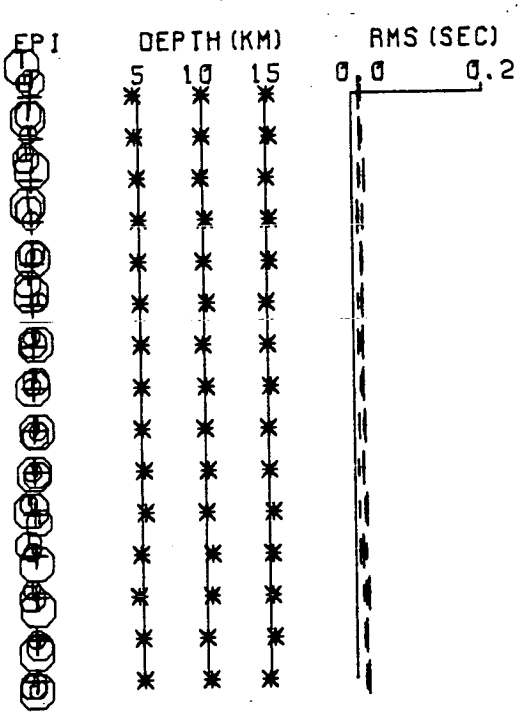
EPI
DEPTH (KM)
5 10 15
RMS (SEC)
0.0 0.2

(c)

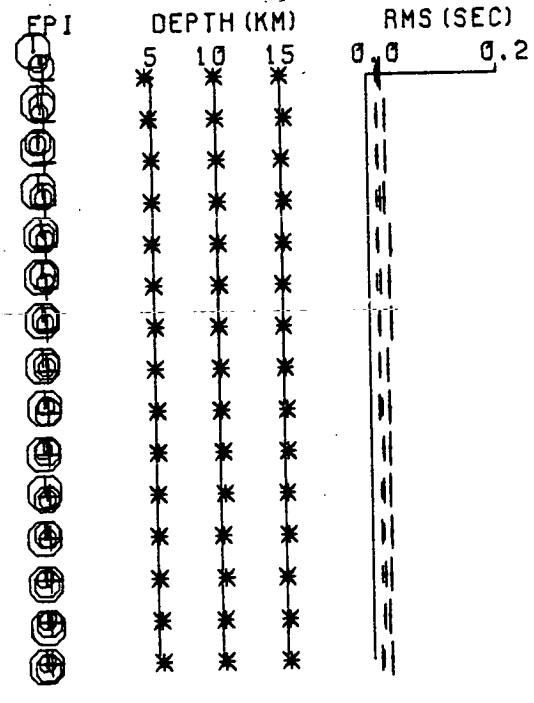
EPI
DEPTH (KM)
5 10 15
RMS (SEC)
0.0 0.2

(d)

Figure 4.7. A summary of the relocations of the events of Fig.3.14 by a program that assumes the structure is an anisotropic half-space. The elastic constants and orientation of the half-space are assumed to be known. The isotropic layer is 3km thick, (Vp = 4.0km/sec, Vp/Vs = 1.73)

(a) Locations using P-arrivals at every station and one S-arrival at a central station.

(b) Locations using P- and S-arrivals at every station.

(c) Location using P-arrivals at every station and one S-arrival at a central station, and where station corrections of 0.2s have been introduced to allow for the effect of the isotropic layer.

(d) Locations using P- and S-arrivals at every station and where station corrections of 0.2s have been introduced to allow for the effect of the isotropic layer.

Notation and format as in Fig.3.4

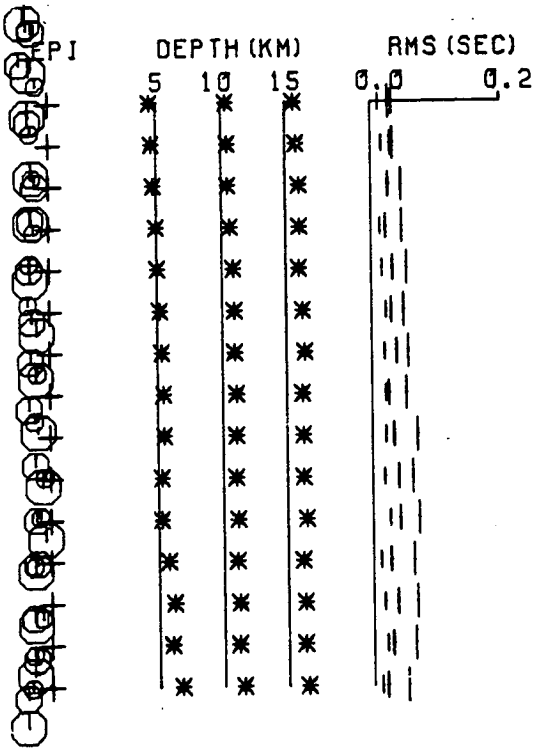
EPI
DEPTH (KM)
5
10
15
RMS (SEC)
0.0
0.2

(a)

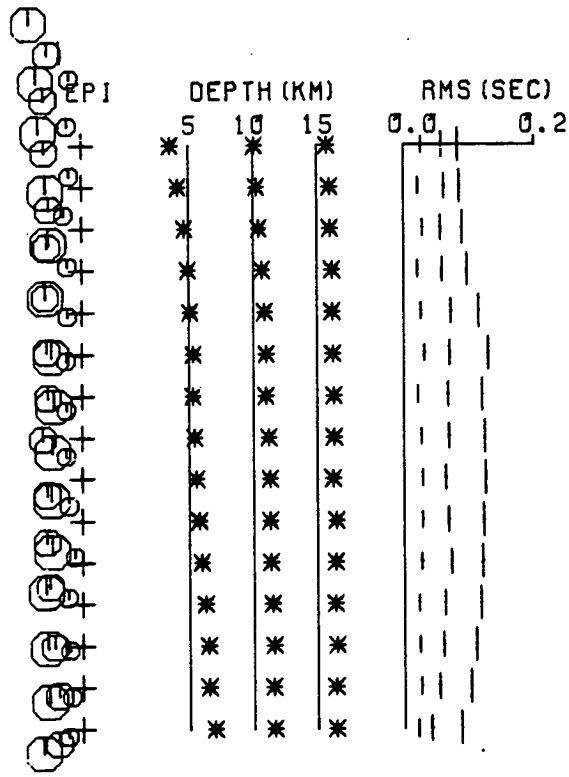
EPI
DEPTH (KM)
5
10
15
RMS (SEC)
0.0
0.2

(b)

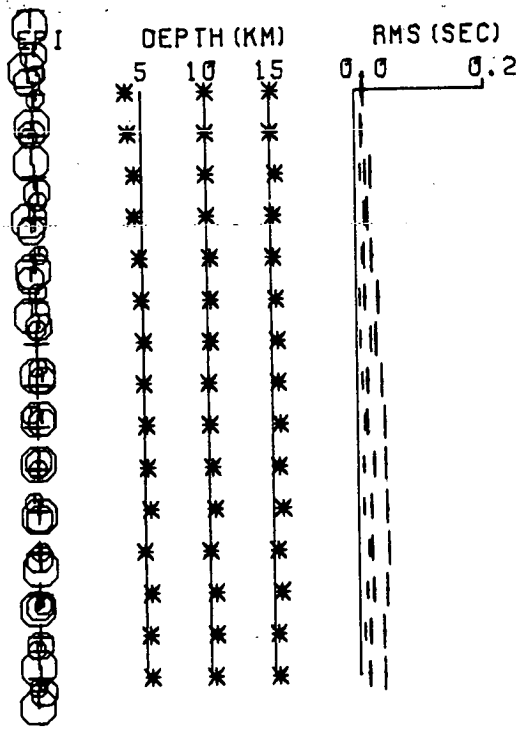
EPI
DEPTH (KM)
5
10
15
RMS (SEC)
0.0
0.2

(c)

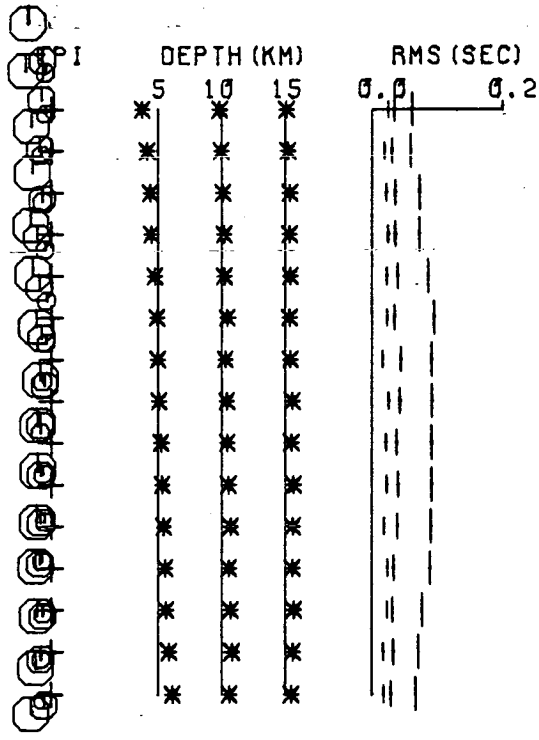
EPI
DEPTH (KM)
5
10
15
RMS (SEC)
0.0
0.2

(d)

4.3.5 The full location procedure

Fig.4.8 shows the locations determined by a location program that models the layered structure exactly. This program uses the routine described in section 4.3.1 to calculate travel-times of the direct wave from a source to a receiver, and calculates all travel-time derivatives numerically. The program uses as trial hypocentres those determined under the assumption of isotropy. For the case of a thin isotropic layer the program has accurately determined the locations of all the events when P- and S-arrivals have been used (Fig.4.8b). The most northerly event at a depth of 5km epicentres has not been located very well. This is an effect of poor network resolution in this more complicated structure. It was found that for convergence, a minimum of two shear-arrivals at central stations are necessary in addition to P-arrivals at all stations. These locations are shown in Fig.4.8a where the most northerly hypocentre at a depth of 5km has again not been determined very accurately. Comparing these two figures with Figs.4.6c and 4.6d, where the isotropic layer has been replaced by constant station corrections and an anisotropic half-space assumed, we can see that there is only a slight improvement in the accuracy of the relocations when the full location procedure is used. The time difference between the two programs, however, is phenomenal. The full location program takes five times as long to locate the events compared to a program that assumes an anisotropic half-space.

Figs.4.8c and 4.8d show the locations determined by the complete location program in the structure consisting of a 3km isotropic layer above an anisotropic half-space. Some of the events have not been accurately determined due to reduced network resolution when the events lie outside the network. The other locations are marginally superior to those determined under the assumption of an an anisotropic half-space with added station corrections (Figs.4.7c and 4.7d). However the level of improvement achieved would not justify the extra computing costs incurred.

Figure 4.8. A summary of the relocations of the events of Fig.3.14 by a program that takes account of the anisotropic half-space and the isotropic layer exactly.
(a) Location using P-arrivals at every station and two S-arrivals at central stations and where the isotropic layer is 1km thick.
(b) Locations using P- and S-arrivals at every station and where the isotropic layer is 1km thick.
(c) Location using P-arrivals at every station and two S-arrivals at central stations and where the isotropic layer is 3km thick.
(d) Locations using P- and S-arrivals at every station and where the isotropic layer is 3km thick.
Notation and format as in Fig.3.4

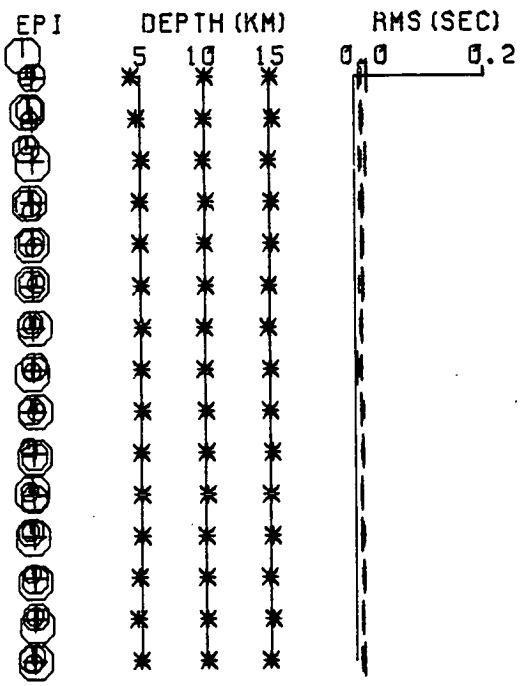
EPI
DEPTH (KM)
5
10
15
RMS (SEC)
0.0
0.2

(a)

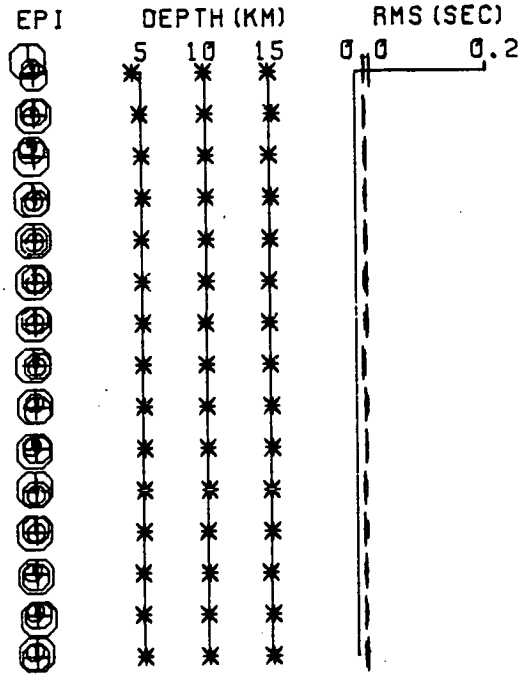
EPI
DEPTH (KM)
5
10
15
RMS (SEC)
0.0
0.2

(b)

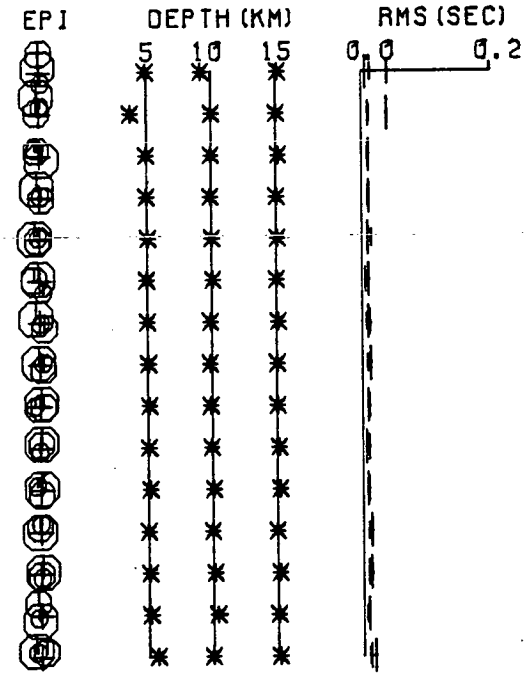
EPI
DEPTH (KM)
5
10
15
RMS (SEC)
0.0
0.2

(c)

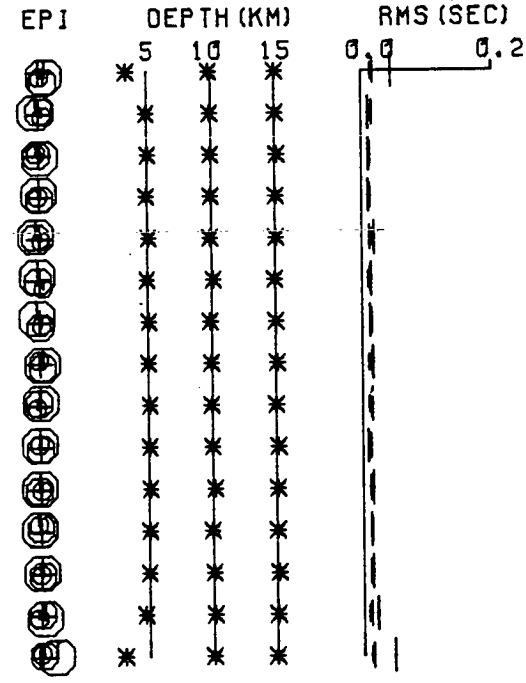
EPI
DEPTH (KM)
5
10
15
RMS (SEC)
0.0
0.2

(d)

4.4 Discussion

This Chapter has illustrated a method of accurately locating local earthquakes in regions of dilatancy-anisotropy where the events occur immediately below a small network as in TDP experiments. If the orientation of the anisotropic variations, and the elastic constants that define seismic-wave propagation through the structure are known, it is possible to accurately locate earthquakes in such regions providing that shear-arrivals are used in addition to the P-arrivals, and providing that reasonable approximations to the true hypocentral locations are known. The first proviso does not present problems for the location of the TDP earthquakes because impulsive shear-arrivals can be accurately read from horizontal seismograms. The second proviso is easily achieved by using the hypocentres determined under the assumption of isotropy. These would be a much closer approximation to the true locations than the nearest station and some arbitrary depth as is the normal practice. An important conclusion for the further analysis of the TDP1 data set in particular, is that it is possible to model the effect of a thin isotropic layer by introducing extra station corrections. This allows the structure to be approximated by a half-space and does not significantly effect the accuracy with which the hypocentres can be determined. However, this is only a good approximation for those events that lie within the network.

For more general use, the anisotropic location programs would ideally require the introduction of an arrival-time weighting scheme, and the layered location program would need to be more efficient, possibly by the introduction of some kind of reference table for calculating the direct wave. More complicated situations, such as a multilayered structure where first arrivals are a mixture of direct and refracted phases would require a much more sophisticated treatment than is possible here. Exact modelling of such structures, if possible, would result in prohibitive computing costs and it would be necessary to employ several simplifying

approximations. An interesting modification to the location programs would be to incorporate shear-wave delays (i.e. the difference in the arrival time between the arrivals of the split shear-waves) into the location procedure. This can be easily achieved and should lead to more accurate hypocentral determinations, particularly for those events outside the network.

CHAPTER 5

DETERMINATION OF DILATANCY-ANISOTROPY. 1) EXISTING METHODS

5.1 Introduction

The previous Chapters have demonstrated that in order to accurately locate earthquakes in regions of dilatancy-anisotropy it is necessary to have some means, not only of diagnosing anisotropy, but also a means of identifying the elastic constants and the orientation parameters that describe seismic-wave propagation through such a structure. This method would have to take account of temporal variations in the structure as the dilatancy-anisotropy varied in response to changes in the magnitude and direction of stress in the source region. At present there are three methods of identifying anisotropy in the Earth's crust using seismic body-waves:-

1. by suitable analysis of shear-wave polarisations;
2. from the delays between the arrival-times of the two almost orthogonally polarised shear-waves; and,
3. from the directional variation of travel-time residuals determined from hypocentral locations in an assumed isotropic structure.

Methods 1 and 2 are related, but are essentially independent of the other method. The first two have received detailed consideration elswhere (Crampin 1978; Crampin & McGonigle 1981). This Chapter will briefly summarise these methods from Crampin & McGonigle (1981) and will examine the variation of travel-time residuals in anisotropic media in more detail.

5.2 Shear-wave polarisations in anisotropic media

Two shear-waves can propagate in every direction in an anisotropic material each with different velocities and different polarisations. These waves

have fixed, orthogonal polarisations for the particular directions of phase-propagation in the particular anisotropic material. However, the velocity vector of energy propagation in anisotropic media is not, in general, coincident with the phase-velocity vector except in certain symmetry directions. The group- and phase- velocities are normally very close to each other in weakly anisotropic media, but can substantially differ in directions close to shear-wave singularities. These are points where the two shear-wave velocity surfaces are analytically continuous through a common point, and the shear-waves exchange polarisations and velocity gradients. Near such directions the group-velocity surface may have cusps and the direction of energy transport may deviate by several degrees from the phase-propagation vector, and the polarisation of a given shear-wave may suddenly swing through 90 degrees. In effect there may be shear-waves from each velocity sheet propagating along a ray in a direction where there are no cusps in the wave-surface. These two arrivals will not, in general, have orthogonal polarisations because they will be associated with different directions on the phase-velocity surfaces. However, for directions of ray inside a cusp, there may be four waves propagating: three waves from the wave-surface with the cusp, and one wavefront from the other shear-wave surface. These four wavefronts may have different orientations and different polarisations. This feature of shear-wave polarisations explains why we only observe shear-wave splitting on a few unrotated horizontal seismograms (Chapter 2). For most shear-wave trains the polarisations will be mixed, and the separate arrivals will only be identified as abrupt changes in the direction of particle motion in polarisation diagrams.

The polarisations of all shear-waves will be a function of the propagation direction and this may allow a unique identification of particular anisotropic structures. Crampin & McGonigle (1981) display

calculated shear-wave polarisations for particular directions through various anisotropic solids on stereographic projections. They illustrate that these polarisation stereograms are sensitive to the orientation and symmetry system of the anisotropy. However, the polarisations only vary slowly with changes in the degree of anisotropy.

5.3 The delay between shear-waves in anisotropic media

The delay between two shear-arrivals propagating along a ray in anisotropic structures is just the difference between the two respective group-velocities in that particular direction. The delays, like the polarisations, will be a function of the propagation direction through the anisotropic structure. Crampin & McGonigle (1981) show that the delays, when displayed on stereographic projections, can identify the symmetry system of the anisotropy and will show marked changes with the degree of anisotropy. For strong anisotropy the form of the projections may show substantial variations. This is because the delays are a function of the group-velocities, and in strong anisotropy the group-velocity may have large deviations from the phase-velocity direction and this may cause mulitple shear-arrivals and major changes in the form of the delay projections.

5.4 The variation of travel-time residuals in anisotropic media

In an ideal situation travel-time residuals should show a three-dimensional directional variation if an isotropic velocity model is used to locate hypocentres in an anisotropic structure. If there are sufficient observations from all directions, the residuals could provide information on the symmetry and orientation of dilatancy-anisotropy as the residuals would vary with azimuth and angle of emergence. However, the variation with angle of emergence will be poorly constrained in practise, due to the

fact that the depth parameter in the location of local earthquakes is not normally very well-determined. The most promising approach would be to examine the variation of residuals with azimuth as this is dependent on the normally well-constrained epicentral location. The major disadvantage of being restricted to the horizontal plane is that for some orientations of the dilatancy-anisotropy there would be no azimuthal variation in propagation velocity and consequently no variation in travel-time residuals. In addition, any weak variation may be obscured in the scatter of real observations. The most important disadvantage with travel-time residuals is that the location of earthquakes is normally performed by minimising travel-time residuals. This would inevitably result in the smoothing of any variations due to velocity-anisotropy. Despite these disadvantages, analysis of travel-time residuals is relatively straightforward and inexpensive, and may provide a useful first look at the data.

This section will illustrate some of the problems discussed above, and attempt to discern how much useful information the azimuthal variation of travel-time residuals can provide about the symmetry and orientation of dilatancy-anisotropy.

5.4.1 Synthetic travel-time residuals

Fig.5.1 illustrates the azimuthal variation of synthetic travel-time residuals for the various crack models of section 3.2. These residuals have been calculated from the look-up tables containing anisotropic velocities used in the generation of synthetic travel-times (section 3.4). They have been calculated about the average velocity in each table for a nominal hypocentral distance of 5km. The number of points at each azimuth angle reflect the different velocities possible according to the angle of incidence of the ray path. The residuals show a marked azimuthal variation

Figure 5.1. The azimuthal variation of exact P- (left-hand diagram) and shear-wave (right-hand diagram) travel-time residuals in various anisotropic models. The residuals have been calculated using the look-up tables of anisotropic velocities, and have been calculated about the mean velocity in the table for a hypocentral distance of 5km.

(a) Dry parallel cracks (model GKFF1) with the axis of rotational symmetry horizontal and striking due North.

(b) Saturated parallel cracks (model GKLF1) with the axis of rotational symmetry horizontal and striking due North.

(c) Dry coplanar normal cracks (model CPFF1) with the axis of rotational symmetry horizontal and striking due North.

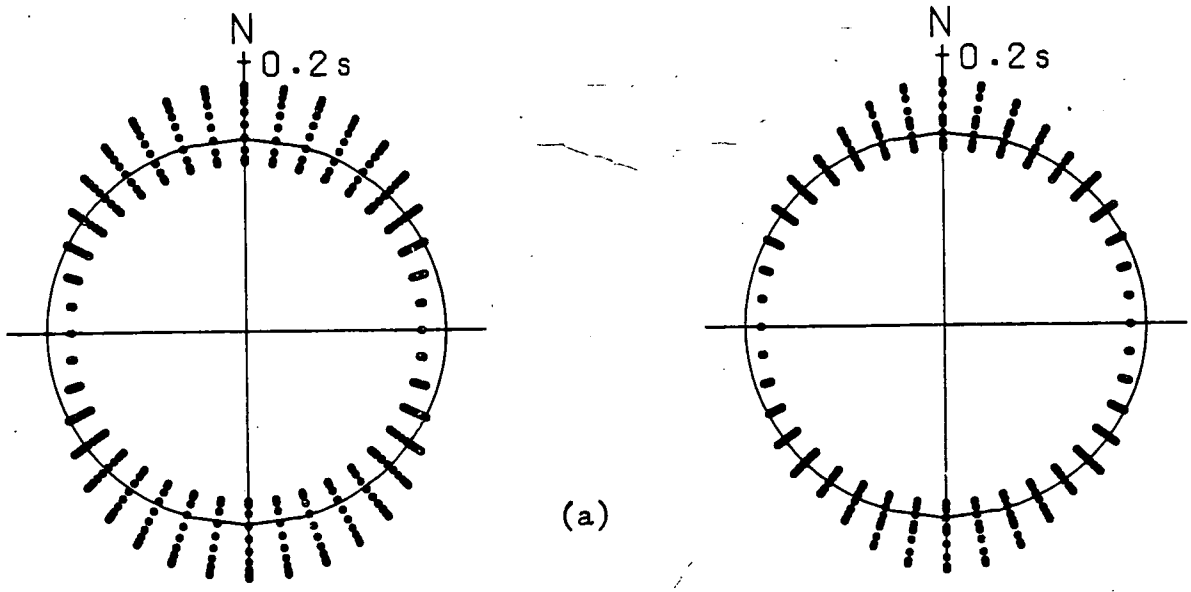

(a)

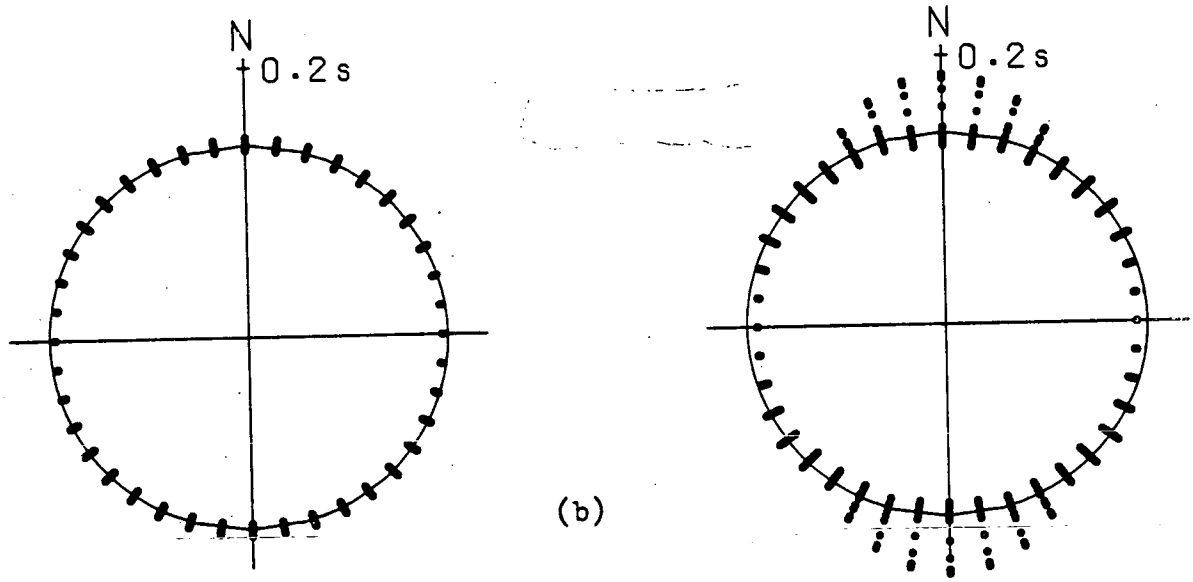

(b)

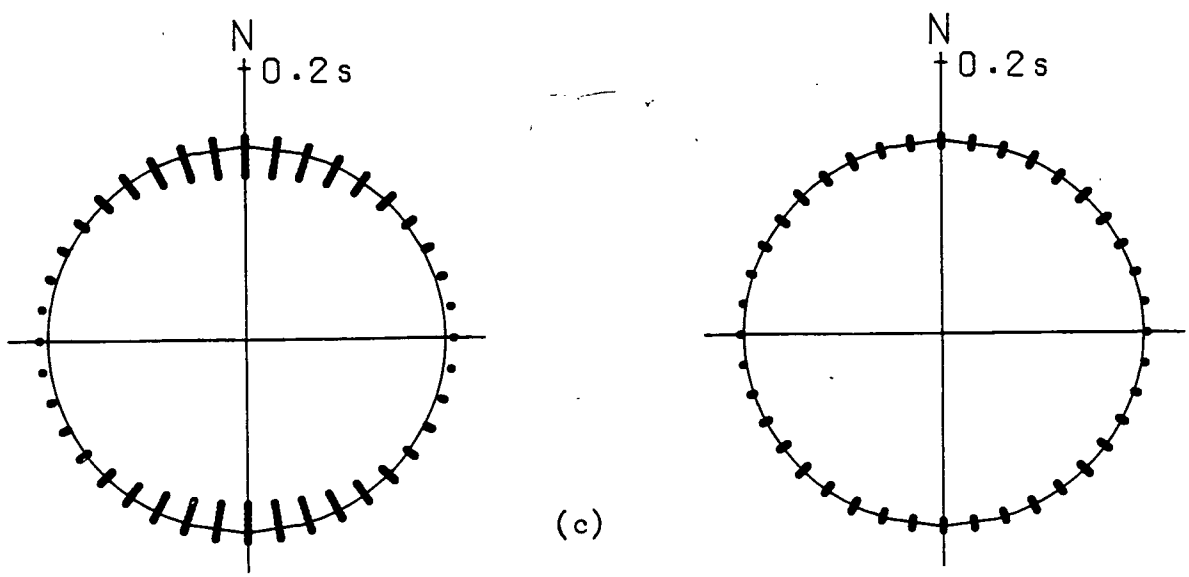

(c)

Figure 5.1 (cont.)

(d) Saturated coplanar normal cracks (model CPLF1) with the axis of rotational symmetry horizontal and striking due North.
(e) Orthogonal, bi-planar dry cracks (model GK2FFA) with the normal to the major crack system horizontal and striking due East, and the normal to the minor crack system horizontal and striking due North.
(f) Orthogonal, bi-planar saturated cracks (model GK2LFA) oriented as in (e).

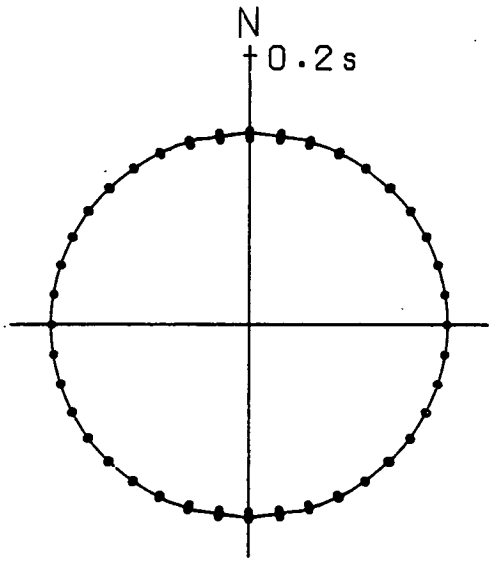

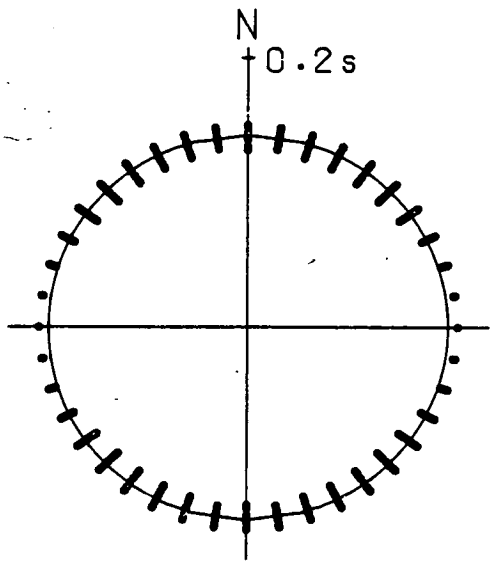

(d)

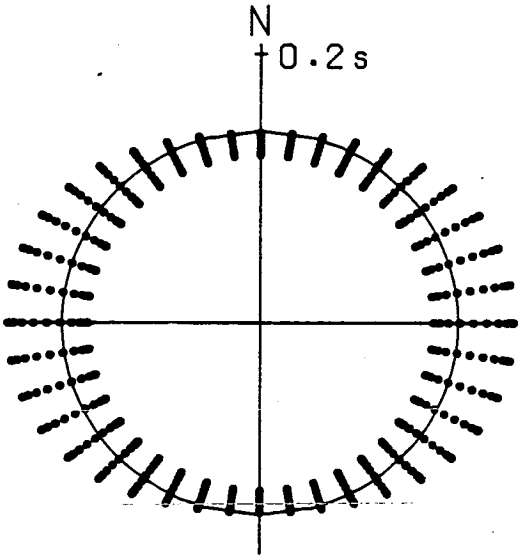

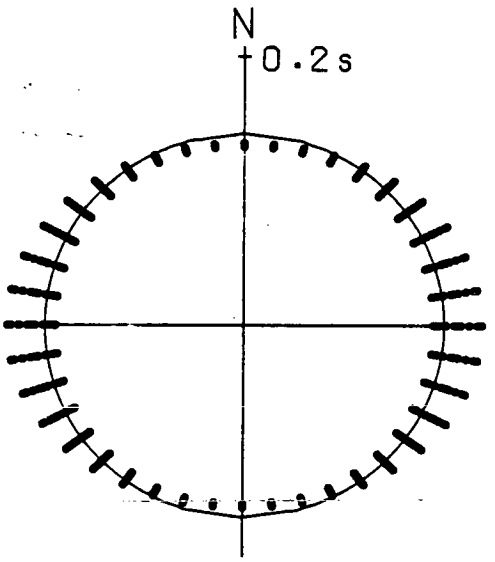

(e)

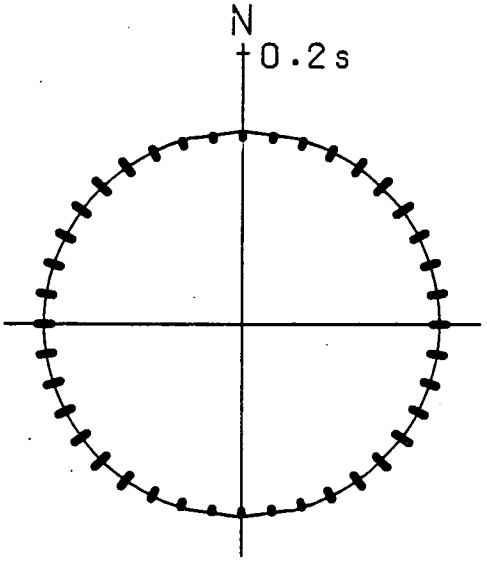

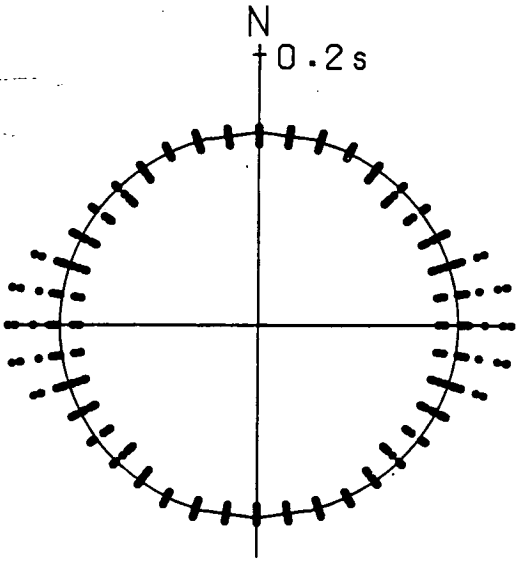

(f)

in each of the models that would be clearly indicative of velocity-anisotropy. There are obvious differences between the dry and saturated cases in each model. Both the P-wave and the shear-wave residuals show a strong variation in the dry crack models, with the P-wave slightly stronger than the shear-waves in all cases. In the saturated crack models the shear-wave still shows a strong variation but the P-wave variation is very much reduced. This suggests that it would be quite straightforward to distinguish between dry and saturated crack-anisotropy on the basis of travel-time residuals. However the form of the azimuthal variation is not significantly different between each of the crack models. Although it is possible to discern the difference in this illustration, where exact travel-time residuals have been calculated, it may be impossible in practice.

5.4.2 Travel-time residuals from earthquake locations

Travel-time residuals, in practice, are calculated as the observed arrival-time minus the calculated arrival-time from the hypocentral location through the assumed structural model to the station recording that particular phase. It will therefore depend on the accuracy of the arrival-time that has been picked, and on the accuracy of the hypocentral location. The need for an accurate hypocentral determination is paramount, because when looking for an azimuthal variation of residuals due to velocity-anisotropy it is necessary to normalise the calculated residual to some nominal hypocentral distance. Differences in path lengths will distort azimuthal variations if the residuals are not normalised. It has already been shown that the assumption of isotropy when locating earthquakes in anisotropic structures can lead to very large mislocations. Therefore it is expected that this will result in severe modifications to the variation of travel-time residuals.

Fig.5.2 shows the azimuthal variation of travel-time residuals from the locations determined by the SQ1 and TDP1 networks (Figs.3.3 and 3.14 respectively) where the model GKFF1, (dry, parallel cracks), is used to model dilatancy-anisotropy surrounding a pure-strike-slip fault. Figs.5.2a and 5.2b are from the locations shown in Fig.3.5b where P- and S-arrivals at stations in the SQ1 network have been used to locate the events. There is a very strong variation in both the P- and S-wave residuals that would indicate that this was a dry crack structure. The large positive residuals in the NW-SE directions indicate that this is the low velocity direction, but the scatter on the residuals would preclude any conclusion as to which particular crack model it is. Figs.5.2c and 5.2d show the travel-time residuals from the locations determined by the TDP1 network using P- and S-arrivals at every station (i.e. those shown in Fig.3.15b). The P-wave residuals show a much reduced variation compared to the SQ1 network, but there is still an indication of late arrivals in an easterly and NW direction. This offset away from the NW-SE direction is due to the effect of poor locations, and is particularly obvious in the shear-wave residuals where there is almost a 90 degree rotation of the late arrivals. This would make any detailed interpretation in terms of anisotropy very difficult. Fig 5.2e shows the P-wave residuals from the locations shown in Fig.3.5a determined by the SQ1 network using only P-arrivals. Again there is a very strong azimuthal variation that would indicate dry crack dilatancy-anisotropy and a low velocity direction in the NW-SE direction. Similarly, Fig.5.2f shows the P-wave residuals calculated from the locations determined by the TDP1 network using only P-arrivals (Fig.3.15a). In this case there is very little azimuthal variation and dilatancy-anisotropy would <u>not</u> be diagnosed.

Fig.5.3 illustrates the variation of travel-time residuals for the case of saturated crack-anisotropy on a pure-strike-slip fault. Again the

Figure 5.2. The azimuthal variation of travel-time residuals from event locations in anisotropic media determined in Chapter 3 under the assumption of isotropy. The anisotropic structure is GKFF1 (dry, parallel cracks) oriented to model dilatancy-anisotropy associated with a strike-slip fault.

(a) P-wave residuals from relocations of the events of Fig.3.3 (the SQ1 network) determined using P- and S-arrivals (i.e. the locations shown in Fig.3.5b).

(b) As (a) for S-wave residuals.

(c) P-wave residuals from relocations of the events of Fig.3.14 (the TDP1 network) determined using P- and S-arrivals (i.e. the locations shown in Fig.3.15b).

(d) As (c) for S-wave residuals.

(e) P-wave residuals from relocations of the events of Fig.3.3 (the SQ1 network) determined using P-arrivals (i.e. the locations shown in Fig.3.5a).

(f) P-wave residuals from relocations of the events of Fig.3.14 (the TDP1 network) determined using P-arrivals (i.e. the locations shown in Fig.3.15a).

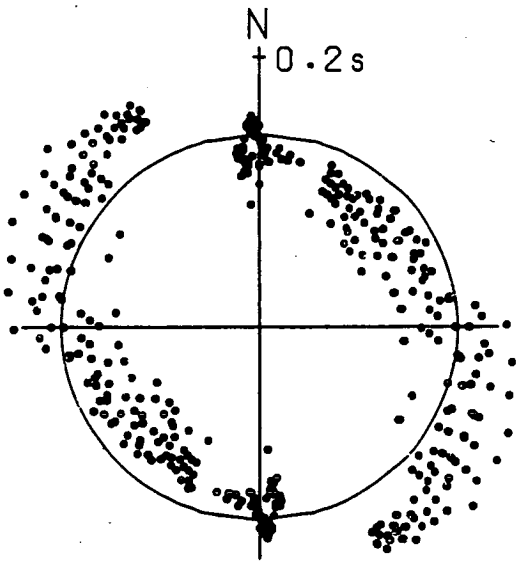

(a)

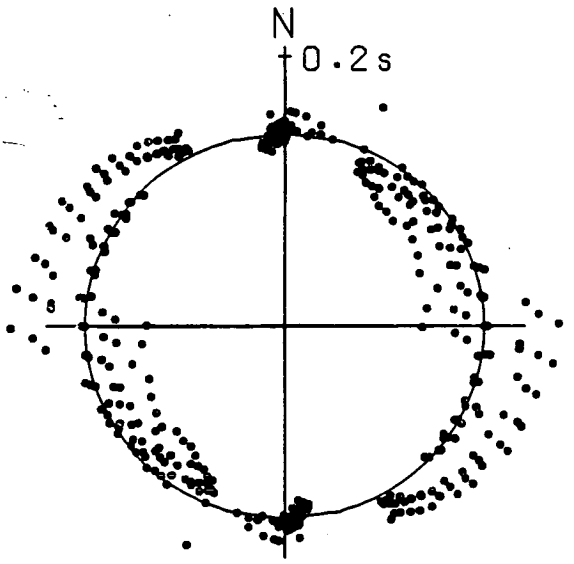

(b)

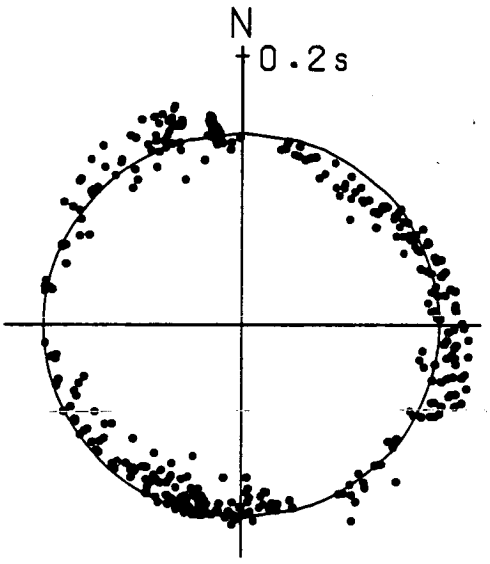

(c)

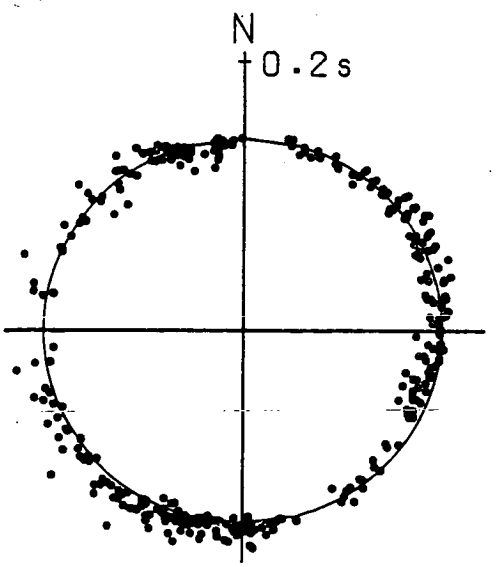

(d)

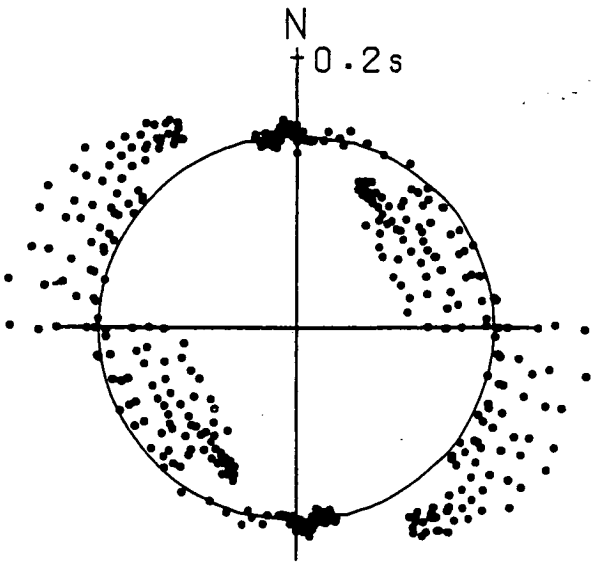

(e)

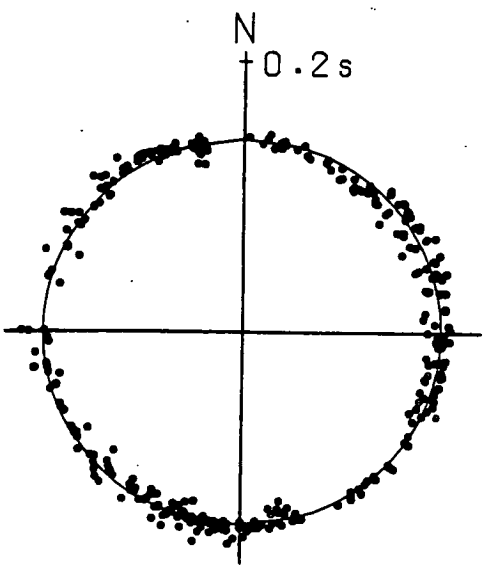

(f)

SQ1 network displays good diagnostic capabilities, with a larger shear-wave variation than P-wave, indicating that the structure is saturated and defining the direction of low velocities. However with the TDP1 network there is no azimuthal variation that would indicate velocity-anisotropy even when shear-wave arrivals are used in the location procedure.

5.4.3 Dipping axis of symmetry

Fig.5.4 illustrates the variation of travel-time residuals in dry crack dilatancy-anisotropy where the axis of rotational symmetry strikes at an azimuth of 135 degrees and is inclined above the surface by 30 degrees. There is no significant difference in the variation of the residuals from the variation for a horizontal axis, when the hypocentres have been determined by the SQ1 network (Fig.5.4a 5.4b and 5.4e). However, when the locations have been determined by the TDP1 network (Figs.5.4c, 5.4d and 5.4f) the positive residuals in the NW quadrant have become negative, but the positive residuals in the easterly direction remain. There is very little variation of the S-wave residuals.

5.4.4 An isotropic structure with an internal dipping interface

A model which may produce an azimuthal variation of travel-time residuals that would be similar to those in an anisotropic half-space, is an isotropic structure with an internal dipping interface and which is assumed to be an isotropic half-space. In order to generate travel-times through such a structure a routine similar to that described in section 4.3.1 can be employed. In that case an iterative scheme was required to calculate the travel-time of the direct wave from a source in an anisotropic half-space overlain by an isotropic layer. A similar routine can be employed here because the problem is the same - namely that the refracted wave no longer lies in the same vertical plane as that defined by the

Figure 5.3. The azimuthal variation of travel-time residuals from event locations in anisotropic media determined in Chapter 3 under the assumption of isotropy. The anisotropic structure is GKLF1 (saturated parallel cracks) oriented to model dilatancy-anisotropy associated with a strike-slip fault.

(a) P-wave residuals from relocations of the events of Fig.3.3 (the SQ1 network) determined using P- and S-arrivals (i.e. the locations shown in Fig.3.5d).

(b) As (a) for S-wave residuals.

(c) P-wave residuals from relocations of the events of Fig.3.14 (the TDP1 network) determined using P- and S-arrivals (i.e. the locations shown in Fig.3.15d).

(d) As (c) for S-wave residuals.

(e) P-wave residuals from relocations of the events of Fig.3.3 (the SQ1 network) determined using P-arrivals (i.e. the locations shown in Fig.3.5c).

(f) P-wave residuals from relocations of the events of Fig.3.14 (the TDP1 network) determined using P-arrivals (i.e. the locations shown in Fig.3.15c).

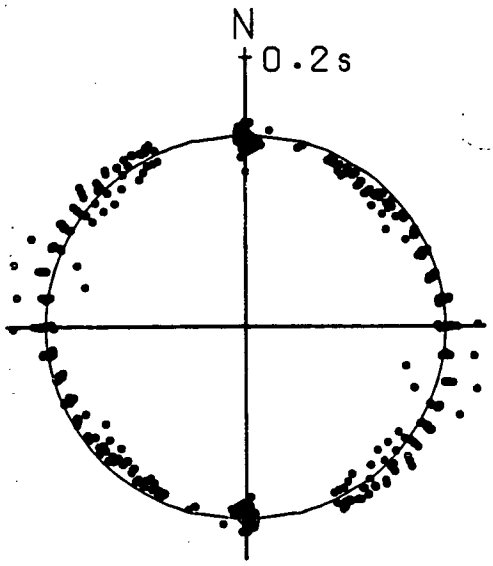

(a)

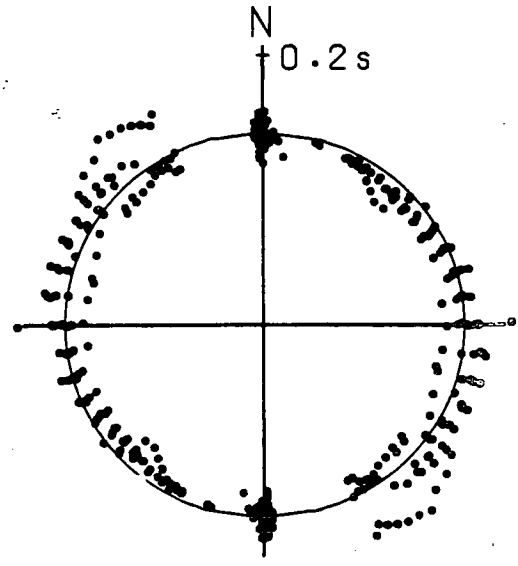

(b)

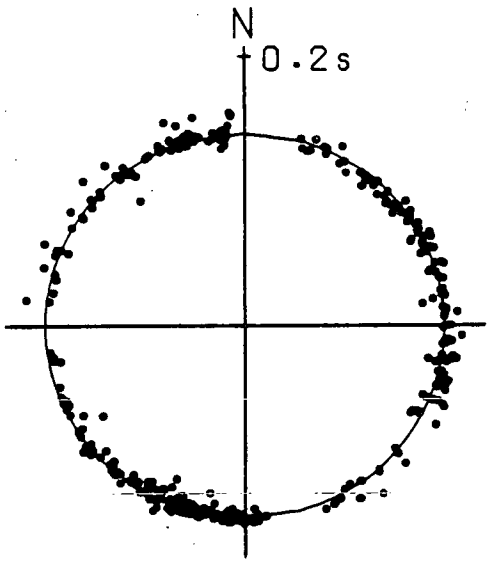

(c)

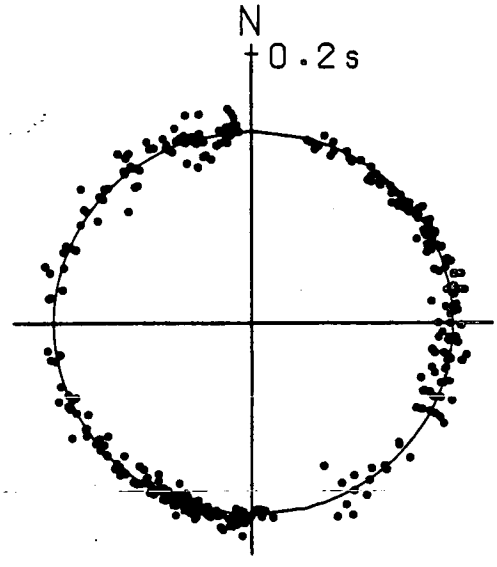

(d)

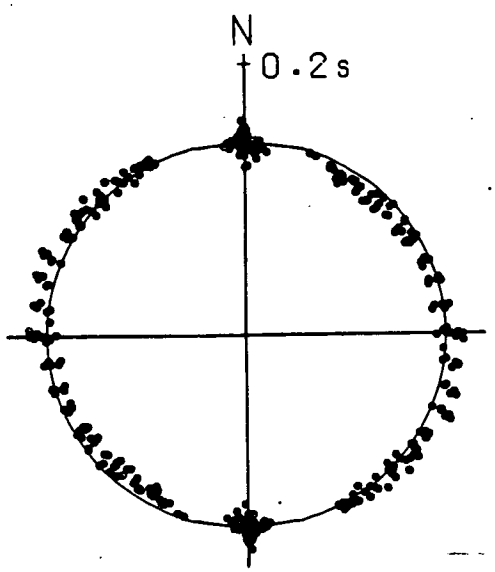

(e)

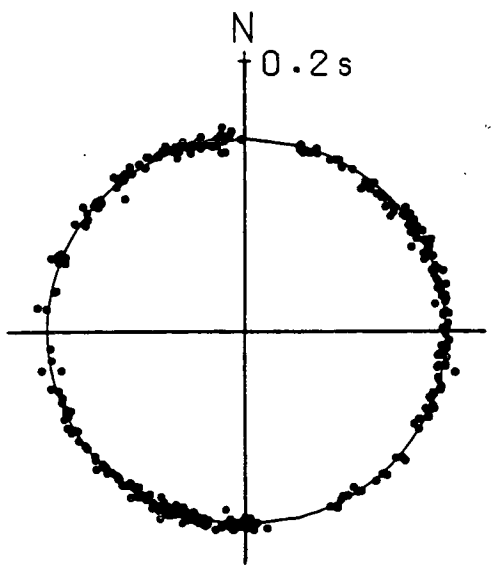

(f)

Figure 5.4 The azimuthal variation of travel-time residuals from event locations in anisotropic media determined under the assumption of isotropy. The anisotropic structure is GKFF1 (dry, parallel cracks) where the axis of rotational symmetry strikes in a direction N135E and is inclined above the surface by 30 degrees.
(a) P-wave residuals from relocations of the events of Fig.3.3 (the SQ1 network) determined using P- and S-arrivals (i.e. the locations shown in Fig.3.20a).
(b) as (a) for S-wave residuals.
(c) P-wave residuals from relocations of the events of Fig.3.14 (the TDP1 network) determined using P- and S-arrivals.
(d) as (c) for S-wave residuals.
(e) P-wave residuals from relocations of the events of Fig.3.3 (the SQ1 network) determined using P-arrivals only (i.e. the locations shown in Fig.3.20b).
(f) P-wave residuals from relocations of the events of Fig.3.14 (the TDP1 network) determined using P-arrivals only.

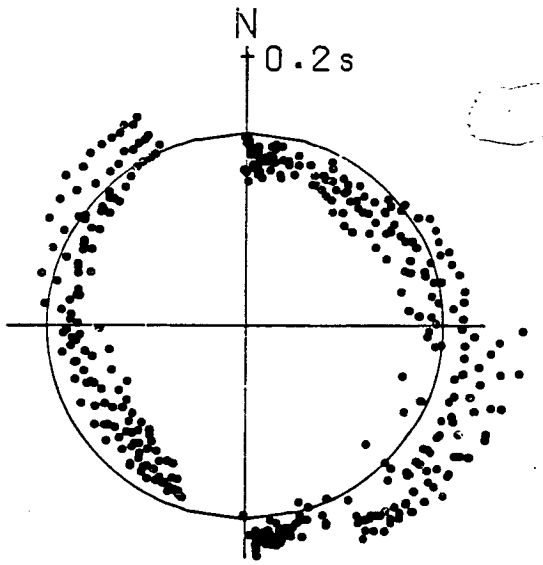

(a)

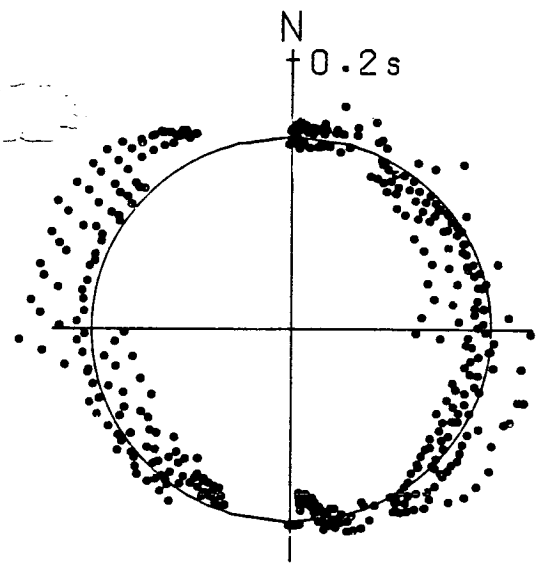

(b)

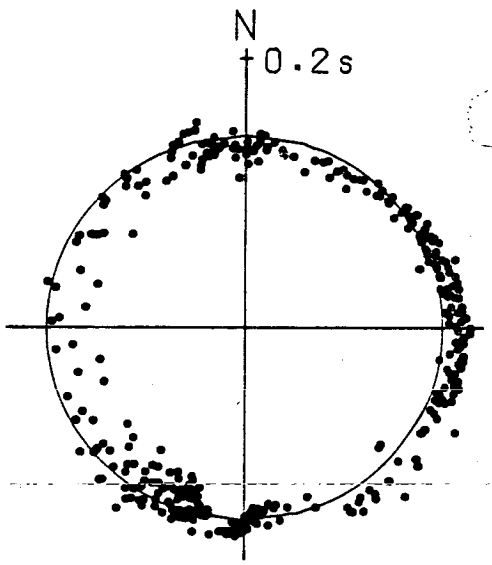

(c)

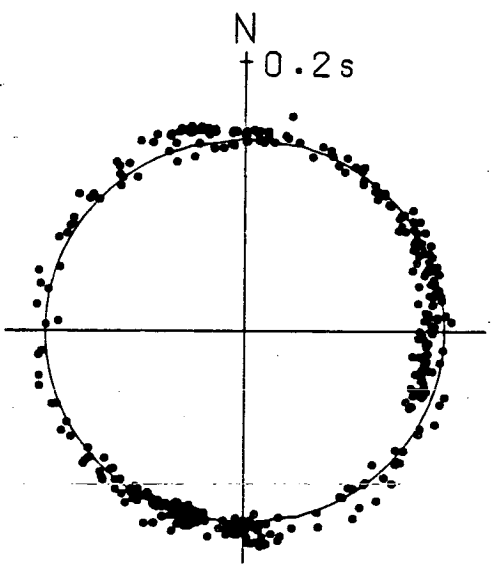

(d)

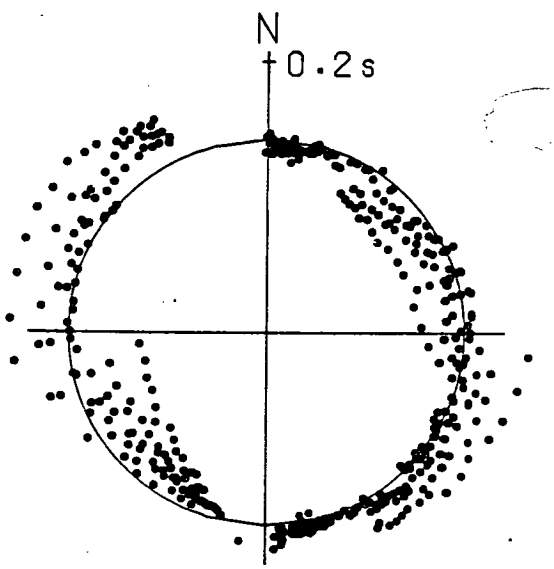

(e)

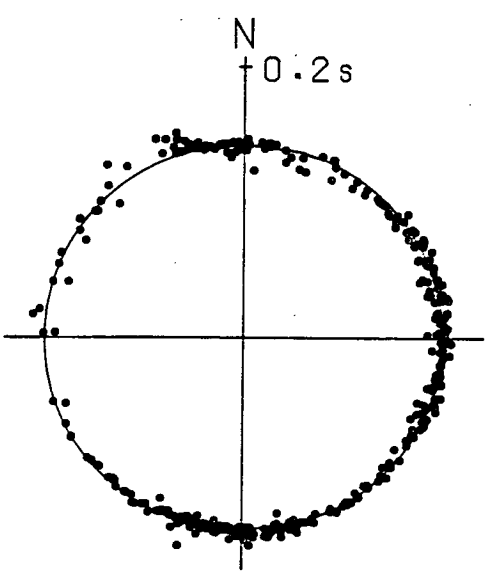

(f)

source and receiver. However the calculation of the refracted wave is different in this case. In this application the refracted wave is calculated by first rotating the interface and incident ray into a new co-ordinate system such that the interface is horizontal. The refracted wave can then be calculated by simple application of Snell's Law at the interface, and by then applying an inverse rotation of the system into its former state. This procedure is repeated using the iterative scheme described in section 4.3.1 until the emergent point of the ray is within 1/50km of the reciever. Providing that Poisson's ratio is the same in both the half-space and the layer, the minimum path for the shear-wave will be the same as that for the P-wave. The travel-times can then be calculated on the basis of the velocities in each section of the model.

Fig.5.5 and 5.6 illustrate the variation of travel-time residuals obtained when an isotropic structure containing a dipping interface is approximated by an isotropic half-space. The model in this case consists of two layers with P-wave velocities of 5.1km/sec and 5.7 km/sec, separated by an interface that strikes along the line of epicentres in Figs.3.3 and 3.14 and dips to the west by 20 degrees. Poisson's ratio in the half-space and the layer is equal to 0.25. The travel-times through this structure have been rounded to 1/20 of a second to simulate the scatter of real data, as in Chapter 3. Figs.5.5a and 5.5b show the P-wave and S-wave residuals determined directly from the calculated travel-times from the true hypocentres to stations of the SQ1 network. The residuals have been determined as the calculated travel-time minus the travel-time based on the hypocentral distance and the highest velocity in the structure. This figure illustrates that there are positive residuals to the west and zero residuals to the east as would be expected. This variation is markedly different from any variation due to velocity-anisotropy that has been modelled here. Figs.5.5c and 5.5d show the variation of residuals after

Figure 5.5 The azimuthal variation of travel-time residuals from the events of Fig.3.3 (the SQ1 network) where an isotropic half-space is used to model an isotropic structure containing a dipping interface. The interface strikes along the line of epicentres and dips below the surface to the west by 20 degrees. The interface separates two sections with Vp = 5.1 km/sec to the west, and Vp = 5.7 km/sec to the east. Possson's ratio in both sections is 0.25.

(a) Exact P-wave residuals calculated from the true hypocentres to each station and assuming a P-wave velocity of 5.7 km/sec.

(b) Exact S-wave residuals calculated from the true hypocentres to each station and assuming a S-wave velocity of 3.3 km/sec.

(c) P-wave residuals calculated from hypocentral locations determined under the assumption of an isotropic half-space with a P-wave velocity of 5.7 km/sec, a Poisson's ratio of 0.25, and using P- and S-arrivals at every station.

(d) As (c) for S-wave residuals.

(e) As (c) for locations determined using only P-arrivals at every station.

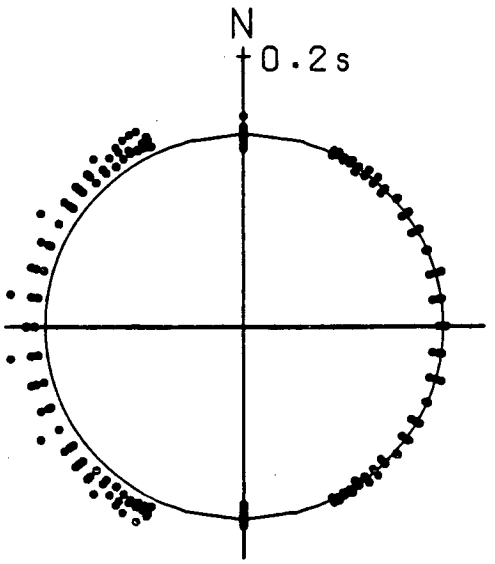

(a)

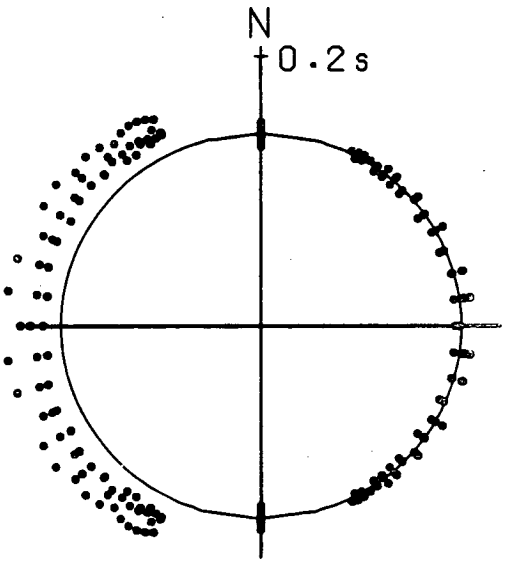

(b)

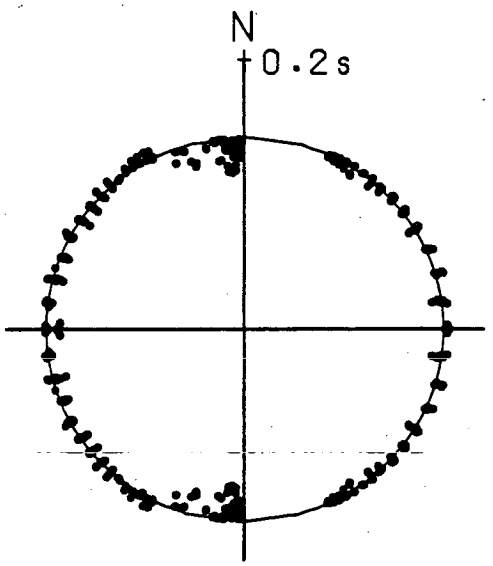

(c)

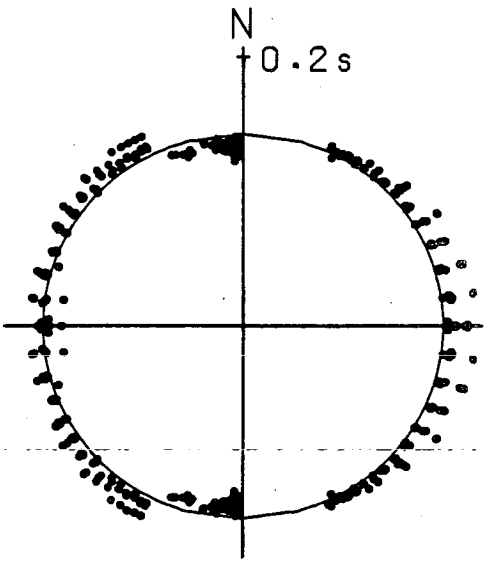

(d)

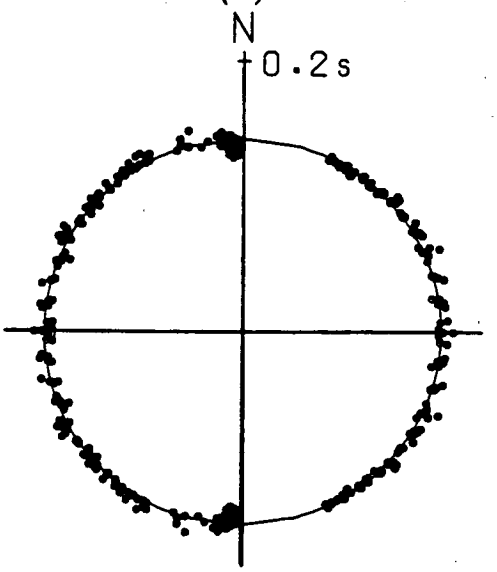

(e)

Figure 5.6 The azimuthal variation of travel-time residuals from the events of Fig.3.14 (the TDP1 network) where an isotropic half-space is used to model an isotropic structure containing a dipping interface. The interface strikes along the line of epicentres and dips below the surface to the west by 20 degrees. The interface separates two sections with Vp = 5.1 km/sec to the west, and Vp = 5.7 km/sec to the east. Possson's ratio in both sections is 0.25.

(a) Exact P-wave residuals calculated from the true hypocentres to each station and assuming a P-wave velocity of 5.7 km/sec.

(b) Exact S-wave residuals calculated from the true hypocentres to each station and assuming a S-wave velocity of 3.3 km/sec.

(c) P-wave residuals calculated from hypocentral locations determined under the assumption of an isotropic half-space with a P-wave velocity of 5.7 km/sec, a Poisson's ratio of 0.25, and using P- and S-arrivals at every station.

(d) As (c) for S-wave residuals.

(e) As (c) for locations determined using only P-arrivals at every station.

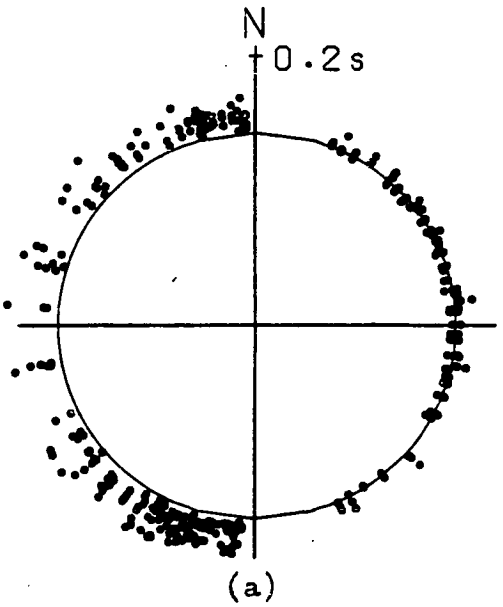

(a)

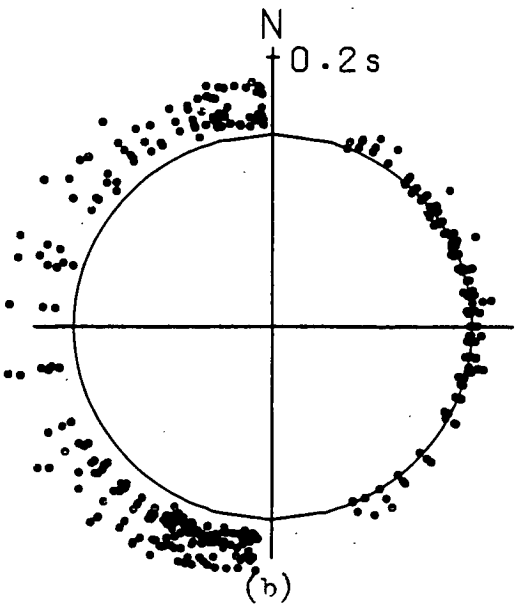

(b)

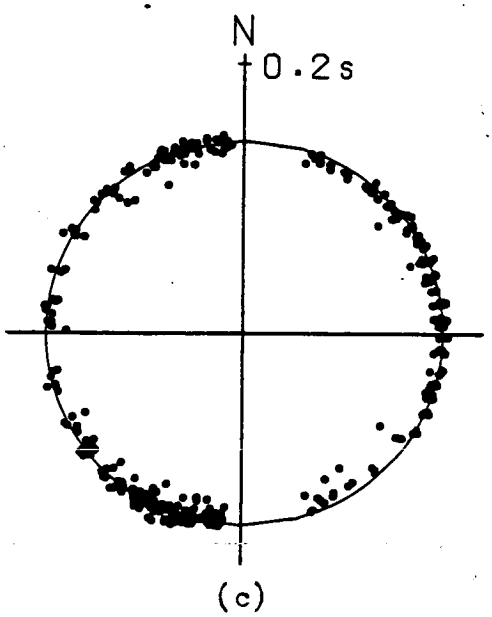

(c)

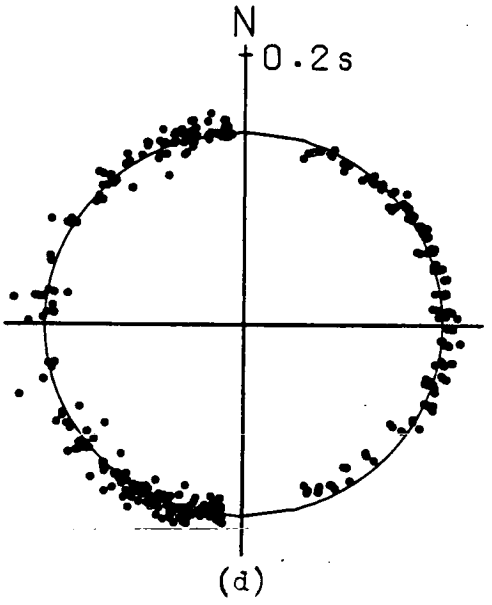

(d)

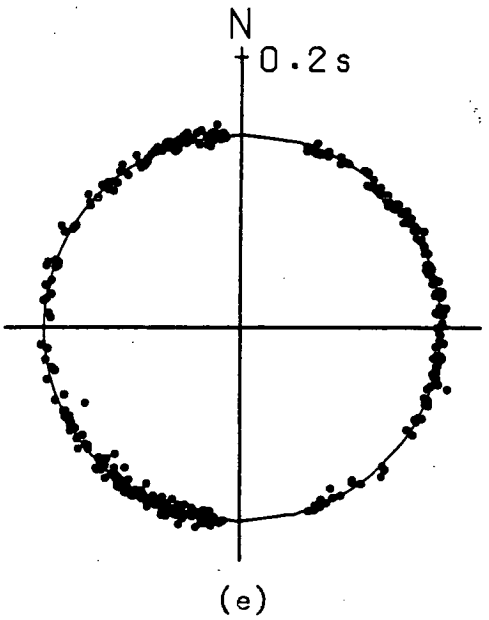

(e)

the events have been relocated under the assumption of an isotropic half-space with a P-wave velocity of 5.7 km/sec. The P-wave residuals show no azimuthal variation, but there is a small variation in S-wave residuals. This example is qualitatively similar to that of saturated crack anisotropy with a horizontal axis of symmetry striking east-west (c.f. Fig.5.3b). Fig.5.5e shows the variation of P-wave residuals when the events have been relocated using only P-arrivals. Again there is no obvious azimuthal variation.

Fig.5.6 illustrates the variation of travel-time residuals in the same structure and under the same assumptions, but when the events have been located by the stations of the TDP1 network. The theoretical variation of residuals is very marked and is completely different from any variation that would be caused by velocity-anisotropy. After relocating the events, there is no variation in either the P-wave or S-wave residuals.

Further work on different isotropic structures with internal dipping interfaces suggests similar conclusions. The theoretical variation of residuals show a very obvious difference from those due to velocity anisotropy, and this variation largely disappears when the residuals are determined from the relocated hypocentres. However with the SQ1 network there is an indication of an azimuthal variation in the S-wave residuals. This suggests that with a regular network at least, velocity-anisotropy could be diagnosed from the analysis of travel-time residuals when the true structure is isotropic with an internal dipping interface. Perhaps more importantly, the variation of travel-time residuals due to velocity-anisotropy could be modelled by an isotropic structure containing a dipping interface. However this problem may not arise with the TDP1 network as it does not appear to have sufficient diagnositic capabilities to identify a dipping interface or velocity-anisotropy from the analysis of travel-time residuals.

5.4.5 An isotropic layer above an anisotropic half-space

It has already been shown (section 4.3) that the assumption of an isotropic structure when locating events in an anisotropic half-space overlain by a horizontal isotropic layer does not result in very different locations from the simple anisotropic half-space case. This is particularly true for a thin layer of 1km thickness. Consequently there is no reason to expect that the variation of travel-time residuals would be significantly different in this case from those illustrated here.

5.5 Discussion

This Chapter has briefly presented three existing methods of determining dilatancy-anisotropy in seismic regions. Of these the most sensitive appears to be the analysis of shear-wave polarisations and shear-wave delays. Crampin & McGonigle (1981) believe that a combined analysis of shear-wave polarisations and delays would offer the best diagnostic capabilities. Once the anisotropic structure has been determined, using observations from many ray directions, only a few observations at particular directions would be necessary to monitor any temporal variations. The analysis of shear-wave polarisations and delays from the TDP experiments is currently in progress.

In a similar study Rothman et al.(1974) suggest that the variation of travel-time residuals may allow the estimation of velocities in anisotropic structures to be used in a location program that takes account of velocity variations. Section 3.8 discussed how the approximations to velocity-anisotropy made by Rothman et al.(1974) are inappropiate. In addition, their analysis uses a high resolution network of stations with regular geometry. It has been demonstrated that such a network can lead to remarkable diagnostic observations which are not possible with the irregular networks actually deployed, particularly if only P-arrivals are

used to locate earthquakes. Even with a regular network of stations, an azimuthal variation in travel-time residuals may, at best, only indicate the direction of high and low velocities in an anisotropic structure. Errors in the arrival-times (not considered by Rothman et al.), and poor determination of the depth parameter of local earthquakes would preclude a more detailed analysis of the three-dimensional anisotropic variations. As demonstrated, travel-time residuals would not provide a sufficiently accurate estimation of velocities to utilise in a location program that allowed for the velocity variations. This is particularly the case for the TDP1 network, and is largely the result of determining hypocentral locations by minimising travel-time residuals.

CHAPTER 6

DETERMINATION OF DILATANCY-ANISOTROPY. 2) THE JOINT DETERMINATION OF HYPOCENTRAL LOCATIONS AND ANISOTROPIC STRUCTURE

6.1 Introduction

A suite of earthquake arrival-times recorded by a given network provides information not only about the earthquake locations, but also about the velocity structure through which the seismic-waves have travelled. If there is sufficient redundancy in the number of observations, then this can be used to determine the velocity structure. The joint-inversion of suites of earthquake arrival-times for hypocentral locations and velocity structure has been successfully applied to many structural investigations. Crosson (1976) describes a technique for determining station corrections and a multi-layered structure that includes low velocity zones. Aki & Lee (1976) invert arrival-times to determine the three-dimensional structure under a seismic array. They parameterize the structure by a number of small rectangular blocks through which a P-wave velocity is to be determined. For simplicity, they restricted the inversion to a one-step procedure. Their method was recently extended to the more usual iterative procedure by Hawley, Zandt & Smith (1981). Ward, Schlue & Sandford (1981), also using an extension of the Aki & Lee method, invert P-arrivals from 40 local events in New Mexico to determine the P-wave velocity in a series of blocks beneath the monitoring network. Spencer & Gubbins (1980) use P-arrivals to determine the velocity structure of a subduction zone beneath the North Island, New Zealand. All of these studies have been concerned with determining the isotropic velocity structure of the area concerned.

It was shown in Chapter 4 that it is possible to accurately locate earthquakes in regions of anisotropy, and so by reasonable inference it seems possible that the joint-inversion technique could be applied to determine the anisotropic structure beneath the TDP networks as indicated

by observations of shear-wave splitting (Chapter 2). This method would be able to take account of the three-dimensional variation in velocities, correctly locate the hypocentres with respect to the current anisotropic model, and also take account of any temporal variations. Such a technique will only be possible if a sufficient number of well-recorded and well-distributed events are available, and that they occur sufficiently often to isolate any temporal variations. The TDP events satisfy these conditions well.

This Chapter will describe the theory of such a program and will illustrate its performance on synthetic data. This will be achieved by inversion of synthetic data with varying degrees of noise added to the arrival-times, and by attempting to determine the dependence of the final solution on the initial model. In addition, we will illustrate the solutions obtained in ten case studies using various isotropic/anisotropic structures. The event and phase distribution used in the case studies corresponds exactly to a real data set from TDP1 that will be used in Chapter 7. At present, application of the inversion process is limited to a homogeneous half-space, but in principle the method is extendable to layered and laterally varying structures, providing that enough data is available and that the calculation of travel-times through such a structure can be accomplished both efficiently and accurately.

6.2 Theory

The theory of a joint-inversion program to determine both the anisotropic structure and the hypocentral locations is very similar to those mentioned above and is an extension of the theory of Appendix B for locating earthquakes in a specified structure.

For a suite of arrival-times from m events recorded at n stations, the travel-time from the ith event to the jth station is;

$$T_{ij} = T_{ij}(p_{1i}, p_{2i}, p_{3i}, p_{4i}, a_1 \ldots\ldots\ldots a_L) \qquad \begin{matrix} i = 1,m \\ j = 1,n \end{matrix} \qquad (6.1)$$

where p_{ki} (k=1,4) are the hypocentre parameters and a_L are the parameters that describe the velocity model. For this particular application these parameters will be the elastic constants that describe seismic-wave propagation through the anisotropic half-space, and the parameters that describe the orientation of the anisotropic variations. Equation (6.1) can be expanded in a first-order Taylor's expansion relating small changes of travel-times to small changes of the hypocentre and model parameters:

$$\delta T_{ij} = \sum_{k=1}^{4} \frac{\partial T_{ij}}{\partial p_{ki}} \delta p_{ki} + \sum_{l=1}^{L} \frac{\partial T_{ij}}{\partial a_l} \delta a_l \qquad (6.2)$$

Equation 6.2 can be written in matrix form as;

$$\underline{A}\,\underline{x} = \underline{B} \qquad (6.3)$$

where $\underline{A}$ contains the partial derivatives of (6.2), $\underline{x}$ contains the hypocentre and model corrections, and $\underline{B}$ is the column vector of residuals based on the current solution.

6.2.1 The forward problem

The forward problem consists of determining the travel-times T_{ij} between the source and the receiver, and of calculating the travel-time derivatives contained in matrix $\underline{A}$. The generation of velocities in an anisotropic solid has been outlined in Appendix A, and the calculation of travel-times in a half-space easily follows. Analytic expressions for travel-time derivatives with respect to the hypocentre parameters in an anisotropic half-space have been described in section 4.2, where they were expressed as functions of the derivatives of the velocity with respect to the propagation direction. In Chapter 4 the anisotropic velocities and their derivatives were referred from look-up tables for particular anisotropic solids. In this application the anisotropic structure is continually changing as the solution progresses and so look-up tables for particular anisotropic solids would be inefficient. In addition, travel-time derivatives with respect to

the elastic constants and orientation parameters are also required. Analytical expressions for these, if they exist, are unlikely to be very simple. For these two reasons, all travel-time derivatives are calculated numerically, and so unlike the anisotropic half-space location program of section 4.2, the routine for calculating anisotropic velocities is an integral part of the joint-inversion program.

Numerical experiments show that the travel-time derivatives with respect to the hypocentre parameters are two orders of magnitude greater than the velocity model derivatives. This would result in an undesirable bias towards corrections to the earthquake locations in the inversion procedure. The travel-time derivatives with respect to the model parameters are therefore weighted so that they are approximately equal to the hypocentre derivatives.

6.2.2 The inverse problem

From Appendix B the solution to Equation (6.3) is given by:

$$\underline{x} = (\underline{A}^T \underline{A})^{-1} \underline{A}^T \underline{B} \qquad (6.4)$$

In this application the matrix $A^T A$ is very large but sparse, and it would be costly in computing time to attempt to invert the matrix. In this program the system is solved by a Gauss-Jordan algorithm modified to ignore zero components.

One of the common problems in the joint-inversion procedure described above is that the normal equation matrix $A^T A$ can be singular or near singular. This arises because the nature of the problem changes from iteration to iteration, and the solution may drift into an area of instability where some partial derivatives in matrix A become zero or near-zero, resulting in zero or near-zero eigenvalues in $A^T A$. This is reflected by large changes in one or more components of the solution vector for only small changes in the model and hypocentre parameters. Such an unstable performance is clearly undesirable and it is necessary to restrict the solution to a sensible region by a process of damping.

There are two ways of achieving damping (Spencer & Gubbins 1980). One method is the generalised inverse where the matrix A^TA is decomposed and its eigenvalues are examined for smallness. Near zero eigenvalues are removed and corresponding solution parameters held constant for that iteration. This method has the advantage of allowing greater control over the way the solution is performed. However it requires a great deal more computing time than the second method. This is the Levenberg-Marquadt algorithm and is described in detail by Crosson (1976). This method involves modifying Equation (6.4) to:

$$\underline{x} = (\underline{A}^T\underline{A} + \lambda^2\underline{I})^{-1}\underline{A}^T\underline{B} \qquad (6.5)$$

where λ is a weighting coeffecient to be adjusted to the requirement of the problem. Crosson (1976) shows that the major result of introducing such a factor is that it prevents the inverse of any small eigenvalue in A^TA becoming large enough to cause instability in the solution. The weighting coefficient needs to be small enough not to modify the solution, but large enough to prevent instability occuring. It is anticipated that this program will be very expensive to use, and so the second approach to the problem, being appreciably less time-consuming, will be adopted. In this application λ is initially assigned a value of 0.01 and is reduced by one order of magnitude whenever a new solution is better than the solution from the previous iteration. When divergence occurs it is increased by one order of magnitude and the iteration is repeated from the previous parameter estimates. This process is repeated until the solution stabilises.

Following the theory outlined above, five programs have been written in Fortran to invert arrival-times and jointly determine hypocentral locations and velocity structure. All of these programs assume the velocity structure is a homogeneous half-space. In summary these programs are as follows:

1) A program to solve for P-wave and shear-wave velocities in a

homogeneous, isotropic half-space. This program can be used to determine trial hypocentres for the anisotropic inversion programs and also to provide a reference solution for statistical tests.

2) A program to solve for anisotropic structures possessing hexagonal symmetry (e.g. parallel and co-planar-normal crack systems). These structures can be fully described by five independent elastic constants and two parameters that describe the orientation. The program uses P- and first shear-wave arrival-times, and calculates group-velocities through the structure.

3) A program to solve for anisotropic structures possessing orthorhombic symmetry (e.g. orthogonal, bi-planar crack systems). Such structures can be described by nine elastic constants and two parameters that describe its orientation. The program again uses P- and first shear-wave arrivals but is restricted to phase-velocity calculations. This is because the calculation of group-velocities in anisotropic solids is performed by the linear interpolation of look-up tables which have to be reset every time the solid is changed. For hexagonal systems a one-dimensional table measured from the symmetry axis is sufficient, but for orthorhombic systems a look-up table of group-velocities for all possible phase-velocity directions is necessary because there is no single direction of axial symmetry. The generation and searching of this table accounts for approximately 60% of the total time required for the inversion. Therefore, limited computing resources restricts the inversion for orthorhombic structures to phase-velocity calculations only.

4) A program to solve for anisotropic structures possessing hexagonal symmetry using P- and both shear-wave arrival-times. The program performs the inversion by calculating the delay between the shear-waves rather than the actual arrival-time of the second shear-wave. This is because although the first shear-wave arrival will have an

unknown error associated with it (due to instrumental and reading errors), the delay between the shear-wave arrivals can be read with greater precision from particle motion diagrams, (as illustrated in Chapter 2), and will also remove the effect of any instrumental errors.

5) As 4) for orthorhombic symmetries using phase-velocities. Although phase-velocities may be a reasonable approximation to observed P- and first shear-wave group-velocities, the delay between the two shear-wave phase-velocities will be a poor approximation to that between group-velocities, particularly in directions where there are cusps on the shear-wave surface (Crampin & McGonigle 1981).

The input data to these programs are the station co-ordinates, station corrections, the trial hypocentral locations and specifications for the trial velocity structure. Programs 1,2 and 3 invert a maximum of two phases (P and first S) recorded at 10 stations from 30 events, while programs 4 and 5 can invert a maximum of three phases (P, first S, and the shear-wave delay), recorded at 10 stations from 20 events. Each of the programs assigns equal weights to all of the arrival-times and, in the anisotropic programs, the model parameters are weighted by a factor of 100 compared to the hypocentre parameters.

The orientation of the anisotropic structure is parameterised by two rotations of the anisotropic solid given as (θ , ϕ). The first rotation, θ , measures an angle of rotation about the vertical anticlockwise from due East in the real Earth. The parameter, ϕ , measures an angle of rotation of the axis pointing due East, about the North-South horizontal, positive below the surface. Therefore an orientation of (0,0) is due East and horizontal, an orientation of (0,90) is vertical, but an orientation of 30,90 strikes due North and is inclined below the surface by 56 degrees. The following set of relations demonstrate how to convert these rotations into direction cosines in the real Earth:

$$x_1 = \cos\theta \cos\phi$$
$$x_2 = \sin\theta \qquad (6.6)$$
$$x_3 = -\cos\theta \sin\phi$$

where x_1 is positive due East, x_2 is positive due North, and x_3 is vertically upwards. The rest of this Chapter will describe the performance of these programs in various structures, and will attempt to develop a technique for applying the program to the analysis of the TDP data.

6.3 The performance of the inversion programs on synthetic data.

This and the following section will attempt to measure the performance of the joint-inversion programs described in the previous section. Inversion with the TDP1 network only will be considered. The major reason for this is that, the assumption of a half-space is likely to be a better approximation to the structure beneath the TDP1 network, than that of the TDP2 network which straddles a major fault zone. It must be emphasised however that the performance of the programs with the TDP1 network will not necessarily be the same as with another network. It has already been shown that the TDP1 network does not possess very good diagnostic capabilities, and so it is likely that improved performances would be possible with other networks.

When using real data there are several factors which will influence the performance of a joint-inversion program. These include :-

1) Inaccuracies in chosen arrival-times arising from reading and instrumental errors which may obscure any weak anisotropic velocity variations if they are too large.
2) The number of arrival-times, their distribution among stations, and the distribution of events.
3) Hetereogeneities in the real Earth that may impose severe restrictions on the assumption of a half-space.

4) The symmetry, elastic constants and orientation of the dilatancy-anisotropy will be unknown.

In order to estimate the performance of the programs and so develop a technique for applying them to the analysis of real data, all of these factors will have to be investigated.

There are two important conclusions from Chapter 4 concerning the anisotropic location programs that can be immediately applied to the inversion programs: 1) shear-arrivals must be used; and 2) the locations determined under the assumption of isotropy must be used as the initial trial hypocentres. These points will be implicitly assumed as pre-requisites for the optimum performance of each program. The first pre-requisite may explain the failure of Ward et al.(1981) to determine an azimuthal variation of P-wave velocity from the inversion of P-arrivals only.

In this section we will only consider solutions for anisotropic structures with hexagonal symmetry using synthetic P- and first shear-wave arrival-times generated to every station in the network from the 30 events shown in Fig.6.1. At each epicentre in this figure there are three hypocentres at depths of 8, 11 and 14km, defining a vertical fault plane. This event distribution satisfies a further pre-requisite that the ray directions from the hypocentres to the receivers should be well-distributed throughout the focal sphere.

6.3.1 Synthetic data without errors

Fig.6.2 shows the solution obtained for the velocity variations and hypocentral locations when the inversion assumes the correct hypocentres and the correct model as the initial solution. The structure is the dry, parallel crack model, GKFF1, of section 3.2, with the axis of rotational symmetry striking perpendicular to the line of epicentres in Fig.6.1 and dipping below the surface at an angle of 45 degrees to the East. P- and

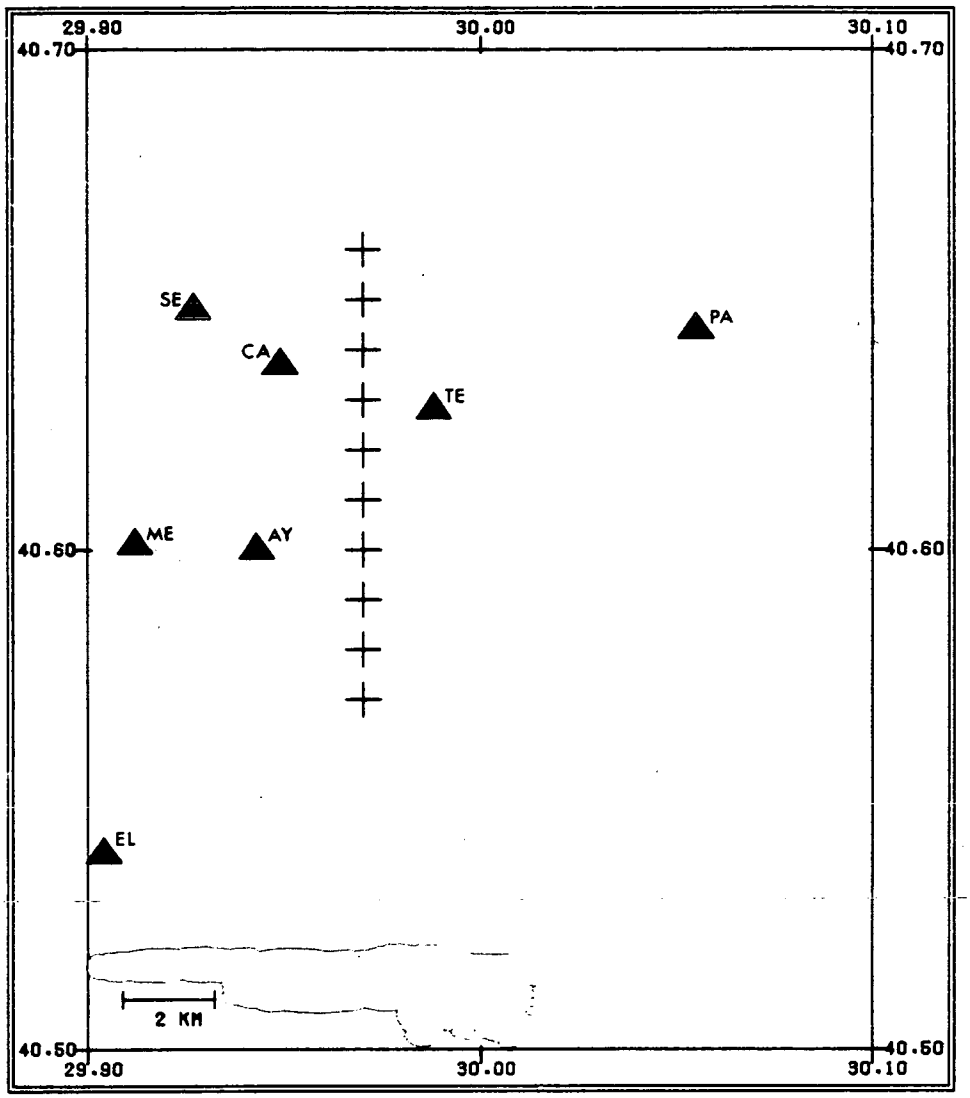

Figure 6.1 A map showing the stations of the TDP1 network in relation to the simulated earthquakes from which synthetic travel-times are generated and inverted for hypocentral locations and anisotropic structure. A cross denotes the epicentral position of three foci at depths of 8, 11 and 14km.

S-arrival times at every station were calculated to the nearest 1/100 of a second. The figure illustrates that the program converged without significantly altering the initial model. This example demonstrates that the inversion procedure is stable within the vicinity of the true solution, and that there are no obvious programming errors.

The next stage is to perturb the initial solution assumed in the inversion. The first step is to use hypocentres determined under the assumption of isotropy as the trial hypocentres, but to keep the initial model parameters correct. Fig.6.3 shows the solution obtained after five iterations. The hypocentres have been accurately determined, but there is a small, systematic departure of the wave-surfaces. This represents an increase of less than 0.1 km/sec in the P- and shear-wave velocity in all directions. Further studies demonstrate that a similar performance is obtained when the anisotropic structure is the corresponding saturated crack model (GKLF1).

6.3.2 Synthetic data with errors

In the rest of this Chapter all inversions of synthetic data will use hypocentres determined under the assumption of isotropy as trial hypocentres, and the arrival-times will be calculated to varying degrees of precision in order to simulate the scatter of real data. The rounding of arrival-times may be a good approximation of the errors associated with the TDP data. As was noted in Chapter 2, the P- and S-phases recorded during the TDP experiments have very impulsive onsets. Therefore, careful selection of arrivals should reduce the usual errors associated with picking arrivals too late. The errors that will be left arise from the precision with which the arrivals were read and instrumental errors. In practise the latter are unknown and so will be assumed to be randomly distributed.

Figs.6.4 and 6.5 illustrate the solutions obtained when the true

Figure 6.2. A summary of the solution obtained by the joint-inversion of synthetic arrival-times, calculated to the nearest 0.01s from the events of Fig.6.1. The true structure is that of dry, parallel cracks (GKFF1) with the axis of rotational symmetry striking perpendicular to the line of epicentres and dipping below the surface by 45 degrees to the East. The trial hypocentres and the trial model used in the inversion correspond to the true solutions. The diagram is divided into three parts.

(a) A vertical section, measured from the axis of rotational symmetry, through the wave surfaces of the true structure (solid lines) and through the structure determined by the inversion (dashed lines - overlain in this particular case). The horizontal axis measures the number of degrees away from the axis of symmetry. Error bars are plotted at each end of the wave-surfaces. These correspond to the maximum and minimum velocities in these directions calculated from the estimated errors of the elastic constants that determine the velocity in the particular direction.

(b) A summary of the relocated hypocentres. Notation and format as in Fig. 3.4.

(c) A summary of the orientation of the axis of rotational symmetry determined by the inversion. The upper diagram shows the horizontal rotation with the line terminated by a double arrow indicating the true direction, and the line terminated by the single arrow indicating the determined direction. Short lines without arrows (overlain here) indicate the estimated error of the solution. The lower diagram indicates the vertical rotation of the symmetry axis with the same line convention as before but with the horizontal line delineating the horizontal.

Figure 6.3. A summary of the solution obtained by the joint-inversion of synthetic arrival-times calculated to the nearest 0.01s from the events of Fig.6.1. The true structure is that of dry, parallel cracks (GKFF1) with the axis of rotational symmetry striking perpendicular to the line of epicentres and dipping below the surface by 45 degrees to the East. The trial hypocentres are those determined under the assumption of isotropy, and the trial model used in the inversion corresponds to the true solution. Notation and format as in Fig.6.2.

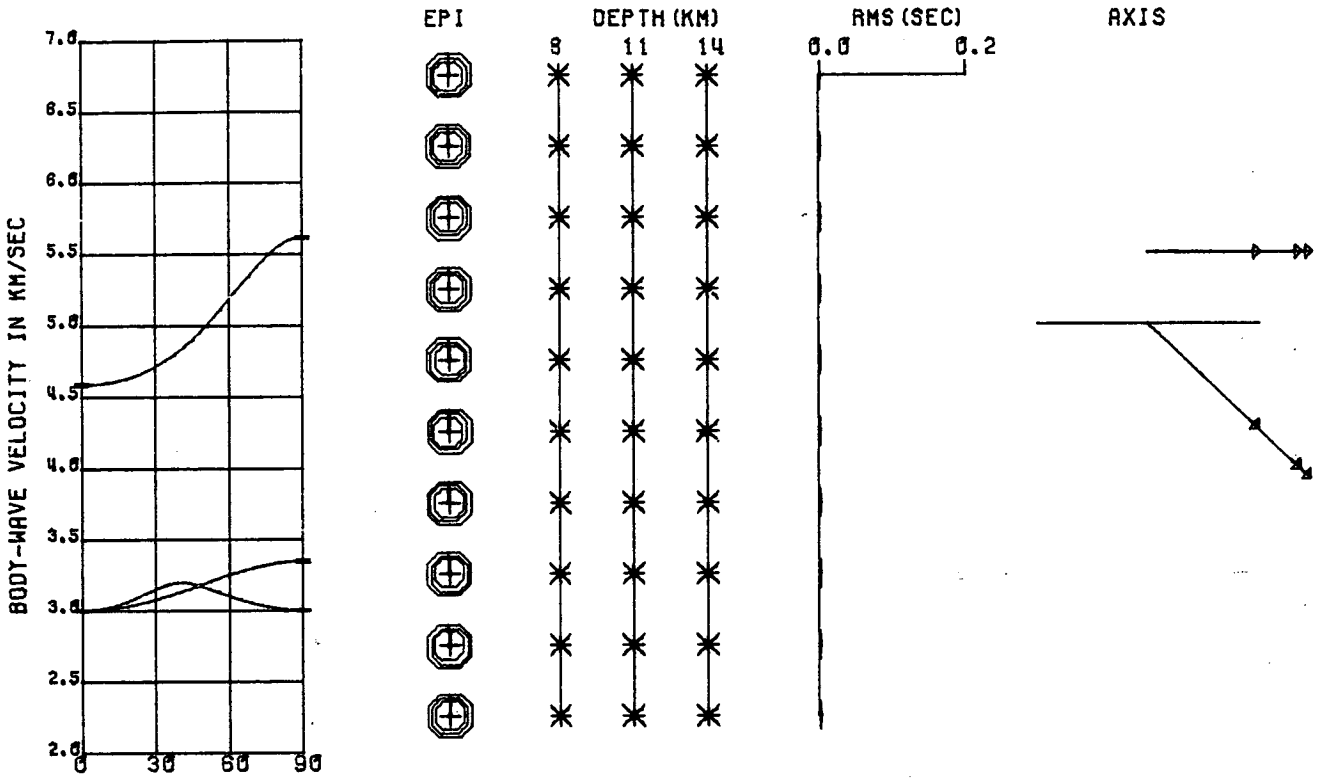

Figure 6.2

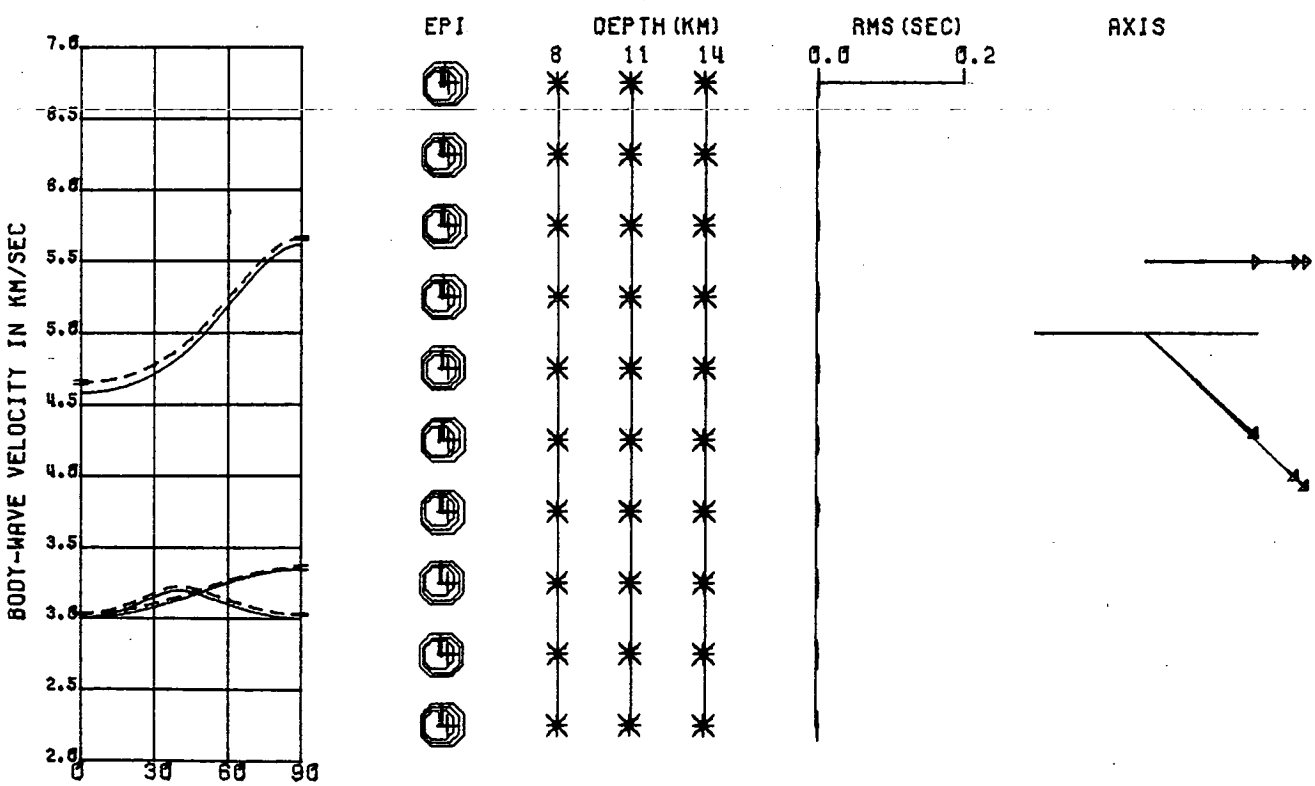

Figure 6.3

structure is GKFF1 and when the arrival-times have been rounded to the nearest 1/10 and 1/5 of a second respectively. In both cases the program has been initialised from the correct model parameters. In the former case the events have been located fairly accurately, but again there is a small departure of the wave-surfaces. However, decreasing the precision of the arrival-times results in a very poor solution (Fig.6.5). The elastic constants and the orientation of the axis of symmetry have been perturbed away from the true solution and this is reflected in the poor hypocentral locations. Figs.6.6 and 6.7 likewise show the performance of the program when the true structure is GKLF1, and where we use the true model as the initial solution. In both cases the inversion has not significantly altered the velocity model and the hypocentres have been well-determined. This difference between the two structures is likely to be the result of the superior trial hypocentres used in the inversion for the weakly anisotropic model GKLF1.

Until now the inversion has always assumed the correct model parameters as an initial model. This is clearly not possible when inverting real data. The remainder of this section will examine the effect of altering the initial model parameters when determining a particular anisotropic structure in order to guage the dependence of the final solution on the initial model.

Fig.6.8 illustrates the solution obtained when the initial model parameters are no longer correct. Fig.6.8a illustrates the solutions obtained for the orientation of the axis of rotational symmetry when the program has assumed six different starting values up to 30 degrees of rotation away from the true orientation. The elastic constants of the initial model in each case correspond to the true values (GKFF1), and the arrival-times are calculated to the nearest 1/10 of a second. The diagram illustrates that the solution progressed towards the true orientation in all cases. Only three solutions converged to the correct orientation, and

Figure 6.4. A summary of the solution obtained by the joint-inversion of synthetic arrival-times calculated to the nearest 0.1s from the events of Fig.6.1. The true structure is that of dry, parallel cracks (GKFF1) with the axis of rotational symmetry striking perpendicular to the line of epicentres and dipping below the surface by 45 degrees to the East. The trial hypocentres are those determined under the assumption of isotropy, and the trial model used in the inversion corresponds to the true solution. Notation and format as in Fig.6.2.

Figure 6.5. A summary of the solution obtained by the joint-inversion of synthetic arrival-times calculated to the nearest 0.2s from the events of Fig.6.1. The true structure is that of dry, parallel cracks (GKFF1) with the axis of rotational symmetry striking perpendicular to the line of epicentres and dipping below the surface by 45 degrees to the East. The trial hypocentres are those determined under the assumption of isotropy, and the trial model used in the inversion corresponds to the true solution. Notation and format as in Fig.6.2.

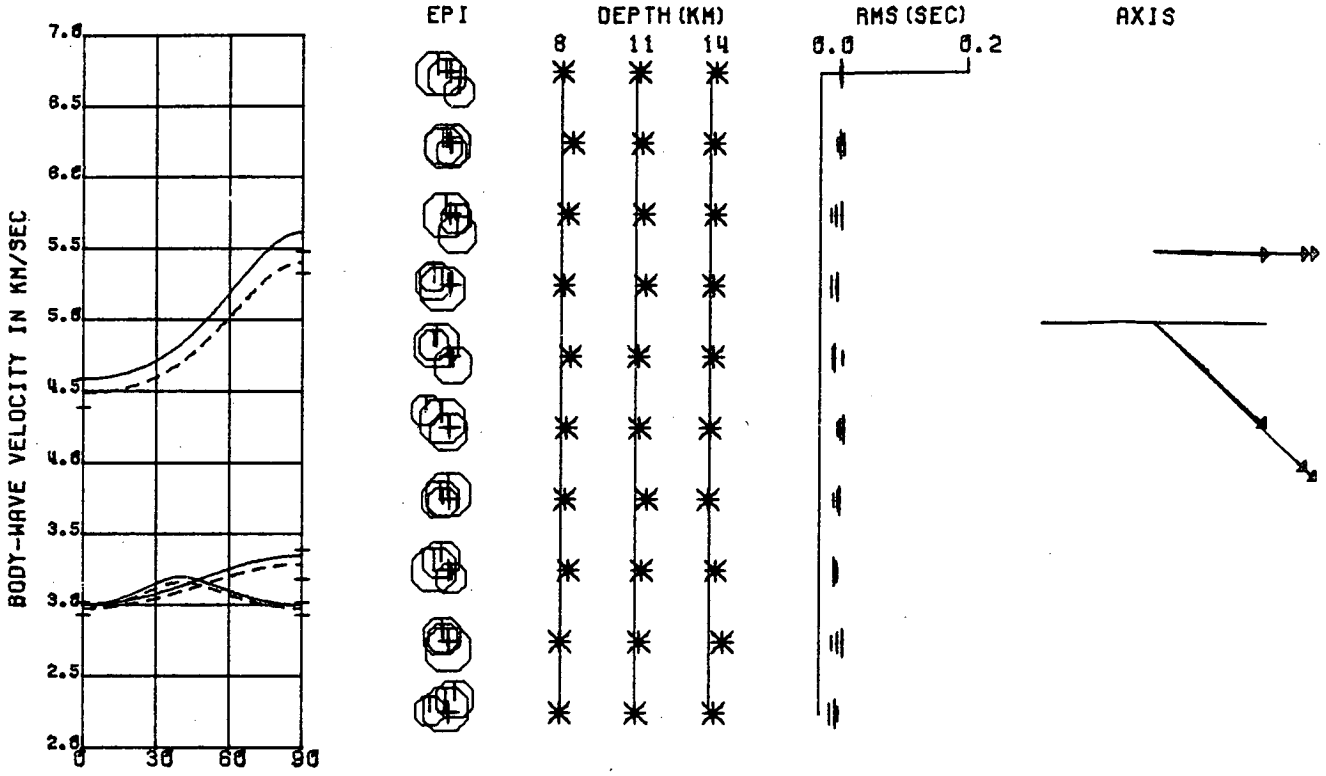

Figure 6.4

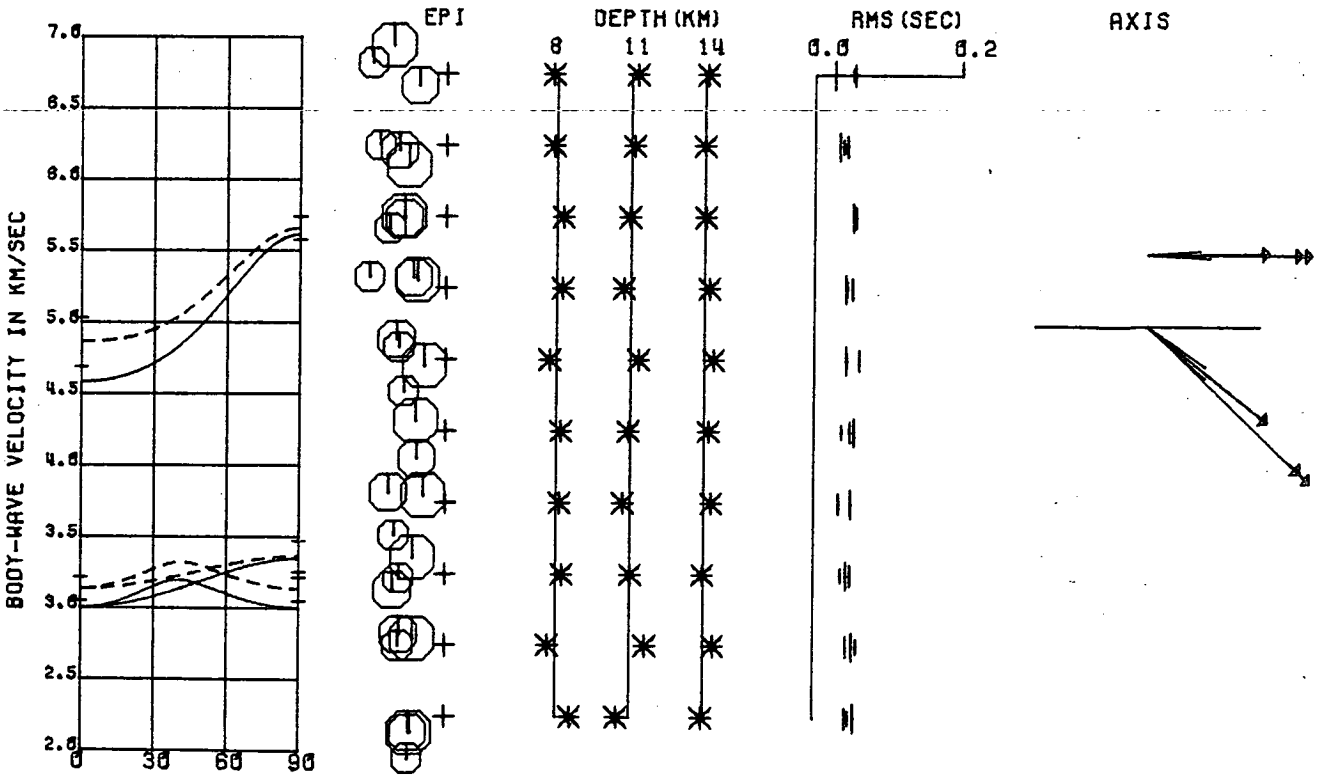

Figure 6.5

Figure 6.6. A summary of the solution obtained by the joint-inversion of synthetic arrival-times calculated to the nearest 0.1s from the events of Fig.6.1. The true structure is that of saturated, parallel cracks (GKLF1) with the axis of rotational symmetry striking perpendicular to the line of epicentres and dipping below the surface by 45 degrees to the East. The trial hypocentres are those determined under the assumption of isotropy, and the trial model used in the inversion corresponds to the true solution. Notation and format as in Fig.6.2.

Figure 6.7. A summary of the solution obtained by the joint-inversion of synthetic arrival-times calculated to the nearest 0.2s from the events of Fig.6.1. The true structure is that of saturated, parallel cracks (GKLF1) with the axis of rotational symmetry striking perpendicular to the line of epicentres and dipping below the surface by 45 degrees to the East. The trial hypocentres are those determined under the assumption of isotropy, and the trial model used in the inversion corresponds to the true solution. Notation and format as in Fig.6.2.

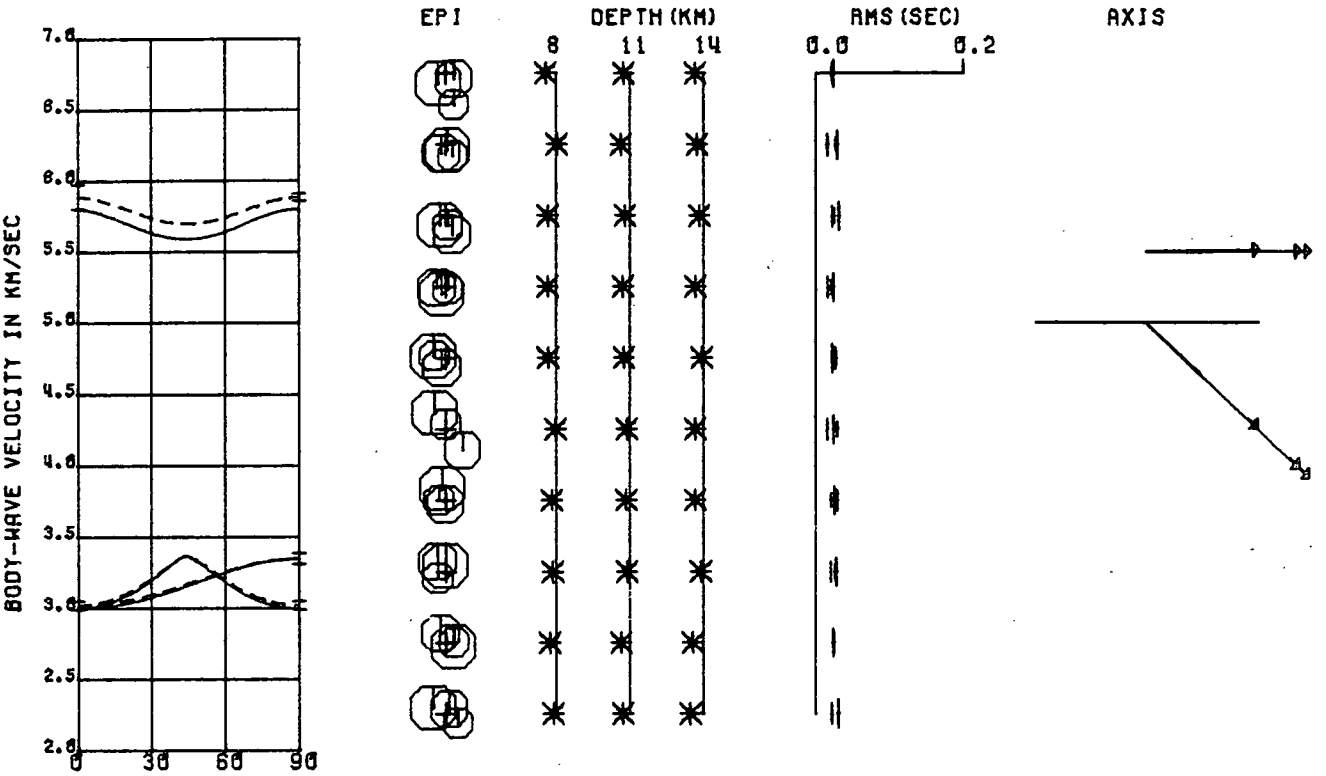

Figure 6.6

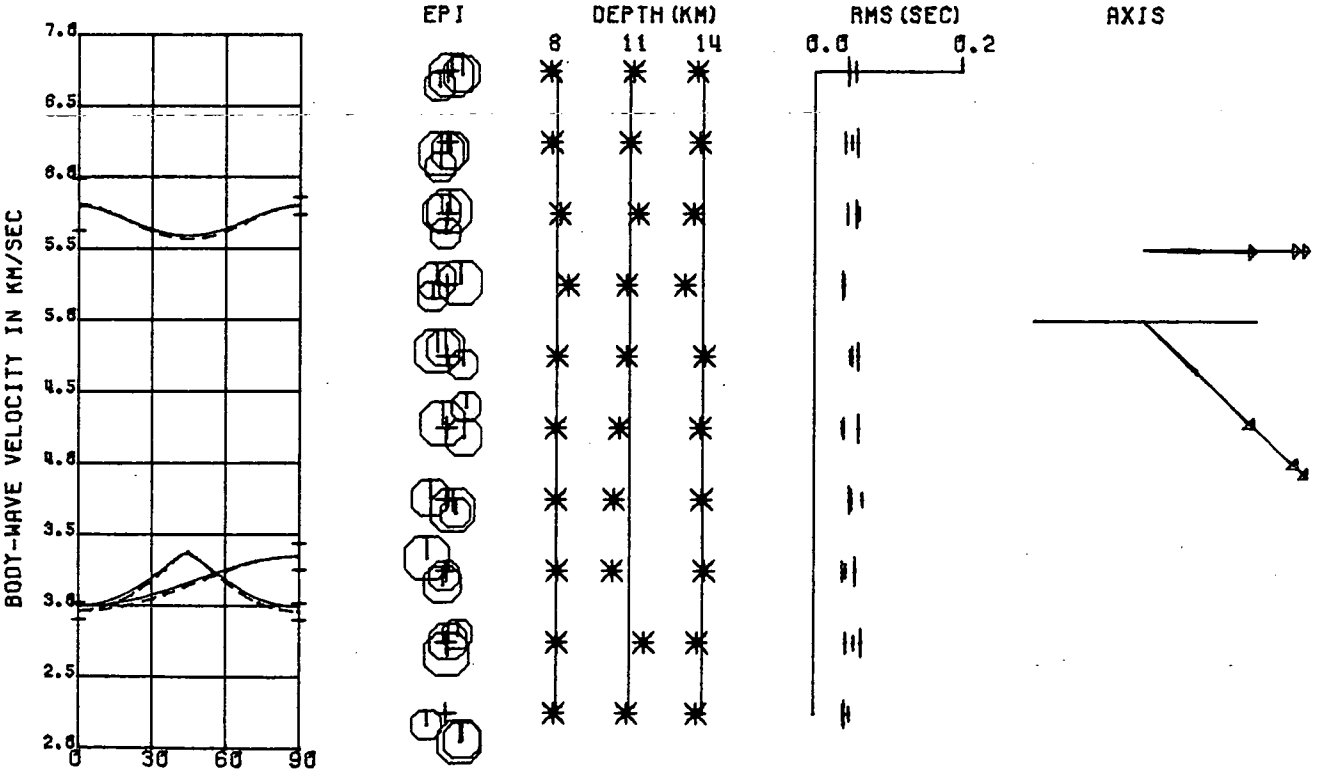

Figure 6.7

Figure 6.8. A summary of the solutions obtained by the joint-inversion of synthetic arrival-times calculated to the nearest 0.1s. The true structure is that of dry, parallel cracks (GKFF1) with the axis of rotational symmetry striking perpendicular to the line of epicentres and dipping below the surface by 45 degrees to the East. The inversion assumes GKFF1 as the initial model (i.e. the true solution).

(a) A summary of solutions obtained for the orientation of the axis of rotational symmetry from six initial values up to 30 degrees of rotation away from the true orientation. The horizontal axis measures the horizontal rotation in degrees, and the vertical axis measures vertical rotation in degrees. The true orientation is at the point 0,45 (marked by an asterisk). A solid line is drawn from the starting point (marked by a dot) to the final solution where estimated errors are plotted. The numbers plotted at each solution are the RMS errors in units from the reference RMS shown in the top left-hand corner (i.e. a value of 201 in this case indicates an RMS error of 0.0401). For future reference an average RMS error will be plotted for closely spaced solutions.

(b) A summary of the solution obtained from the weighted average of the three solutions at an orientation of 0,45 in (a). Notation and format as Fig.6.2.

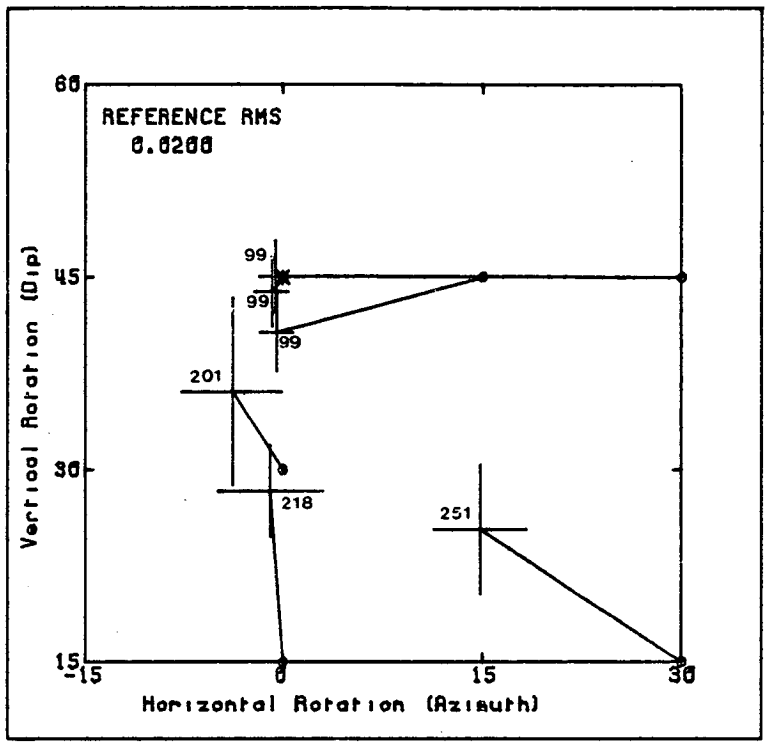
REFERENCE RMS
0.0200
Vertical Rotation (Dip)
Horizontal Rotation (Azimuth)
60
45
30
15
-15
0
15
30
99
99
99
201
218
251

(a)

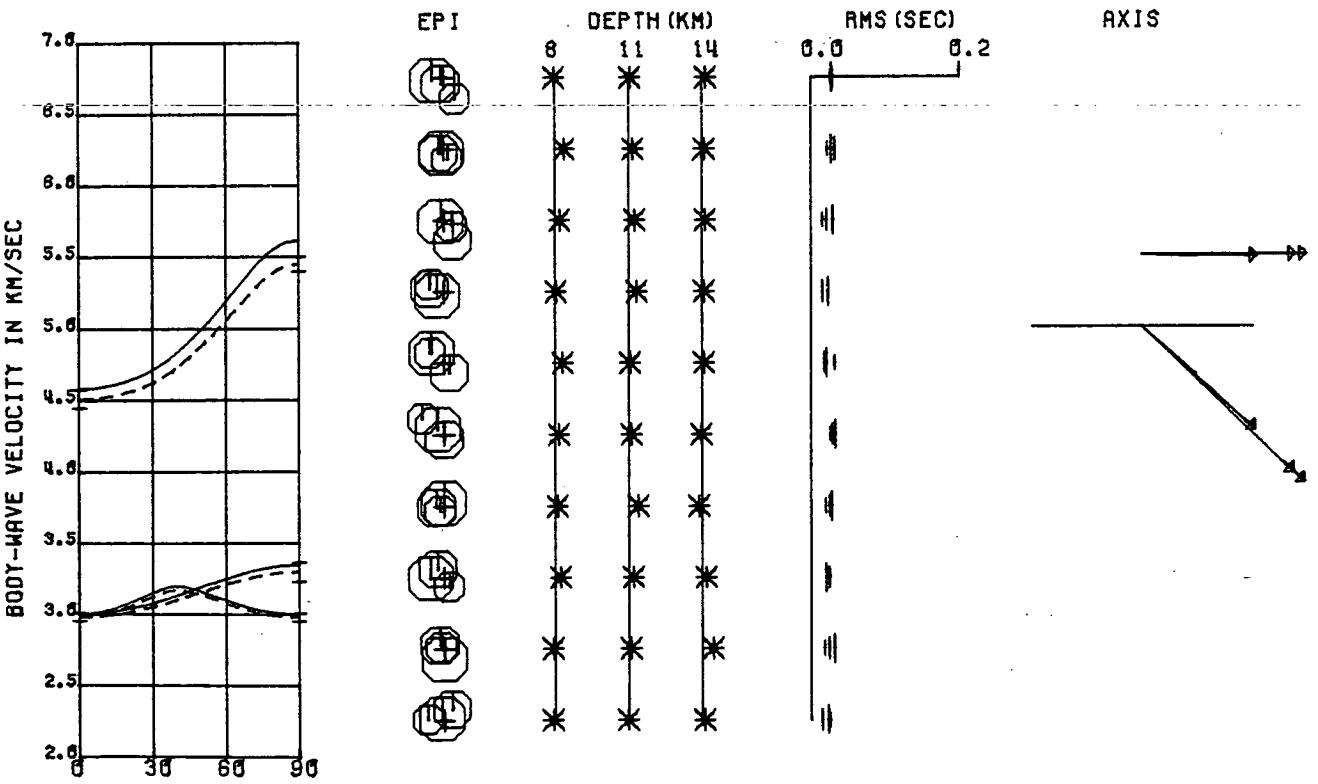
EPI
DEPTH (KM)
8
11
14
RMS (SEC)
0.0
0.2
AXIS
BODY-WAVE VELOCITY IN KM/SEC
7.0
6.5
6.0
5.5
5.0
4.5
4.0
3.5
3.0
2.5
2.0
0
30
60
90

(b)

this is reflected in the low RMS and orientation errors associated with these solutions. Taking the weighted average of these three solutions for the anisotropic structure, and relocating the events in this new structure, produces the results shown in Fig.6.8b. This solution is a very good fit to the true velocity variations and the hypocentre locations. Inverting again for the structure from this weighted average does not improve this solution. We can immediately see from this example that the inversion is not globally convergent and that the solutions obtained are dependent on the initial model. However the correct solution is indicated by the lowest RMS and orientation errors.

Decreasing the precision of the arrival-times to 1/5 of a second produces the solution shown in Fig.6.9. The initial model and the true structure are the same as above. In this case there are four solutions near the correct orientation and with similar RMS and standard errors. As before, taking the weighted average of these solutions and relocating the events produces the results shown in Fig.6.9b. The wave-surfaces are a very good fit to the correct model and the hypocentral locations are as accurate as can be expected given the large errors associated with the arrival-times.

The next step is to perturb the elastic constants at the same time as perturbing the orientation of the initial model. Fig.6.10 illustrates the case where the inversion has assumed the elastic constants of GKLF1 as the initial model, and where the arrival-times have been calculated to the nearest 1/10 of a second. Fig.6.10a shows that two solutions converge to the correct orientation, but the other four solutions, although at the correct azimuth, are 20 degrees in error for the dip of the axis of symmetry. Notice that the solutions at the correct orientation are those that were initialised from the furthest orientations (i.e. from points 0,15 and 30,15), while the solution initialised from the correct orientation has drifted away to the same solution as the remainder. This

Figure 6.9. A summary of the solutions obtained by the joint-inversion of synthetic arrival-times calculated to the nearest 0.2s. The true structure is that of dry, parallel cracks (GKFF1) with the axis of rotational symmetry striking perpendicular to the line of epicentres and dipping below the surface by 45 degrees to the East. The inversion assumes GKFF1 as the initial model (i.e. the true solution). (b) shows the solutions from the weighted average of the four solutions near the correct orientation at 0,45. Notation and format as in Fig.6.8.

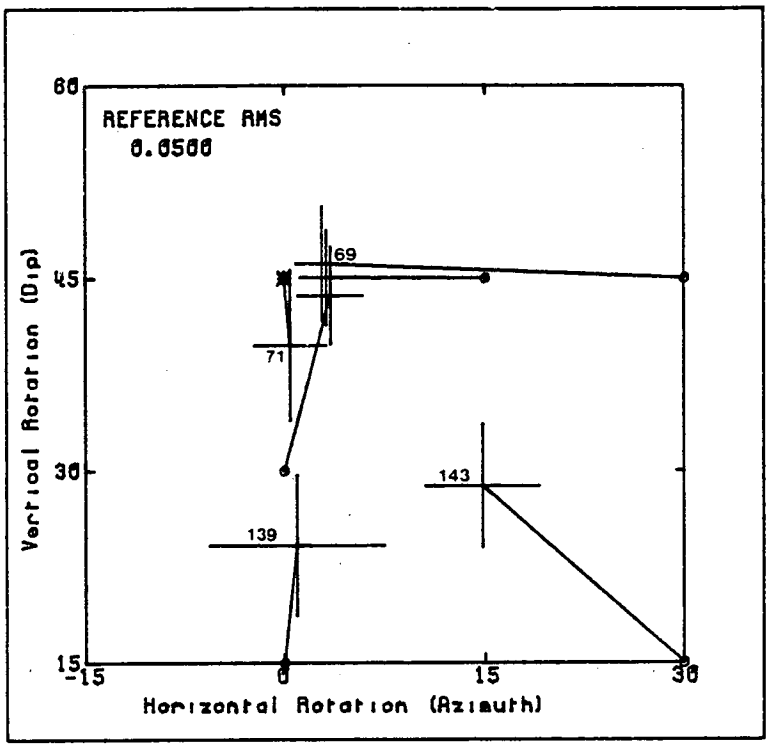
REFERENCE RMS
0.0500
60
45
30
15
-15
0
15
30
69
71
143
139
Vertical Rotation (Dip)
Horizontal Rotation (Azimuth)

(a)

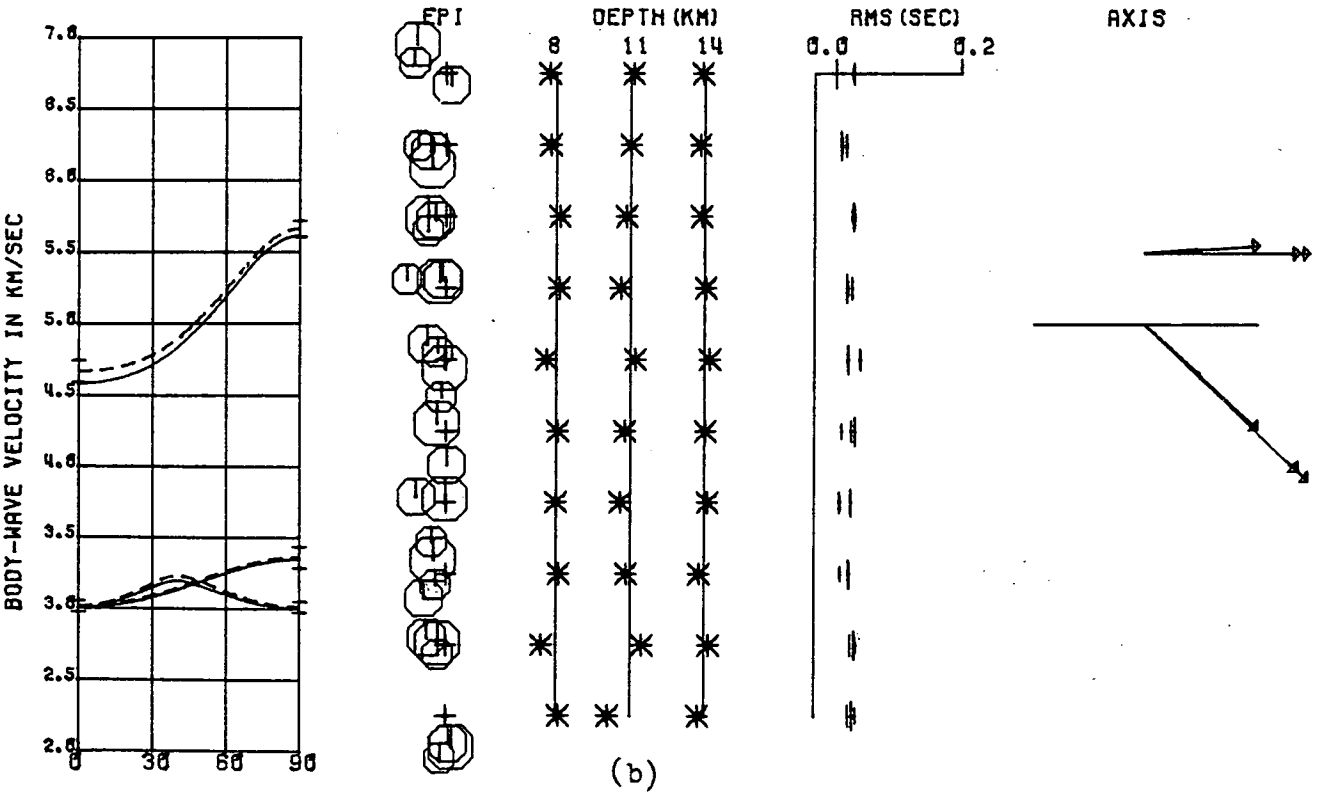
BODY-WAVE VELOCITY IN KM/SEC
7.0
6.5
6.0
5.5
5.0
4.5
4.0
3.5
3.0
2.5
2.0
0
30
60
90
EPI
DEPTH (KM)
8
11
14
RMS (SEC)
0.0
0.2
AXIS

(b)

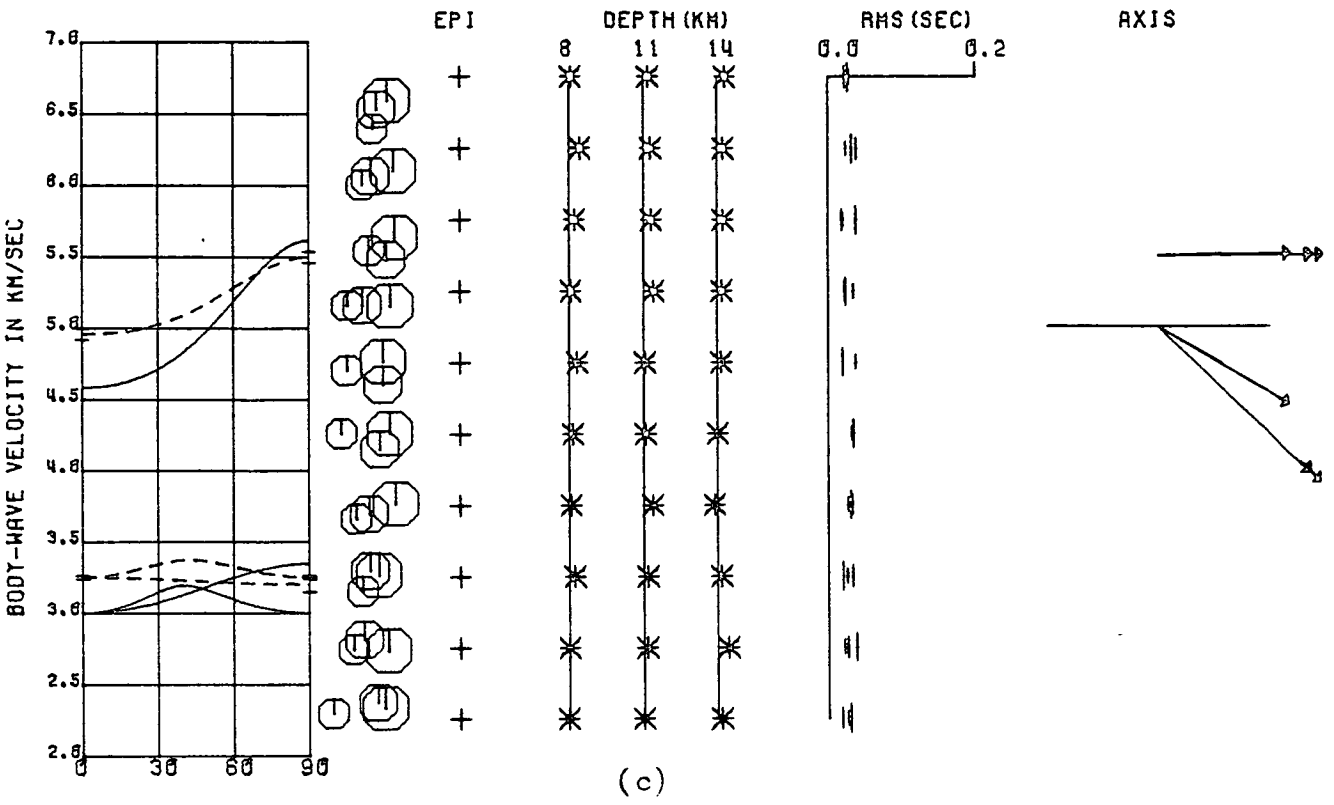

Figure 6.10. A summary of the solutions obtained by the joint-inversion of synthetic arrival-times calculated to the nearest 0.1s. The true structure is that of dry, parallel cracks (GKFF1) with the axis of rotational symmetry striking perpendicular to the line of epicentres and dipping below the surface by 45 degrees to the East. The inversion assumes GKLF1 as the initial model. (b) shows the weighted average of the two solutions at an orientation of 0,45 in (a), and (c) is the weighted average of all the solutions in (a). Notation and format as in Fig.6.8.

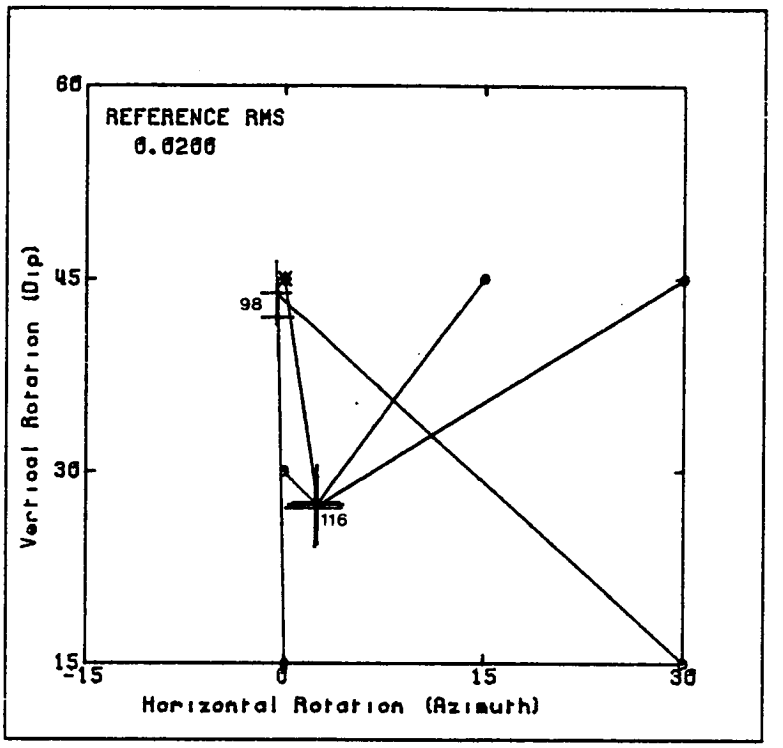
REFERENCE RMS
0.0200
60
45
30
15
-15
0
15
30
98
116
Vertical Rotation (Dip)
Horizontal Rotation (Azimuth)

(a)

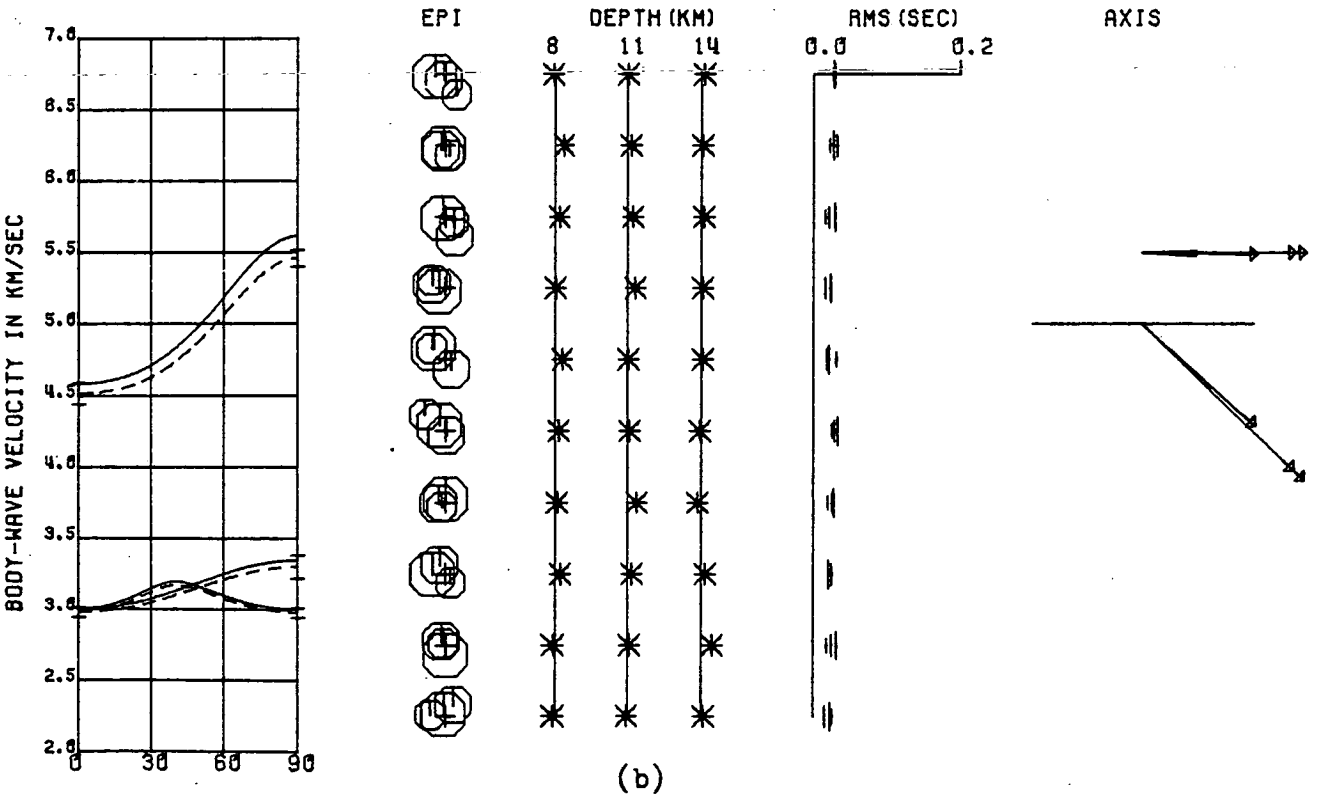
BODY-WAVE VELOCITY IN KM/SEC
7.0
6.5
6.0
5.5
5.0
4.5
4.0
3.5
3.0
2.5
2.0
0
30
60
90
EPI
DEPTH (KM)
8
11
14
RMS (SEC)
0.0
0.2
AXIS

(b)

illustrates the complicated nature of the inversion procedure and that it is not sufficient for part of the initial model to be near the correct solution. The solution quality is marginally better for the solutions at the correct orientation and when these are averaged, following the same procedure as before, they produce the overall solution shown in Fig.6.10b. However as there is little difference in the quality of all the solutions, it may be more consistent to take the weighted average of all the solutions. This produces the results shown in Fig.6.10c which is clearly inadequate, but does at least indicate a strong 2θ P-wave variation. This suggests the importance of considering those solutions with the lowest formal errors when the actual parameters of various solutions are significantly different.

Decreasing the precision of the arrival-times to 0.2 seconds produces the results shown in Fig.6.11. There are four solutions with similar, low RMS and orientation errors. The azimuth of the axis of symmetry defined by these solutions is correct, but the dip and elastic constants are very poorly determined. This has resulted in very inaccurate locations (Fig.6.11b), but again the solution indicates a strong 2θ P-wave variation.

Figs.6.12 and 6.13 show the solutions obtained for arrival-time precision of 0.1s and 0.2s respectively and where the initial model was that of a quasi-isotropic structure. (It is not possible to initialise the program from an exactly isotropic structure. In such a structure the travel-time derivatives with respect to the orientation of the structure are not defined, and the normal equation matrix would be singular). Again, in both cases, the azimuth of the axis of symmetry has been well-determined, but its dip, the elastic constants and consequently the hypocentral locations have been poorly determined. However, the solutions still indicate a strong 2θP-wave variation.

[It is recognised that in some cases the small orientation errors associated with some solutions (e.g. Fig.6.12) do not reflect the

Figure 6.11. A summary of the solutions obtained by the joint-inversion of synthetic arrival-times calculated to the nearest 0.2s. The true structure is that of dry, parallel cracks (GKFF1) with the axis of rotational symmetry striking perpendicular to the line of epicentres and dipping below the surface by 45 degrees to the East. The inversion assumes GKLF1 as the initial model. (b) shows the weighted average of the four solutions in (a) with the lowest RMS error. Notation and format as in Fig.6.8.

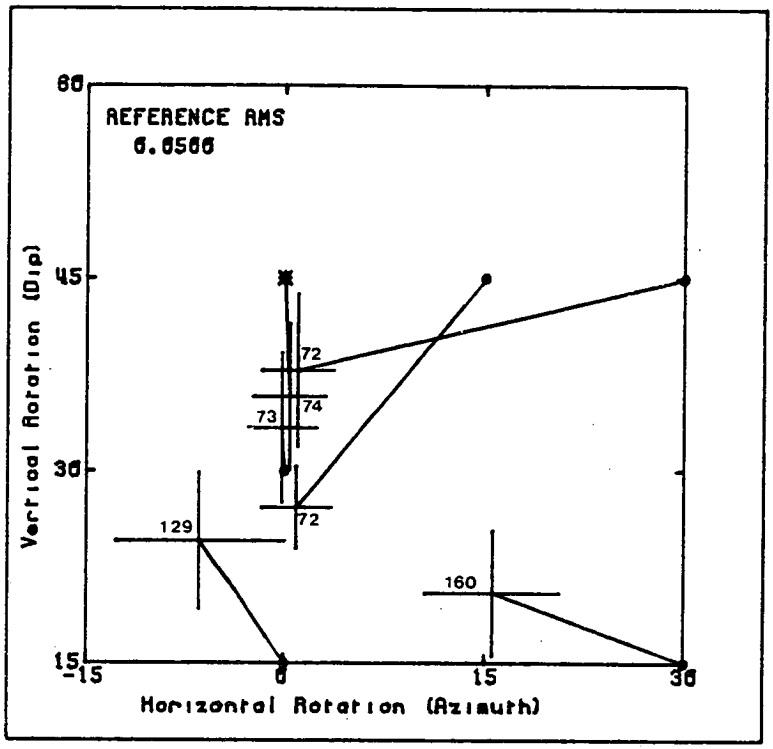
REFERENCE RMS
0.0500
60
45
30
15
-15
0
15
30
Vertical Rotation (Dip)
Horizontal Rotation (Azimuth)
72
73
74
72
129
160

(a)

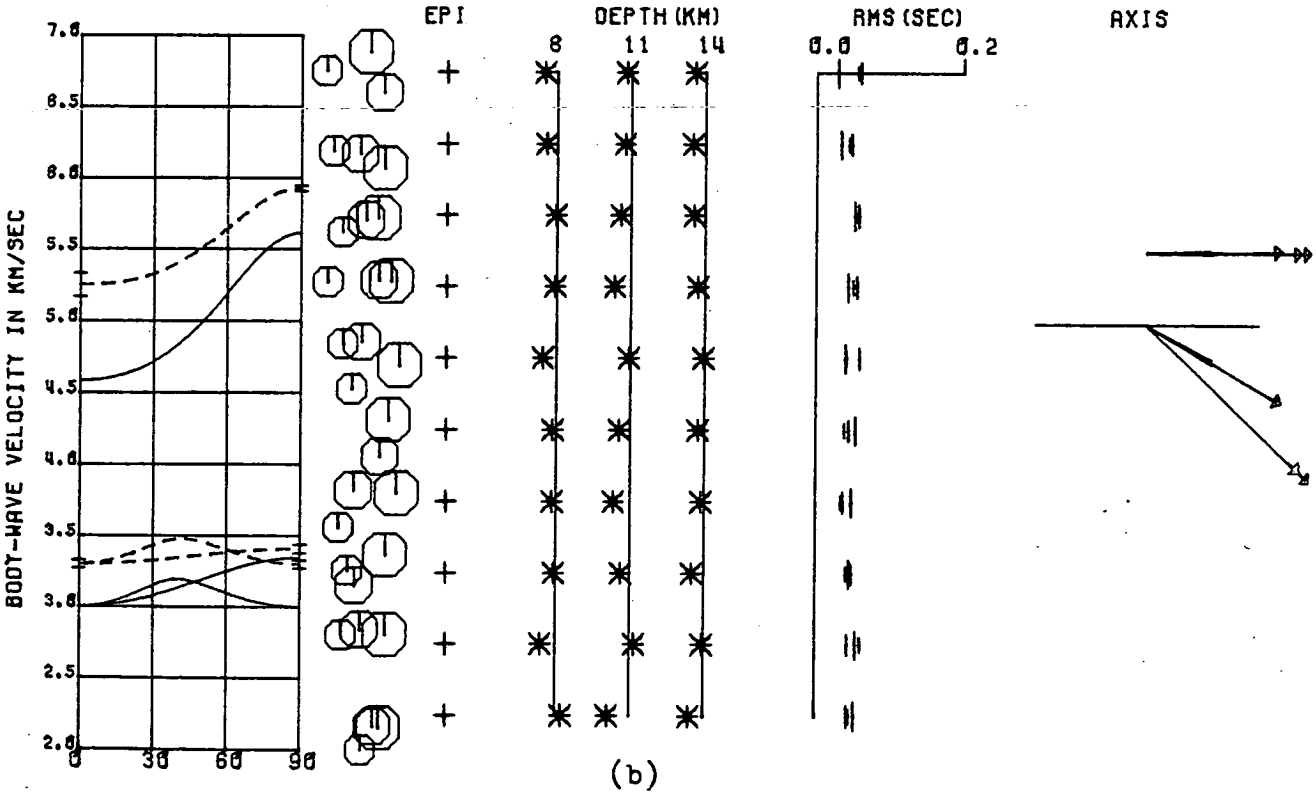
EPI
DEPTH (KM)
8
11
14
RMS (SEC)
0.0
0.2
AXIS
BODY-WAVE VELOCITY IN KM/SEC
7.0
6.5
6.0
5.5
5.0
4.5
4.0
3.5
3.0
2.5
2.0
0
30
60
90

(b)

Figure 6.12. A summary of the solutions obtained by the joint-inversion of synthetic arrival-times calculated to the nearest 0.1s. The true structure is that of dry, parallel cracks (GKFF1) with the axis of rotational symmetry striking perpendicular to the line of epicentres and dipping below the surface by 45 degrees to the East. The inversion assumes a quasi-isotropic structure as the initial model. (b) shows the weighted average of the three solutions in (a) with the lowest RMS error. Notation and format as in Fig.6.8.

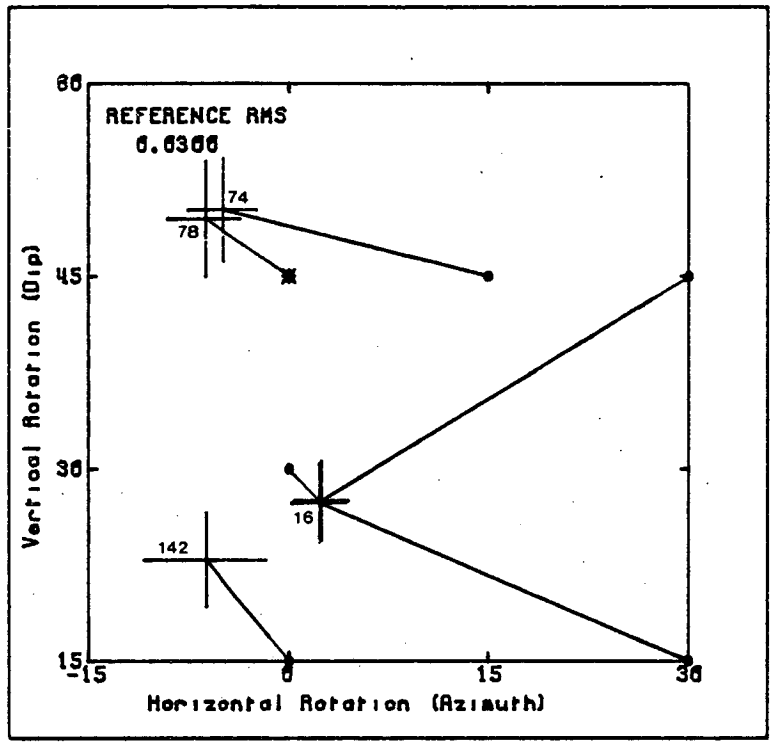
REFERENCE RMS
0.0300
74
78
16
142
60
45
30
15
-15
0
15
30
Vertical Rotation (Dip)
Horizontal Rotation (Azimuth)

(a)

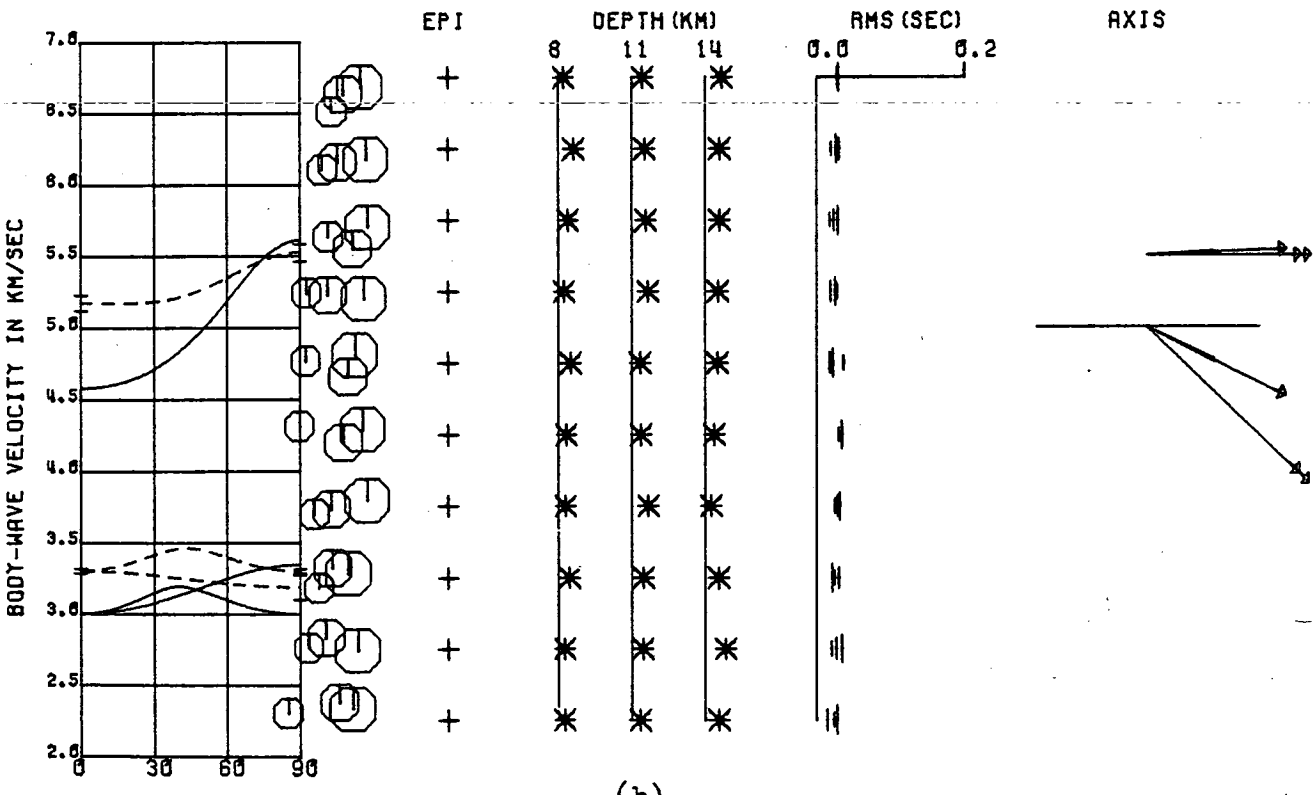
EPI
DEPTH (KM)
8
11
14
RMS (SEC)
0.0
0.2
AXIS
BODY-WAVE VELOCITY IN KM/SEC
7.0
6.5
6.0
5.5
5.0
4.5
4.0
3.5
3.0
2.5
2.0
0
30
60
90

(b)

Figure 6.13. A summary of the solutions obtained by the joint-inversion of synthetic arrival-times calculated to the nearest 0.2s. The true structure is that of dry, parallel cracks (GKFF1) with the axis of rotational symmetry striking perpendicular to the line of epicentres and dipping below the surface by 45 degrees to the East. The inversion assumes a quasi-isotropic structure as the initial model. (b) shows the weighted average of the four solutions in (a) with the lowest RMS error. Notation and format as in Fig.6.8.

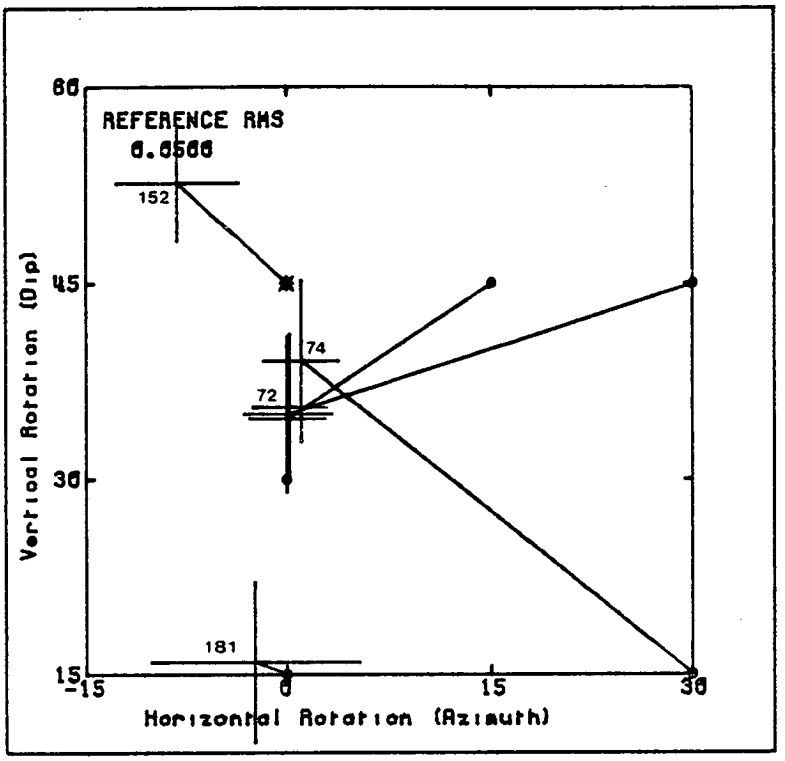
REFERENCE RMS
0.0500
152
74
72
181
60
45
30
15
-15
0
15
30
Vertical Rotation (Dip)
Horizontal Rotation (Azimuth)

(a)

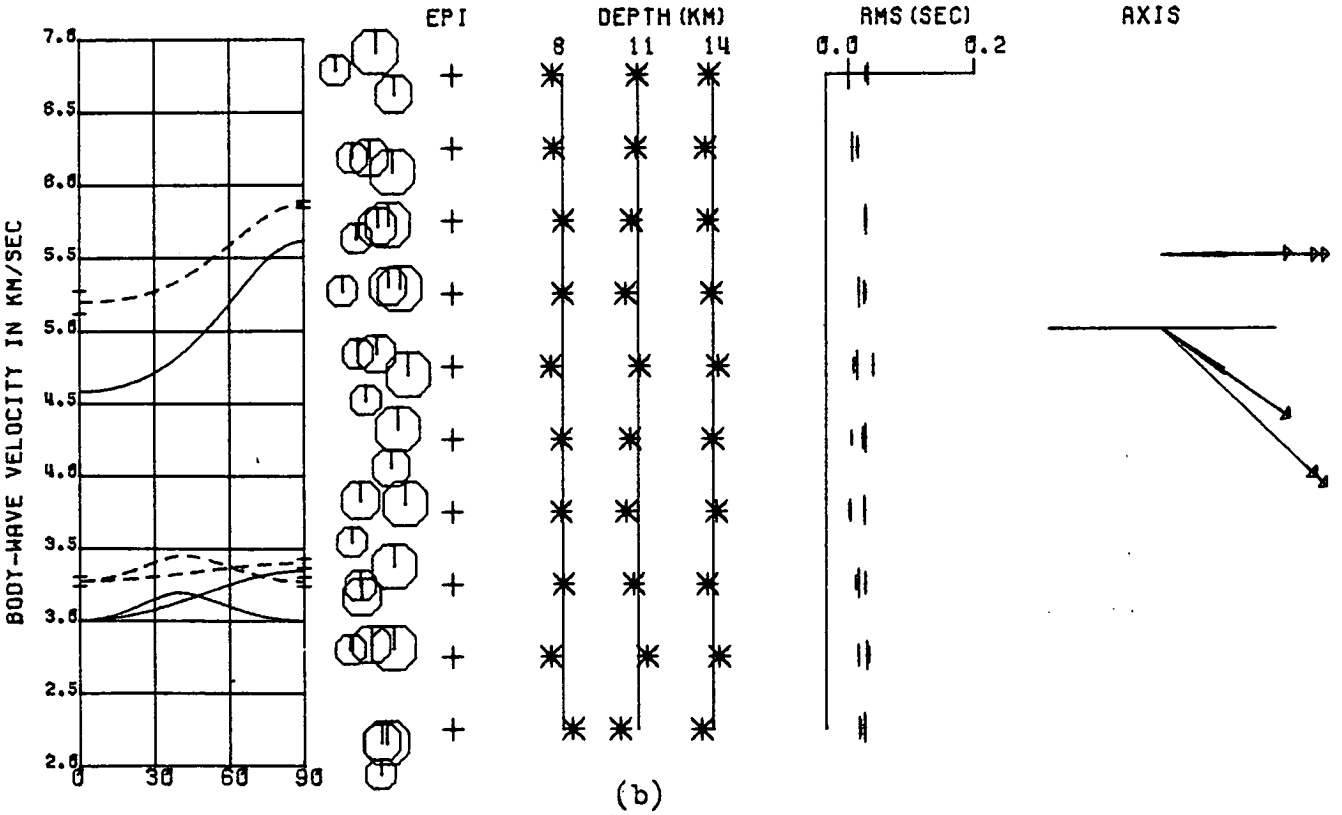
EPI
DEPTH (KM)
8
11
14
RMS (SEC)
0.0
0.2
AXIS
BODY-WAVE VELOCITY IN KM/SEC
7.0
6.5
6.0
5.5
5.0
4.5
4.0
3.5
3.0
2.5
2.0
0
30
60
90

(b)

departure of the solution from the true values. Aki & Lee (1976) also observed a similar phenomena with their joint-inversion program, and ascribe it to neglecting higher order terms in the expansion of the travel-time equation (equation 6.1). In addition, the expansion, and the procedure for estimating errors is based on linear assumptions and so are only valid in the vicinity of the true solution. Aki & Lee (1976) also note that the resolution matrix calculated in their (more costly) inverse procedure also provides little indication of this departure. These explanations also apply to the small errors for the elastic constants. Another reason, in some cases, is that the procedure for calculating the weighted average (Bevington 1969) of the solutions, produces a solution with lower errors than any individual solution.]

It is clear from this section that the joint-inversion for hypocentral locations and anisotropic structure is not globally convergent. The trial model used in the inversion has to be close to the true solution for convergence to be obtained. However it has also been shown that in most cases the azimuth of the axis of symmetry is normally well-constrained, and that there is usually an indication of the nature of the velocity variations even when a poor initial model has been chosen. This suggests that it may be possible to iterate the inversion process itself in a similar way to that of Aki & Lee (1976). They found it was necessary to continually improve their solutions by using the hypocentres determined by the previous inversion as trial hypocentres for a following inversion using the same initial velocity model. In our situation we can use the same hypocentres in each inversion but continually improve the initial model until it is obvious that the true structure has been obtained. This approach will be examined in more detail in the following section.

It must be emphasised again that this feature of the inversion process is probably symptomatic of the TDP1 network. The TDP1 network provides a good azimuthal coverage for events inside the network and so, as observed,

the horizontal orientation of the structure is well-constrained. However, the distribution of ray paths from deep events to the stations of the network only define a narrow cone through the focal sphere and so the dip of the axis of symmetry is poorly constrained. This characteristic of the TDP1 network was recognised in Chapter 2 and was one of the reasons for the subsequent TDP2 experiment with a greater aperture network.

6.4 A series of case studies with the TDP1 network

The preceding section has demonstrated that the joint-inversion of earthquake arrival-times for hypocentral locations and anisotropic structure is not globally convergent. The solution obtained by the inversion is dependent on the initial model and the true solution cannot be obtained unless the trial solution is in the close vicinity. What is required is an iterative process of using the inversion programs to find a good approximation to the true solution and for recognising when the correct solution has been found. That this may be possible is suggested by the observation in the preceding section that the horizontal orientation of the structure is normally well-constrained with the TDP1 network even though the other parameters are poorly determined because of a poor initial approximation. This section will illustrate how solutions for particular velocity models can be obtained using an iterative process of continually refining the initial model. We will again invert suites of synthetic arrival-times generated to the stations of the TDP1 network.

6.4.1 The models

Table 6.1 summarises the velocity models that are considered in this section. No attempt has been made to orientate these models to correspond to the possible structure that may exist beneath the TDP1 network. This section concentrates on finding a consistent approach of identifying the correct structure using the various joint-inversion programs. The only assumption that is made in the determination of these models is that the

Table 6.1 Velocity models used in case studies.

MODEL	SYMMETRY	VELOCITY STRUCTURE	COMMENTS
A	isotropic	half-space	Vp = 5.7 km/sec Vs = 3.3 km/sec
B	isotropic	half-space with internal dipping interface	striking along 29.953E dipping to west by 20° Vp1 = 4.0km/sec (West) Vp2 = 5.7km/sec (East) Vp/Vs = 1.73
C	hexagonal	parallel dry cracks (GKFF1)	axis of rotational symmetry at an orientation of 30,0
D	hexagonal	parallel saturated cracks (GKLF1)	as C
E	hexagonal	co-planar-normal dry cracks (CPFF1)	as C
F	hexagonal	co-planar-normal saturated cracks (CPLF1)	as C
G	hexagonal	isotropic layer overlying half-space of parallel dry cracks (GKFF1)	layer - 1km thick Vp = 4.0 km/s Vp/Vs = 1.73 half-space - as C
H	hexagonal	isotropic layer overlying half-space of parallel saturated cracks (GKLF1)	as G
I	orthorhombic	orthogonal, bi-planar dry cracks (GK2FFA)	normal to major cracks vertical - normal to minor cracks at 60,0 intermediate at -30,0
J	orthorhombic	orthogonal, bi-planar saturated cracks (GK2LFA)	as I

specifications of the isotropic layer in models H and G are known.

Two types of data set are used. The first consists of synthetic P- and first shear-wave travel-times generated through each model from the 30 events shown in Fig.6.14. This distribution of events corresponds to a suite of actual earthquake locations determined under the assumption of isotropy in the TDP1 experiment. The arrival-times from this data set will be used in Chapter 7 to determine the anisotropic structure beneath the TDP1 network. The depths of these events lie in the range 5 - 11km with an average depth of 8km. In addition the number, (261), and distribution of recorded phases in the synthetic data set corresponds exactly to that in the TDP1 data set. All synthetic travel-times are rounded to the nearest 1/10 of a second to simulate the scatter of real data. The overall RMS error obtained by the correct inversion of such data is similar to that obtained in Chapter 7 for the inversion of the real data set. The second type of data set is a subset of 20 events from the first data set, and contains 16 shear-wave delays. Again this corresponds to the number and distribution in a subset of the TDP1 data set. The depth range and the average depth is the same as in the larger data set. As explained in section 6.2 the delay between the first and second shear-wave synthetic arrivals is calculated to the nearest 1/100 of a second, but the arrival-time of the first shear-wave is still rounded to the nearest 1/10 of a second. We have used this data set in order to model the real problem as closely as possible. It is anticipated that the results of the inversion of these data sets will assist in the interpretation of the inversion of the real data set.

The distribution of the events of Fig.6.14 is such that there are no horizontal or near-horizontal ray paths through the structure. This will mean that a large part of the wave-surfaces in the anisotropic models will be unsampled by rays from events to receivers. This is illustrated in Fig.6.15 where the apparent velocities have been calculated on the basis of

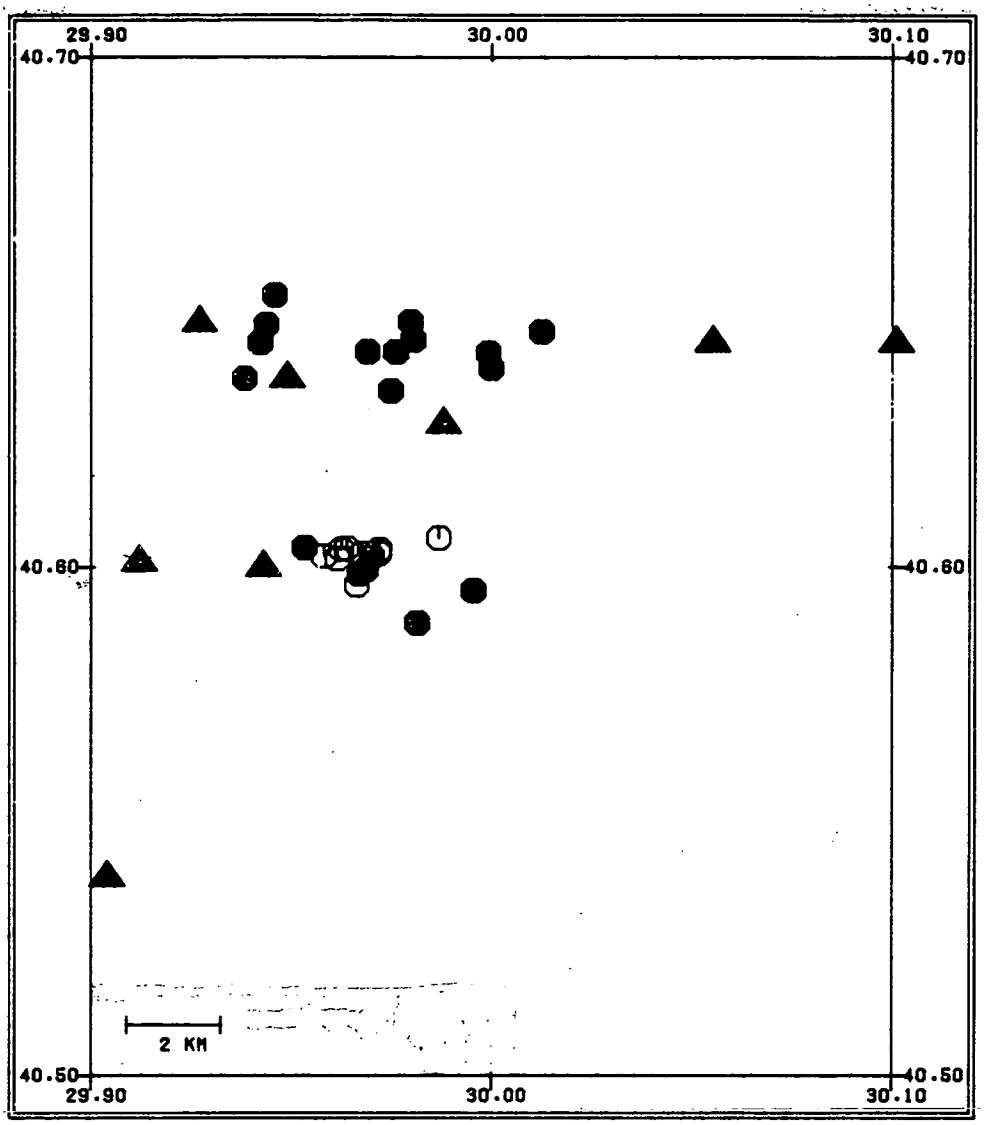

Figure 6.14. A map of the epicentral distribution of 30 events in the depth range 5-11km used to determine various anisotropic structures using synthetic P- and first shear-wave arrival-times to the stations (▲) of the TDP1 network. Average depth of these events is 8km. The solid circles are a subset of 20 events from which synthetic P- and first shear-wave arrival-times, and shear-wave delay data are used to determine the structure. The average depth is the same as in the larger data set.

the synthetic arrival-times and the correct hypocentres, and where the ray directions, based on a half-space model, have been rotated into the vertical plane measured from a principal axis (30,0 for the hexagonal models, and -30,0 for the orthorhombic models). The correct hypocentres have been used to determine the apparent velocities in order to illustrate the best possible performance of the inversion programs given the errors associated with the arrival-times. (N.B. the apparent velocities determined from the locations based on the assumption of isotropy, which are used as trial hypocentres for the anisotropic inversion programs, show no directional variations). These diagrams demonstrate that approximately only 50% of each wave-surface is sampled, and so it is anticipated that the elastic constants that largely determine velocities in the unsampled region will be poorly constrained. The reason that a slightly larger section of the orthorhombic structure appears to be sampled is because the section is measured from a different direction (-30,0) compared to the hexagonal models (at 30,0). (Note also that the increased scatter of the velocities in the orthorhombic structures is not real. This particular method of presenting the data is slightly misleading for a structure that does not possess an axis of rotational symmetry).

Several inferences on the performance of the inversion programs can be made from Fig.6.15. The apparent velocities in models E and F, and the apparent shear-wave velocities in model I, show little directional variation and it is anticipated that these surfaces may be difficult to resolve. In addition, in the same models and model I, the second shear-wave surface is not very well-defined and the use of shear-wave delay data may not improve the solution obtained for these structures. The degree of scatter on the arrival-times may make it difficult to distinguish between a system of parallel cracks and a system of bi-planar cracks. Note however, that these comments only apply to these models and are not general. Different orientations of these structures will mean that

Figure 6.15. An illustration of the region of the wave-surfaces of each anisotropic model actually sampled by ray paths from the events of Fig.6.14 to stations of the TDP1 network. Points marked on the true surfaces (solid lines) have been calculated on the basis of the rounded arrival-time, the correct hypocentres, and the ray directions in a half-space from the source to the receiver and rotated into the vertical plane measured from a principal axis, (30,0 for hexagonal models, and -30,0 for orthorhombic models). Upper diagrams are from the data set of P- and first shear-wave arrival-times. Lower diagrams are from the data set that includes shear-wave delays. (a) to (h) correspond to models C to J (Table 6.1) respectively. For the orthorhombic models, I and J, phase velocities have been plotted. The horizontal dashed lines correspond to P- and S-velocities determined by an inversion of the data set for isotropic velocities in a half-space (section 6.4.2).

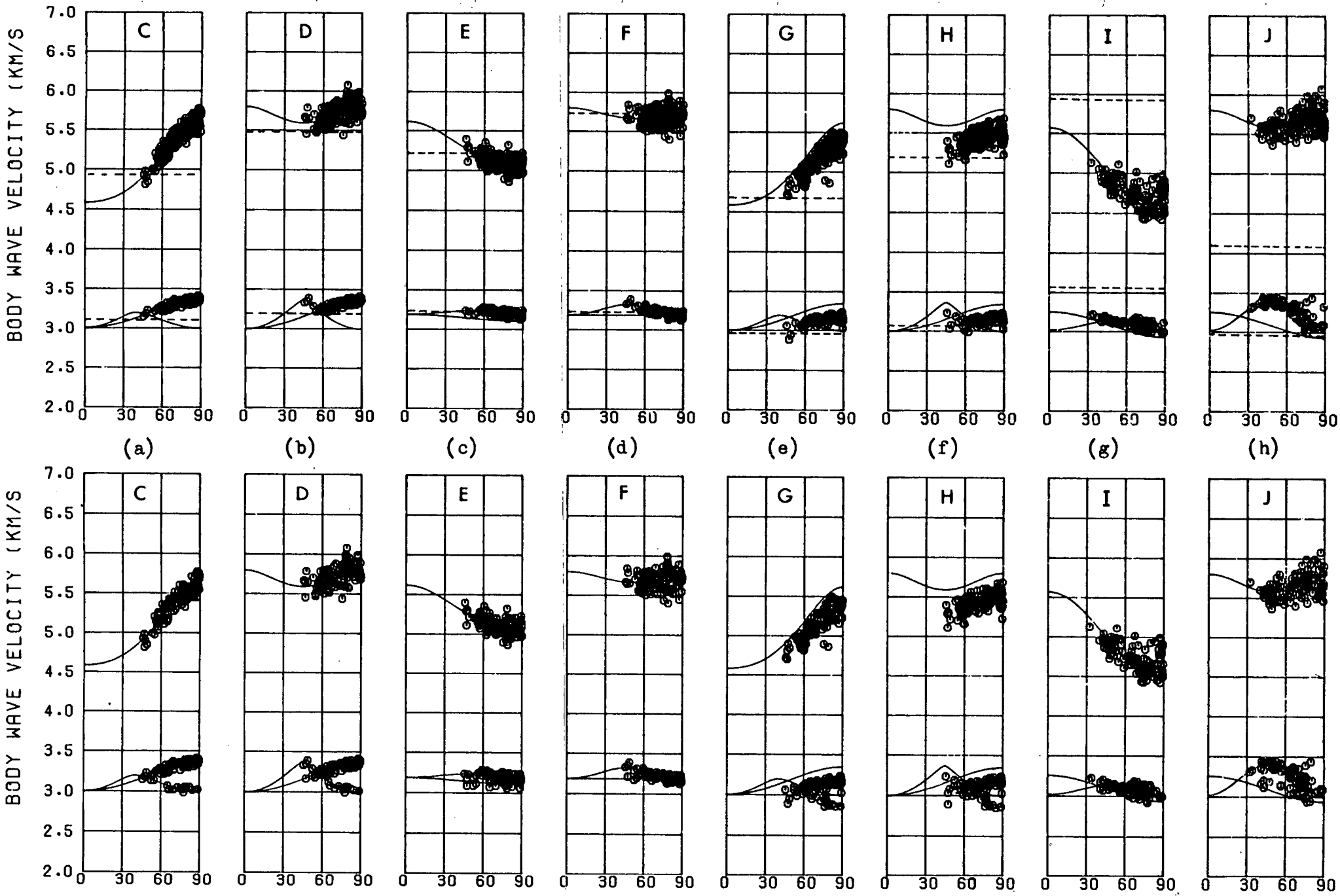
BODY WAVE VELOCITY (KM/S
7.0
6.5
6.0
5.5
5.0
4.5
4.0
3.5
3.0
2.5
2.0
0
30
60
90
C
D
E
F
G
H
I
J
(a)
(b)
(c)
(d)
(e)
(f)
(g)
(h)

different regions of the wave-surfaces will be sampled and this will effect the degree of resolution possible in the inversion.

6.4.2 The isotropic solutions

Table 6.2 shows the solutions obtained in each of the models by the joint-inversion for isotropic P- and shear-wave velocities in a half-space. The solutions for most of the anisotropic models (all except models E and F) indicate that there is a trade-off between the isotropic velocities and the origin-time. That this is due to the anisotropic variations is suggested by the good solutions obtained for the isotropic structures. The velocities determined in this inversion have been plotted as dashed lines in Fig.6.15. Notice that in the hexagonal models where the P- or shear-wave surface displays a strong variation, the corresponding velocity determined by the inversion is approximately the lowest velocity actually sampled through the structure. In models E and F, where there is no noticeable variation, an average velocity is determined. In the orthorhombic models, with much more complicated variations, there is a large trade-off between the isotropic velocities, the origin-time and, in model J, the depth of the hypocentral locations. For the orthorhombic structures very poor hypocentral locations have been determined and this will create problems later in this section when they are used as trial hypocentres for an anisotropic inversion. (For this reason the events in these structures have also been relocated using constant P- and S-wave velocities with HYP071, and are summarised in Table 6.2 under models I1 and J1). The difference in the errors associated with the solutions for P- and shear-wave velocity is the result of adding the same errors to both P- and shear-wave arrival-times. This introduces more scatter onto the P-wave velocities, as illustrated in Fig.6.15, and results in the superior determination of the shear-wave velocity as observed. Notice that only in model J where there are very large absolute errors are the estimated errors

Table 6.2. The isotropic solutions for model A to J

The solutions obtained by the inversion of the arrival-times generated through models A to J for P- and shear-wave velocities in an isotopic half-space.

MODEL	Vp	Vs	AVERAGE HYPOCENTRE PARAMETERS				OVERALL
			long. (29.9696)	lat. (40.6177)	depth (8.02)	origin time (0.00)	RMS ERROR
A	5.70 (0.11)	3.29 (0.02)	29.9699 (0.16)	40.6173 (0.24)	8.00 (0.25)	0.00 (0.07)	0.0289
B	5.53 (0.11)	3.22 (0.02)	29.9735 (0.16)	40.6176 (0.24)	8.08 (0.26)	-0.03 (0.07)	0.0302
C	4.88 (0.13)	3.10 (0.04)	29.9746 (0.19)	40.6099 (0.28)	7.88 (0.36)	-0.20 (0.11)	0.0383
D	5.49 (0.12)	3.21 (0.03)	29.7240 (0.17)	40.6146 (0.24)	7.85 (0.27)	-0.51 (0.07)	0.0310
E	5.22 (0.11)	3.26 (0.03)	29.9684 (0.16)	40.6191 (0.24)	8.05 (0.29)	0.04 (0.08)	0.0311
F	5.75 (0.13)	3.27 (0.03)	29.9693 (0.19)	40.6180 (0.28)	8.12 (0.29)	0.00 (0.08)	0.0343
G	4.67 (0.14)	2.98 (0.04)	29.9728 (0.20)	40.6121 (0.29)	8.35 (0.38)	-0.29 (0.12)	0.0409
H	5.20 (0.10)	3.09 (0.02)	29.9710 (0.15)	40.6154 (0.22)	8.20 (0.25)	-0.12 (0.08)	0.0294
I	5.91 (0.14)	3.59 (0.03)	29.9683 (0.19)	40.6196 (0.28)	8.07 (0.32)	0.40 (0.08)	0.0327
I1	5.00	3.30	29.9694	40.6186 (0.39)	8.88 (0.32)	-0.05	0.0416
J	4.13 (0.20)	2.97 (0.08)	29.9696 (0.29)	40.6171 (0.41)	11.99 (0.72)	-1.48 (0.30)	0.0492
J1	5.70	3.30	29.9701	40.6171 (0.68)	8.22 (0.47)	-0.02	0.0697

The correct longitude, latitude, depth and origin-time averages are given in brackets at the head of each column. Average estimated errors in km/sec and km are given in brackets in each column. Models I1 and J1 have been located by HYPO71 and only an epicentral and the focal depth error are calculated.

noticeably larger than those in the isotropic structures. This feature of the inversion could have been anticipated from the conclusions of Chapter 3.

6.4.3 The anisotropic solutions

Section 6.3 suggests that a more systematic approach to determining the anisotropic structure is required which allows us to continually refine the initial model until the correct solution is clearly indicated. This suggests a combined approach of searching parameter space and straightforward least-squares inversion. In general the anisotropic inversion programs will only converge to the correct orientation of the anisotropic structure if the trial model is less than 30 degrees of rotation from the true orientation. This means that for a complete search for the correct orientation, a series of inversions can initially be performed from directions spaced at 30 degree intervals throughout the semi-focal sphere. (Only half the focal sphere needs to be considered because the anisotropic variations possess 180 degree symmetry). Initial work suggested that although essentially searching for the orientation of the anisotropic structure in this stage it is important not to constrain the elastic constants. This is because certain elastic constants are a very poor fit to particular orientations of other anisotropic structures and will therefore restrict the solutions to regions where they are a good fit. The actual values of the elastic constants in this first stage are also important in order that a clear indication of the correct solution can be obtained. It was found that using GKFF1 as the initial model provided the best indication. The reason for this is that, as demonstrated in Chapter 5, locating earthquakes in anisotropic structures with the TDP1 network under the assumption of isotropy effectively reduces the travel-time residuals to zero. Searching for second-order anisotropic variations by initialising the program from an isotropic structure,

(perhaps the obvious choice), will clearly not produce any further minimising of the travel-time residuals and a similar isotropic solution will be obtained. This can be avoided if the program is purposely initialised away from the first-order solution.

Once an indication of the correct orientation has been achieved the solution can be refined by altering the initial model and by only searching from a few directions surrounding this orientation. The model GKLF1 was found to be suitable in this stage, as this is sufficiently close to models of weak anisotropy and isotropy. These two stages should be sufficient to produce a good approximation to the structure. Further refinement of this solution using shear-wave delay data, can proceed using the hypocentral locations and structure defined by the first two stages as initial solutions.

This section will now illustrate how solutions for each of the models in Table 6.1 can be obtained following the process outlined above. We will describe in detail the solution obtained for model A and briefly summarise the solutions for the other models. The detailed solutions for these models are described in Appendix D. In addition we shall only illustrate the performance of the program in obtaining the velocity structure under the assumption that if this is accurately determined then by necessity so are the hypocentral locations. For reference, the solutions obtained for each of the models are summarised in Table 6.3 (for model A) and Table D.1 (for the other models), where the solution labels are referred to from the corresponding figure captions. These tables also list the F-test ratios between the square of the RMS error for the corresponding isotropic solution (Table 6.2), and the square of the RMS error for the particular anisotropic solution. The F-test, (Bevington 1969), tests the hypothesis that small changes in the square of the RMS error imply a statistically significant improvement in quality of fit from one solution to another. Bamford & Nunn (1979), and Bamford, Jentsch and Prodehl (1979), in field

studies of anisotropic propagation, have used this test to compare the quality of fit to their data of a model which allows for anisotropy, with that for a model that does not. For the number of degrees of freedom (approx. 135) involved in the inversion of our data set, F-ratios greater than 1.36 and 1.55 are required for an improvement in quality of fit to be significant at the 95% an 99% confidence levels respectively. No ratio is calculated for the solution obtained by the inversion of the data set containing shear-wave delays as there can be no isotropic equivalent.

MODEL A

Fig.6.16a illustrates the solutions obtained for the orientation of an axis of rotational symmetry in model A. In general, each solution is very dependent on the initial orientation; the RMS errors associated with each solution are very similar with no obvious minimum; and the orientation errors are very large as would be expected for an isotropic structure. In addition, the elastic constants associated with each solution suggest a very weakly anisotropic structure. There is perhaps an indication of two solutions for the orientation of a symmetry direction; one at an orientation of 45,5 and the other at one of 70,-70. We can attempt to clarify this by searching for a solution from 8 of the surrounding orientations and use GKLF1 as the initial model. The resulting solutions are shown in Fig.6.16b. Each inversion has not altered the initial orientation and the errors associated with these orientations are very large, again suggesting that the inversion has converged to an isotropic solution. In addition, the RMS errors associated with each solution are very similar to that of the isotropic solution (Table 6.2). An isotropic solution is confirmed by analysis of the elastic constants associated with each solution. These are all very similar, and the weighted average of these solutions produces the wave-surfaces shown in Fig.6.16c. The two shear-wave surfaces are almost coincident and the wave-surfaces show very

Figure 6.16. A summary of the solutions obtained by the inversion of synthetic arrival-times generated through model A.

(a) A summary of the solutions obtained for the orientation of the axis of rotational symmetry when the inversion assumes GKFF1 as an initial model, and is initialised from orientations spaced at 30 degree intervals throughout the semi-focal sphere. The horizontal axis measures the rotation about the vertical in tens of degrees measured anticlockwise from due East, and the vertical axis measures the rotation in tens of degrees about the North-South horizontal, from due East to the downward vertical. The left-hand diagram illustrates the initial and final solutions for the orientation. The right-hand diagram is a plot of the estimated errors associated with the final solution for the orientation. Each error bar has been scaled by a factor SF (bottom left) for convenience of presentation. A question mark in place of an error bar indicates that one or both errors are greater than 200 degrees. The number plotted beside each solution is the RMS error for that particular solution measured in units from the reference value of 0.0200 (i.e. 99 represents an RMS error of 0.0299). An average RMS error is plotted for closely spaced solutions.

(b) A summary of the solutions obtained from particular orientations using GKLF1 as an initial model. Notation and format as in (a).

(c) Dashed lines - a summary of the wave-surfaces obtained by taking the weighted average of all solutions shown in (b) (Solution A in Table 6.3). Solid lines - for reference, the wave-surfaces in model GKFF1. Error bars plotted at each extreme of the surfaces have been calculated on the basis of error estimates of the elastic constants that solely determine the velocity in that particular direction.

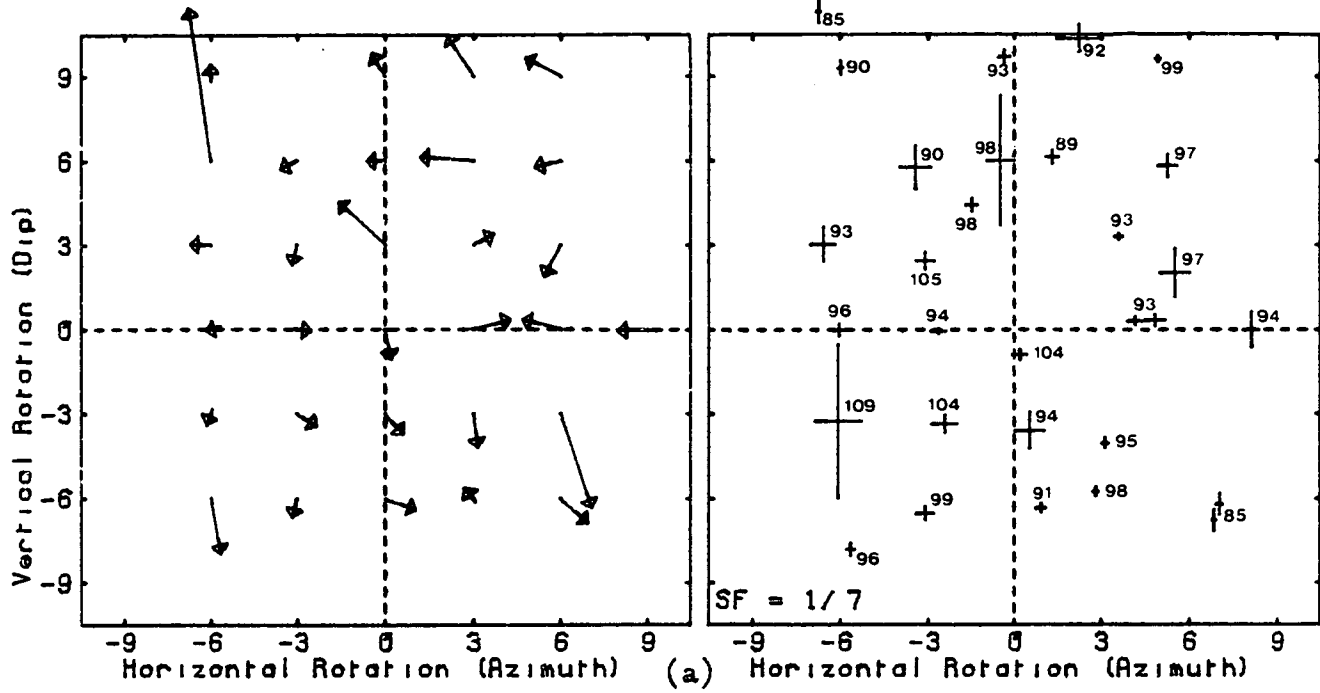
Vertical Rotation (Dip)
Horizontal Rotation (Azimuth)
SF = 1/7
(a)

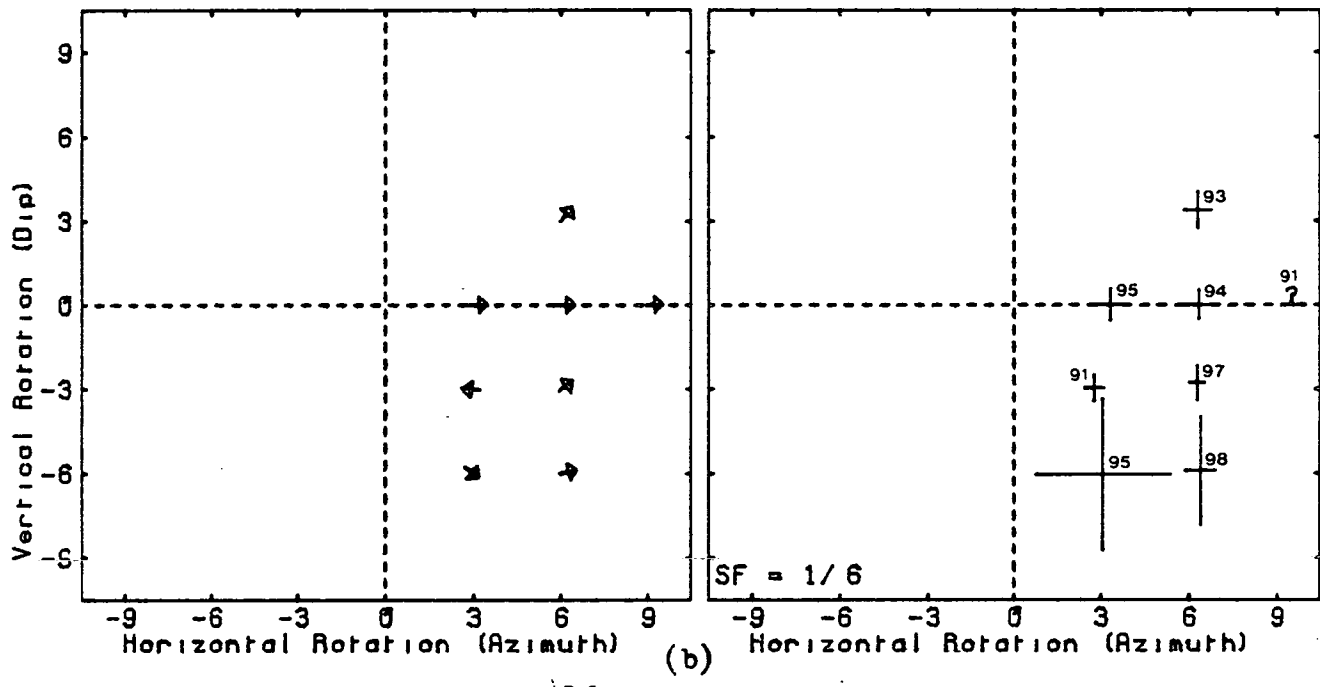
Vertical Rotation (Dip)
Horizontal Rotation (Azimuth)
SF = 1/6
(b)

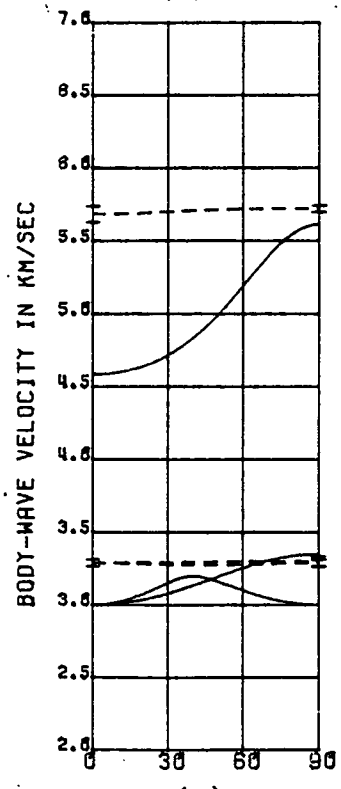
BODY-WAVE VELOCITY IN KM/SEC
(c)

little directional variations. The solution indicates P- and S-velocities of 5.71km.sec and 3.27km/sec, respectively - almost exactly the true solution. The RMS and estimated velocity errors associated with this solution are similar to those determined in the isotropic inversion (Table 6.2).

MODEL B

The inversion of the synthetic arrival-times generated through model B appeared to define two orientations for the symmetry direction when GKFF1 was used as the initial model. The orientations, symmetric about the horizontal and due East, define slight minima in the RMS errors, but these are not superior to that obtained by the isotropic inversion, and the orientation errors are large. Inversion of the data set using GKLF1 as the initial model also produces solutions with large orientation errors and with RMS errors that are similar to that obtained by the isotropic inversion. Most importantly, the elastic constants associated with each solution indicate an isotropic structure with P- and shear-wave velocities similar to that in the corresponding solution in Table 6.2.

MODEL C

Model C is the most straightforward structure to determine - the structure is strongly anisotropic and we initially assume the correct elastic constants as the initial model. Nine solutions converge to the correct orientation with very low orientation errors and which define a marked minimum in the RMS errors which is statistically superior to the isotropic solution at the 99% confidence limit. The weighted average of the elastic constants of these solution produces a very good fit to the true wave-surfaces. This solution is improved by the inversion of the subset containing shear-wave delays.

MODEL D

The first series of inversion assuming GKFF1 as the initial model defined a horizontal rotation of 30 degrees for model D. Solutions for all dip angles at this direction have low RMS errors, but only the solutions at low dip angles have low orientation errors as well. This orientation is confirmed in the second series of inversions using GKLF1 as the initial model, when three solutions define a minimum in both the RMS and orientation errors at the correct orientation. The corresponding elastic constants define a structure that is a good fit to the true structure, but the F-test ratio suggests that the solution is not statistically superior to the isotropic solutions at the 95% confidence level. The solution is confirmed and improved by inversion of the subset containing shear-wave delays.

MODEL E

As anticipated in section 6.4.1 the velocity variations in model E cannot be accurately resolved by the TDP1 network given the errors on the arrival-times. The clearest indication of a solution for the axis of rotational symmetry is 90 degrees of azimuth in error, suggesting that the azimuthal variation of velocities is well-constrained, but not the vertical variation. The inversion of the subset containing shear-wave delays does not improve the solution. No solution has a better RMS error than the isotropic solution and the orientation errors are large in all cases. In practise, this structure would have to be dismissed as being isotropic within the accuracy of the data.

MODEL F

The inversion for model F produces solutions that are similar to that of model D. The first series of inversions, using GKFF1 as the initial model, define a horizontal orientation of 30 degrees for the axis of rotational

symmetry. The second series of inversions, using GKLF1 as the initial model, define a minimum in both the RMS and orientation errors at the correct orientation. The elastic constants define a structure that is a good fit to the true structure. The solution is statistically significant at the 95% confidence level compared to the isotropic solution, and is confirmed and improved by inversion of the subset containing shear-wave delays.

MODEL G

The effect of the isotropic layer in model G is to completely mask the variations in the shear-wave surfaces. However the orientation of the structure and the strong 2θ P-wave variation are clearly defined, and the solution is statistically significant compared to the isotropic solution. The solution can be improved by introducing station corrections to take account of the known isotropic layer and by inversion of the data set containing shear-wave delays.

MODEL H

The effect of the isotropic layer in model H is to almost completely mask the orientation of the structure. However, as in model D (but to a lesser extent), the horizontal orientation of the structure is indicated. The true orientation of the structure is resolved by introducing station corrections to allow for the isotropic layer, and by changing the initial model to GKLF1. The resulting solution is a reasonable fit to the true structure but is only marginally superior in a statistical sense to the isotropic solution. The fit to the true structure is improved by using the subset containing shear-wave delays.

MODEL I

Inversion of the arrival-times generated through model I for hexagonal

structure appears to define the orientation of both horizontal principal axes, (i.e. the direction of the crack intersections, and the direction of the normal to the minor crack system). The solutions at these orientations have the lowest RMS and orientation errors in both series of inversions (i.e when both GKFF1 and GKLF1 are used as initial models). This apparent duality of the solutions and the fact that inversion of shear-wave delays does not confirm either solution suggests that the assumption of hexagonal symmetry is insufficient to describe this structure. Inversion for orthorhombic symmetry confirms both orientations, and the nature of the P-wave variation of both solutions are consistent with the same structure, but there are very large estimated errors on the surface. As anticipated in section 6.4.1 the shear-wave surfaces are not a good fit to those of the true structure, even after inversion of shear-wave delays. The RMS errors of the best solutions indicate that they are almost statistically significant compared to the isotropic solutions.

MODEL J

As in model I, the inversion of the arrival-times generated through model I for hexagonal symmetry appear to define two orientations, but in this case ~~they are the orientations of the normals to each crack system. The~~ wave-surfaces associated with both solutions are a very poor fit to the true velocity-surfaces because of the very poor trial hypocentres used in the inversion (Table 6.2). The duality of the solutions for the orientation, and the fact that inversion of the shear-wave delays does not confirm either solution suggests that the assumption of hexagonal symmetry is insufficient to describe this structure. Inversion for orthorhombic structure, using revised hypocentres defines all three principal axes, the solutions at which are consistent with the same structure, but again with very large estimated errors. The fit to the structure is improved by inversion of the shear-wave delays and the error bars are also improved.

The RMS error associated with each solution suggests that they are statistically significant compared to the isotropic solutions at the 99% confidence level.

6.5 Joint-inversion with the TDP2 network

The TDP2 network covers a much larger area than the TDP1 network and so it is expected that the performance of the inversion programs with the TDP2 network will be better. This is suggested by Fig.6.17 which shows the region of the models GKFF1 and GKLF1 sampled by ray paths from a suite of events that will be used in Chapter 7, to the stations of the TDP2 network (but not including HE to the west of the main network). The synthetic arrival-times have been rounded to the nearest 0.1s. Comparison with the equivalent figure (Fig.6.15) for the TDP1 network reveals that a further 30% of the wave-surfaces are sampled. It is anticipated that this feature will provide a greater constraint on the dip of any symmetry direction in the real structure. However, as noted previously, the TDP2 network straddles a major fault zone and any lateral hetereogeneities may mask the anisotropic variations.

6.6 Discussion

This Chapter has presented a new method of determining the orientation and the elastic constants of an anisotropic structure. This is achieved by inverting suites of earthquake arrival-times and simultaneously solving for the hypocentral locations, two parameters that define the orientation of the structure, and either five or nine elastic constants that describe seismic-wave propagation through structures of hexagonal or orthorhombic symmetry respectively. It has been demonstrated that the inversion procedure is not globally convergent and that the initial model used in the inversion needs to be in the close vicinity of the correct solution for convergence to be obtained. To achieve this requires a combined approach

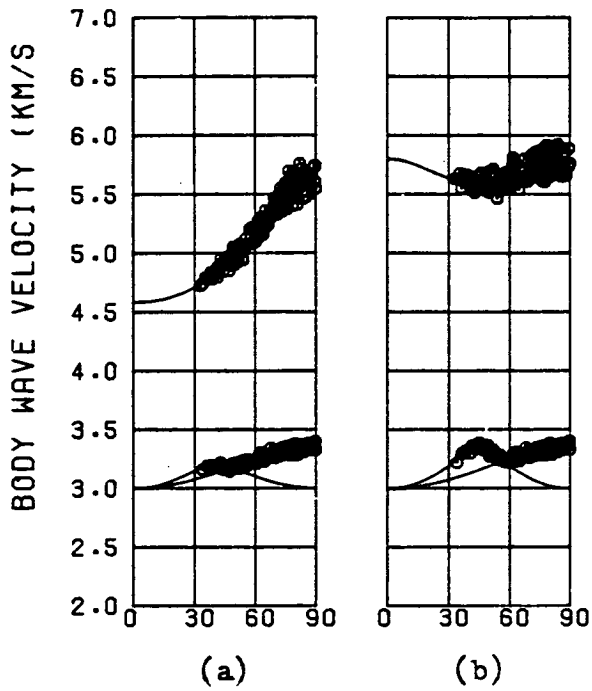

Figure 6.17. An illustration of the region of the wave-surfaces of models GKFF1 (part (a)) and GKLF1 (part (b)) sampled by ray paths from a suite of events that will be used in Chapter 7, to stations of the TDP2 network (not including HE). Points marked on the true surfaces have been calculated from synthetic arrival-times (rounded to 0.1s), the actual hypocentral locations, and the ray directions in a half-space rotated into the a vertical section measured from the axis of rotational symmetry. In both models the axis of rotational symmetry is at an orientation of 30,0.

of searching parameter space for the solution, and iterative least-squares inversion from specified directions in the focal sphere. Once an indication of the true solution has been obtained it is then possible to refine the initial model until convergence to the correct solution is obtained. The correct solution is indicated by low RMS and orientation errors and by the consistent convergence of the inversion to this one solution from surrounding points in parameter space. It has been shown that for most structures it is possible to find reasonable solutions using P-and first-shear arrival data. A much more accurate solution for the elastic constants can be achieved by using this solution as an initial model and incorporating shear-wave delay data into the inversion. This is only possible if the shear-wave surfaces in the region sampled by the ray paths are sufficiently distinct so as not to be obscured or distorted by the errors on the first shear-arrival times. However, it is not always possible to find accurate solutions, particularly for structure with either weak or very complicated velocity variations. Nevertheless in these cases there is still an indication of the true structure (in particular, the orientation and the nature of the P-wave variation) even though the exact solution cannot be resolved given the accuracy of the data.

At present the inversion is limited by the assumption of a half-space but it has been shown that for structures possessing strong anisotropic variations the effect of a thin near-surface layer can be modelled by the introduction of extra station corrections. However, the layer, and any other departure from a half-space, is likely to mask the variations due to weak anisotropy such as in models E, F and H, in which case the inversion would not define a solution that is significantly superior to an isotropic solution.

A summary of how to recognise particular structures is outlined below.

ISOTROPIC STRUCTURES

Isotropic structures can be recognised by the strong dependence of the final orientation on the initial orientation; large estimated orientation errors; and by the RMS error of any solution being similar to that obtained by an isotropic inversion. More importantly, when the initial model assumed in the inversion is only weakly anisotropic, the elastic constants of all solutions indicate no directional variation in the wave-surfaces, and the two shear-wave surfaces are almost coincident. This is the case even when the structure is not a half-space but is inhomogeneous due to an internal dipping interface. Although not demonstrated, by inference from the half-space case we can suggest that an isotropic solution would be obtained if the structure consists of a series of horizontal and isotropic layers. This is clearly the most important and encouraging aspect of the inversion synthetic data. Providing that the initial model is reasonably close to isotropy, then inversion of arrival-times in a laterally varying isotropic structure will produce a recognisably isotropic solution.

HEXAGONAL STRUCTURES

Strongly anisotropic structures with hexagonal symmetry are recognisable by consistent convergence of the solutions to one particular orientation with low RMS and parameter errors. This is also the case if the anisotropic variations are slightly masked by the effect of a thin isotropic surface layer. However for structures that possess only weak P- and shear-wave anisotropy, the scatter in the arrival-times may obscure the anisotropic variations. In this case the solutions obtained have similar RMS errors to that of an isotropic solution. Notice also that even though it is possible to obtain a good fit to the true structure, it is not always statistically superior to the solution obtained by an isotropic inversion (e.g. model H). However, such solutions are associated with lower estimated errors

than those for an isotropic solutions. In some of the models there was evidence of secondary solutions that were incorrect, but which were still significantly superior to the isotropic solution. These may be caused by poor network resolution (there are large azimuthal gaps to the north and south-east with the data set used), but these were always associated with higher RMS errors than those of the correct solution.

ORTHORHOMBIC STRUCTURES

At present, the inversion for orthorhombic structures is limited to the inversion of phase-velocities. It is not anticipated that this restriction will be important for weakly anisotropic structures and where only P- and first S-arrival data are used. It will be a severe restriction for strongly anisotropic structures where the observed group-velocity deviates markedly from the phase-velocity, particularly in structures where there are cusps on the shear-wave surface. In such structures it would be inconsistent to use this program to invert a data set that includes shear-wave delays.

It was shown that for the particular models used here it is not possible to obtain a close enough initial model, in particular close hypocentres, for the inversion to converge to the correct solution. An orthorhombic structure may be difficult to distinguish from a hexagonal structure, but would be indicated by consistent solutions for orthogonal orientations at each of the principal axes. It is anticipated that this duality of the solutions would be better defined in the hexagonal inversion if the orthorhombic models used here were oriented differently or if the minor crack system was of greater density. Inversion for orthorhombic symmetry should confirm the orientations, and the elastic constants obtained at each orthogonal orientation should be consistent with the same structure, particularly for the P-wave surface. However, there were very large model errors associated with these solutions, and it may be

impossible to say with any certainty which are the high and low velocity directions from the inversion alone.

In summary, this Chapter has illustrated that it is possible to accurately invert suites of arrival-times for both hypocentral locations and anisotropic structure, providing that the arrival-times of P- and S-phases are accurately known, and that the structure is reasonably simple. This is possible even with a very small and irregular network using a distribution of events with large azimuthal gaps. We have not attempted to model an inhomogeneous anisotropic structure, such as a laterally varying structure with the same anisotropic variations superimposed. Such structures are likely to invalidate tha assumption of a half-space and lead to confusing results. In addition, the shear-wave surfaces in the models used here do not exhibit cusps. The velocity variations in such structures may be particularly difficult to resolve.

CHAPTER 7

FURTHER ANALYSIS OF THE TDP DATA SETS

7.1 Introduction

This Chapter will attempt to determine the anisotropic structure beneath the TDP networks, as indicated by consistent and clear observations of shear-wave splitting (Chapter 2). This will be achieved by the analysis of the travel-time residuals and by the joint-inversion of suites of earthquake arrival-times for anisotropic structure and hypocentral locations using the techniques developed in Chapter 6. We shall firstly, however, briefly review the TDP experiments and relocate the earthquakes with improved arrival-times, but still using an isotropic approximation for the velocity structure.

Several hundred earthquakes have been recorded during the TDP1 and TDP2 surveys. The events have been located, under the assumption of isotropy, in a diffuse pattern beneath the networks and so sample a substantial volume of the structure. Most records display impulsive P- and S-arrivals that can be accurately read from three-component seismograms. Shear-wave splitting, strongly indicative of shear-wave propagation through anisotropic media, has been identified in the majority of shear-wave trains in the records. It is anticipated that the anisotropy is due to the preferential alignment of pre-existing cracks under the action of a deviatoric stress system and is not necessarily related to an impending large earthquake. The detailed analysis of the TDP data sets will rely on accurate hypocentres. However, as demonstrated in Chapter 3, failure to take account of such anisotropy may result in systematic mislocations of a few kilometres.

The TDP1 network, in particular, has a small aperture (15km) and all stations are to the south of the main fault zone and situated on bedrock. This suggests that a half-space is a reasonable approximation to the

structure. This is not likely to be the case for the TDP2 network which straddles the fault zone, although a strongly anisotropic structure seems likely to dominate any lateral velocity discontinuities. That the dilatancy-anisotropy is likely to be homogeneous is suggested by P-wave first motion studies which indicate that the dominant mechanism of the TDP2 events is strike-slip with a small component of normal motion. It is not possible to undertake a complete analysis of the source mechanisms of the TDP1 events, due to the poor azimuthal coverage, but all first motions are consistent with those determined for the TDP2 events. The fault-plane solutions indicate P and T axes at azimuths of N112E and N27E, inclined above the surface by 29 degrees, and dipping below the surface by 12 degrees, repectively. We therefore anticipate that the principal axes of the anisotropic structure will be close these directions.

7.2 Repicking arrival-times and the relocation of events

The arrival-times of the events in the TDP experiments were originally picked to the nearest 1/20 of a second from analogue records. Chapter 6 demonstrated that it is important that the arrival-times be as accurate as possible. The degree of scatter of the arrival-time data will influence the precision with which weakly anisotropic structures can be determined. In addition, improved arrival-times should result in improved hypocentral locations which will be used as initial solutions in the joint-inversion of the data sets. For this reason the arrival-times were repicked to the nearest 1/100 of a second from digitised seismograms using a partially automatic process.

The TDP events were digitised, at a sampling rate of 100 samples/sec, and stored on magnetic tape. The P- and S-arrivals were read from these seismograms using an automatic computer program. This program is very simple in comparison with other routines that are commonly used for real time data processing and earthquake location (Stewart, Lee & Eaton 1971;

Crampin & Fyfe 1974). This simplicity is possible for several reasons: 1) we can use the preliminary event locations to set a narrow window surrounding the correct arrival-times; 2) it is not necessary to cross-check a picked phase with phases on other channels in order to identify it as a seismic signal; and 3) we are only improving the arrival-times of known phases in a given, small time-interval, and we are not attempting to distinguish between local events, teleseisms, drop-outs, and noise, etc..

For P-arrivals, read from the vertical seismogram, the program initially determines the maximum amplitude, (A), in one second of time series immediately before the beginning of the 'P-window'. The program then searches through the P-window for a sample that exceeds a certain fraction of this amplitude. A sample (X_k) is initially chosen as an arrival if:

$$B\,|X_{k+1}| > |A| \qquad (7.1)$$

where B is a constant. This sample is confirmed as an arrival if

$$B\,|X_{k+3}| > |A| \qquad (7.2)$$

and $B\,|X_{k+7}| > |A|$

A value of 1.2 for B was found to be suitable for picking impulsive P-arrivals. If no arrival is picked within the P-window, the constant is increased to 2.5 and the window is searched again. This value was found to be suitable for very emergent arrivals. If no arrival is selected in these two searches, a nominal P-arrival is assigned based either on the preliminary event location or the arrival picked from the analogue records. This arrival is used by the shear-wave arrival routine, but no actual arrival is declared to the operator.

The program uses a similar routine to search for a shear-wave arrival on the horizontal seismograms. The seismograms are first rotated into

radial and transverse components using the preliminary event location in order to increase the amplitude of the shear-wave on the horizontal components. The program uses 0.5s of data, beginning 0.5s after the P-arrival, to determine a maximum amplitude (A), and then searches for an arrival in the 'S-window' using the criteria in 7.1 and 7.2. In this case a suitable value for B was found to be 1.6, increasing to 2.5 if no arrival was found in the first search. This procedure was repeated on the second horizontal seismogram. The operator then selects which, (if any), of the two selected arrivals is the true first shear-wave arrival.

This routine will accurately pick 75% of the P- and shear-wave arrivals that can be read by the operator. An example from the TDP1 data set is shown in Fig.7.1. (Notice the example of shear-wave splitting on the horizontal seismograms at AY and the marked difference between the new arrivals and the arrivals read from analogue records). In this particular example the operator chose all the P-arrivals selected by the program, together with the S-arrivals on the radial component at SE and on the transverse component at AY. The S-arrival at TE was revised to 59.59 by the operator.

Approximately 200 events from TDP1 and 300 from TDP2 were relocated using the arrival-times that had been automatically picked from digitised records using the routine described above. The locations are shown in Figs.7.2a and 7.2b, and were determined by HYPO71 using the crustal model in Table 2.1. It is now possible to see much more detail in the earthquake locations, and linear trends in seismic activity are apparent (c.f. Figs.2.2 and 2.5). The most notable features in TDP1 are the cluster to the east of AY, the NW-SE trend south of PA, and the very well-defined N-S trend to the north-east of SE. The first two features are also apparent to a lesser degree in the TDP2 locations. The most notable feature of the TDP2 locations is the very dense cluster immediately beneath DP just south of the main fault zone. The repicking of arrival-times has resulted in an

Figure 7.1 An example of the output from a program that automatically reads P- and shear-wave arrivals from digitised seismograms. Details of the preliminary earthquake location are shown in the right-hand column. The traces from top to bottom are: time-code with one second marks and with the first complete second decoded; three groups of three-component seismograms (vertical, radial and transverse) at stations SE, TE and AY respectively; a repeat of the time-code. A vertical mark is placed above each trace at every 4s from the first second mark. A vertical line across each three-component set marks the selected P-arrival. A single arrow above each horizontal seismogram marks the selected shear-wave arrival for that particular component. The position of the these two arrivals is also indicated by a single arrow above the vertical seismogram. The time of each arrival is printed at the end of each respective trace. Double arrows below each trace indicate the original arrival-time read from analogue records. This arrival-time is also written at the end of each trace and labelled JP. AZ denotes the azimuth of the station from the epicentre measured clockwise from North, and HD denotes the hypocentral distance in kilometres.

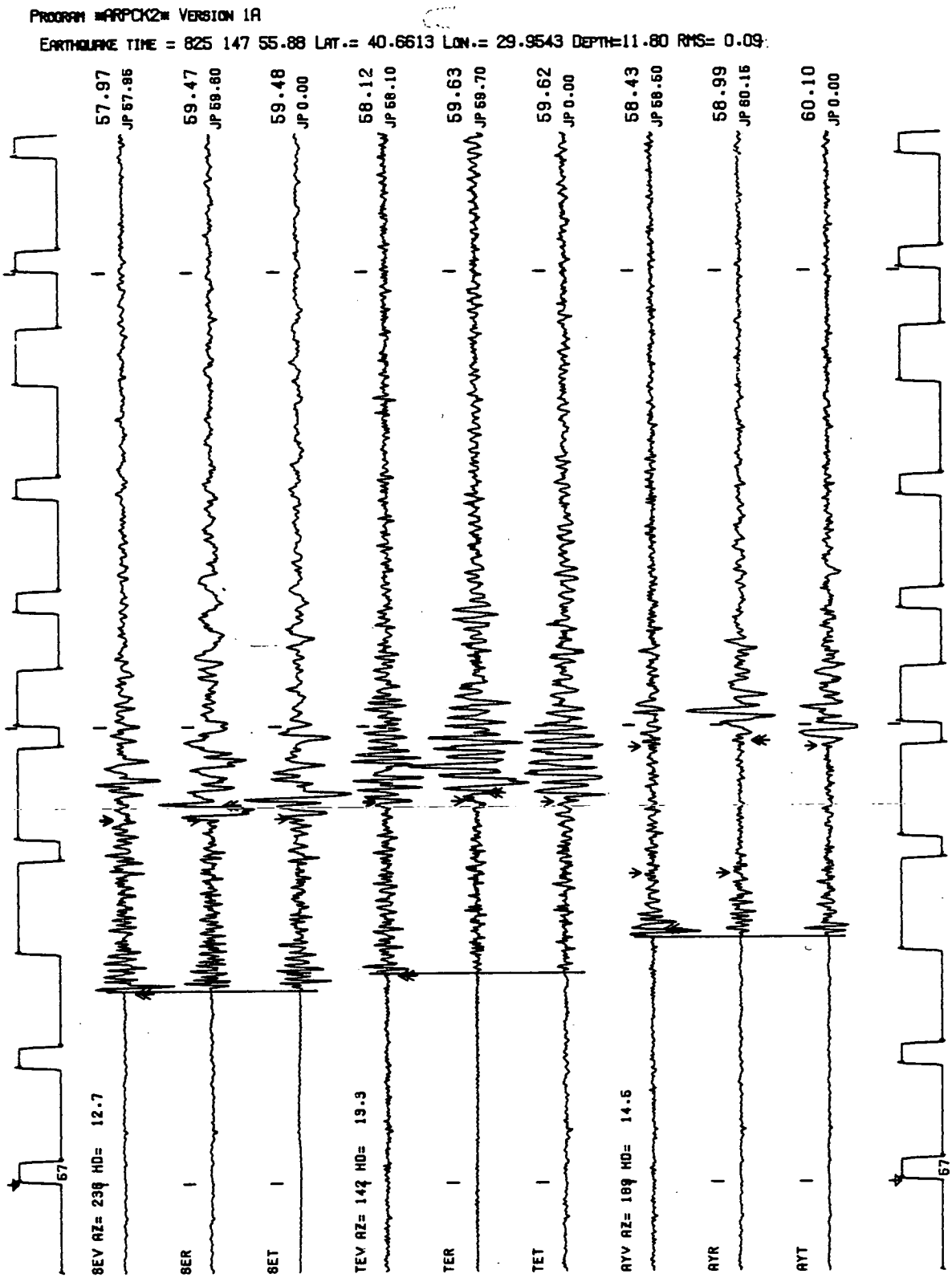
PROGRAM =ARPCK2= VERSION 1A
EARTHQUAKE TIME = 825 147 55.88 LAT.= 40.6613 LON.= 29.9543 DEPTH=11.80 RMS= 0.09
57.97
JP 57.96
59.47
JP 59.80
59.48
JP 0.00
58.12
JP 58.10
59.63
JP 59.70
59.62
JP 0.00
58.43
JP 58.50
58.99
JP 60.15
60.10
JP 0.00
BEV AZ= 239 HO= 12.7
BER
BET
TEV AZ= 142 HO= 19.3
TER
TET
AYV AZ= 189 HO= 14.5
AYR
AYT
67
67

Figure 7.2 A map of epicentral locations in TDP1 and TDP2 using arrival-times automatically picked from digitised seismograms.
(a) 199 events from TDP1
(b) 276 events from TDP2

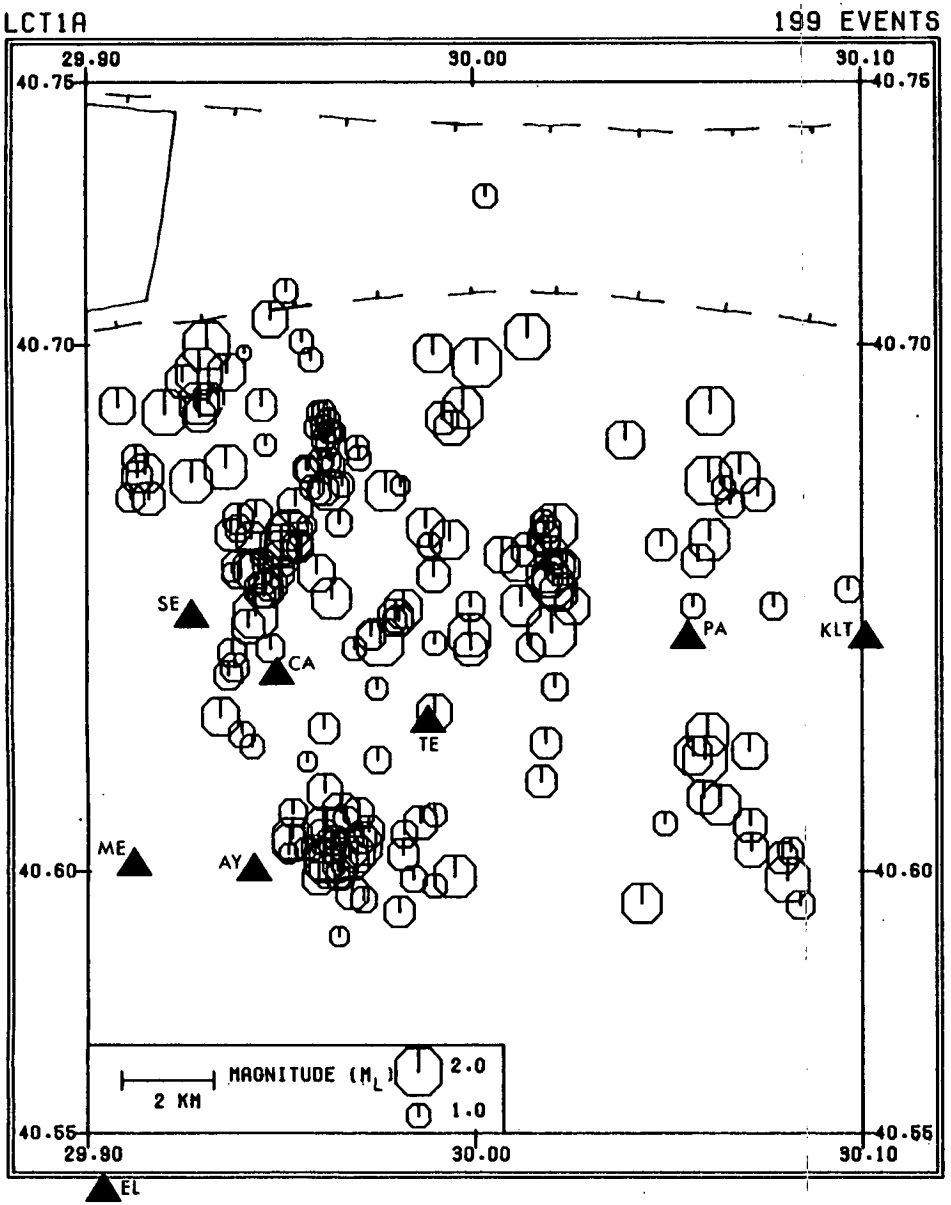
LCT1A
199 EVENTS
29.90
30.00
30.10
40.75
40.70
40.60
40.55
SE
CA
TE
PA
KLT
ME
AY
EL
MAGNITUDE (M_L)
2.0
1.0
2 KM

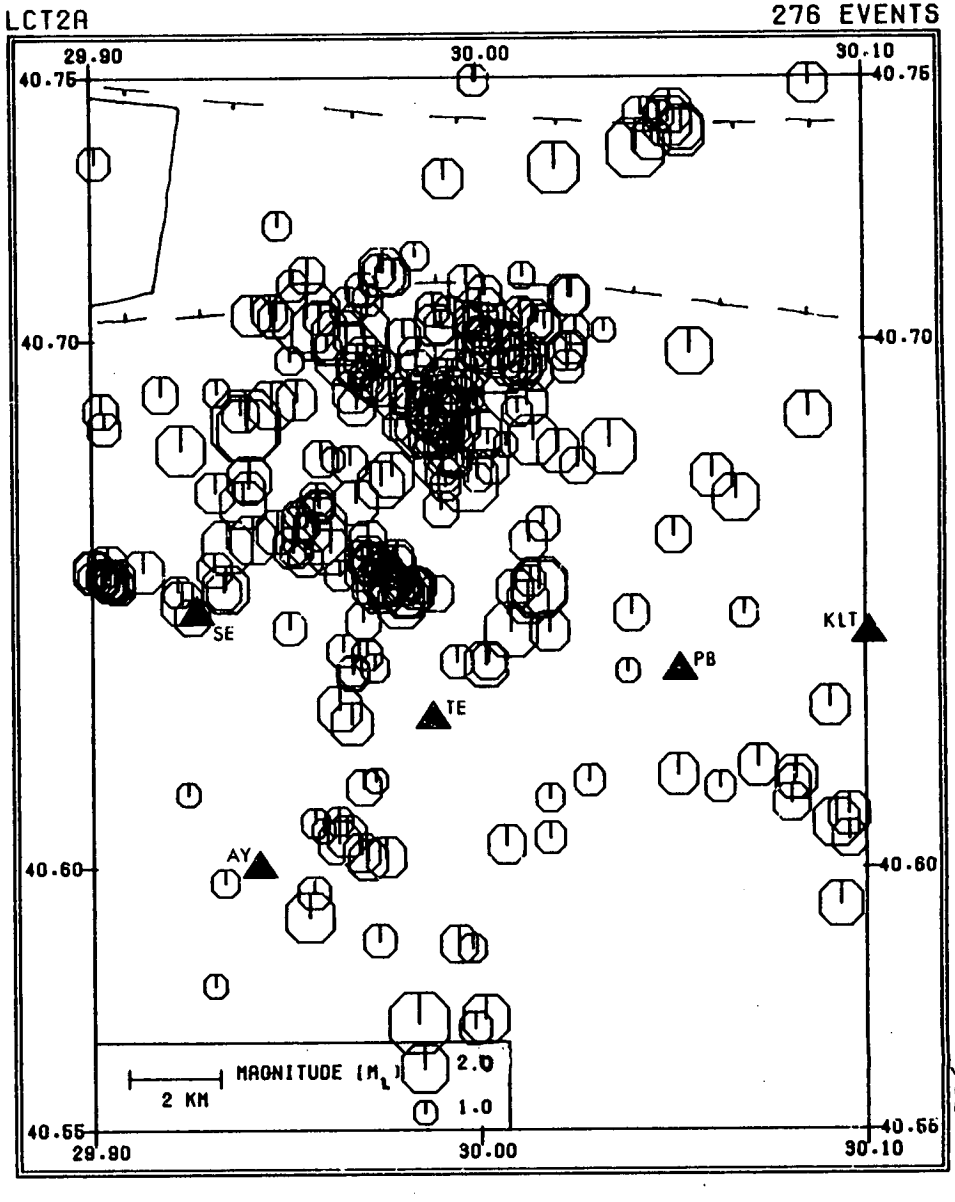
LCT2A
276 EVENTS
29.90
30.00
30.10
40.75
40.70
40.60
40.55
SE
TE
PB
KLT
AY
MAGNITUDE (M_L)
2.0
1.0
2 KM

average decrease of 50% in the RMS errors and a decrease of approximately 25% and 30% in the standard errors associated with the epicentral and focal depth determinations respectively.

7.3 Analysis of the TDP1 travel-time residuals

From Chapter 5, as a first step in the procedure to identify the anisotropic structure we can plot an azimuthal variation of travel-time residuals. This may indicate which are the high and low velocity directions and so provide an indication of a symmetry direction which will reduce the area needed to be searched in the inversion procedure. Fig.7.3a shows plots of P- and S-wave travel-time residuals from all of the events in Fig.7.2a. There is a large amount of scatter, particularly in the NE quadrant. The near zero residuals in the NW quadrant probably reflect the high azimuthal weighting given to arrivals at PA by HYPO71. Fig.7.3b shows the variation of residuals from those events that have at least 8 recorded arrivals. The scatter has been reduced but there is still no indication of any variation that could be ascribed to velocity-anisotropy.

Table 7.1 (Model A) lists the average station residuals after relocation of the TDP1 events. There is a large delay at AY that is statistically significant at the 95% confidence level (i.e. more than twice its standard deviation). This is also apparent in a plot of the travel-time residuals at AY in Fig.7.4a. Normally a positive delay at a station is ascribed to anomalous low-velocity structure immediately beneath the station. This station is at an altitude of 1000m and insufficient allowance for this may be a factor. Alternatively it may be a reflection of instrumental errors. The most likely source of such an error is from skewness of the tape heads in both the recording and playback systems. The station AY was recorded at one end of the tape head, and so an unfortunate combination of such errors could easily account for the observed delays. Another source of this delay could be velocity-anisotropy. AY receives

Figure 7.3 The azimuthal variation of P-and shear-wave travel-time residuals from the events of Fig.7.2a. The circle marks a zero residual and the 0.1s residual is labelled. All residuals have been normalised to a hypocentral distance of 10km. Symbol size is proportional to the weight assigned to the particular phase. The residuals are plotted with the station in the middle of the diagram.
(a) P- and shear-wave travel-time residuals from all events.
(b) P- and shear-wave travel-time residuals from all the events with at least eight recorded arrivals.

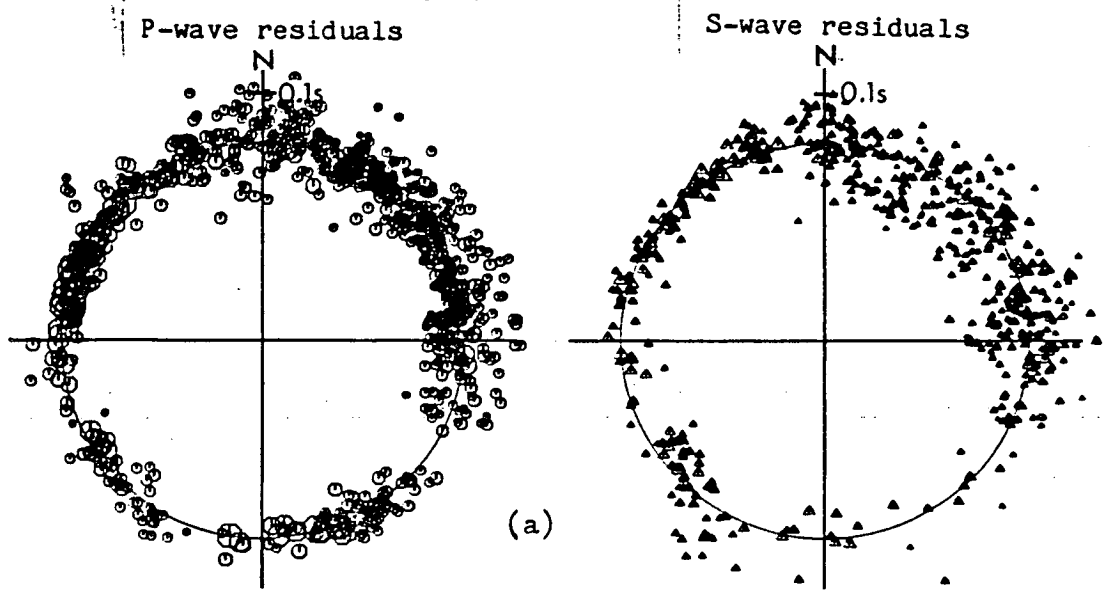
P-wave residuals
N
0.1s
S-wave residuals
N
0.1s
(a)

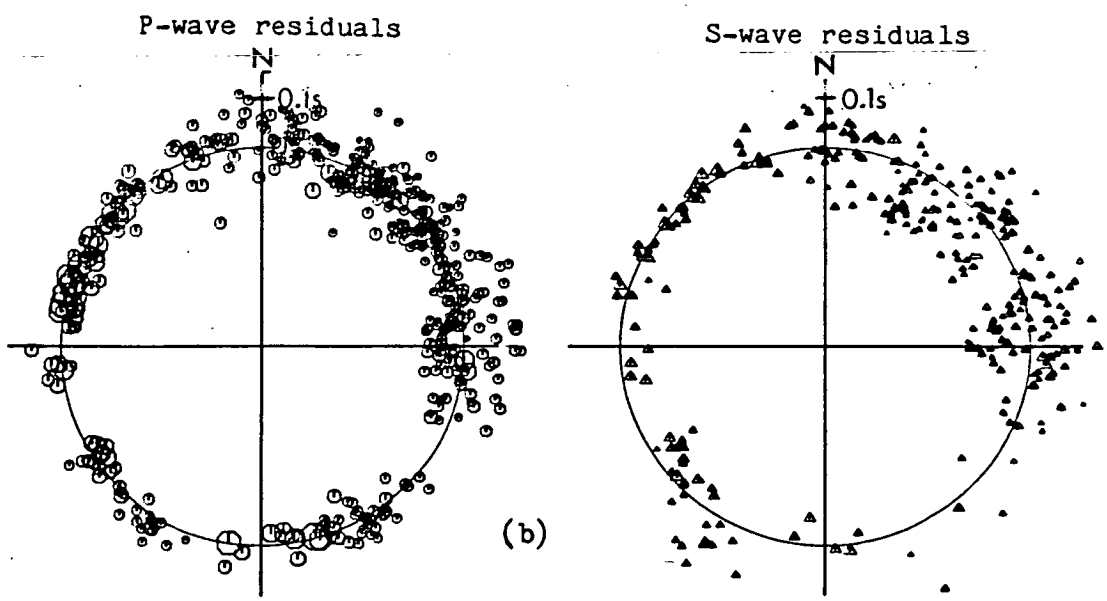
P-wave residuals
N
0.1s
S-wave residuals
N
0.1s
(b)

Figure 7.4 The azimuthal variation of travel-time residuals from the events of Fig.7.2a at particular stations. Notation and format as in Fig.7.3.
(a) P- and shear-wave residuals at station AY
(b) P- and shear-wave residuals at station ME

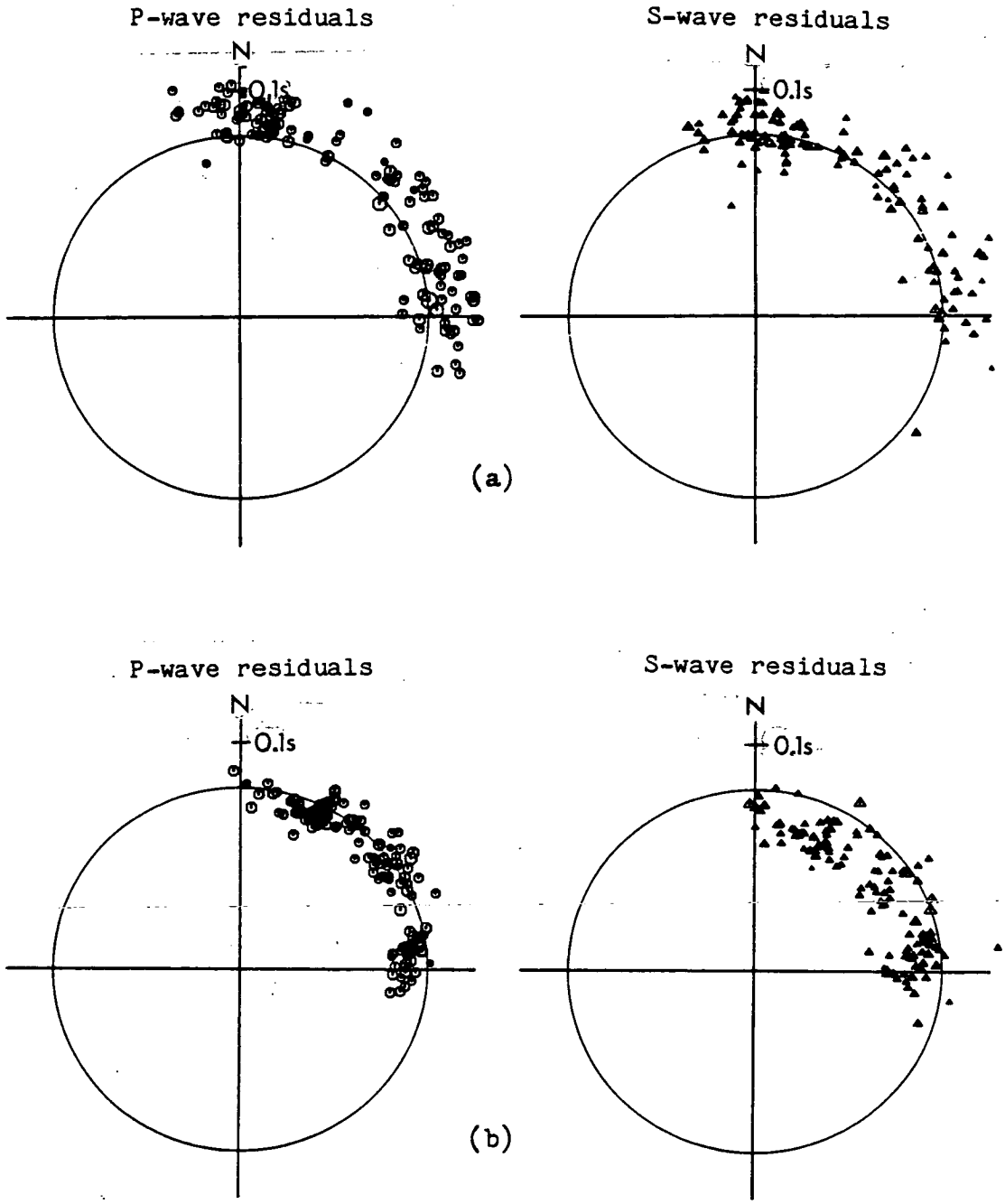
P-wave residuals
N
0.1s
S-wave residuals
N
0.1s
(a)
P-wave residuals
N
0.1s
S-wave residuals
N
0.1s
(b)

rays from a predominantly north-easterly direction. If this direction is a low velocity direction then a positive delay is to be expected at this station. If this is the case, then altering the station correction so that the average residual is zero will effectively smooth any variations due to anisotropy.

Fig.7.5 illustrates a very clear example of such a smoothing effect. In Chapter 3 the SQ1 network was used to locate the events of Fig.3.3, under the assumption of isotropy, using only P-arrivals and where the true structure was a system of dry parallel cracks (model GKFF1) oriented to model dilatancy-anisotropy associated with a strike-slip fault. The resulting locations are shown in Fig.7.5a, and the P-wave residuals are shown in Fig.7.5b. The average station residual at four stations is non-zero and can be reduced by introducing station corrections. The resulting locations and residuals are shown in Figs.7.5c and 7.5d respectively. There is now no obvious variation in the residuals that would indicate anisotropy. In addition, this process has resulted in no appreciable improvement to the earthquake locations although there is a very noticeable improvement in the nominal quality of the locations as indicated by the RMS errors. This illustrates that great care must be exercised with the station corrections when attempting to determine the anisotropic structure. In addition, any inversion program that solves for station corrections (e.g. Crosson 1976; Aki & Lee, 1976; Ward et al.1981) will inevitably result in some smoothing of any variations due to velocity-anisotropy, and its possible elimination if stations are receiving rays from particular directions. This is possibly another explanation for the failure of Ward et al. to observe P-wave anisotropy.

There are two arguments against this delay being due to velocity-anisotropy. Firstly, as demonstrated in Chapter 5, the TDP1 network places insufficient constraint on the earthquake locations for variations in residuals due to velocity-anisotropy to be apparent. Secondly, station ME

Figure 7.5 An illustration of the effect of altering the station corrections when locating earthquakes in regions of dilatancy-anisotropy under the assumption of isotropy. The events of Fig.3.3 have been located using P-arrivals at the station of the SQ1 network in a structure where a system of dry parallel cracks is oriented to model dilatancy-anisotropy on a strike-slip fault.

(a) Locations determined without any station corrections. Notation and format as in Fig.3.4.

(b) The azimuthal variation of P-wave travel-time residuals from the locations shown in (a).

(c) Locations determined with corrections at four stations so that all stations have an average residual of zero. Notation and format as in Fig.3.4.

(d) The azimuthal variation of P-wave travel-time residuals from the locations shown in (c).

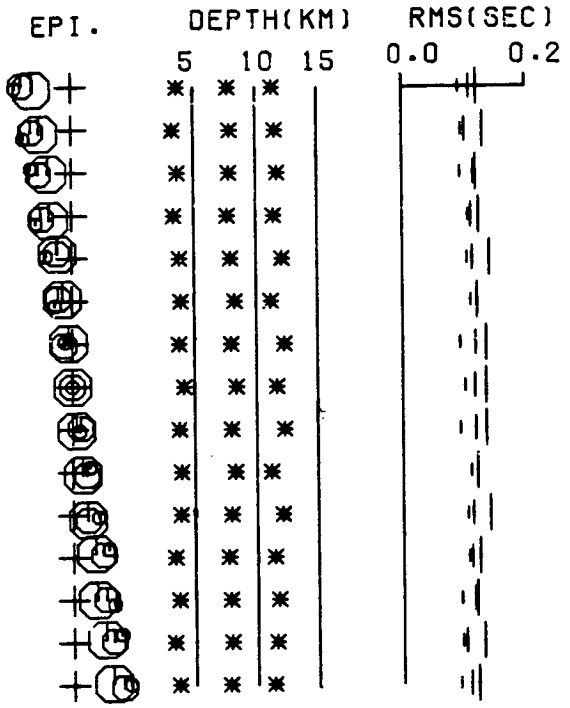
EPI.
DEPTH(KM)
5
10
15
RMS(SEC)
0.0
0.2

(a)

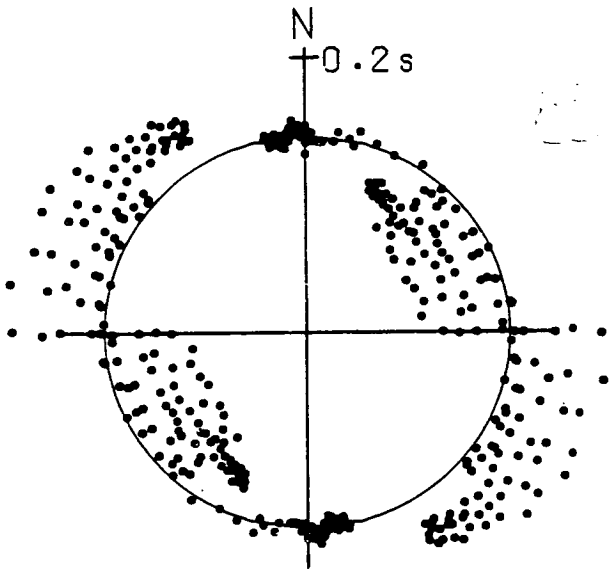
N
0.2s

(b)

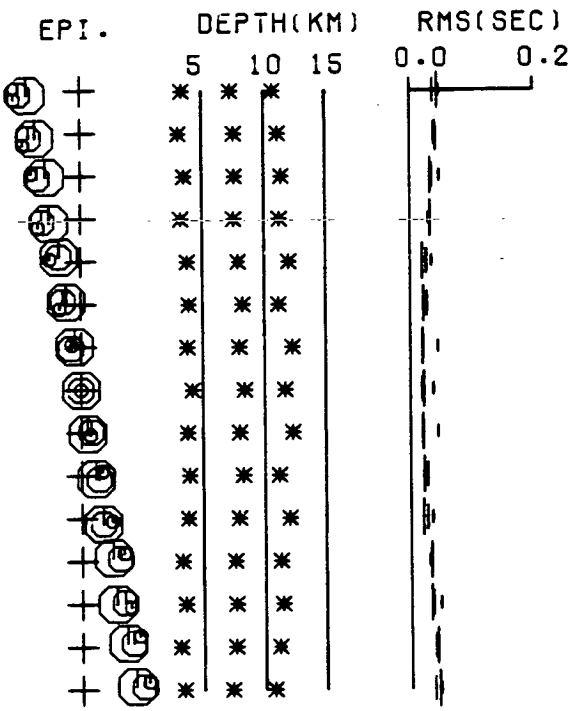
EPI.
DEPTH(KM)
5
10
15
RMS(SEC)
0.0
0.2

(c)

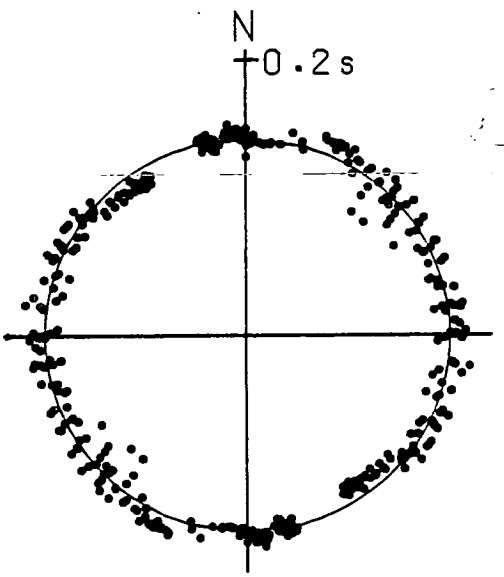
N
0.2s

(d)

Table 7.1. A list of the average delays for the TDP1 stations after relocation of approximately 200 events. Model A - normal station corrections based on the station elevation. Model B - an extra station correction of 0.05s introduced at station AY. Standard deviations are given in brackets.

Station	Model A	Model B
SE	-0.002 (0.012)	-0.002 (0.013)
TE	0.006 (0.012)	0.009 (0.012)
AY	0.052 (0.018)	0.024 (0.019)
CA	-0.012 (0.012)	-0.012 (0.012)
PA	-0.008 (0.009)	-0.010 (0.009)
ME	-0.017 (0.015)	-0.003 (0.010)
EL	0.013 (0.008)	0.024 (0.013)

Table 7.2. Isotropic solutions for the TDP1 data sets.
The average of the estimated errors (in km and km/sec) are given in brackets beneath the corresponding parameters. HYPO71 only estimates epicentral and focal depth errors and used the model in Table 2.1 to locate the events.

Data set	Location by	Vp	Vs	Long.	Lat.	Depth	Origin time	Overall RMS error
F1	HYPO71	—	—	29.9686 (0.52)	40.6146	8.49 (0.37)	32.46	0.0513
	Inversion	5.48 (0.22)	3.36 (0.05)	29.9679 (0.32)	40.6146 (0.45)	9.29 (0.51)	32.29 (0.15)	0.0488
F2	HYPO71	—	—	29.9707 (0.63)	40.6174	7.76 (0.38)	28.55	0.0489
	Inversion	5.56 (0.30)	3.33 (0.07)	29.9698 (0.50)	40.6163 (0.85)	8.29 (0.59)	28.84 (0.17)	0.0491
F3	HYPO71	—	—	29.9695 (0.47)	40.6179	7.99 (0.35)	30.15	0.0498
	Inversion	5.47 (0.20)	3.33 (0.05)	29.9682 (0.28)	40.6180 (0.41)	8.60 (0.47)	30.01 (0.13)	0.0498

receives rays from almost the same direction as AY and would therefore be expected to show positive residuals. Table 7.1 and Fig.7.4b indicate that there are negative residuals at ME. We therefore suggest that the positive delay at AY may be due to combination of a local structural anomaly, and instrumental errors, and may be allowed for by introducing an extra station correction.

We modified the station corrections by a step-wise process of altering the station correction of the station with the most significant delay and then of relocating the events. By introducing an extra correction of 0.05s at AY we reach a situation where no station delay is significantly different from zero (Model B, Table 7.1). The revised locations are shown in Fig.7.6. Compared to the original locations based on arrivals picked from analogue records, (Chapter 2), the average RMS error has been reduced by 55%, and the average standard errors associated with the epicentral and depth determinations have been reduced by 35% and 30% respectively. This is an improvement of 10%, 14% and 2% respectively, on the locations based on the automatically picked arrivals with the original station correction at AY. The travel-time residuals from these revised locations are shown in Fig.7.7. Again there is still no obvious variation that would indicate the presence of velocity-anisotropy. There is, however, a slight indication of late arrivals, particularly for the shear-waves, in the SW quadrant. This is at most only suggestive and cannot be taken to indicate a symmetry direction.

7.4 Inversion of TDP1 data for anisotropic structure

The events from the TDP1 data set were divided into two approximately equal time-intervals, and a suite of events were selected from each. This may be sufficient to isolate any temporal variation during the experiment. These two sets (F1 and F2) consist of 26 events (with 131 P- and 81 shear-wave arrivals) and 25 events (with 117 P- and 73 shear-wave arrivals)

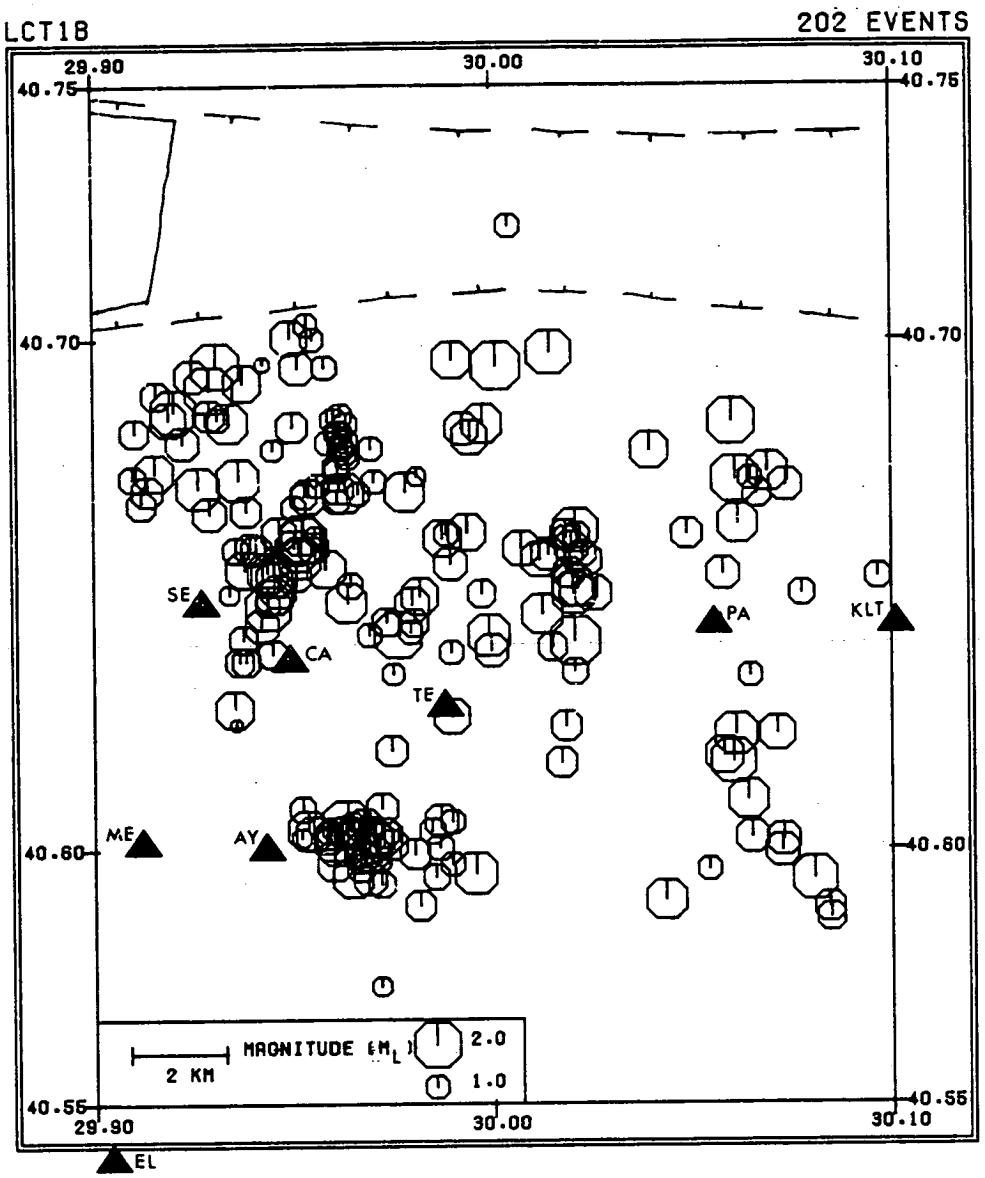

Figure 7.6 A map of the revised epicentres from TDP1. The locations have been determined using an isotropic velocity model and where an extra station correction at AY has been introduced.

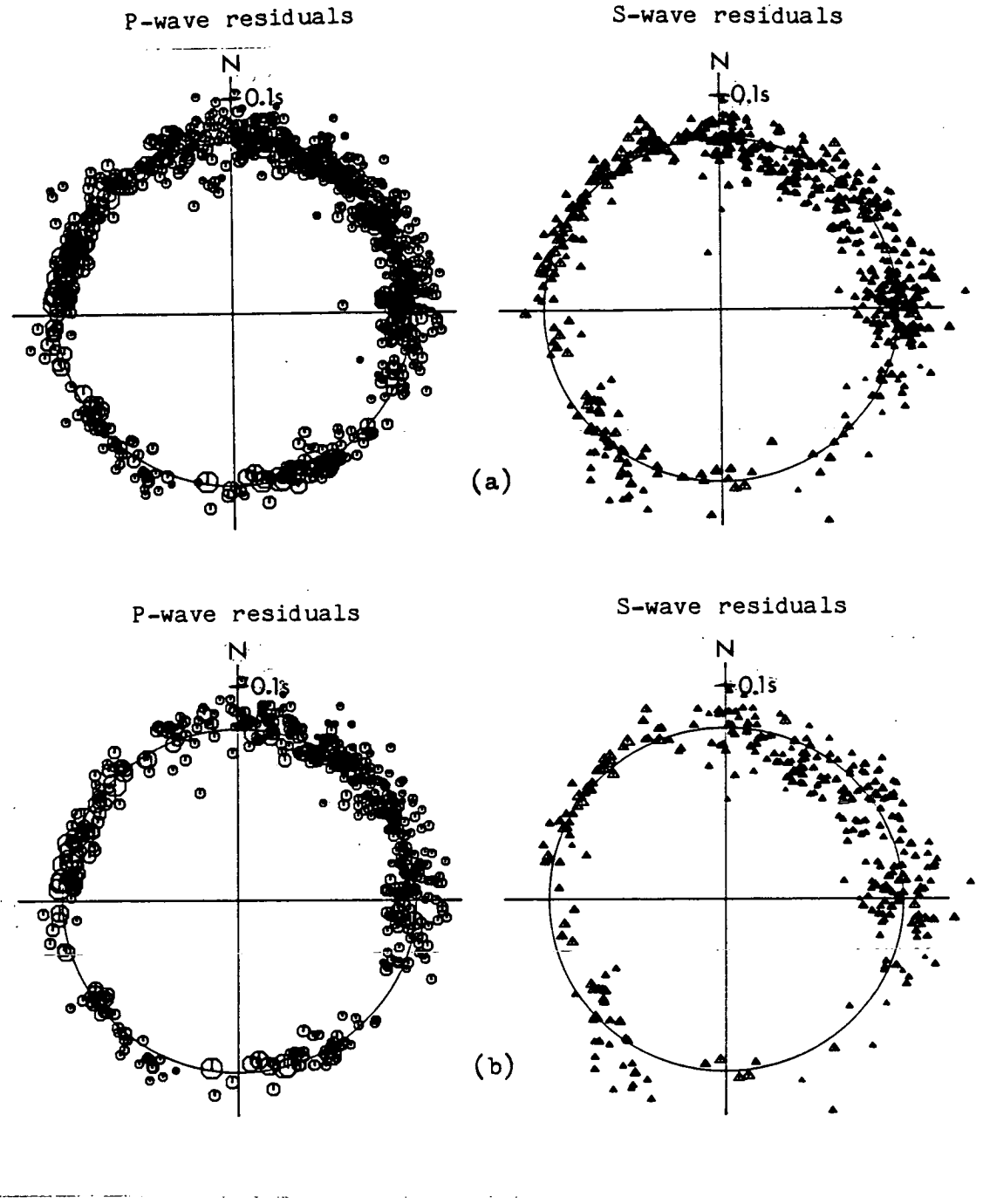

Figure 7.7 The azimuthal variation of P-and shear-wave travel-time residuals from the events of Fig.7.6. Notation and format as in Fig.7.3.
(a) P- and shear-wave travel-time residuals from all events.
(b) P- and shear-wave travel-time residuals from all the events with at least eight recorded arrivals.

Figure 7.8 A map of the epicentres in two data sets from TDP1 that are used to determine the anisotropic structure by joint-inversion of arrival-times.
(a) Data set F1 with 26 events.
(b) Data set F2 with 25 events.

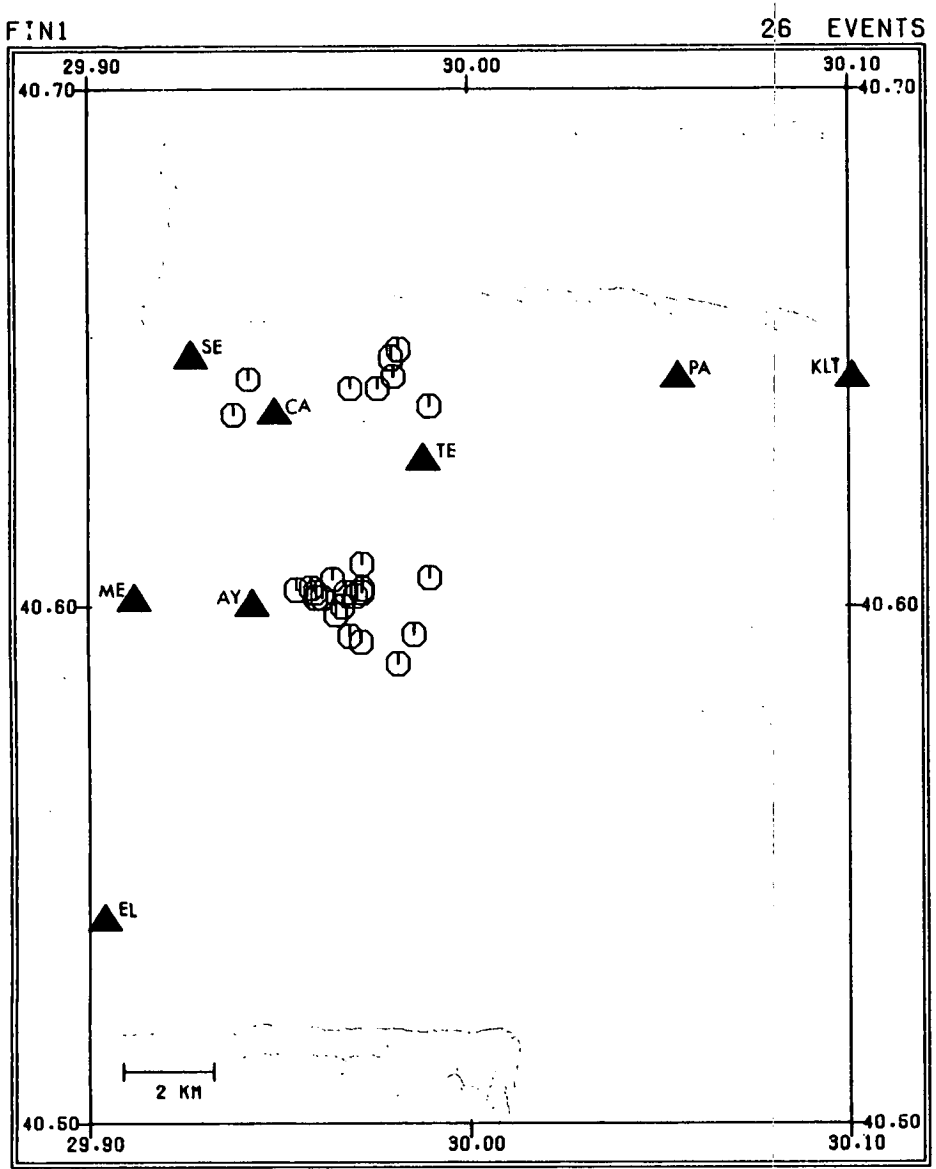
FIN1
26 EVENTS
29.90
30.00
30.10
40.70
40.60
40.50
SE
CA
PA
KLT
TE
ME
AY
EL
2 KM

(a)

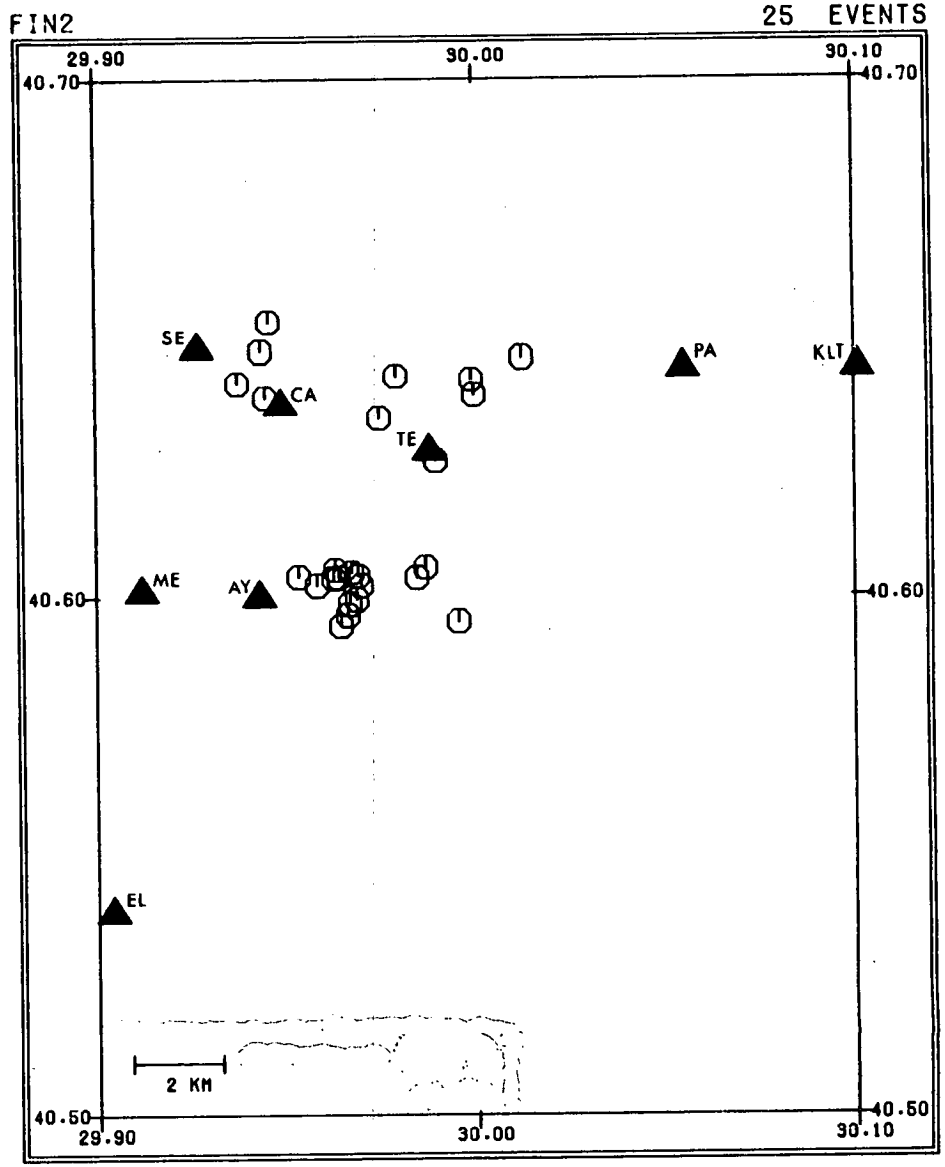
FIN2
25 EVENTS
29.90
30.00
30.10
40.70
40.60
40.50
SE
CA
PA
KLT
TE
ME
AY
EL
2 KM

(b)

clearest. The author was not involved in reading the shear-wave delays, but selected those that had been given the highest weighting.

Table 7.2 summarises the hypocentral solutions determined by HYPO71 and by the joint-inversion for P- and shear-wave velocities, and hypocentres in an isotropic half-space for each of the data sets. Notice that the joint-inversion of the data results in slightly greater focal depths than those determined by HYPO71, and also obtains lower velocities and a lower Vp/Vs ratio (approximately 1.65) than those of the crustal model in Table 2.1. This may be an effect of near-surface structure. Note also that although the inversion program produces similar locations as HYPO71, (as well as similar estimated and RMS errors), this does not provide any indication of possible large errors in the locations due to velocity-anisotropy. The inversion indicates P- and shear-wave velocities of approximately 5.5 and 3.3km/sec respectively. This suggests that the anisotropic models listed in Appendix A can be used directly as initial models in the joint-inversion procedure. In view of the necessity of having accurate trial hypocentres for the inversion procedure, it was decided to use those determined by HYPO71, as the velocity model used by HYPO71 is likely to be slightly more realistic than an isotropic half-space.

The first stage in the inversion procedure is to search for solutions throughout the whole focal sphere in order to find an indication of the orientation of the anisotropic structure. In this stage we use the data sets containing P- and first shear-wave arrival-times, assume an initial structure corresponding to the strongly anisotropic model GKFF1, and assume a structure with hexagonal symmetry. Fig.7.9a shows the solutions obtained for the orientation of the structure by inverting data set F1. Two clear minima have been defined each at a horizontal rotation of approximately -40 degrees. The two orientations of the axis of rotational symmetry are inclined above and below the surface by approximately 50 degrees of

Figure 7.9 A summary of the solutions obtained by the joint-inversion of the data sets F1 and F2 for an anisotropic structure with hexagonal symmetry.

(a) A summary of the solutions obtained for the orientation of an axis of rotational symmetry by the inversion of data set F1, assuming GKFF1 as an initial model. Notation and format as in Fig.6.16a, with a reference RMS error of 0.0300.

(b) A summary of the solutions obtained for the orientation of an axis of rotational symmetry by the inversion of data set F2, assuming GKFF1 as an initial model. Notation and format as in Fig.6.16a, with a reference RMS error of 0.0300.

(c) Dashed lines - the wave-surfaces obtained by taking the weighted average of eight solutions at an orientation of -42,-57 in (a) (solution F1A in Table 7.3). Solid lines - for reference, the wave-surfaces in model GKFF1.

(d) Dashed lines - the wave-surfaces obtained by taking the weighted average of seven solutions at an orientation of -46,54 in (a) (solution F1B in Table 7.3). Solid lines - for reference, the wave-surfaces in model GKFF1.

(e) Dashed lines - the wave-surfaces obtained by taking the weighted average of eight solutions at an orientation of -47,-58 in (b) (solution F2A in Table 7.3). Solid lines - for reference, the wave-surfaces in model GKFF1.

(f) Dashed lines - the wave-surfaces obtained by taking the weighted average of three solutions at an orientation of -35,49 in (b) (solution F2B in Table 7.3). Solid lines - for reference, the wave-surfaces in model GKFF1.

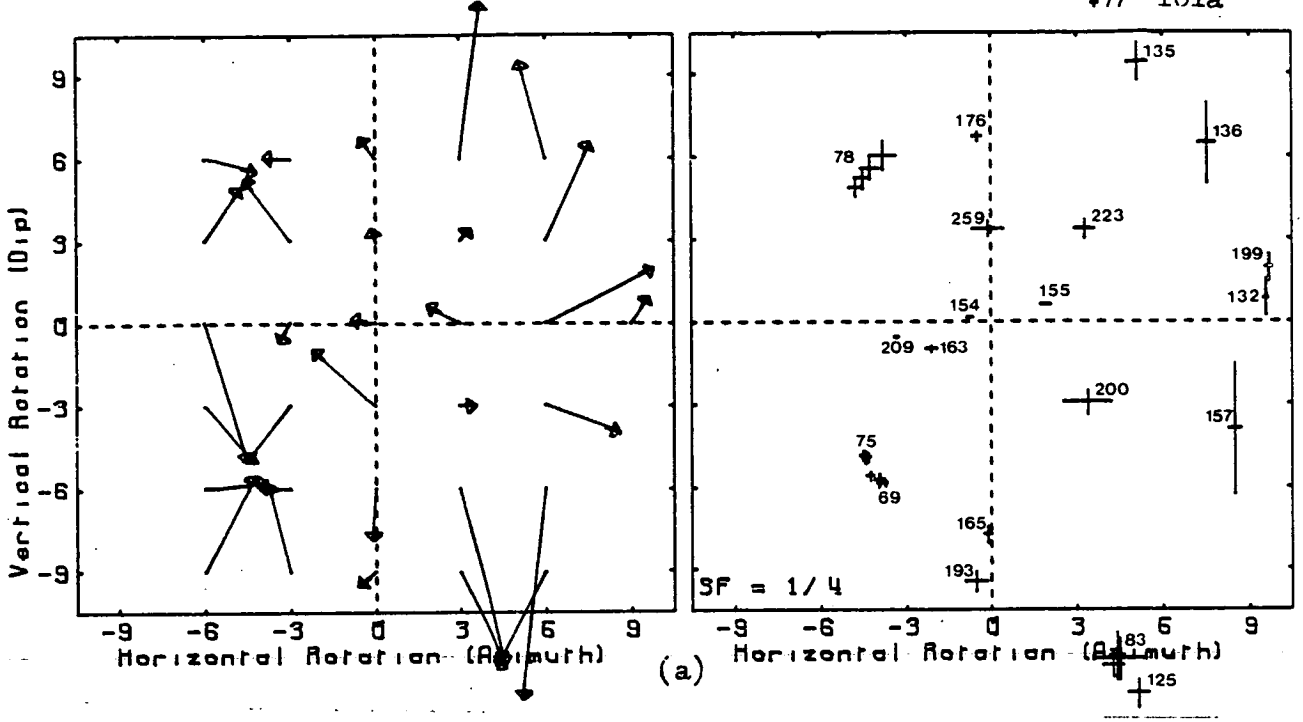
Vertical Rotation (Dip)
Horizontal Rotation (Azimuth)
SF = 1/4
(a)

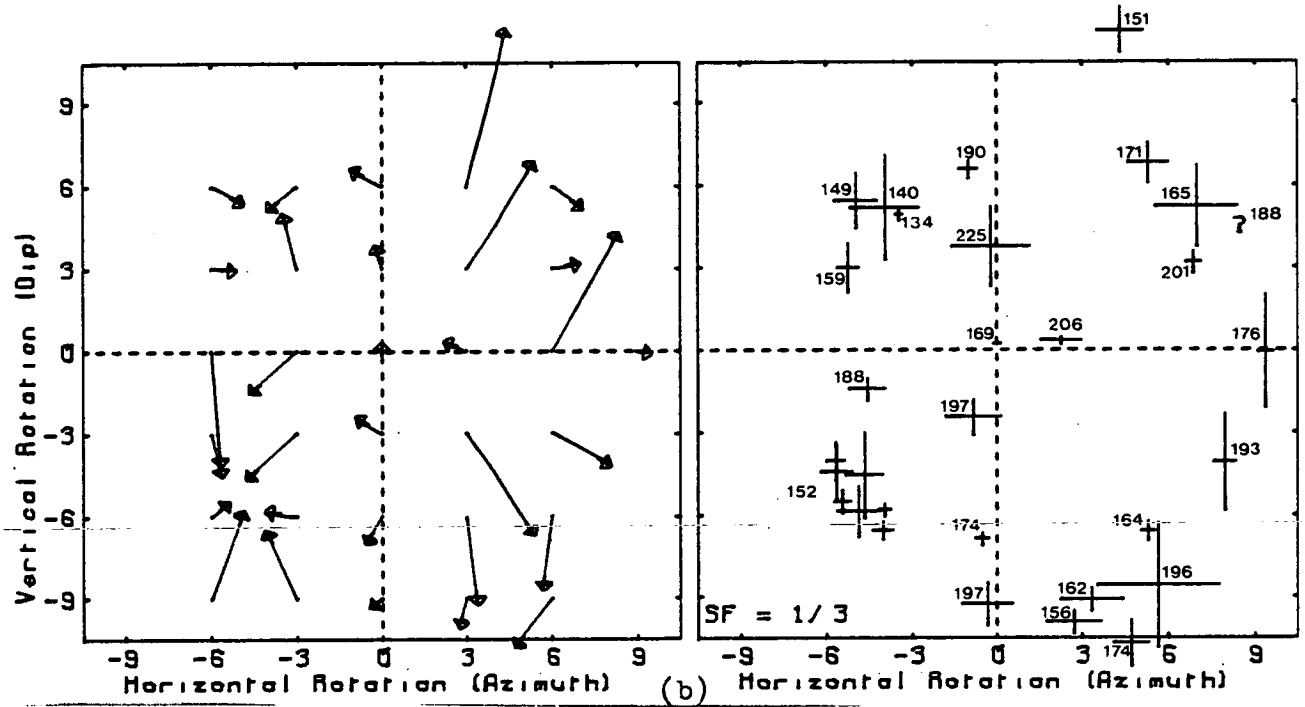
Vertical Rotation (Dip)
Horizontal Rotation (Azimuth)
SF = 1/3
(b)

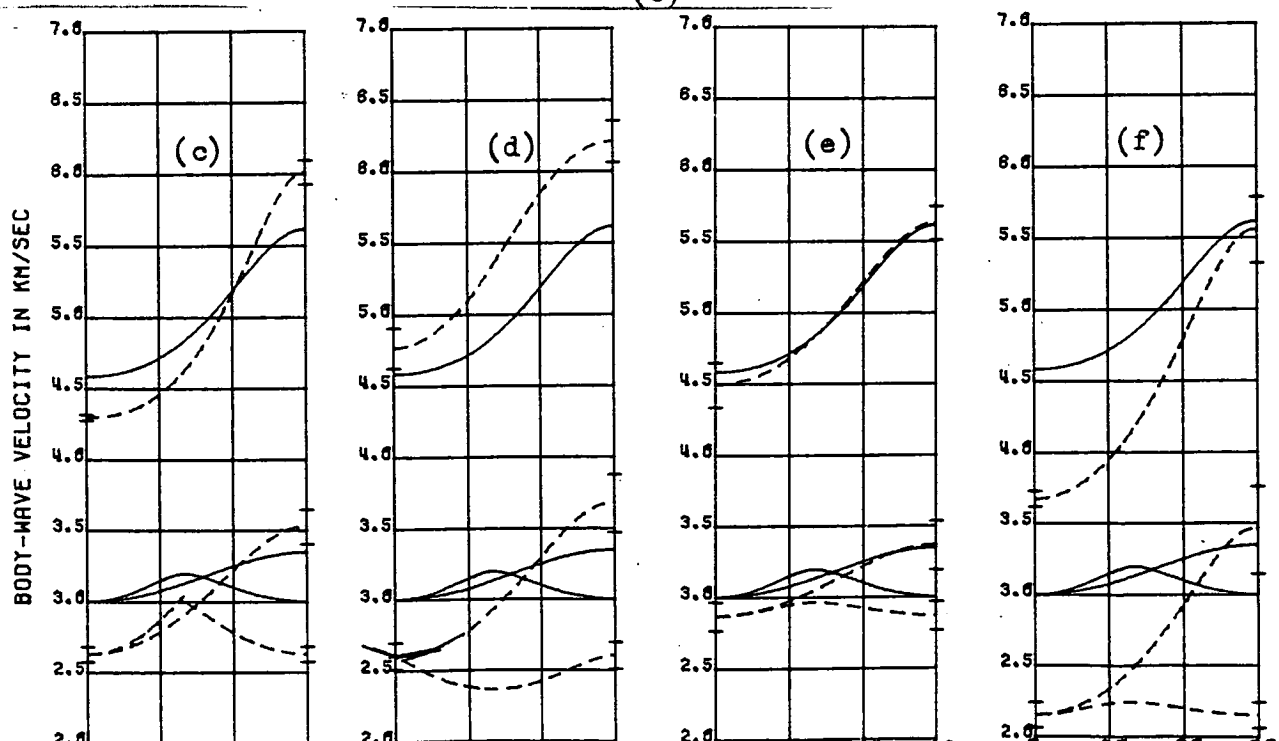
BODY-WAVE VELOCITY IN KM/SEC
(c)
(d)
(e)
(f)

rotation. Each solution has small orientation errors and the RMS error indicates that the solutions are statistically significant (at the 99% confidence level) compared to the isotropic solutions. Fig.7.9b shows the solutions obtained for the orientation of the structure by inverting data set F2. In this case the same two solutions are apparent but are not so well-defined. The RMS error of each solution, although clearly superior to the isotropic solution, is not statistically significant at the 95% level. Figs.7.9(c,d,e and f) show the wave-surfaces obtained from each of the solutions above. (For reference, parameters of each solution are listed in Table 7.3 where the solution labels are referred from the corresponding figure captions). These sections indicate that the inversion has converged to a similar solution in both data sets. This suggests that the apparent difference between the two data sets is just a reflection of the fewer degrees of freedom in F2 (i.e 81 against 101) and cannot be interpreted as any temporal variation.

Having dismissed the possibilty of any resolvable temporal variation during TDP1, we can invert the combined data set F3 for hexagonal symmetry using GKFF1 as the initial model. Fig.7.10 illustrates the solutions obtained for the orientation of an axis of rotational symmetry. The same two orientations are defined, each with an RMS error indicating that the solution is statistically significant compared to the isotropic solution. Both solutions indicate an axis of rotational symmetry striking at N130E, close to where we are anticipating a solution associated with the directions of maximum and intermediate compression, and are approximately 75 degrees apart.

The remainder of this section will concentrate on finding a solution for the structure by inversion of data set F3 and its subset containing shear-wave delays. Fig.7.11 illustrates the solutions obtained from the next stage in the inversion process where we invert for hexagonal symmetry, use GKLF1 as an initial model and search for solutions from directions

Figure 7.10 A summary of the solutions obtained by the joint-inversion of data set F3 for an anisotropic structure with hexagonal symmetry.
(a) A summary of the solutions obtained for the orientation of an axis of rotational symmetry assuming GKFF1 as an initial model. Notation and format as in Fig.6.16a with a reference RMS error of 0.0300.
(b) Dashed lines - the wave-surfaces obtained by taking the weighted average of eight solutions at an orientation of -41,-62 in (a) (solutions F3A in Table 7.3). Solid lines - for reference, the wave-surfaces in model GKFF1.
(c) Dashed lines - the wave-surfaces obtained by taking the weighted average of four solutions at an orientation of -47,52 in (a) (solution F3B in Table 7.3). Solid lines - for reference, the wave-surfaces in model GKFF1.

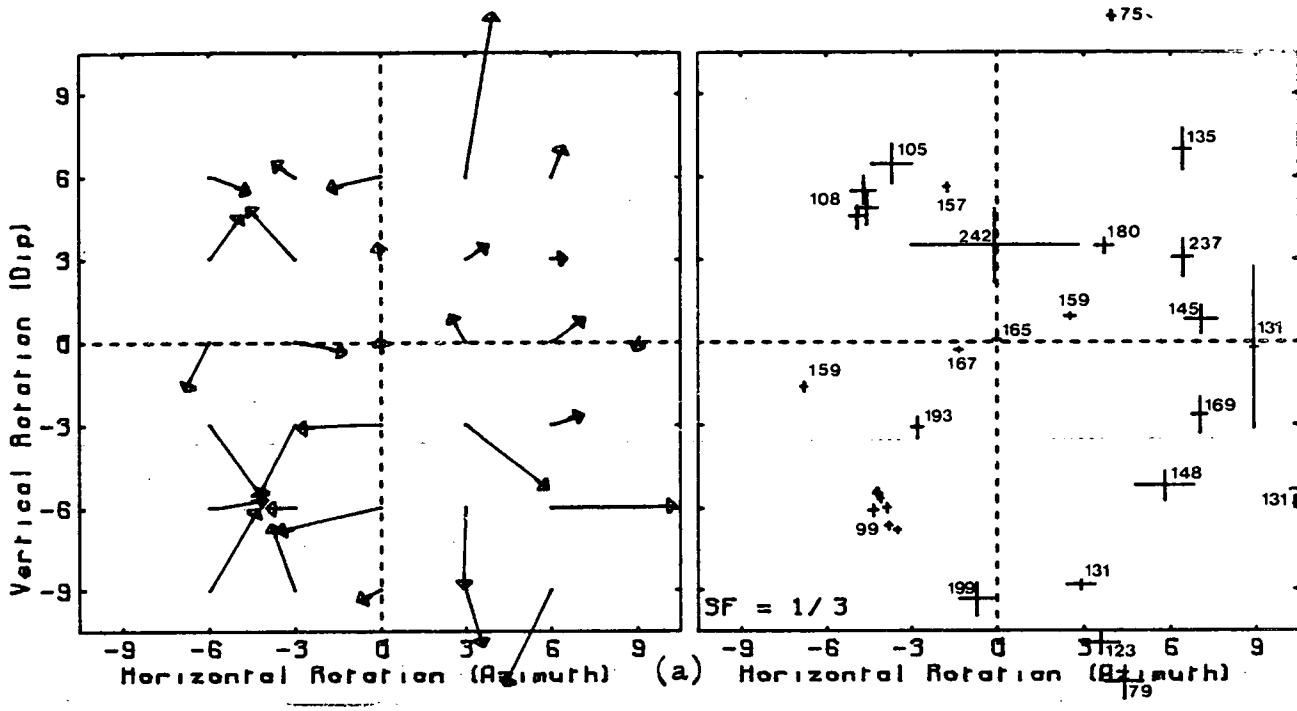
Vertical Rotation (Dip)
Horizontal Rotation (Azimuth)
(a)
SF = 1/3
105
108
157
242
180
135
237
159
145
131
165
167
159
193
169
148
99
131
199
123
79
75

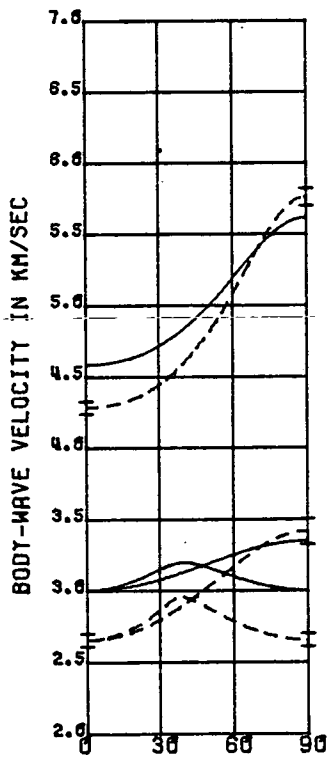
BODY-WAVE VELOCITY IN KM/SEC
(b)

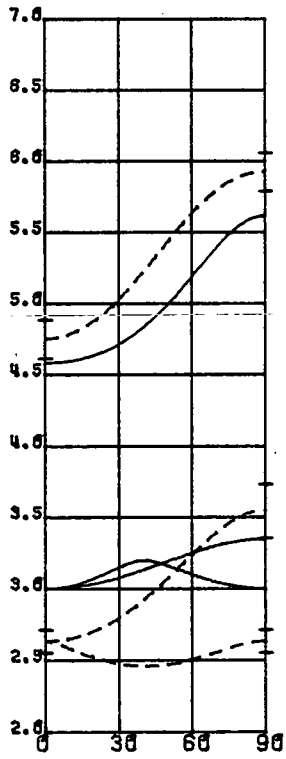
(c)

Figure 7.11 A summary of the solutions obtained by the joint-inversion of data set F3 for an anisotropic structure with hexagonal symmetry.
(a) A summary of the solutions for the orientation of an axis of rotational symetry when the inversion assumes GKLF1 as the initial model, and is initialised from particular directions in the focal sphere. Notation and format as in Fig.6.16a with a reference RMS error of 0.0300.
(b) Dashed lines - the wave-surfaces obtained by taking the weighted average of three solutions at an orientation of -39,-60 in (a) (solution F3C in Table 7.3). Solid lines - for reference, the wave-surfaces in model GKFF1.
(c) Dashed lines - the wave-surfaces obtained by taking the weighted average of the solution at an orientation of -39,58 in (a) (solution F3D in Table 7.3). Solid lines - for reference, the wave-surfaces in model GKFF1.
(d) Dashed lines - the wave-surfaces obtained by the inversion of the data set containing shear-wave delays using the solution in (b) as the initial model (solution F3E in Table 7.3). Solid lines - for reference, the wave-surfaces in model GKFF1.
(e) Dashed lines - the wave-surfaces obtained by the inversion of the data set that contains shear-wave delays using the solution in (c) as the initial model (solution F3F in Table 7.3). Solid lines - for reference, the wave-surfaces in model GKFF1.

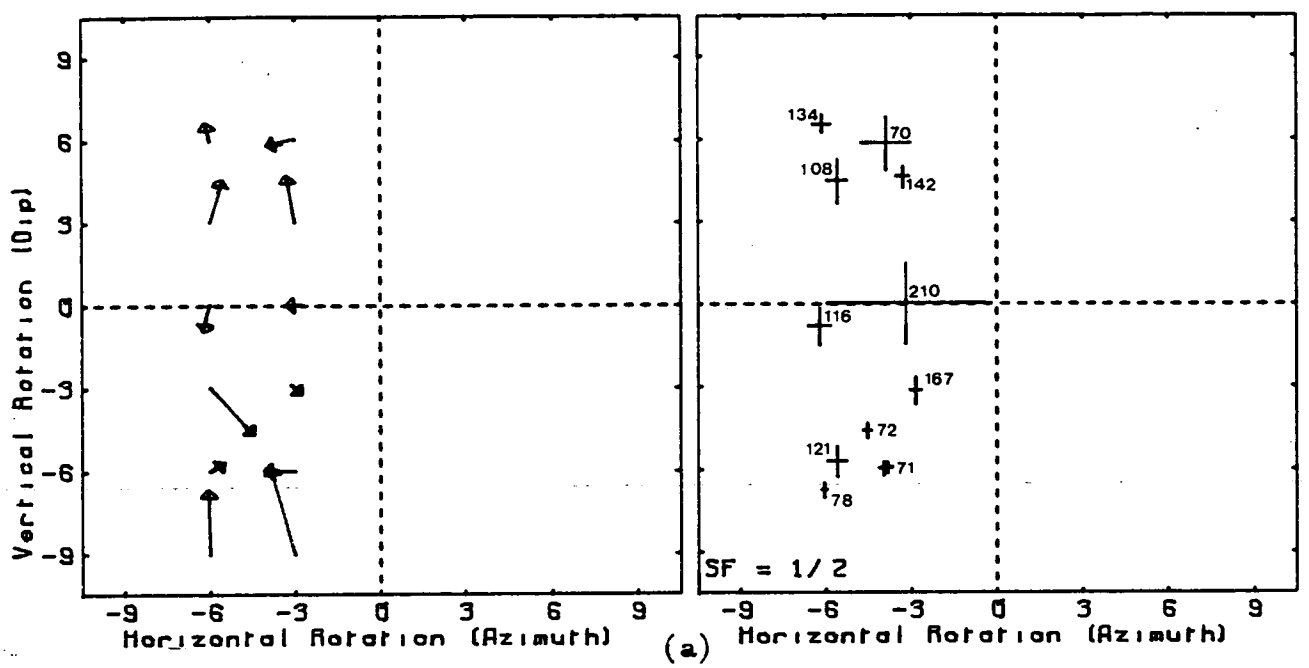
Vertical Rotation (Dip)
Horizontal Rotation (Azimuth)
Horizontal Rotation (Azimuth)
SF = 1/2
134
70
108
142
210
116
167
72
121
71
78

(a)

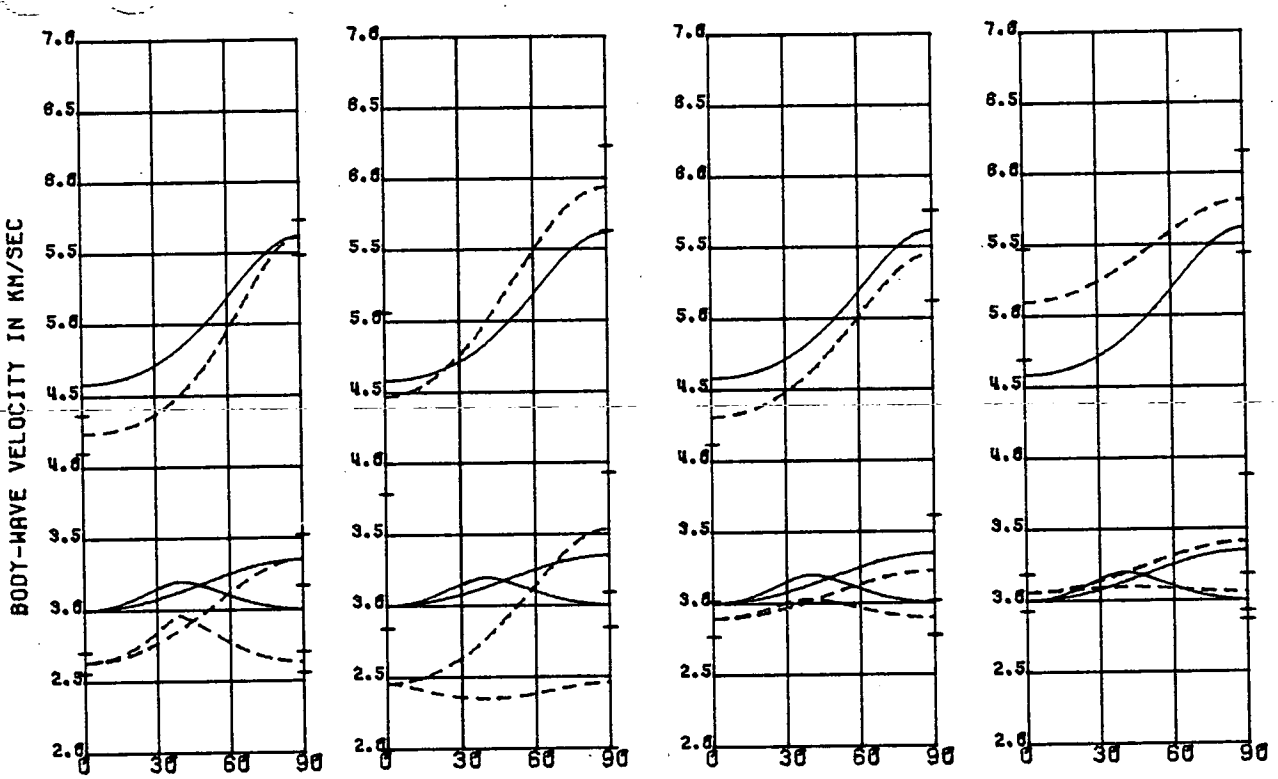
BODY-WAVE VELOCITY IN KM/SEC

(b) (c) (d) (e)

surrounding the horizontal rotation of -40 degrees. We can see that the solutions with the lowest RMS and orientation errors are found at the same orientations but are not as well-defined as previously. A plot of the wave-surfaces (Figs.7.11b and c) reveals essentially the same solution as before. Figs.7.11(d and e) show the wave-surfaces obtained by inverting the data set that includes shear-wave delays, for hexagonal symmetry, and using each of the solutions above as initial models. The degree of anisotropy, particularly the shear-wave anisotropy, has been reduced in both cases but the orientation of each final solution does not differ appreciably from the initial orientation. The RMS and parameter errors are much larger, possibly reflecting inaccuracies in the shear-wave delays.

The inversion of the TDP1 data sets for hexagonal structure has identified two possible orientations for an axis of rotational symmetry. The RMS error associated with both solutions indicate that each is statistically significant (at the 99% confidence level) compared to the isotropic solution. Each solution is obtained when either model GKFF1 or GKLF1 is used as the initial model in the inversion. The inversion of the data set that includes shear-wave delays apparently confirms each solution but the model errors are increased. The two solutions are approximately orthogonal. The solution at an orientation of -40,-60 indicates low velocities close to the direction where we are anticipating high velocities associated with the direction of maximum compression. All of these features are similar to those of model I in Appendix D, suggesting that the assumption of hexagonal symmetry is insufficient to describe the structure, and that inversion for orthorhombic symmetry is required.

Fig.7.12a shows the solutions obtained for the orientation of the structure by inversion for orthorhombic symmetry using GKFF1 as the initial model. All solutions have low orientation errors, and all solutions, except that with an RMS error of 0.0472, are statistically superior to the isotropic solution at the 95% confidence level. The solutions with the

Table 7.3. Anisotropic solutions from the inversion of the TDP1 data sets.

Errors are given in brackets. Estimated errors for solutions determined under the assumption of hexagonal symmetry are only given for the independent elastic constants. F-test ratio at 95% and 99% significance levels: data set F1 - 1.39,1.59; F2 - 1.45,1.70; F3 - 1.35,1.54. Azimuth and dip refer to horizontal and vertical rotations respectively.

SOLUTION	ELASTIC CONSTANTS									ORIENTATION		OVERALL RMS ERROR	F-TEST RATIO
	C11	C22	C33	C23	C13	C12	C44	C55	C66	Azimuth	Dip		
F1A	48.04 (0.49)	93.99 (2.61)	93.99	29.22 (1.90)	17.44	17.44 (1.31)	32.39	17.99	17.99 (0.74)	-41.71 (1.21)	-57.00 (1.97)	0.0372	1.72
F1B	59.19 (3.53)	100.39 (4.73)	100.39	29.87 (3.00)	47.39	47.39 (3.17)	35.26	17.63	17.63 (1.28)	-45.93 (4.54)	53.56 (6.78)	0.0380	1.65
F2A	52.53 (3.67)	82.42 (3.43)	82.42	23.38 (2.61)	19.17	19.17 (2.13)	29.52	21.41	21.41 (1.49)	-47.49 (3.78)	58.38 (4.87)	0.0452	1.18
F2B	35.12 (1.10)	80.39 (6.71)	80.39	17.92 (4.29)	25.48	25.48 (4.62)	31.24	12.04	12.04 (1.00)	-35.01 (3.12)	49.35 (6.90)	0.0441	1.24
F3A	47.72 (0.99)	86.26 (1.86)	86.26	25.55 (1.30)	16.88	16.88 (1.03)	30.36	18.32	18.32 (0.63)	-40.90 (1.10)	-61.62 (1.67)	0.0396	1.58
F3B	58.74 (3.36)	91.28 (4.20)	91.28	25.76 (2.76)	41.25	41.25 (3.12)	32.76	18.08	18.08 (1.08)	-47.19 (5.16)	52.00 (7.37)	0.0402	1.53
F3C	46.67 (2.93)	81.18 (3.61)	81.18	23.43 (2.55)	14.71	14.71 (1.60)	28.88	18.00	18.00 (1.01)	-38.93 (2.09)	-59.64 (3.20)	0.0371	1.80
F3D	51.94 (14.65)	91.64 (9.30)	91.64	26.72 (6.08)	39.57	39.57 (6.37)	32.46	15.69	15.69 (5.32)	-38.63 (17.05)	58.00 (19.71)	0.0370	1.81
F3E	48.36 (4.27)	77.17 (8.97)	77.17	23.11 (4.95)	12.36	12.36 (3.00)	27.03	21.80	21.80 (1.87)	-41.54 (8.61)	-63.06 (7.68)	0.1205	—

Table 7.3 (continued)

SOLUTION	ELASTIC CONSTANTS									ORIENTATION		OVERALL RMS ERROR	F-TEST RATIO
	C11	C22	C33	C23	C13	C12	C44	C55	C66	Azimuth	Dip		
F3F	67.57 (10.32)	87.74 (10.79)	87.74	27.27 (6.90)	26.83	26.83 (5.31)	30.24	24.34	24.34 (2.03)	-39.45 (15.08)	67.39 (13.15)	0.1043	—
F3G	53.93 (4.48)	87.11 (3.14)	90.27 (3.79)	29.07 (2.90)	18.17 (2.78)	21.38 (2.58)	30.94 (0.46)	14.45 (1.86)	18.06 (1.93)	-43.70 (2.83)	-49.79 (3.18)	0.0364	1.87
F3H	44.38 (6.61)	80.95 (4.89)	82.05 (6.14)	17.33 (4.01)	38.51 (8.79)	45.52 (9.04)	30.52 (1.08)	13.61 (3.29)	14.87 (1.89)	-39.86 (6.92)	40.56 (4.60)	0.0345	2.08
F3I	65.65 (5.80)	85.85 (4.33)	89.79 (4.78)	34.27 (3.25)	24.22 (3.08)	30.70 (3.33)	28.87 (0.77)	26.40 (0.87)	28.74 (0.94)	-52.90 (4.67)	-43.62 (5.65)	0.0611	—
F3J	82.90 (5.25)	81.38 (3.01)	81.98 (4.04)	25.50 (2.18)	33.41 (3.40)	30.95 (3.47)	27.47 (0.64)	27.55 (0.67)	27.12 (1.60)	-46.19 (11.54)	31.79 (9.89)	0.0634	—
F3K	112.52 (18.38)	76.77 (7.56)	96.54 (11.70)	54.18 (16.09)	45.99 (16.63)	29.94 (7.80)	26.95 (3.46)	32.33 (1.71)	33.33 (2.23)	-16.93 (4.19)	47.49 (3.79)	0.0379	1.73
F3L	75.37 (7.90)	108.86 (16.73)	94.05 (11.12)	42.40 (14.33)	53.23 (16.02)	28.31 (7.98)	32.09 (1.73)	26.30 (4.48)	32.90 (2.06)	72.91 (3.69)	47.49 (3.62)	0.0380	1.72
F3M	113.32 (9.65)	79.52 (5.93)	96.49 (7.75)	34.73 (6.20)	44.14 (6.04)	29.90 (4.30)	30.47 (1.39)	30.27 (1.34)	33.61 (1.61)	-15.98 (7.03)	48.36 (12.17)	0.0746	—
F3N	77.51 (5.74)	109.77 (9.15)	93.60 (7.40)	41.30 (5.71)	33.05 (6.00)	27.98 (4.07)	30.13 (1.32)	30.14 (1.37)	33.47 (1.59)	73.55 (7.23)	48.34 (12.45)	0.0744	—
F3O	111.24 (5.85)	77.62 (3.29)	95.06 (4.46)	36.36 (4.03)	42.80 (3.88)	28.94 (2.61)	28.90 (0.92)	30.95 (0.74)	33.38 (0.91)	-16.83 (2.43)	47.46 (2.51)	—	—

lowest RMS errors (but not the lowest orientation errors) are those at the orientations defined previously under the assumption of hexagonal symmetry. The velocity-surfaces (Figs.7.12b and c) are also similar to those obtained previously. From Chapter 6, we would expect to see solutions for an orthorhombic structure at two or three orthogonal orientations. These two solutions are 85 degrees apart and so satisfy this condition. However, another condition is that the elastic constants associated with each solution should indicate the same structure, and, obviously, that the hypocentral locations should be the same. Fig.7.12(d) is a section through each solution in the same plane, and Table 7.4 shows the average hypocentral locations from each solution. The two solutions clearly do not indicate the same structure. In addition, inversion of the subset containing shear-wave delays using these solutions as initial models, produces the solutions shown in Figs.7.12e and f. The orientation of both solutions in noticeably different from those of the initial models, and the form of one solution, F3G, is dramatically altered.

Table 7.4. The average hypocentral parameters from solutions F3G and F3H in Table 7.3. The initial hypocentral parameters are given at the head of each column.

Solution	Long	Lat	Depth	OT
	(29.9696)	(40.6177)	(8.02)	(30.14)
F3G	29.9775	40.6103	8.36	30.06
F3H	29.9545	40.6332	9.04	29.94

As noted previously, however, most of the solutions shown in Fig.7.12a are statistically superior to the isotropic solution. By plotting the velocity-surfaces of each solution in the same section we can attempt to see if any of the remaining solutions satisfy the conditions for an orthorhombic structure - namely that the solutions are orthogonal and indicate the same structure. Fig.7.13 shows sections of those solutions in Fig.7.12a which have an RMS error of less than 0.0400. We can see that the

Figure 7.12 A summary of the solutions obtained by the joint inversion of data set F3 for an anisotropic structure with orthorhombic symmetry.

(a) A summary of the solutions obtained for orientation of the structure when the inversion assumes GKFF1 as an initial model. Notation an format as in Fig.6.16a with a reference RMS error of 0.0300.

(b) Dashed lines - the wave-surfaces obtained by taking the weighted average of four solutions at an orientation of -44,-48 in (a) (solution F3G in Table 7.3). Solid lines - for reference, the wave-surfaces in model GKFF1.

(c) Dashed lines - the wave-surfaces obtained by taking the weighted average of two solutions at an orientation of -40,41 in (a) (solution F3H in Table 7.3). Solid lines - for reference, the wave-surfaces in model GKFF1.

(d) Dashed lines - a vertical section, measured from 0,0, through the wave-surfaces of the solution shown in (c). Solid lines - the solution in (b) in the same section.

(e) Dashed lines - the wave-surfaces obtained by the inversion of the data set containing shear-wave delays using the solution in (b) as the initial model (solution F3I in Table 7.3). Solid lines - for reference, the wave-surfaces in model GKFF1.

(f) Dashed lines - the wave-surfaces obtained by the inversion of the data set that contains shear-wave delays and using the solution in (c) as the initial model (solution F3J in Table 7.3). Solid lines - for reference, the wave-surfaces in model GKFF1.

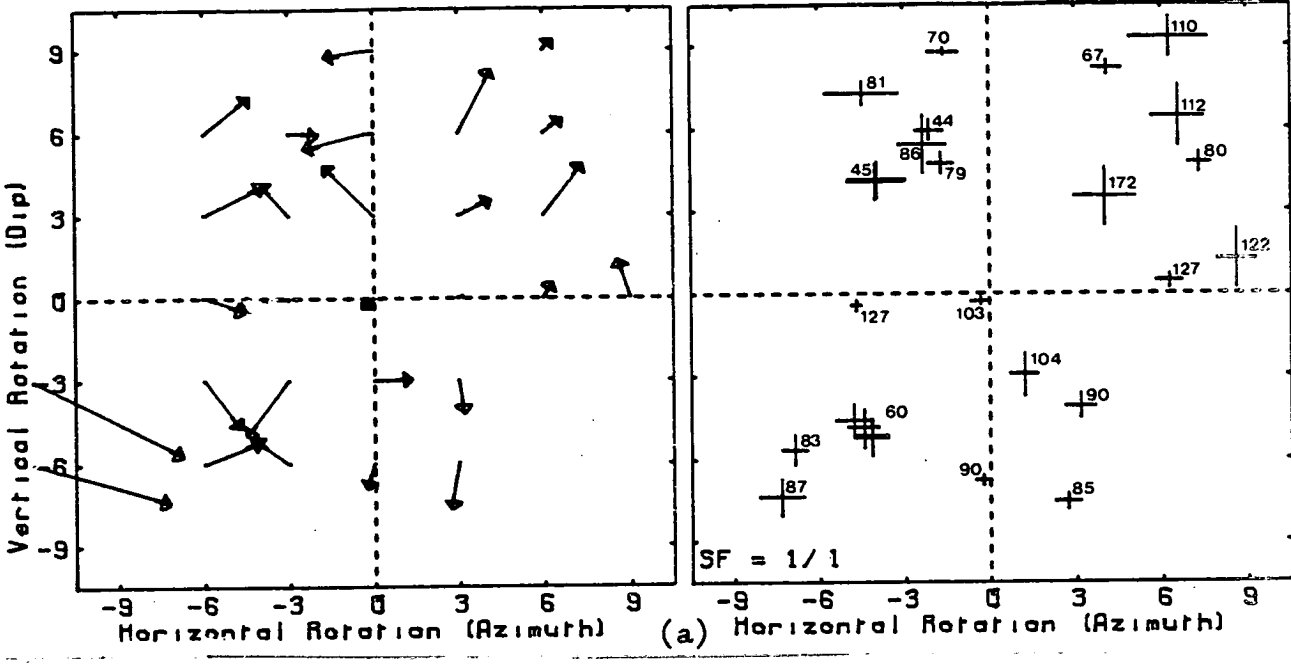
Vertical Rotation (Dip)
Horizontal Rotation (Azimuth)
SF = 1/1
Horizontal Rotation (Azimuth)

(a)

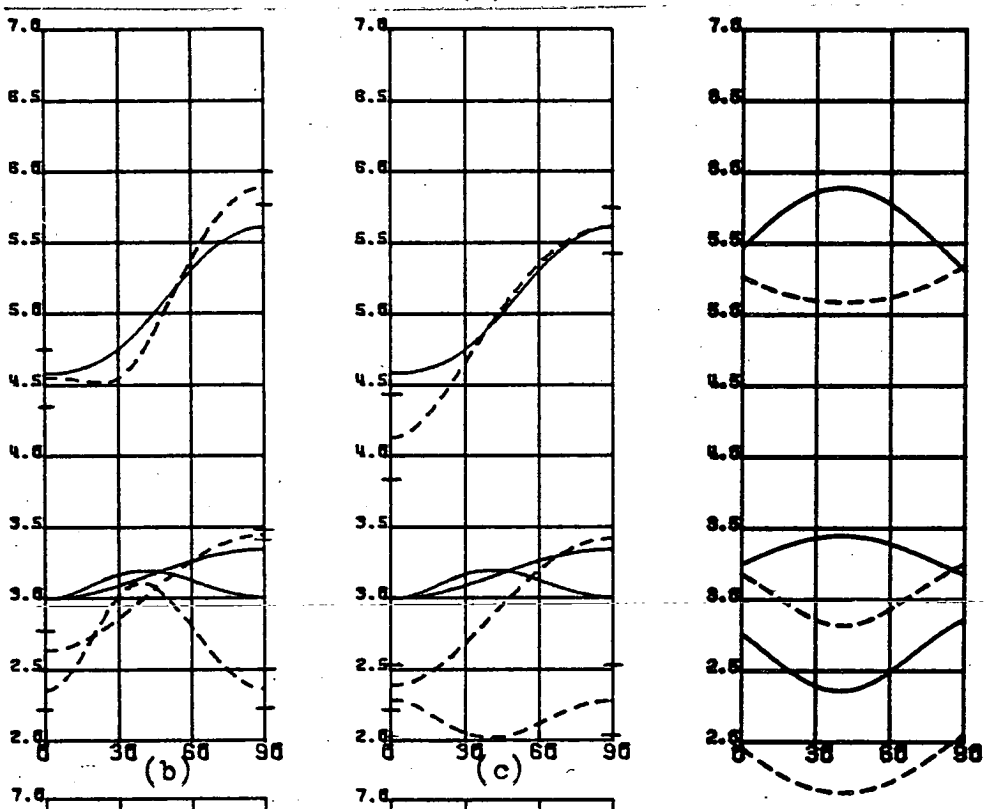

(b) (c) (d)

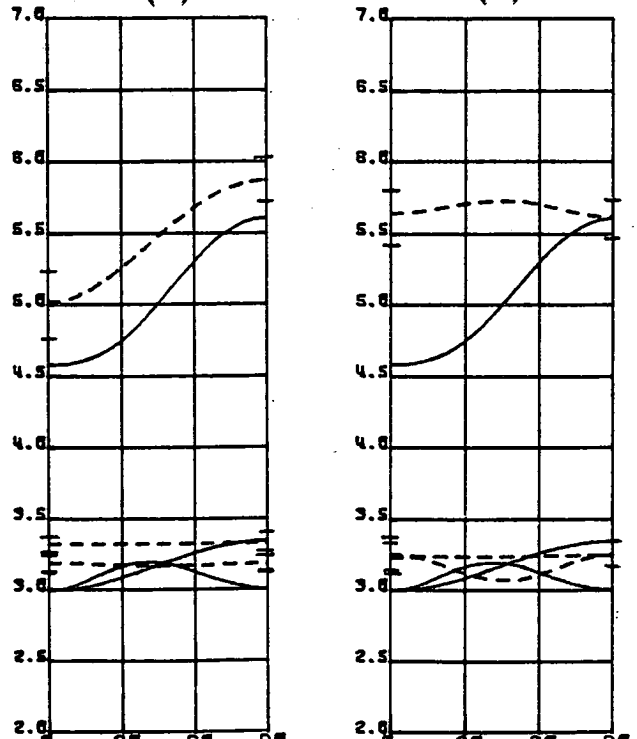

Figure 7.13 Vertical sections through the velocity-surfaces of those solutions in Fig.7.12a with an RMS error of less than 0.0400. In each case the section is measured from an orientation of (0,0). The labels in the centre of each diagram are for reference in the text. The solutions are those at orientations of : (a) -17,47; (b) -45,73; (c) -23,54; (d) -16,88; (e) -21,59; (f) 41,82; (g) 73,47; (h) 27,-76; (i) 32,-41; (j) 12,-29; (k) -2,-68.

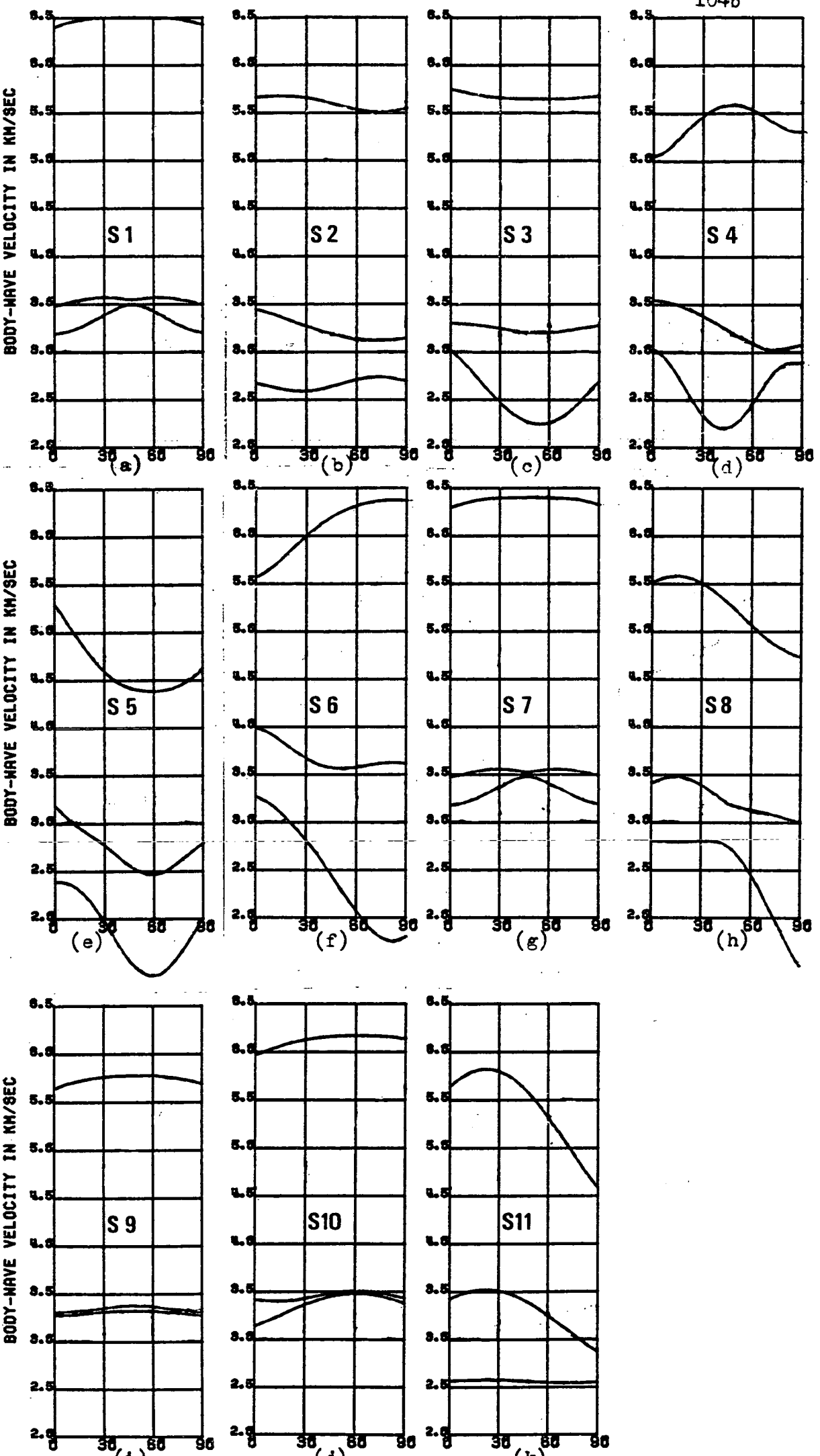
BODY-WAVE VELOCITY IN KM/SEC
S 1
S 2
S 3
S 4
S 5
S 6
S 7
S 8
S 9
S10
S11
(a)
(b)
(c)
(d)
(e)
(f)
(g)
(h)
(i)
(j)
(k)

two solutions, S1 and S7, at an orientation of (-17,47) and (73,47) respectively, satisfy these conditions almost exactly. The velocity-surfaces are very similar and the two solutions are almost exactly 90 degrees apart. No other pair of solutions satisfy these conditions, and similarly none of the solutions shown are consistent with either of the solutions shown previously (c.f. Fig.7.12c). The direction that is orthogonal to both of these orientations is 0,-43, and solutions S8 to S11 are near this orientation. Two of these indicate very strong variations that are not consistent with solutions S1 and S7, but solutions S9 and S10, at orientations of 12,-29 and 32,-41 respectively, are reasonably similar.

Close examination of the solutions for orthorhombic symmetry, therefore, reveals only one solution for the structure that has been determined at two (and possibly three) orthogonal orientations. Figs.7.14(a and b) show the velocity-surfaces of the two solutions. We can attempt to confirm each solution by inversion of the subset containing shear-wave delays using each solution as an initial model. This produces the solutions shown in Figs.7.14(c and d). The orientation of each solution and the form of the velocity-surfaces are very similar to the initial models, and the error bars have been reduced. However, the degree of shear-wave anisotropy has been reduced in both cases, in a similar fashion to that observed in model I (Figs.D.8c and e). Figs.7.14(e and f) show sections through the velocity-surfaces of each of these solutions in the same section as those shown in Fig.7.13. These figures illustrate that both solutions are still consistent with the same structure, and that the solutions are similar to those obtained by inversion of the larger data set.

We can attempt to find the third principal axis by inversion of the subset containing shear-wave delays. As noted, the direction that is orthogonal to both these solutions is at 0,-43. Using the elastic constants of the solution obtained above as the initial model, and using

Figure 7.14 Sections through the velocity-surfaces of various solutions determined by inversion for orthorhombic structure.

(a) Section from the x_1 - axis to the x_3 - axis of the solution at an orientation of -17,47 in Fig.7.12a (Solution F3K in Table 7.3).

(b) Section from the x_1 - axis to the x_3 - axis of the solution at an orientation of 73,47 in Fig.7.12a (Solution F3L in Table 7.3).

(c) Section from the x_1 - axis to the x_3 - axis of the solution obtained by inverting the data set containing shear-wave delays and using the solution in (a) as the initial model (solution F3M in Table 7.3).

(d) Section from the x_1 - axis to the x_3 - axis of the solution obtained by inverting the data set containing shear-wave delays and using the solution in (b) as the initial model (solution F3N in Table 7.3).

(e) A vertical section , measured from an orientation of 0,0, through the velocity surfaces of the solution shown in (c).

(f) A vertical section , measured from an orientation of 0,0, through the velocity surfaces of the solution shown in (d).

(g) Dashed lines - a section from the x_1-axis to the x_3-axis through the velocity-surfaces of a solution obtained by taking the weighted average of two solutions at an orientation of 19,-62. These were obtained by inverting the data set containing shear-wave delays, initialised from orientations of 0,-30 and 0,-60, and using a suitably rotated version of solution F3K as the initial model. Solid lines - a vertical section through the same solution measured from an orientation of 0,0.

(h) As (g) for a solution obtained by inverting the large data set, without the extra station correction at station AY, and using solution F3K as the initial model.

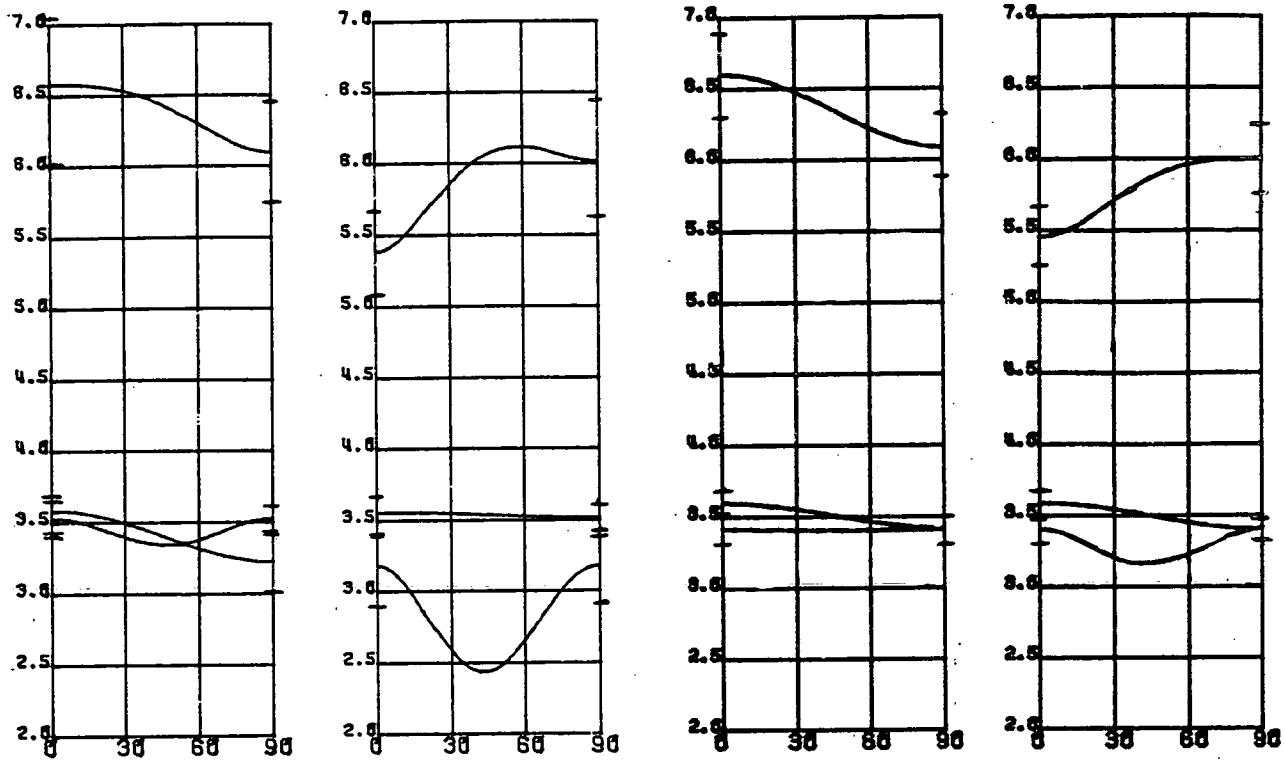
7.0
6.5
6.0
5.5
5.0
4.5
4.0
3.5
3.0
2.5
2.0
0
30
60
90

(a) (b) (c) (d)

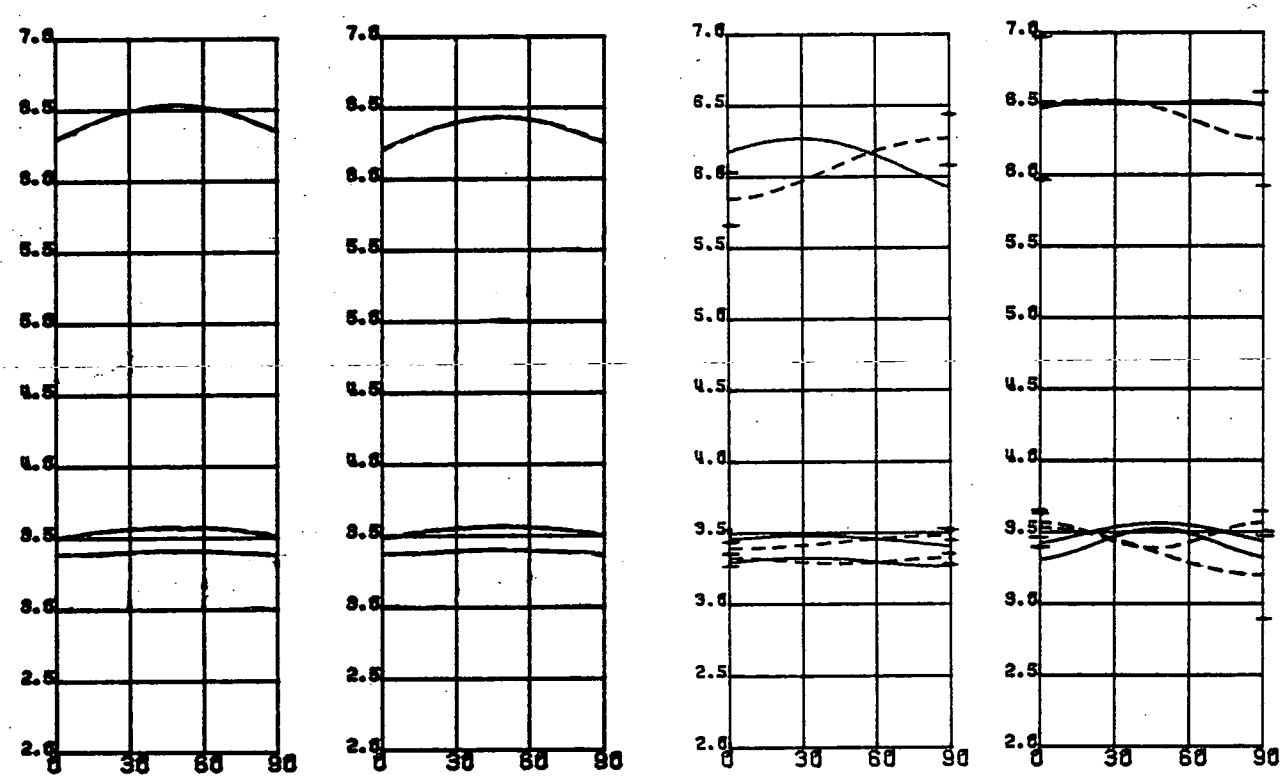
7.0
6.5
6.0
5.5
5.0
4.5
4.0
3.5
3.0
2.5
2.0
0
30
60
90

(e) (f) (g) (h)

0,-30 and 0,-60 as initial orientations, both inversions converge to similar solutions at an orientation of 19,-62. This orientation is 27 degrees away from the third axis. The velocity-surfaces shown in Fig.7.14g are reasonably similar to the solution defined previously, and still indicate intermediate velocities in this direction.

A second test is to remove the extra station correction at AY that was the introduced in section 7.4. Inversion for an anisotropic structure with orthorhmobic symmetry, using solution F3K as the initial model, produces the solution in Fig.7.14h. The horizontal orientation is altered by 10 degrees, but the dip and the elastic constants are very similar to those of the initial model, and this solution still indicates high velocities in this direction. We can also investigate solutions F3G and F3H defined previously, in the same way. The inversion does not find a numerically consistent solution when solution F3H is used as the initial model. The inversion progresses to a solution such that an eigenvalue in the Kelvin-Christoffel equation, (Equation A.1), is negative. This suggests that this solution may be a secondary minimum, possibly the result of poor network resolution. However, the inversion of this data set does not significantly alter the initial model when solution F3G is used.

In summary, inversion of the TDP1 data sets has defined several anisotropic solutions for the half-space structure that are statistically superior to an isotropic half-space approximation at the 95% confidence level. The inversion for hexagonal symmetry clearly defines two orthogonal orientations for the axis of rotational symmetry. Both of these solutions, F3C and F3D, are confirmed by inversion of the data set containing shear-wave delays. They are both obtained when we invert for orthorhombic symmetry (solutions F3G and F3H). However, the two solutions do not represent solutions for the same orthorhombic structure, and both solutions still appear to indicate a hexagonal structure. Inversion of the data set containing shear-wave delays, slightly alters solutions F3G, but

dramatically modifies solution F3H. Examination of the other solutions reveals only one pair of orthogonal solutions (F3K and F3L) that indicate the same structure. Both solutions are confirmed by inversion of shear-wave delays (F3M and F3N), and there is a similar solution within 30 degrees of the third principal axis of these two solutions. The weighted average of these four solutions (i.e. F3K, F3L, F3M and F3N) is labelled F30 in Table 7.3. Further discussion of these solutions will take place in section 7.7.

7.5 Analysis of the TDP2 travel-time residuals

Fig.7.15 shows the azimuthal variation of travel-time residuals from the events that were relocated from TDP2 and shown in Fig.7.2b, and where we rejected the arrivals at station HE to the west of the main network. There is a lot of scatter even though a cut-off at 0.2s has been introduced, and even when those residuals from event locations based on eight or more arrivals are plotted. The large scatter may reflect the poor model used to locate the earthquakes. As with the TDP1 data, there is no obvious indication of any variation that might be ascribed to dilatancy-anisotropy.

Table 7.5 lists the average station residuals after relocating the events shown in Fig.7.2b. There is a significant negative delay at station DP, and a significant positive delay at PB. There is no delay at AY, suggesting that the delay observed in TDP1 was a consequence of instrumental errors. There are several important differences between the delays at the TDP2 stations and the delay at AY in the TDP1 network. 1) Although two of the delays are statistically significant, no station delay is clearly larger than at other stations. 2) We cannot ignore the presence of the major fault zone striking through the centre of the TDP2 network. Our simple layered, isotropic approximation to the structure is likely to be unrealistic, and may introduce spurious effects. 3) We cannot rule out the possiblity of velocity-anisotropy being a factor in these observations.

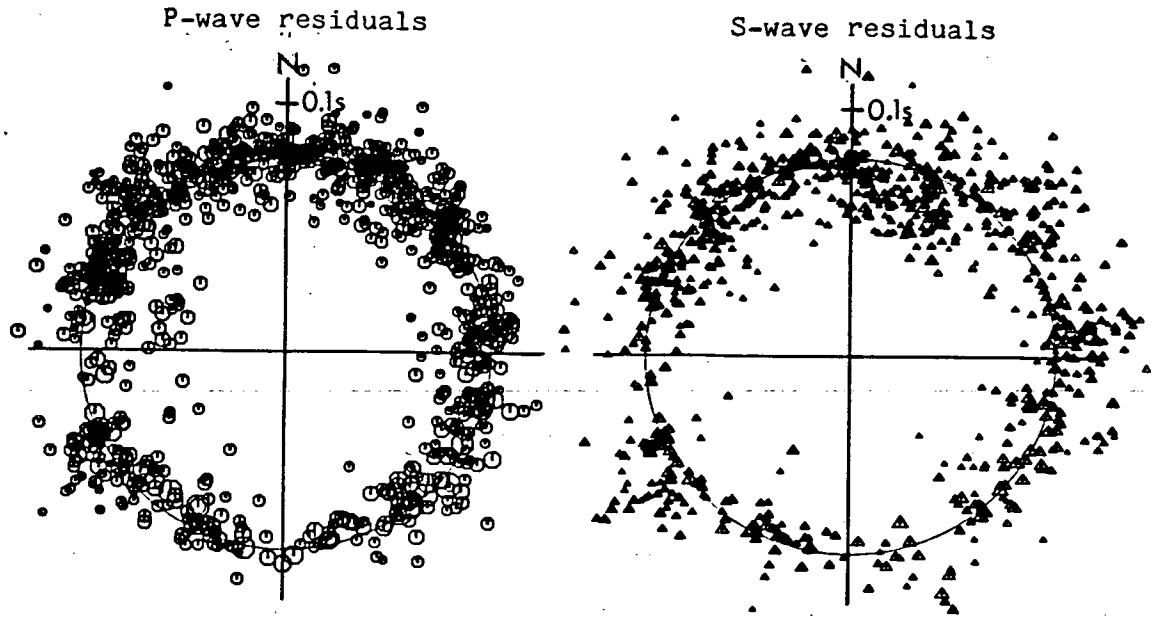

(a)

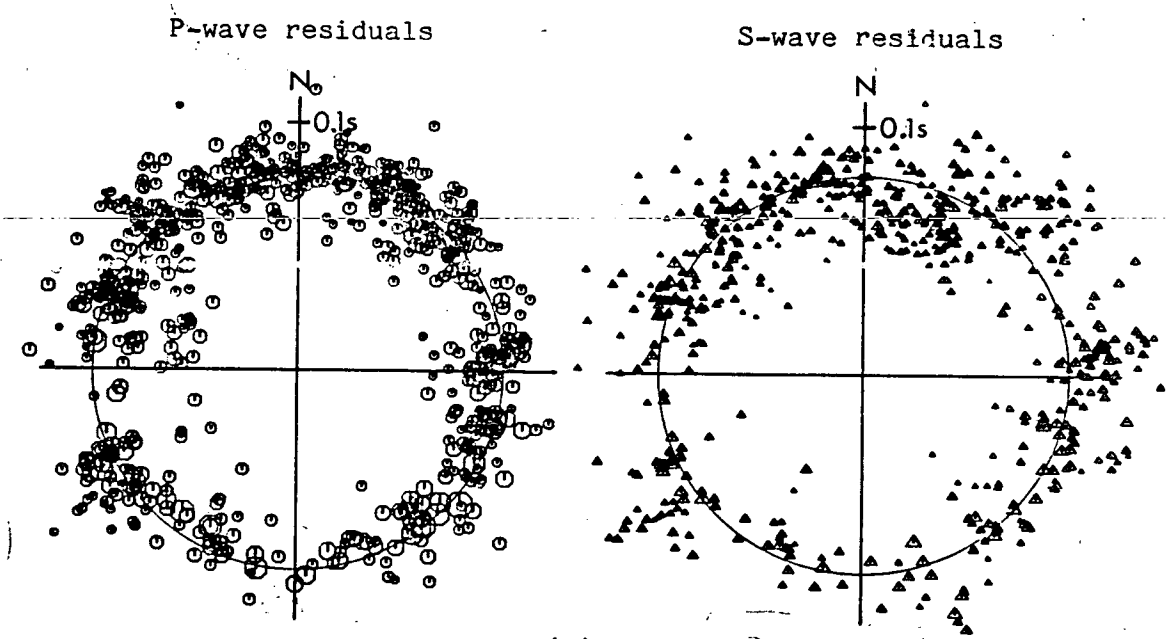

(b)

Figure 7.15 The azimuthal variation of P-and shear-wave travel-time residuals from the events of Fig.7.2b. Notation and format as in Fig.7.3. A cut-off at 0.2s has been introduced in order to reduce the scatter of the residuals.
(a) P- and S-residuals from all the events.
(b) P- and S- residuals from all the events with at least eight recorded arrivals.

Table 7.5. A list of the average delays at the TDP2 stations after relocation of approximately 300 events. Standard deviations are given in brackets.

Station	Residual
SE	0.001 (0.011)
TE	-0.011 (0.012)
AY	0.017 (0.010)
DP	-0.037 (0.013)
KE	-0.036 (0.041)
IZ	-0.018 (0.018)
PB	0.028 (0.013)
HI	-0.035 (0.019)
KT	0.000 (0.001)

Table 7.6. Isotropic solutions for the TDP2 data set

The average of the estimated errors (in km/sec and km) are given in brackets beneath the corresponding parameters. HYPO71 only estimates the epicentral and focal depth errors, and used the crustal model in Table 2.1 to relocate the events.

Data set	Location by	Vp	Vs	Long.	Lat.	Depth	Origin time	Overall RMS error
F4	HYPO71	—	—	29.9725 (0.55)	40.6833	9.85 (0.67)	29.93	0.1068
	Inversion	4.99 (0.15)	3.00 (0.04)	29.9732 (0.36)	40.6840 (0.35)	9.72 (0.74)	29.64 (0.19)	0.1025

There is no station in the network that is receiving rays from the same directions as either DP or PB, and we cannot compare delays, as was possible with ME and AY in TDP1. In addition, the TDP2 network will place greater constraint on the earthquake locations and it may be possible to observe an azimuthal variation of travel-time residuals due to velocity-anisotropy. For these reasons, we shall not alter any station corrections in the TDP2 network.

7.6 Inversion of TDP2 data for anisotropic structure

A suite of 30 events was selected from TDP2 for further analysis by the joint-inversion procedure. This data set consists of 183 P- and 153 shear-wave arrivals. The distribution of epicentres is shown in Fig.7.16. These events were carefully selected using similar criteria to those used in the selection of the TDP1 data sets. The author was not involved in the re-picking of arrivals from TDP2, but selected those that were given the highest weighting. In addition, arrivals at HE (Fig.2.1) have been rejected, and the analysis of the TDP2 data has not reached a stage where shear-wave delays are available. Table 7.6 summarises the location parameters for this data set determined by HYPO71 and by the joint-inversion for P- and shear-wave velocities in an isotropic half-space. The velocities determined by the inversion are lower than those determined from the TDP1 events and this may be a reflection of the lower velocities within the fault zone. As with the TDP1 events, we use the hypocentres determined by HYPO71 as the trial solutions for the inversion for anisotropic structure.

Initially, we invert the data set for anisotropic structure under the assumption of hexagonal symmetry, use GKFF1 as the initial model and initialise the inversion from directions spaced at 30 degree intervals throughout the semi-focal sphere. The solutions are shown in Fig.7.17, and appear to be different from the solutions obtained from TDP1 (Fig.7.9 and

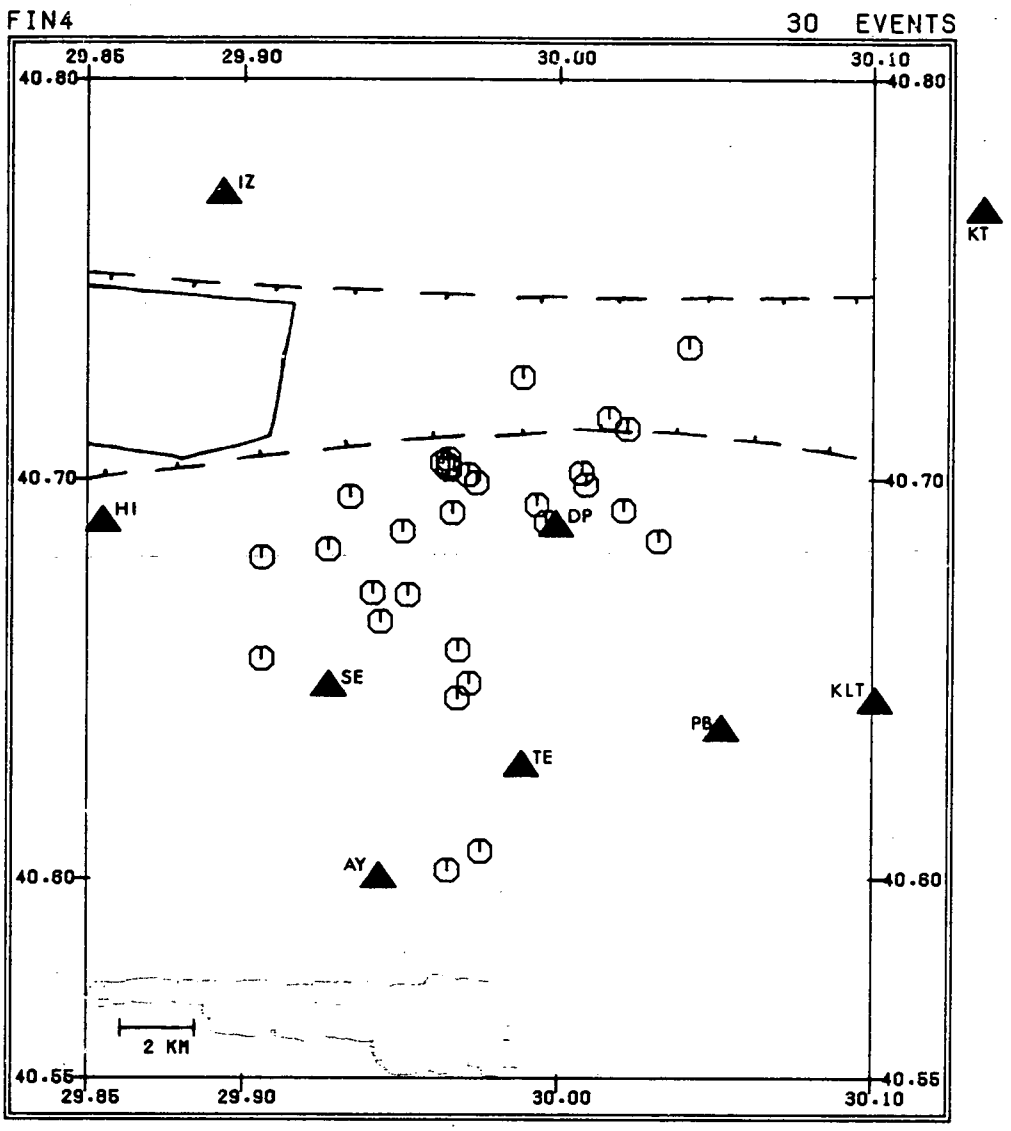

Figure 7.16 A map of the epicentral positions of 30 events from TDP2 used to determine the anisotropic structure by the joint-inversion of arrival-times.

7.10). There is one well-defined solution at an orientation of -70,0. The weighted average of the solutions at this orientation produce the wave-surfaces shown in Fig.7.17b. (For reference, the parameters of each solution are listed in Table 7.7, where the solution labels are referred from the corresponding figure captions). There is also another well-defined solution at an orientation of 20,-5 with lower RMS errors and similar orientation errors. These produce the wave-surfaces shown in Fig.7.17c. However, there are solutions with still lower RMS errors at orientations of -45,60, 20,60 and 60,60. The wave-surfaces from these solutions are shown in Figs.7.17(d,e and f). Notice that solutions F4C and F4E are at similar orientations, and similar velocity variations, as the orthorhombic solution (F3K and F3L, Fig.7.14) obtained from TDP1.

Following the procedure used previously, we now invert the data set using GKLF1 as the initial model. The resulting solutions are shown in Fig.7.18a. The same two horizontal orientations have been defined and produce similar wave-surfaces (Figs.7.18b and c), but there are solutions with lower RMS errors at orientations of -50,-20, -40,60, 15,55 and 60,50. These are shown in Fig.7.18(d,e,f and g) and again the solutions F4I and F4K are similar to the orthorhombic solution obtained from TDP1 at similar orientations. In particular, solution F4I has lower RMS and orientation errors than any other solution.

The inversion for hexagonal system has defined several solutions for the orientation of an axis of rotational symmetry. As with TDP1, this suggests that the assumption of hexagonal symmetry is insufficient to describe this structure, and that inversion for orthorhombic symmetry is required. Fig.7.19a shows the solutions obtained by inversion for orthorhombic symmetry using GKFF1 as an initial model. As with the TDP1 data set, the inversion for orthorhombic symmetry has produced several solutions with very low RMS and parameter errors, but these are at similar orientations to those defined by the hexagonal inversion. Adopting the

Figure 7.17 A summary of the solutions obtained by the joint-inversion of the TDP2 data set for anisotropic structure with hexagonal symmetry.
(a) A summary of the solutions for the orientation of an axis of rotational symmetry when the inversion assumes GKFF1 as an initial model. Notation and format as in Fig.6.16a with a reference RMS error of 0.0700.
(b) Dashed lines - the wave-surfaces obtained by taking the weighted average of the four solutions at an orientation of -66,2 in (a) (solution F4A in Table 7.7). Solid lines - for reference, the wave-surfaces in model GKFF1.
(c) Dashed lines - the wave-surfaces obtained by taking the weighted average of the five solutions at an orientation of 19,-5 in (a) (solution F4B in Table 7.7). Solid lines - for reference, the wave-surfaces in model GKFF1.
(d) Dashed lines - the wave-surfaces obtained by taking the weighted average of the solution at an orientation of -43,57 in (a) (solution F4C in Table 7.7). Solid lines - for reference, the wave-surfaces in model GKFF1.
(e) Dashed lines - the wave-surfaces obtained by taking the weighted average of the two solutions at an orientation of 17,53 in (a) (solution F4D in Table 7.7). Solid lines - for reference, the wave-surfaces in model GKFF1.
(f) Dashed lines - the wave-surfaces obtained by taking the weighted average of the solutions at an orientation of 65,50 in (a) (solution F4E in Table 7.7). Solid lines - for reference, the wave-surfaces in model GKFF1.

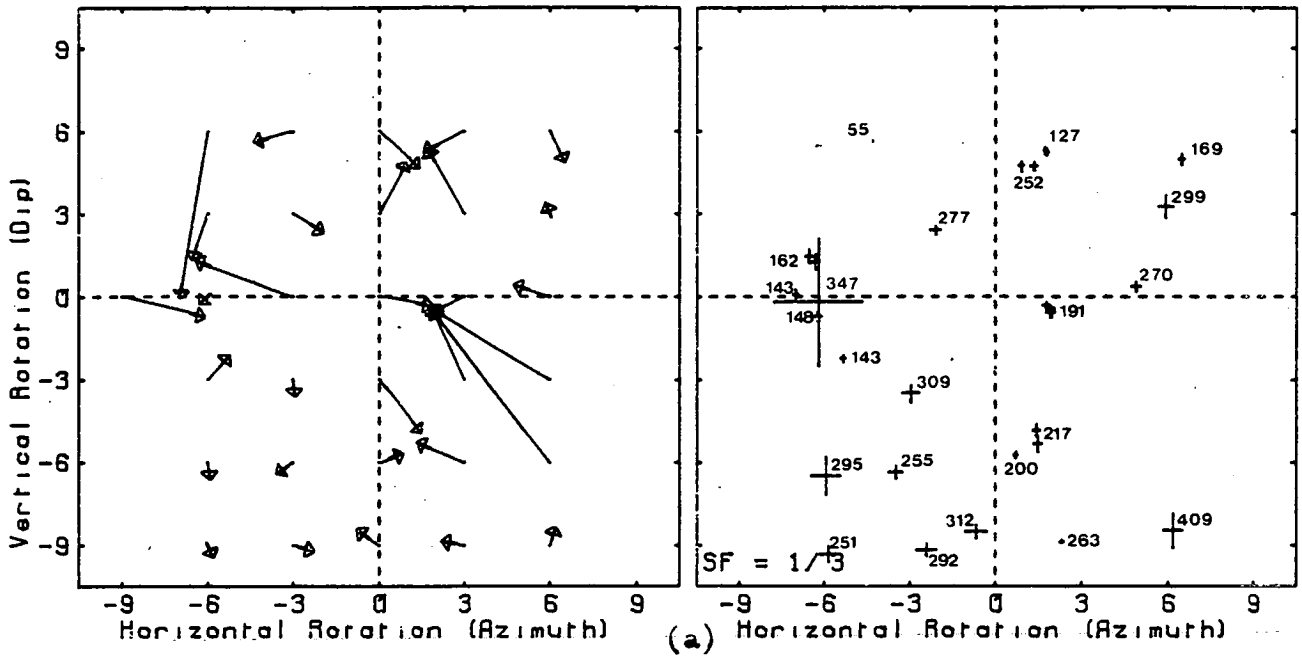
Vertical Rotation (Dip)
Horizontal Rotation (Azimuth)
SF = 1/3
55
127
169
252
277
299
162
143
347
148
270
191
143
309
217
295
255
200
312
409
251
263
292
Horizontal Rotation (Azimuth)

(a)

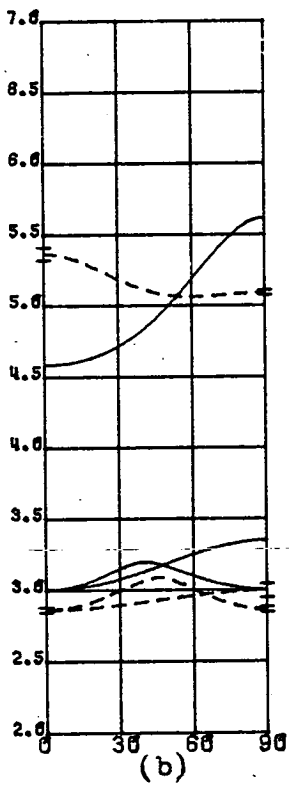

(b)

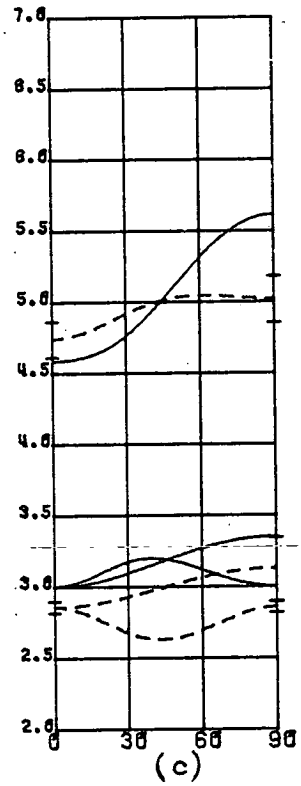

(c)

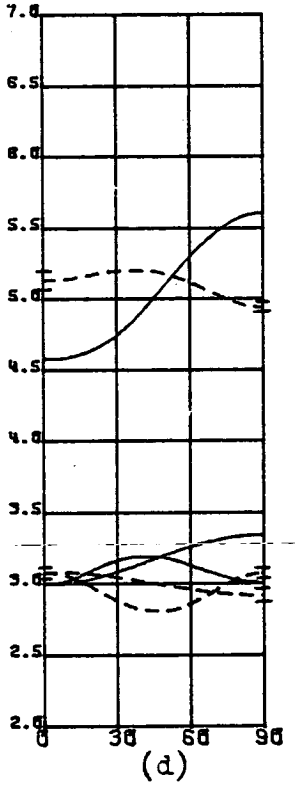

(d)

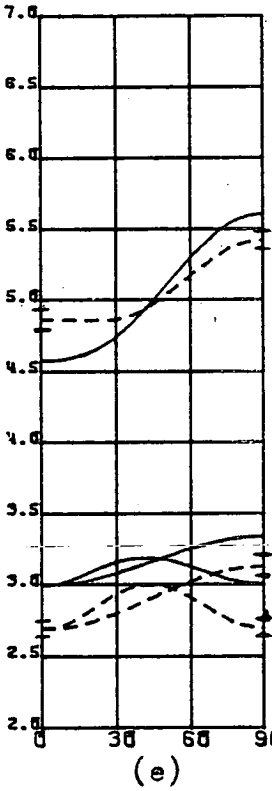

(e)

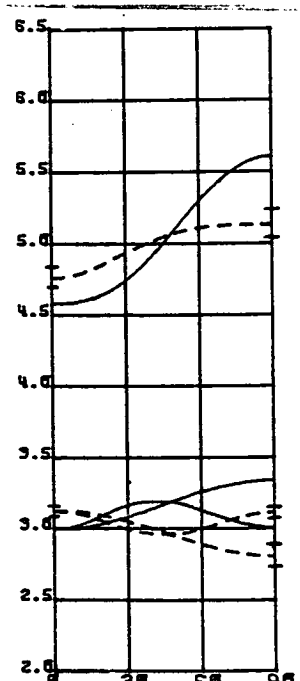

Figure 7.18 A summary of the solutions obtained by the joint-inversion of the TDP2 data set for anisotropic structure with hexagonal symmetry.

(a) A summary of the solutions for the orientation of an axis of rotational symmetry when the inversion assumes GKLF1 as an initial model. Notation and format as in Fig.6.16a with a reference RMS error of 0.0700.

(b) Dashed lines - the wave-surfaces obtained by taking the weighted average of the two solutions at an orientation of 18,-5 in (a) (solution F4F in Table 7.7). Solid lines - for reference, the wave-surfaces in model GKFF1.

(c) Dashed lines - the wave-surfaces obtained by taking the weighted average of the three solutions at an orientation of -71,5 in (a) (solution F4G in Table 7.7). Solid lines - for reference, the wave-surfaces in model GKFF1.

(d) Dashed lines - the wave-surfaces obtained by taking the weighted average of the three solutions at an orientation of -53,-21 in (a) (solution F4H in Table 7.7). Solid lines - for reference, the wave-surfaces in model GKFF1.

(e) Dashed lines - the wave-surfaces obtained by taking the weighted average of the two solutions at an orientation of -41,58 in (a) (solution F4I in Table 7.7). Solid lines - for reference, the wave-surfaces in model GKFF1.

(f) Dashed lines - the wave-surfaces obtained by taking the weighted average of the solutions at an orientation of 17,52 in (a) (solution F4J in Table 7.7). Solid lines - for reference, the wave-surfaces in model GKFF1.

(g) Dashed lines - the wave-surfaces obtained by taking the weighted average of the solutions at an orientation of 62,53 in (a) (solution F4K in Table 7.7). Solid lines - for reference, the wave-surfaces in model GKFF1.

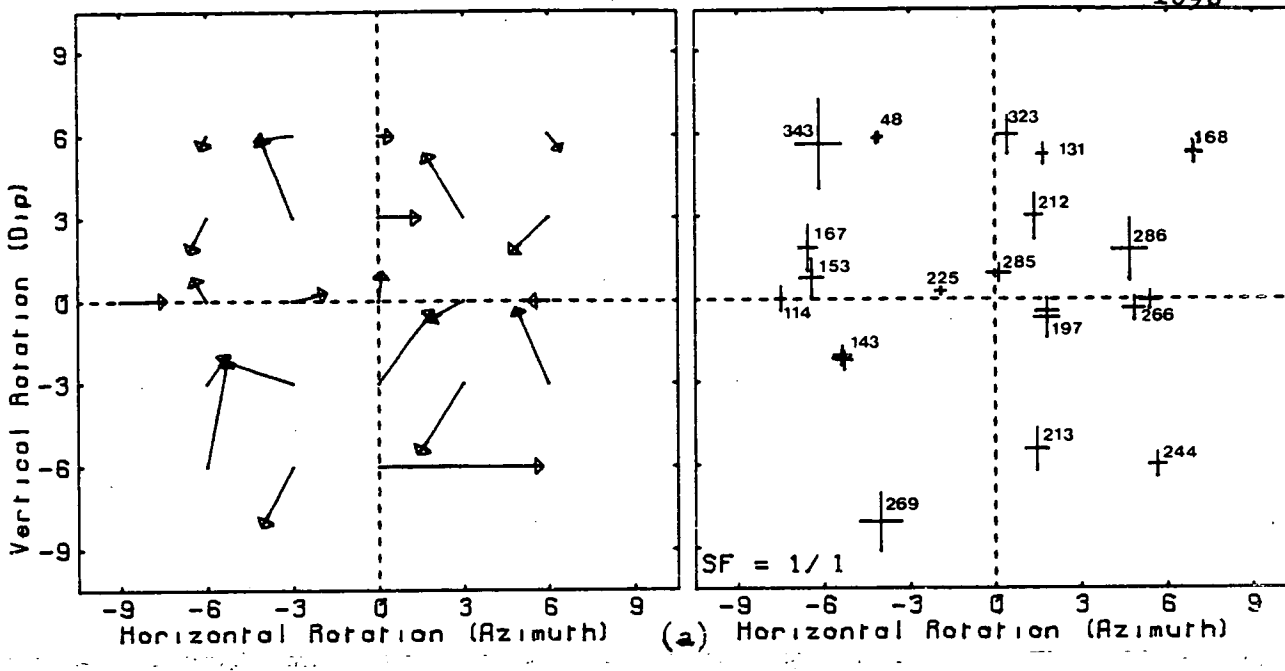
Vertical Rotation (Dip)
Horizontal Rotation (Azimuth)
343
48
323
131
168
212
167
153
225
285
286
114
197
266
143
213
244
269
SF = 1/ 1
Horizontal Rotation (Azimuth)

(a)

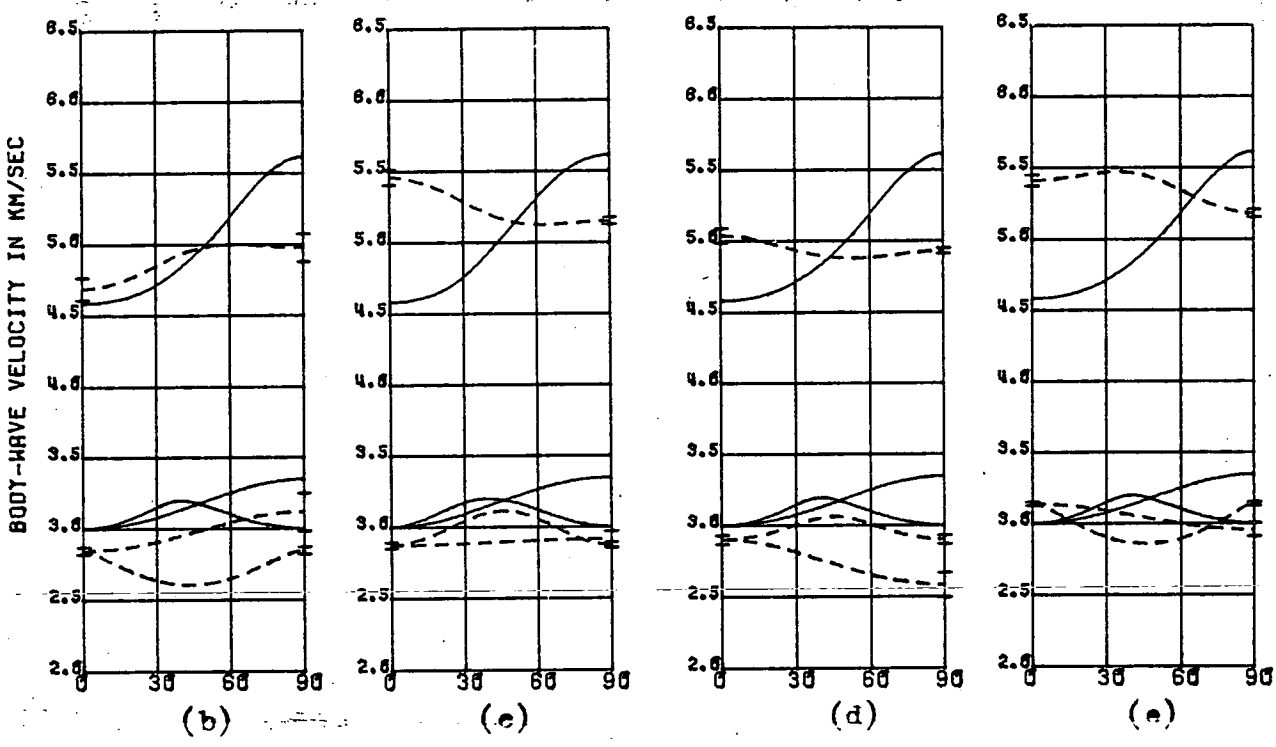
BODY-WAVE VELOCITY IN KM/SEC

(b) (c) (d) (e)

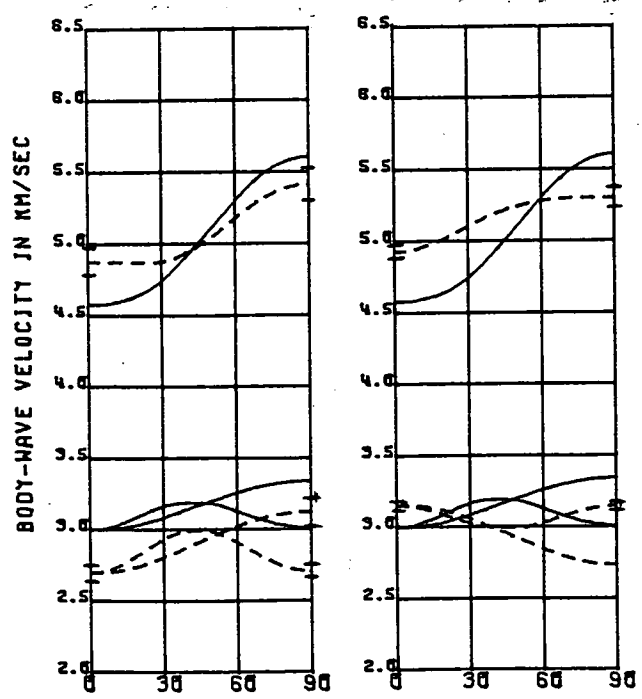
BODY-WAVE VELOCITY IN KM/SEC

(f) (g)

Table 7.7. Anisotropic solutions from the inversion of the TDP2 data sets.

Errors in brackets. Estimated errors for solutions determined under the assumption of hexagonal symmetry are only given for the independent elastic constants. F-test ratio at 95% and 99% significance levels are approximately 1.25 and 1.39 respectively. Azimuth and dip refer to horizontal and vertical rotations respectively.

SOLUTION	ELASTIC CONSTANTS									ORIENTATION		OVERALL RMS ERROR	F-TEST RATIO
	C11	C22	C33	C23	C13	C12	C44	C55	C66	Azimuth	Dip		
F4A	74.87 (1.22)	67.41 (0.51)	67.41	20.73 (1.01)	21.32	21.32 (0.51)	23.34	21.32	21.32 (0.28)	-66.11 (1.65)	1.92 (3.24)	0.0854	1.44
F4B	57.18 (1.91)	64.43 (2.57)	64.43	13.87 (1.76)	25.26	25.26 (2.35)	25.28	21.08	21.08 (0.38)	18.70 (1.69)	-4.74 (2.00)	0.0891	1.32
F4C	68.71 (1.40)	63.36 (0.87)	63.36	19.27 (0.84)	25.03	25.03 (1.16)	22.05	24.67	24.67 (0.32)	-42.83 (1.35)	57.35 (2.18)	0.0755	1.84
F4D	61.70 (1.61)	76.60 (1.94)	76.60	25.45 (1.30)	21.53	21.53 (1.09)	25.58	18.85	18.85 (0.56)	17.42 (1.25)	52.78 (2.46)	0.0827	1.54
F4E	59.08 (1.28)	68.72 (1.61)	68.72	27.99 (2.42)	18.15	18.15 (0.84)	20.37	25.33	25.33 (0.50)	64.50 (2.89)	49.87 (5.84)	0.0869	1.39
F4F	58.43 (3.10)	65.59 (4.26)	65.59	14.67 (2.99)	25.92	25.92 (3.93)	25.46	21.24	21.24 (0.59)	18.31 (2.81)	-5.21 (3.69)	0.0897	1.31
F4G	77.54 (1.53)	68.98 (0.67)	68.98	24.77 (1.02)	22.73	22.73 (0.65)	22.11	21.49	21.49 (0.30)	-71.43 (1.45)	-5.19 (3.43)	0.0843	1.48
F4H	66.05 (1.31)	63.25 (0.50)	63.25	28.51 (0.82)	15.78	15.78 (0.54)	17.37	21.92	21.92 (0.47)	-53.45 (1.64)	-21.48 (1.85)	0.0843	1.48
F4I	76.17 (1.04)	69.80 (0.69)	69.80	24.36 (0.73)	31.45	31.45 (0.12)	22.72	25.60	25.60 (0.23)	-41.02 (0.99)	58.42 (1.29)	0.0748	1.88
F4J	61.92 (2.30)	76.45 (2.53)	76.45	25.53 (1.70)	21.80	21.80 (1.41)	25.46	18.92	18.92 (0.84)	16.93 (1.84)	52.34 (3.67)	0.0831	1.52

Table 7.7 (continued)

SOLUTION	ELASTIC CONSTANTS									ORIENTATION		OVERALL RMS ERROR	F-TEST RATIO
	C11	C22	C33	C23	C13	C12	C44	C55	C66	Azimuth	Dip		
F4K	63.30 (1.31)	73.25 (1.53)	73.25	34.51 (2.74)	21.63	21.63 (0.83)	19.37	25.84	25.84 (0.47)	62.42 (2.95)	52.67 (4.91)	0.0868	1.39
F4L	71.31 (1.45)	63.66 (1.12)	64.95 (1.38)	19.08 (1.20)	26.74 (2.29)	22.68 (1.25)	22.31 (0.33)	23.50 (0.27)	25.63 (0.32)	-32.90 (1.85)	58.31 (2.57)	0.0762	1.81
F4M	77.86 (2.41)	58.60 (2.23)	63.24 (2.11)	26.23 (3.44)	24.71 (1.52)	20.30 (1.62)	19.16 (0.46)	24.26 (0.39)	18.61 (0.53)	-74.12 (0.72)	73.90 (1.81)	0.0736	1.94
F4N	65.12 (2.01)	61.98 (1.68)	68.21 (2.59)	32.45 (2.79)	16.62 (1.65)	19.32 (1.73)	21.30 (0.41)	24.16 (0.41)	21.22 (0.46)	-45.08 (1.08)	-30.73 (1.16)	0.0788	1.69

technique used for TDP1, we plot vertical sections through each solution, measured from the same direction, in order to see which solutions satisfy the criteria for an orthorhombic structure (i.e. that solutions are orthogonal and imply the same structure). Fig.7.19(b to i) show sections through those solutions in part (a) that have an RMS error of less than 0.0800s. Solutions T1 and T5 are not similar to any other solution and can be dismissed. However, solutions T2 and T6, T3 and T7, and solutions T4 and T8 each satisfy this condition. Solutions T2 and T6 are very similar to those determined from TDP1. The other two solutions, although at different orientations also suggest a similar structure but indicate a greater degree of shear-wave anisotropy. These three pairs of solutions have been individually averaged, and are labelled F4L, F4M and F4N in Table 7.7.

The absence of shear-wave delays for this data set precludes much further analysis of this data set, and these solutions in particular. However, all three solutions are obtained in the same form when we introduce extra station corrections of 0.2s to model the effect of any near-surface, horizontal isotropic layer. Solution F4M is apparent when we invert for orthorhombic symmetry using GKLF1 as the initial model. In this case, we obtain the other solutions at only one of the orientations.

In summary, inversion of the TDP2 data set, as with the TDP1 data sets, defines several solutions for anisotropic structure that are statistically superior to the solution obtained by inverting for an isotropic structure. The inversion for hexagonal symmetry defines several possible orientations for an axis of rotational symmetry, but there is only one solution, F4I, that is clearly superior to the others. Inversion for orthorhombic symmetry again defines several possible structures. Unlike for the TDP1 analysis, these solutions are at similar orientations to those defined by the hexagonal inversion. Examination of these solutions reveals three pairs of orthogonal solutions (F4L, F4M and F4N) that indicate the

Figure 7.19 A summary of the solutions obtained by the joint-inversion of the TDP2 data set for anisotropic structure with orthorhombic symmetry.
(a) A summary of the solutions for the orientation of an axis of rotational symmetry when the inversion assumes GKFF1 as an initial model. Notation and format as in Fig.6.16a with a reference RMS error of 0.0700.
The velocity-surfaces are vertical sections, measured from (0,0), through those solutions in (a) with an RMS error of less than 0.0800. Solution labels are for reference from the text. The velocity-surfaces are from those solutions at an orientation of:
(b) -23,41; (c) -32,59; (d) -75,74; (e) -45,-31; (f) -72,54;
(g) 57,58; (h) 16,74; (i) 45,-31.

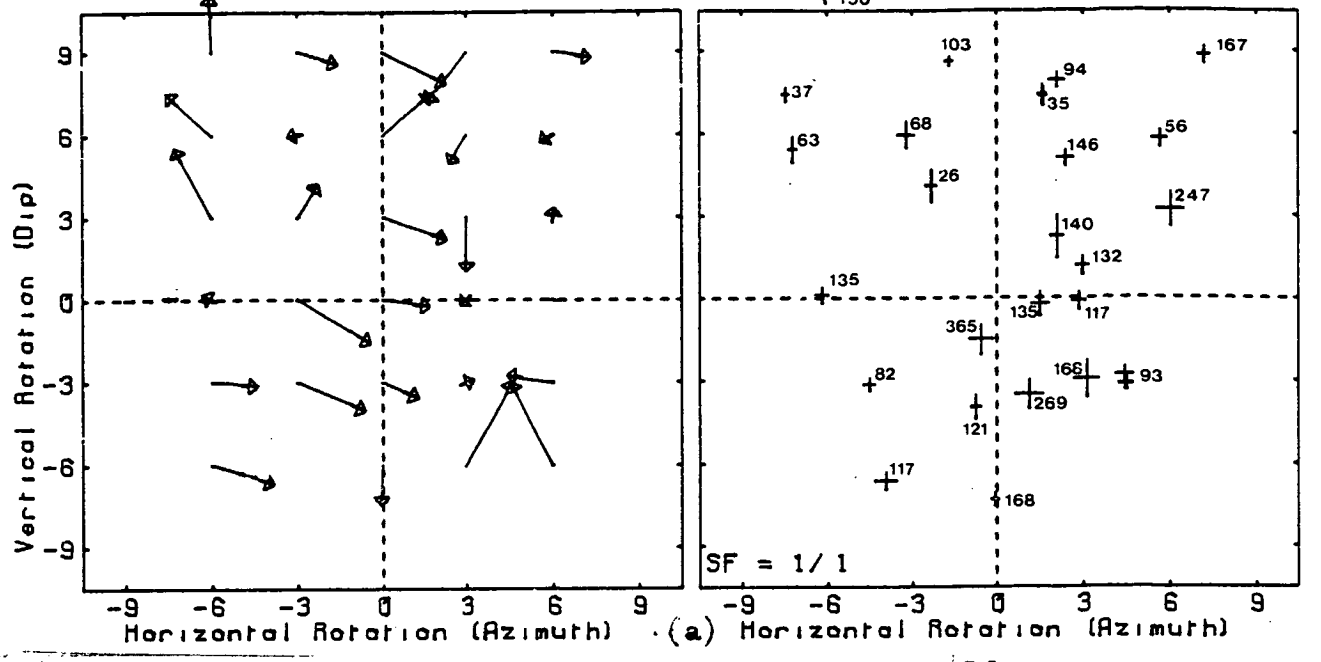
Vertical Rotation (Dip)
Horizontal Rotation (Azimuth)
SF = 1/ 1
(a)
Horizontal Rotation (Azimuth)

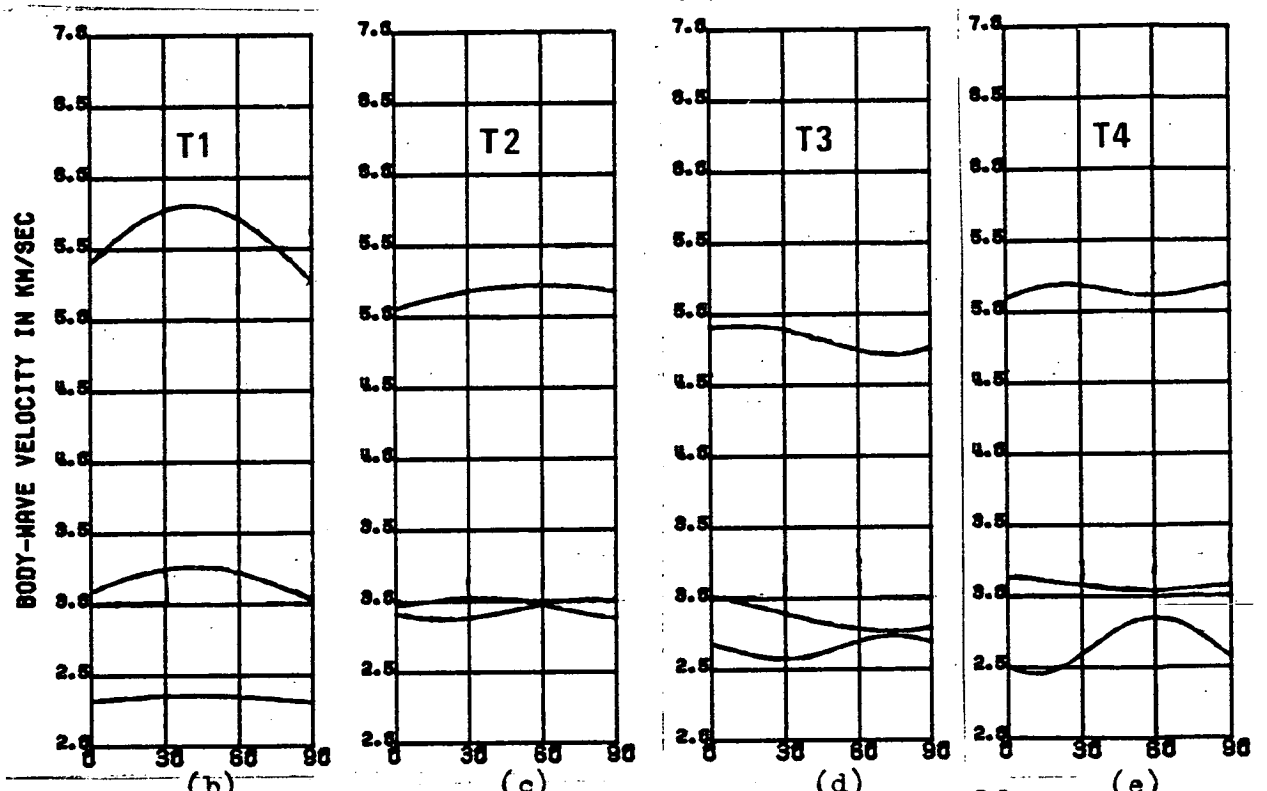
BODY-WAVE VELOCITY IN KM/SEC
T1
T2
T3
T4
(b)
(c)
(d)
(e)

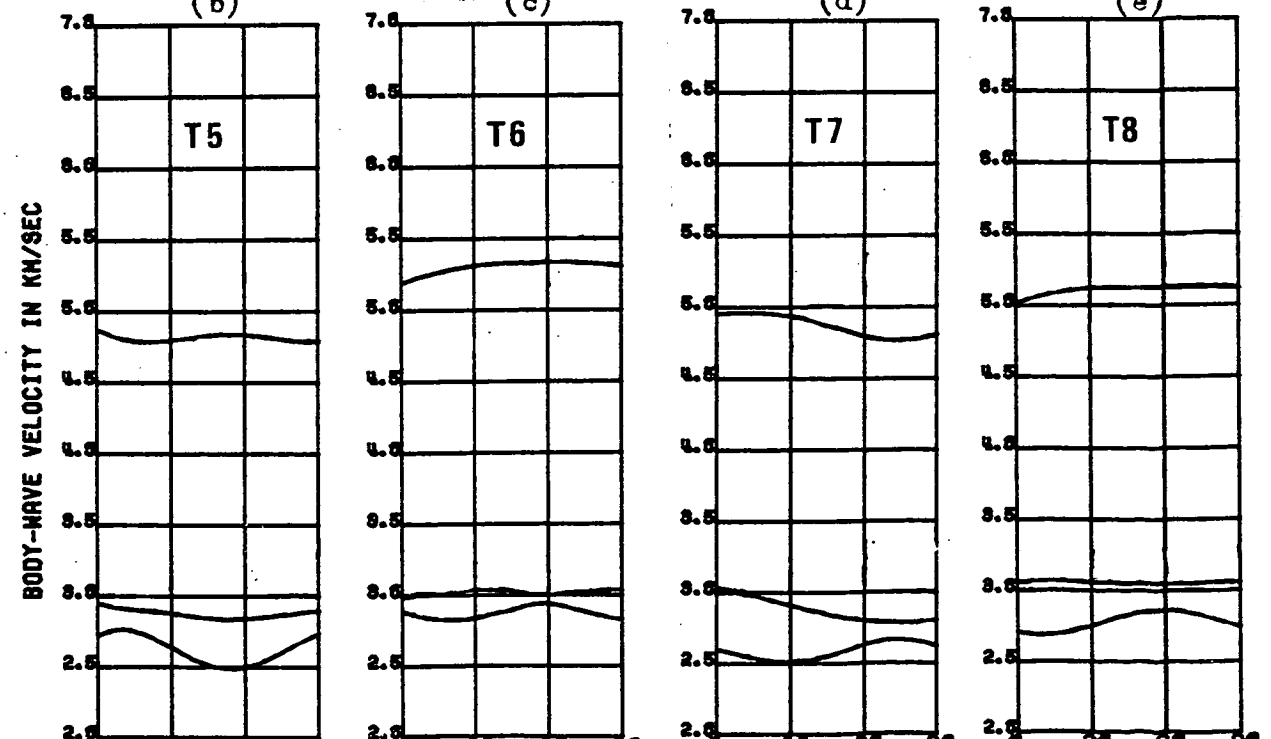
BODY-WAVE VELOCITY IN KM/SEC
T5
T6
T7
T8

same structure. Only one of these, F4M, is obtained when we use both GKFF1 and GKLF1 as initial models in the inversion, although the other two are still apparent. Solution F4L is similar to the orthorhombic solution (F30) obtained from inversion of TDP1 data. Further discussion of these solutions will take place below.

7.7 Discussion

This Chapter has attempted to apply the techniques developed in Chapters 5 and 6, to the determination of the anisotropic structure beneath the TDP networks. As anticipated in Chapter 5, the azimuthal variation of travel-time residuals did not provide any indication of high or low velocity directions that could have been ascribed to velocity-anisotropy. The joint-inversion of particular data sets from each experiment, however, defines numerous solutions for an anisotropic half-space that are statistically superior to the assumption of a simple isotropic structure, at the 95%, and sometimes the 99%, confidence level. However, only a few solutions are consistent with the behaviour of the inversion procedure when analysing synthetic data. Before we discuss individual solutions for the structure, it is worthwhile to remind ourselves of the limitations in our inversion procedure.

1) Our most serious limitation is that we assume the structure to be a homogeneous half-space. This may be a reaonable approximation for analysis of the TDP1 data sets, but we should not ignore the presence of the North Anatolian Fault in the analysis of the TDP2 data. This represents a major discontinuity striking through the centre of the network, and will undoubtedly lead to some spurious effects.

2) Computing costs restricts our inversion procedure to a relatively simple one. We do not use the Generalised Inverse technique which would lead to a more detailed interpretation of the stabilty and resolution of our solutions, and we have to rely on the information provided by the

estimated and RMS errors. Chapter 6 demonstrated that the estimated errors do not always reflect the departure from the true solution, although the lowest RMS error was always associated with the correct solution. In the isotropic models, inversion for an anisotropic half-space never provided a solution that was superior to the inversion for an isotropic half-space.

3) We do not use arrival-time or parameter weighting in our inversion scheme. We have attempted to resolve the absence of arrival-time weighting by careful selection of the data, but this may be insufficient, particularly for the shear-waves. All model parameters have been assigned equal weight, and this may be inadequate, as the elastic constants do not have equal effect on the form of the anisotropic variations.

4) For the TDP1 network, in particular, there are large aziumthal gaps both to the north and to the south-east for the event distribution that we have used. This may lead to spurious effects due to poor network resolution, but there was little obvious evidence of this during the inversion of synthetic data.

5) The inversion for structures of orthorhombic symmetry is restricted to calculation of phase-velocities. This may preclude any detailed interpretation of the shear-wave surfaces in the orthorhombic solutions.

6) We only invert for symmetry systems up to orthorhombic. If the cracks are not aligned in an orthogonal manner, then it may be necessary to invert for higher systems.

7.7.1 The TDP1 solutions

The joint-inversion of the TDP1 data sets defined three solutions, two hexagonal and one orthorhombic, that demand further consideration. We can examine the solutions by using each as a model to relocate all the events detected during TDP1, and then comparing the resulting statistical

parameters of the relocated events. This may provide an indication of how dependent the solutions are on the inversion procedure, and on the distribution of events that we used to determine the structure. We will use the anisotropic half-space location program of Chapter 4 to relocate the events with each model. This program has no weighting scheme, and so we remove arrivals that have been assigned a low weight. (There are four levels of weighting with HYPO71, and we use those arrivals assigned one of the two highest). Secondly, we remove those events with less than six arrivals, and any that do not have a shear-wave arrival. Finally we remove those events that cannot be located by the location program (i.e. these are mainly those that lie a significant distance outside the network). The process reduces the number of events in the TDP1 data set to approximately 160.

Fig.7.20 shows the epicentral locations of approximately 140 of these events, together with four vertical sections through the hypocentres. These locations have been determined by HYPO71 using the velocity model in Table 2.1, and using all the arrival-times (and their weights), originally assigned to the events. These hypocentres will be used as trial hypocentres for subsequent hypocentral determinations. Fig.7.21 shows the epicentral locations of the events, with the same sections, determined by the anisotropic half-space program using an <u>isotropic</u> model with velocities corresponding to those determined by inversion for isotropic structure of data set F3 (Table 7.2). The arrival-times, the trial hypocentres, and the location procedure are therefore equivalent to that which we shall use to locate the events in each of the anisotropic models. The parameters of each set of locations are summarised in Table 7.8, where the HYPO71 locations are referenced L1A, and the isotropic half-space locations are referenced L1B. Notice that there is little difference in the epicentral locations, the sections, and the location parameters between these two models, and that most of these events are located on the periphery of the

Figure 7.20 A map of the hypocentral locations of a reduced set of events from TDP1 determined by HYPO71 using the crustal model in Table 2.1. On the right are four vertical sections through the hypocentres with the vertical axis measuring depth in kilometers. The horizontal axis measures distance along the correspondingly labelled lines on the epicentral map. XWD indicates the width of the cross-section in kilometres, centred on the lines on the epicentral map. The size of each symbol is proportional to magnitude, and is plotted on the same scale as those on the epicentral map.

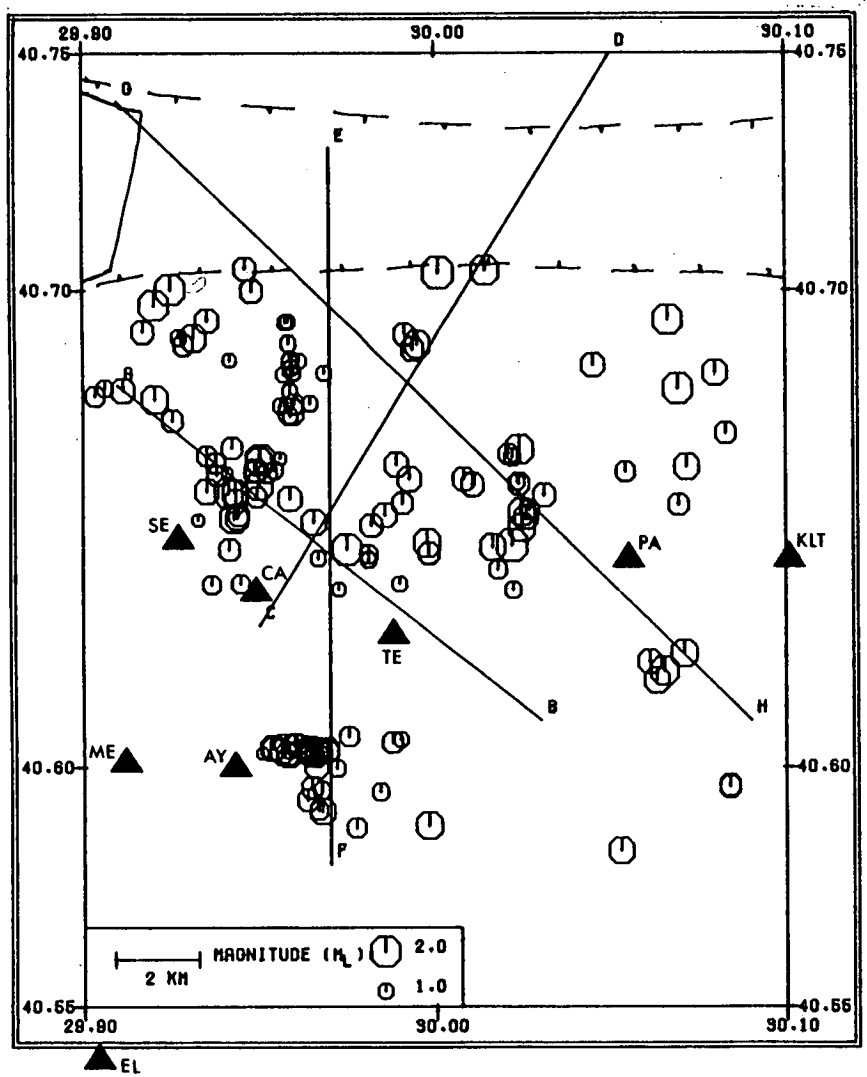
29.80
30.00
30.10
40.75
40.70
40.60
40.55
D
E
F
G
H
B
C
SE
CA
PA
KLT
TE
ME
AY
EL
MAGNITUDE (M_L)
2.0
1.0
2 KM

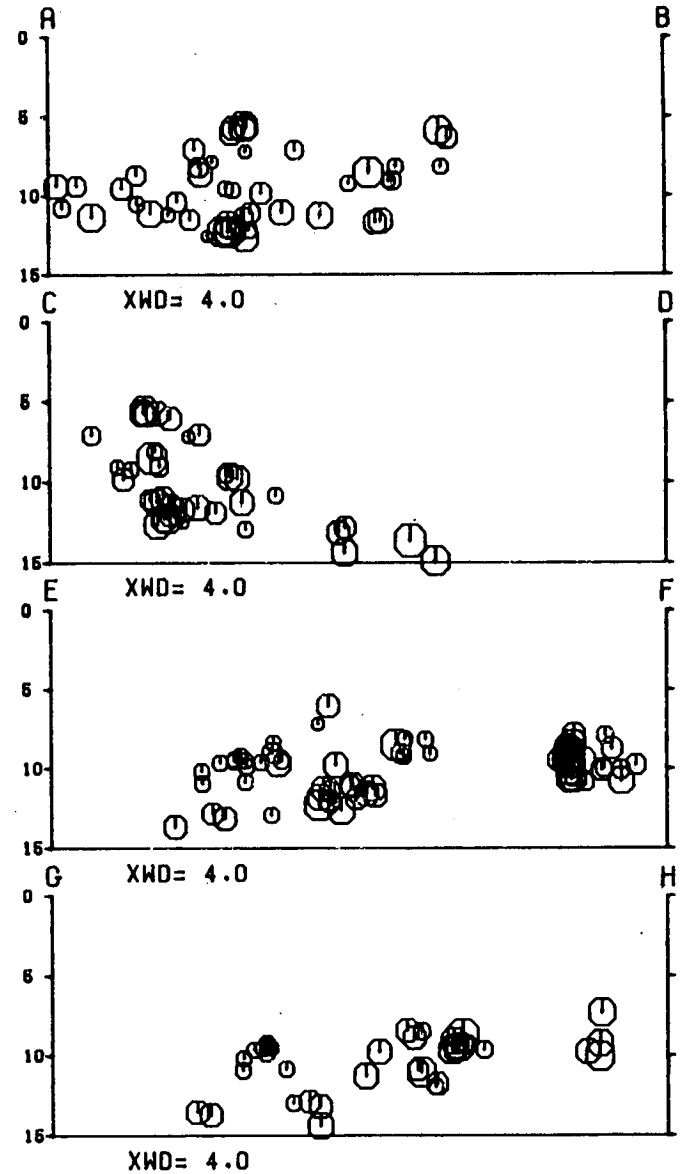
A
B
C
D
E
F
G
H
0
5
10
15
XWD= 4.0
XWD= 4.0
XWD= 4.0
XWD= 4.0

Figure 7.21 A map of the hypocentral locations of a reduced set of events from TDP1 determined by the anisotropic half-space location program using an isotropic model with P- and S- velocities corresponding to those determined by inversion of data set F3 (Table 7.2). Format as in Fig.7.20.

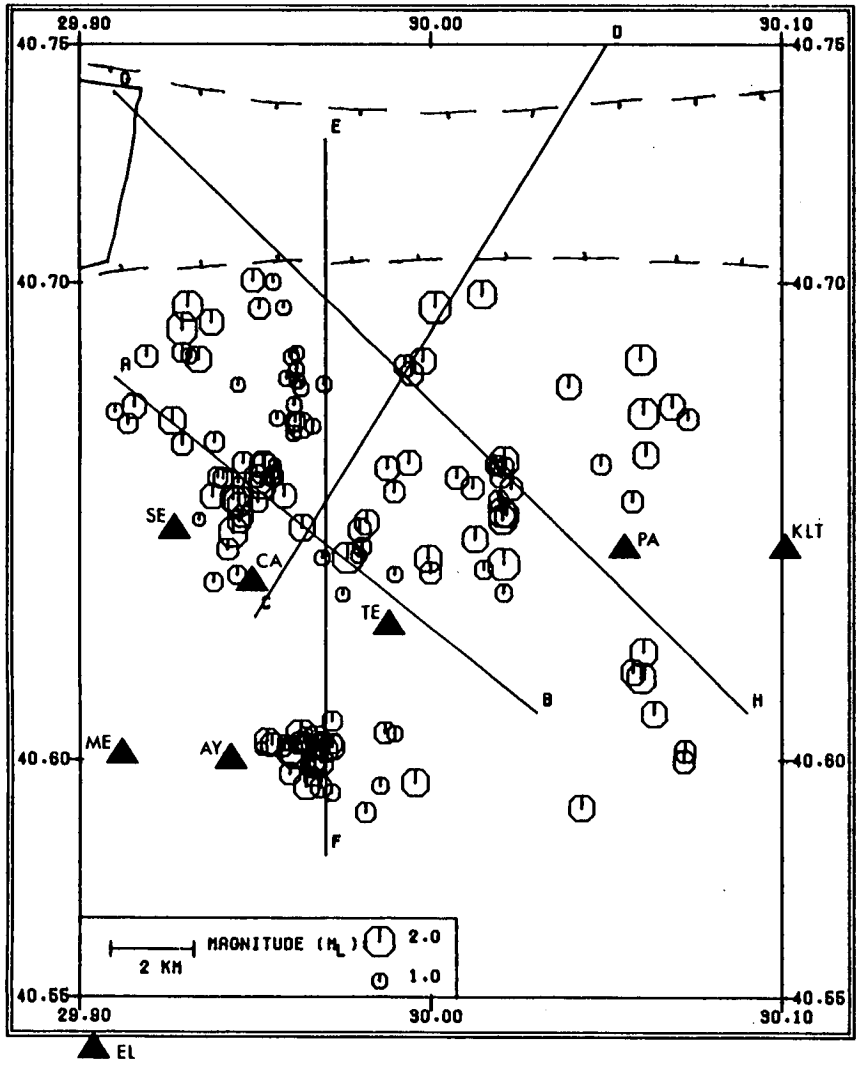
29.80
30.00
30.10
40.75
40.70
40.60
40.55
A
B
C
D
E
F
G
H
SE
CA
TE
PA
KLT
ME
AY
EL
MAGNITUDE (M_L)
2.0
1.0
2 KM

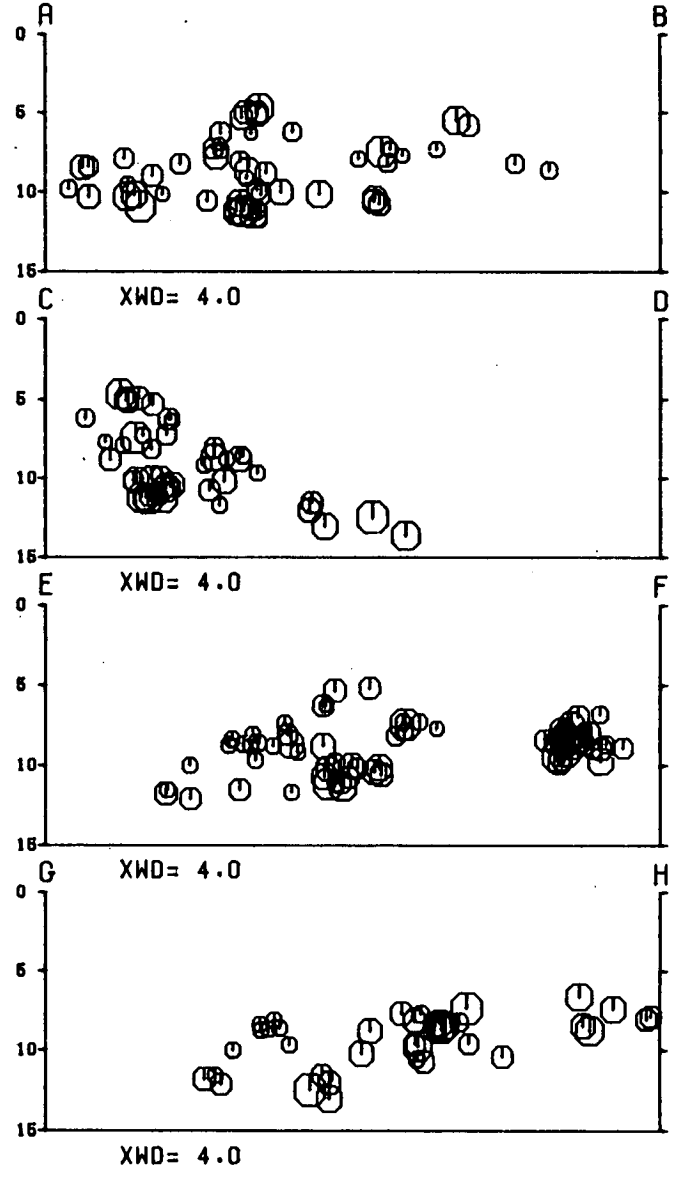
A
B
C
D
E
F
G
H
0
5
10
15
XWD= 4.0
XWD= 4.0
XWD= 4.0
XWD= 4.0

network. The sections through the hypocentres define a significant dip towards the North - this is likely to be the result of poor network resolution. We shall see later that this dip is not so marked in the TDP2 locations.

We use the F-test again, (i.e. the ratio of the squares of the overall RMS errors) to estimate the significance of any improvement in the fit to the data by locating the earthquakes in an anisotropic half-space. We will compare any anisotropic solution with the isotropic solution with the lowest error, (in this case the half-space case, L1B). In the revised TDP1 data set, there are approximately 500 degrees of freedom, and so F-ratios of approximately 1.15 and 1.25 would indicate that the anisotropic solutions represent a significant improvement at the 95% and the 99% levels respectively.

The first model that we shall consider is that obtained at an orientation of -40,60 by inversion for a structure with hexagonal symmetry. We take the weighted average of solutions F3D and F3F (Table 7.3), and relocate all the events in the revised data set. A summary of the relocation parameters are referenced L1C in Table 7.8. All parameters of these locations are slightly worse than those in the isotropic structures. This is contrary to what we would expect. Section 4.2 demonstrated that the locations by the TDP1 network in the correct anisotropic model should produce hypocentres with slightly lower RMS and hypocentral errors. This suggest that this solution cannot be real and must reflect some deficiency in our inversion procedure.

The next model that we shall consider is the hexagonal structure that was consistently obtained at an orientation of approximately -40,-45 in all the inversions of the TDP1 data sets. We shall first use the weighted average of solutions F3C and F3E, which were obtained by inversion of data set F3 under the assumption of hexagonal symmetry. The location parameters are referenced L1D in Table 7.8. As in the previous model, the RMS errors

and the hypocentral errors are greater than those in the isotropic structures, and again this is contrary to what we would expect. The inversion for orthorhombic symmetry finds a similar solution at this orientation but with a slightly lower RMS error, although it is still confirmed by inversion of shear-wave delays. We take the weighted average of the two orthorhombic solutions, F3G and F3I and relocate the events. This produces a set of locations with parameters referenced L1E in Table 7.8. This model produces locations with much lower average RMS and hypocentre errors than the hexagonal model at the same orientation. However, the overall RMS error suggests that the solution is not statistically significant, when compared to the isotropic solutions. As with the previous model, this suggests that the solutions consistently obtained at an orientation of -40,40 do not represent true solutions for the anisotropic structure.

We are left with one other possible solution from the inversion of the TDP1 data set, that of the orthorhombic solution F3O. The parameters of the relocation using this structure are referenced L1F in Table 7.8. With this model there is a noticeable improvement in the average RMS and hypocentral errors, and the F-ratio indicates that this structure represents a statistically significant improvement in the fit to the data compared to the isotropic approximations. Fig.7.22 shows the epicentral relocations in this case, together with the same vertical section through the hypocentres as before.

Comparison of the relocations shown in these figures reveals some very interesting features. In the isotropic locations, there is a pronounced NNE-SSW trend of epicentres to the north-east of station SE. In the anisotropic locations, there is still an indication of this trend, but in addition there are two very well-defined NW-SE trends. There is also a very tight cluster of epicentres 1km to the ENE of SE which was not apparent in either of the isotropic locations. Of course, not too much

Figure 7.22 A map of the hypocentral locations of a reduced set of events from TDP1 determined by the anisotropic half-space location program using an anisotropic model corresponding to solution F30 in Table 7.3. Format as in Fig.7.20.

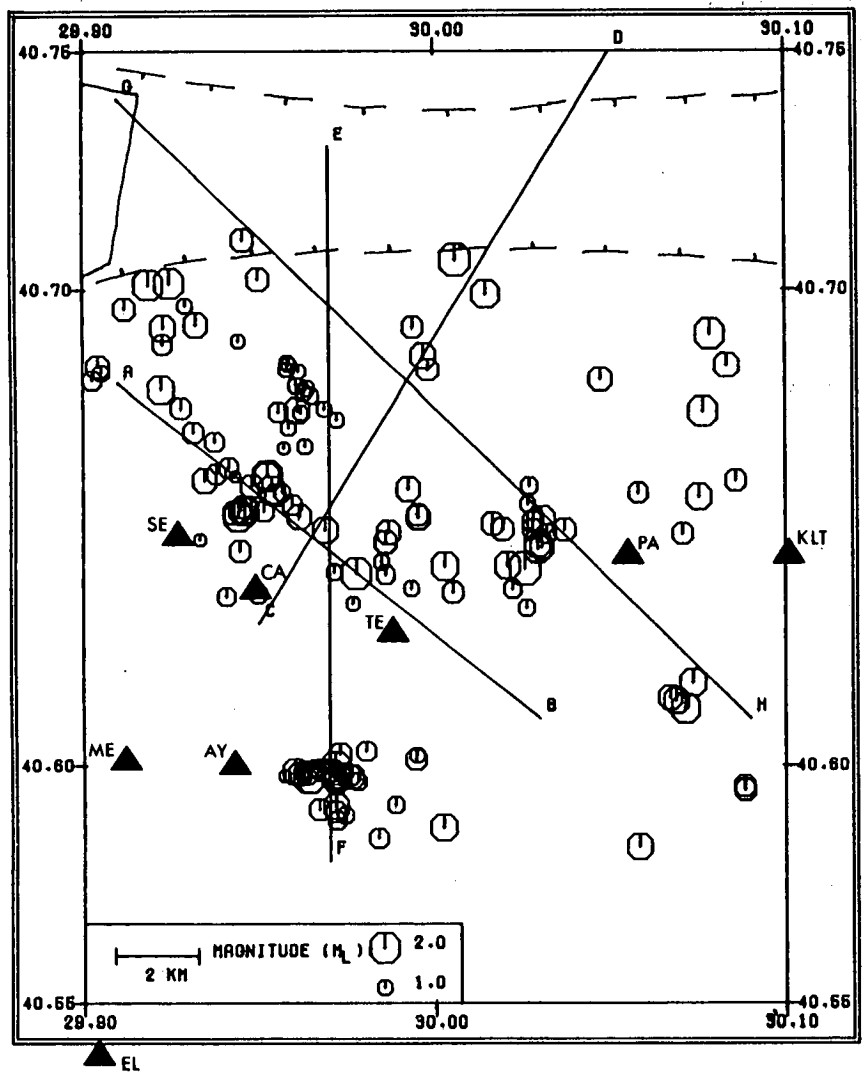
29.90
30.00
30.10
40.75
40.70
40.60
40.55
A
B
C
D
E
F
G
H
SE
CA
TE
PA
KLT
ME
AY
EL
MAGNITUDE (M_L)
2.0
1.0
2 KM

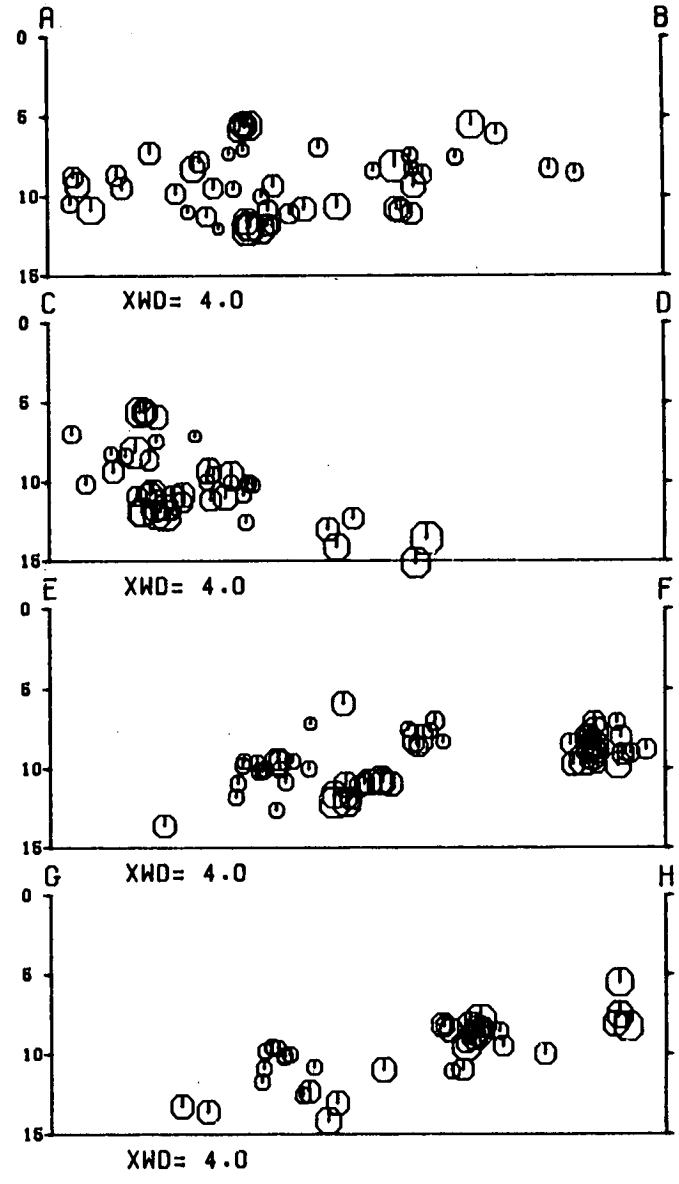
A
B
C
D
E
F
G
H
0
5
10
15
XWD= 4.0
XWD= 4.0
XWD= 4.0
XWD= 4.0

emphasis should be placed on these locations, as they occur mainly outside the network, but it is encouraging that not only does this solution represent a statistically superior fit to the data, but that the locations appear to define more detail.

In summary, of the three solutions for anisotropic structure obtained by inversion of the TDP1 data sets, only one of these, F30, produces a suite of relocations of all the TDP1 events that have superior average hypocentral and RMS errors, and where the F-ratio indicates that the improvement is statistically significant at more than the 95% confidence level. The two hexagonal solutions that we consistently obtained produce a suite of relocations with average errors that are worse than those of an isotropic model. A possible interpretation of these two solutions is revealed by re- examination of the inversion of synthetic data generated through an isotropic structure with a dipping interface (model B, Appendix D). In that case, inversion for a structure with hexagonal symmetry produces two solutions for the orientation of an axis of rotational symmetry, each symmetric about the horizontal and displaying strong anisotropic variations. This is very similar to the two hexagonal solutions here. However, in the synthetic case, the RMS error associated with these solutions were not superior to the isotropic solution, and an isotropic structure was obtained when we used GKLF1 as the initial model. This is contrary to what we observe here. Nevertheless, we must remember that we are inverting real data with unknown errors, and we are assuming a homogeneous half-space, and using a simple inverse scheme that does not provide any information on how well particular parameters are resolved. The fact that the estimated and the RMS errors of these solutions are less than the corresponding isotropic solutions, may reflect the fact that the structure is anisotropic, and that the solutions may be accounting for some of the variations. We therefore suggest that these two solutions represent numerical solutions only, and possibly reflect the deficiencies in our

Table 7.8 A summary of the average errors, and the overall RMS errors obtained by relocating a large subset of the TDP events in various velocity models. F-ratios of approximately 1.15 and 1.25 for the TDP1 locations indicate a statistically significant improvement in the fit to the data at the 95% and 99% confidence levels respectively. The corresponding values for the TDP2 locations are 1.1 and 1.2.

Reference	Number of events (arrivals)	Average RMS error	Average epicentral error	Average focal depth Error	Overall RMS error	F-ratio	Model
L1A	139 (1126)	0.0342	0.62	0.43	0.0534	____	Table 2.1 determined by HYPO71
L1B	139 (1114)	0.0338	0.62	0.40	0.0531	____	Isotropic half-space using F3 velocities in Table 7.3
L1C	138 (1106)	0.0349	0.65	0.46	0.0554	0.97	Solution F3D/F3F
L1D	139 (1114)	0.0366	0.58	0.42	0.0781	0.46	Solution F3C/F3E
L1E	139 (1114)	0.0327	0.61	0.41	0.0521	1.04	Solution F3G/F3I
L1F	139 (1114)	0.0289	0.56	0.41	0.0460	1.33	Solution F3O
L2A	199 (1839)	0.0682	0.66	0.63	0.1437	____	Table 2.1 determined by HYPO71
L2B	202 (1740)	0.0592	0.57	0.56	0.1076	____	Isotropic half-space using F4 velocities in Table 7.6
L2C	201 (1730)	0.0572	0.56	0.55	0.1041	1.07	Solution F4I

Table 7.8 (cont.)

Reference	Number of events (arrivals)	Average RMS error	Average epicentral error	Average focal depth Error	Overall RMS error	F-ratio	Model
L2D	201 (1730)	0.0496	0.48	0.51	0.0929	1.34	Solution F4L
L2E	198 (1709)	0.0532	0.45	0.50	0.0975	1.22	Solution F4M
L2F	200 (1718)	0.0566	0.59	0.56	0.1012	1.13	Solution F4N
L1G	139 (1114)	0.0320	0.58	0.40	0.0504	1.11	Hexagonal version of solution F30
L1H	136 (1093)	0.0337	0.62	0.45	0.0537	0.98	Solution F30 with principal axes interchanged
L2G	200 (1725)	0.0575	0.56	0.57	0.1029	1.09	Hexagonal version of solution F4L
L2H	202 (1740)	0.0602	0.56	0.55	0.1088	0.98	Hexagonal version of solution F4M
L1I	139 (1114)	0.0518	0.76	0.58	0.0828	0.41	TDP1 locations using solution F4L
L1J	139 (1114)	0.0531	0.66	0.57	0.0850	0.39	TDP1 locations using solution F4M
L2I	186 (1605)	0.0713	0.84	0.79	0.1397	0.59	TDP2 locations using solution F30

assumptions and in our inversion procedure. Note as well that there was no suggestion of any similar solutions from the inversion of the TDP2 data set. If we ignore the possibility of a temporal variation, this suggests that these solutions are peculiar to the TDP1 network, which again suggests poor network resolution.

However, to re-iterate, we have identified one solution that produces superior hypocentral parameters; is a statistically significant improvement over the isotropic models; and appears to produce hypocentres that display much more detail. We shall discuss the possible interpretation of this solution in section 7.7.3.

7.7.2 The TDP2 solutions

As with the TDP1 data sets, inversion of the single TDP2 data set defined several possible solutions for the anisotropic structure. We can investigate these solutions by using the respective models to relocate all the TDP2 events using the anisotropic half-space location program of Chapter 4. We initially modify the arrival-time data set by removing all arrivals that have been given a low weight; rejecting all arrivals at station HE; discarding those events with less than 6 arrivals, or with no shear-wave arrivals; and finally, we reject those events outside the network that the location program fails to determine. This reduces the number of events in the TDP2 data set to about 230. Fig.7.23 shows the epicentral locations of about 200 of these events in the centre of the network, from the original locations determined by HYPO71 using the crustal model in Table 2.1. The vertical sections through the hypocentres are in the same planes as those for the TDP1 events. The parameters of these locations are listed in Table 7.8 (reference L2A). Fig.7.24 shows the corresponding locations in an isotropic half-space with velocities corresponding to those determined by the isotropic inversion of data set F4 (Table 7.6). The locations have again been determined by the program that will be used to locate the events in an anisotropic half-space, using the

Figure 7.23 A map of the hypocentral locations of a reduced set of events from TDP2 determined by HYPO71 using the crustal model in Table 2.1. Format as in Fig.7.20.

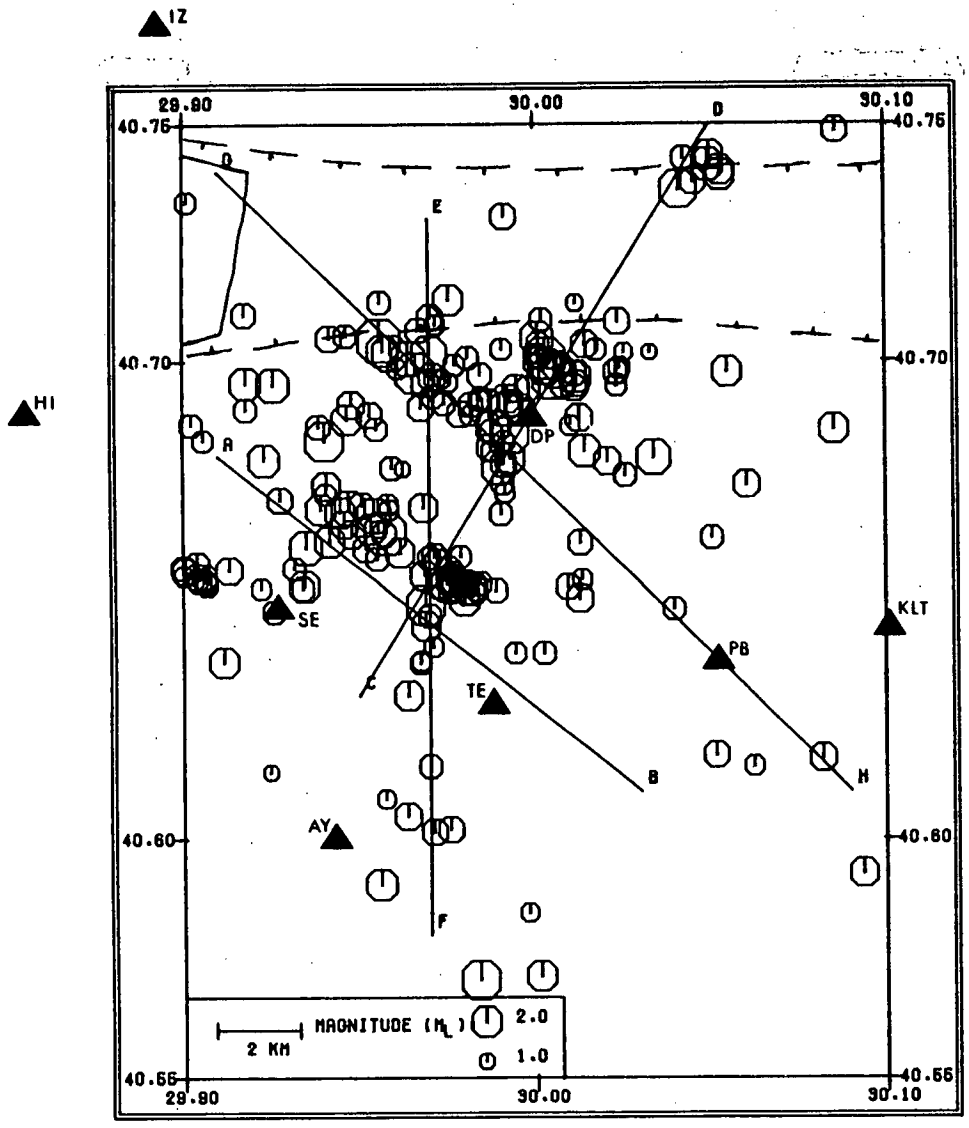
IZ
HI
29.80
30.00
30.10
40.75
40.70
40.60
40.55
A
B
C
D
E
F
G
H
DP
SE
PB
KLT
TE
AY
2 KM
MAGNITUDE (M_L)
2.0
1.0

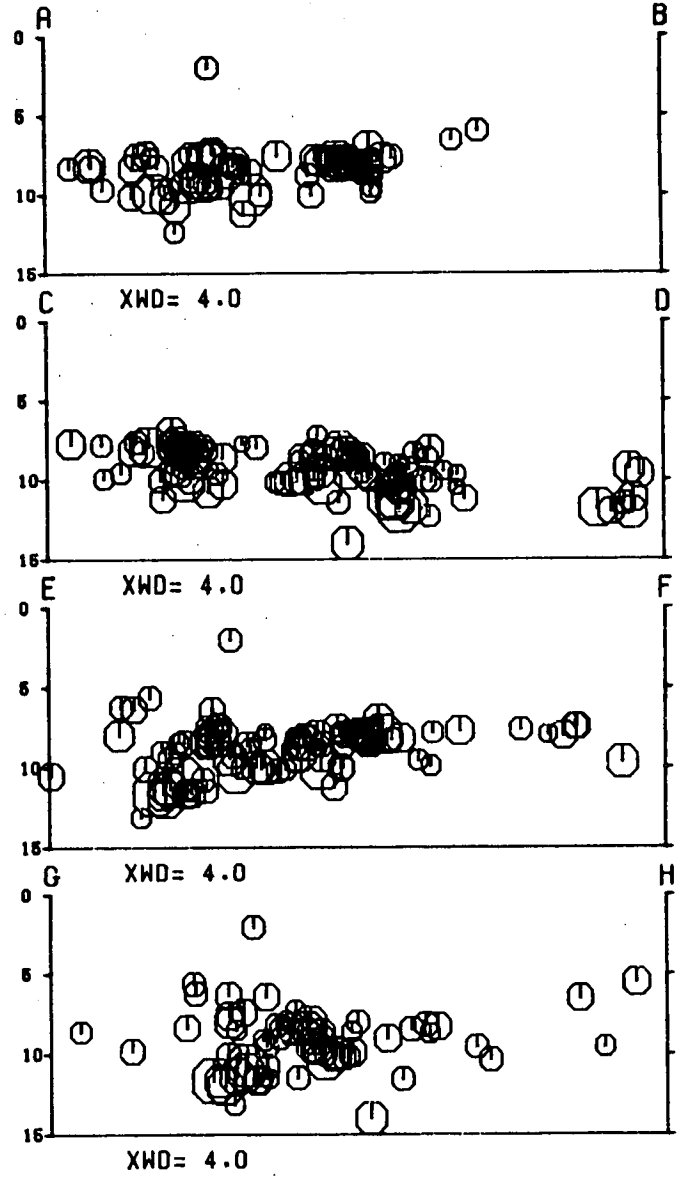
A
B
C
D
E
F
G
H
0
5
10
15
XWD= 4.0
XWD= 4.0
XWD= 4.0
XWD= 4.0

Figure 7.24 A map of the hypocentral locations of a reduced set of events from TDP1 determined by the anisotropic half-space location program using an isotropic model with P- and S- velocities corresponding to those determined by inversion of data set F4 (Table 7.6). Format as in Fig.7.20.

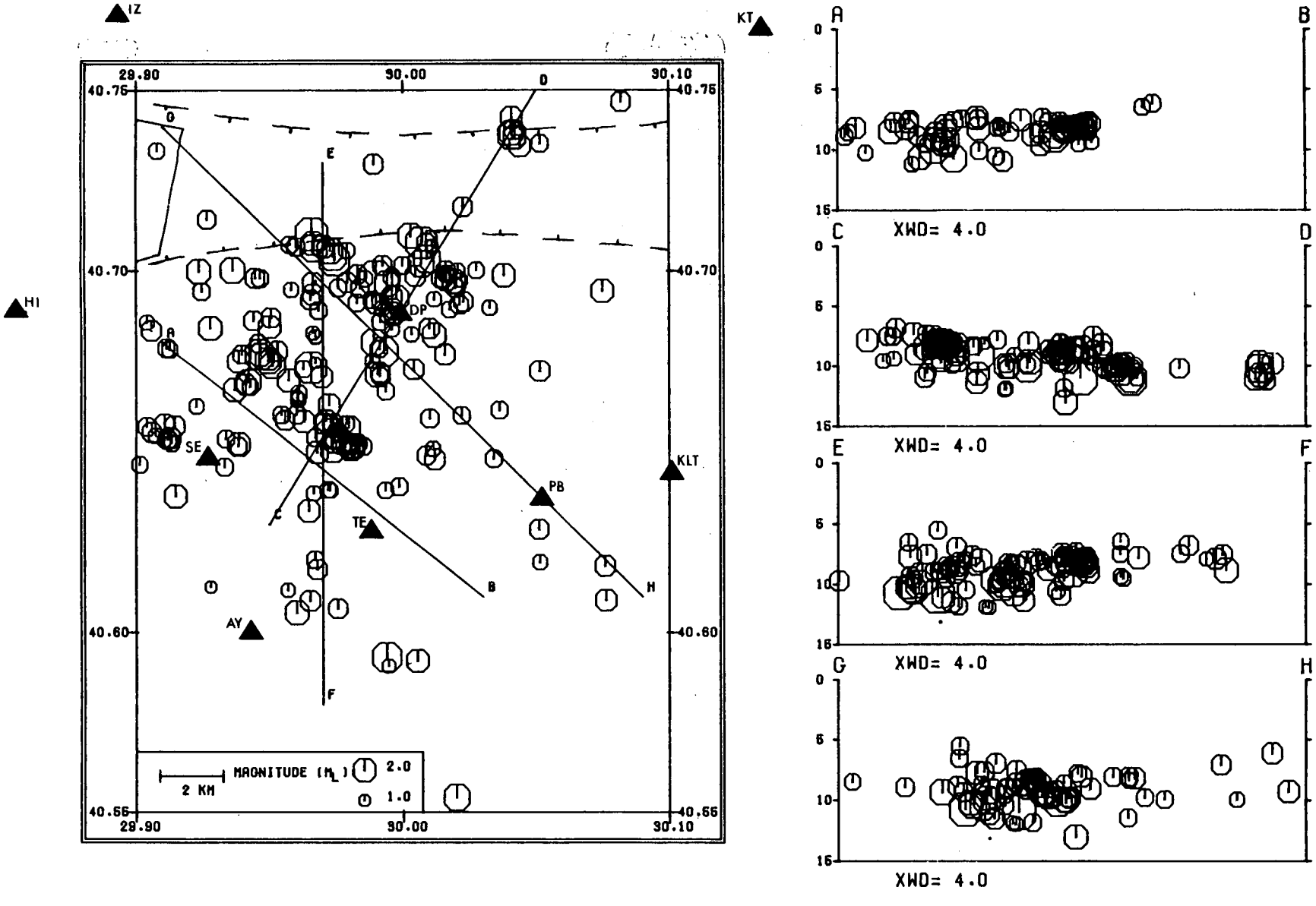
IZ
KT
HI
29.80
30.00
30.10
40.75
40.70
40.60
40.55
SE
DP
TE
PB
KLT
AY
A
B
C
D
E
F
G
H
2 KM
MAGNITUDE (M_L) 2.0
1.0
0
5
10
15
XWD= 4.0
XWD= 4.0
XWD= 4.0
XWD= 4.0

same arrival-times, and the same trial hypocentres (i.e. those from Fig.7.23). The parameters of these locations are referenced L2B in Table 7.8. The removal of the poorer arrivals has resulted in a decrease in the RMS and hypocentral errors, and a substantial improvement in the overall RMS error. This process has also caused a northward shift in the epicentres. Notice that the cross sections only indicate a very shallow dip to the north, as opposed to the very marked dip in the TDP1 locations. This was clearly an effect of poor resolution with the TDP1 network.

As with the TDP1 data set, we shall use the F-test to estimate the significance of any improvement in the locations by using the anisotropic models. We shall compare the anisotropic solutions with the isotropic solutions with the lowest overall RMS error (i.e. the half-space solution, L2B). There are approximately 900 degrees of freedom with this data set, and so F-ratios of approximately 1.1 and 1.2 indicate a significant improvement at the 95% and the 99% confidence levels respectively.

The first model that we shall consider is solution F4I, which indicated an axis of rotational symmetry at an orientation of -41,58. This model produces a set of relocation parameters referenced L2C in Table 7.8. There has been a slight reduction in the average RMS and hypocentral errors, but the overall RMS error indicates that the improvement is not statistically significant at the 95% level. The orthorhombic solutions, F4L, F4M and F4N produce the relocation parameters referenced L2D, L2E and L2F, respectively in Table 7.8. Of these, only the solutions F4L and F4M produce a set of relocation parameters with improved average errors and represent a statistically significant improvement in the fit to the data. In addition, an F-ratio of 1.1 indicates that solution F4L is statistically superior to solution F4M, although the latter has lower estimated hypocentral errors. Figs.7.25 and 7.26 show the epicentral locations determined in these two models, together with vertical sections through the hypocentres. Both models tend to increase the epicentral clustering and

Figure 7.25 A map of the hypocentral locations of a reduced set of events from TDP1 determined by the anisotropic half-space location program using an anisotropic model corresponding to solution F4L in Table 7.7. Format as in Fig.7.20.

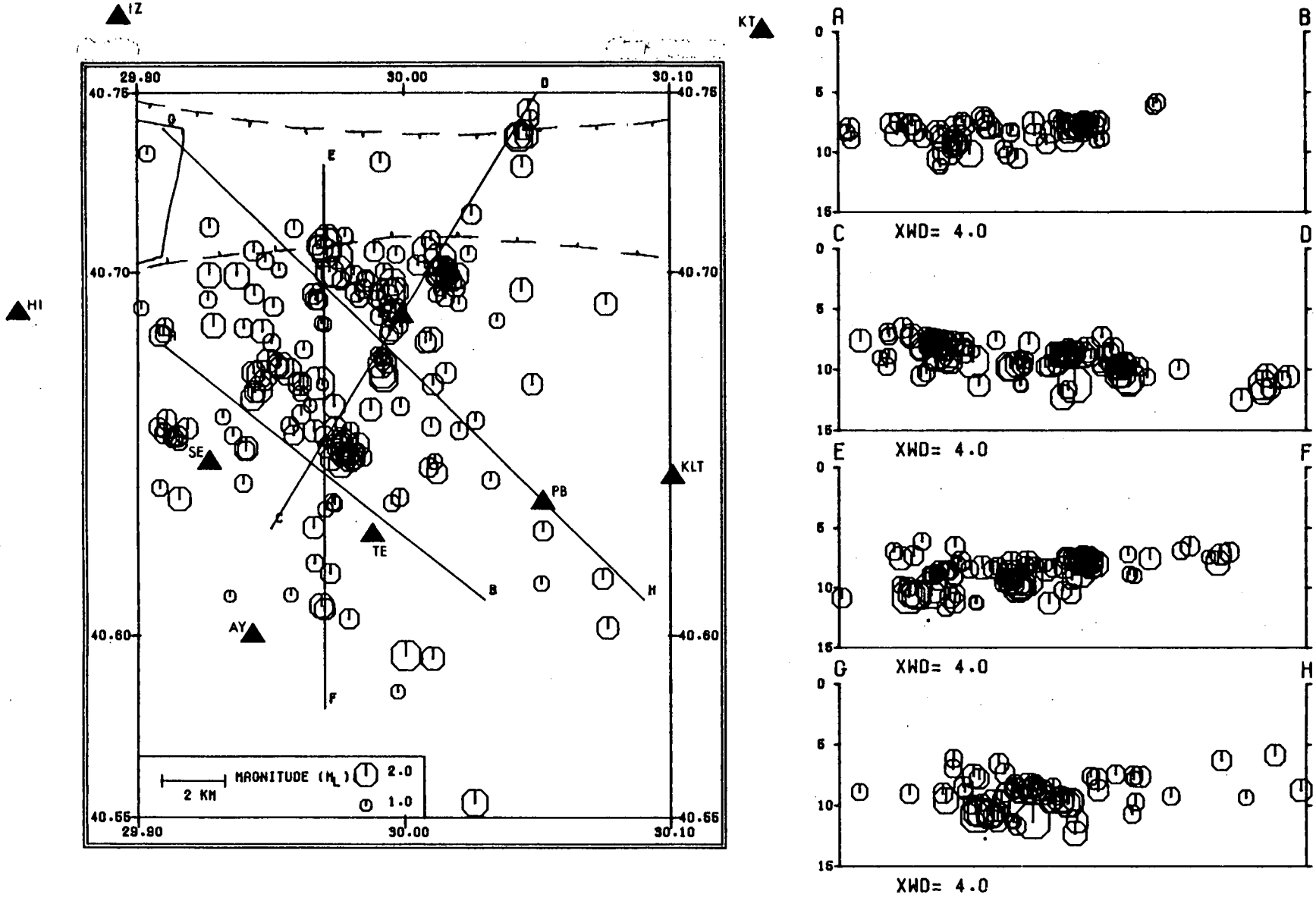
IZ
KT
HI
29.90
30.00
30.10
40.75
40.70
40.60
40.55
A
B
C
D
E
F
G
H
SE
TE
PB
KLT
AY
2 KM
MAGNITUDE (M_L)
2.0
1.0
0
5
10
15
XWD= 4.0
XWD= 4.0
XWD= 4.0
XWD= 4.0

Figure 7.26 A map of the hypocentral locations of a reduced set of events from TDP1 determined by the anisotropic half-space location program using an anisotropic model corresponding to solution F4M in Table 7.7. Format as in Fig.7.20.

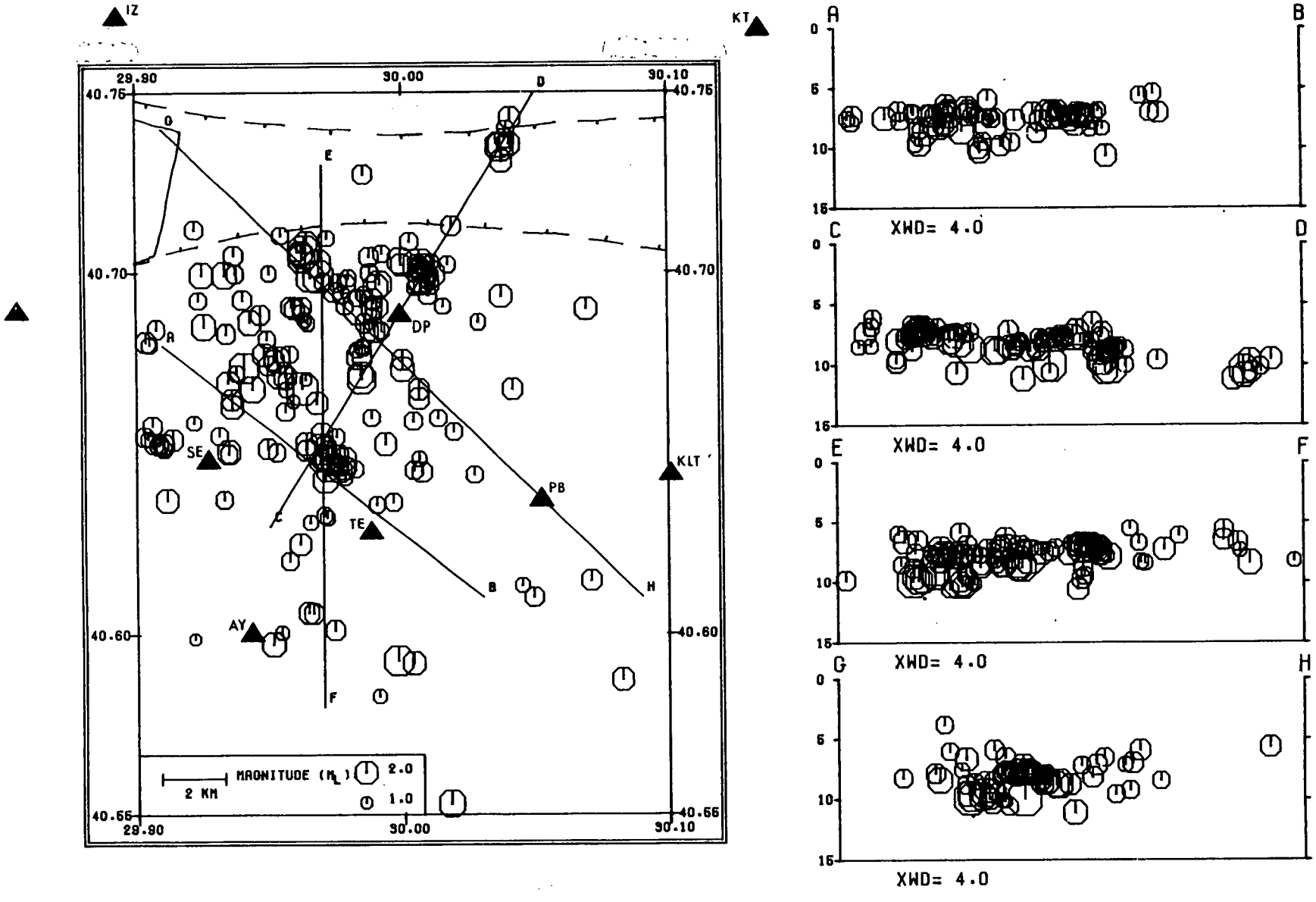
IZ
KT
29.90
30.00
30.10
40.75
40.70
40.60
40.55
D
E
C
DP
A
SE
KLT
PB
TE
B
H
AY
F
MAGNITUDE (M_L)
2.0
1.0
2 KM
A
B
C
D
E
F
G
H
XWD= 4.0
XWD= 4.0
XWD= 4.0
XWD= 4.0
0
5
10
15

reduce the spread of the focal depths when compared to both isotropic models. Notice in particular, the crescent-shaped pattern of the epicentres, 2km to the north-east of station SE in Fig.7.25. This feature is apparent in the locations in the other models, but nowhere is it as clear as in this case. We should not place too much emphasis on the fact that the hypocentres tend to cluster more tightly when an anisotropic model is used to locate the events. The estimated errors in the isotopic locations would be such that clusters on this scale could be considered as being from the same source. However, as with the TDP1 relocations, it is encouraging that an anisotropic model produces locations, not only with superior statistical parameters, but which also appears to provide a clearer definition of possible structural features.

In summary, although all four solutions obtained by inversion of the TDP2 data set produce a suite of 200 locations with a statistically significant improvement in the fit to the arrival-time data, only two of these, F4L and F4M, have superior estimated errors and also seem to produce clearer hypocentral locations. However, solution F4L is statistically superior to solution F4M. We shall consider the interpretation of these two solutions in terms of dilatancy-anisotropy in more detail in the following section.

Before discussing the possible interpretation, it would be informative to examine various approximations to the three solutions from TDP1 and TDP2 in order to investigate how well-constrained they are. Of the three elastic constants in solution F30 defining P-wave velocity along a principal axis, (C11, C22 and C33), only C22 is statistically distinct - being more than two standard errors away from each of the others. This means that, at least for P-waves, we cannot strictly say that this solution is statistically different from a hexagonal solution (this is a very similar feature to that which we observed in the inversion of model I, Appendix D). As a first test, we can convert this model to a hexagonal

solution with an axis of rotational symmetry at an orientation of 73,47. The parameters of the relocations are referenced L1G in Table 7.8. This solution is almost superior to the isotropic solution L1B at the 95% confidence level, but is statistically inferior to the orthorhombic solution at the same level of confidence (an F-ratio of 1.2). We can also rotate the solution so that the constants C11 and C33 are interchanged (with corresponding rotations for the other elastic constants). The relocations parameters in this case are referenced L1H in Table 7.8, and they indicate that the solution is no better than the isotropic solutions. We can perform similar tests on the two TDP2 orthorhombic solutions. In these cases, only the elastic constant C11 is statistically distinct. However, this is not strictly correct because the elastic constants that determine shear-wave velocity along the principal axes are statistically distinct. A hexagonal version of these solutions produces a suite of location parameters referenced L2G and L2H in Table 7.8. We can see that both solutions are inferior to the orthorhombic solutions, and that one is actually worse than the isotropic half-space approximation. This demonstrates that in these models, the shear-wave surfaces play an important role in improving the fit to the arrival-times. These tests indicate that the solutions determined by the inversion programs represent the best fit to the data despite the errors associated with each of the parameters.

It would be interesting to interchange these solutions and try locating the TDP1 events with the solutions determined from TDP2, and vice-versa. The parameters of the TDP1 locations using models F4L, and F4M are referenced L1I and L1J in Table 7.8. The parameters of the TDP2 locations are referenced L2I in the table. We can see that these results suggest that the models are not interchangeable, (at least, not in exactly the same form), and that the solutions are only valid for the particular networks and data sets. This is probably a reflection of the fact that a

half-space is not a good approximation to the TDP2 structure, and that the anisotropic variations in this case are likely to masked to some extent by lateral variations, and the solution will have been modified.

Finally, it is necessary to consider how much reliance can be placed on these orthorhombic solutions. Re-examination of the solutions obtained for the orthorhombic models in Appendix D, suggests that we can only be certain about the orientation of the principal axes in these solutions, and the nature of the P-wave variations. In model I, the shear-wave surface was not well-determined, and there was a large departure of the P-wave surface. For the shear-wave surfaces in particular, we are inverting group-velocity arrivals with a program that calculates phase-velocities. However, it was demonstrated that for model F4L the shear-wave surface has significant influence in improving the fit to the data.

7.7.3 Possible interpetations in terms of dilatancy-anisotropy

We have identified three possible solutions for the anisotropic structure, one from TDP1 and two from TDP2. These solutions are not only indicated by the joint-inversion procedure devloped in Chapter 6, they also produce statistically superior locations. In addition, the locations in each model appear to display clearer patterns than those in the isotropic models. The anisotropic models are clearly taking account of some variation in the structure. In this section we will attempt to interpret the solutions in terms of dilatancy-anisotopy. We shall consider solutions F30 and F4L, (being the 'best' solutions from TDP2), in detail and briefly discuss the other solutions.

The velocity-surfaces, in each symmetry plane, of the two solutions are shown in Fig.7.27. The most obvious feature of these solutions, is that the form of the P-wave surface in each case, and the form of the shear-wave surfaces to a certain extent, are very similar. The apparent differences between the two solutions may be the result of the masking effect of lateral variations in the case of solution F4L, and poor network

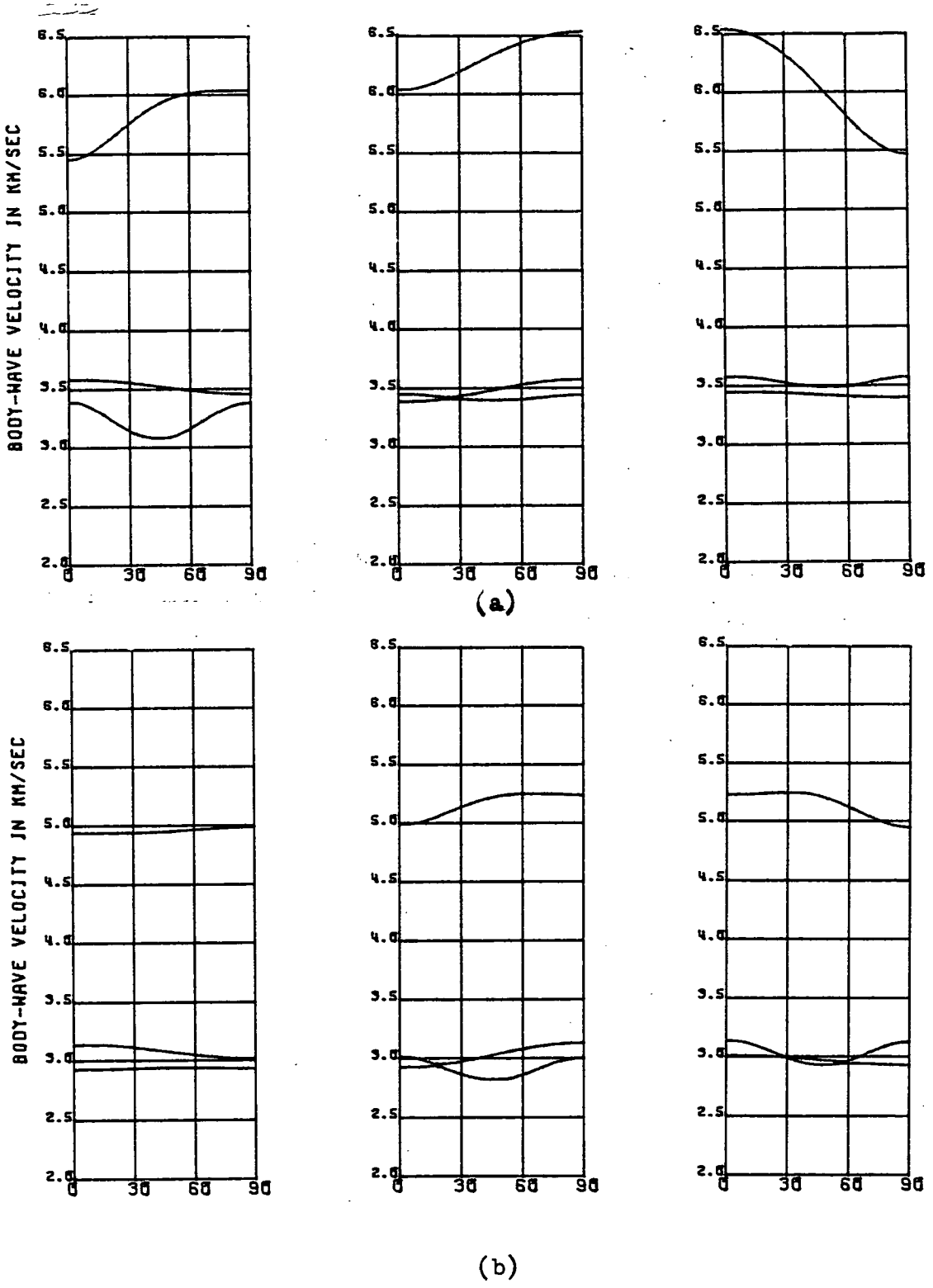

Figure 7.27 Sections through the velocity-surfaces of:
(a) solution F30 (Table 7.3),
(b) solution F4L (Table 7.7).
Using the terminology of Fig.3.2, the sections are, from left to right; a section perpendicular to the direction of crack intersections; a section parallel to the major crack system; a section parallel to the minor crack system.

resolution in the case of TDP1. Both solutions indicate a 2θ P-wave variation, which is characteristic of a dry crack system. The P-wave variation is much greater than the shear-wave variation and this is another characteristic of wave propagation through a dry crack system. There are several possible explanations for this feature. Any one of the limitations in our inversion procedure, discussed at the beginning of this section, could explain why we observe a 2θ variation. In addition, there are several other reasons why we might appear to observe such a variation, or why the cracks may indeed be dry.

1) The 4θ P-wave variation in the saturated crack systems may be an artefact of the modelling procedure which is based on seismic-wave propagation through infinitesimally thin, penny-shaped cracks. Cracks in the Earth are unlikely to be so regular and may be wide enough to invalidate the assumption. The 4θ P-wave variation is a reflection of the fact that the compressional component of stress, normal to the crack faces, is continuous across a saturated crack, but is not continuous across a dry crack (Garbin & Knoppoff, 1975). If the cracks are wide, there may be little transmission of compressional stress across the crack, even though they are still saturated, and we would only see a 2θ variation. It is not known how wide the cracks would need to be in order to invalidate the modelling procedure. However Crampin, McGonigle & Bamford (1980) observed a 4θ P-wave variation due to aligned, saturated cracks which had crack densities of up to 0.25 (Equation 3.1). It is difficult to see how cracks of even greater dimensions could be maintained at depth in the Earth.

2) Toksöz et al. (1979) suggest that the TDP area may be a seismic gap with a potential for an earthquake of magnitude 6 or more. This is supported by Evans et al. (1982) who suggest that this branch of the fault represents the true extension of the North Anatolian Fault, and so major earthquakes can be expected here. Using the well known precursor

time/magnitude relations (Kasahara, 1979), we expect the dilatancy process to occur over approximately 1.5 and 9 years for magnitude 6 and 7 events respectively. Therefore we could tentatively suggest that the dry crack system might be part of a dilatancy-diffusion episode precursory to a magnitude 7 earthquake. However, there is no other evidence to substantiate this, and it is only mentioned as a possibility.

3) Gold (1979) suggests that cracks at depth in the Earth may be maintained by high gas pressure. This would mean that the cracks are effectively dry to seismic-waves.

Table 7.9 lists the directions of azimuth and dip of the principal axes of the solutions in terms of whether they indicate high, intermediate or low velocities. In addition, we have also indicated the direction of the P, null and T axes of the composite fault plane solution shown in Fig.2.6 (labelled CFPS1). This has been expressed in terms of whether we anticipate high, intermediate or low velocities along these directions, in a dry crack system. We can immediately see that solutions F30 and F4L are oriented in a very similar fashion, and that they both indicate low velocities within approximately 15 degrees of the T axis of the fault plane solution. The directions of high velocities in both solutions are within 20 degrees of each other, but these directions are more than 70 degrees away from the direction of maximum velocities as suggested by the orientation of the P-axis. In fact, the high velocity directions are within 20 degrees of the null axis, and the intermediate velocities are within 20 degrees of the P-axis. We know that rotating solution F30 so that the intermediate and high P-wave velocity directions are interchanged, produces a suite of locations with inferior statistical parameters. We can therefore be reasonably sure that this orientation of the principal axes is not an artefact of the inversion procedure. Therefore, the two solutions cannot be conclusively related to the stress axes of the composite fault

Table 7.9. A summary of the directions of the stress axes determined from two composite fault-plane solutions, (CFPS), of the TDP2 events, and the principal axes of solutions obtained by the joint-inversion of various TDP data sets for anisotropic structure. Each direction is given as corresponding to high, intermediate or low velocities in a dry crack structure. The labels of each velocity solution are from Tables 7.3 and 7.7. Dip is positive below the surface.

Solution	High		Intermediate		Low	
	Azimuth	Dip	Azimuth	Dip	Azimuth	Dip
CFPS1	N112E	-29	N137E	58	N27E	12
F30	N114E	45	N90E	-43	N12E	12
F4L	N141E	45	N90E	-32	N19E	28
CFPS2	N175E	36	N150E	-51	N76E	12

plane solution. However, there are several possible explanations of this effect.

1) The North Anatolian Fault is a dominantly tensional feature, (it is a graben in the TDP area), and so it is encouraging that both solutions indicate low velocities close to the T-axis. It is difficult to envisage a mechanism where the minor crack system opens perpendicular to the direction of maximum compressive stress. However, as the area is dominantly tensional, we might expect the other directions to be particularly effected by pre-existing rock fabric.

2) We are sampling a structure that is very close to a major fault zone, and this may have a modifying effect on the orientation of dilatancy-anisotropy in its immediate vicinity.

3) We should not assume that the dilatancy-anisotropy is homogeneous from the surface to the source region at a depth of 10km. It could be argued that it is likely that the high confining pressure at such a depth would preclude the existence of dry cracks. If the zone of anisotropy lies closer to the surface than the source region, then we should not assume that the stress system responsible for the earthquakes at a depth of 10km, is exactly the same as that at a depth of, say, 5km. However, the whole structure would still be dominated by the tensional component, and this fits well with our results.

4) Another possible factor has recently come to light from the work of Evans and Asudeh (1982) on fault plane solutions. They have identified a sequence of 10 events that appear to have a slightly different mechanism from that shown in Fig.2.6. A composite fault plane solution of these events is shown in Fig.7.28 and the orientation of the stress axes are referenced CFPS2 in Table 7.9. We can see that the stress axes bear little relation to the principal axes of the orthorhombic solutions. It is not known at this stage whether this indicates a temporal or spatial variation in the orientation of the stress axes.

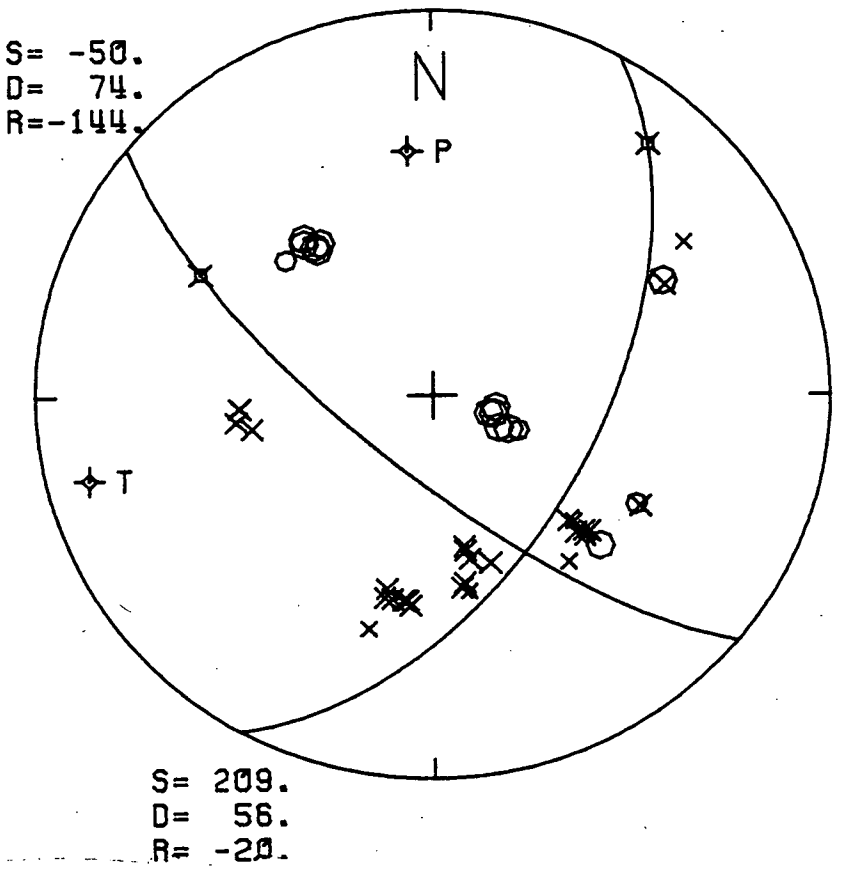

Figure 7.28 A composite fault-plane solution of the P-wave first motions of 10 events that are not consistent with the solution shown in Fig.2.6. Notation and format as in Fig.2.6. (Courtesy of Evans et al. 1982).

However it demonstrates that the orientation of the stress axes determined from fault plane solutions can vary, and may not reflect the orientation of dilatancy-anisotropy. Of this set of 10 events, five were included in data set F4, which we inverted for anisotropic structure.

Finally we should mention the other three solutions determined from the inversion of the TDP2 data set. (We have already suggested a reason for the other apparent solutions from TDP1). The velocity variations of the other TDP2 solutions are very similar to those in the solutions discussed above (see Figs.7.18e and 7.19). The hexagonal solution, F4I, is at similar orientation to one of the principal axes of the orthorhombic solution F4L, and so is similar to those hexagonal solutions obtained by inversion of synthetic data generated through the orthorhombic models in Appendix D. The two other orthorhombic solutions, F4M and F4N, although displaying similar velocity variations, are oriented differently, and produce statistically inferior locations. This is similar to the effect we observed in the hexagonal models C and G in Appendix D. In these cases the inversion defined secondary minima which had reasonably similar velocity variations but were oriented differently, and were statistically inferior to the correct solution. We therefore suggest that these solutions represent secondary minima in solution space.

7.8 Summary

The joint-inversion of the TDP data sets for anisotropic structure and hypocentral locations defines several hexagonal and orthorhombic solutions that appear to be statistically superior to the solution obtained by inversion of the same data sets for isotropic structure. Of these only one solution, F30, from TDP1 produces statistically superior hypocentral locations for a set of 140 events. The other two solutions from TDP1 can be dismissed as being an effect of poor network resolution when using real

data, and possibly reflect lateral variations in the structure. Four of the solutions from TDP2 produce statistically superior hypocentral locations for a set of 200 events. However, there is one solution, F4L that is statistically superior to both the isotropic and the other anisotropic solutions. This solution is similar to solution F30 from TDP1. The other solutions from TDP2 can be dismissed as being secondary minima in solution space.

The two solutions, F30 and F4L, display similar variations and are oriented within 20 degrees of each other. This orientation is within 20 degrees of the stress axes determined from a composite fault plane solution shown in Fig.2.6. The solutions indicate a dry, biplanar crack system with low velocities close to the direction of least compression. However, the solutions indicate high velocities in the direction of intermediate compression, and intermediate velocties along the direction of maximum compression. This may be due to complicated variations in the stress field, the presence of the North Anatolian Fault, differences in the orientation of the stress system with depth, or the effect of pre-existing rock fabric.

CHAPTER 8

CONCLUSIONS

Two micro-earthquake surveys (TDP1 and TDP2) were conducted on a section of the North Anatolian Fault in Western Turkey. Analysis of the three-component seismograms and polarisation diagrams identified clear and consistent observations of shear-wave splitting. Shear-wave splitting is strongly indicative of seismic-wave propagation through an anisotropic structure. The most likely mechanism to cause such anisotropy in seismic regions is the preferential alignment of pre-existing cracks under the action of a deviatoric stress system. This dilatancy-anisotropy is not necessarily related to an impending major earthquake, but may merely be a reflection of the ambient stress field.

Failure to model the anisotropic velocity variations when locating earthquakes can result in systematic mislocations of hypocentres of up to 20% of the average path length through the structure, and is particularly pronounced when only P-arrivals are used and when a network of irregular geometry is employed. Even location with a highly regular network can lead to large mislocations if the anisotropic variations are not symmetrical with the source/receiver geometry. In such cases, the normal tests of location quality, (i.e. the RMS error and the estimated hypocentral errors), do not provide any indication of the departure of the hypocentres from their true locations. In addition, changes in the nature and the orientation of the anisotropic variations, (such as in the precursory period to a large earthquake), may lead to apparent migrations of hypocentres. Such 'anomalous' earthquake locations have been observed many times in regions of possible dilatancy-anisotropy.

A simple modification to the location procedure, and the use of look-up tables containing anisotropic velocities and their directional derivatives, allows the accurate locations of earthquakes in a homogeneous,

anisotropic half-space. In general, this is only possible if shear-wave arrival-times are used in addition to the P-wave arrival-times, and if the hypocentres determined under the assumption of isotropy are used as trial solutions. It is possible to introduce further modifications into the location procedure and exactly model the effect of an isotropic layer above the anisotropic half-space. This is achieved at the expense of a five-fold increase in computation time compared to the half-space case. However, it is possible to model the effect of a known, thin, isotropic layer by introducing extra station corrections, and assuming the structure to be an anisotropic half-space. The major problem with these location programs, (as with all location procedures), is that they require accurate information on the velocity structure, and in this case, on the nature and the orientation of the anisotropic variations.

There are several methods that may allow the detailed identification of the anisotropic variations. The most sensitive appears to be from the analysis of shear-wave polarisations and delays (Crampin & McGonigle 1981). It was demonstrated that the more usual method of analysing the azimuthal variation of travel-time residuals, may provide no indication of dilatancy-anisotropy, particularly if only P-arrivals are used to locate the hypocentres with an irregular network. The use of a regular network, and incorporating shear-waves into the location procedure, may at best (if the anisotropic variations are of sufficient amplitude and are conveniently oriented), only provide an indication of high and low velocity directions, and would certainly not provide sufficient information on the three-dimensional variations to employ in any location procedure.

However, it was demonstrated that it is possible to invert suites of earthquake (P- and S-) arrival-times for both the hypocentral locations and the parameters that describe seismic-wave propagation through an anisotropic half-space. This was possible with a small network, with only

a few stations, and using an event distribution which possessed very large azimuthal gaps - certainly far from ideal. The inversion procedure is very dependent on the initial model and a large number of inversions from various starting positions are required. It was demonstrated that convergence to very reasonable solutions can be achieved by employing a combined approach of searching parameter space and by least-squares inversion from the various starting models. The method is limited by the assumption of a half-space, the lack of any data or parameter weighting, and by the lack of any information concerning the resolution with which various parameters are determined.

Inversion of real data from each TDP experiment defined several possible solutions for the anisotropic structure in each case. This may reflect deficiencies in the inversion procedure and in the assumption of a half-space. It was demonstrated that it is possible to reduce this number of solutions by using each model to relocate all the events in each experiment and by comparing the quality of the fit to the data with the locations in an isotropic model. This method reduces the number of solutions from each experiment to a single, orthorhombic structure which is also statistically superior to the other anisotropic solutions. These solutions are very similar and have principal axes close to the directions of the stress axes of a composite fault-plane solution - as we would expect for stress induced dilatancy-anisotropy. In addition, both solutions indicate a low velocity direction close to the direction of least compression, which is also what we would expect. However, the solutions indicate high and intermediate velocities along the null axis and the P-axis of this fault-plane solution. This is contrary to what we would expect but may be the result of spatial or temporal variations in the stress field, amongst other possibilities.

CHAPTER 9

SUGGESTIONS FOR FURTHER WORK

There are several developments in this thesis that require further improvement and analysis. We need to know more about the structure of the TDP area. A possible technique is that of Aki & Lee (1978), later developed by Hawley et al. (1981), in order to determine any lateral variations in the structure. This new information may be introduced into the anisotropic inversion procedure by suitable modification of the station corrections. For the TDP2 network, in particular, it may be necessary to have station corrections that are dependent on the source region. However, we must remember that the anisotropic variations are likely to influence any results obtained under the assumption of isotropy. It would also be of interest to compare the quality of the solution for a more complicated isotropic structure with that obtained in this thesis for an anisotropic half-space.

The anisotropic location programs of Chapter 4 ideally require the introduction of some scheme for weighting arrivals if they are to be used on a routine basis for locating real events. The layered location program could be expanded to include more isotropic layers and to incorporate refracted phases. However, in this case, we would really need to consider methods of improving the efficiency of the program. One obvious way is to reduce the number of iterations required to calculate the direct wave by relaxing the criteria for convergence. Ideally we would need to perform numerical tests to find an optimum value for the convergence test that also minimised the errors. Secondly we could investigate the use of look-up tables to assist in the calculation of the direct wave. Both location programs can be easily modified to incorporate shear-wave delays. This may result in better constrained hypocentres if we have accurate information on the anisotropic variations. In addition it would be interesting, and

possibly of future use, to undertake network resolution studies, in a similar way to that of Peters & Crosson (1972), and Buland (1976), to investigate the optimum network geometry necessary to accurately locate earthquakes in regions of possible dilatancy-anisotropy.

The inversion programs of Chapter 6 also need to be made more efficient. It is difficult to see how this can be achieved as the most time-consuming aspect of the inversion is also the most fundamental. However, inversion of the normal equation matrix for error estimates accounts for 10% of the CPU time, and these may not be required in the early stages of the inversion procedure. We most definitely require a program that calculates group-velocities through an orthorhombic structure. This would be very expensive to use, but may only be required to check solutions obtained using the phase-velocity approximation, and to improve the solution for the shear-wave surfaces. A system of arrival-time weighting may improve the interpretation of the inversion of real data, and may help to remove the effect of poor network resolution observed with the TDP1 data. This would ideally require the addition of another large matrix to the program, probably at the expense of some degrees of freedom, but it may be sufficient to just reduce the weighting assigned to all the shear-arrivals in comparison to the P-arrivals. Other possible improvements include the introduction of parameter weighting (not all elastic constants have the same effect on the structure), and the adoption of the Generalised Inverse procedure to provide resolution information. Finally we could undertake further synthetic studies such as introducing lateral variations into the anisotropic half-space. The most interesting would be to consider two welded quarter-spaces with <u>different</u> isotropic properties, but with the <u>same</u> anisotropic variations superimposed. This is likely to be a more realistic approximation of the structure in a major fault zone.

Further work can be done with the TDP data, particularly the TDP2 data. In this case, inversion of data set that include shear-wave delays is an obvious necessity, together with different data sets. A more detailed analysis of the locations in the anisotropic models can be undertaken to see if the clustered events are from the same source and that this is not an effect of the anisotropic variations coupled with the effect of phases recorded at different stations; or if the linear trends that are more apparent in the anisotropic locations are related to any structural features. We could use the locations determined in the anisotropic models to recalculate fault-plane solutions and the variation of shear-wave polarisations to see if they help to provide a clearer interpretation. In addition, we could use the models to calculate the theoretical variation of shear-wave polarisations and delays. However, not too much emphasis should be placed on this analysis as the shear-wave polarisations will be critically dependent on group-velocity propagation. We could also attempt to invert these solution for crack density. However, we would ideally require information from the analysis of shear-wave polarisations and delays which would place a greater constraint on the anisotropic variations before undertaking such a detailed analysis.

Finally, it would be interesting to apply the inversion technique to the analysis of arrival-time data from other seismic regions. We would require a small, dense network of three component stations with as simple a basic structure as possible. This may provide information on whether such dilatancy-anisotropy, as appears to exist in the TDP area, is a general characteristic of most seismic regions.

REFERENCES.

Aggarwal, Y.P., Sykes, L.R., Simpson, D.W. & Richards, P.G., 1975. Spatial and temporal variations in ts/tp and in P-wave residuals at Blue Mountain Lake, New York: application to earthquake prediction. J. geophys. Res., 80, 718-732.

Aki, K. & Lee, W.H.K., 1976. Determination of three-dimensional velocity anomalies under a seismic array using first P-arrival times from local earthquakes. 1. A homogeneous initial model. J. geophys. Res., 81, 4381-4399.

Aki, K. & Richards, P.G., 1980. Quantitative Seismology: theory and methods. W.H. Freeman and Company, 932pp.

Bamford, D., Jentsch, M. & Prodehl, C., 1979. Pn anisotropy studies in northern Britain and the eastern and western United States. Geophys. J.R. astr. Soc., 57, 397-429.

Bamford, D. & Nunn, K.R., 1979. In situ seismic measurements of crack-anisotropy in the Carboniferous Limestone of North-West England. Geophys. Prosp., 27, 322-338.

Batzle, M.L., Simmons, G. & Siegfried, R.W., 1980. Microcrack closure in rocks under stress: direct observation. J. geophys. Res., 85, 7072-7090.

Bevington, P.R., 1969. Data reduction and error analysis for the physical sciences. McGraw-Hill, New York, 336pp.

Bowman, R. & Kisslinger, C., 1981. Changes in focal mechanism of small earthquakes before an Mb = 4.6 earthquake in the Central Aleutian seismic zone (Abstract). Earthquake notes, 52, p69.

Brace, W.F., 1978. Volume changes during fracture and frictional sliding: A review. Pure appl. Geophys., 116, 603-614.

Brady, B.T., 1975. Theory of earthquakes. II Inclusion theory of crustal earthquakes. Pure Appl. Geophys., 113, 149-168.

Bufe, C.G., Pfluke, J.H. & Wesson, R.L., 1974. Premonitory vertical migration of micro-earthquakes in Central California - evidence of dilatancy biasing ? Geophy. Res. Letts., 1, 221-224.

Buland, R., 1976. The mechanics of locating earthquakes. Bull. seis. Soc Amer., 66, 173-187.

Byerlee, J., 1978. A review of rock mechanics studies in the United States pertinent to earthquake prediction. Pure appl. Geophys., 116, 586-602.

Crampin, S & Fyfe, C.J., 1974. Automatic analysis of tape recordings from seismic networks. Geophys. J.R. astr. Soc., 39, 155-168.

Crampin, S., 1977. A review of the effects of anisotropic layering on the propagation of seismic-waves. Geophys. J.R. astr. Soc., 49, 9-27.

Crampin, S., 1978. Seismic-wave propagation through a cracked solid: polarisation as a possible dilatancy diagnostic. Geophys. J.R. astr. Soc., 53, 467-496.

Crampin, S., Evans, J.R., Üçer, S.B., Doyle, M., Davis, J.P., Yegorkina, G.V., & Miller, A., 1980. Observations of dilatancy-induced polarisation-anomalies and earthquake prediction. Nature, 286, 874-877.

Crampin, S., McGonigle, R. & Bamford, D., 1980. Estimating crack parameters from observations of P-wave velocity anisotropy. Geophys., 45, 345-360.

Crampin, S., Evans, J.R., Doyle, M. & Davis, J.P., 1981. Comments on papers about shear-wave splitting in dilatancy-induced anisotropy by I.N. Gupta and by A. Ryall and W.U. Savage. Bull. seis. Soc. Amer., 71, 375-377.

Crampin, S. & Kirkwood, S., 1981. Velocity variations in systems of anisotropic symmetry. J. Geophys., 49, 35-42.

Crampin, S. & McGonigle, R., 1981. The variation of delays in stress-induced polarisation-anomalies. Geophys. J.R. astr. Soc., 64, 115-131.

Crampin,S. & Evans, J.R., 1982. Earthquake prediction: a new physical basis. Nature, in preparation.

Crampin, S., Stephen, R.A. & McGonigle, R., 1982. The polarisation of P-waves in anisotropic media. Geophys. J.R. astr. Soc., in press.

Crosson, R.S., 1976. Crustal structure modelling of earthquake data. 1. Simultaneous least-squares estimation of hypocentre and velocity parameters. J. geophys. Res., 81, 3036,3046.

Das, S. & Scholz, C.H., 1981. Off-fault aftershock clusters caused by a shear stress increase. Bull. seis. Soc. Amer., 71, 1669-1675.

Engdahl, E.R. & Kisslinger, C., 1978. Seismological precursors to a magnitude 5 earthquake in the Central Aleutian Islands, in Earthquake Precursors (AEPS 2), ed. C. Kisslinger and Z. Suzuki.

Engdahl, E.R. & Lee, W.H.K., 1976. Relocation of local earthquakes by seismic ray-tracing. J. geophys. Res., 81, 4400-4406.

Evans, J.R., Asudeh, I. & Crampin, S., 1982. Crustal stresses in North Western Analtolia from micro-earthquake fault-plane solutions. Geophys. J.R. astr. Soc., in preparation.

Garbin, H.D. & Knopoff, L., 1975. Elastic moduli of a medium with liquid filled cracks. Q. appl. Math., 33, 301-303.

Gold, T., 1979. Terrestial sources of carbon and earthquake outgassing. J. petrol. Geol., 1, 3-19.

Griggs, D.T., Jackson, D.D., Knopoff, L. & Shreve, R.L., 1975. Earthquake prediction: modelling the anomalous Vp/Vs source region. Science, 187, 537-540.

Gupta, I.N., 1973a. Premonitory variations in S-wave velocity anisotropy before earthquakes in Nevada. Science, 182, 1129-1132.

Gupta, I.N., 1973b. Seismic velocities in rock subjected to axial loading up to fracture. J. geophys. Res., 78, 6936-6942.

Gupta, I.N., 1974. Dilatancy and spatial distributions of aftershocks. Bull. seis. Soc. Amer., 64, 1707-1713.

Haber, A. & Runyon, R.P., 1973. General Statistics. Addison - Wesley, London, 401pp.

Hadley, K., 1975. Azimuthal variation of dilatancy. J. geophys. Res., 80, 4845-4850.

Haimson, B.C., 1981. Large-scale testing of hydraulic fracturing. Geophys. Res. Letts., 8, 715-718.

Hawley, B., Zandt, G. & Smith, R.B., 1981. Simultaneous inversion for hypocentres and lateral velocity variations: and iterative solution with a layered model. J. geophys. Res., 86, 7073-7086.

Healy, J.H. & Peake, L.G., 1975. Sesimic velocity structure along a section of the San Andreas Fault near Bear Valley, California. Bull. seis. Soc. Amer., 65, 1177-1197.

Kasahara, K., 1979. Earthquake mechanics. Cambridge Univ. Press, 248pp.

Lee, W.H.K. & Lahr, J.C., 1975. HYP071(revised): a computer program for determining hypocentre, magnitude and first motion pattern of local earthquakes. U.S. Geol. Surv., Open File Rept., 75-311.

Lindh, A.G., Lockner, D.A. & Lee, W.H.K., 1978. Velocity anomalies: an alternative explanation. Bull. seis. Soc. Amer., 68, 721-734.

Lindh, A.G., Fuis, G. & Mantis, C., 1978. Seismic amplitude measurements suggest foreshocks have different mechanisms than aftershocks. Science, 201, 56-59.

McGonigle, R. & Crampin, S., 1982. A FORTRAN program to evaluate the phase and group velocities in an anisotropic solid. Computers and Geosciences, in press.

McNally, K.C., Kanamori, H. & Pechman, J.C., 1978. Earthquake swarm along the San Andreas Fault near Palmdale, Southern California, 1976-1977. Science, 201, 814-817.

Mjachkin, V.I., Brace, W.F., Sobolev, G.A. & Dieterich, J.H., 1975. Two models for earthquake forerunners. Pure Appl. Geophys., 113, 169-181.

Musgrave, M.J.P., 1970. Crystal acoustics. Holden-Day Inc., 280 pp.

Nur, A., 1972. Dilatancy, pore fluids and premonitory variations of ts/tp travel-times. Bull. seis. Soc. Amer., 62, 1217-1222.

Nur, A., 1975. A note on the consitutive law for dilatancy. Pure Appl. Geophys., 113, 197-206.

Nur, A. & Simmons, G., 1969. The effect of saturation on velocity in low porosity rocks. Earth Planet. Sci. Lett., 7, 183-193.

Osokina, D.N., Nikonov, A.A. & Tsvetkova, N.Yu., 1979. Modelling the stress field and kinematics of the San Andreas fault system. Tectonophys. 52, 647-663.

Peters, D.C. & Crosson, R.S., 1972. Application of prediction analysis to hypocentre determination using a local array. Bull. seis. Soc. Amer., 62, 775-788.

Robinson, R., Wesson, R.L. & Ellsworth, W.L., 1974. Variation of P-wave velocity before the Bear Valley earthquake of 24 February 1972. Science, 184, 1281-1283.

Rothman, R.L., Greenfield, R.J. & Hardy Jr., H.R., 1974. Errors in hypocentral location due to velocity anisotropy. Bull. seis. Amer., 64, 1993-1996.

Scholz, C.H., Sykes, L.P. & Aggarwal, Y.P., 1973. Earthquake prediction: a physical basis. Science, 181, 803-810.

Scholz, C.H. & Kranz, R., 1974. Notes on dilatancy recovery. J. geophys. Res., 79, 2132-2135.

Scholz, C.H. & Koczynski, T.A., 1979. Dilatancy-anisotropy and the response of rocks to large cyclic loads. J. geophys. Res., 84, 5525-5534.

Semenov, A.N., 1969. Variations in the travel-time of transverse and longitudinal waves before violent earthquakes. Izv. Acad. Sci. USSR, Phys. Solid Earth, (English translation), 4, 245-248.

Simmons, G. & Richter, D., 1969. Microcracks in Rocks, in Physics and Chemistry of Minerals and Rocks, pp105-137, ed. Strens, R.G.J., John Wiley, New York.

Sobolev, G.A. & Slavina, L.B., 1977. The spatial and temporal change of Vp/Vs before strong earthquakes in Kamchatka. Pure Appl. Geophys., 115, 1047-1060.

Spencer, C. & Gubbins, D., 1981. Travel-time inversion for simultaneous earthquake location and velocity structure determination in laterally varying media. Geophys. J.R. astr. Soc., 63, 95-116.

Spetzler, H.A., Sobolev, G.A., Sondergeld, C.H., Salov, B.G., Getting, I.C. & Koltsov, A., 1981. Surface deformation, crack formation and acoustic velocity changes in pyrophyllite under polyaxial loading. J. geophys. Res., 86, 1070-1080.

Steppe, J.A., Bakun, W.P. & Bufe, C.G., 1977. Temporal stability of P-velocity anisotropy before earthquakes in Central California. Bull. seis. Soc. Amer., 67, 1075-1090.

Stewart, S.W., Lee, W.H.K. & Eaton, J.P., 1971. Real-time detection and location of local seismic events in Central California. Bull. seis. Soc. Amer., 67, 433-452.

Stewart, G.S., Chael, E.P. & McNally, K.C., 1981. The November 29 1978, Oaxaca, Mexico earthquake: a large simple event. J. geophys. Res., 86, 5053-5060.

Stuart, W.D., 1974. Diffusionless dilatancy model for earthquake precursors. Geophys. Res. Letts., 1, 261-264.

Synge, J.L., 1957. Elastic waves in anisotropic media. J. Math. Phys., 35, 323-335.

Toksöz, M.N., Shakal, A.F. & Michael, A.J., 1979. Space-time migration of earthquakes along the North Anatolian Fault Zone and seismic gaps. Pure Appl. Geophys., 117, 1258-1270.

Üçer, S.B., Crampin, S. & Miller, A., 1981. The MARNET radio-linked seismometer network spanning the Marmara Sea, and the seismicity of Western Anatolia. Geophys. J.R. astr. Soc., in preparation.

Ward, R.M., Schlue, J.W. & Sandford, A.R., 1981. Three-dimensional velocity anomalies in the upper crust near Socorra, New Mexico. Geophys. Res. Letts., 8, 553-556.

Whitcomb, J.H., Garmany, J.D. & Anderson, D.L., 1973. Earthquake prediction: variation of seismic velocities before the San Francisco earthquake. Science, 180, 632-635.

Wu, C. & Crosson, R.S., 1975. Numerical investigation of dilatancy biasing of hypocentre locations. Geophys. Res. Letts., 6, 205-208.

Wyss, M., 1975. Precursors to the Garm Earthquake of March 1969. J. geophys. Res., 80, 2926-2930.

Wyss, M., Johnston, A.C. & Klein, F.W., 1981. Multiple asperity model for earthquake prediction. Nature, 289, 231-234.

Yegorkina, G.V., Rakitov, V.A., Garetovsky, I.V. & Yegorova, L.M., 1977. Anisotropy of velocities of seismic waves and the stress state of the Earth's crust in the territory of Armenia. Izv. Akad. Nauk. SSSR. Fiz. Zemli, No. 8, 43-55 (in Russian), 554-562 (AGU, English translation).

APPENDIX A.

THE COMPUTATION OF VELOCITIES IN AN ANISOTROPIC SOLID.

A.1 Phase velocities.

The velocities of phase-propagation in an anisotropic solid, normal to the surface of constant phase may be considered as forming concentric phase velocity-surfaces, which are more formally, the solution space of a third order eigenvalue problem (Crampin 1977). Points on the velocity-surface are given by the Kelvin-Christoffel equation (Musgrave 1970):

$$(\Gamma - \rho V^2 \underline{I})\,\underline{a} = 0 \qquad (A.1)$$

where ρ is the density, $\underline{V}$ is the phase velocity, $\underline{a}$ is the polarisation vector, Γ is a 3x3 matrix of Kelvin-Christoffel stiffnesses, which are quadratic functions of elastic constants, c_{ij}, and direction cosines, n_{ij}, within the solid. For solids of orthorhombic symmetry there are nine non-zero, independent elastic constants, and the elements Γ_{ij} of the matrix can be written;

$$\begin{aligned}
\Gamma_{11} &= c_{11}n_1^2 + c_{66}n_2^2 + c_{55}n_3^2, & \Gamma_{23} &= (c_{23} + c_{44})\,n_2n_3 \\
\Gamma_{22} &= c_{66}n_1^2 + c_{22}n_2^2 + c_{44}n_3^2, & \Gamma_{13} &= (c_{13} + c_{55})\,n_1n_3 \\
\Gamma_{33} &= c_{55}n_1^2 + c_{44}n_2^2 + c_{33}n_3^2, \text{ and} & \Gamma_{12} &= (c_{12} + c_{66})\,n_1n_2
\end{aligned} \qquad (A.2)$$

For solids of hexagonal symmetry there are only five independent elastic constants, and the above equations can be reduced using the following symmetry relations;

$$c_{22} = c_{33}\ ,\ c_{55} = c_{66}\ ,\ c_{13} = c_{12}\ ,\ \text{and}\ c_{44} = (c_{33} - c_{23})/2 \qquad (A.3)$$

with x_1 as the axis of rotational symmetry.

A.2 Group velocities.

In anisotropic media energy propagates with a component, usually small, parallel to the wavefront, and the energy travels along a ray at an angle to

the propagation direction (Crampin, 1977; Crampin, Stephen & McGonigle, 1982). The surface traced by energy radiating along rays from a point source in a given time is known as the wave-surface, and is the envelope of the wavefronts (Synge 1957). The corresponding velocity is termed the wave, ray or group-velocity. The phase-velocity is the velocity that appears in equations of motion and in most other analytical expressions, whereas it is the group-velocity that is measured in most observations of arrival-times. The group-velocity vectors g_j for the wave-surface in a crystal possessing orthorhombic symmetry are given by (Musgrave 1970):

$$g_j = p_j^2(\rho v^2 - \Gamma_{jj})/(\rho v n_j) + (n_j/\rho v)\sum_{k=1}^{3} a_k^2 S_{jk} \quad \text{for } j=1,2,3 \qquad (A.4)$$

where $S_{11}= c_{11}$; $S_{22}= c_{22}$; $S_{33}= c_{33}$;
$S_{23}= S_{32}= c_{44}$; $S_{31}= S_{13}= c_{55}$; and $S_{12}= S_{21}= c_{66}$.

and where the symmetry relations (A.3) hold for hexagonal symmetry. The method of identifying the appropiate body wave surface that any phase- or group-velocity belongs to is outlined in McGonigle & Crampin (1982).

This theory provides the basis for a computer routine which generates phase- and group-velocities in any anisotropic solid. The routine can be used to generate look-up tables containing velocities at specified angles of incidence and azimuth throughout the focal sphere, and the derivatives of the velocities with respect to these angles at the same points. These look-up tables can then be used to generate synthetic travel-times in an anisotropic half-space (section 3.4), and as a reference table for a program that will locate earthquakes in such a structure (section 4.2). Alternatively the routine can be used as a subroutine of a larger program such as the layered location program (section 4.3), or the joint-inversion programs (Chapter 6).

The elastic constants used for the various anisotropic models used in this thesis are listed in Table A.1.

Table A.1. Elastic constants for models of dilatancy-anisotropy used in this Thesis

MODEL	COMMENTS	C11	C22	C33	C23	C13	C12	C44	C55	C66
GKFF1	Hexagonal dry, parallel cracks, model 1 (section 3.2)	54.665	81.977	81.977	23.675	12.855	12.855	29.161	23.418	23.418
GKLF1	Hexagonal saturated, parallel cracks model 1 (section 3.2)	87.464	87.464	87.464	29.142	28.393	28.393	29.161	23.352	23.352
GKLF4	Hexagonal saturated, parallel cracks (increased crack density) model 1 (section 3.2)	87.464	87.464	87.464	29.142	22.643	22.643	29.161	11.990	11.990
CPFF1	Hexagonal co-planar, dry cracks model 2 (section 3.2)	81.997	66.732	66.732	16.497	19.081	19.081	25.117	26.443	26.443
CPLF1	Hexagonal co-planar, saturated cracks model 2 (section 3.2)	87.464	84.368	84.368	31.483	28.387	28.387	26.443	26.443	26.443
GK2FFA	Orthorhombic orthogonal, bi-planar, dry model 3 (section 3.2)	80.665	71.308	53.779	12.529	13.455	19.923	22.443	23.729	27.581
GK2LFA	Orthorhombic orthogonal, bi-planar saturated cracks, model 3 (section 3.2)	87.464	87.464	87.464	27.131	27.627	29.060	22.443	23.729	27.581

APPENDIX B.

THE LOCATION OF EARTHQUAKES BY A LEAST-SQUARES PROCEDURE.

The problem of earthquake location is a non-linear, least-squares problem where we minimise the goodness of fit (Bevington 1969) between observed and calculated data. That is, we minimise:-

$$\chi^2 = \sum_i^N [\, t_i - T_i]^2 \Big/ \sigma_i^2 \qquad (B.1)$$

where t_i are the (N) observed arrival-times, T_i are the calculated arrival-times, and σ_i are the standard deviations of the observed arrival-times. In practise σ_i are unknown and are assumed to be equal to unity, so they can be ommitted at this stage for clarity. The calculated arrival-time T_i for a particular velocity model can be expressed as;

$$T_i = T_i(p_1, p_2, p_3, p_4) \qquad (B.2)$$

where p_1 is the origin-time and p_2, p_3, and p_4 are the hypocentral co-ordinates. Equation (B.2) can be expanded in a first order Taylor's expansion relating small changes in travel-time to small changes in hypocentral parameters:

$$T_i = T_0 + \sum_{k=1}^{4} \frac{dT_i}{dp_k} \delta p_k \qquad (B.3)$$

where summation over i is implicitly assumed. Equation (B.3) can be substituted in Equation (B.1), and the expression $t_i - T_0$ can be associated with the travel-time residuals R_i. Therefore Equation (B.1) becomes:

$$\chi^2 = \sum_i \left(R_i - \sum_k^4 \frac{dT_i}{dp_k} \delta p_k\right)^2 \qquad (B.4)$$

Minimising this expression by taking the derivatives with respect to the parameters p_k, and setting the result equal to zero, produces a set of equations known as the normal equations;

$$\sum_i R_i \frac{dT_i}{dp_k} = \sum_{j=1}^{4} \sum_i \frac{dT_i}{dp_k} \frac{dT_i}{dp_j} \delta p_k \quad \text{for } k = 1,2,3,4 \qquad (B.5)$$

This can be written in matrix form as;

$$\underline{A}^T \underline{B} = \underline{A}^T \underline{A}\, \underline{x} \qquad (B.6)$$

where the superscript T denotes a matrix transpose; $\underline{x}$ is a 4x1 column vector containing the required adjustments p_k; $\underline{B}$ is a Nx1 column vector containing the travel-time residuals R_i; and $\underline{A}$ is a 4xN matrix of partial derivatives given in Equation (B.5). A solution to (B.6) is;

$$\underline{x} = (\underline{A}^T \underline{A})^{-1} \underline{A}^T \underline{B} \qquad (B.7)$$

The problem is non-linear because coefficients in $\underline{A}$ are dependent on the corrections in $\underline{x}$, so small changes in $\underline{x}$ produces small changes in $\underline{A}$. Therefore earthquake location is performed by an iterative adjustment of the hypocentral parameters from an initial estimate of the solution, until some convergence criteria is satisfied. The normal starting parameters are the time of the first arrival, the co-ordinates of the nearest station, and some arbitrary depth (5km in Chapter 3). The convergence criteria is normally taken as being insignificant changes (to any required degree) in the adjustment vector $\underline{x}$.

The unknown standard deviations, σ_i, of the observed arrival-times are required in order to estimate the errors of the hypocentral parameters p_k. Bevington (1969) shows that these errors E_k may be estimated as;

$$E_k^2 = S^2 \varepsilon_{kk} \qquad (B.8)$$

where $\varepsilon_{kk} = (\underline{A}^T \underline{A})^{-1}_{kk}$ for $\sigma_i = 1$

and $S = \left[\sum_i (t_i - T_i)^2 \right] / \nu$

where $\nu = N - 4$, is the number of degrees of freedom, and T_i are the calculated travel-times from the final solution.

In an isotropic half-space the travel-times and their derivatives can be easily found from the travel-time equation;

$$T_i = p_1 + [(x_i - p_2)^2 + (y_i - p_3)^2 + (z_i - p_4)^2]^{\frac{1}{2}}/V \qquad (B.9)$$

where x_i, y_i, z_i are the co-ordinates of the ith station, and V is the half-space velocity.

This theory provides the basis for the location programs of Chapters 3 and 4, and for the joint-inversion programs of Chapter 6.

APPENDIX C.

TABLES OF ESTIMATED AND TRUE HYPOCENTRAL LOCATION ERRORS.

This appendix contains tables comparing the estimated and the true hypocentral location errors from section 3.5, where an isotropic location program was used to locate events in an anisotropic half-space. The estimated hypocentral error, E_H is calculated as (Bevington 1969):

$$E_H^2 = X^2\left[\sum_i C_{ii} + 2*\left[\sum_i \sum_j C_{ij}\right]\right] \quad \begin{array}{l} i = 2,3,4 \\ j = 2....i \\ j \neq i \end{array} \qquad (C.1)$$

where $\underline{C}$ is the inverse of the normal equation matrix A^TA, and X^2 is the square of the sum of the travel-time residuals divided by the number of degrees of freedom. This error is expressed in kilometres and is averaged over each set of fifteen events at each depth interval. The true error, expressed in the same way, is the difference between the true hypocentral position and the relocated position. If the ratio between the true and the estimated error is greater than two, then the error is statistically signifiant at the 95% confidence level. The model references are from various figure captions for the the relocations presented in Figs.3.5 to 3.22 and in Fig.4.1.

C.1 Isotropic half-space

MODEL	DEPTH	AVERAGE ERRORS		RATIO
		ESTIMATED	TRUE	
ASQ1XZ	5.00	0.20	0.22	1.10
	10.00	0.36	0.34	0.95
	15.00	0.38	0.52	1.37
ASQ1XY	5.00	0.07	0.08	1.12
	10.00	0.09	0.06	0.69
	15.00	0.08	0.09	1.13
HYPOP	5.00	0.17	0.24	1.43
	10.00	0.34	0.35	1.01
	15.00	0.39	0.62	1.56
HYPOPS	5.00	0.06	0.07	1.11
	10.00	0.11	0.05	0.41
	15.00	0.12	0.09	0.72

C.2 Pure-strike-slip fault

MODEL	DEPTH	AVERAGE ERRORS		RATIO
		ESTIMATED	TRUE	
MSQ1SZ	5.00	2.12	1.44	0.68
	10.00	2.70	2.16	0.80
	15.00	3.46	3.41	0.98
MSQ1SY	5.00	0.65	0.70	1.06
	10.00	0.62	0.54	0.86
	15.00	0.63	0.63	1.00
NSQ1SZ	5.00	0.53	0.21	0.39
	10.00	0.80	0.68	0.85
	15.00	1.40	1.26	0.90
NSQ1SY	5.00	0.31	0.19	0.60
	10.00	0.22	0.25	1.16
	15.00	0.28	0.34	1.23
OSQ1SZ	5.00	0.93	0.58	0.63
	10.00	1.28	0.76	0.60
	15.00	1.42	0.85	0.60
OSQ1SY	5.00	0.25	0.21	0.84
	10.00	0.23	0.22	0.93
	15.00	0.21	0.38	1.85
PSQ1SZ	5.00	0.24	0.25	1.05
	10.00	0.36	0.29	0.81
	15.00	0.47	0.47	1.00
PSQ1SY	5.00	0.20	0.14	0.70
	10.00	0.25	0.18	0.71
	15.00	0.30	0.31	1.04
QSQ1SZ	5.00	2.11	0.70	0.33
	10.00	2.55	1.33	0.52
	15.00	3.24	1.48	0.46
QSQ1SY	5.00	0.61	0.40	0.66
	10.00	0.53	0.44	0.82
	15.00	0.47	0.52	1.11
RSQ1SZ	5.00	0.51	0.18	0.35
	10.00	0.94	1.03	1.10
	15.00	1.42	1.87	1.32
RSQ1SY	5.00	0.24	0.19	0.79
	10.00	0.32	0.41	1.28
	15.00	0.37	0.24	0.65

C.3 Pure-thrust fault

MODEL	DEPTH	AVERAGE ERRORS		RATIO
		ESTIMATED	TRUE	
MSQ1TZ	5.00	0.35	1.74	4.96
	10.00	0.40	2.16	5.47
	15.00	0.62	2.03	3.30
MSQ1TY	5.00	0.22	0.47	2.12
	10.00	0.33	0.54	1.62
	15.00	0.40	1.21	3.04
NSQ1TZ	5.00	0.26	0.21	0.80
	10.00	0.44	1.21	2.76
	15.00	0.46	2.33	5.07
NSQ1TY	5.00	0.14	0.26	1.82
	10.00	0.44	0.34	0.77
	15.00	0.56	1.66	2.96
OSQ1TZ	5.00	0.51	0.70	1.37
	10.00	0.63	0.64	1.02
	15.00	0.68	0.68	0.99
OSQ1TY	5.00	0.18	0.18	1.00
	10.00	0.18	0.22	1.22
	15.00	0.16	0.39	2.47
PSQ1TZ	5.00	0.17	0.18	1.04
	10.00	0.33	0.42	1.26
	15.00	0.48	0.33	0.69
PSQ1TY	5.00	0.23	0.06	0.25
	10.00	0.24	0.14	0.58
	15.00	0.21	0.17	0.81
QSQ1TZ	5.00	0.42	2.34	5.50
	10.00	0.73	3.75	5.17
	15.00	1.06	4.59	4.33
QSQ1TY	5.00	0.21	0.81	3.83
	10.00	0.32	0.32	1.00
	15.00	0.37	0.73	1.98
RSQ1TZ	5.00	0.26	0.30	1.16
	10.00	0.37	1.45	3.88
	15.00	0.41	2.59	6.32
RSQ1TY	5.00	0.24	0.28	1.20
	10.00	0.55	0.82	1.48
	15.00	0.73	0.79	1.09

C.4 Pure-normal fault

MODEL	DEPTH	AVERAGE ERRORS		RATIO
		ESTIMATED	TRUE	
MSQ1NZ	5.00	1.41	2.30	1.63
	10.00	1.55	3.02	1.95
	15.00	1.96	4.04	2.06
MSQ1NY	5.00	0.46	0.88	1.91
	10.00	0.49	0.37	0.77
	15.00	0.45	0.26	0.58
NSQ1NZ	5.00	0.41	0.81	1.97
	10.00	0.71	1.44	2.02
	15.00	0.93	1.76	1.90
NSQ1NY	5.00	0.17	0.47	2.72
	10.00	0.27	0.22	0.80
	15.00	0.25	0.24	0.99
OSQ1NZ	5.00	0.15	0.94	6.09
	10.00	0.26	1.49	5.71
	15.00	0.41	2.39	5.85
OSQ1NY	5.00	0.14	0.24	1.73
	10.00	0.20	0.37	1.81
	15.00	0.25	1.22	4.84
PSQ1NZ	5.00	0.18	0.24	1.36
	10.00	0.20	0.89	4.53
	15.00	0.44	1.28	2.93
PSQ1NY	5.00	0.12	0.20	1.66
	10.00	0.24	0.44	1.79
	15.00	0.27	0.38	1.41
QSQ1NZ	5.00	0.77	2.02	2.62
	10.00	0.80	2.24	2.81
	15.00	0.99	3.24	3.28
QSQ1NY	5.00	0.30	0.79	2.64
	10.00	0.33	0.16	0.50
	15.00	0.34	0.49	1.45
RSQ1NZ	5.00	0.45	0.81	1.81
	10.00	0.56	1.54	2.74
	15.00	0.64	1.62	2.54
RSQ1NY	5.00	0.23	0.47	2.08
	10.00	0.20	0.38	1.88
	15.00	0.22	0.34	1.53

C.5 Additional cases - TDP1 network

MODEL	DEPTH	AVERAGE ERRORS		RATIO
		ESTIMATED	TRUE	
MTP1SZ	5.00	0.54	1.55	2.87
	10.00	0.62	2.01	3.24
	15.00	0.91	2.31	2.55
MTP1SY	5.00	0.26	0.67	2.54
	10.00	0.25	0.75	3.04
	15.00	0.25	0.93	3.70
NTP1SZ	5.00	0.26	0.53	2.00
	10.00	0.39	0.82	2.12
	15.00	0.68	1.10	1.61
NTP1SY	5.00	0.14	0.24	1.70
	10.00	0.12	0.46	3.75
	15.00	0.12	0.59	4.87
MTP1TZ	5.00	0.39	1.97	5.04
	10.00	0.47	2.48	5.26
	15.00	0.78	2.62	3.35
MTP1TY	5.00	0.25	0.51	2.05
	10.00	0.30	0.98	3.28
	15.00	0.35	1.64	4.67
NTP1TZ	5.00	0.29	0.32	1.14
	10.00	0.41	0.93	2.24
	15.00	0.65	2.08	3.19
NTP1TY	5.00	0.15	0.24	1.60
	10.00	0.41	0.95	2.34
	15.00	0.65	2.31	3.56
MTP1NZ	5.00	0.80	2.05	2.57
	10.00	0.92	3.17	3.44
	15.00	1.21	4.29	3.54
MTP1NY	5.00	0.40	0.82	2.04
	10.00	0.44	0.99	2.27
	15.00	0.46	1.40	3.07
NTP1NZ	5.00	0.29	0.37	1.28
	10.00	0.49	0.97	2.01
	15.00	0.74	1.86	2.51
NTP1NY	5.00	0.22	0.32	1.48
	10.00	0.17	0.34	2.02
	15.00	0.19	0.56	2.99

C.6 Additional cases - increased crack density

MODEL	DEPTH	AVERAGE ERRORS		RATIO
		ESTIMATED	TRUE	
N1SQSZ	5.00	1.39	0.52	0.37
	10.00	2.61	1.97	0.76
	15.00	4.01	3.60	0.90
N1SQSY	5.00	2.21	1.39	0.63
	10.00	1.49	2.07	1.39
	15.00	1.36	2.57	1.89

C.7 Additional cases - dipping crack systems

MODEL	DEPTH	AVERAGE ERRORS		RATIO
		ESTIMATED	TRUE	
MDSQSZ	5.00	1.60	1.13	0.70
	10.00	1.87	2.09	1.12
	15.00	2.25	3.24	1.44
MDSQSY	5.00	0.54	0.63	1.17
	10.00	0.54	1.15	2.16
	15.00	0.57	1.73	3.03
NDSQSZ	5.00	0.50	0.21	0.42
	10.00	0.89	0.55	0.62
	15.00	1.26	0.95	0.75
NDSQSY	5.00	0.39	0.30	0.77
	10.00	0.40	0.53	1.32
	15.00	0.36	0.66	1.83
MDSQTZ	5.00	0.43	1.55	3.60
	10.00	0.57	2.78	4.90
	15.00	0.98	3.96	4.04
MDSQTY	5.00	0.32	0.66	2.08
	10.00	0.38	1.18	3.12
	15.00	0.42	1.80	4.30
NDSQTZ	5.00	0.35	0.35	1.01
	10.00	0.80	0.55	0.69
	15.00	1.33	0.91	0.69
NDSQTY	5.00	0.18	0.28	1.52
	10.00	0.42	0.69	1.61
	15.00	0.67	1.22	1.82
MDSQNZ	5.00	0.94	1.40	1.49
	10.00	1.01	2.20	2.17
	15.00	1.06	3.38	3.18
MDSQNY	5.00	0.37	0.68	1.81
	10.00	0.45	1.17	2.58
	15.00	0.58	1.74	3.01
NDSQNZ	5.00	0.40	0.21	0.52
	10.00	0.48	0.63	1.33
	15.00	0.60	1.16	1.93
NDSQNY	5.00	0.27	0.28	1.04
	10.00	0.20	0.48	2.42
	15.00	0.26	0.48	1.82

C.8 Comparison with HYPO71

MODEL	DEPTH	AVERAGE ERRORS		RATIO
		ESTIMATED	TRUE	
HYP2P	5.00	2.02	1.40	0.69
	10.00	2.48	2.72	1.10
	15.00	2.95	4.84	1.64
HYP2PS	5.00	0.64	0.72	1.12
	10.00	0.57	0.46	0.81
	15.00	0.60	0.49	0.83
MSQ1SZ	5.00	2.12	1.44	0.68
	10.00	2.70	2.16	0.80
	15.00	3.46	3.41	0.98
MSQ1SY	5.00	0.65	0.70	1.06
	10.00	0.62	0.54	0.86
	15.00	0.63	0.63	1.00

C.9 Anisotropic locations

MODEL	DEPTH	AVERAGE ERRORS		RATIO
		ESTIMATED	TRUE	
XBSQNY	5.00	0.06	0.06	0.96
	10.00	0.06	0.07	1.20
	15.00	0.07	0.06	0.85
Y1BQNZ	5.00	0.10	0.07	0.69
	10.00	0.10	0.12	1.17
	15.00	0.15	0.15	1.01
XBTPNY	5.00	0.06	0.11	1.69
	10.00	0.07	0.10	1.39
	15.00	0.09	0.10	1.13
Y1BTNZ	5.00	0.11	0.17	1.60
	10.00	0.14	0.16	1.13
	15.00	0.23	0.27	1.16
MSQ1SY	5.00	0.65	0.70	1.06
	10.00	0.62	0.54	0.86
	15.00	0.63	0.63	1.00
MSQ1SZ	5.00	2.12	1.44	0.68
	10.00	2.70	2.16	0.80
	15.00	3.46	3.41	0.98
MTP1SY	5.00	0.26	0.67	2.54
	10.00	0.25	0.75	3.04
	15.00	0.25	0.93	3.70
MTP1SZ	5.00	0.54	1.55	2.87
	10.00	0.62	2.01	3.24
	15.00	0.91	2.31	2.55

APPENDIX D

A SERIES OF CASE STUDIES WITH THE JOINT-INVERSION PROGRAMS

This appendix describes in detail the solutions for nine different isotropic and anisotropic models determined by the joint-inversion of suites of synthetic arrival-times for both the hypocentral locations and the velocity structure, following the procedure outlined in section 6.4. These models are described as models B to J in Table 6.1, (page 77a), and the reader should consult section 6.4 for the necessary background information. For reference, the parameters of each illustrated solution are listed in Table D.1 where the solution labels are referred to from the corresponding figure captions.

MODEL B

Fig.D.1a illustrates the solution obtained for the orientation of an axis of rotational symmetry in model B when GKFF1 is used as the initial model. There appear to be two favoured orientations centred on 0,40 and 0,-40. The RMS and orientation errors associated with solutions at these orientations are marginally lower than those of the other solutions. The elastic constants associated with both solutions indicate quite strong 2θ variations in both the P-wave and fastest shear-wave surface, with little variation in the slower shear-wave surface (Figs.D.1c and d). We can check these solutions by searching for solutions from the six surrounding orientations using GKLF1 as the initial model. The solutions for the orientation in this case are shown in Fig.D.1b. The RMS errors are similar to those in Fig.D.1a and there is no favoured orientation. The estimated orientation errors are large in most cases suggesting that the structure is isotropic, and the RMS error of any solution is no better than the isotropic solution (Table 6.2). An isotropic solution is confirmed by

Figure D.1. A summary of the solutions obtained by the inversion of synthetic arrival-times generated through model B.

(a) A summary of the solutions obtained for the orientation of the axis of rotational symmetry when the inversion assumes GKFF1 as an initial model, and is initialised from orientations spaced at 30 degree intervals throughout the semi-focal sphere. Notation and format as in Fig.6.16a, with a reference RMS error of 0.0200.

(b) A summary of the solutions obtained from particular orientations using GKLF1 as an initial model. Notation and format as in Fig.6.16a with a reference RMS error of 0.0200.

(c) Dashed lines - a vertical section through the wave-surfaces obtained by taking the weighted average of six solutions near an orientation of 0,30 in (a). Solid lines - for reference, the wave-surfaces in model GKFF1. Error bars as in Fig.6.16c.

(d) Dashed lines - a vertical section through the wave-surfaces obtained by taking the weighted average of four solutions near an orientation of -10,-50 in (a). Solid lines - for reference, the wave-surfaces in model GKFF1. Error bars as in Fig.6.16c.

(e) Dashed lines - a vertical section through the wave-surfaces obtained by taking the weighted average of all solutions in the upper part of (b) (solution B1 in Table D.1). Solid lines - for reference, the wave-surfaces in model GKFF1. Error bars as in Fig.6.16c.

(f) As (c) for the solutions in the lower part of (b) (solution B2 in Table D.1).

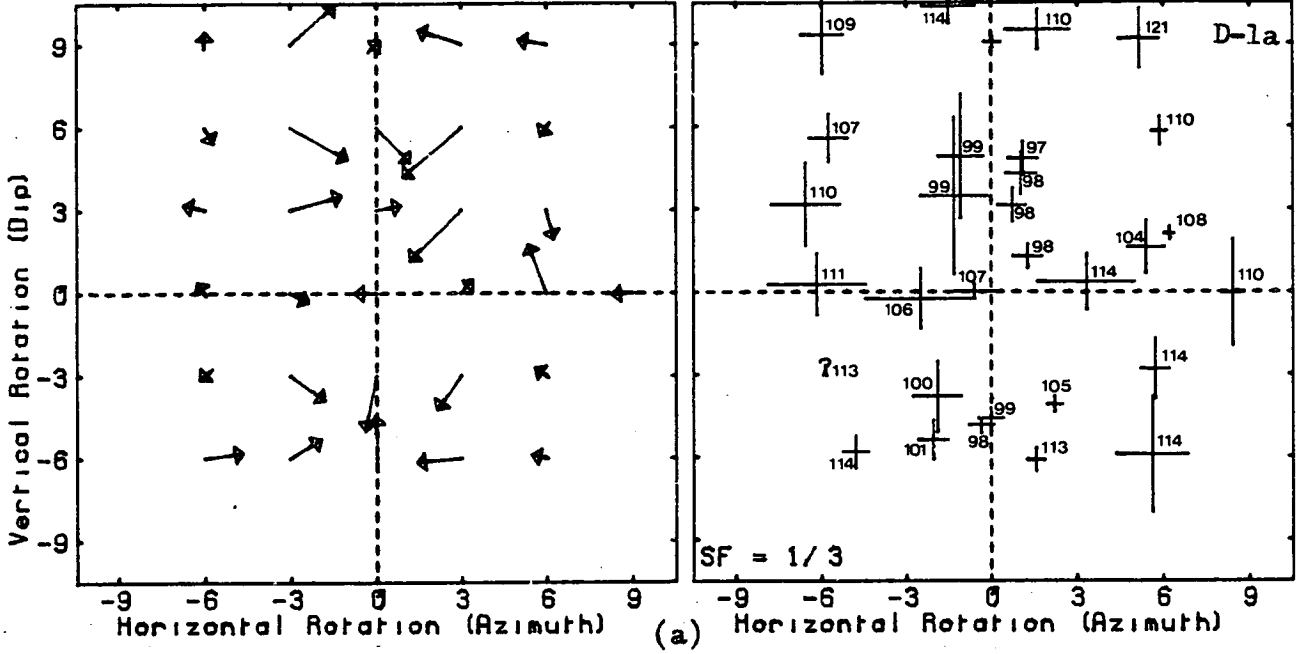
Vertical Rotation (Dip)
Horizontal Rotation (Azimuth)
D-1a
SF = 1/3
(a)

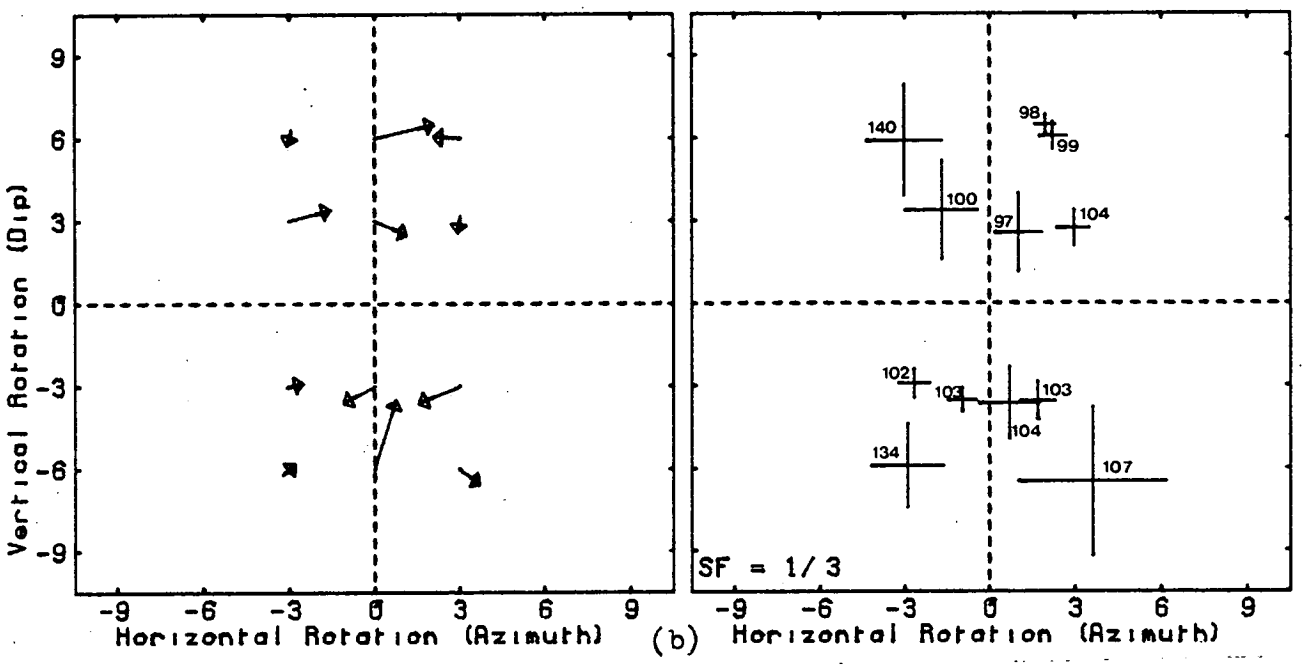
Vertical Rotation (Dip)
Horizontal Rotation (Azimuth)
SF = 1/3
(b)

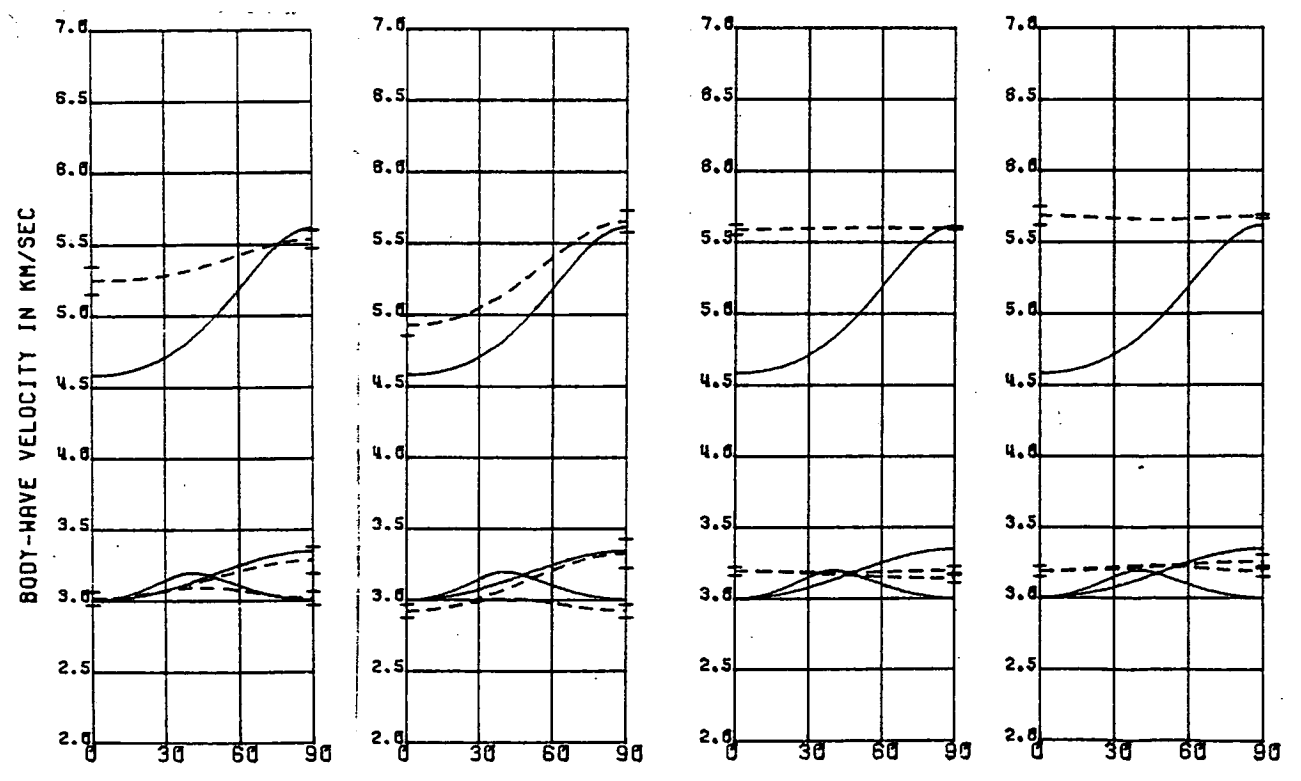
BODY-WAVE VELOCITY IN KM/SEC
(c)
(d)
(e)
(f)

plotting the weighted average of the elastic constants at each orientation (Figs.D.1e and D.1f). The solutions display very little variation in the P-wave or shear-wave surfaces, and the two shear-wave surfaces are almost coincident. The P-wave and shear-wave velocities, and the RMS and estimated velocity errors, are similar to those determined by the isotropic inversion program (Table 6.2).

MODEL C

Model C should be the most straightforward structure to determine. The model is strongly anisotropic and initially we assume the correct elastic constants as an initial model. Fig.D.2a shows the solutions for the orientation of the axis of symmetry obtained from each of the initial orientations. Nine solutions have defined a very clear minimum in the RMS errors at the true orientation (30,0). The elastic constants for eight of these solutions are all very similar (the exception being the solution from initialised 60,0 - which also has a much larger RMS error, and which may have been the result of premature terminations of the inversion process). The weighted average of these solutions produces the wave-surfaces shown in Fig.D.2b. The shear-wave surfaces are almost an exact fit to the true surfaces and the P-wave surface deviates only slightly from the true surface in the unsampled region. Notice that there are three other orientations defined by two or more solutions that have similar orientation errors to the correct solution. The elastic constants associated with each of the orientations defined by two solutions (i.e. those at 20,-45 and -65,70) are not consistent and can be dismissed as coincidental. However the elastic constants of the three solutions at 15,45 are mutually consistent, and the weighted average of these, plotted in the same section as that in Fig.D.2b, produce the wave-surfaces shown in Fig.D.2c. The P- and first shear-wave surfaces are a reasonable fit to the true surfaces,

Figure D.2. A summary of the solutions obtained by the inversion of synthetic arrival-times generated through model C.

(a) A summary of the solutions obtained for the orientation of the axis of rotational symmetry when the inversion assumes GKFF1 as an initial model, and is initialised from orientations spaced at 30 degree intervals throughout the semi-focal sphere. Notation and format as in Fig.6.16a. The RMS error at the point 60,0 is an anomalous value from the solutions at 30,0 and is not included in the average of those solutions. The reference RMS error is 0.0200.

(b) Dashed lines - a vertical section, measured from 30,0, through the wave-surfaces obtained by taking the weighted average of eight solutions at 30,0 in (b) (solution C1 in Table D.1). Solid lines - the wave-surfaces in the true model in the same section. Error bars as in Fig.6.16c.

(c) As (b) for the two solutions at an orientation of 20,45. No error bars have been plotted because the section is not measured from a principal axis.

(d) As (b) for the solution obtained by inversion of the data set that includes shear-wave delays using the solution in (b) as an initial model (solution C2 in Table D.1).

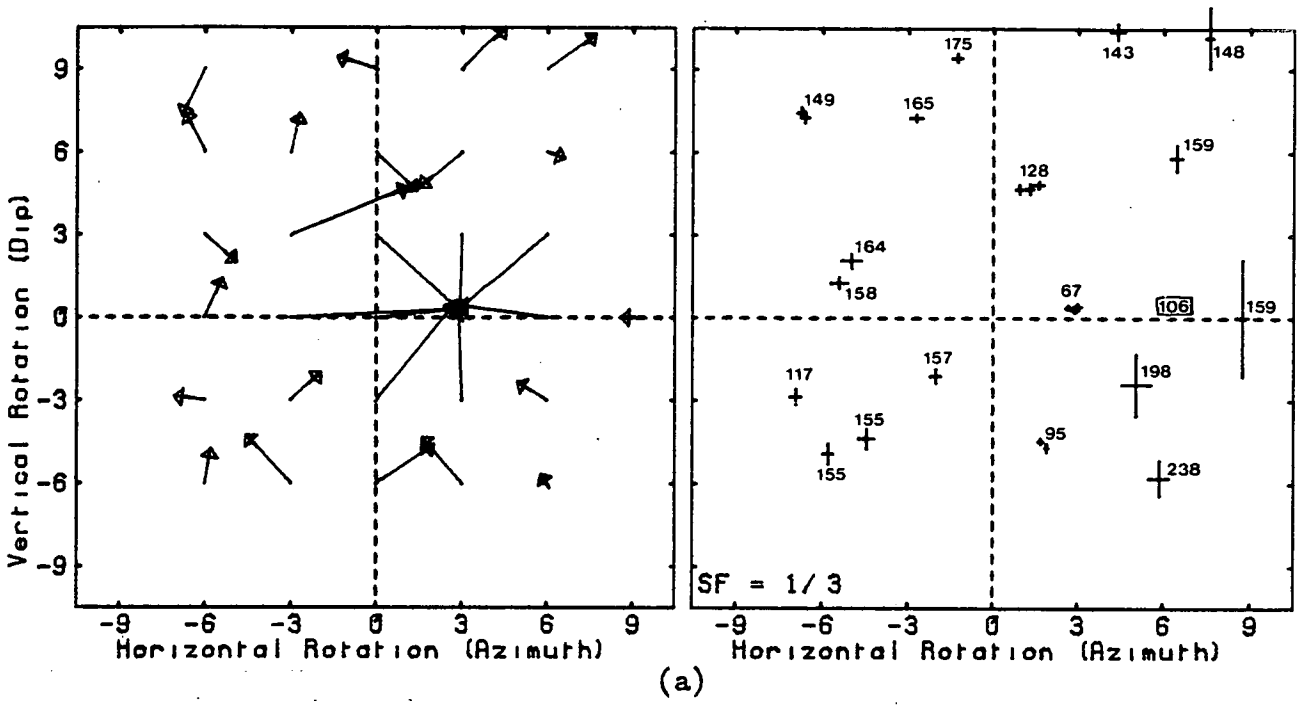
Vertical Rotation (Dip)
Horizontal Rotation (Azimuth)
Horizontal Rotation (Azimuth)
SF = 1/3
175
143
148
149
165
159
128
164
158
67
106
159
157
117
198
155
95
155
238

(a)

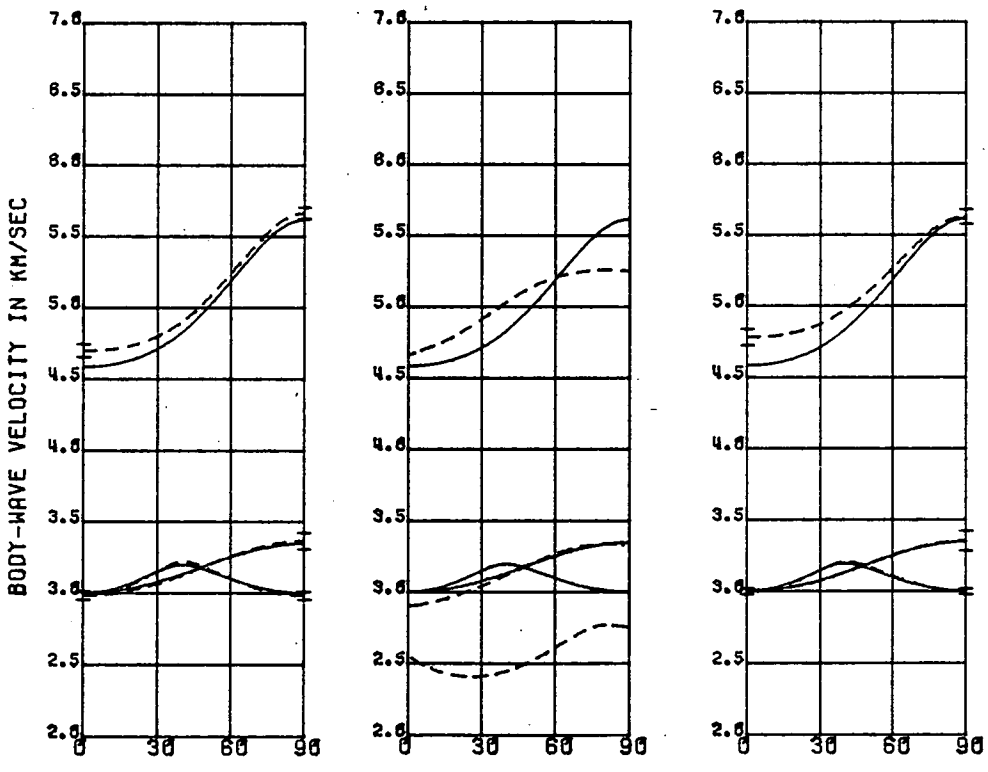
BODY-WAVE VELOCITY IN KM/SEC

(b) (c) (d)

but the second shear-wave surface is not. The F-test ratio with this solution (equal to 1.36) indicates that it is statistically superior to the isotropic solution, but a corresponding ratio of 1.5 indicates that the solution at the correct orientation is statistically superior to this solution.

The clear indication of the orientation of the structure, the low errors at this orientation and on the corresponding elastic constants, and the statistically significant improvement in the fit to the data, all suggest that the structure has been well-determined, and that it is not necessary to refine the initial model. However we can attempt to improve the solution by using the data set containing shear-wave delay data. In this inversion we use the velocity structure and the hypocentral locations determined in the previous stage as the initial model. The wave-surfaces from the subsequent solution are shown in Fig.D.2d. Again the shear-wave surfaces are an identical fit but the P-wave surface is slightly poorer than before and this is reflected in the increased error bars on this surface.

MODEL D

Fig.D.3a shows the solutions obtained for the orientation of model D. No clear orientation has been defined in this stage but a favoured horizontal orientation at 30 degrees is clearly indicated. There is little indication of the dip of the axis of symmetry but there are three solutions at 30,0 with low RMS and orientation errors. We can attempt to refine this solution by altering the initial model to GKLF1. In this stage we will initialise the inversion from the nine orientations surrounding and including the correct orientation. Fig.D.2b illustrates the subsequent solutions. Three solutions have defined a clear minimum in both the RMS and the orientation errors at the correct orientation. The other solutions

Figure D.3. A summary of the solutions obtained by the inversion of synthetic arrival-times generated through model D.

(a) A summary of the solutions obtained for the orientation of the axis of rotational symmetry when the inversion assumes GKFF1 as an initial model, and is initialised from orientations spaced at 30 degree intervals throughout the semi-focal sphere. Notation and format as in Fig.6.16a with a reference RMS error of 0.0200.

(b) A summary of the solutions obtained from particular orientations using GKLF1 as an initial model. Notation and format as in Fig.6.16a with a reference RMS error of 0.0200.

(c) Dashed lines - a vertical section, measured from 30,0, through the wave-surfaces obtained by taking the weighted average of the three solutions at 30,0 in (b) (solution D1 in Table D.1). Solid lines - the wave-surfaces in the true model in the same section. Error bars as in Fig.6.16c.

(d) As (c) for the solution obtained by inversion of the data set that includes shear-wave delays using the solution in (c) as an initial model (solution D2 in Table D.1).

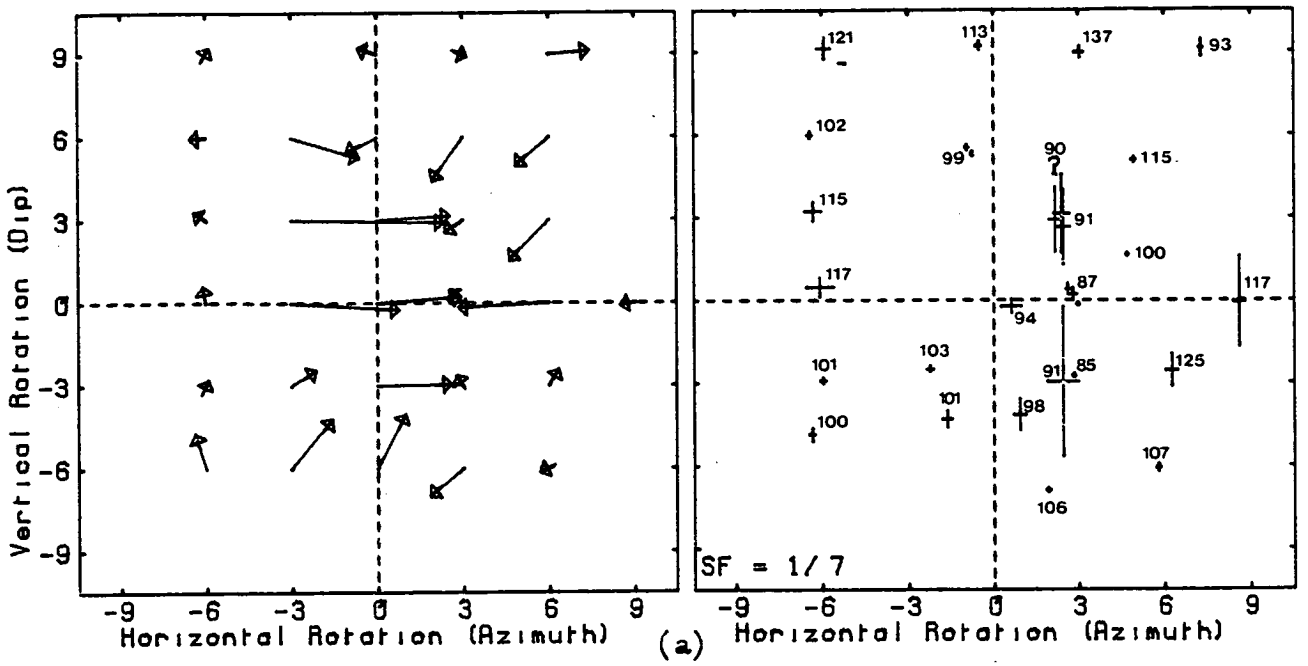
Vertical Rotation (Dip)
Horizontal Rotation (Azimuth)
SF = 1/7
(a)

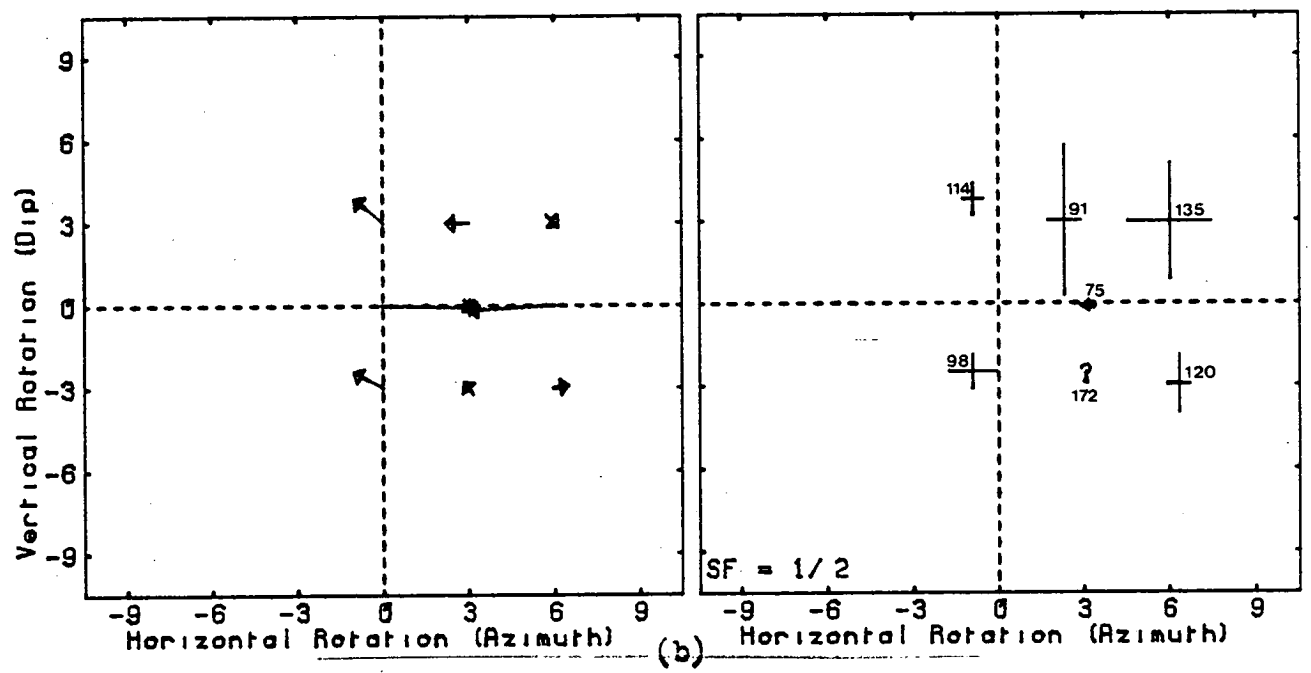
Vertical Rotation (Dip)
Horizontal Rotation (Azimuth)
SF = 1/2
(b)

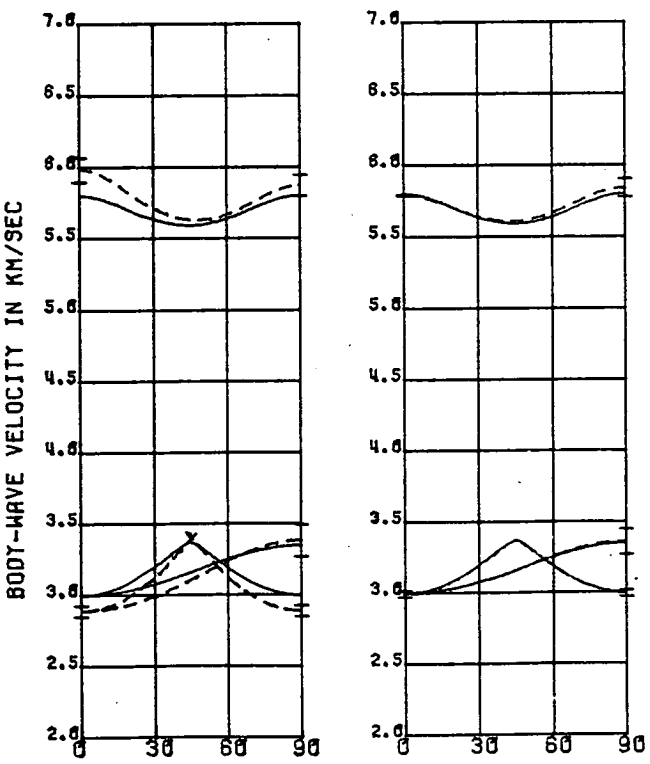
BODY-WAVE VELOCITY IN KM/SEC

do not show any tendency to consistently converge to any other orientation. Averaging the elastic constants from these three solutions produces the wave-surfaces shown in Fig.D.3c and are a good fit to each of the wave-surfaces. The F-test ratio of 1.27 indicates that although this solution is a very good fit to the true wave-surfaces, it is not statistically superior to the isotropic solution. We can improve this solution by inverting the data set containing shear-wave delays using the solution in Fig.D.3c as the initial model. This produces the solution shown in Fig.D.3d where the wave-surfaces are almost identical to the true wave-surfaces.

MODEL E

Fig.D.4a illustrates the solution obtained for the orientation of model E. The RMS errors associated with each solution are very similar in all cases. However there appears to be a convergence of four solutions to an orientation of -60,0. This is 90 degrees away from the correct solution for the orientation of the axis of rotational symmetry. The reason for this is that the velocity variations in this model are dominated by the 2θ variation in the P-wave surface, which is 90 degrees out of phase, (in a horizontal section), with the 2θ P-wave velocity variation in the initial model (GKFF1). The weighted average of the elastic constants of these four solutions produces the wave-surfaces shown in Fig.D.4c. Notice that this figure is slightly misleading. The solution indicates that there is an axis of rotational symmetry at an orientation of -60,0. This means that both a horizontal and vertical section from this direction would produce the wave-surfaces shown. However, in the real structure, a vertical section at this orientation would show no directional variations - the wave-surfaces shown for the true structure are for a horizontal section. The fact that the P-wave surface of the solution is a reasonable fit to a

Figure D.4. A summary of the solutions obtained by the inversion of synthetic arrival-times generated through model E.

(a) A summary of the solutions obtained for the orientation of the axis of rotational symmetry when the inversion assumes GKFF1 as an initial model, and is initialised from orientations spaced at 30 degree intervals throughout the semi-focal sphere. Notation and format as in Fig.6.16a with a reference RMS error of 0.0300.

(b) A summary of the solutions obtained from particular orientations using GKLF1 as an initial model. Notation and format as in Fig.6.16a with a reference RMS error of 0.0300.

(c) Dashed lines - a horizontal section, measured from -60,0, through the wave-surfaces obtained by taking the weighted average of four solutions at -60,0 in (a) (solution E1 in Table D.1). Solid lines - the wave-surfaces in the true model in the same section. Error bars as in Fig.6.16c.

(d) Dashed lines - a vertical section measured from 30,0, through wave-surfaces obtained by taking the weighted average of the six solutions with the lowest orientation errors in (b) (solution E2 in Table D.1). Solid lines - the wave-surfaces in the true model in the same section.

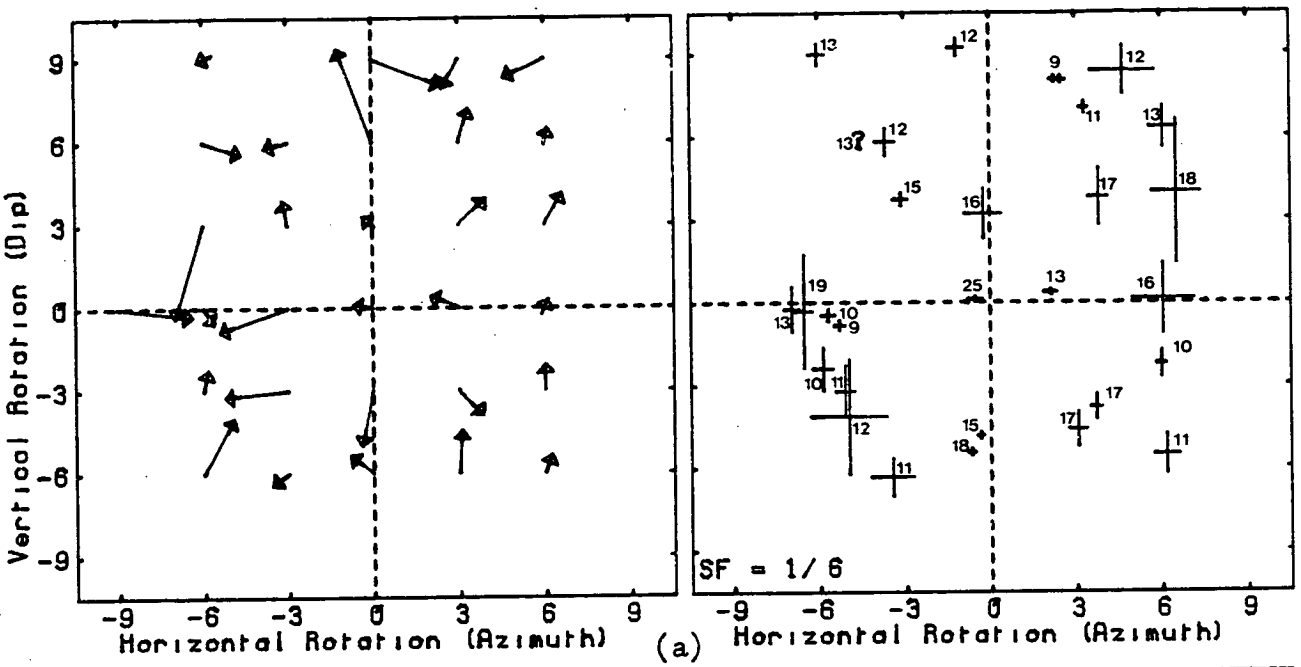
Vertical Rotation (Dip)
Horizontal Rotation (Azimuth)
SF = 1/6
(a)

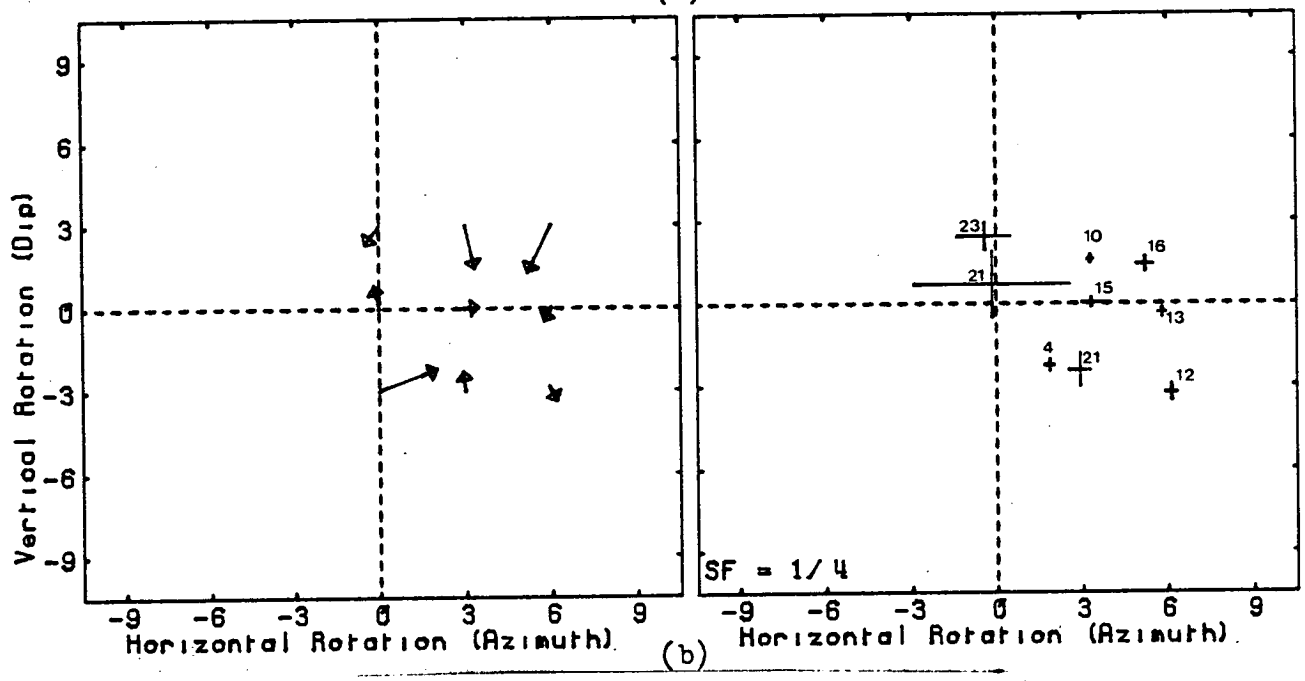
Vertical Rotation (Dip)
Horizontal Rotation (Azimuth)
SF = 1/4
(b)

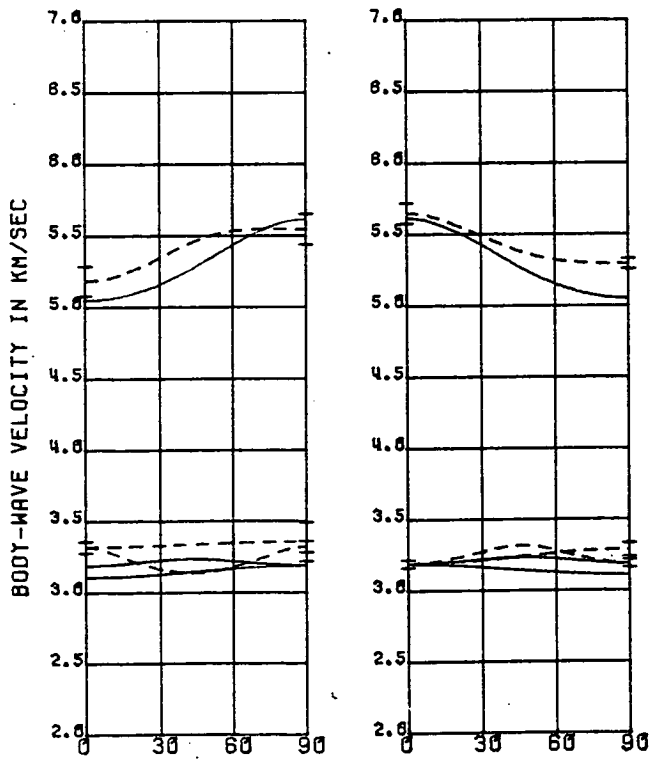
BODY-WAVE VELOCITY IN KM/SEC

horizontal section is a reflection of the greater constraint placed on the horizontal orientation of the structure by the TDP1 network, as noted in section 6.3.

We can see if it is possible to find a better fit to the data by searching for a solution from the nine grid points centred on 30,0 and using GKLF1 as the initial model. Fig.D.4b illustrates the solutions obtained in this stage. There is no obvious minimum and the solutions are of a similar quality to those shown in Fig.D.4a. Examination of the elastic constants associated with these solutions indicates that five of the solutions are consistent with each other. These are the five with the lowest orientation errors. The weighted average of these produces the variations shown in Fig.D.4d, and are still only a reasonable fit to the true wave-surfaces. The solution is not improved by inversion of the data set that includes shear-wave delays.

As anticipated in section 6.4.1, the errors in the arrival-times effectively mask the anisotropic variations in this structure and it is not possible to find a clear indication of the structure even when using shear-wave delay data. In practise the large orientation errors, the weak variations in the wave-surfaces, and the fact that the RMS errors of all solutions are not better than that of the isotropic solution would mean that this structure would have to be dismissed as being isotropic within the accuracy of the data.

MODEL F

Fig.D.5a illustrates the solutions obtained for the orientation of model F. The RMS errors of all the solutions are similar but there is a tendency for convergence to three different orientations. These solutions all lie at a horizontal orientation of 30 degrees and dip at -50, 0 and 50 degrees respectively, and are associated with the lowest RMS and orientation

Figure D.5. A summary of the solutions obtained by the inversion of synthetic arrival-times generated through model F.

(a) A summary of the solutions obtained for the orientation of the axis of rotational symmetry when the inversion assumes GKFF1 as an initial model and is initialised from orientations spaced at 30 degree intervals throughout the semi-focal sphere. Notation and format as in Fig.6.16a with a reference RMS error of 0.0300.

(b) A summary of the solutions obtained from particular orientations using GKLF1 as an initial model. Notation and format as in Fig.6.16a with a reference RMS error of 0.0200.

(c) Dashed lines - a vertical section, measured from 30,0, through the wave-surfaces obtained by taking the weighted average of the six solutions at 30,-50 in (a). Solid lines - the wave-surfaces in the true model in the same section. No error bars have been plotted because the section is not measured from a principal axis.

(d) As (c) for the two solutions at an orientation of 30,0 in (a). Error bars as in Fig.6.16c.

(e) as (c) for the three solutions at 30,0 in (b) (solution F1 in Table D.1). Error bars as in Fig.6.16c.

(f) As (c) for the solution obtained by the inversion of the data set that includes shear-wave delays using the solution in (e) as the initial model (solution F2 in Table D.1). Error bars as in Fig.6.16c.

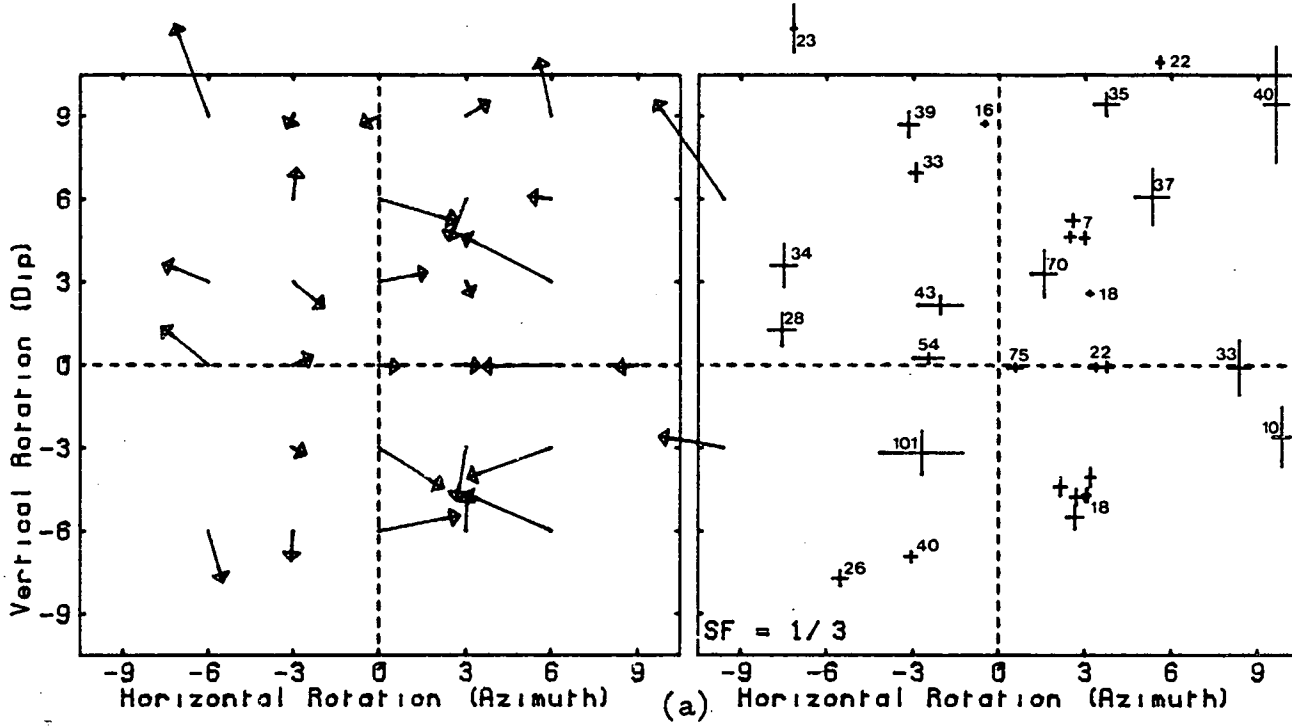
Vertical Rotation (Dip)
Horizontal Rotation (Azimuth)
SF = 1/3
(a)

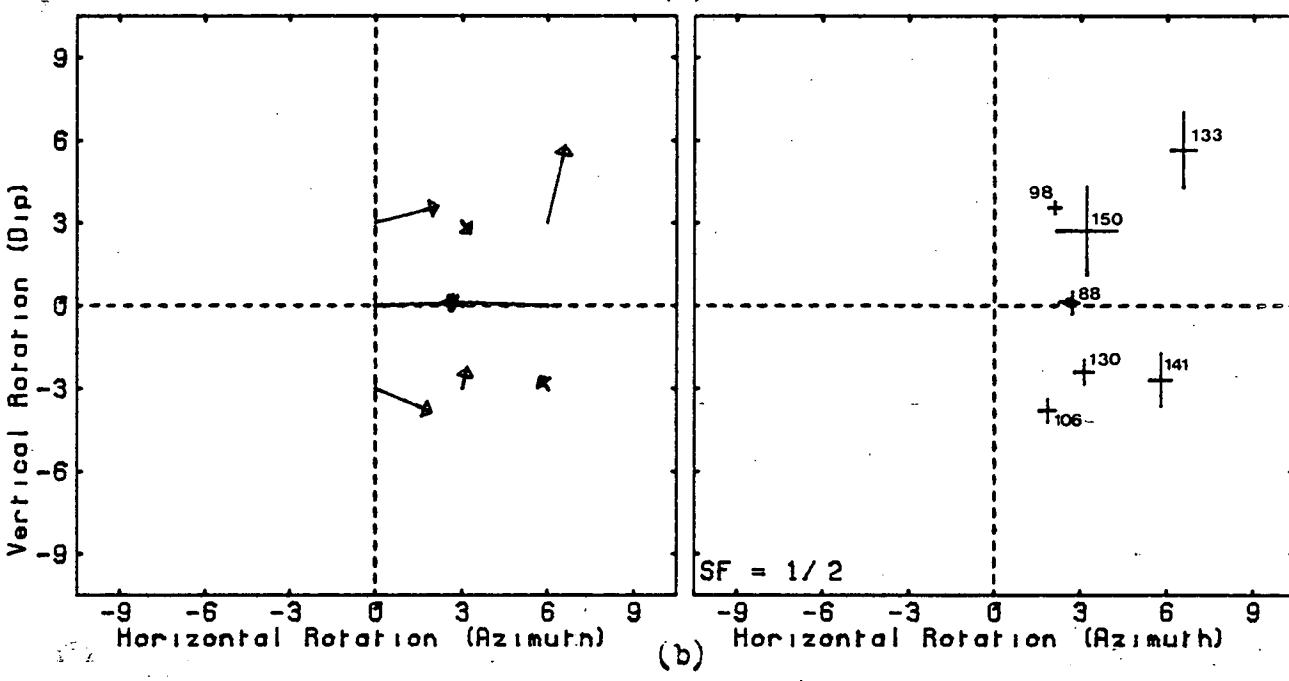
Vertical Rotation (Dip)
Horizontal Rotation (Azimuth)
SF = 1/2
(b)

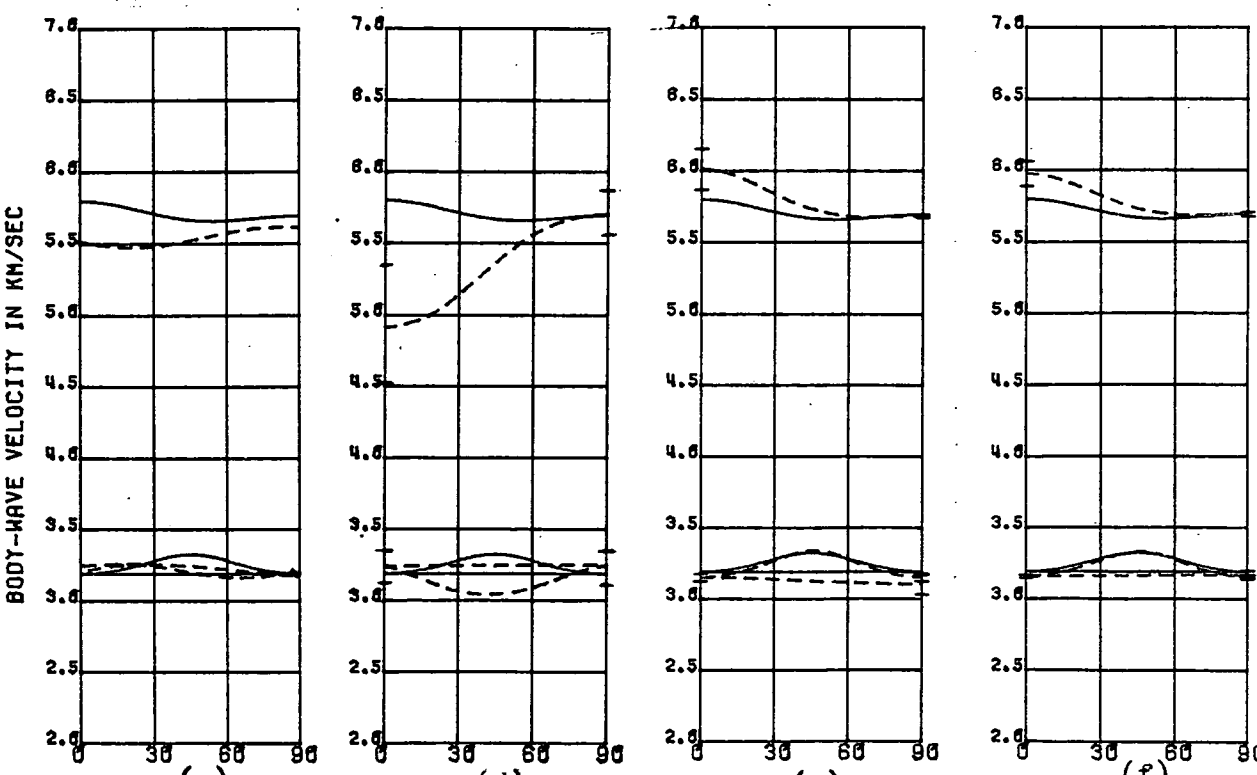
BODY-WAVE VELOCITY IN KM/SEC
(c)
(d)
(e)
(f)

Table D.1. The anisotropic solutions for models B to J.

Estimated errors are given in brackets. Estimated errors for solutions determined under the assumption of hexagonal symmetry are given for the independent elastic constants only. The F-test ratios in brackets for models I and J are calculated from the isotropic solutions I1 and J1 in Table 6.2. Azimuth and dip refer to horizontal and vertical rotations respectively.

SOLUTION	ELASTIC CONSTANTS									ORIENTATION		OVERALL RMS ERROR	F-TEST RATIO
	C11	C22	C33	C23	C13	C12	C44	C55	C66	Azimuth	Dip		
B1	81.22 (1.01)	81.49 (0.23)	81.49	30.18 (0.79)	28.66	28.66 (0.73)	25.16	26.53	26.53 (0.50)	____	____	0.0309	0.96
B2	84.06 (1.90)	83.83 (0.34)	83.83	28.62 (1.27)	29.65	29.65 (0.98)	27.16	26.47	26.47 (0.60)	____	____	0.0306	0.97
C1	57.44 (1.10)	83.39 (1.17)	83.39	24.44 (0.82)	14.47	14.47 (0.70)	29.48	23.14	23.14 (0.45)	28.87 (0.85)	3.11 (0.80)	0.0267	2.07
C2	59.45 (1.42)	82.39 (1.47)	82.39	23.87 (0.91)	15.86	15.86 (0.87)	29.26	23.39	23.39 (0.31)	29.59 (1.56)	3.53 (0.85)	0.0296	—
D1	93.04 (2.68)	89.58 (2.26)	89.58	30.05 (1.68)	30.22	30.22 (1.39)	29.77	21.65	21.65 (0.61)	31.51 (2.40)	-1.29 (1.38)	0.0275	1.27
D2	87.14 (0.12)	88.73 (1.91)	88.73	30.00 (1.24)	29.00	29.00 (0.90)	29.37	23.31	23.31 (0.36)	29.00 (2.36)	-0.62 (0.99)	0.0316	—
E1	69.92 (2.76)	80.00 (3.09)	80.00	21.39 (1.65)	23.46	23.46 (2.93)	29.31	28.67	28.67 (0.69)	-59.37 (6.97)	-6.57 (7.49)	0.0313	0.99
E2	83.03 (2.07)	72.90 (1.00)	72.90	16.66 (0.64)	20.44	20.44 (1.11)	28.12	26.50	26.50 (0.43)	31.03 (2.94)	4.51 (3.38)	0.0313	0.99
F1	94.03 (4.49)	84.03 (0.32)	84.03	33.98 (1.94)	30.68	30.68 (0.54)	25.03	25.83	25.83 (0.41)	26.24 (2.70)	1.42 (1.52)	0.0288	1.42

Table D.1. The anisotropic solutions (cont.)

SOLUTION	ELASTIC CONSTANTS									ORIENTATION		OVERALL RMS ERROR	F-TEST RATIO
	C11	C22	C33	C23	C13	C12	C44	C55	C66	Azimuth	Dip		
F2	92.89 (2.71)	84.32 (0.44)	84.32	32.10 (0.53)	30.69	30.69 (1.07)	26.11	25.92	25.92 (0.16)	26.80 (2.94)	1.68 (1.37)	0.0296	—
G1	54.05 (1.56)	75.81 (0.97)	75.81	22.66 (0.83)	13.13	13.13 (1.00)	26.58	24.14	24.14 (0.63)	27.01 (1.39)	-1.64 (0.97)	0.0299	1.87
G2	56.62 (1.40)	77.39 (0.46)	77.39	22.90 (0.35)	15.27	15.27 (0.80)	27.25	22.49	22.49 (0.24)	31.52 (1.78)	0.57 (0.99)	0.0308	—
H1	75.53 (3.50)	79.76 (2.14)	79.76	25.70 (1.45)	23.95	23.95 (1.44)	27.03	23.71	23.71 (1.03)	37.95 (2.01)	-6.83 (1.99)	0.0285	1.06
H2	80.42 (2.78)	80.08 (1.82)	80.08	25.73 (1.11)	25.14	25.14 (1.31)	27.18	22.53	22.53 (0.36)	33.47 (3.03)	-2.37 (1.41)	0.0321	—
I1	93.00 (3.57)	131.81 (8.26)	131.81	49.68 (5.30)	51.89	51.89 (5.03)	41.07	33.47	33.47 (0.97)	67.12 (3.96)	-5.36 (8.78)	0.0303	1.16
I2	107.69 (3.95)	86.43 (0.97)	86.43	21.89 (0.59)	30.39	30 39 (1.45)	32.27	31.23	31.23 (0.30)	-16.28 (2.40)	3.39 (1.76)	0.0301	1.18
I3	98.36 (2.96)	107.15 (5.27)	107.15	33.24 (3.28)	34.62	34.62 (2.37)	36.96	35.77	35.77 (0.81)	46.84 (13.85)	16.16 (11.41)	0.0386	—
I4	98.94 (4.52)	92.09 (2.26)	92.09	23.70 (1.35)	31.89	31.89 (2.08)	34.20	32.44	32.44 (0.63)	-23.70 (10.30)	-3.32 (5.02)	0.0347	—

Table D.1. The anisotropic solutions (cont.)

SOLUTION	ELASTIC CONSTANTS									ORIENTATION		OVERALL RMS ERROR	F-TEST RATIO
	C11	C22	C33	C23	C13	C12	C44	C55	C66	Azimuth	Dip		
I5	103.12 (15.45)	76.25 (8.59)	68.08 (15.10)	15.99 (6.09)	29.16 (17.55)	40.22 (18.12)	27.68 (3.75)	21.64 (4.08)	32.93 (2.18)	149.16 (3.43)	-0.16 (1.30)	0.0288	1.29
I6	76.61 (10.85)	104.32 (21.90)	68.85 (18.90)	22.89 (13.43)	20.83 (20.12)	34.36 (11.96)	28.14 (3.52)	26.98 (4.03)	27.77 (3.41)	63.68 (3.21)	0.02 (1.12)	0.0286	1.31
I7	95.57 (5.15)	82.90 (2.40)	74.61 (5.23)	18.39 (1.90)	24.89 (2.98)	32.10 (2.50)	29.90 (1.48)	28.17 (1.34)	32.63 (0.78)	148.08 (5.46)	0.26 (1.60)	0.0352	—
I8	84.31 (3.35)	93.59 (4.40)	73.57 (6.58)	21.20 (2.91)	20.63 (2.15)	28.34 (3.55)	29.32 (1.81)	27.67 (1.68)	31.99 (0.71)	63.12 (8.00)	1.17 (1.58)	0.0340	—
I9	88.82 (13.44)	66.25 (8.15)	56.15 (11.54)	9.24 (4.85)	20.22 (13.81)	32.01 (15.54)	25.54 (3.33)	20.11 (3.48)	30.41 (2.19)	-32.11 (2.95)	-0.17 (1.06)	0.0289	1.28 (2.03)
I10	69.38 (18.15)	99.98 (42.27)	65.96 (34.98)	16.94 (21.71)	18.49 (30.95)	35.22 (19.99)	29.38 (8.21)	23.07 (4.93)	25.39 (5.77)	60.49 (3.45)	-0.38 (1.36)	0.0286	1.31 (2.08)
I11	79.85 (4.92)	68.73 (2.05)	61.82 (4.59)	9.08 (1.26)	15.01 (2.16)	22.56 (2.37)	28.29 (1.53)	26.73 (1.44)	28.48 (0.96)	-29.88 (6.70)	-2.12 (1.72)	0.0367	—
I12	77.01 (2.51)	85.01 (5.24)	81.62 (5.23)	19.81 (2.69)	16.58 (1.56)	27.48 (3.13)	34.25 (1.52)	32.11 (1.46)	29.12 (0.94)	59.57 (7.62)	-8.49 (2.46)	0.0393	—
J1	59.84 (1.68)	67.55 (1.46)	67.55	7.18 (0.84)	1.59	1.59 (0.93)	30.19	24.75	24.75 (0.41)	63.71 (1.88)	8.04 (2.25)	0.0410	1.44

Table D.1. The anisotropic solutions (cont.)

SOLUTION	ELASTIC CONSTANTS									ORIENTATION		OVERALL RMS ERROR	F-TEST RATIO
	C11	C22	C33	C23	C13	C12	C44	C55	C66	Azimuth	Dip		
J2	32.13 (2.70)	49.63 (3.43)	49.63	25.39 (14.14)	1.07	1.07 (1.01)	12.12	16.03	16.03 (0.68)	1.72 (0.94)	8.89 (0.63)	0.0346	2.02
J3	84.47 (3.64)	83.27 (6.54)	83.27	33.80 (4.62)	22.53	22.53 (2.24)	24.74	26.18	26.18 (1.22)	25.22 (5.04)	-0.90 (1.97)	0.0665	—
J4	32.33 (1.43)	51.79 (1.58)	51.79	14.35 (1.61)	1.41	1.41 (0.31)	18.72	15.98	15.98 (0.54)	2.47 (0.95)	90.08 (0.70)	0.0472	—
J5	83.65 (6.57)	83.50 (7.15)	77.61 (10.52)	23.40 (5.80)	22.91 (5.54)	30.71 (34.31)	22.88 (0.93)	20.85 (0.74)	24.96 (15.45)	57.19 (6.07)	-0.69 (0.42)	0.0301	2.67 (5.67)
J6	84.21 (11.57)	84.21 (10.19)	76.11 (17.70)	22.23 (8.98)	22.89 (9.63)	43.52 (62.90)	20.92 (1.12)	23.02 (1.53)	20.89 (28.63)	152.03 (6.69)	-0.92 (0.47)	0.0296	2.76 (5.87)
J7	79.63 (22.74)	83.85 (13.47)	82.05 (13.75)	24.68 (31.40)	22.89 (12.09)	22.95 (11.75)	29.08 (12.94)	23.36 (1.90)	21.34 (1.69)	-0.56 (1.16)	89.06 (0.91)	0.0305	2.60 (5.53)
J8	83.08 (1.89)	83.71 (3.10)	77.44 (3.16)	23.79 (1.56)	22.87 (1.36)	29.43 (2.12)	22.83 (0.57)	21.42 (0.55)	26.86 (0.96)	57.03 (10.46)	-0.81 (0.76)	0.0338	—
J9	84.52 (3.99)	80.78 (2.33)	77.53 (3.51)	21.55 (1.52)	23.66 (1.89)	27.38 (2.40)	22.14 (0.64)	23.33 (0.63)	26.51 (1.40)	155.41 (9.82)	-1.23 (1.07)	0.0458	—
J10	79.75 (3.65)	82.88 (2.57)	82.04 (2.69)	25.24 (1.65)	23.08 (1.60)	23.14 (1.57)	28.57 (0.94)	22.96 (0.57)	21.97 (0.63)	-0.88 (0.94)	88.84 (0.88)	0.0347	—

errors. The solutions at 30,50 and 30,-50 indicate very weak anisotropy. Fig.D.5c shows the wave-surfaces obtained by taking the weighted average of the six solutions at 30,-50 in a vertical section measured from the true symmetry direction. The two solutions at 30,0 indicate very strong P-wave anisotropy, as illustrated in Fig.D.5d, but notice that the large error bar on this surface in the symmetry direction indicates that this direction cannot conclusively be associated with low velocities. However these solutions are not a statistical improvement over the isotropic solutions (Table 6.2).

The solutions in Fig.D.5a suggest that there is a symmetry direction at a horizontal rotation of 30 degrees. We can repeat the procedure used for previous models and search for a solution from the nine grid points centred on 30,0 using GKLF1 as the initial model. The solutions obtained for the orientation in this case are shown in Fig.D.5b. There is now a clear minimum at the correct orientation defined by three solutions, and the RMS errors of these solutions are clearly superior to those in the previous stage. The weighted average of these solutions produce the wave-surfaces shown in Fig.D.5e and are a good fit to the true surfaces, although the P-wave surface deviates slightly in the unsampled region. This is reflected by the larger estimated error in this direction. The F-test ratio for this solution indicates that it is statistically superior to the isotropic solution, and the fit to the true wave-surfaces is marginally improved by using shear-wave delays (Fig.D.5f).

MODEL G

Fig.D.6a shows the solutions obtained for the orientation of model G. Nine solutions have converged to the correct orientation and this is reflected in the low RMS and orientation errors. As for the half-space case, the inversion has clearly defined the orientation of the structure and it is

Figure D.6. A summary of the solutions obtained by the inversion of synthetic arrival-times generated through model G.

(a) A summary of the solutions obtained for the orientation of the axis of rotational symmetry when the inversion assumes GKFF1 as an initial model, and is initialised from orientations spaced at 30 degree intervals throughout the semi-focal sphere. Notation and format as in Fig.6.16a with a reference RMS error of 0.0300.

(b) A summary of the solutions obtained from particular orientations using GKFF1 as an initial model and with revised station corrections to take account of the isotropic layer. Notation and format as in Fig.6.16a with a refernce RMS of 0.0300.

(c) Dashed lines - a vertical section, measured from 30,0, through the wave-surfaces obtained by taking the weighted average of the nine solutions at 30,0 in (a). Solid lines- the wave-surfaces in the true model in the same section. Error bars as in Fig.6.16c.

(d) Dashed lines - a horizontal section, measured from -70,0, through the wave-surfaces obtained by taking the weighted average of the three solutions at -70,0 in (a). Solid lines - the wave-surfaces in the true model in the same section. Error bars as in Fig.6.16c.

(e) As (c) for the six solutions at 30,0 in (b) (solution G1 in Table D.1).

(f) As (c) for the solution obtained by the inversion of the data set that includes shear-wave delays, using the solution in (e) as the initial model (solution G2 in Table D.1).

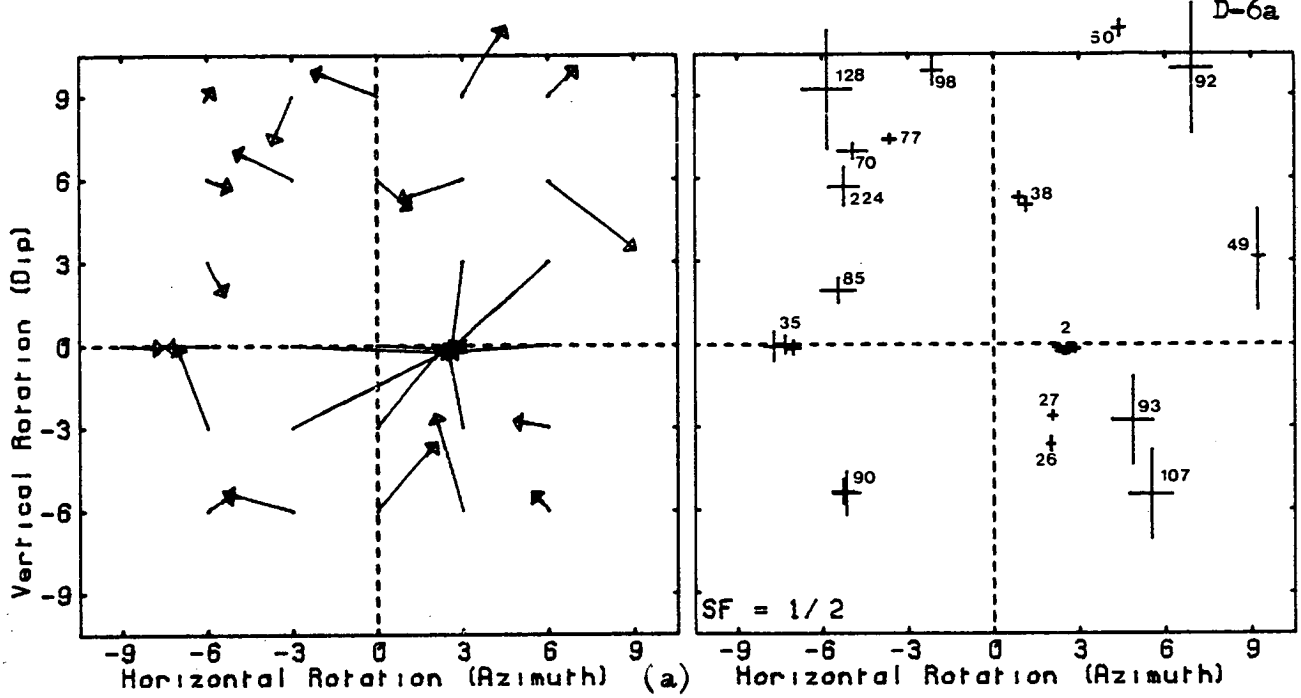
Vertical Rotation (Dip)
Horizontal Rotation (Azimuth)
(a)
SF = 1/2
50
128
98
92
77
70
224
38
49
85
35
2
27
26
93
90
107

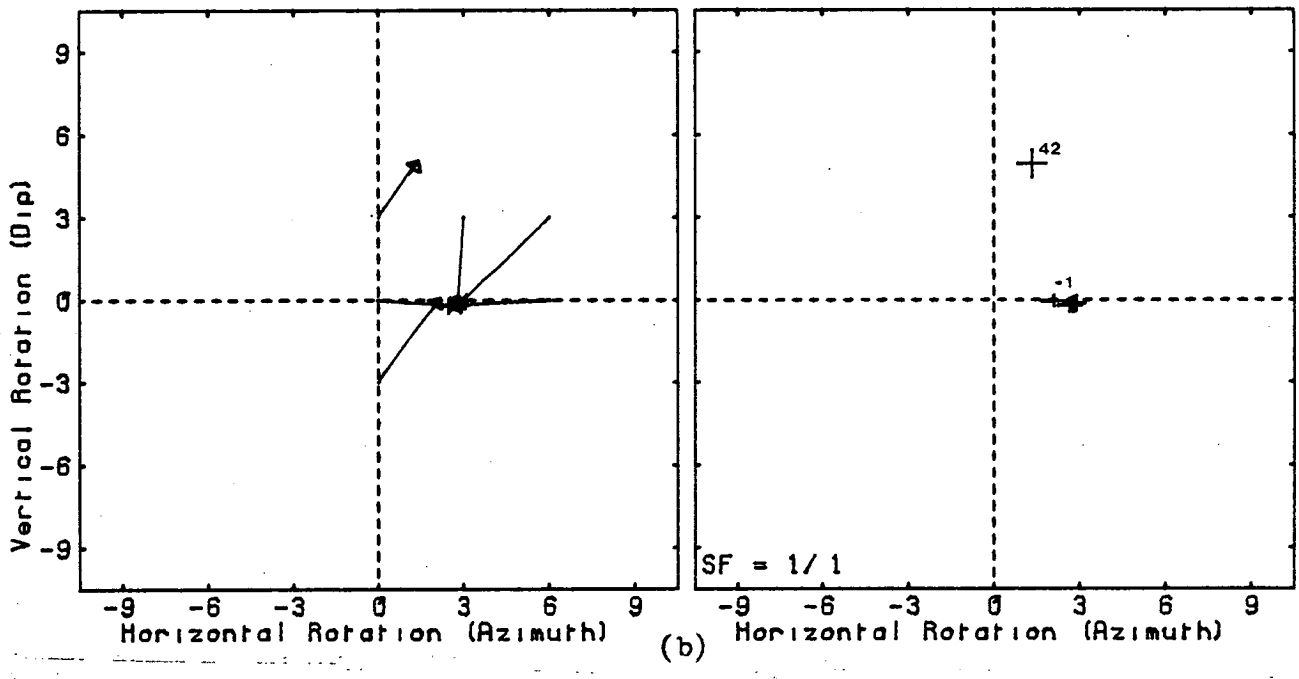
Vertical Rotation (Dip)
Horizontal Rotation (Azimuth)
(b)
SF = 1/1
42
-1

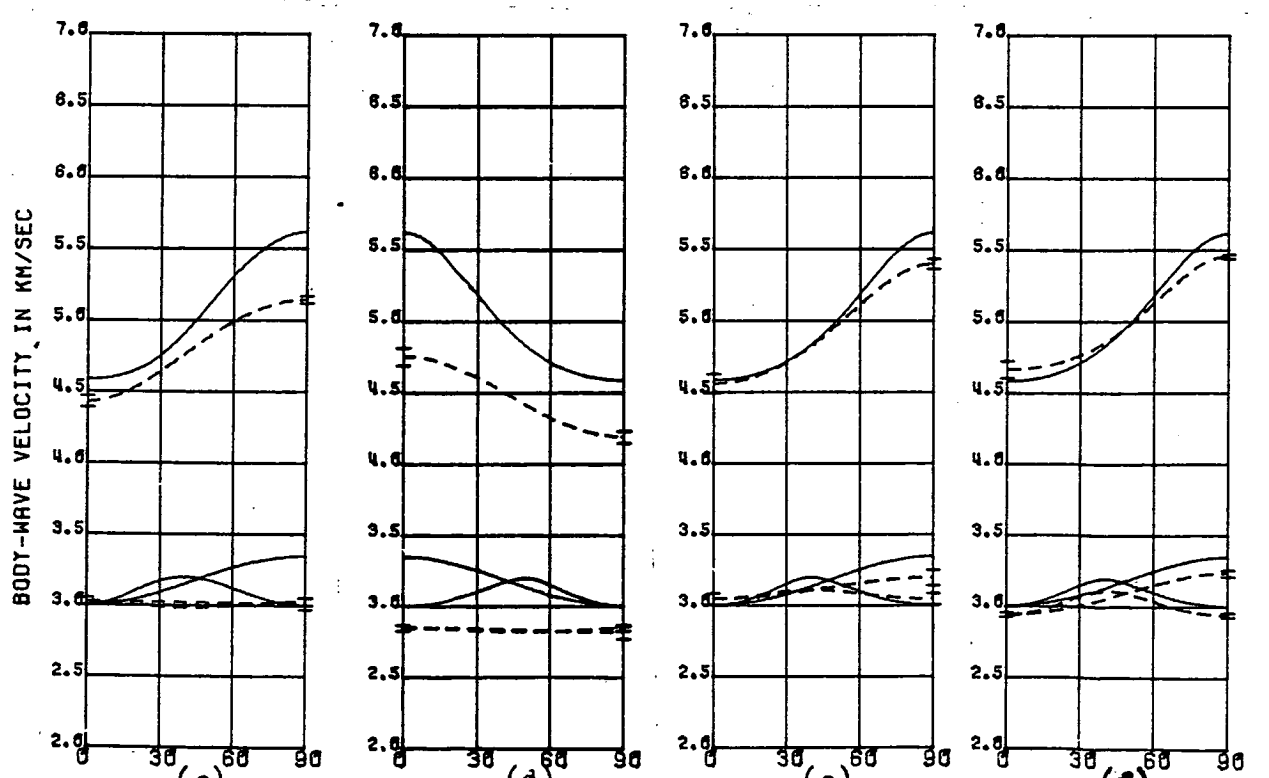
BODY-WAVE VELOCITY, IN KM/SEC
(c)
(d)
(e)
(f)

not necessary to refine the initial model. Fig.D.6c illustrates the wave-surfaces obtained by taking the weighted average of the nine solutions at an orientation of 30,0 in (a). The figure illustrates that the effect of the isotropic layer is to completely mask the shear-wave variation and reduce the P-wave variation. Also similar to the half-space case is the secondary minimum at an orientation of 20,50. The wave-surfaces from this solution, in a vertical section measured from the true symmetry direction, are similar to those shown in Fig.D.6c. In addition there is also a mimina at -70,0. This is a similar phenomena to that observed in model E where the inversion attempts to fit the well-constrained horizontal P-wave variation. This solution is shown in Fig.D.6d. As in the half-space case (model C) the RMS errors at these secondary minima are clearly inferior to those at the true orientation but are nevertheless statistically superior to the isotropic solution.

We can allow for the effect of the known isotropic layer by introducing corrections to each of the stations of the network. It was demonstrated in Chapter 4 that this is a reasonable approximation for a very thin isotropic layer as modelled here. Fig.D.6b shows that the orientation of the anisotropic structure is still clearly defined (although some inversions have not converged in the allotted time), and Fig.D.6e illustrates that the P-wave and the fastest shear-wave surfaces are well-determined, but the second shear-wave surface displays very little directional variation. The RMS error suggests that this solution is marginally superior to the solution shown in Fig.D.6c, and the F-test ratio again indicates that this solution is statistically superior to the isotropic solution. This solution is improved by inversion of the data set that includes shear-wave delays using the revised station corrections (Fig.D.6f). The form of the wave-surfaces are almost correct but there is a small offset in the shear-wave surfaces.

MODEL H

Fig.D.7a shows the solutions obtained for the orientation of model H. In this case there is only a slight tendency for some solutions to converge to a horizontal orientation of 30 degrees (c.f. Fig.D.3 for the half-space case). Following the procedure used previously we can attempt to refine the solution by using GKLF1 as the initial model, introducing station corrections to allow for the effect of the thin isotropic layer, and by searching for a solution surrounding the correct orientation. The resulting solutions are shown in Fig.D.7b. There is a minimum in the RMS and orientation errors defined by three solutions near the correct orientation. The wave-surfaces from the weighted average of these solutions are shown in Fig.D.7c and are a reasonable fit to the true surfaces. Again this solution is improved slightly using shear-wave delays, but there is a still a small offset in all the wave-surfaces (Fig.D.7d). This example illustrates the masking effect that a thin isotropic layer may have on weak anisotropic variations. The solution obtained, although a good fit, is only marginally superior, in a statistical sense, to the isotropic solution.

MODEL I

Fig.D.8a illustrates the solution obtained for the orientation of an axis of rotational symmetry in the orthorhombic model, model I. (Note that we are inverting phase-velocities with a program that calculates group-velocities. For this model, and model J, there is no marked difference between phase- and group-velocities and so we do not anticipate that this will significantly effect any conclusions). The inversion has not clearly defined any minimum in the RMS or orientation errors. This is similar to the solution for an isotropic structure (Fig.6.16), but there are solutions with low RMS and orientation errors at low dip angles, at a

Figure D.7. A summary of the solutions obtained by the inversion of synthetic arrival-times generated through model H.

(a) A summary of the solutions obtained for the orientation of the axis of rotational symmetry when the inversion assumes GKFF1 as an initial model and is initialised from orientations spaced at 30 degree intervals throughout the semi-focal sphere. Notation and format as in Fig.6.16a with a reference RMS of 0.0200.

(b) A summary of the solutions obtained from particular orientations when the inversion assumes GKFF1 as an initial model and with revised station corrections to take account of the thin isotropic layer. Notation and format as in Fig.6.16a with reference RMS error of 0.0200.

(c) Dashed lines - a vertical section measured from 30,0 through the wave-surfaces obtained by taking the weighted average of three solutions near 30,0 in (b) (solution H1 in Table D.1). Solid lines - the wave-surfaces in the true model in the same section. Error bars as in Fig.6.16c.

(d) As (c) for the solution obtained by the inversion of the data set that includes shear-wave delays using the solution in (c) as the initial model (solution H2 in Table D.1).

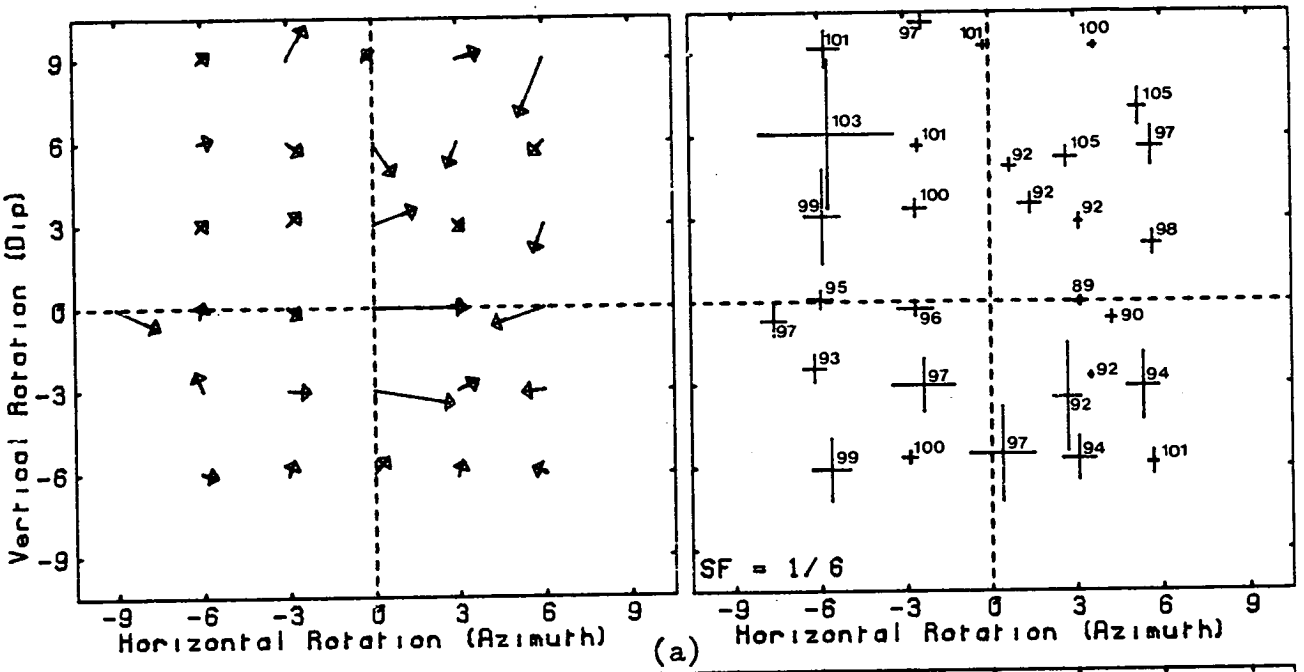
Vertical Rotation (Dip)
Horizontal Rotation (Azimuth)
SF = 1/6
(a)

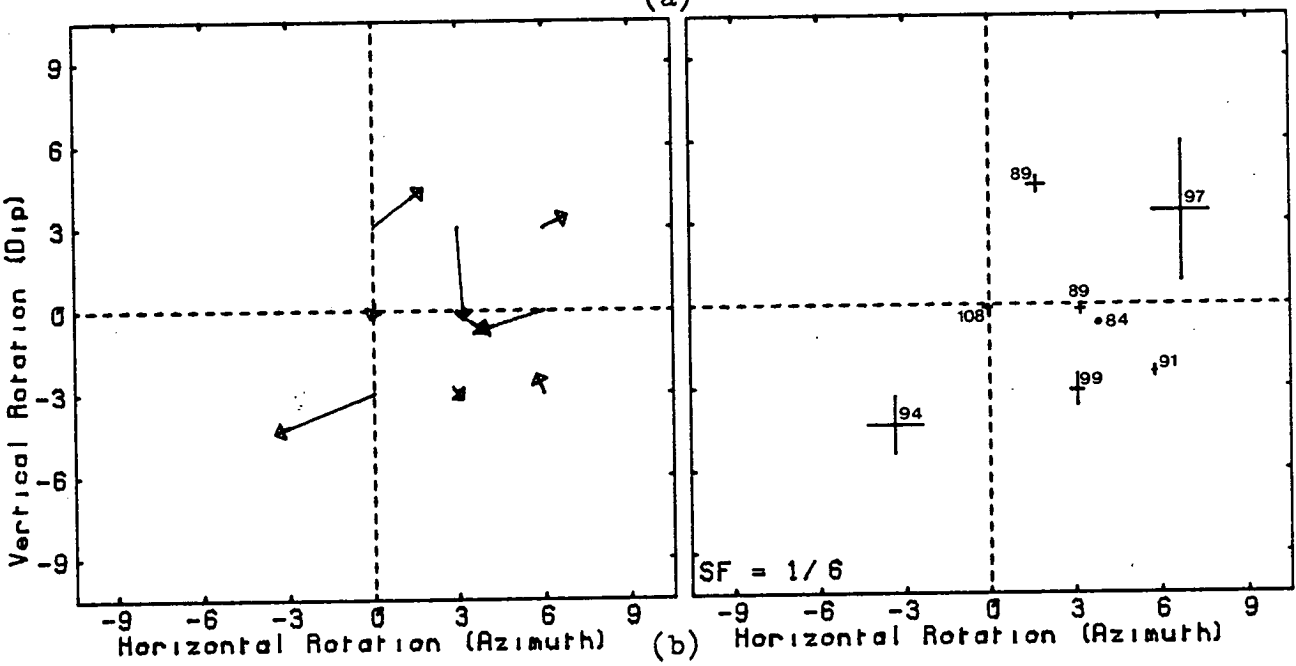
Vertical Rotation (Dip)
Horizontal Rotation (Azimuth)
SF = 1/6
(b)

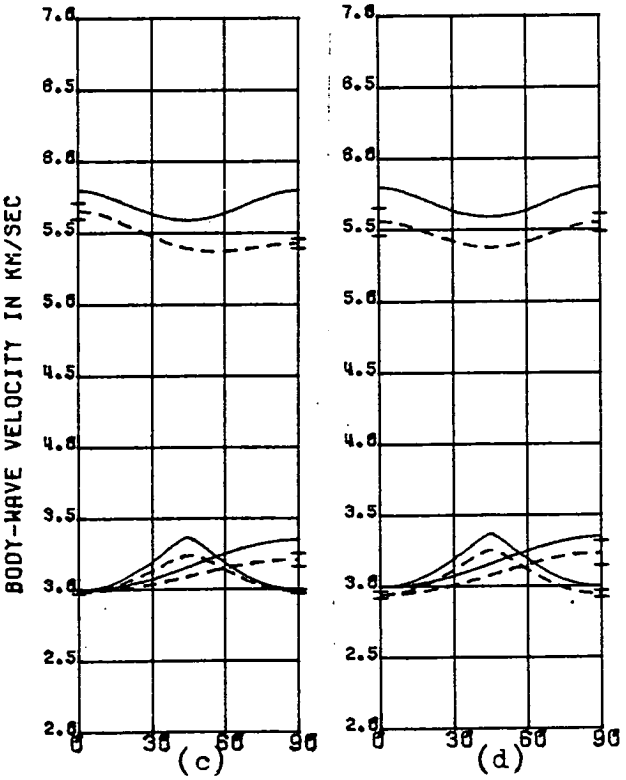
BODY-WAVE VELOCITY IN KM/SEC
(c)
(d)

horizontal rotation of -20, and surrounding the orientation of 0,90. We can attempt to clarify this by altering the initial model to GKLF1 and by searching for solutions in this region. Fig.D.8b shows the results of this search and again there is no clear indication of the orientation of the structure, although there are two groups of solutions with low RMS errors (i.e. less than 0.0310s), low orientation errors and similar elastic constants at 65,-5 and -15,5. More importantly, the elastic constants associated with these solutions indicate an anisotropic structure with a strong P-wave variation. Fig.D.8c shows the wave-surfaces obtained by taking the weighted average of the four solutions converging to the point 65,-5 and Fig.D.8d shows the wave-surfaces of the four solutions at -15,5. Notice that the solution at 65,5 indicates high velocities in a vertical direction, when this is a low velocity direction in the true model. The form of the velocity variations is correct for a horizontal section from this orientation, and so this may be an exaggeration of the phenomenon noted in models E and G where the inversion attempts to fit the better constrained horizontal velocity variations.

The inversion of the arrival-times in this structure has not produced any clear solution for the structure. The lack of any indication of the orientation of the structure in the first series of inversions suggests that the structure is not a hexagonal system of dry cracks. In the second series of inversions using GKLF1 as the initial model there is a slight indication of two solutions for the orientation of the structure. The elastic constants at both orientations suggest that the structure is not a system of saturated cracks and that it is not isotropic. We can attempt to refine each solution by inversion of the data set that includes shear-wave delays. This produces the solutions shown in Figs.D.8e and D.8f. The form wave-surfaces have changed and the orientation of one solution is altered by more than 20 degrees. This ambiguity, and the fact that there appear to

be two favoured orientations, almost 90 degrees apart, suggests that the assumption of hexagonal symmetry is insufficient to describe this structure and we can attempt to find a solution by inverting for an orthorhombic structure.

For the orthorhombic inversion we will use the same trial hypocentres as before, assume GKLF1 as the initial model and search for solutions at low dip angles. The solutions are shown in Fig.D.8g and suggest two orientations centred at -30,0 and 60,0 with low RMS and orientation errors. These are the orientations of two of principal axes in the true structure, and are close to the orientations suggested by the hexagonal inversion. Notice that the RMS and orientation errors are superior to the solutions for a hexagonal structure, and that the solutions are almost statistically superior to the isotropic solutions. The velocity-surfaces for these two solutions are shown in Fig.D.8h and D.8i. The form of the P-wave surface is correct but the P-wave velocity is too large in all directions and the shear-wave surfaces are poorly determined. Although the P-wave surfaces do imply the same structure, the large error bars on the elastic constants and the fact that the shear-wave surfaces in each solution do not imply the same structure, indicate that the structure is very poorly determined.

The poor results from the orthorhombic inversion may be result of the large errors in the trial hypocentres used in the inversion, and in particular the large errors in the origin-times (Table 6.2). There are two ways that this solution may be improved. Firstly we can use shear-wave delay data with the initial model corresponding to the solutions above. This produces the solutions shown in Figs.D.8(j and k) for the two orientations of -30,0 and 60,0 respectively. Again the P- and the shear-wave velocities are too large in all directions, but the two solutions are now much more consistent and the error bars have been reduced. The second method involves revising the trial hypocentres used in

Figure D.8. A summary of the solutions obtained by the inversion of synthetic arrival-times generated through model I.

(a) A summary of the solutions obtained for the orientation of an axis of rotational symmetry when the inversion assumes hexagonal symmetry, uses GKFF1 as an initial model, and is initialised from orientations spaced at 30 degree intervals throughout the semi-focal sphere. Notation and format as in Fig.6.16a with a reference RMS error of 0.0300.

(b) A summary of the solutions obtained from particular orientations using GKLF1 as an initial model and under the assumption of hexagonal symmetry. Notation and format as in Fig.6.16a with a reference RMS error of 0.0300.

(c) Dashed lines - a vertical section measured from 65,-5 through the wave-surfaces obtained by taking the weighted average of the four solutions at 65,-5 in (b) (solution I1 in Table D.1). Solid lines - the velocity-surfaces in the true model in the same section. Error bars as in Fig.6.16c.

(d) Dashed lines - a vertical section measured from -15,5 through the wave-surfaces obtained by taking the weighted average of the four solutions at 15,5 in (a) (solution I2 in Table D.1). Solid lines - the velocity-surfaces in the true model in the same section. Error bars as in Fig.6.16c.

(e) As (c) for the solution obtained by inverting the data set that includes shear-wave delays using the solution in (c) as the initial model (solution I3 in Table D.1).

(f) As (d) for the solution obtained by inverting the data set that includes shear-wave delays using the solution in (d) as the initial model (solution I4 in Table D.1).

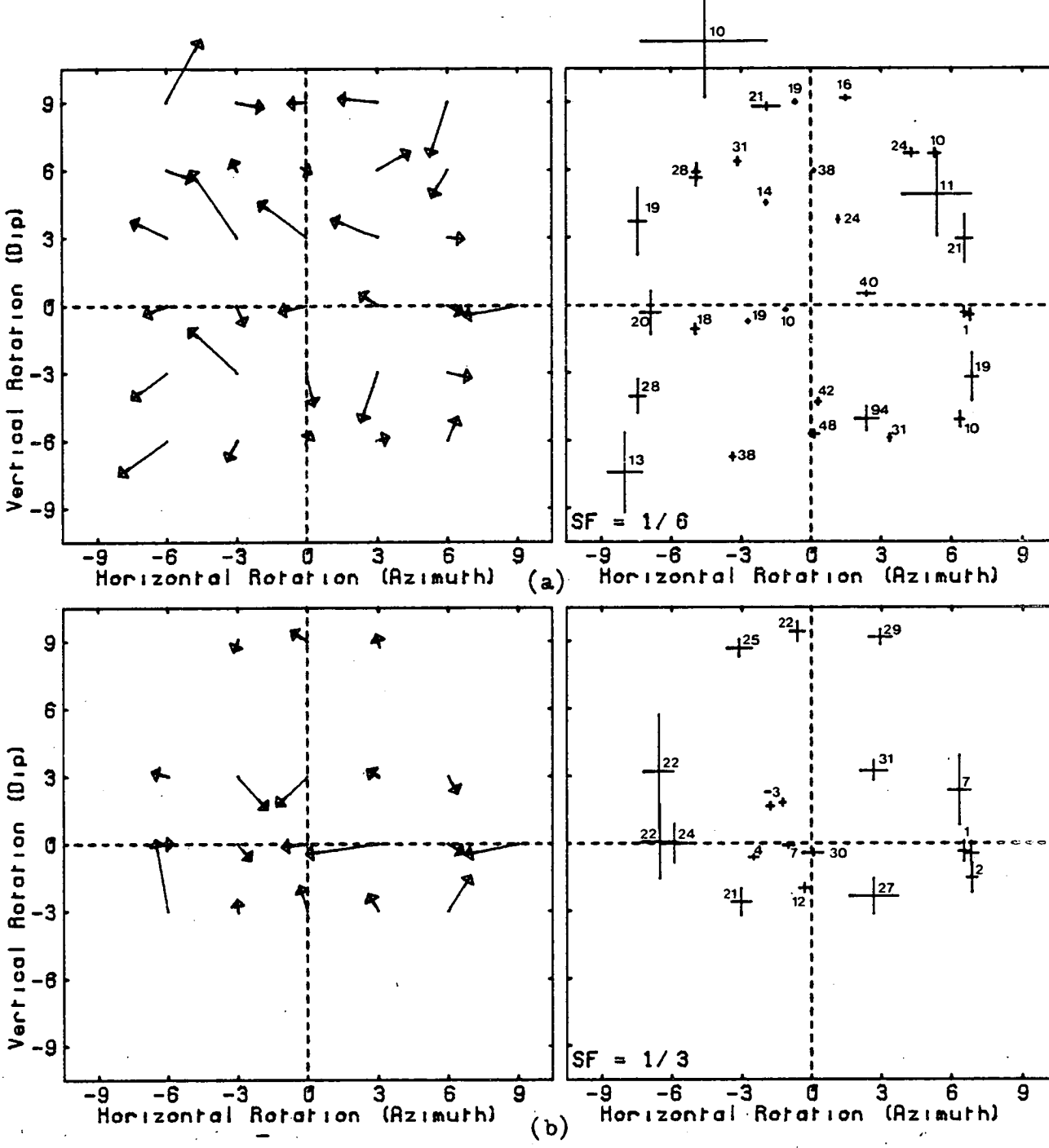
Vertical Rotation (Dip)
Horizontal Rotation (Azimuth)
(a)
SF = 1/6
SF = 1/3
(b)

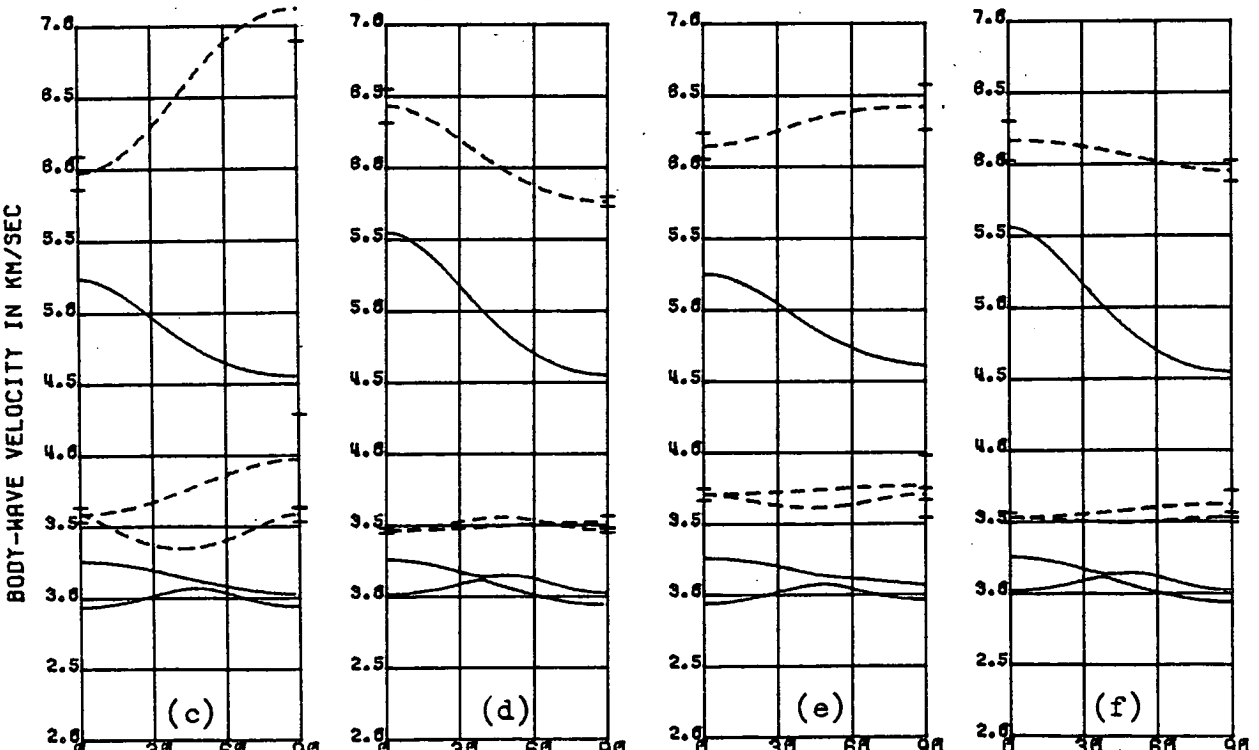
BODY-WAVE VELOCITY IN KM/SEC
(c)
(d)
(e)
(f)

Figure D.8 (cont.)

(g) A summary of the solutions obtained for the orientation of model I by performing an inversion for an orthorhombic structure using GKLF1 as an initial model. The reference RMS error is 0.0200.

(h) Dashed lines - a vertical section measured from -30,0 through the velocity-surfaces of the solution at -30,0 in (g) (solution I5 in Table D.1). Solid lines - the velocity-surfaces in the true model in the same section. Error bars as in Fig.6.16c.

(i) As (h) for the solution at 60,0 in (g) (solution I6 in Table D.1).

(j) As (h) for the solution using shear-wave delay data and where the solution in (h) is used as the initial model (solution I7 in Table D.1).

(k) As (h) for the solution using shear-wave delay data and where the solution in (i) is used as the initial model. (solution I8 in Table D.1).

(l) As (h) for the solution at -30,0 using revised trial hypocentres (solution I9 in Table D.1).

(m) As (h) for the solution at 60,0, using revised trial hypocentres (solution I10 in Table D.1). The upper error bar for the P-wave velocity in the symmetry direction is at 7.4km/sec.

(n) As (h) for the solution using shear-wave delay data and where the solution in (l) is used as the initial model (solution I11 in Table D.1).

(o) As (h) for the solution using shear-wave delay data and where the solution in (m) is used as the initial model (solution I12 in Table D.1).

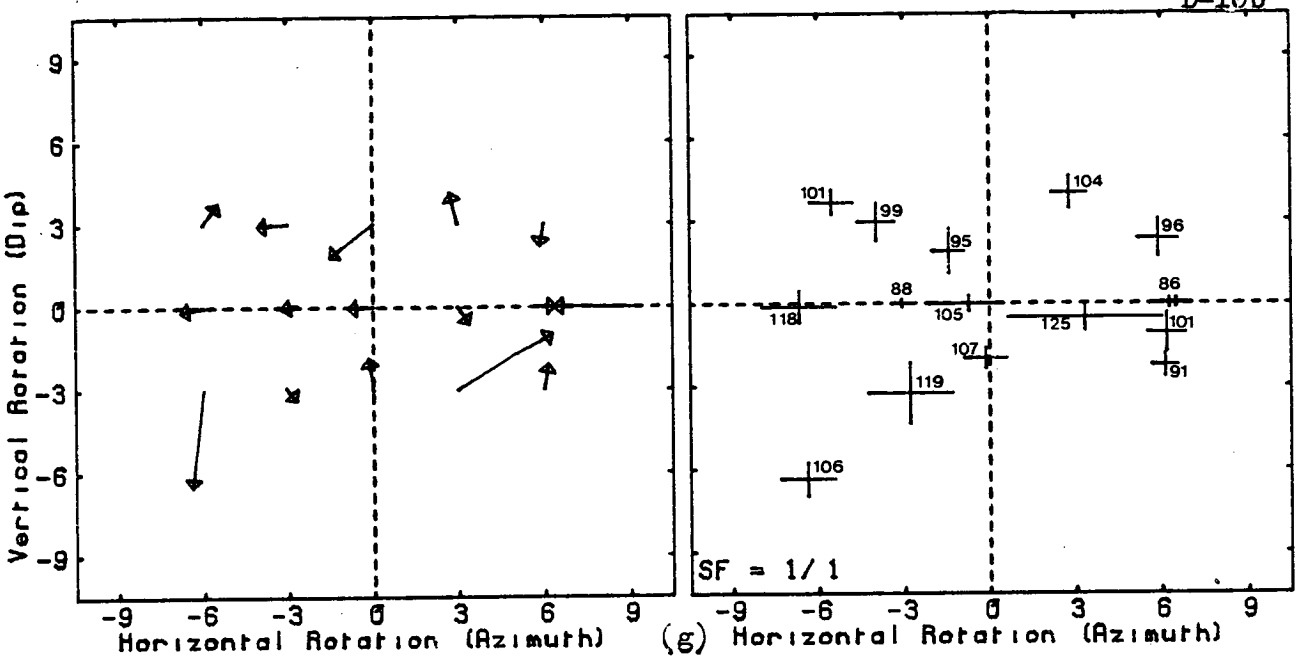
Vertical Rotation (Dip)
Horizontal Rotation (Azimuth)
101
99
95
104
96
88
86
118
105
125
101
107
91
119
106
SF = 1/1
(g) Horizontal Rotation (Azimuth)

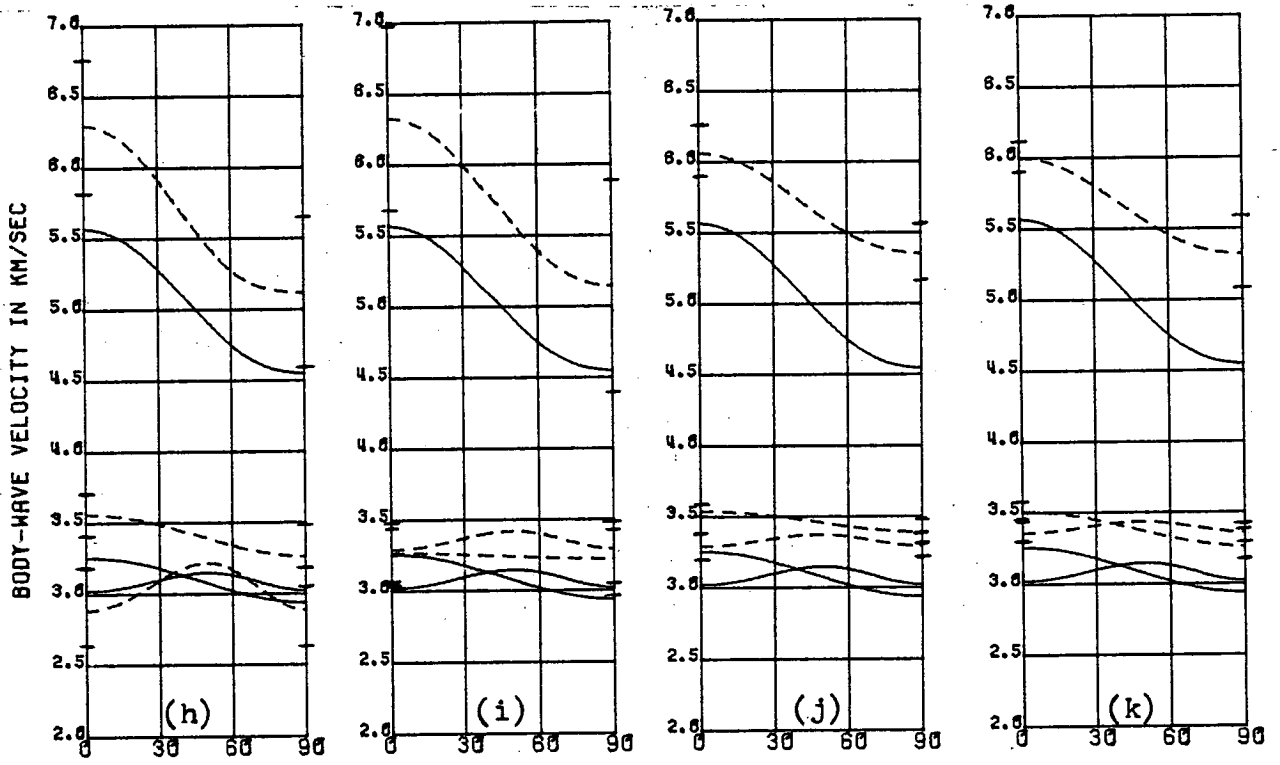
BODY-WAVE VELOCITY IN KM/SEC
(h)
(i)
(j)
(k)

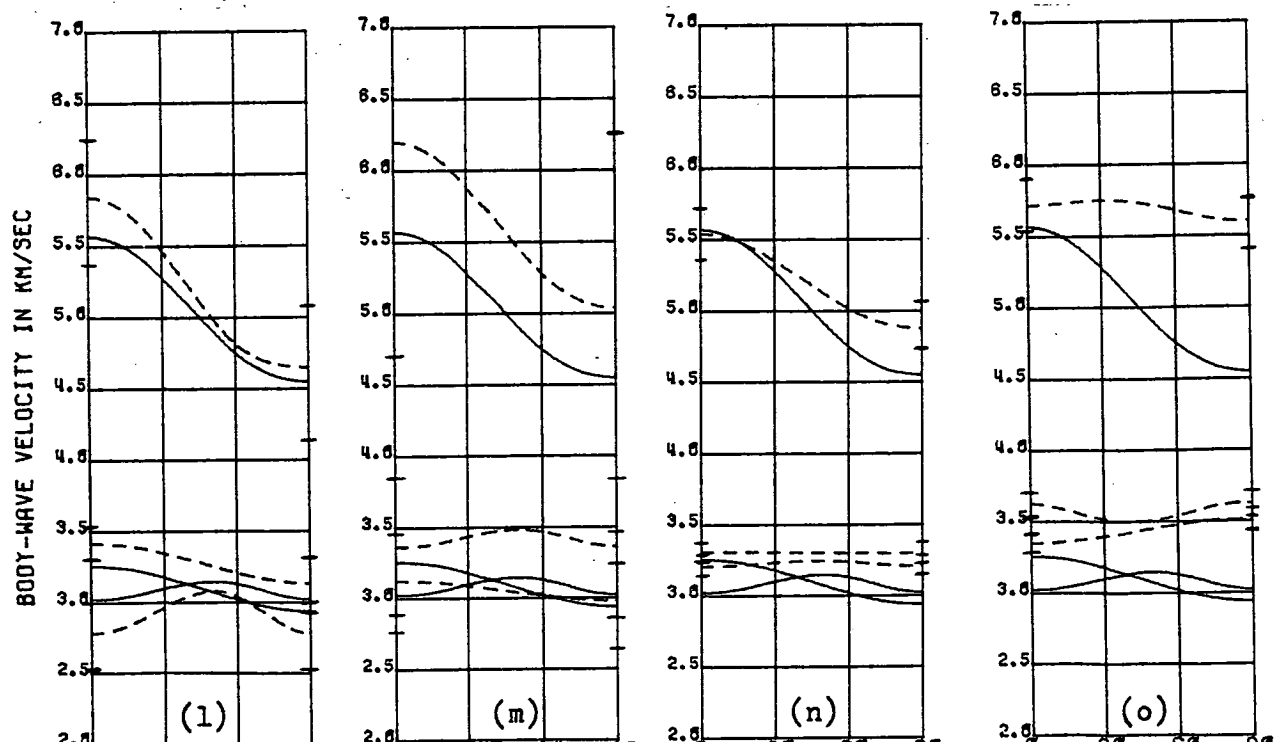
BODY-WAVE VELOCITY IN KM/SEC
(l)
(m)
(n)
(o)

the inversion. Using those hypocentres located in the structure determined above does not improve the solution. However, we can revise the hypocentres by using different isotropic velocities from those determined by the isotropic inversion. Figs.D.8(l and m) illustrate the solutions obtained at the two orientations using hypocentres determined under the assumption of constant isotropic P- and shear-wave velocities of 5.0 and 3.3 respectively (model I1 in Table 6.2). These velocities were chosen as being similar in relation to the sampled velocities (Fig.6.15) as those determined in the hexagonal models. This has resulted in a slight improvement of the absolute values of the P-wave velocity in all directions and in the form of the shear-wave surfaces. There are still very large errors on the elastic constants and the shear-wave surfaces do not imply the same structure. The use of shear-wave delay data using the model determined in these solutions produces the solutions shown in Fig.D.8n and D.8o. These solutions are a poorer fit to the data than obtained previously with the same data set, particularly for the solution shown in Fig.D.8c, and this is reflected in the poorer RMS errors. The substantial modifications of the elastic constants in the model may be a reflection of the indistinct nature of the two shear-wave surfaces, (see Fig.6.15), together with the reduced number of degrees of freedom in the data set.

As anticipated in section 6.4.1 this model has proven to be very difficult to resolve and the poor resolution is reflected in the large estimated errors of the elastic constants. However the inversion has correctly defined the orientations of two of the principal axes, and the solution is almost statistically superior to the isotropic solution. Although the form of the P-wave surface has been correctly determined, the large estimated errors associated with each of the elastic constants are such that none are significantly different. The weighted average of the elastic constants, C11, C22 and C33, from solutions I5 to I8, are 95.31,

82.90 and 73.94, with standard deviations 3.03, 1.61 and 3.85 respectively. In this case, only the high velocity direction (C11) is different from the others at more than two standard deviations. This suggests that in practise it may be difficult to conclusively determine which are the high, intermadiate and low velocity directions from the inversion procedure alone.

MODEL J

Fig.D.9a illustrates the solutions obtained for the orientation of an axis of rotational symmetry in model J. Four solutions define a minimum in both the RMS and orientation errors at an orientation of 65,5, with a suggestion of another solution at -50,-10. There is one solution with a much lower RMS error at an orientation of 0,90. Notice that there are some solutions with lower RMS errors but displaying no consistent pattern, and that all these RMS errors are much larger than obtained in the previous models. Fig.D.9b shows the solutions obtained in the second stage of the structure determination using GKLF1 as the initial model. The minima at 65,5 and 0,90 have again been well-defined and produce the wave-surfaces shown Figs.D.9c and D.9d. The inversion of shear-wave delay data does not confirm either solution (Figs.D.9e and f). The axis of rotational symmetry moves 40 degrees in one case and the form of the wave-surfaces is altered. As in model I, this suggests that a hexagonal system is insufficient to describe this structure.

In this model a solution cannot be obtained by inversion for orthorhombic symmetry when the very poor trial hypocentral locations (Table 6.2) are used. In practise the very low velocities obtained by the isotropic inversion may conflict with evidence of the velocity structure from refraction surveys. As in the case of the previous model we can re-determine the trial hypocentres using fixed isotropic velocities. In

Figure D.9. A summary of the solutions obtained by the inversion of synthetic arrival-times generated through model J.

(a) A summary of the solutions obtained for the orientation of an axis of rotational symmetry when the inversion assumes hexagonal symmetry, uses GKFF1 as an initial model and is initialised from orientations spaced at 30 degree intervals throughout the semi-focal sphere. Notation and format as in Fig.6.16a with a reference RMS error of 0.0200.

(b) A summary of the solutions obtained from particular orientations assuming hexagonal symmetry and using GKLF1 as an initial model. Notation and format as in Fig.6.16a with a reference RMS error of 0.0200.

(c) Dashed lines - a vertical section measured from -30,0 through the wave-surfaces obtained by taking the weighted average of the six solutions at 65,5 in (b) (solution J1 in Table D.1). Solid lines - the velocity-surfaces of the true model in the same section. Error bars as in Fig.6.16c.

(d) Dashed lines - a vertical section measured from 0,90 through the wave-surfaces obtained by taking the weighted average of the two solutions at 0,90 in (b) (solution J2 in Table D.1). Solid lines - the velocity-surfaces of the true model in the same section. Error bars as in Fig.6.16c.

(e) As (c) for the solution obtained by inverting the data set that includes shear-wave delays and using the solution in (c) as the initial model (solution J3 in Table D.1).

(f) As (c) for the solution obtained by inverting the data set that includes shear-wave delays and using the solution in (d) as the initial model (solution J4 in Table D.1).

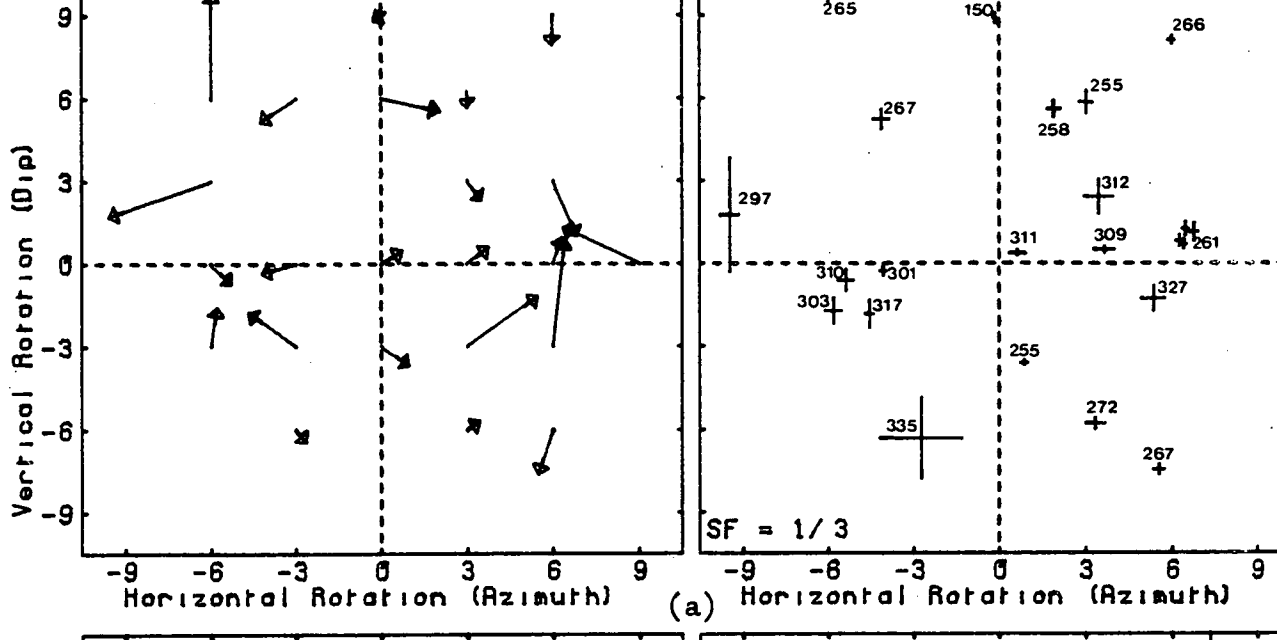
Vertical Rotation (Dip)
Horizontal Rotation (Azimuth)
SF = 1/3
(a)

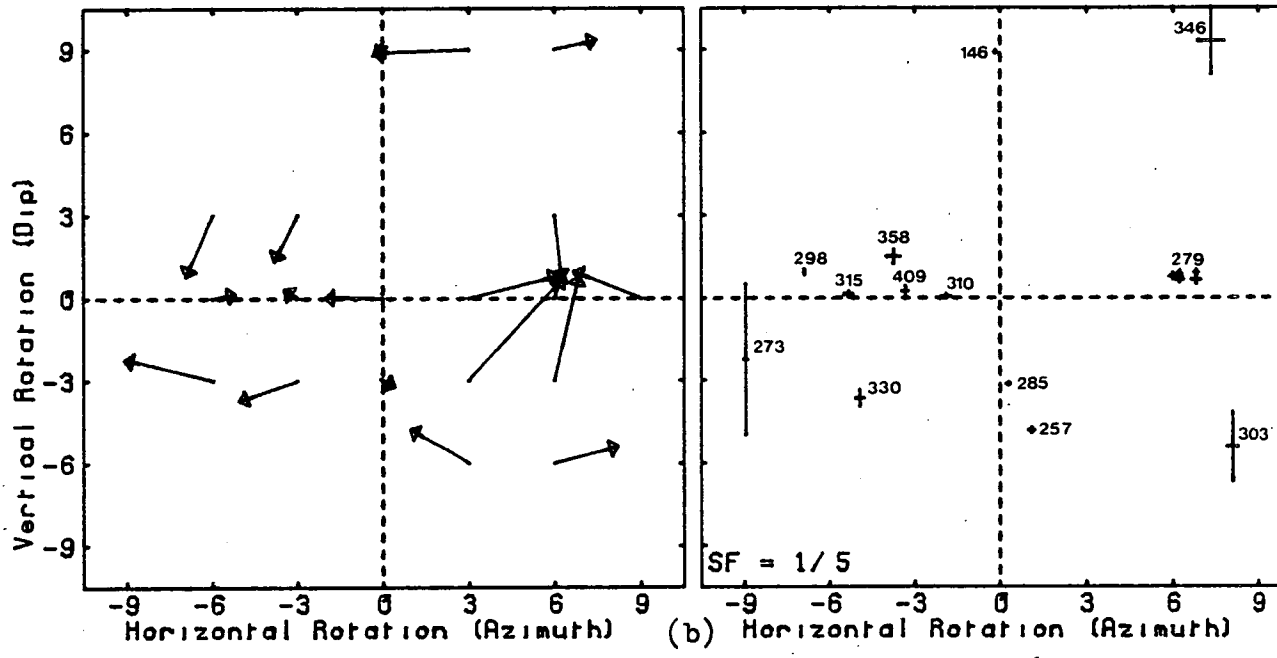
Vertical Rotation (Dip)
Horizontal Rotation (Azimuth)
SF = 1/5
(b)

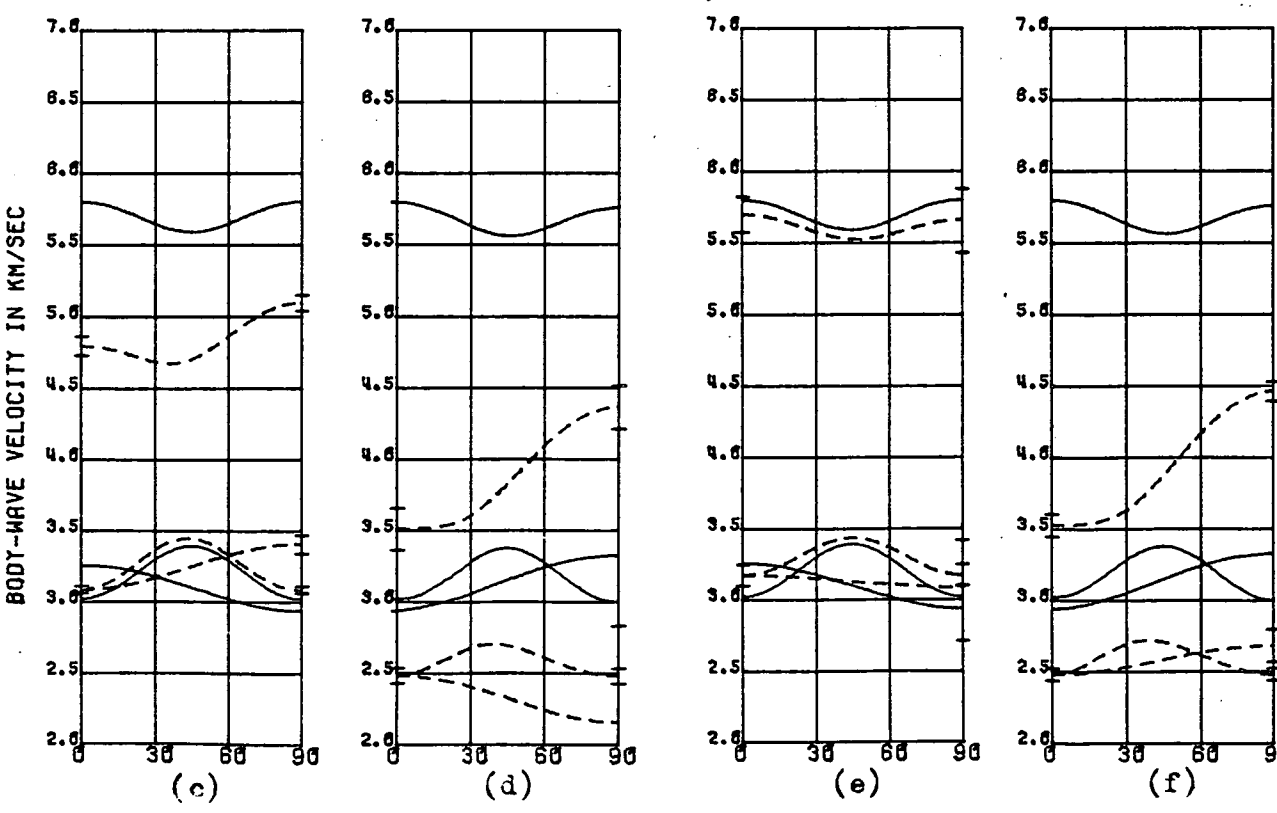
BODY-WAVE VELOCITY IN KM/SEC
(c)
(d)
(e)
(f)

Figure D.9 (cont.)

(g) A summary of the solutions obtained for the orientation of model J by performing an inversion for an orthorhombic structure using GKLF1 as an initial model. The reference RMS error is 0.0200.

(h) Dashed lines - a vertical section measured from -30,0 through the velocity-surfaces obtained by taking the weighted average of the solutions at 60,0 in (g) (solution J5 in Table D.1). Solid lines - the velocity-surfaces in the true model in the section. Error bars as in Fig.6.16c. The lower error bar on the first-shear-wave in the symmetry direction is at 1.91km/sec.

(i) As (h) for the solutions at -30,0 in (g) (solution J6 in Table D.1).

(j) As (h) for the solution at 0,90 in (g) (solution J7 in Table D.1).

(k) As (h) for the solution using shear-wave delay data and where the solution in (h) is used as the initial model (solution J8 in Table D.1).

(l) As (h) for the solution using shear-wave delay data and where the solution in (i) is used as the initial model (solution J9 in Table D.1)

(m) As (h) for the solution using the data set that includes shear-wave delays and where the solution in (j) is used as the initial model (solution J10 in Table D.1).

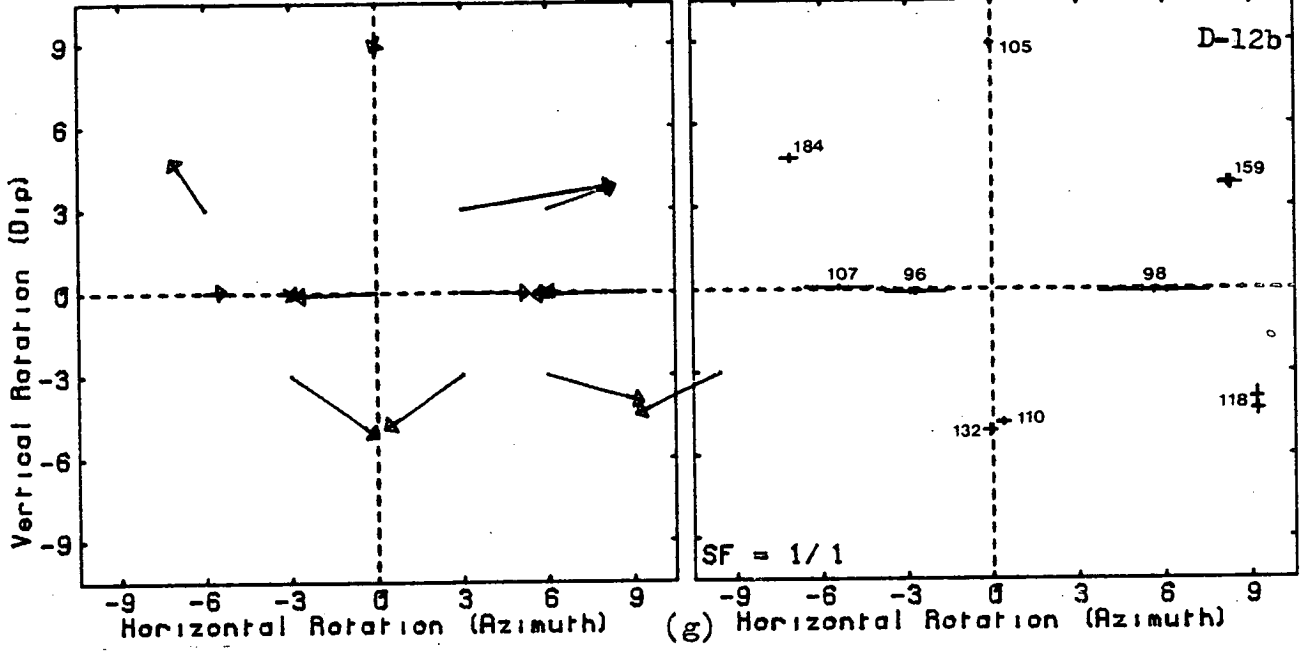
Vertical Rotation (Dip)
Horizontal Rotation (Azimuth)
SF = 1/1
D-12b
105
184
159
107
96
98
118
132
110
(g) Horizontal Rotation (Azimuth)

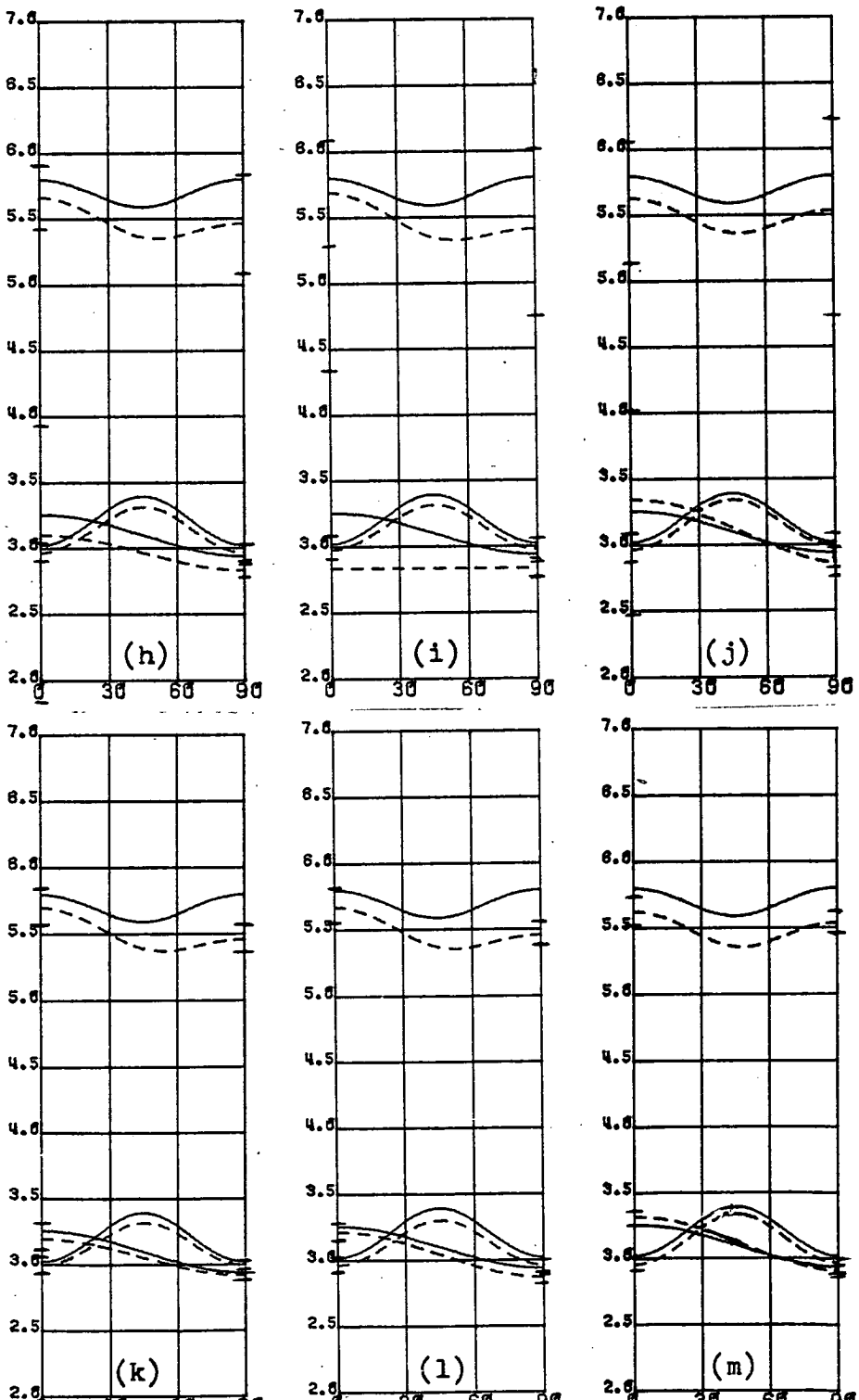
(h)
(i)
(j)
(k)
(l)
(m)

this case we use P- and S-wave velocities of 5.7 and 3.3km/sec respectively (Model J1 - Table 6.2). We will search for an orthorhombic solution at low dip angles and at 0,90 using GKLF1 as the initial model. The solutions are shown in Fig.D.9g. Three minima have been defined at the orientations of the principal axes at 60,0, -30,0 and 0,90. The velocity-surfaces associated with these solutions are shown in Figs.D.9h to j. The solutions at 60,0 and 0,90 are a good fit to all the surfaces but the velocities are too low in all directions. The solution at -30,0 is similar but the second shear-wave surface shows no directional variations. In all cases the errors on the elastic constants are very large but the solutions are statistically superior to the isotropic solution. All three solutions are improved by inversion of the data set containing shear-wave delays (Figs.D.9k to m). The error bars have been reduced and all three solutions are now consistent with the same structure.

APPENDIX E

PUBLISHED PAPERS

This appendix lists the papers that are in various stages of publication and which I have co-authored. In addition I briefly indicate my contribution to each of them. Copies of the published papers are bound at the end of this thesis.

E.1 Published papers

1) Crampin, S., Evans, J.R., Üçer, S.B., Doyle, M., Davis, J.P., Yegorkina, G.V., & Miller, A.,1980. Observations of dilatancy-induced polarisation anomalies and earthquake prediction. Nature, 286, 874-877.

2) Crampin ,S., Evans, J.R., Doyle, M., & Davis, J.P., 1981. Comments on papers about shear-wave splitting in dilatancy-induced anisotropy by I.N. Gupta and by A. Ryall and W.U. Savage. Bull. seis. Soc. Amer., 71, 375-377.

3) Evans, J.R., Doyle M., Üçer, S.B., Miller, A., & Crampin, S., 1980. An experiment to investigate polarisation-anomalies in North Anatolia, in Proc. Interdis. Conf. on Earthq. Pred. Res. in the North Anatolian Fault Zone, Istanbul, Friedr. Vieweg & Sohn, Weisbaden.

4) Doyle, M., McGonigle, R. & Crampin, S.,1981. The effects of crack anisotropy on hypocentral locations (Abstract). Geophys. J.R. astr. Soc., 65, p.250.

Paper 1) presents the preliminary observations of shear-wave splitting from the TDP1 experiment and my contribution was to assist Russ Evans in the data acquisition and in writing the program to plot polarisation diagrams on a routine basis. My contribution to paper 2) was to draw attention to, and discuss the mentioned papers. Crampin and Evans were responsible for the text. Papers

3) and 4) are the text and abstract of papers that I presented to conferences in Istanbul and Cambridge, respectively. Paper 4) is the abstract from the paper currently in press, and is not bound at the end of this thesis.

E.2 Paper in press

Doyle, M., McGonigle, R. & Crampin, S., 1982. The effects of crack-anisotropy on the hypocentral locations of local earthquakes. Geophys. J.R. astr. Soc., 68.

This paper is taken from Chapters 3, 4 and 5 of this thesis. Bob McGonigle supplied the routines for calculating velocities in an anisotropic solid, provided useful advice in the writing of various location programs, and commented on the text. Stuart Crampin made extensive comments on numerous drafts of the text.

E.3 Paper in preparation

Doyle, M., McGonigle, R., Crampin, S. & Evans, J.R., 1982. The joint-inversion of arrival-times in regions of dilatancy-anisotropy. Intended for publication in Geophys. J.R. astr. Soc..

This paper will be condensed from Chapters 6 and 7 of this thesis. Bob McGonigle again supplied the routines for calculating velocities in an anisotropic solid and helpled extensively in writing the inversion programs. All three co-authors have made extensive comments on the text.

Reprinted from Natuture. Vol. 286. No. 5776. pp. 874-877. August 28 1980

Observations of dilatancy-induced polarization anomalies and earthquake prediction

Stuart Crampin*, Russ Evans*, Balamir Üçer†, Mark Doyle*‡, J. Peter Davis*§, Galia V. Yegorkina|| & Alistair Miller*¶

* Institute of Geological Sciences. Murchison House. West Mains Road. Edinburgh EH9 3LA. UK
† Kandilli Observatory, Çengelköy, Istanbul, Turkey
‡ Department of Geophysics, University of Edinburgh. James Clerk Maxwell Building, Edinburgh EH9 3JZ. UK

Much of the search for earthquake prediction schemes has centred on the expectation that rocks in the impending source area will show dilatancy: the opening of cracks at high stress-levels. Recent developments in the theory of seismic wave propagation in cracked media[1] demonstrate that shear-wave splitting will occur in seismic-wave propagation through cracked structures, when the cracks have any overall alignment. This splitting causes polarization anomalies in the seismograms, and it has been suggested[1] that dilatancy, induced by the build-up of stress before earthquakes, might be recognized and monitored by analysis of these anomalies. We present here new observations which support this hypothesis.

The crust and upper mantle of the Earth are thoroughly permeated by cracks. Sedimentary rocks contain joints and fractures, which can lead to pronounced seismic velocity-anisotropy in shallow beds[2,3]. Igneous rocks in the crust, and possibly the crystalline upper-mantle[4], contain microcracks within grains and along grain boundaries[5]. These various cracks are essentially closed and transparent to seismic waves under high isotropic confining-pressure and low pore-pressure[4]. The primary action of non-hydrostatic stress on rock will be to modify the existing lines of weakness (cracks) in the rock, and the effects will depend on whether the cracks are initially open or closed, and on the relative confining and pore-pressures. At low ambient-stress and low pore-pressure, systems of open cracks may be differentially closed[6], and at high ambient-stress, systems of closed cracks may be differentially opened, if the pore pressure and non-lithostatic stresses are sufficiently high. The term 'dilatancy' is used here to cover both these differential processes, in addition to the usual meaning of the opening of fresh cracks under high local stress-levels. This differential opening of existing cracks may occur over substantial distances, and is probably the direct cause of many of the precursory phenomena, which are sometimes observed hundreds of kilometres from impending epicentres[7]. Laboratory experiments demonstrate that, in stressed rock-samples, existing cracks[6] and newly opened cracks[8-10] both take up pronounced alignments, and certainly all stress-induced dilatancy in the Earth will open cracks in preferred directions. Note that there is now a hypothesis that gas at high pore-pressure may exist at deep levels in seismic regions[11], so that dilatancy cracks could be gas filled even in the upper mantle.

The wavelengths of seismic waves are so much greater than the likely dimensions of any stress-induced cracks, that the velocity variations of seismic waves propagating through a dilatancy zone of aligned cracks can be modelled by propagation through purely-elastic anisotropic media[1]. Theoretical and numerical calculations demonstrate[1,12,13] that, except in a few specific symmetry-directions, anisotropy writes a characteristic signature into the polarization of the shear wavetrain. This

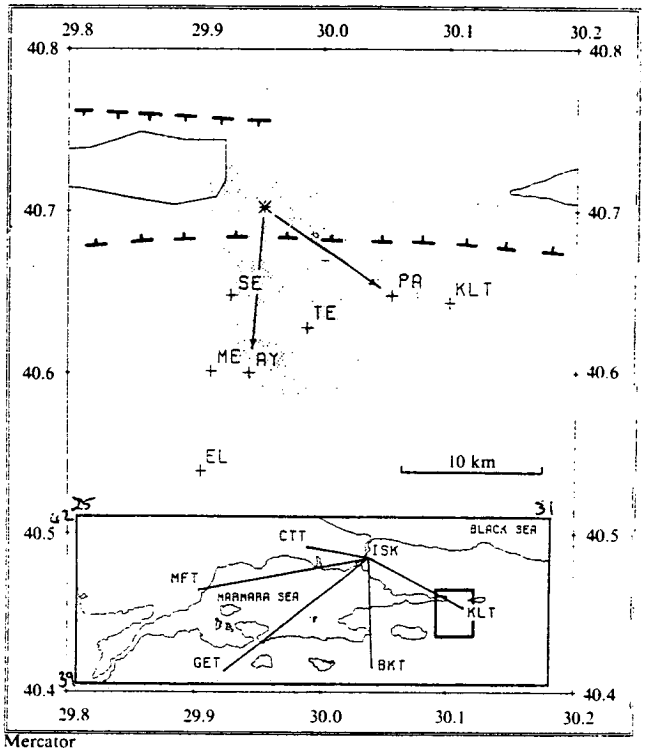

Fig. 1 Map showing the TDPNET three-component stations, with inset of MARNET stations. Most of the local earthquakes occurred within the shaded area, and the epicentre of the earthquake used for Fig. 2 is marked by an asterisk. The heavy dashed line shows the approximate lines of the Northern Anatolian Fault, which in this area appears to be a graben structure.

signature is a distinctive feature of seismic waves propagating through anisotropic media and will persist for any following isotropic-segments of the path. A plane shear-wave splits on entry into a dilatancy zone into two orthogonally-polarized phases, which are not, in general, parallel to either the vertical or horizontal directions (curved wavefronts show more complicated effects). These split waves travel with different velocities, and result in the shear-wave particle-motion being resolvable into nearly-orthogonally polarized components[1,13]. The arrival of these 'split' shear-waves may be identified by abrupt changes in direction (anomalies) of the particle motion, when plotted in polarization diagrams[1]. The time delay between the phases may be estimated from suitable rotated seismograms, or more directly from polarization diagrams. This delay is proportional to the degree of differential shear-wave anisotropy, and the length of the path through the anisotropic rock, which for long paths will be the dimensions of the dilatancy zone. Consequently, the delay is not very sensitive to small errors in epicentral location or focal depth. However, it is sensitive even to quite weak crack-anisotropy[1], and seems to be a way of monitoring the whole dilatancy episode from initiation of the stress-induced cracking, through the possible influx of water[14], to the conclusion of the earthquake sequence. An example of the sensitivity is that saturation of dry cracks by water would approximately double the differential shear-wave anisotropy for about half of all directions of propagation through any given system of cracks[1]. This should be recognizable on the seismograms, and may help to resolve whether cracks are gas filled at depth in the crust, and whether the influx of water is an essential part of the source process. Thus, if they can be observed, shear-wave polarization-anomalies could lead to a better understanding of the whole earthquake source-process.

We believe that such anomalies have now been observed. For several years, delays between shear-wave arrivals on pairs of

Present addresses: § Department of Geological & Geophysical Sciences, Princeton University, Princeton, New Jersey 08540; || Institute of Physics of the Earth, Bolshaya Grouzinskaya 10, Moscow 123810, USSR; ¶ Overseas Development Administration, Eland House, Stag Place, London SW1E 5DH, UK.

unrotated horizontal-component seismograms have been recorded[15] on arrays of three-component seismometers in seismic regions in Armenia, and Fergana, USSR. The delays were observed on between 5 and 10% of all seismograms from local and regional events at all azimuths and at distances up to 450 km. These delays were interpreted[15] as being due to shear-wave splitting caused by anisotropy directly induced by the build-up of stress before an earthquake. Recently, the magnitudes of these delays have been shown to vary before large earthquakes, and to be correlated with the directions of nearby geological faults[16]. However, we consider that anisotropy due to crack dilatancy is likely to dominate any anisotropy directly induced by stress in the Earth.

Gupta[17] probably observed similar anomalies to those of Yegorkina *et al.*[15] from several series of earthquakes in Nevada, US, at distances of >100 km from a single three-component seismic station. However, the small range of azimuths did not allow any convincing interpretation[18], and Gupta was misled into seeking shear-waves split only into SV and SH components, when the seismic traces clearly did not display such polarizations. Gupta's observations will be discussed in detail elsewhere.

Similar delays have been observed on records from a small closely-spaced network in Turkey, TDPNET (Fig. 1), of three-component seismometers specifically designed to monitor polarization anomalies. A centre of low-magnitude seismic activity was identified near the Northern Anatolian Fault from MARNET records (MARNET is a radio-linked seismic network spanning the Marmara Sea, Turkey). A collaborative project between the Institute of Geological Sciences and Kandilli Observatory deployed TDPNET over the swarm activity for eight weeks during the summer of 1979. High-quality recordings were obtained from several hundred small earthquakes at epicentral distances of <20 km, and depths between 8 and 15 km. The analogue magnetic-tape records were digitized at 100 samples s^{-1}, and display impulsive P- and S-wave arrivals very suitable for polarization analysis. A few records show shear waves arriving at different times on the unrotated horizontal-seismograms from events at all azimuths, similar to the observations of Yegorkina *et al.*[15,16]. The majority, however, show shear waves arriving at the same time on both horizontal traces, and display shear-wave splitting only when plotted in polarization diagrams.

Figure 2 shows examples of both types of record from the same earthquake at different stations. The seismograms are typical of the data set: almost every shear wavetrain with sufficient signal-to-noise ratio (several hundred examples) shows shear-wave splitting in polarization diagrams, and a few show splitting in the unrotated horizontal-seismograms, as in the observations of Yegorkina *et al.* Figure 2*a* shows separate shear-wave arrivals on the two horizontal-components, despite the azimuth to the epicentre being 40° from the instrument orientations: the shear arrival on the east-west component is about 0.2 s later than the arrival on the north-south. Figure 2*b* shows shear waves arriving simultaneously on both horizontal components. Splitting is not easily identified on the original or the rotated seismograms, but is clearly visible in the horizontal projection of the polarization diagrams.

The horizontal polarizations diagrams show abrupt changes in the direction of the particle motion. We interpret these anomalies as the arrival of phases with different linear polarizations due to shear-wave splitting in propagation through anisotropic material. Any other explanation is untenable: the anomalies cannot be caused by isotropic discontinuities, because no isotropic structure can split shear waves propagating in almost all directions; and it is unlikely to be a source effect, when the sources are small and the P-wave arrivals comparatively simple. There are very few previous studies of short-period particle-motion so it is difficult to know what sort of phenomena to expect. Local and regional earthquakes that we have examined in a region of low seismicity (Scotland) have elliptical shear-motion without the characteristic abrupt turning points of the

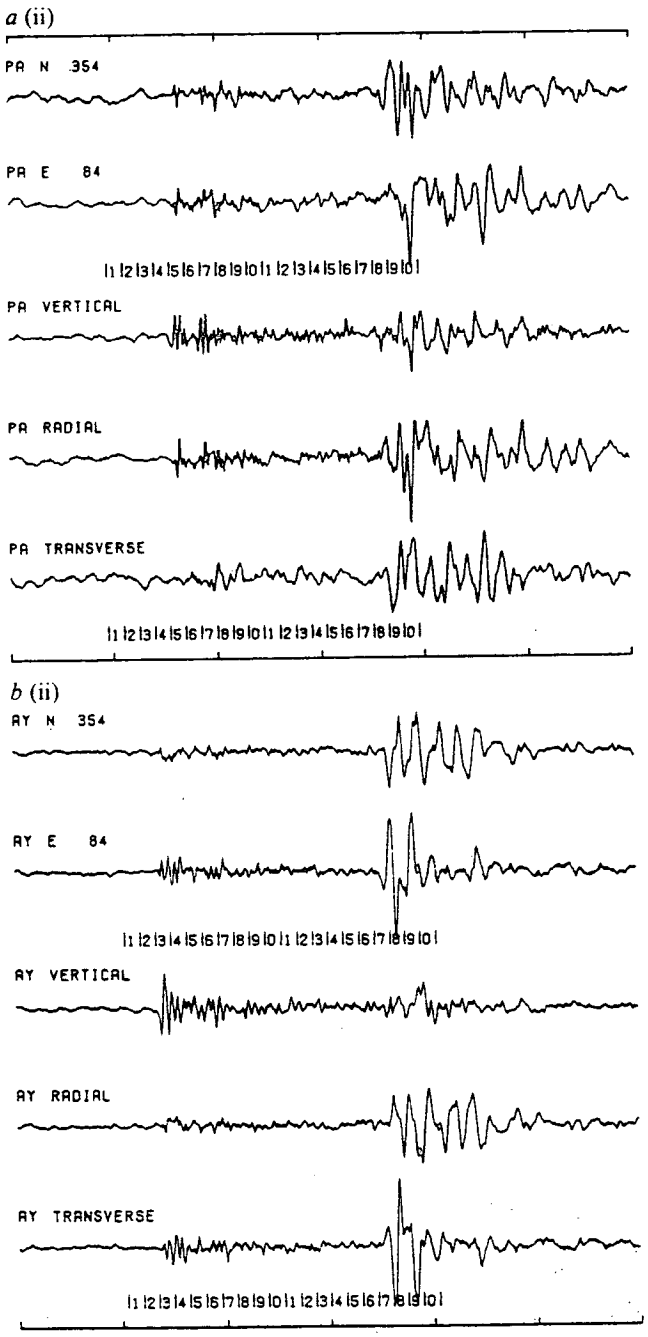

Fig. 2 Examples of seismograms and polarization diagrams for a small earthquake on 15 September 1979 with epicentre 40°42'10" N, 29°57'13" E, depth 13 km, and magnitude $M_L = 1.5$. The seismograms are, from the top: unrotated horizontals N 354° E and N 84° E, vertical, and rotated radial and transverse components. The numbered polarization-diagrams for P- and S-wave arrivals are the projections of the particle motion on to three orthogonal-planes for the correspondingly numbered 0.15-s time-windows marked either side of the rotated traces. Directions: U, up; D, down; T, towards; A, away from the source. L, left; R, right in the direction of the station. Each set of three diagrams has been normalized and the relative multiplication factor is marked at the bottom left of each diagram. The heavy arrows on the horizontal projection of the S waves mark the first S-wave arrival, and the subsequent arrivals of phases with different polarizations. Cross bars marked on the polarization diagrams at every 1/100 s, allow delays to be estimated. *a*, Seismograms at PA: hypocentral distance 17 km; azimuth of arrival N 305° E. *b*, Seismograms at AY: hypocentral distance 18 km; azimuth of arrival N 5° E.

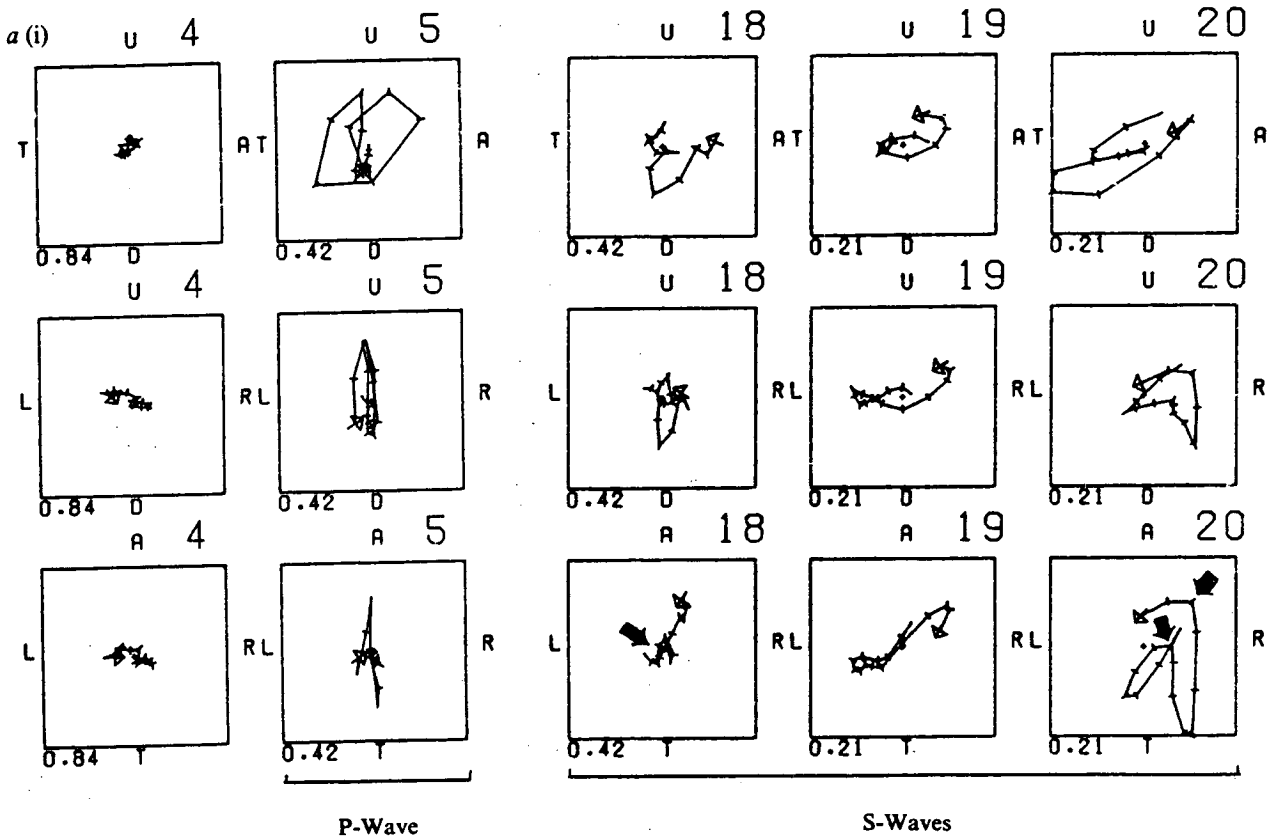
a (i)
U 4
U 5
U 18
U 19
U 20
T
AT
A
L
RL
R
0.84
0.42
0.21
D
T
P-Wave
S-Waves

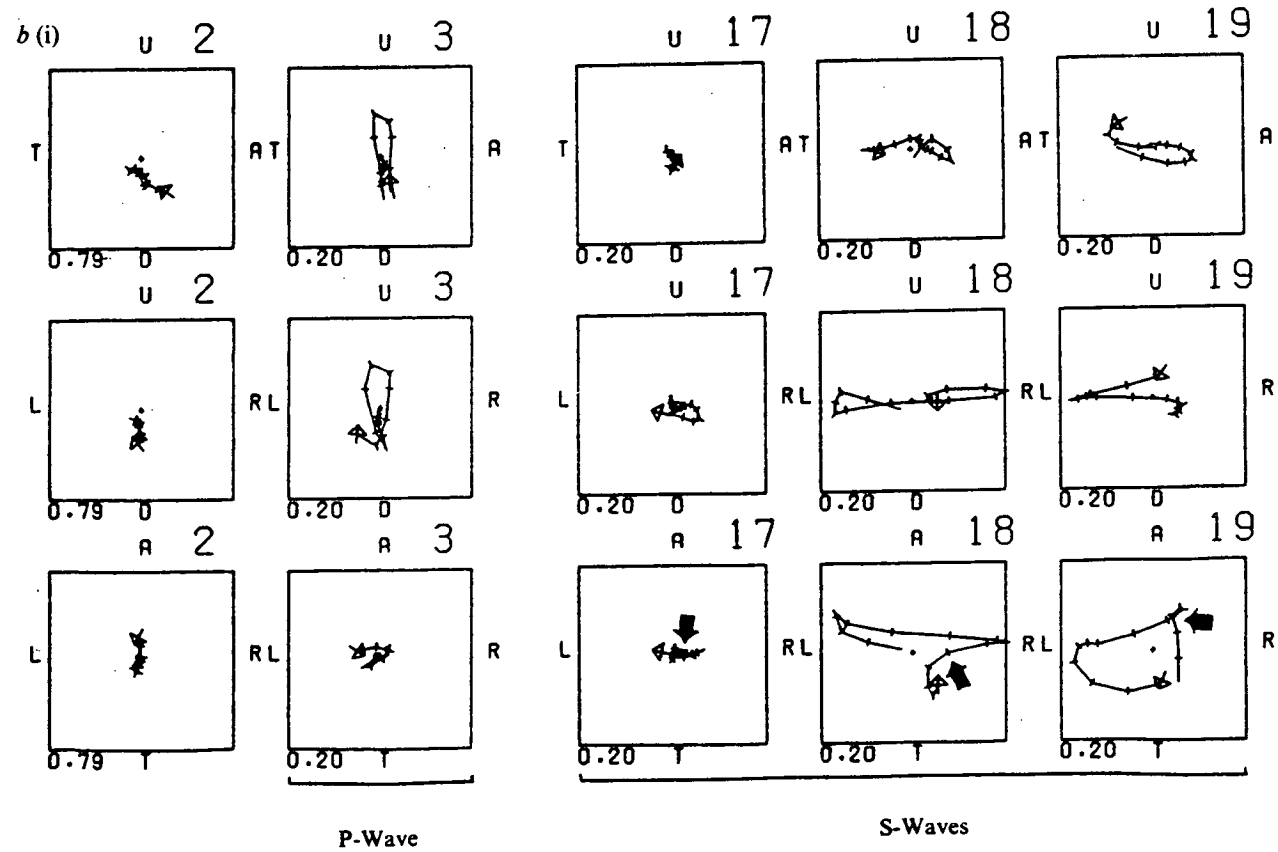
b (i)
U 2
U 3
U 17
U 18
U 19
T
AT
A
L
RL
R
0.79
0.20
D
T
P-Wave
S-Waves

TDPNET records. Orthogonal changes in polarization are sometimes observed in local and regional events, when there is a mixture of Rayleigh and Love surface-waves present. However, this cannot account for orthogonal polarizations in the first half-second following the initial shear-arrival, particularly when the paths are direct rays with little possibility of head-wave, channel-wave, or surface-wave interactions. We consider that some form of anisotropy must be the cause of the split shear-arrivals.

We suggest that dilatancy is the only possible explanation of this anisotropy. Stress on cracked rock (all crustal rocks are heavily cracked[2,5], although many of these cracks may be initially sealed) causes the cracks to open and close anisotropically[6], and such dilatant structures are expected to cause shear-wave splitting[1]. Dilatancy is the only possible explanation of anisotropy, which can have such large, if not dominating, effects in such otherwise heterogeneous regions as Turkey and Armenia. A demonstration that the delays between the shear waves vary with time (stress) would confirm our interpretation.

Clearly, such splitting is not easy to analyse. However, some conclusions can be drawn from the existing data: many of the shear waves in the TDPNET records (Fig. 2*a*) and Armenia[15] do not split parallel to SH or SV, but into more general orientations. This supports the hypothesis that the splitting is not caused by isotropic conversions. It also suggests that the dilatancy is unlikely to consist of horizontal cracking as suggested by Wang[19], which would result in transverse isotropy and splitting only into SH or SV components.

Figure 2 shows several abrupt changes in direction of the shear-wave polarizations. These may be due to complicated local structure, but may also be due to a curved wavefront propagating through a structure with comparatively strong anisotropy. The group-velocity vector is not, in general, parallel to the phase-velocity vector in anisotropic media[12]. Consequently, the map of the positions reached by the energy of two shear-waves radiating from a point in a given time, the wave surface, may be extremely complicated, with three-dimensional cusps, ridges, and multiple points. Cusps, in particular, are very common features of shear-wave energy propagation in anything other than very weak anisotropy. Rays propagating in directions within a cusp may have four shear-wave arrivals, with different velocities, different polarizations, and wavefronts which are not parallel. The density of cracks in Earth structures is large enough to produce strong anisotropy: the only detailed field measurements of velocity anisotropy known to us[2] were interpreted[3] as due to two sets of intersecting cracks, each with crack density of the order of 0.2. The large crack densities were due to large dimensions and aspect ratios. Thus, some crack anisotropy in the Earth is strong enough to produce complicated wave-surfaces containing cusps, and this is preferred explanation for the several abrupt changes of polarization in Fig. 2.

Our comparatively simple hypothesis of extensive dilatancy links several previously unrelated earthquake phenomena, and seems to be present to the several seismic regions of North Anatolia, Armenia, Fergana, and possibly Nevada. Our suggestion that stress in the Earth can be monitored by examining shear wavetrains in polarization diagrams would be very important for earthquake prediction studies. All previous precursors, including V_P/V_S anomalies[1], are probably indirect effects of this dilatancy, and seem to occur unpredictably. The TDP experiment suggests that polarization anomalies may occur in almost all shear wavetrains propagating through dilatancy zones, and might be generally available for estimating changes in the Earth's stress.

We thank Dr J. C. Savage for helpful comments. This research has been supported by various organizations, but mostly by the Natural Environment Research Council and Kandilli Observatory. This letter is published with the approval of the director of the Institute of Geological Sciences.

Received 16 May; accepted 2 July 1980.

1. Crampin, S. *Geophys. J. R. astr. Soc.* **53**, 467–496 (1978).
2. Bamford, D. & Nunn, K. R. *Geophys. Prosp.* **27**, 322–338 (1979).
3. Crampin, S., McGonigle, R. & Bamford, D. *Geophysics* **45**, 345–360 (1980).
4. Brace, W. F. *Flow and Fracture in Rocks* (eds Heard, H. C., Borg, I. Y., Carter, N. L. & Raleigh, C. B.) (*Geophys. Monogr.*, 16, AGU, Washington, 1972).
5. Simmons, G. & Richter, D. *Physics and Chemistry of Minerals and Rocks*, 105–137 (ed Strens, R. G. J.) (Wiley, New York, 1976).
6. Nur, A. & Simmons, G. *J. geophys. Res.* **74**, 6667–6674 (1969).
7. Dobrovolsky, I. P., Zubkov, S. I. & Miachkin, V. I. *Pure appl. Geophys.* **117**, 1025–1044 (1979).
8. Brace, W. F., Paulding, B. W. & Scholz, C. *J. geophys. Res.* **71**, 3939–3953 (1966).
9. Gupta, I. N. *Bull. seism. Soc. Am.* **63**, 1157–1165 (1973).
10. Hadley, K. *J. geophys. Res.* **80**, 4845–4850 (1975).
11. Gold, T. *J. petrol. Geol.* **1**, 3–19 (1979).
12. Crampin, S. *Geophys. J. R. astr. Soc.* **49**, 9–27 (1977).
13. Keith, C. M. & Crampin, S. *Geophys. J. R. astr. Soc.* **49**, 181–245 (1977).
14. Myachkin, V. I., Brace, W. F., Sobolev, G. A. & Dieterich, J. H. *Pure appl. Geophys.* **113**, 169–181 (1975).
15. Yegorkina, G. V., Rakitov, V. A., Garetovskaya, I. V. & Yegorova, L. M. *Izv. Akad. Nauk. SSSR. Fiz. Zemli. No. 8*, 43–55 (in Russian), 554–562 (English edition) (1977).
16. Volvovsky, I. S., Egorkina, G. V. & Popov, E. A. *Pap. Workshop on Modern Methods of Registration and Interpretation of Seismic Observations*, Yalta (1979).
17. Gupta, I. N. *Science* **182**, 1129–1132 (1973); *Bull. seis. Soc. Am.*, **64**, 1997–2001 (1974), **65**, 425–437 (1975).
18. Ryall, A. & Savage, W. U. *Bull. seism. Soc. Am.* **64**, 1943–1951 (1974).
19. Wang, C.-Y. *Nature* **251**, 405–406 (1974).

Printed in Great Britain by Macmillan Production Ltd., Basingstoke, Hampshire

Bulletin of the Seismological Society of America, Vol. 71, No. 1, pp. 375–377, February 1981

COMMENTS ON PAPERS ABOUT SHEAR-WAVE SPLITTING IN DILATANCY-INDUCED ANISOTROPY BY I. N. GUPTA AND BY A. RYALL AND W. U. SAVAGE

BY STUART CRAMPIN, RUSS EVANS, MARK DOYLE, AND J. PETER DAVIS*

Gupta (1973b) reports shear waves splitting into *SH* and *SV* components on unrotated seismograms from two series of earthquakes in Nevada recorded at a three-component station, TNP, at epicentral distances of 100 and 130 km, respectively. He interprets the splitting as due to dilatancy-induced anisotropy in the source region. These seismograms have been variously interpreted by Gupta (1973b, 1974) and by Ryall and Savage (1974), and all three papers seem to be in error as a result of some misunderstandings of the nature of anisotropic propagation.

These misunderstandings are summarized in Table 1 of Gupta (1973a). Gupta made rock-fracturing experiments in the laboratory, and measured *P*- and *S*-wave velocity variations (the shear-wave polarizations were undifferentiated) along the compressional, null, and tensional axes under increasing load. The velocity variations demonstrate, as would be expected (Brace *et al.*, 1966), that dilatancy cracks open perpendicular to the tensional axis and parallel to the compressive axis (except during the last 10 per cent of the stress increase immediately before failure, when more general cracking occurs). Gupta then infers (probably correctly, to a first approximation) that these results can be used to identify the anisotropic orientations before the three basic types of earthquake fault-mechanisms; thrust, normal, and strike-slip. However, Gupta then goes on to quote Nur and Simmons (1969) and Nur (1971) in support of statements in Table 1 suggesting that dilatancy before all three types of mechanisms will cause shear waves to split into *SH* and *SV* components for many directions of propagation. These are not correct inferences from the work of Nur and Simmons, and almost all the statements in Table 1 (Gupta, 1973a) are either wrong or require severe qualifications.

All shear waves propagating in anisotropic media split into two components with orthogonal particle-motion polarization relative to the direction of phase propagation. These polarizations are *fixed* for the particular direction of propagation in the particular anisotropic structure, and generally will not have *SH* and *SV* polarizations except in a few particular directions of anisotropic symmetry (Crampin, 1977). The only cracked media, where shear waves split into components with *SH* and *SV* polarizations for all directions of propagation, are transversely isotropic structures consisting of a uniform distribution of parallel-horizontal cracks (Crampin, 1978), a random distribution of vertical cracks (cracks with co-planar normals; Crampin and Radovich, in preparation), or any other arrangement of cracks with a vertical axis of cylindrical symmetry. Dilatancy with parallel-horizontal cracks might be expected before thrust fault-mechanisms (Gupta, 1973a), but the earthquakes in Nevada do not have thrust mechanisms (Gupta, 1973b). Without transversely isotropic symmetry, splitting into *SH* and *SV* would only be expected in a few isolated directions, and it would be a remarkable coincidence if the two distinct 5°-azimuthal ranges covered from TNP both happen to be such symmetry directions. In fact, many of the shear-wave seismograms illustrated in Gupta (1973b) and in Ryall and Savage (1974) do not split into *SH* and *SV*. For example, Figure 2 of Gupta and Figure 1 of

* Rotary International Foundation Fellow.

Ryall and Savage show shear waves, identified as *SH*, but having polarizations at 45° or less to the radial direction, that cannot be classified as *SH* in the usual sense. These various misunderstandings lead Gupta and Ryall and Savage into seeking features on the seismograms that are not necessarily implied by anisotropy.

Observations of shear-wave splitting due to stress-induced anistropy have been made by Yegorkina *et al.* (1977), who observed splitting as distinct shear-wave arrivals on unrotated horizontal seismograms on records from all azimuths in Armenia, USSR. Note that these are not necessarily *SH* or *SV* polarizations. Crampin *et al.* (1980) have observed splitting in polarization diagrams of records of small earthquakes immediately beneath a small closely spaced network of three-component instruments near the Northern Anatolian Fault in Turkey. Crampin *et al.* identified shear-wave splitting as the cause of abrupt changes in the direction of the observed particle motion, and such abrupt changes in direction, as a split shear wave arrives with nearly orthogonal particle motion, are diagnostic of anisotropic propagation (Crampin, 1977, 1978). Ryall and Savage (1974) show a few plots of particle motion for the Nevada earthquakes. However, the seismograms are too noisy (with signal-to-noise ratios of barely two on some components), the sampling rate too coarse, and the anticipated abrupt arrivals are smoothed and cannot easily be recognized. Yegorkina *et al.* (1977), using similar analysis to Gupta (1973b), but in a region of much higher seismicity, confine their attention to the small percentage of seismograms *from all azimuths*, which demonstrate shear-wave splitting on unrotated horizontal seismograms.

Shear-wave splitting is strongly diagnostic of anisotropy. It is difficult to devise combinations of isotropic features that can produce distinct shear-wave arrivals with nearly orthogonal polarizations for almost all directions of propagation. The fact that splitting is rarely identified on *unrotated seismograms* (Ryall and Savage, 1974), is expected, and agrees with the observations of Yegorkina *et al.* (1977) and Crampin *et al.* (1980). Shear waves will be split for all directions of propagation in anisotropic media. This splitting will be visible in appropriate polarization diagrams, but will only be seen on unrotated seismograms in a few directions of propagation.

Gupta (1975) presents further observations of shear-wave splitting, which he interprets as showing temporal variations during two (more distant) earthquake sequences at another location in Nevada. However, he presents no illustrations of seismograms, and implies that he uses the same criteria for recognizing splitting as in his previous papers. The comments in this letter should still apply.

We conclude that, although the Nevada records may show dilatancy-induced shear-wave splitting, it is impossible to confirm this from unrotated seismograms in isolated directions. If observations can be obtained over a suitable range of directions, as in Yegorkina *et al.* (1977) and Crampin *et al.* (1980), they can indicate the presence of dilatancy-induced anisotropy, and may be important for monitoring stress changes before earthquakes.

Acknowledgments

This work was supported by the Natural Environment Research Council, and is published with the approval of the Director of the Institute of Geological Sciences.

References

Brace, W. F., B. W. Paulding, and C. Scholz (1966). Dilatancy in the fracture of crystalline rock, *J. Geophys. Res.* **71**, 3939–3953.

Crampin, S. (1977). A review of the effects of anisotropic layering on the propagation of seismic waves, *Geophys. J.* **49**, 9–27.

Crampin, S. (1978). Seismic-wave propagation through a cracked solid: polarization as a possible dilatancy diagnostic, *Geophys. J.* **53**, 467–496.

Crampin, S., R. Evans, S. B. Üçer, M. Doyle, J. P. Davis, G. V. Yegorkina, and A. Miller (1980). Observations of dilatancy-induced polarization anomalies and earthquake prediction, *Nature* **286**, 874–877.

Gupta, I. N. (1973a). Dilatancy and premonitory variations of *P*, *S* travel times. *Bull. Seism. Soc. Am.* **63**, 1157–1161.

Gupta, I. N. (1973b). Premonitory variations in *S*-wave velocity anisotropy before earthquakes in Nevada, *Science* **182**, 1129–1132.

Gupta, I. N. (1974). Comments on "*S*-wave splitting: a key to earthquake prediction?" by A. Ryall and W. U. Savage, *Bull. Seism. Soc. Am.* **64**, 1997–2001.

Gupta, I. N. (1975). Premonitory seismic-wave phenomena before earthquakes near Fairview Peak, Nevada, *Bull. Seism. Soc. Am.* **65**, 425–437.

Nur, A. (1971). Effects of stress on velocity anisotropy in rocks with cracks, *J. Geophys. Res.* **76**, 2022–2034.

Nur, A. and G. Simmons (1969). Stress-induced velocity anisotropy in rocks with cracks: an experimental study. *J. Geophys. Res.* **74**, 6667–6674.

Ryall, A. and W. U. Savage (1974). *S*-wave splitting: key to earthquake prediction?, *Bull. Seism. Soc. Am.* **64**, 1943–1951.

Yegorkina, G. V., V. A. Rakitov, I. V. Garetovskaya, and L. M. Yegorova (1977). Anisotropy of velocities of seismic waves and the stress state of the Earth's crust in the territory of Armenia (in Russian), *Izv. Akad. Nauk SSSR. Fiz. Zemli, No. 8*, 43–55 (554–562 of the English edition).

INSTITUTE OF GEOLOGICAL SCIENCES
MURCHISON HOUSE
WEST MAINS ROAD
EDINBURGH EH9-3LA, SCOTLAND
(S.C., R.E., M.D.)

DEPARTMENT OF GEOPHYSICS
UNIVERSITY OF EDINBURGH
JAMES CLERK MAXWELL BUILDING
EDINBURGH EH9-3JZ, SCOTLAND (M.D.)

DEPARTMENT OF GEOLOGICAL AND
GEOPHYSICAL SCIENCES
PRINCETON UNIVERSITY
PRINCETON, NEW JERSEY 08544 (J.P.D.)

Manuscript received July 16, 1980

An experiment to investigate polarization anomalies in North Anatolia

by Russ Evans[*], Mark Doyle[*+], S.Balamir Üçer[@], Alistair Miller[*@£] & Stuart Crampin[*]

[*]Institute of Geological Sciences, Murchison House, West Mains Road, Edinburgh EH9-3LA, UK

[+]Department of Geophysics, University of Edinburgh, James Clerk Maxwell Building, Edinburgh EH9-3JZ, UK

[@]Kandilli Observatory, Çengelköy, Istanbul,

[£]Overseas Development Ministry, London, UK

A three-component seismometer network, TDPNET, was set up during the summer of 1979 a few kilometres South of Izmit, near the Northern Anatolian Fault at the Eastern margin of the Marmara Sea. The network was designed to monitor the polarization anomalies suggested by theoretical and numerical investigations (Crampin 1978). A site was chosen on the basis of swarm activity recognised during routine epicentral locations at Kandilli Observatory (see Fig. 1 of Üçer, Crampin & Miller 1980, this volume). One of the MARNET stations, KLT, recorded a high level of local activity throughout the winter of 1978/79. This activity, centred a few kilometres to the South of the Northern branch of the Northern Anatolian Fault, was monitored for eight weeks by a closely-spaced radio-linked network of six three-component stations recording on analogue magnetic-tape.

Several hundred earthquakes were recorded within and near TDPNET during this period (Fig. 1). They were located with HYPO71 (Lee & Lahr 1973) at depths between 8 and 15 km, by assuming an isotropic crustal-structure determined by using local quarry blasts. The magnitudes (M_L) range from 0.8 to 2.5, and an event of 3.5 M_L occurred at the start of the recording interval. The majority of the events had impulsive P and S arrivals, and the records are very suitable for investigating polarization anomalies (Crampin, Evans, Üçer, Doyle, Davis, Yegorkina & Miller 1980).

The hypothesis of shear-wave splitting in seismic regions has been outlined by Crampin (1980, this volume): the crust of the Earth is permeated by a large variety of cracks, which will be opened and closed differentially by non-hydrostatic stresses, such as occur before earthquakes. On entry into such effectively anisotropic structures of aligned cracks, shear waves split into components with different velocities and nearly orthogonal polarizations (Crampin 1978). The delay between these arrivals is proportional to the differential shear-wave velocity-anisotropy and to the path length through the anisotropy. Such split arrivals can be recognised by abrupt changes in direction of the shear-wave particle-motion, when the wave forms are drawn in polarization-diagrams. These diagrams are projections of the particle motion on to the three orthogonal-planes defined by the rotated seismograms. On the evidence of the high level of seismic activity in this swarm, the whole region around TDPNET seems to be stressed and crack dilatancy is expected along all paths near the swarm activity.

The majority of shear wavetrains recorded by TDPNET display the abrupt changes in direction of particle motion indicative of dilatancy (see Crampin et al. 1980). In a small proportion of shear arrivals, not necessarily from Cardinal directions, the shear-wave splitting is clearly visible as separate arrivals on the unrotated horizontal seismograms. This phenomenon is similar to that observed by Yegorkina, Rakitov, Garetovskaya & Yegorova (1977) in seismic regions in Armenia, USSR. Thus it seems that dilatancy may be a comparatively widespread phenomenon in seismic regions.

Although the data processing is still at a preliminary stage, we suggest that the observed shear-wave splitting is due to propagation through dilatancy anisotropy. A demonstration that the splitting has appropriate three-dimensional variations, and that the delays between the two shear arrivals vary with time (that is with stress accumulation and release) would confirm our interpretation.

This work has been supported by a variety of organization, but the major support has come from the Natural Environment Research Council, U.K., and Kandilli Observatory, Turkey, and is published with the approval of the Director of Kandilli Observatory and the Director of the Institute of Geological Sciences.

References

Crampin,S., 1978. Seismic-wave propagation through a cracked solid: polarization as a possible dilatancy diagnostic, Geophys. J.R.astr.Soc., 53, 467-496

Crampin,S., 1980. Polarization anomalies as diagnostics of dilatancy, Proc.Interdis.Conf.Earthq.Pred.Res.in N.Anatolian Fault Zone, Friedr.Vieweg & Sohn, Wiesbaden.

Crampin,S., Evans,R., Üçer,S.B., Doyle,M., Davis,J.P., Yegorkina,G.V. & Miller,A., 1980. A preliminary report on observations of dilatancy-induced polarization-anomalies: the potential for earthquake prediction, Nature, submitted.

Lee,W.H.K. & Lahr,J.C., 1975. 'HYP071 (revised): A computer program for determining hypocenter, magnitude and first motion pattern of local earthquakes, US Geol.Survey, Open File Report 75-311.

Üçer,S.B., Crampin,S. & Miller,A., 1980. Identification of swarm activity using the MARNET telemetered seismometer-network, Proc.Interdis,Conf.Earthq,Pred.Res.in N.Anatolian Fault Zone, Friedr. Vieweg & Sohn, Wiesbaden.

Yegorkina,G.V., Rakitov,V.A., Garetovskaya,I.V. & Yegorova,L.M., 1977. Anisotropy of velocities of seismic waves and the stress state of the Earth's crust in the territory of Armenia, Izv.Acad.Sci.USSR.Earth Phys.(English tranl.), 13, 554-562.

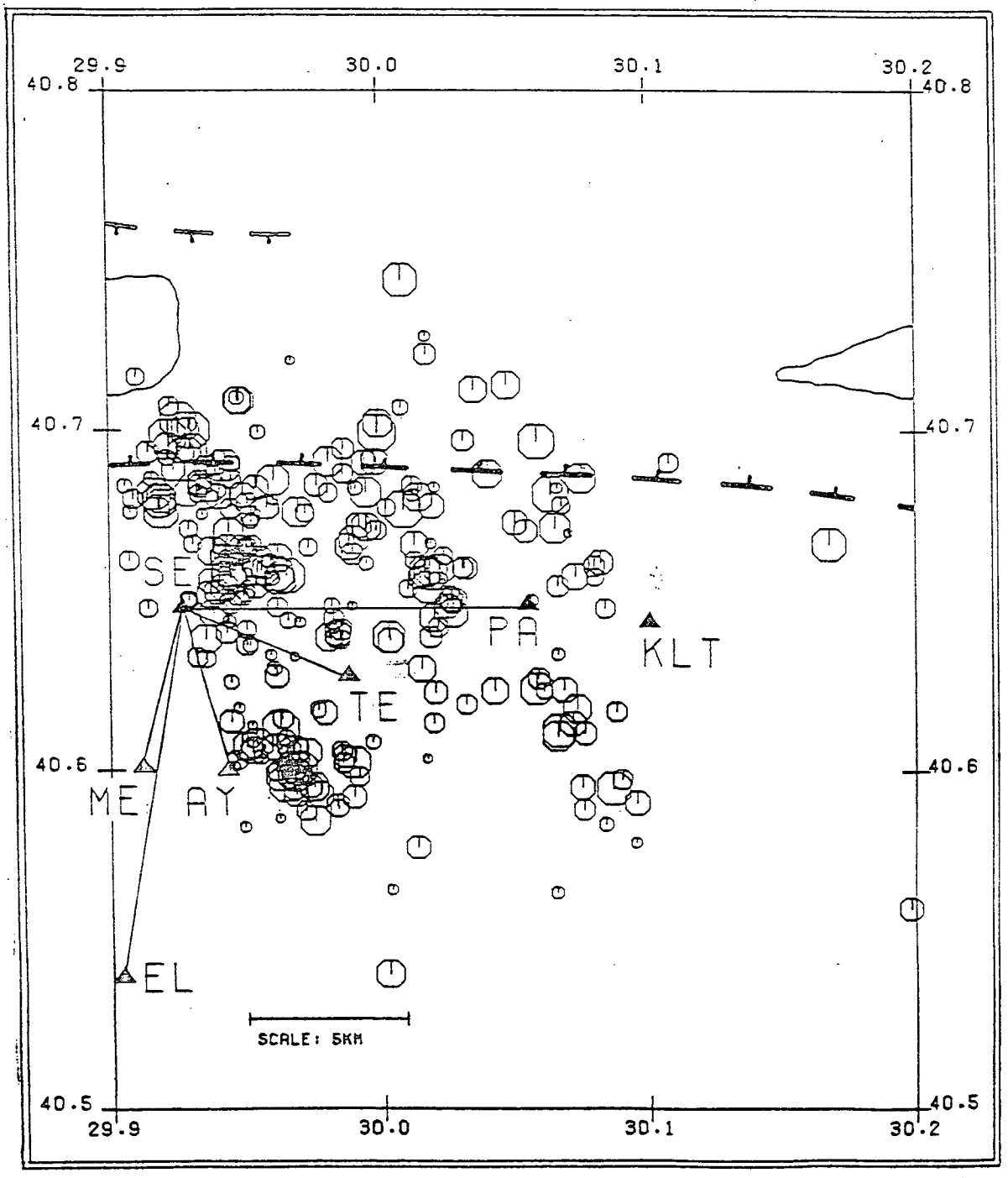

Fig. 1: Earthquakes located during the Turkish Dilatancy Project, with magnitudes ranging from 0.8 M_L to 2.0 M_L. AY, EL, ME, PA, SE, and TE are three-component TDPNET stations, and KLT is a vertical MARNET station. The dashed lines mark geological faults associated with the Northern Anatolian Fault.